



UNIVERSITAT DE
BARCELONA

Paleoseismic transect across the Alhama de Murcia Fault and implications of a fault-based seismic hazard assessment for the Eastern Betics

Octavi Gómez Novell

ADVERTIMENT. La consulta d'aquesta tesi queda condicionada a l'acceptació de les següents condicions d'ús: La difusió d'aquesta tesi per mitjà del servei TDX (www.tdx.cat) i a través del Dipòsit Digital de la UB (diposit.ub.edu) ha estat autoritzada pels titulars dels drets de propietat intel·lectual únicament per a usos privats emmarcats en activitats d'investigació i docència. No s'autoritza la seva reproducció amb finalitats de lucre ni la seva difusió i posada a disposició des d'un lloc aliè al servei TDX ni al Dipòsit Digital de la UB. No s'autoritza la presentació del seu contingut en una finestra o marc aliè a TDX o al Dipòsit Digital de la UB (framing). Aquesta reserva de drets afecta tant al resum de presentació de la tesi com als seus continguts. En la utilització o cita de parts de la tesi és obligat indicar el nom de la persona autora.

ADVERTENCIA. La consulta de esta tesis queda condicionada a la aceptación de las siguientes condiciones de uso: La difusión de esta tesis por medio del servicio TDR (www.tdx.cat) y a través del Repositorio Digital de la UB (diposit.ub.edu) ha sido autorizada por los titulares de los derechos de propiedad intelectual únicamente para usos privados enmarcados en actividades de investigación y docencia. No se autoriza su reproducción con finalidades de lucro ni su difusión y puesta a disposición desde un sitio ajeno al servicio TDR o al Repositorio Digital de la UB. No se autoriza la presentación de su contenido en una ventana o marco ajeno a TDR o al Repositorio Digital de la UB (framing). Esta reserva de derechos afecta tanto al resumen de presentación de la tesis como a sus contenidos. En la utilización o cita de partes de la tesis es obligado indicar el nombre de la persona autora.

WARNING. On having consulted this thesis you're accepting the following use conditions: Spreading this thesis by the TDX (www.tdx.cat) service and by the UB Digital Repository (diposit.ub.edu) has been authorized by the titular of the intellectual property rights only for private uses placed in investigation and teaching activities. Reproduction with lucrative aims is not authorized nor its spreading and availability from a site foreign to the TDX service or to the UB Digital Repository. Introducing its content in a window or frame foreign to the TDX service or to the UB Digital Repository is not authorized (framing). Those rights affect to the presentation summary of the thesis as well as to its contents. In the using or citation of parts of the thesis it's obliged to indicate the name of the author.



UNIVERSITAT DE
BARCELONA

Paleoseismic transect across the Alhama de Murcia Fault and implications of a fault-based seismic hazard assessment for the Eastern Betics

OCTAVI GÓMEZ NOVELL

Ph.D. Thesis

2021



Institut de Recerca Geomodels
Grup de Recerca RISKNAT
Departament de Dinàmica de la Terra i l'Oceà
Facultat de Ciències de la Terra
Universitat de Barcelona

Paleoseismic transect across the Alhama de Murcia Fault and implications of a fault-based seismic hazard assessment for the Eastern Betics

Memòria de Tesi Doctoral com a compendi d'articles presentada per:

Octavi Gómez Novell

per a optar al títol de Doctor per la Universitat de Barcelona.

Aquesta tesi s'ha realitzat dins del Programa de Doctorat de Ciències de la Terra
(HDK09) de la Universitat de Barcelona sota la direcció de:

Dra. María Ortuño Candela i Dr. Julián García Mayordomo

i tutoria de:

Dra. Eulàlia Masana Closa

Barcelona, juliol de 2021

The Ph.D. candidate has benefited from a predoctoral FPI grant (“Formación de Personal Investigador”) (BES-2016-077048) in the period between 2017 and 2021, funded by the Spanish Ministry of Science and Innovation and within the framework of the PREVENT project “Prevención de desastres sísmicos en las Béticas Orientales mediante la integración de paleosismología, geodesia GPS, reevaluación del peligro sísmico y concienciación social” (CGL2015-66263-R).

The research of this thesis has also received funds from the Department of Earth and Ocean Dynamics (Faculty of Earth Sciences, University of Barcelona), the Geomodels Research Institute and the Bosch i Gimpera Foundation (project: FBG 309386).

© Octavi Gómez Novell · 2021

Contact: ogomezno@gmail.com

*Al la meva família, amigues, amics,
i a tots els investigadors que lluiten per seguir
fent recerca malgrat tota la precarietat.*

AGRAÏMENTS

He donat moltes voltes pensant com escriure aquests agraïments i la veritat és que estic una mica nerviós perquè no m'agradaria deixar-me a ningú. Quan miro enrere, m'adono que aquests quatre anys han estat dels millors que he viscut i, malgrat l'experiència científica ha estat immillorable, això es deu a totes les persones que m'heu acompanyat al llarg del camí. D'una manera o altra, heu fet que aquesta tesi sigui una realitat.

Vull començar donant les gràcies als meus directors, la Maria i en Julián. No només heu confiat plenament en mi des del principi, sinó que m'heu donat suport en totes les decisions, us heu entregat, i m'heu fet sentir com un més de la família en tots els aspectes. Gràcies Maria per saber-me escoltar com ningú, per pensar sempre més enllà i per contagiar-me la teva passió i afecte cap a la ciència. Gracias Julián por tu serenidad, por tus consejos y por saber acortar siempre la distancia entre Barcelona y Madrid. Aquí també vull sumar-hi la meua tutora, l'Eulàlia, per implicar-se tant en la tesi, i per l'entusiasme i energia constants. Soc conscient que he estat molt afortunat tenint-vos com a guies d'aquesta aventura i espero que allà on vagi a partir d'ara, sàpiga exportar ni que sigui una mica de la vostra manera de fer ciència. Gràcies de tot cor!

Als meus companys i companyes de lluita, alegries i penúries: els del despatx 329b. Xabier, Pere, Rober, Albert, Llani, Mar i Ane, gràcies per crear el millor ambient que es pot demanar, pel bon rollo i per l'amistat de tots aquests quatre anys. M'heu fet molt feliç! Vull agrair-vos, en especial, totes les vegades que heu dedicat el vostre temps a escoltar-me, animar-me i, fins i tot, a posar el vostre granet de sorra en aquesta tesi. A en Xabier i en Pere per les xerrades arreglant el sistema universitari i pels tants dubtes informàtics que m'han resolt. A en Rober per les bromes enginyoses i per ser una mà salvadora, sobretot quan no sabia res de com organitzar una campanya de camp. A l'Albert per portar la seva vitalitat arreu i per no dubtar a acompanyar-me (i donar-ho tot) a les trinxeres. A la Llani per reestablir el positivisme i la juerga quan ha calgut. A la Mar per l'alegria i per il·luminar-me les matemàtiques dels errors. I a l'Ane per la serenitat, tant necessària a l'inici de tesi. Gràcies a tots, sense vosaltres aquesta experiència no hagués estat el mateix; espero que en puguem viure moltes més!

A los equipazos de tectónica activa en Madrid (Complutense, IGME...) que tan bien me acogieron en mi primera campaña de trincheras (cuando aún era un pipiolo) y que han contado conmigo a lo largo de estos años. En especial a Josechu y a Juanmi por todo el conocimiento que habéis aportado a esta tesis, tanto en el campo, como en las muchas charlas y discusiones que hemos tenido. He aprendido un montón con vosotros y, sobretodo, me lo he pasado genial. ¡Gracias!

A la resta de membres del projecte PREVENT que m'heu acollit, m'heu fet créixer com a investigador i que heu posat el vostre granet de sorra en aquesta tesi: Raimon, Gia, Tom, Stéphane, Raquel... Gràcies/thank you for bringing your experience to the field and meetings, and for always being available to teach me with any question I had. I have learned a lot from you and hope we can work together in the years to come. You make the best environment during the field campaigns (especially after long days of removing dust from 7m deep trenches!). They certainly would not be the same without you, glass(es) of wine for dinner and pancakes for breakfast included.

To the amazing team of the Fault2SHA working group: Oona, Thomas, Bruno, Francesco, Lucilla, Laura... Thanks for creating this great initiative and for letting me be a small part of it, I have learned a lot from the meetings, workshops, and courses, especially in Paris; one of my first experiences as a Ph.D. student, and kind of a kick-off for this thesis. Special thanks to Thomas Chartier for the outstanding help and knowledge provided all along with SHERIFS and the hazard modelling, and for always being reachable and ready to discuss (even when I sent too many emails). I enjoyed a lot working with you!

A todos los que trabajáis en tectónica activa en las Béticas, el Fault2SHA Betics team, por facilitar siempre vuestros datos, tan vitales para esta tesis. En especial a Paula Herrero por su interés y por las discusiones de estos últimos meses.

A Ana Luisa Rodrigues y a Miren del Val por venir al campo a medir dosimetría y, junto con Alicia Medialdea, por estar dispuestas siempre a resolver cualquier duda y discutir los resultados. ¡Gracias, obrigado!

A tots els companys i amics del “mundillo” que m’he anat trobant en congressos, campanyes de camp, etc. i amb qui m’ho he passat tan bé. En especial a la Sara Pena pels molts riures (sobretot a la campanya de Carboneras), al Marc Viaplana pel bon rotllo sempre i per donar-me un cop de mà en aquesta tesi, a Alba Peiro por apuntarse a un

bombardeo y venirse a Murcia a excavar, y a Andrés Núñez por hacer del despacho un sitio mucho menos solitario durante unos meses.

Als membres del RISKNAT i del Departament de Dinàmica de la Terra i l'Oceà, pel bon ambient de treball, per l'escalf i per la proximitat que s'hi respira. En especial a tots els que m'heu donat un cop de mà alguna vegada durant aquests anys: Anna Martí, Núria Carrera, Marta Guinau... També a tots els membres del PAS del departament i de la facultat (Maria José, Ana, Mònica) i, com no, a les magnífiques dones del servei de neteja (Silvia, Luisa...) que dia a dia fan possible que tots tinguem un bon entorn de treball.

A nivell més personal vull començar agraïnt a la meva “germana” en aquesta experiència, la quasi Dra. Cristina. Sense tu aquest camí hagués sigut molt més difícil. Gràcies per saber escoltar, per les xerrades, pels consells, per compartir la histèria en alguns moments i, en definitiva, per ser una de les millors amigues que hom pot demanar, i més en una etapa així. Gràcies també per llegir-te i millorar tants fragments d'aquesta tesi.

A la Nia i a la Marta per tots els dinars i desenes de cafès de màquina als quals ja som addictes, i que tant m'han fet desconnectar quan ho necessitava aquest darrer any. Gràcies també a l'Amanda i en Kevin per ser-hi sempre presents, per creure en mi, escoltar-me i per ser dels pocs que em riuen les bromes absurdes de geòleg.

A totes les meves amigues i amics de Sant Celoni i rodalies pels infinits riures, per tot el suport que m'heu donat, pels ànims, i per la comprensió quan he hagut de dedicar un pèl massa de temps a la tesi. Martí, Nuries, Laura, Marta, Yurena, Marina, Martina, Annes, Laia, Alba, Agnès, Keila... Gràcies de tot cor!

A la Mariajo, perquè gràcies a tu vaig decidir-me a fer geologia i, per tant, ets coresponsable de que estigui escrivint aquestes línies avui.

A la meva família, pares, Eloi i a en Pasqual; no crec que pugui plasmar en quatre línies tot el que signifiquen per mi ni tot el que m'heu donat perquè avui sigui on soc. Aquesta tesi és també vostra, encara que potser hi hagi escrites coses que us semblaran molt rares... Gràcies per confiar en mi de forma incondicional (a vegades més del que jo mateix ho faig), per estar sempre al meu costat i per aguantar-me fins i tot en els dies en que ho veig tot gris i només tinc ganes de discutir. Sou els millors!!

I finalment a tu, estimat lector/a. Gràcies per decidir-te a obrir aquesta tesi i a llegir-ne les seves pàgines. Espero que gaudeixis tant com jo he gaudit fent-la!

TABLE OF CONTENTS

SUMMARY	1
RESUM	5
RESUMEN	9
PREFACE AND THESIS STRUCTURE	13
I. INTRODUCTION	15
1 GENERAL INTRODUCTION	17
1.1 Interest and motivation.....	17
1.2 Hypotheses	21
1.3 Objectives.....	22
1.4 Published articles and coherency within the thesis.....	23
2 BASIC CONCEPTS AND BACKGROUND.....	25
2.1 Methodological overview and state of the art.....	25
2.1.1 Paleoseismology.....	25
2.1.2 Probabilistic seismic hazard assessment	32
2.2 Geological and tectonic setting.....	38
2.2.1 The Eastern Betics Shear Zone	42
2.2.2 The Alhama de Murcia Fault	43
2.2.2.1 Geomorphic expression and seismogenic nature.....	46
2.3 Background.....	48
2.3.1 Paleoseismic studies of the Eastern Betics Shear Zone	48
2.3.2 Seismic hazard studies of southeastern Spain.....	51
II. METHODS	55
3 METHODS FOR PALEOSEISMIC CHARACTERIZATION OF THE ALHAMA DE MURCIA FAULT.....	57
3.1 Geomorphological mapping	57
3.2 Trenching survey	59
3.3 Dating of stratigraphic units	64
3.3.1 Optical Stimulated Luminescence (OSL)	64
3.3.1.1 Dated samples and dating procedure.....	65
3.3.2 Radiocarbon	67
3.3.2.1 Dated samples and dating procedure.....	67
3.4 Deformation quantification.....	68
3.4.1 Vertical slip estimation	69
3.4.1.1 Limits of the deformation.....	69
3.4.1.2 Structure simplification	70
3.4.1.3 Measurements.....	72
3.4.2 Lateral slip estimation.....	72
3.4.3 Net slip estimation.....	74
3.4.4 Shortening estimation.....	74
3.5 Seismic and paleoseismic parameters.....	74
3.5.1 Earthquake chronosequences and recurrence.....	75
3.5.2 Slip rates and shortening rates.....	76

3.5.3	Slip per event and single event displacement.....	77
4	METHODS FOR FAULT-BASED PROBABILISTIC SEISMIC HAZARD ASSESSMENT.....	79
4.1	Data and methods to compute fault rupture hypotheses in the Eastern Betics Shear Zone	79
4.1.1	Definition of fault rupture hypotheses	79
4.1.1.1	Fault rupture hypotheses.....	81
4.1.2	Geological fault parameters as inputs for the calculations.....	85
4.1.2.1	Slip rates.....	86
4.1.2.2	Other parameters	89
4.1.3	SHERIFS method.....	89
4.1.4	Seismic and paleoseismic data to check the results	91
4.1.4.1	Seismicity rates from the regional catalogue.....	91
4.1.4.2	Paleoearthquake rates	92
4.2	Source models for the seismic hazard calculations	94
4.2.1	Fault sources.....	94
4.2.1.1	FM model	95
4.2.1.2	Fault sources with background: FM_bg model	95
4.2.2	Area sources.....	97
4.2.3	Final composite seismogenic source models for the hazard calculations	101
4.2.4	Ground motion prediction equation	101
4.2.5	Rupture model weighting and logic trees explored.....	102
4.2.6	Hazard calculations	103
III.	RESULTS AND PARTIAL DISCUSSIONS.....	105
5	STRUCTURAL AND PALEOSEISMIC CHARACTERIZATION OF A MULTI-BRANCH TRANSECT OF THE LORCA-TOTANA SEGMENT OF THE ALHAMA DE MURCIA FAULT..	107
5.1	Introduction	107
5.2	Geological setting of the Lorca-Totana segment.....	109
5.3	Mapping of the Lorca-Totana segment	112
5.4	Structure of the Lorca-Totana segment	117
5.4.1	Fault branches	117
5.4.1.1	N-AMF	117
5.4.1.2	S-AMF.....	122
5.4.1.3	F-AMF.....	123
5.4.2	Kinematic distribution.....	125
5.4.2.1	N-AMF	125
5.4.2.2	S-AMF.....	127
5.4.2.3	F-AMF.....	128
5.5	Paleoseismic study.....	129
5.5.1	Site selection	129
5.5.2	Sedimentary units of the trenches	130
5.5.3	Geochronology of the stratigraphic units: sedimentary interpretation.....	147
5.5.3.1	T-2 (La Tercia site).....	148
5.5.3.2	T-1 (El Roser site)	149
5.5.3.3	T-16 (El Saltador site)	150
5.5.3.4	T-3 (La Hoya site)	155
5.5.3.5	Sedimentary evolution.....	156
5.5.4	Paleoearthquake evidence	157
5.5.4.1	N ₁ -AMF.....	157
5.5.4.2	N _{2b} -AMF.....	161
5.5.4.3	S-AMF.....	162

5.5.4.4	F-AMF.....	167
5.5.5	Fault slips.....	168
5.5.5.1	Vertical slips.....	168
5.5.5.2	Lateral slips.....	172
5.5.5.3	Net slips.....	175
5.5.5.4	Shortenings.....	177
5.6	Seismic and paleoseismic parameters of the Lorca-Totana segment.....	180
5.6.1	Event chronosequence and recurrence intervals.....	180
5.6.1.1	N ₁ -AMF.....	181
5.6.1.2	N _{2b} -AMF.....	183
5.6.1.3	S-AMF.....	185
5.6.1.4	F-AMF.....	187
5.6.2	Slip rates.....	190
5.6.2.1	Vertical slip rates.....	192
5.6.2.2	Lateral slip rates.....	194
5.6.2.3	Net slip rates.....	195
5.6.3	Shortening rates.....	198
5.6.4	Mean slips per event and event displacements.....	200
5.6.4.1	Slip per event (SPE).....	200
5.6.4.2	Event displacement (ED).....	202
5.7	Discussion on the paleoseismic parameters of the Lorca-Totana segment.....	204
5.7.1	Slip rates.....	204
5.7.1.1	Slip rate variability over time.....	206
5.7.1.2	Shortening rate evaluation and variability over time.....	209
5.7.1.3	Implications of the slip rates within the Eastern Betics Shear Zone.....	210
5.7.2	Paleoearthquakes in the Lorca-Totana segment.....	214
5.7.2.1	Event chronosequence and correlation.....	214
5.7.2.2	Recurrence intervals and seismic behavior.....	219
5.7.2.3	Implications of the constrained recurrences within the Eastern Betics Shear Zone setting.....	222
5.8	Discussion on the seismic potential of the AMF.....	225
5.9	Overview: structure and tectonic evolution of the Lorca-Totana segment.....	228
6	STRUCTURAL DATA FOR POTENTIAL FUTURE PALEOSEISMIC SITES IN THE TOTANA-ALHAMA SEGMENT OF THE ALHAMA DE MURCIA FAULT.....	233
6.1	Introduction.....	233
6.2	Cartography and structure of the Totana-Alhama segment.....	235
6.3	Deformation related to the Amarguillo Fault.....	239
6.4	Potential site for paleoseismic survey.....	243
6.5	Overview.....	244
7	FAULT-BASED PROBABILISTIC SEISMIC HAZARD ASSESSMENT OF THE EASTERN BETICS SHEAR ZONE.....	247
7.1	Introduction.....	247
7.2	Evaluation of earthquake rupture models for the Eastern Betics Shear Zone.....	248
7.2.1	Modelled earthquake rates from SHERIFS.....	248
7.2.1.1	Performance of the models.....	249
7.2.2	Consistency check of the models.....	250
7.2.2.1	Seismicity rates from the regional earthquake catalogue.....	250
7.2.2.2	Paleoearthquake rates from paleoseismic research.....	252
7.3	Logic tree weighting.....	254
7.4	Probabilistic seismic hazard assessment results.....	256
7.4.1	Mean hazard maps and magnitude-distance disaggregation.....	256

7.4.1.1	Fault influence.....	256
7.4.1.2	Background influence.....	260
7.4.1.3	Area sources influence	261
7.4.2	Mean hazard curves.....	263
7.5	Discussion on earthquake rupture models in the Eastern Betics	264
7.5.1	Analysis of the modelling results with the datasets (consistency check).....	264
7.5.1.1	Earthquake catalogue.....	264
7.5.1.2	Paleoearthquake rates	265
7.5.2	Considerations of the fault sources modelling and perspectives.....	267
7.6	Discussion on the seismic hazard results.....	268
7.6.1	Comparison with previous probabilistic seismic hazard assessments in southeastern Spain: implications on the modelling.....	268
7.6.1.1	Comparison with a hazard assessment using the ZESIS areal model	268
7.6.1.2	Comparison with Rivas-Medina et al. (2018) fault-based approach	271
7.6.2	Implications for moderate magnitude earthquakes	274
7.6.3	Implications of the Ground Motion Prediction Equation selection (GMPE)..	275
7.6.4	Implications of the fault slip rates.....	277
7.6.5	Testing the impact of updated slip rate data into the seismic hazard.....	279
7.6.5.1	Model performance and consistency check.....	281
7.6.5.2	New hazard results and implications for the Eastern Betics Shear Zone	284
7.6.6	Overview: limitations and perspectives	287
IV.	GLOBAL DISCUSSIONS	289
8	CONNECTION BETWEEN PALEOSEISMIC DATA AND SEISMIC HAZARD ASSESSMENT AT THE EASTERN BETICS SHEAR ZONE; FORWARD LOOK.....	291
8.1	The impact of paleoseismic data in fault-based approaches in the EBSZ.....	291
8.1.1	Slip rates.....	292
8.1.2	Earthquake recurrences (Paleorates)	293
8.1.3	Fault rupture complexity and fault geometry	296
8.1.4	Time variability of slip rates and earthquake recurrence model	300
8.1.4.1	Slip rates.....	301
8.1.4.2	Earthquake recurrence model	302
9	STRENGTHENING THE BRIDGE BETWEEN DATA COLLECTORS AND HAZARD PRACTITIONERS.....	305
V.	CONCLUSIONS.....	309
CONCLUSIONS ON THE STRUCTURAL AND PALEOSEISMIC CHARACTERIZATION OF THE ALHAMA DE MURCIA FAULT		311
CONCLUSIONS ON THE PROBABILISTIC SEISMIC HAZARD ASSESSMENT IN THE EASTERN BETICS SHEAR ZONE		313
GLOBAL CONCLUSIONS.....		315
REFERENCES		317
ANNEXES		341
ANNEX I.....		343
ANNEX II.....		385

ACRONYMS

AD: *Anno Domini*; standing for Gregorian calendar years

AF: Amarguillo Fault

AMF: Alhama de Murcia Fault

BC: Before Christ

BP: Before Present

BSF: Bajo Segura Fault

CAF: Carrascoy Fault

CF: Carboneras Fault

CV: Coefficient of Variation

DEM: Digital Elevation Model

EBSZ: Eastern Betics Shear Zone

ED: Event displacement

EMS: European Macrosesimic Scale

F-AMF: Frontal Alhama de Murcia Fault

GMPE: Ground Motion Prediction Equation

GPS: Global Positioning System

GR: Gutenberg-Richter distribution

IRSL: Infrared Stimulated Luminiscence

ka: kilo years ago (thousands of years ago)

kyr: kilo years (thousands of years)

LTF: Los Tollos Fault

LiDAR: Light Detection and Ranging

m.a.s.l.: meters above sea level

MFD: Magnitude-Frequency Distribution

M_{max}: Maximum magnitude

M_{min}: Minimum magnitude

M_w: Moment magnitude

N-AMF: Northern Alhama de Murcia Fault

OSL: Optical Stimulated Luminiscence

PDF: Probability density function

PF: Palomares Fault

PGA: Peak ground acceleration

PSHA: Probabilistic Seismic Hazard Assessment

RI: Recurrence interval

RP: Return period

S-AMF: Southern Alhama de Murcia Fault

SHERIFS: Seismic Hazard Earthquake Rates In Fault Systems

SPE: Slip per event

TL: Thermoluminiscence

yr: years

SUMMARY

The SE of Spain is one of the most seismically active regions of the Iberian Peninsula. In this framework, the Eastern Betics Shear Zone (EBSZ) is one of the most prominent fault systems absorbing an important part of the Eurasia-Africa convergence. The EBSZ has caused damaging earthquakes in historical times, the most recent being the 2011 Lorca earthquake (Mw 5.2). The unexpected damage associated to this moderate event evidenced that the hazard estimations for the region needed to be reviewed. This context has motivated the development of several paleoseismic studies within the EBSZ for over two decades aiming to characterize its faults for the seismic hazard assessments. Despite this, the available data is usually too local and, for some faults, reliable and representative parameters are still lacking. Such heterogeneity in the fault parameters of the EBSZ has usually hampered the development of seismic hazard models based on geological data, yet they could provide more realistic hazard estimations as proven in regions such as California, New Zealand or Italy.

Based on the outlined issues, this thesis has been designed to be a comprehensive study that allows to: i) contribute to the completion of the paleoseismic record of one of the most active faults within the EBSZ, the Alhama de Murcia Fault (AMF), by obtaining more representative paleoseismic data in one of the fault transects, and ii) include faults and paleoseismic data as the primordial inputs to derive earthquake occurrence in a probabilistic seismic hazard assessment (PSHA) of the EBSZ. To achieve so, the study is divided in two main parts. The first part (**A**) is a local study and presents a structural characterization and integral paleoseismic study in four sites across a complete transect of the AMF, where previous studies focused only on a single fault site. The second part (**B**) is a regional study and presents a fault-based PSHA of the EBSZ where the main faults of the system and their available data are used to define scenarios of fault ruptures and to calculate their respective earthquake rates for the seismic source modelling.

A) The structural characterization has been carried out in the two central segments of the AMF, Lorca-Totana and Totana-Alhama, by means of geomorphological mapping and field analysis. In the former segment, five subparallel fault branches (N50-65°) have been identified in a ~2 km wide transect with partitioning of the overall sinistral-reverse deformation. From N to S: N₁-AMF (lateral), N_{2a} and b-AMF (dip slip), S-AMF (lateral)

and F-AMF (dip slip). Four of these structures bound two pressure ridges developed parallel to the main mountain front. The Totana-Alhama segment shows more diffuse deformation over a wider transect ($>2\text{km}$), where the most prominent structure is the Amarguillo Fault (AF), a $\sim\text{N}10^\circ$ ramification of the AMF. The AF is composed by at least five branches forming a transtensional bend with left-lateral component. Based on these results, a paleoseismic survey has been carried out in the Lorca-Totana segment, which implied the excavation of eight paleoseismic trenches across four fault branches in a NW-SE transect. In each trench, we have performed i) a paleoseismic analysis to identify the paleoearthquake record and to derive the recurrence intervals (RI) of major events for the four branches, and ii) a structural analysis of the vertical and lateral slips to estimate the slip rates in each branch and for the whole segment. To do so, we relied on new radiocarbon and OSL dates, along with previous ones.

The work allowed to obtain one of the completest paleoearthquake records in the Iberian Peninsula. This is especially relevant in the S-AMF, where seventeen events for the last $\sim 100\text{ ka}$ are identified. The RI varies from 5.7 ± 1.7 to $4.3\pm 0.4\text{ kyr}$ for the last 73-31 ka, which yields a Poissonian to weakly periodic recurrence behavior based on the coefficient of variation ($\text{CV}=0.8\text{-}1.0$). This RI is reduced to $3.1\pm 1.4\text{ kyr}$ if only the last five events for the last 18 ka in the F-AMF are accounted. Conversely, in the two N-AMF branches the paleoearthquake record is more unreliable due to the presence of large sedimentary gaps in the sequences at the apical areas of alluvial fans. The total net slip rate for the last 18 ka is $1.55^{+0.14}/_{-0.18}\text{ mm/yr}$ (four branches), considerably higher than the previous estimations ($0.9\pm 0.1\text{ mm/yr}$). In this segment, the S-AMF is the controlling fault, and its slip rate evolution since 73 ka shows fluctuations marked by two short accelerations and respective longer slower phases (super-cycles). The most marked acceleration is observed between 31 and 25 ka, coinciding in time and duration with an acceleration in the Carrascoy Fault (34-28 ka). This suggests a possible activity synchronicity between different faults for the first time in the EBSZ. The vertical slip rate evolution reveals that the S-AMF and F-AMF show increased activity with respect to northern parts of the fault system since $\sim 18\text{ ka}$. Furthermore, their nearly identical vertical slip rates in this period, along with the time compatibility of the last five events in both branches, suggests that they could rupture synchronously.

B) The fault-based PSHA of the EBSZ relied, for the first time in Spain, on a particular source modelling with relaxed segmentation, in which different hypotheses of multi-fault

ruptures have been envisaged in two models (FM and FM_bg). To do so, we used the SHERIFS code and geological fault data as inputs to compute earthquake probabilities. Each hypothesis has been weighted in a logic tree for PSHA based on their fit with the seismic catalogue and paleoearthquake rates. From this analysis, we suggest that multi-fault ruptures involving lengths up to single to several whole faults of the EBSZ are feasible, while the rupture of the whole system (~400 km) seems unfeasible based on the misfit with the available data. The hazard results of both models show a clear control of the EBSZ faults in the seismic hazard for all return periods, increasing drastically the hazard levels in the regions close to the fault traces and influencing up to 20 km farther with respect to an area source PSHA. The seismic hazard is dependent on the fault slip rates as peak ground accelerations and territorial extension of the fault influence appear higher around the AMF and Carboneras Fault, while lower slip rate faults (Palomares Fault; PF or the northeastern termination of the AMF) show much less contribution to the hazard. For the return period of 475 years and near-fault locations, our models are more consistent with the ground motion values reached in the 2011 Mw 5.2 Lorca event than the building code or national seismic hazard map. This suggests that our fault system-based model performs more accurate estimations for this return period. Paleoseismic parameters, mainly slip rates and its uncertainties, have a clear impact on the seismic hazard and, for some faults (PF), the lack of detailed paleoseismic studies can compromise the reliability of the hazard estimations. This is a key discussion point in the present study, marking the need for better constrained and reliable slip rates in the EBSZ.

The integral paleoseismic study of the AMF performed in this thesis has revealed to be a crucial step towards a more representative characterization of the paleoseismic parameters of this fault (slip rates, recurrences, rupture behavior), and thus, of the EBSZ. The acquisition of refined and reviewed paleoseismic parameters is one of the key practices to improve seismic hazard evaluations. In this respect, further paleoseismic studies should focus on poorly researched faults and on performing integrative studies in other faults of the EBSZ, as we do for the AMF. The comprehensive approach followed here, from paleoseismic data collection to PSHA, contributes to perform more critical interpretations of the seismic hazard, and aims to serve as a case example for other low-to-moderate seismicity regions worldwide.

RESUM

El SE d'Espanya és una de les regions sísmicament més actives de la Península Ibèrica. En aquest marc, la Zona de Cisalla de les Bètiques Orientals (ZCBO) és un dels sistemes de falles més rellevant que absorbeix una part important de la convergència Euràsia-Àfrica. La ZCBO ha causat grans terratrèmols des d'èpoques històriques, entre els quals hi ha el terratrèmol de Lorca del 2011 (Mw 5.2). L'elevat impacte i danys causats per aquest esdeveniment de moderada magnitud va evidenciar la necessitat de revisar les estimacions de perillositat sísmica a la regió. Aquest context ha motivat el desenvolupament de diversos estudis paleosísmics a la ZCBO durant més de dues dècades, amb l'objectiu de caracteritzar l'activitat de les falles per a les avaluacions de la perillositat sísmica. Malgrat això, les dades disponibles actualment acostumen a ser massa locals i, en alguns casos, encara manquen estimacions fiables i representatives dels paràmetres sísmics. Aquesta heterogeneïtat en els paràmetres de les falles a la ZCBO ha dificultat el desenvolupament de models de perillositat sísmica basats en dades geològiques, tot i que podrien implicar estimacions més realistes de la perillositat, tal i com s'ha demostrat en regions com Califòrnia, Nova Zelanda o Itàlia.

En base a les qüestions esmentades, aquesta tesi s'ha dissenyat amb l'objectiu de ser un estudi exhaustiu que permeti: i) contribuir a completar el registre paleosísmic d'una de les falles més actives de la ZCBO, la falla d'Alhama de Murcia (FAM), mitjançant l'obtenció de dades paleosísmiques representatives d'un dels transectes de falla, i ii) incloure falles i dades paleosísmiques com a base per calcular l'ocurrència de terratrèmols en una avaluació probabilista de la perillositat sísmica (PSHA) a la ZCBO. Per aconseguir-ho, l'estudi s'ha dividit en dues parts principals. La primera part (**A**) és un estudi local i presenta una caracterització estructural i un estudi paleosísmic integral en quatre localitats d'un transecte complet de la FAM, on estudis previs s'havien centrat en una sola localitat. La segona part (**B**) és un estudi regional i presenta un PSHA de la ZCBO on s'han utilitzat les falles principals del sistema i les seves dades disponibles per definir escenaris de ruptura de falla i calcular les seves respectives taxes de terratrèmols per a la modelització de la font sísmica.

A) La caracterització estructural s'ha dut a terme als dos segments centrals de la FAM, Lorca-Totana i Totana-Alhama, mitjançant cartografia geomorfològica i anàlisi de camp.

En el primer segment, s'han identificat cinc branques de falla subparal·leles (N50-65°) en un transecte d'uns 2 km d'amplada amb partició de la deformació sinistral-inversa. De N a S: N₁- FAM (lateral), N_{2a i b}- FAM (salt en cabussament), S- FAM (lateral) i F-FAM (salt en cabussament). Quatre d'aquestes estructures delimiten dues crestes de pressió desenvolupades paral·leles al front muntanyós. El segment Totana-Alhama presenta una deformació més difusa en un transecte més ample (> 2 km), on l'estructura més destacada és la falla de l'Amarguillo (FA), una ramificació ~ N10° de la FAM. La FA està formada per almenys cinc branques que formen un sector transtensional amb component lateral esquerra. En base a aquests resultats, s'ha realitzat un estudi paleosísmic al segment Lorca-Totana, que ha implicat l'excavació de vuit trinxeres paleosísmiques en quatre branques de falla d'un transecte NW-SE. A cada trinxera, s'ha realitzat i) una anàlisi paleosísmica per identificar el registre de paleoterratrèmols i derivar els intervals de recurrència de grans esdeveniments (IR) a les quatre branques, i ii) una anàlisi estructural dels salts verticals i laterals per tal d'estimar les velocitats de desplaçament de cada branca i de tot el segment. Per fer-ho s'han realitzat noves datacions de radiocarboni i OSL, així com utilitzat algunes ja existents.

En aquesta tesi s'ha pogut obtenir un dels registres de paleoterratrèmols més complets de la Península Ibèrica. Això és especialment rellevant per la S-FAM, on s'han identificat disset esdeveniments pels darrers ~ 100 ka. L'IR varia de $5,7 \pm 1,7$ a $4,3 \pm 0,4$ ka pels darrers 73-31 ka, cosa que evidencia un comportament de poissonià a aperiòdic en base al coeficient de variació (CV = 0,8-1,0). Aquest IR s'escurça a 3.1 ± 1.4 ka si es tenen en compte els últims cinc esdeveniments pels darrers 18 ka a la F-FAM. A les dues branques N-FAM, en canvi, el registre de paleoterratrèmols no és fiable degut a la poca resolució de la seqüència sedimentària a les zones apicals dels ventalls al·luvials. La velocitat de desplaçament neta pels darrers 18 ka és de $1,55^{+0,14}_{-0,18}$ mm/any (quatre branques), considerablement superior a les estimacions anteriors ($0,9 \pm 0,1$ mm/any). En aquest segment, la S-FAM és la falla principal i l'evolució temporal de la seva velocitat de desplaçament pels darrers 73 ka presenta fluctuacions marcades per dues acceleracions curtes i fases lentes més llargues (supercicles). L'acceleració més marcada s'observa entre els 31 i 25 ka, coincidint en el temps i durada amb una acceleració a la falla de Carrascoy (34-28 ka). Per primera vegada a la ZCBO, això suggereix una possible sincronia en l'activitat de dues falles diferents. L'evolució de la velocitat de desplaçament vertical revela que la S-FAM i la F-FAM mostren una major activitat respecte a les parts

septentrionals del sistema pels darrers 18 ka. A més, les seves velocitats de desplaçament verticals gairebé idèntiques en aquest període, juntament amb la compatibilitat temporal dels darrers cinc esdeveniments en ambdues branques, suggereix que podrien trencar de forma sincrònica.

B) El PSHA de la ZCBO portat a terme s'ha basat, per primera vegada a Espanya, en una modelització de fonts sísmiques en la que s'han considerat diverses hipòtesis de ruptura multi-falla en dos models (FM i FM_bg). Per fer-ho, s'ha utilitzat el codi SHERIFS i dades geològiques de les falles per tal de calcular les taxes d'ocurrència de terratrèmols. Cada hipòtesi s'ha ponderat en un arbre lògic per al PSHA en funció del seu ajust amb el catàleg sísmic i les taxes de paleoterratrèmols. A partir d'aquesta anàlisi es suggereix que les ruptures multi-falla que involucren longituds de fins a una o varies falles de la ZCBO són factibles, mentre que la ruptura de tot el sistema (~400 km) sembla improbable en base al desajust amb les dades disponibles. Els resultats de perillositat d'ambdós models (FM i FM_bg) mostren un control clar de les falles en la perillositat sísmica per tots els períodes de retorn. Aquestes augmenten dràsticament els nivells de perillositat de les regions properes a les traces (fins a 20 km) respecte a d'altres PSHA que no consideren falles. La perillositat sísmica depèn de la velocitat de desplaçament de les falles, ja que les acceleracions màximes del terreny i l'extensió territorial d'aquestes són més altes al voltant de la FAM i la falla de Carboneras, mentre que les falles amb menor velocitat de desplaçament (falla de Palomares; FP o la terminació nord-est de la FAM) mostren una menor contribució a la perillositat. Pel període de retorn de 475 anys i ubicacions properes a les falles, els models presentats aquí són més coherents amb els valors d'acceleració del terreny assolits durant el terratrèmol de Lorca del 2011 (Mw 5.2) que la normativa sismoresistent o el mapa nacional de perillositat sísmica. Això suggereix que els models PSHA basats en falles realitzen estimacions més precises per a aquest període de retorn. Els paràmetres paleosísmics, principalment les velocitats de desplaçament i les seves incerteses, tenen un impacte clar sobre la perillositat sísmica i, per a algunes falles (FP), la manca d'estudis paleosísmics detallats pot comprometre la fiabilitat de les estimacions. Aquest és un punt de debat clau en el present estudi que posa de manifest la necessitat d'obtenir velocitats de desplaçament més ben acotades i fiables a la ZCBO.

L'estudi paleosísmic integral de la FAM realitzat en aquesta tesi ha revelat ser un pas clau per una caracterització més representativa dels paràmetres paleosísmics d'aquesta falla (velocitats de desplaçament, recurrències, comportament sísmic) i, en conseqüència, de

la ZCBO. L'adquisició de paràmetres paleosísmics refinats i revisats és una de les pràctiques clau per millorar les avaluacions de la perillositat sísmica. En aquest sentit, futurs estudis paleosísmics haurien de centrar-se en falles poc investigades i en realitzar estudis integrals en d'altres falles de la ZCBO, com s'ha fet per la FAM. L'enfocament integral que s'ha seguit aquí, des de la recopilació de dades paleosísmiques fins al PSHA, contribueix a realitzar interpretacions més crítiques de la perillositat sísmica i pretén servir d'exemple per d'altres regions de sismicitat baixa-moderada.

RESUMEN

El SE de España es una de las regiones sísmicamente más activas de la Península Ibérica. En este marco, la Zona de Cizalla de las Béticas Orientales (ZCBO) es uno de los sistemas de fallas más relevante que absorbe una parte importante de la convergencia Eurasia-África. La ZCBO ha causado grandes terremotos desde épocas históricas, entre los que está el terremoto de Lorca de 2011 (Mw 5.2). El elevado impacto y daños causados por este evento de moderada magnitud evidenció la necesidad de revisar las estimaciones de peligrosidad sísmica en la región. Este contexto ha motivado el desarrollo de distintos estudios paleosísmicos en la ZCBO durante más de dos décadas, con el objetivo de caracterizar la actividad de las fallas para las evaluaciones de la peligrosidad sísmica. A pesar de ello, los datos disponibles actualmente suelen ser demasiado locales y, en algunos casos, aún faltan estimaciones fiables y representativas de los parámetros sísmicos. Esta heterogeneidad en los parámetros de las fallas de la ZCBO ha dificultado el desarrollo de modelos de peligrosidad sísmica basados en datos geológicos, aunque podrían implicar estimaciones más realistas de la peligrosidad, tal y como se ha demostrado en regiones como California, Nueva Zelanda o Italia.

En base a las cuestiones mencionadas, esta tesis se ha diseñado con el objetivo de ser un estudio exhaustivo que permita: i) contribuir a completar el registro paleosísmico de una de las fallas más activas de la ZCBO, la falla de Alhama de Murcia (FAM), mediante la obtención de datos paleosísmicos representativos de uno de los transectos de falla, e ii) incluir fallas y datos paleosísmicos como base para calcular la ocurrencia de terremotos en una evaluación probabilista de la peligrosidad sísmica (PSHA) en la ZCBO. Para ello, el estudio se ha dividido en dos partes principales. La primera parte (**A**) es un estudio local y presenta una caracterización estructural y un estudio paleosísmico integral en cuatro localidades de un transecto completo de la FAM, donde estudios previos se habían centrado en una sola localidad. La segunda parte (**B**) es un estudio regional y presenta un PSHA de la ZCBO donde se han utilizado las fallas principales del sistema y sus datos disponibles para definir escenarios de ruptura de falla y calcular sus respectivas tasas de terremotos para la modelización de la fuente sísmica.

A) La caracterización estructural se ha llevado a cabo en los dos segmentos centrales de la FAM, Lorca-Totana y Totana-Alhama, mediante cartografía geomorfológica y análisis

de campo. En el primer segmento, se han identificado cinco ramas de falla subparalelas (N50-65°) en un transecto de unos 2 km de ancho con partición de la deformación siniestral-inversa. De N a S: N₁- FAM (lateral), N_{2a y b}- FAM (salto en buzamiento), S-FAM (lateral) y F-FAM (salto en buzamiento). Cuatro de estas estructuras delimitan dos crestas de presión desarrolladas paralelas al frente montañoso. El segmento Totana-Alhama presenta una deformación más difusa en un transecto más ancho (> 2 km), donde la estructura más destacada es la falla del Amarguillo (FA), una ramificación ~ N10° de la FAM. La FA está formada por al menos cinco ramas que forman un sector transtensivo con componente lateral izquierda. En base a estos resultados, se ha realizado un estudio paleosísmico en el segmento Lorca-Totana, que ha implicado la excavación de ocho trincheras paleosísmicas en cuatro ramas de falla de un transecto NW-SE. En cada trinchera, se ha realizado i) un análisis paleosísmico para identificar el registro de paleoterremotos y derivar los intervalos de recurrencia de grandes eventos (IR) en las cuatro ramas, y ii) un análisis estructural de los saltos verticales y laterales con el fin de estimar las velocidades de desplazamiento de cada rama y de todo el segmento. Para ello se han realizado dataciones de radiocarbono y OSL, así como utilizado algunas ya existentes.

En esta tesis se ha podido obtener uno de los registros de paleoterremotos más completos de la Península Ibérica. Esto es especialmente relevante para la S-FAM, donde se han identificado diecisiete eventos para los últimos ~ 100 ka. El IR varía de $5,7 \pm 1,7$ a $4,3 \pm 0,4$ ka para los últimos 73-31 ka, lo que evidencia un comportamiento de poissoniano a aperiódico en base al coeficiente de variación ($CV = 0,8- 1,0$). Este IR se acorta a $3,1 \pm 1,4$ ka si se tienen en cuenta los últimos cinco eventos para los últimos 18 ka en la F-FAM. En las dos ramas N-FAM, en cambio, el registro de paleoterremotos no es fiable debido a la poca resolución de la secuencia sedimentaria en las zonas apicales de los abanicos aluviales. La velocidad de desplazamiento neta para los últimos 18 ka es de $1,55^{+0,14}_{-0,18}$ mm / año (cuatro ramas), considerablemente superior a las estimaciones anteriores ($0,9 \pm 0,1$ mm/año). En este segmento, la S-FAM es la falla principal y la evolución temporal de su velocidad de desplazamiento para los últimos 73 ka presenta fluctuaciones marcadas por dos aceleraciones cortas y fases lentas más largas (superciclos). La aceleración más marcada se observa entre los 31 y 25 ka, coincidiendo en el tiempo y duración con una aceleración en la falla de Carrascoy (34-28 ka). Por primera vez en la ZCBO, esto sugiere una posible sincronía en la actividad de dos fallas

diferentes. La evolución de la velocidad de desplazamiento vertical revela que la S-FAM y la F-FAM muestran una mayor actividad respecto a las partes septentrionales del sistema en los últimos 18 ka. Además, sus velocidades de desplazamiento verticales casi idénticas en este periodo, junto con la compatibilidad temporal de los últimos cinco eventos en ambas ramas, sugiere que podrían romper de forma sincrónica.

B) El PSHA de la ZCBO llevado a cabo se ha basado, por primera vez en España, en una modelización de fuentes sísmicas en la que se han considerado varias hipótesis de ruptura multi-falla en dos modelos (FM y FM_bg). Para ello, se ha utilizado el código SHERIFS y datos geológicos de las fallas para calcular las tasas de ocurrencia de terremotos. Cada hipótesis se ha ponderado en un árbol lógico para el PSHA en función de su ajuste con el catálogo sísmico y las tasas de paleoterremotos. A partir de este análisis se sugiere que las rupturas multi-falla que involucran longitudes de hasta una o varias fallas de la ZCBO son factibles, mientras que la ruptura de todo el sistema (~ 400 km) parece improbable en base al desajuste con los datos disponibles. Los resultados de peligrosidad de ambos modelos (FM y FM_bg) muestran un control claro de las fallas en la peligrosidad sísmica para todos los periodos de retorno. Estas aumentan drásticamente los niveles de peligrosidad de las regiones cercanas a las trazas (hasta 20 km) respecto a otros PSHA que no consideran fallas. La peligrosidad sísmica depende de la velocidad de desplazamiento de las fallas, ya que las aceleraciones máximas del terreno y la extensión territorial de éstas son más altas alrededor de la FAM y la falla de Carboneras, mientras que las fallas con menor velocidad de desplazamiento (falla de Palomares; FP o la terminación noreste de la FAM) muestran mucho menos contribución a la peligrosidad. Para el periodo de retorno de 475 años y ubicaciones cercanas a las fallas, los modelos presentados aquí son más coherentes con los valores de aceleración del terreno alcanzados durante el terremoto de Lorca de 2011 (Mw 5.2) que la normativa sismorresistente o el mapa nacional de peligrosidad sísmica. Esto sugiere que los modelos PSHA basados en fallas realizan estimaciones más precisas para este periodo de retorno. Los parámetros paleosísmicos, principalmente las velocidades de desplazamiento y sus incertidumbres, tienen un impacto claro sobre la peligrosidad sísmica y, para algunas fallas (FP), la falta de estudios paleosísmicos detallados puede comprometer la fiabilidad de las estimaciones. Este es un punto de debate clave en el presente estudio que pone de manifiesto la necesidad de obtener velocidades de desplazamiento más bien acotadas y fiables en la ZCBO.

El estudio paleosísmico integral de la FAM realizado en esta tesis ha revelado ser un paso clave para una caracterización más representativa de los parámetros paleosísmicos de esta falla (velocidades de desplazamiento, recurrencias, comportamiento sísmico) y, en consecuencia, de la ZCBO. La adquisición de parámetros paleosísmicos refinados y revisados es una de las prácticas clave para mejorar las evaluaciones de la peligrosidad sísmica. En este sentido, futuros estudios paleosísmicos deberían centrarse en fallas poco investigadas y en realizar estudios integrales en otras fallas de la ZCBO, como se ha hecho para la FAM. El enfoque integral que se ha seguido aquí, desde la recopilación de datos paleosísmicos hasta el PSHA, contribuye a realizar interpretaciones más críticas de la peligrosidad sísmica y pretende servir de ejemplo para otras regiones de sismicidad baja-moderada.

PREFACE AND THESIS STRUCTURE

The contents of this thesis are based on the results of two published articles indexed in the Journal of Citation Reports (JCR) along with other results that have not been published to date. The research has been developed in the Department of Earth and Ocean Dynamics of the Faculty of Earth Sciences, University of Barcelona, and as part of the RISKMAT research group and Geomodels research institute.

The thesis is structured in five chapters, divided in a total of nine subsections, along with references and annexes. The text of the published articles has been adapted and modified in other to fit and ensure a better coherency and linearity with the structure, and to avoid potential redundant information.

Chapter I is the introduction to the thesis. In the first section (section 1), the interest and motivation of the research are exposed, the principal objectives are presented and the relationship between the published articles as well as their coherency within the rest of the thesis is stated. In the second section (section 2), the chapter contains the main theoretical aspects of the approaches used, the geological and tectonic setting of the Eastern Betics and Alhama de Murcia Fault (AMF), and a literature background of the study area. It is aimed for non-expert readers to fully understand the topics discussed in the thesis.

Chapter II explains the data and methodologies followed. The first section (section 3) explains the principal methods used to perform a structural and paleoseismic analysis in active faults and the second one (section 4) explains the methods used to perform a source modelling for a probabilistic seismic hazard assessment (PSHA) focused on the Eastern Betics Shear Zone (EBSZ), providing specifications for the hazard calculations. This includes a compilation and critical revision of previously published fault data in the EBSZ and characteristics of the hazard models used.

Chapter III contains the main results of the thesis. The first section (section 5) of this chapter presents the results of the research that has not been published during the development of the thesis. These concern a comprehensive structural and paleoseismic study in the AMF, where structural and paleoseismic data from different sites are integrated to obtain more representative slip rates of the whole fault, more complete

paleoearthquake records and recurrence estimations. The implications of these data are discussed at the end of the section. From these results, in a second section we characterize and propose a new site to develop future paleoseismic studies in another segment of the AMF (section 6). The third section (section 7) describes the results of the two published JCR articles and presents a fault-based PSHA of the EBSZ. First, we present the results of a source modelling using geological fault data from the EBSZ and a state-of-the-art methodology to model complex patterns of fault ruptures at a whole fault system scale. Then we calculate the seismic hazard for different return periods, depicted in hazard maps, curves and disaggregation plots. The implications of the source modelling and hazard results are discussed at the end of the section and compared with previous studies in southeastern Spain. As a final step, the parameters obtained for the AMF in the first section 5 of the chapter are used as inputs to perform a new hazard model, test the impact of the new data into the seismic hazard values and deepen the discussion on the relationship between fault data and seismic hazard.

Chapter IV presents the global discussions of this thesis where all the topics discussed in chapter III are reviewed and integrated. Mainly, we set the importance of including fault data into the seismic hazard assessments and justify how the fault parameters obtained the multi-site paleoseismic approach in the AMF can improve the reliability of the seismic hazard estimations (section 7). Based on the results and limitations described, a second section (section 9) presents a thorough discussion on how both geologists and seismic hazard modellers could improve their future work to produce eventually more reliable PSHAs.

Chapter V presents the main conclusions of the thesis. We first present the specific conclusions of the paleoseismic study in the AMF and the seismic hazard assessment, and, finally, the global conclusions of the thesis.

At the end of the thesis the main **References** of the thesis are listed followed by the **Annexes**. **Annex I** contains the two published articles in the original journal format. **Annex II** contains, in a digital repository, **A)** uninterpreted digital elevation models, **B)** OSL dating laboratory reports, **C)** uninterpreted field photographs of the figures in the thesis, **D)** raw trench photologs and interpretations, **E)** the codes written to establish chronosequences in the trenches and **F)** probability density function graphs computed to calculate slip rates.

I. INTRODUCTION

This chapter introduces the motivation, hypotheses and objectives of the thesis, as well as the basic concepts of paleoseismology and seismic hazard, and their background at the Eastern Betics.

View of Sierra de La Tercia and Las Estancias from La Salud (Lorca).

1 General introduction

1.1 Interest and motivation

Earthquakes are one of the most damaging natural phenomena and represent half of the casualties related to natural disasters with nearly 750,000 worldwide in the 1998-2017 period alone (WHO, 2021). To this date, earthquakes remain unpredictable. However, the characterization of their occurrence in terms of territorial location, size and frequency has improved noticeably and is one of the principal motivations of the seismic hazard-related studies to prevent and mitigate the potential damaging effects of such phenomena.

Earthquakes happen on active faults and, historically, the occurrence of large earthquakes causing surface ruptures has been crucial to unveil the location and extent of such structures. The 1906 San Francisco earthquake is conceived as a paradigmatic case that allowed to undoubtedly relate the origin of earthquakes to the faults (e.g., Lawson, 1908; Reid, 1910). In this sense, the study of faults from both seismological and geological perspectives has become essential for the understanding of earthquake mechanics and location (e.g., Kanamori, 1972; Berberian, 1979; Archuleta, 1984).

Despite the increasing knowledge of faults as sources able to generate earthquakes (i.e., seismogenic sources), prior to the 1980s the probabilistic seismic hazard assessments (PSHA) characterized earthquake occurrence solely based on the records of historical and instrumental seismicity. In such studies the information on faults was not included for the source definition or source modelling, also because very few studies were able to provide detailed fault parameters useful for the hazard assessments (e.g., earthquake frequency or recurrence) (McCalpin, 2009). The exclusive use of seismicity data, however, proved to be an inaccurate way to estimate the seismic hazard because in most regions earthquake catalogues only cover a few centuries to over a thousand of years, a time span insufficient to capture the larger seismic cycles of most faults (Schwartz and Coppersmith, 1984). This is especially problematic in low seismicity regions, where faults have recurrence periods much longer than the extent of the catalogues (e.g., Spain). It gets even more challenging in those active regions where there is no record of large earthquakes. In this context, the interest on the inclusion of pre-historic earthquake data from faults into PSHA increased with the development of studies focused on the active tectonics, more specifically on the subdiscipline of paleoseismology (e.g., Sieh, 1978a, 1978b; Sieh and Jahns, 1984 in California).

Active tectonics focuses on the study of deformations in the Earth crust on timescales significant for the society (Keller and Pinter, 1996) and in this field, paleoseismology focuses on studying the time, location and size (magnitude) of pre-historic earthquakes (paleoearthquakes) based on structural-stratigraphic records and geomorphological expression (McCalpin, 2009; Kondo and Owen, 2013). The novelty of paleoseismological studies, emerging during the late 1970s, relied on that they were allowing to extend the earthquake record of historical catalogues and to characterize long-term earthquake recurrences and other parameters such as fault slip rates and magnitudes to assist in PSHA.

Nowadays paleoseismology is one of the main approaches to obtain fault parameters for the seismic hazard, commonly slip rates, earthquake recurrence and maximum magnitude. In high seismicity regions, this approach is vastly implemented in hazard assessments and combined with a variety of fault data from other methods (geodetic or geophysical) to characterize the seismogenic sources. Well known examples of this are found in California with the UCERF-3 model (Field et al., 2014) or in New Zealand (e.g., Stirling et al., 2012). In Europe, countries with high seismicity such as Italy or Greece, have developed many active tectonics studies over the last years that have allowed to characterize the activity on faults. For instance, the DISS database (Database of Individual Seismogenic Sources) (Basili et al., 2008) compiles all the data available on active faults in Italy gathered for over two decades and to be used in PSHA. Contrarily, in low or moderate seismicity regions, such as southeastern Spain, paleoseismic studies encounter a series of additional difficulties in the quantification of the seismic parameters related to: i) surface processes like erosion or intermittent sedimentation that can easily erase or mask the geological evidence of seismic activity or ii) distribution of the deformation over a wider area and between fault branches. The study of these regions is more challenging as requires more effort and resources on integrating data from multiple paleoseismic sites and methods to obtain sufficiently reliable fault parameters (Cowie et al., 2012). For this reason, the inclusion of fault data into PSHA is usually less frequent, although in these regions it is more crucial because seismic catalogues are more incomplete and can potentially underestimate the seismic hazard.

The SE of Spain is a low-to-moderate seismicity region where several large earthquakes have occurred in historical times, highlighting the seismic potential of this zone. Some of the most damaging with larger maximum intensities ($I_{EMS}=VIII-IX$) happened in

Almería (1522 AD), Lorca (1674 AD), Dalías-Berja (1804 AD) or Torrevieja (1829 AD), whose effects on the population was compiled in the historical records of the time (Mezcua, 1982; Martínez Solares, 2003; Silva et al., 2014). The active faults of southeastern Spain are suspected to have caused many of these earthquakes, although the level of knowledge and characterization in terms of paleoseismic research varies strongly between them. For this reason, the importance of applying paleoseismic approaches in the Iberian Peninsula to properly characterize active faults was highlighted, at least, since the early 2000s (Santanach and Masana, 2001).

The severe damage caused by the 2011 Mw 5.2 Lorca earthquake generated in the Alhama de Murcia Fault (AMF) raised awareness on the necessity of the study of active faults in the Eastern Betics, especially because the earthquake evidenced that the seismic hazard estimations in the area, which did not consider faults, underestimated the ground motions experienced. In addition, earthquake peculiarities (source effects) such as its shallow epicenter, rupture directivity towards Lorca city and heterogeneity in the slip distribution, aggravated its damaging effects (Martínez-Díaz et al., 2012a; Alguacil et al., 2014). This motivated the development of paleoseismic studies focused on constraining fault parameters and homogenization over the territory with the aim to be used and improve seismic hazard studies. The AMF is one of the most prominent faults of southeastern Spain and has been the subject of many of these studies in the last decade leading to one of the most complete paleoseismic records of Spain with more reliable parameters. These studies, however have developed mostly on a single segment of the fault and in a single fault branch out of several that also accommodate deformation (Martínez-Díaz et al., 2003; Masana et al., 2004). This means that the seismic parameters previously calculated for the AMF (e.g., slip rates or recurrence) might be underestimated or underrepresented and therefore characterizing the other branches is a required step to obtain more representative estimations of the whole fault. In addition, paleoseismic data throughout the Eastern Betics are still heterogeneous and fault parameters have still large uncertainties in some zones (e.g., 0.01-0.08 mm/yr for the Palomares fault; García-Mayordomo, 2005 or 0.16 to 1.37 mm/yr for the Góñar-Lorca segment of the AMF; Ortuño et al., 2012)

The inclusion of faults into PSHA in Spain is still an emerging and scarce practice, with only a few applications in southeastern Spain (i.e., García-Mayordomo et al., 2007; Rivas-Medina et al., 2018). In these works, faults are considered both as non-interacting and

independent sources, which may be unrealistic according to many nature observations of linked ruptures during earthquakes (e.g., multi-fault ruptures; Wei et al., 2011; Zhang et al., 2012). In addition, discussing and revising the impact that the reliability of fault data has for the PSHA in the Eastern Betics is pending, yet crucial to understand and interpret the hazard assessments, especially given the large uncertainties of the parameters in some faults. Unreliable fault data leads to unreliable hazard estimations and consequent impact for the society. If seismic hazard is underestimated, the lack of preparedness and seismic planification may become a thread for the society, but if it is overestimated it can also imply greater costs than required for the governments and populations.

Acknowledging the reliability and limitations of the fault parameters is crucial when incorporating them in earthquake forecasts (Field et al., 2014). It is then important, yet not frequent, that both geologists (data collectors) and hazard modellers work together to understand the sources of error or uncertainty in the fault data and how these might propagate into the seismic hazard. In this sense, the creation of synergies and works that encompass the whole seismic hazard calculation process, from data collection to final hazard results, might be fruitful to have better trained specialists able to fully understand and assess the problems involved in each step and, in the end, to perform overall better hazard estimations (e.g., Fault2SHA initiative: Scotti and Peruzza, 2017; García-Mayordomo et al., 2019).

Therefore, the main driving motives of the present thesis can be summarized in three:

- i) The lack of representativeness of paleoseismic data for some faults in the Eastern Betics, either because their paleoseismic investigations focus on single branches out of several that accommodate deformation or because the paleoseismic research is heterogeneous over the different seismogenic faults.
- ii) The lack of fault-based PSHA in the Eastern Betics that consider nature-observed patterns of complex linked fault ruptures in the source modelling and that put the focus on evaluating the impact of the reliability and uncertainties of fault data into the seismic hazard results.
- iii) The importance of understanding the whole process of estimating the seismic hazard of a region to understand the problematics and uncertainties related to every step and its propagation to the hazard; from the collection of fault data in the field (paleoseismic studies) to the seismic hazard calculations.

1.2 Hypotheses

Given the motives explained in the previous section, the starting hypotheses of this thesis are the following:

- i) Performing a comprehensive paleoseismic study across different unstudied fault branches in a transect of the Alhama de Murcia Fault (AMF) and integrating data from multiple sites allows for an improved and more realistic characterization of the seismic and paleoseismic parameters of this fault, namely slip rates and earthquake recurrences. This implies that:
 - a) The AMF has more than one active branch absorbing deformation and that has produced large earthquakes during the recent Quaternary.
 - b) The slip rates of the AMF are probably higher than anticipated from previous studies and among the highest within the Eastern Betics.
 - c) The paleoearthquake catalogue to date is likely incomplete and the integration of data from different sites will contribute to its completion. Moreover, paleoseismic trenching in more recent materials than previous studies will likely evidence the Holocene activity in the AMF.
 - d) Integrating data from different fault branches might shed light on the fault behavior in terms of possible simultaneous ruptures and recurrence models.
- ii) Including faults as seismogenic sources into the probabilistic seismic hazard assessments (i.e., fault-based PSHA) of the Eastern Betics Shear Zone increases the near-fault hazard values and enhances the reliability of the results respect to previous estimations in southeastern Spain. In detail:
 - a) Considering the EBSZ as a whole and exploring complex fault rupture patterns within the system allows for a more realistic modelling of earthquake occurrence.
 - b) Fault slip rates are critical and controlling parameters for the PSHA.
 - c) The new paleoseismic data obtained in the AMF will contribute to increase the seismic hazard estimations around this fault.
- iii) The reliability and uncertainties of the fault parameters play a significant role in the reliability of the PSHA. Therefore, proper acknowledgement of such limitations, discussion and sharing between geologists and hazard modellers is beneficial in the light of improved fault-based PSHA.

1.3 Objectives

In agreement with the main topics explained in the previous sections, the main objectives of this thesis are to:

- i) Improve the reliability and representativeness of the seismic parameters and seismic potential of the Alhama de Murcia Fault (AMF) by quantifying more precisely the fault slip rates, extending the knowledge of the paleoearthquake record and constraining better the earthquake recurrences. To achieve this, we aim to:
 - a) Refine the surface characterization of the AMF by performing a detailed geomorphological mapping and structural analysis of its two central segments.
 - b) Demonstrate the Quaternary seismogenic activity of several branches conforming these segments.
 - c) Locate a transect in each central segment suitable to perform a paleoseismic study based on the geomorphological and field data acquired.
 - d) Perform a comprehensive paleoseismic survey in one of the segments, across the different branches composing it, by integrating the data from all the sites explored. This is done to ensure more representative paleoseismic parameters of the whole fault segment (slip rates and recurrences) and evaluate possible simultaneous fault ruptures.
- ii) Evaluate the seismic hazard of the Eastern Betics with a fault-based probabilistic seismic hazard assessment (PSHA), considering the available geological and paleoseismic data of the main faults as inputs for the source modelling, and also including the new data obtained in the AMF. With this, we also aim to:
 - a) Perform a state-of-the-art source modelling considering the fault system as a whole by relaxing segmentation criteria and allowing linked ruptures between faults (multi-fault ruptures), in agreement with more realistic fault behaviors observed in nature.
 - b) Evaluate the improvements and limitations of including faults as the main seismogenic sources into the PSHA of the Eastern Betics compared to previous studies.
 - c) Discuss the relevance of including faults into PSHA in the Eastern Betics as opposed to using non-fault-based approaches. This also implies evaluating the relevance of performing integral paleoseismic studies to obtain more reliable fault parameters for the hazard assessment.

iii) Evaluate the reliability and uncertainties of the fault data in the Eastern Betics and its impact for the robustness of the hazard estimations. In this line, we aspire to recommend where future paleoseismic studies should be developed to mitigate bias into the seismic hazard.

1.4 Published articles and coherency within the thesis

This thesis is presented as a compilation of the results from two published journal articles indexed in the Journal of Citation Reports (JCR). The original articles can be found in the Annex I and their full reference is:

1. Gómez-Novell, O., Chartier, T., García-Mayordomo, J., Ortuño, M., Masana, E., Insua-Arévalo, J. M., et al. (2020a). Modelling earthquake rupture rates in fault systems for seismic hazard assessment: The Eastern Betics Shear Zone. *Engineering Geology* v. 265. <https://doi.org/10.1016/j.enggeo.2019.105452>.
2. Gómez-Novell, O., García-Mayordomo, J., Ortuño, M., Masana, E., and Chartier, T. (2020b). Fault System-Based Probabilistic Seismic Hazard Assessment of a Moderate Seismicity Region: The Eastern Betics Shear Zone (SE Spain). *Frontiers in Earth Science* v. 8. doi:10.3389/feart.2020.579398.

The first article (Gómez-Novell et al., 2020a) is focused on performing a fault-based source modelling for a seismic hazard assessment of the EBSZ. To do so a novel method has been applied to model the earthquake rates of fault and multi-fault rupture hypotheses at the system-level for the whole EBSZ and using published geological fault data as the main inputs (geometry, slip rates and recurrences). The reliability of each hypothesis is discussed based on the fit with the rates derived from the seismic catalogue and paleoseismic studies. Based on this fit, a relative weight is assigned for each hypothesis in a logic tree in PSHA.

The second article (Gómez-Novell et al., 2020b) uses the source modelling and logic tree weights from the first article to perform a full fault-based hazard assessment of the EBSZ. The seismic hazard is presented in the form of hazard maps, curves and hazard disaggregation for different return periods (475, 975, 2475 and 4975 years). The article also discusses the implications of the study, i.e., the improvements with respect to previous fault and non-fault-based PSHA in Spain and the limitations concerning the fault input data used, mainly about slip rates.

As explained in the preface, the two published articles concern one part of the results from the thesis. The other part of the results corresponds to unpublished research from a comprehensive paleoseismic characterization across the Alhama de Murcia Fault (AMF). Despite this, both parts are importantly related because they conform essential steps of the seismic hazard assessment: first, the field reconnaissance and fault mapping (sections 5 and 6), followed by the paleoseismic characterization of fault parameters (section 5); second, the use of such parameters as inputs for the source modelling (article 1) and computation of the seismic hazard (article 2) (section 7). Thereby and in agreement with the outlined objectives, the thesis is organized in the coherent order of the hazard assessment process. In a fault-based PSHA, well-constrained fault input data (slip rates, recurrence) is crucial as it controls the earthquake probabilities; a driving factor to estimate the hazard (see section 2). In this respect, the paleoseismic study in the AMF (section 5) allows to better understand the nature of data, limitations and uncertainties coming from paleoseismology, enabling to identify more precisely how it affects the reliability of the seismic hazard from the articles. The fault data for the AMF presented in this thesis was not considered for the hazard assessment in the two publications because it was not available at the time. Therefore, the updated data of the AMF has been included here in a new hazard model for the EBSZ (section 7.6.5) as complementary to the papers to better relate both topics in the general discussion (chapter IV). This allowed to compare with the results strictly from the papers, to identify how data from a multi-site paleoseismic study, as we do in the AMF, can help to increase the reliability of the hazard estimations and overall enrich the analysis on the implications of including fault data in PSHA for the EBSZ. Furthermore, the effects that poorly studied faults in the EBSZ have to the reliability of the seismic hazard results (section 7) justify the proposal for a future paleoseismic survey in an unstudied zone of the AMF (section 6).

2 Basic concepts and background

2.1 Methodological overview and state of the art

In this section we present a brief overview of the most relevant characteristics and implications of the two main approaches used in this thesis: paleoseismology and probabilistic seismic hazard assessment (PSHA).

2.1.1 Paleoseismology

Paleoseismology is a subdiscipline of the active tectonics focused on constraining the timing, size and location of pre-historic earthquakes, i.e., previous to the existence of historical records, based on geomorphological and geological evidence (sensu McCalpin, 2009; Kondo and Owen, 2013). The method is important because it allows to extend the earthquake record beyond the time coverage of the historical catalogues (Figure 2.1) that, most times, are too short to correctly depict the seismic cycles of faults. Paleoseismic studies are mainly focused on the study of the effects that earthquakes have on tectonic landforms (geomorphology) (Figure 2.2 and Figure 2.3) and sedimentary sequences (Figure 2.4), mainly the ones occurring in the pre-historical period, but also those in the historical (pre-instrumental) and even nowadays (Kondo and Owen, 2013). These effects comprehend mainly fault displacements, rupturing or folding caused by coseismic or postseismic faulting, but also other off-fault indirect effects derived from ground shaking such as liquefactions or mud flows (Fletcher et al., 2014; Rockwell et al., 2014).

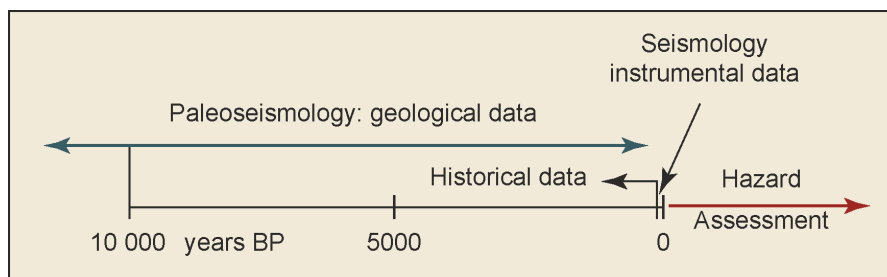


Figure 2.1. Time span of paleoseismological studies (geological record) with respect to historical and seismological data. Seismic hazard assessments require the combination of the three types of data to perform estimations of the future. From Kondo and Owen (2013), after Mörner (2011). Used with permission from Elsevier under the STM Permissions Guidelines.

The scope of studying earthquake effects in geological records is, on the one hand, identifying evidence of past earthquakes (paleoearthquakes), establish chronosequences and obtaining critical parameters such as the earthquake recurrences. In the sedimentary sequences, evidence of paleoearthquakes is identified in contacts between units called

event horizons representing the topographic surface right after the occurrence of an event. Some common evidences are, among others, truncations of faults at the base of a sedimentary unit, disconformities evidencing differential deformation between units, liquefacted units or colluvial deposits coming from the erosion of a previous scarp (colluvial wedges) (McCalpin, 2009) (Figure 2.4). See details on types of paleoearthquake evidence used in this thesis in chapter II (section 3).

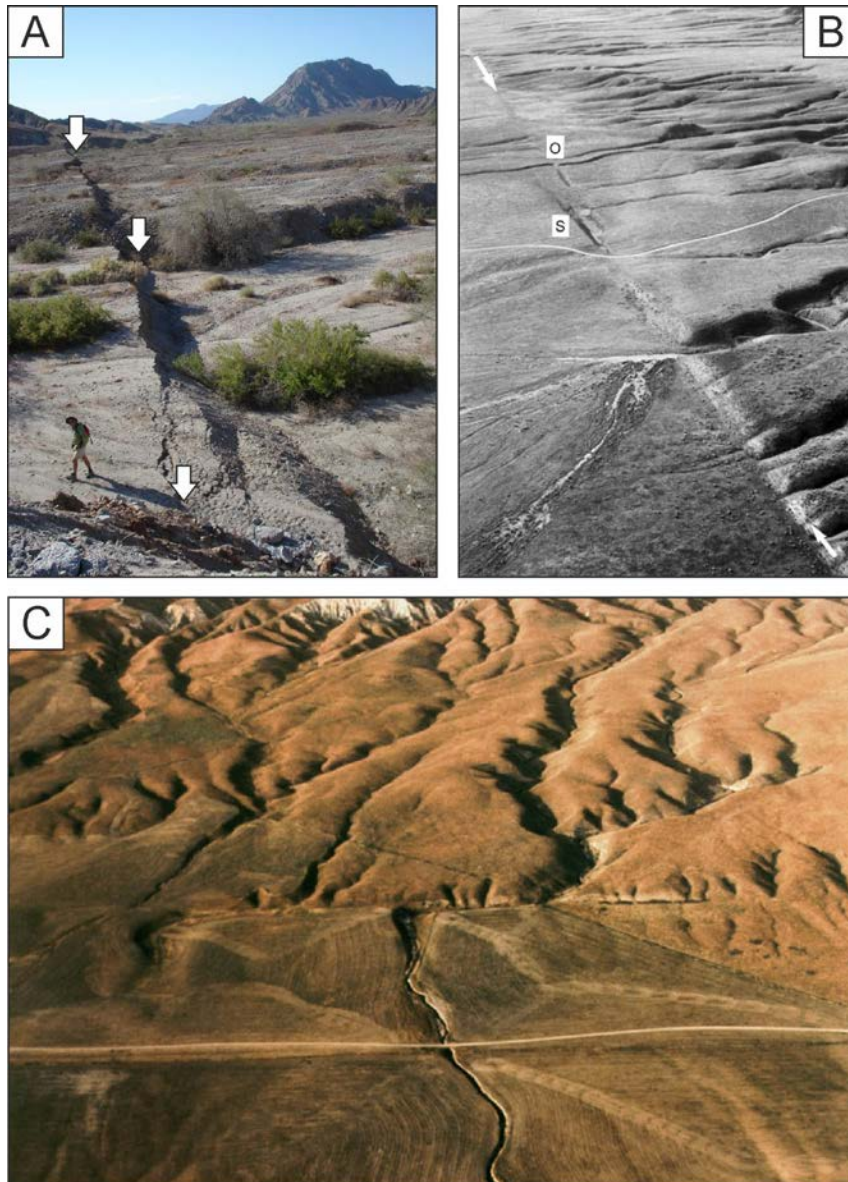


Figure 2.2. Examples of geomorphological features in paleoseismology **A)** Surface rupture of the 2010 Mw 7.2 El Mayor-Cucapah earthquake, Baja California. Photo courtesy of María Ortuño. **B)** Aerial image of the San Andreas Fault (between arrows) in the Carrizo Plain, California. “O” indicates a dextral offset in a drainage channel crossing the fault; “S” indicates a sag pond (see Figure 2.3). Figure from McCalpin (2009) interpreted on a photograph from Wallace (1990). Used with permission from Elsevier under the STM Permissions Guidelines. **C)** Laterally offset channels in the San Andreas Fault along the Carrizo Plain, California. From Wallace (1990).

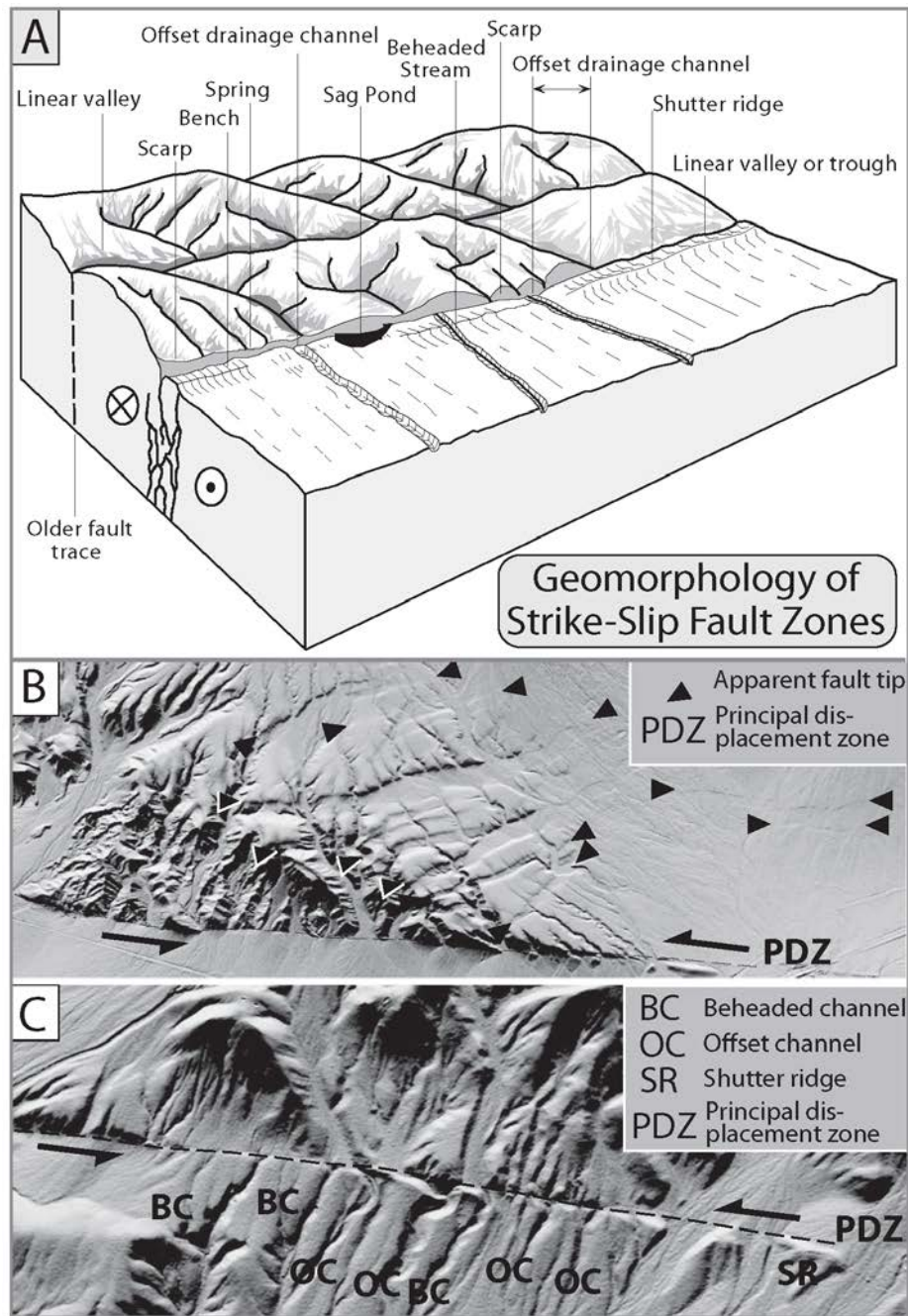


Figure 2.3. Geomorphological features in strike-slip faults. Figure from Burbank and Anderson (2011), used with permission from John Wiley and Sons. **A)** Sketch of typical geomorphological features defined in strike-slip faults. Originally from Wesson et al. (1975). **B)** and **C)** Geomorphological features along the Garlock Fault Zone in southern California in a shaded relief extracted from LiDAR data.

On the other hand, paleoseismology focuses on the quantification of the deformation (fault displacements) to characterize the slip rate of the faults and parameters such as the slip per event. This is done by measuring the displacements that faults generate on certain markers whether they are geomorphological or geological, for instance drainage channel incisions (Figure 2.2), laterally continuous sedimentary units or terrace surfaces

(Kondo and Owen, 2013). In all cases, fault displacements may be the result of one or more repeated paleoearthquakes and thus is necessary to identify individual events.

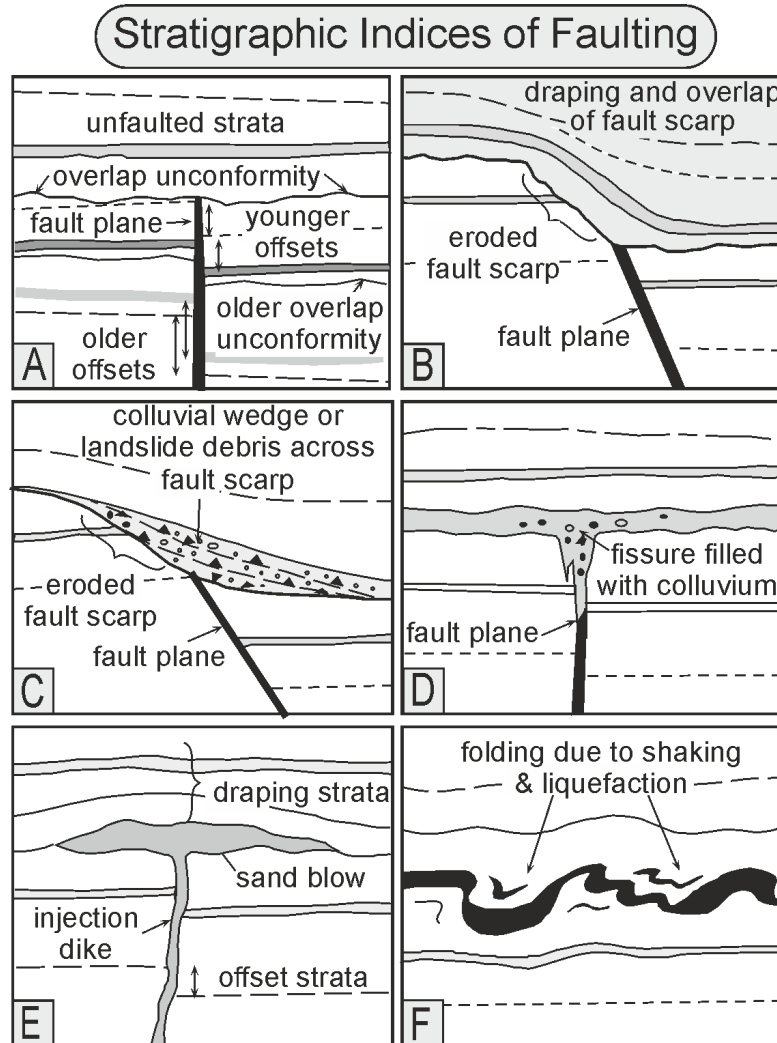


Figure 2.4. Stratigraphic evidence of past faulting events. Figure from Burbank and Anderson (2011), modified after Allen (1986). Used with permission from John Wiley and Sons. **A)** Fault offsets covered by an unconformity developed after the last earthquake. **B)** Unconformity on top of an eroded fault scarp. Same as in A), the unconformities are the event horizon. **C)** Colluvial wedge from the erosion of a fault scarp. The base of the wedge is the event horizon. **D)** Fissures filled with colluvial materials in the fault zone. The base of the colluvium is the event horizon. **E)** Injection dikes of sand generating offsets in the underlying strata and folding in the overlying. The first horizontal layer is the event horizon **F)** Liquefaction related to earthquake shaking.

The most used approach to study active faults is the excavation of paleoseismic trenches because they allow to expose the fault zones and clearly observe and characterize the sedimentary units and relationships. Such trenches can have very different dimensions and orientations depending on the scope of the specific study in question. Trenches dug perpendicular to the faults allow to directly observe the fault zones and to identify individual paleoearthquakes from fault-related evidence. They also allow to quantify

vertical displacements of the units, especially in dip-slip faults (Pantosti et al., 1996; Papanikolaou et al., 2005; DuRoss et al., 2021).

Conversely, trenches dug parallel to the faults are commonly used in strike-slip faults to characterize and quantify the lateral displacements. This is done by measuring the displacement of piercing points in linear features such as buried paleochannels that cross the fault zone and are offset by it (Figure 2.5).

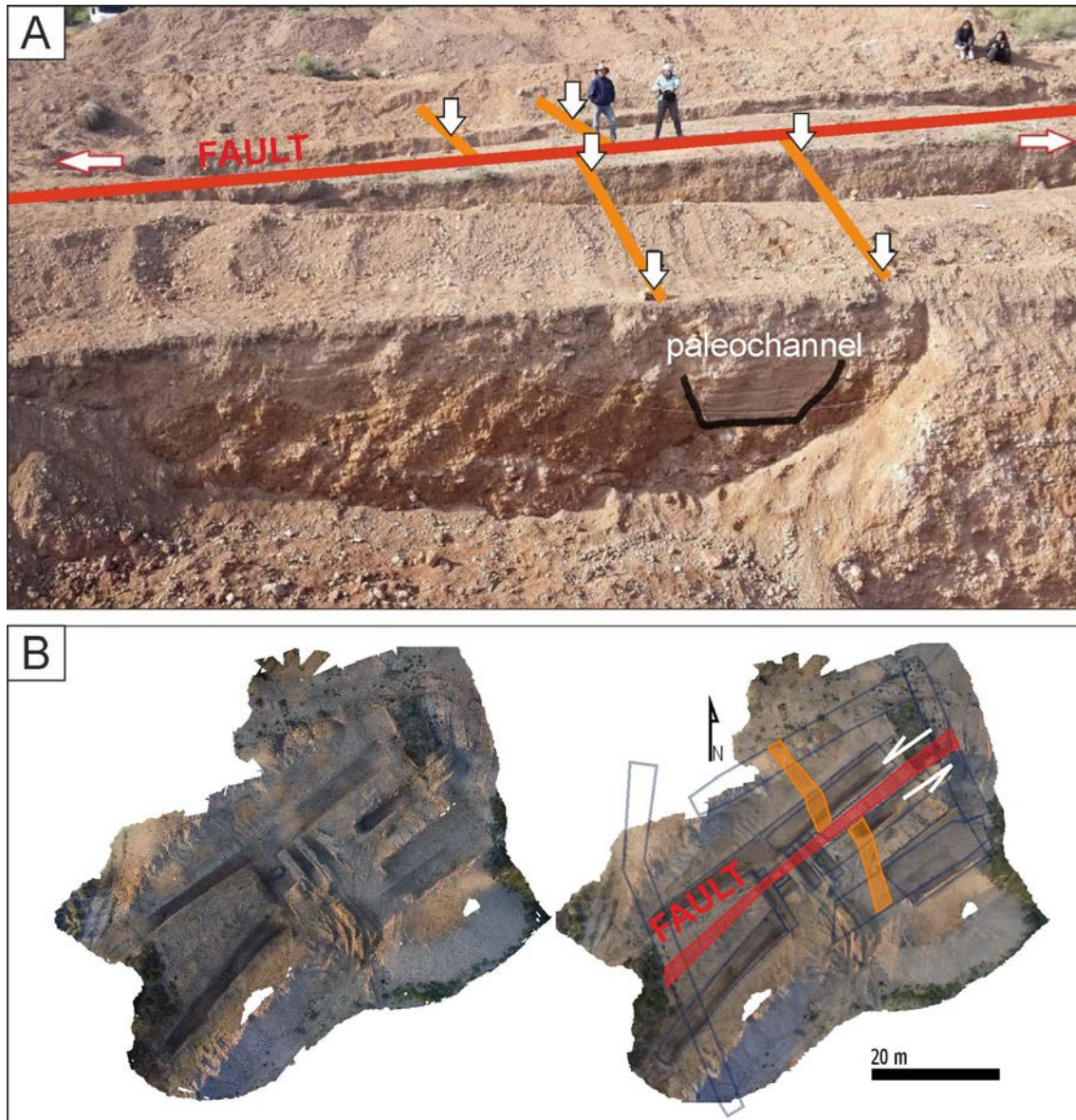


Figure 2.5. **A)** Image of a left-lateral offset paleochannel recognized in trenches excavated parallel to a fault. It corresponds to the Carboneras Fault in the Tostana site, near Níjar, SE Spain ($36^{\circ}52'22.0''\text{N}$, $2^{\circ}08'42.8''\text{W}$). Photo courtesy of Stéphane Baize. **B)** Plan view photomosaic of a 3D paleoseismic trenching survey in the Carboneras Fault. In the right sketch, the disposition of the paleochannel and fault (figure A) are indicated and inferred from discrete exposures in the different trenches parallel to the fault. Figure courtesy of Robert López-Escudero (ongoing research).

The combination of both perpendicular and parallel trenching is called 3D trenching (Figure 2.5B) and it is used to completely characterize the displacements and paleoearthquake history of a fault (Marco et al., 2005; Dikbaş et al., 2018; Wechsler et al., 2018). Other paleoseismic approximations include the study of sedimentary sequences in natural outcrops such as creek margins or morphotectonic analyses. In the latter, geomorphological features are used to measure displacements caused by faults in geomorphic features such as channel incisions and drainage networks, terrace surfaces or scarps (Hessami et al., 2003; Gold et al., 2009) (Figure 2.3).

Other used paleoseismic approaches focus on the study of bedrock fault scarps to unveil the earthquake histories. To do so, fault scarps are analyzed to identify evidence of coseismic slip. Classically, variations in the lichen developments along the fault scarp vertical profile have been used to identify and date different exposure times and hence evidence for repeated paleoearthquakes (lichenometry) (e.g., Bull, 1996; De Guidi et al., 2019). More recently, most paleoseismic studies on fault scarps rely on the cosmogenic technique, which measures the ^{36}Cl from cosmogenic radiation accumulated over the years on the exposed fault scarp (Benedetti et al., 2013; Benedetti and Van Der Woerd, 2014; Mechernich et al., 2018). Higher ^{36}Cl concentrations indicate longer exposure times, and thus, variations of this cosmogenic nuclide concentration in the fault scarp indicate different episodes of exposure, i.e., repeated coseismic slips.

Knowing the age of the sediments and landforms affected by deformation is fundamental to place in time the recognized paleoearthquakes and to calculate the slip rate of the faults. To do so, paleoseismologists sample the sediments deposited before and after the interpreted paleoearthquakes to constrain their ages. Alternatively, bedrock landforms (such as scarps or erosional surfaces on bedrock) are systematically sampled using vertical profiles to unveil exposure dates. One of the first used and most widespread dating techniques in paleoseismology is radiocarbon due to its accuracy during the Holocene time span (e.g., Sieh et al., 1989). However, the time limitation of radiocarbon (usually <40 ka) and development of paleoseismic approaches in lower slip rate faults, required the implementation of other dating techniques to extend the record beyond the Holocene. Some of these techniques are the Optical Stimulated Luminescence (OSL), Thermoluminescence (TL), Uranium series and Cosmogenic isotopes (Noller, 2000),

which allow to date materials within the Pleistocene period. For bedrock, the cosmogenic dating of the ^{36}Cl cosmonuclide is the most frequently used to date fault scarp exposures.

Besides the usefulness of paleoseismic approaches for assessing the seismic hazard related to faults, the methodology has several important limitations, such as the difficulty of determining if the slip per event in a site is representative of the average/maximum slip, or the fact that the number of paleoearthquakes identified is always a minimum. This latter is due to several causes:

The first is that paleoseismology only records earthquakes large enough to produce surface deformation. This means that other smaller earthquakes are underrepresented in the record, although they could have caused damage as well. The magnitude threshold to cause surface rupture has been thoroughly debated among researchers. Although classically it has been regarded that most likely earthquakes producing surface ruptures have magnitudes above Mw 6.0-6.5, as mentioned in McCalpin (2009) and reflected in the Unified Database of Surface Ruptures (SURE) (Baize et al., 2019), several lower magnitude earthquakes have produced surface rupture as well. One of the most paradigmatic cases is the 2019 Mw 4.9 Le Teil earthquake in France (Ritz et al., 2020). The second cause for earthquake underdetection in paleoseismology is that the sedimentary deposition is often not continuous, which causes that some earthquakes cannot be individually distinguished in the exposed sequences if they happened during depositional hiatuses. The third is that superficial processes, such as erosion or bioturbation, might erase evidence of paleoearthquakes. Moreover, bioturbated units are typically related to lower depositional rates, which enhances the likelihood of paleoearthquake underestimation (Yeats et al., 1997). Finally, paleoseismological studies are usually localized in specific branches and portions of a fault although earthquakes can imply complex ruptures in wide deformation areas and irregular slips along strike (e.g., Kearse et al., 2018), meaning that paleoearthquake evidence can be missed.

The first paleoseismic studies appeared during the late 1960s with the observations of geological effects of surface ruptures and their relationship with magnitude (Matsuda et al., 1978; Bonilla, 1982, in McCalpin, 2009 and references therein). Nonetheless, the modern-day paleoseismology was established from the late 1970s in the San Andreas Fault (California) when the excavation of trenches to expose the fault zones started to be used extensively, paired with radiocarbon datings to establish detailed earthquake chronosequences (Sieh, 1978a, 1978b; Weldon and Sieh, 1985; Sieh et al., 1989). From

there, paleoseismic studies have been commonly used in different regions of the world to characterize active faults for the sake of more reliable seismic hazard assessments, including lower deforming regions such as in Central Ecuador (Baize et al., 2015), the lower Rhine graben (Camelbeeck et al., 2000; Meghraoui et al., 2000), Germany (Grützner et al., 2016), France (Sébrier et al., 1997) or in the Eastern Betics (see details in section 2.3). In these regions, the paleoseismic methodologies have been adapted to accommodate issues not found in higher seismicity regions. One of the common issues is the rate of surface processes (e.g. erosion) overcoming the tectonic deformation rates and masking deformed markers, which has motivated methodological adaptations such as the proposed for the fault lateral offsets in the Alhama de Murcia Fault (Ferrater et al., 2015a).

2.1.2 Probabilistic seismic hazard assessment

Probabilistic seismic hazard assessments (PSHAs) are one of the most widespread approaches to assess earthquake probabilities in seismic regions because they allow to express the hazard statistically computing the probabilities of exceeding certain parameters of the ground motion (e.g., peak ground acceleration or PGA) considering all the possible seismic sources, their characteristics and magnitude ranges that could affect a particular site (Cornell, 1968; Youngs and Coppersmith, 1985). This contrasts with deterministic seismic hazard approaches in which the seismic hazard is not computed as probabilities, but only considering the effects of a maximum earthquake in a study site.

In the probabilistic approach, the seismic hazard in a site is the probability of exceedance of a given ground motion level in a determined period of time (UNDRO, 1979; Benito and Jimenez, 1999). This means that the seismic hazard at a given site depends on the probability of exceedance of a ground motion value in a period of time, and on the individual probabilities of that earthquake reaching a magnitude at a given distance, as shown in Equation 2.1 (McGuire, 1995).

$$\lambda a = \lambda \iint P(A > a | m, r) f_M(m) f_R(r) dm dr \quad \text{Equation 2.1}$$

In the equation λa is the hazard expressed as the annual rate of exceedance of a ground motion parameter, λ is the activity rate of the source, $P(A > a | m, r)$ is the probability of a ground motion parameter A to exceed a certain value a given a magnitude m and a distance r to the source. $f_M(m)$ and $f_R(r)$ are the individual probability density functions of the earthquake magnitude and distance to the site. Both distance and magnitude are

fundamental as they control the ground motion that a site will experience and therefore, are significant terms in the definition of ground motion attenuation.

PSHAs treat earthquake occurrence as Poissonian, meaning that earthquakes are fully independent events and, consequently, their related ground motions occur in a random pattern and are independent in time. In this sense, the probability of exceedance of a ground motion level at least once during a certain period of time is represented by Equation 2.2 (Cornell, 1968).

$$P(A > a, t) = 1 - e^{-(\lambda_a t)} \quad \text{Equation 2.2}$$

λ_a is the annual exceedance rate of the ground motion parameter and t is the investigation time, i.e., the number of years for which the prediction is made. The inverse of λ_a is the so-called return period (RP). A RP of 475 years, commonly used in building codes, implies a 10% probability of exceedance considering an investigation time of 50 years, which implies the standard lifespan considered for conventional buildings. Despite this, other newer probabilistic approaches consider earthquake probabilities as time-dependent functions since they have shown to fit better the occurrence of seismicity (e.g., Matthews et al., 2002).

The final seismic hazard is expressed as the mean of all the obtained exceedance values of ground motion considering all the magnitudes and distances influencing a site in a given time. Common representations of the seismic hazard are maps in terms of PGA or curves in terms of PGA or spectral acceleration (SA) for engineering purposes. The maps allow to easily depict the most relevant sources for the hazard over a territory with colored scales or contours, although they are usually limited only to a few representative return periods. Hazard curves represent in more detail the probabilities of exceedance of certain ground motion values in a specific site. These outputs from the hazard integrate the contribution of all the sources. In this sense, to estimate the magnitude and distance with a higher contribution to the hazard in a site and for a given return period, i.e., controlling earthquake, the hazard disaggregation is required (e.g., Bazzurro and Cornell, 1999).

The performance of PSHAs can be summarized into two steps as defined from the equations presented. The first step corresponds to the source modelization or source modelling. It relies on the definition of the seismogenic sources including their geometry,

dimensions and spatial characteristics. It also encompasses the characterization of these sources in terms of earthquake frequency and expected magnitudes. This is achieved by modelling the mathematic distributions or magnitude frequency distributions (MFDs) that fit better the seismicity of a certain area. A widely used distribution is the Gutenberg-Richter (sensu Gutenberg and Richter, 1944), in which the frequency of earthquakes follows a magnitude-dependent exponential distribution, meaning that larger earthquakes happen less frequently than smaller (Figure 2.6). The frequency is controlled by the slope of the distribution, i.e., the so-called b value. Another common distribution is the characteristic earthquake (Schwartz and Coppersmith, 1984), which assumes that faults only generate maximum earthquakes of a given “characteristic” magnitude, while they remain quiescent in between these events (Wesnousky, 1994) (Figure 2.6). Paleoseismic studies are highly valuable for the source modelling in fault-based PSHAs because they can help to characterize their activity in terms of earthquake rates and suitable MFD models, especially when the seismic catalogues are not able to provide them (Figure 2.7).

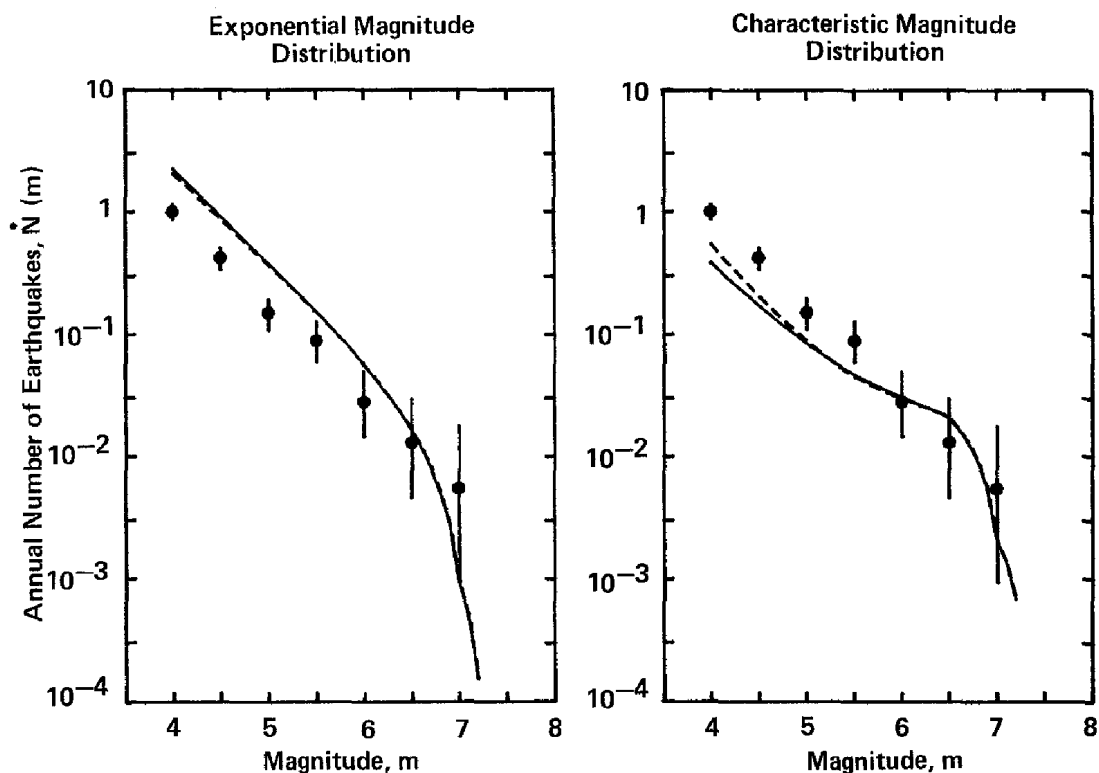


Figure 2.6. Comparison of magnitude-frequency distribution (MFD) models based on slip rate and seismicity. Point and bars are the seismicity data and one standard deviation. The left plot corresponds to an exponential distribution (i.e., Gutenberg-Richter) and the right plot corresponds to a characteristic earthquake model. Figure from Youngs and Coppersmith (1985), used with permission from the Seismological Society of America under the STM Permissions Guidelines.

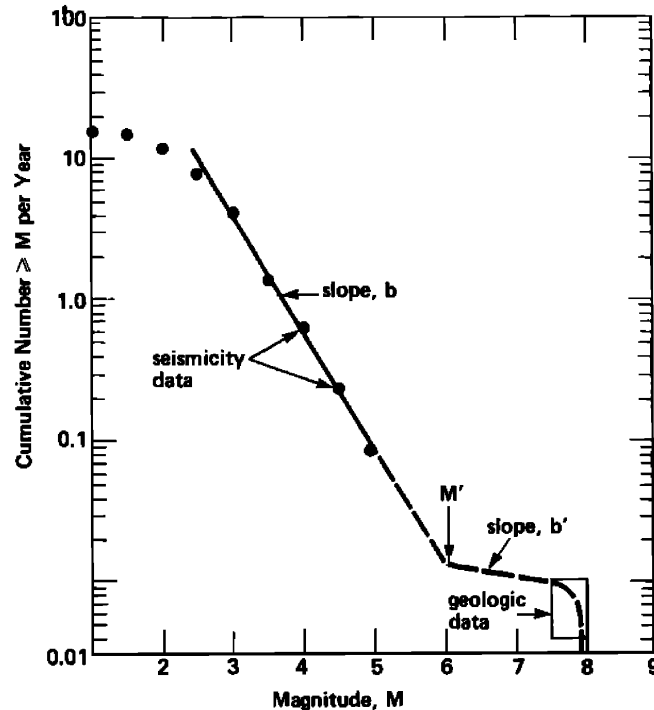


Figure 2.7. Synthetic magnitude-frequency distribution (MFD) of a characteristic earthquake distribution in a fault showing the constraints provided from seismicity and geological (paleoseismic) data. Figure from Schwartz and Coppersmith (1984), used with permission from John Wiley and Sons.

The second step corresponds to the modelization of the ground motion attenuation of the propagating seismic waves to calculate the expected ground motion at a given site and time. This implies the selection of so-called Ground Motion Prediction Equations (GMPE), which take into account many variables including earthquake magnitude, distance, rheological characteristics and fault geometries, among others. The selection of GMPEs is crucial for the hazard assessment as it strongly influences the predicted ground motion in a certain site, for this reason a thorough exploration of different equations is necessary.

A crucial part in PSHA is the assessment of the uncertainties linked to the parameters used for the calculations, whether they concern the source modellings (e.g., earthquake recurrence models, maximum magnitudes) or the GMPEs used to model the attenuation. For this reason, most PSHA studies are built following logic trees that allow capturing and exploring these uncertainties (Bommer et al., 2005). The resulting hazard is expressed as the mean of all the branches, the contribution of which is controlled by an assigned weight. Among the advantages, this allows including hypotheses that are regarded as unlikely in the modelling by assigning them a lower weight.

The first PSHA approaches were developed during the late 1960-70s (Cornell, 1968; McGuire, 1976) in the United States as a methodological novelty that allowed to consider all the potential sources affecting the hazard of a site rather than only considering single sources. This allowed to calculate the seismic hazard in a region in the form of hazard maps, contrasting to previous assessments in which the hazard was exclusively expressed as site curves. The definition of the seismogenic sources in these first studies relied exclusively on the seismicity data from the earthquake catalogues as paleoseismological approaches were still underdeveloped at that time. The most common approach consisted on defining point, line or more commonly, areal sources (zonifications or zonations; Figure 2.8) over the territory, in which the seismicity was characterized by the catalogue and considered equiprobable in time and space (Cornell, 1968). Despite this, catalogues do not typically extend more than a few centuries to a thousand years (e.g., Spain, Italy, Greece, China or Middle East), which is a very short time window for characterizing the occurrence of major events, especially in regions of moderate seismic activity. Therefore, they usually fail to adequately picture the seismic cycle of the faults, which can be thousands of years long. In this sense, the use of geological data in PSHA has become increasingly important since the mid 1980s.



Figure 2.8. Example of seismogenic zonifications for Portugal based on seismic catalogue data. Earthquake epicenters are depicted by circles and stars. Black star corresponds to the 1755 Lisbon earthquake. Figure from Vilanova and Fonseca (2007), used with permission from the Seismological Society of America under the STM Permissions Guidelines.

Traditionally, geological data and fault data have been used to characterize the occurrence of maximum or characteristic events and to complement the high magnitude region of the MFDs (Wesnousky, 1986; Schwartz and Coppersmith, 1986). Because maximum events usually have a very low impact in seismic hazard for the return periods considered in conventional building (e.g., 475 years or 10% probability of exceedance in 50 years), this type of fault-based PSHA was regarded in studies interested in long return periods (e.g. critical infrastructures like nuclear power plants). Nonetheless, over the years, there has been increasing awareness of the fact that low-to-moderate magnitude events (Mw 4.0-6.0) are also able to produce significant strong ground motions and thus damage, especially at sites located on top or very close to fault sources subject to rupture directivity site effects (e.g., in Japan; Dhakal, 2021 or in the 2011 Lorca earthquake; Alguacil et al., 2014). In this context, the identification and characterization of active faults as seismogenic sources able to produce all the range of earthquake magnitudes has become a critical task in the PSHAs of seismically active regions. In accordance with the increasing availability and refinement of paleoseismic and geological studies, the incorporation of fault data in PSHA is nowadays an important part of the source modelling aiming to estimate earthquake activity beyond the coverage of seismic catalogues. The use of faults in PSHA is a well-established practice worldwide with examples such as Frankel (1995) in eastern US, WGCEP (2003) or Field et al. (2014) (UCERF-3) in California (Figure 2.9), Stirling et al. (2012) in New Zealand and Woessner et al. (2015) in Europe. In most cases, faults are modelled as independent sources following a characteristic earthquake model (Youngs and Coppersmith, 1985; Wesnousky, 1986) or an exponential model, typically a Gutenberg-Richter distribution (e.g., Bungum, 2007).

Years of fault studies have shown that faults can rupture in very complex configurations involving several structures simultaneously and with contrasting kinematics or geometries. Earthquakes such as the 2010 Mw 7.2 Cucapah (Fletcher et al., 2014), the 2012 Mw 8.6 Sumatra (Zhang et al., 2012) or the 2016 Mw 7.8 Kaikoura (Little et al., 2018) are known examples. Accordingly, in the recent years seismic hazard modelers have developed new approaches to relax fault segmentation and to model faults as complex and interacting sources in seismic hazard. Including this complexity has demonstrated to be a turning point to model fault processes in PSHA because it allowed to perform more reliable and accurate hazard estimations. Approaches like UCERF-3

(Field et al., 2014) (Figure 2.9) or the recent SHERIFS (Chartier et al., 2019) are emerging methodologies whose principle is modelling earthquake occurrence considering scenarios of multi-fault ruptures for source characterization in PSHA. In both cases fault rupturing is treated as an aleatory variable, whose occurrence is assumed to be linked to the randomness of the seismic process.

Most fault-based PSHA approaches are usually carried out in high seismicity regions with advanced paleoseismic fault knowledge (e.g., Stirling et al., 2012; Field et al., 2014 for New Zealand and California, respectively). Conversely, the scarcity of paleoseismic and geological data on faults has been one of the major challenges faced by PSHA analysts in low-to-moderate seismicity regions, such as western Europe. Consequently, fault-based approaches in these regions are not as implemented to date.

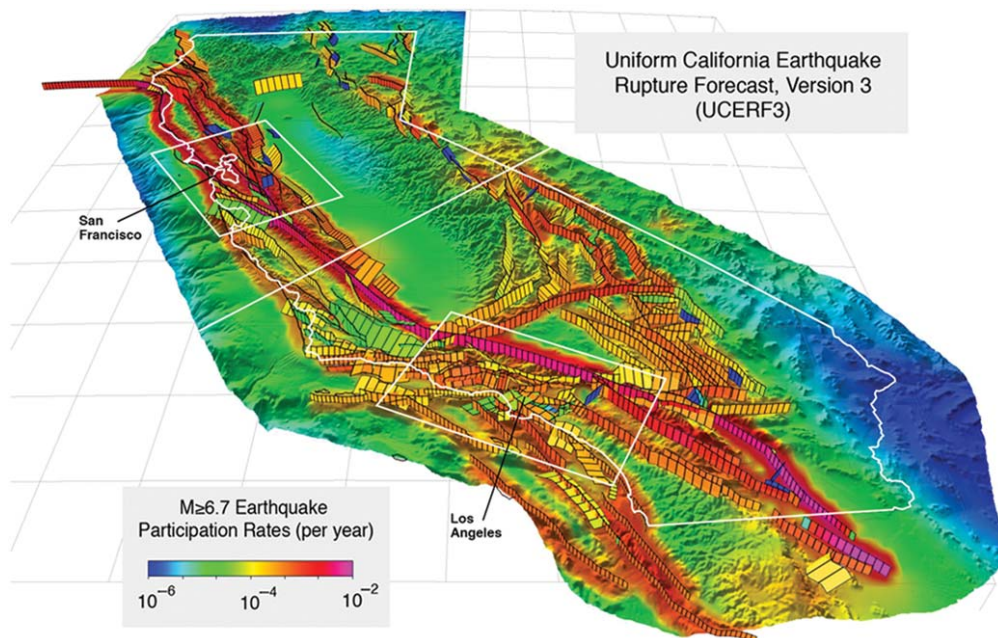


Figure 2.9. Fault model for the Uniform California Earthquake Rupture Forecast version 3 (UCERF-3). Black rectangles depict the fault sections considered in the model, and colors the annual participation rates for magnitudes $M \geq 6.7$. Figure from Field et al. (2014), used with permission from the Seismological Society of America under the STM Permissions Guidelines.

2.2 Geological and tectonic setting

The study area of this thesis is focused on the eastern part of the Betic Cordillera, southeastern Spain, which is one of the most seismically active regions of the Iberian Peninsula absorbing an important part of the NNW-SSE convergence between the Africa and Eurasia (4-6 mm/yr; DeMets et al., 2015). This Cordillera is part of an arc-shaped subduction-related orogenic belt linked with the Rif and Tell ranges in the North African

coast through the Gibraltar arc (Figure 2.10A) (Platt and Vissers, 1989). This orogen was formed in the context of slow convergence between the African and Iberian plates from late Cretaceous to the present (Dercourt et al., 1986; Dewey et al., 1989; Rosenbaum et al., 2002; Vergés and Fernández, 2012). The Betic Cordillera comprises two main geological domains: the Internal Zones, where the present study is located, and the External Zones (Figure 2.10). The Internal Zones are mainly composed by Paleozoic and lower Mesozoic rocks with variable metamorphic degrees, stacked in three main tectonic complexes (Nevadofilábride, Alpujárride and Maláguide) (Egeler and Simon, 1969; Aldaya, 1970; Goffe et al., 1989; Lonergan, 1993; Azañón and Goffé, 1997; Rodríguez-Cañero et al., 2018; Santamaría-López and Sanz de Galdeano, 2018). The External Zones, are formed by the Subbetic and Prebetic units, composed by deformed but non-metamorphic Mesozoic and Cenozoic rocks of the Iberian cover (e.g., García-Hernández et al., 1980). From the late Oligocene and during the Neogene, backarc extension coeval with compression occurred in the Betics, causing the exhumation of the Internal Zones along with the formation of the Alborán Basin and several other intra-montane basins controlled by the activity of normal faults (Rodríguez-Fernández et al., 2012). Some of these Neogene basins correspond to the Fortuna and Lorca basins (Figure 2.10B and Figure 2.11B), located in the study area of this thesis (see section 2.2.2). The origin, timing and evolution of the Neogene extension has been extensively debated due to the many different models proposed to date (e.g., Faccenna et al., 2004; Spakman and Wortel, 2004; Jolivet et al., 2009; Vergés and Fernández, 2012; Do Couto et al., 2016).

In the Betics, the onset of the neotectonic activity under the nowadays NNW-SSE compressional transpressive regime occurred during the Late Miocene-early Pliocene due to a shift of the compressional stress field from the convergence (e.g., Meijninger and Vissers, 2006; Rodríguez-Fernández et al., 2012). According to Calais et al. (2003), the convergence vector has changed since ~3 Ma with a 20° counter-clockwise rotation, which might have implied a 25% decrease in the convergence rates with respect to the start of the neotectonic activity. The transpressive regime caused the tectonic inversion of the extensional intramontane basins formed during the Neogene, and thus the reactivation of normal faults as sinistral-reverse faults. During this period, new NE-SW strike-slip faults also formed together with structures related to the sinistral motion, such as pull apart basins and pressure ridges (Montenat, 1973; De Larouzière et al., 1988; Montenat and Ott D'Estevou, 1999; Meijninger and Vissers, 2006; Rodríguez-Fernández

et al., 2012) (Figure 2.11). The main active faults of the Betic Cordillera are located in the Internal Zones, in the southeastern margin. One of the most prominent and active regions there is the Eastern Betics Shear Zone (EBSZ) (Bousquet, 1979; De Larouzière et al., 1988; Sanz de Galdeano et al., 2019), which is the focus of the present study.

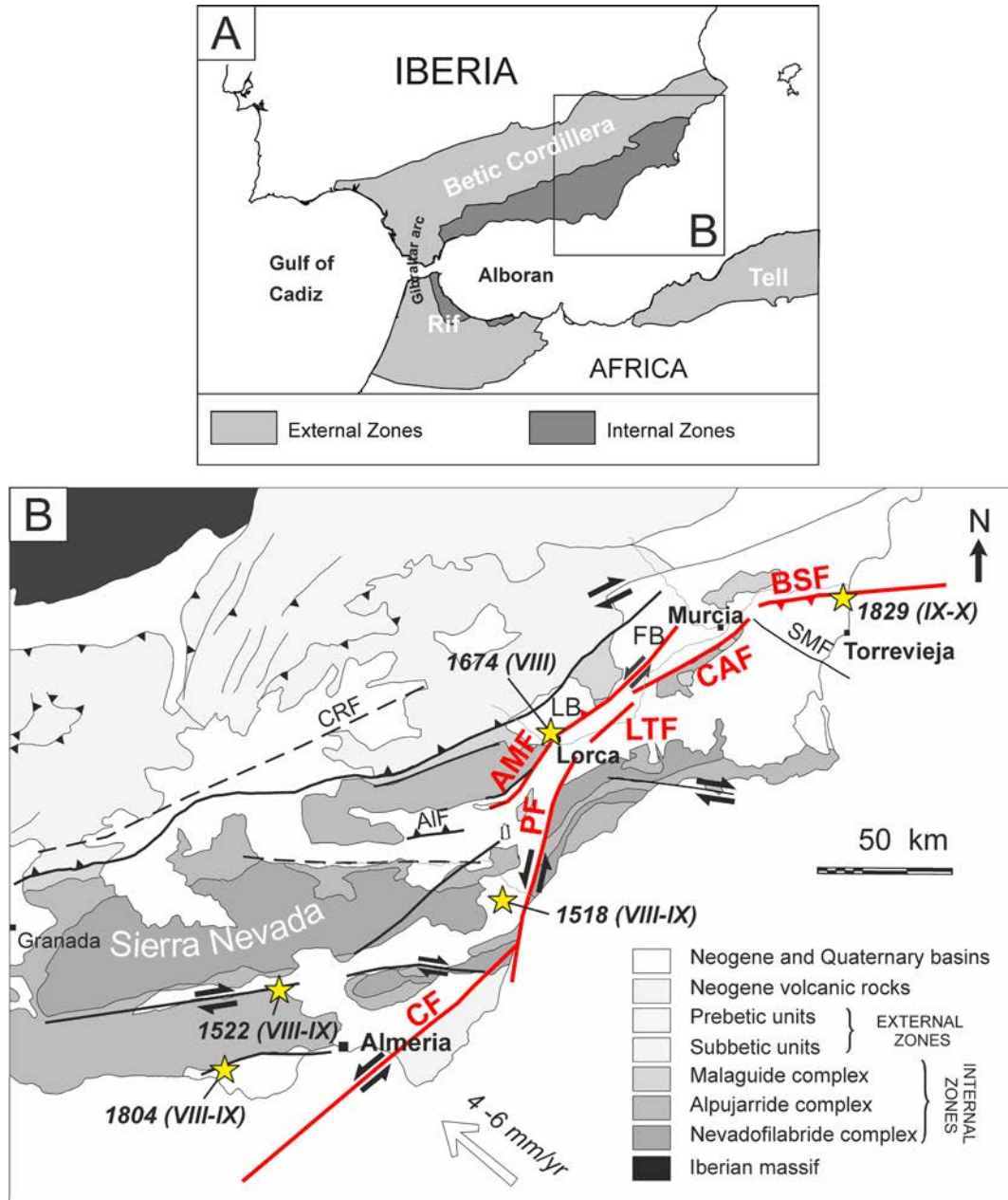


Figure 2.10. A) Location of the Eastern Betics within the Betic Cordillera. Modified from Masana et al. (2018). B) Principal geological complexes conforming the Eastern Betics and main active faults depicted with solid lines. The faults of the Eastern Betics Shear Zone are highlighted in red and the most relevant historical earthquakes with a yellow star. Event intensities refer to the European Macroseismic Scale (EMS98). CF: Carboneras Fault; PF: Palomares Fault; AMF: Alhama de Murcia Fault; LTF: Los Tollos Fault; CAF: Carrascoy Fault; BSF: Bajo Segura Fault; AIF: Albox Fault; CRF: Crevillente Fault; SMF: San Miguel de Salinas Fault; LB: Lorca Basin; FB: Fortuna Basin. Modified from Ortuño et al. (2012), with permission from the authors. Units are based on the geological map of Spain (1:50000) (Marín-Lechado et al., 2011).

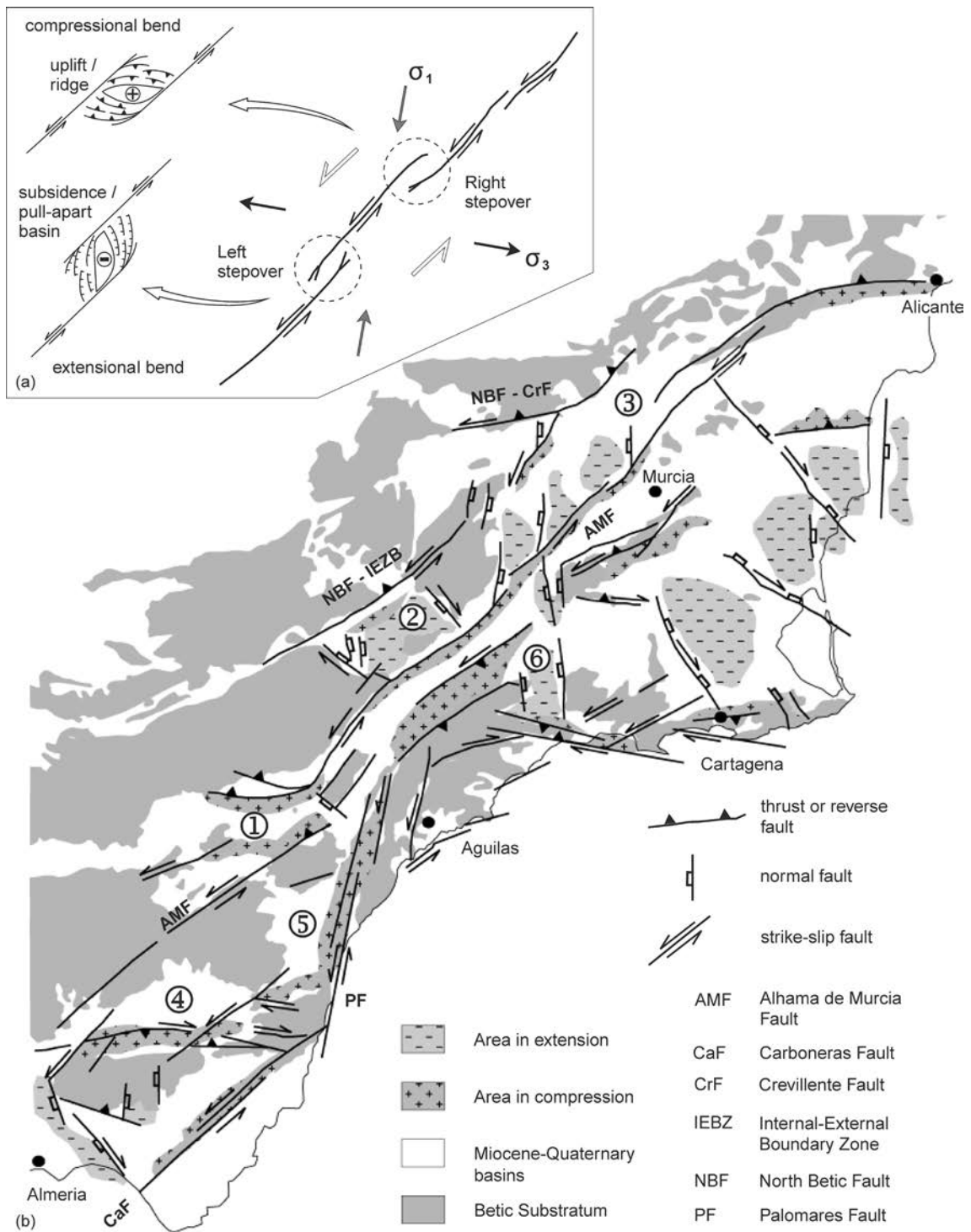


Figure 2.11. A) Sketch of the structures formed on non-coplanar fault strands in a sinistral shear context similar to the Eastern Betics. Releasing stepovers form extension and subsidence (pull-apart basins), while restraining stepovers form compression and uplift (pressure ridges). **B)** Tectonic map of Eastern Betics with the main faults and Neogene intramontane basins indicated by numbers. After Montenat et al. (1987). 1: Huerca-Overa Basin, 2: Lorca Basin, 3: Fortuna Basin, 4: Sorbas Basin, 5: Vera Basin, 6: Hinojar-Mazarrón Basin. Figure from Meijninger and Vissers (2006), used with permission from John Wiley and Sons.

2.2.1 The Eastern Betics Shear Zone

The Eastern Betics Shear Zone (EBSZ) is a ~400 km long transpressive tectonic corridor of mainly oblique reverse and left-lateral strike-slip kinematics with a characteristic NE-SW sigmoidal trend (Bousquet, 1979; De Larouzière et al., 1988; Silva et al., 1993). It accommodates most part of the convergence rate from the Eurasia and Nubian plates in the southeastern margin of the Iberian Peninsula (Masana et al., 2004). Based on geodetic data from Echeverria et al. (2013), 1-3 mm/yr of the total 4-6 mm/yr of convergence shortening are accommodated in the Eastern Betics, while according to Serpelloni et al. (2007) this is within the range of 1.6 - 2.7 (± 0.6) mm/yr.

Although the EBSZ is a moderate seismicity region with rates lower than other European regions (as Italy or Greece), many destructive earthquakes with intensities up to IX-X (IEMS98) have affected this region since historical times (e.g., 1518 VIII-IX Vera, 1522 VIII-IX Almería, 1674 VIII Lorca, 1804 VIII-IX Dalías-Berja, 1829 IX-X Torreveja; (Mezcua, 1982; Martínez Solares, 2003; Silva et al., 2014). More recently, moderate magnitude earthquakes have taken place (e.g., 1993-1994 Adra; the 1999 Mw 4.8 Mula, 2002 Mw 5.0 Bullas; the 2005 Mw 4.8 La Paca seismic series; Rodríguez-Escudero et al., 2014), including the damaging 2011 Mw 5.2 Lorca earthquake (e.g., Martínez-Díaz et al., 2012a).

Some of the damaging earthquakes in the area have been related to the main active faults of the system, which from SW to NE are (Figure 2.10B): Carboneras Fault (CF), Palomares Fault (PF), Los Tollos Fault (LTF), Alhama de Murcia Fault (AMF), Carrascoy Fault (CAF) and Bajo Segura Fault (BSF) (Bousquet, 1979; De Larouzière et al., 1988; Silva et al., 1993; Insua-Arévalo et al., 2015), along with other important faults such as the Crevillente (CrF), Albox (AlF) and San Miguel de Salinas (SMF) (Figure 2.10B). The 1518 Vera earthquake has been attributed to PF (e.g., García-Mayordomo, 2005), the 1522 Almería earthquake to CF (e.g., Reicherter and Hübscher, 2007), the 1674 Lorca earthquake to AMF (Martínez-Díaz et al., 2018), the 1829 Torreveja earthquake to BSF (e.g., Alfaro et al., 2012) or, in recent times, the 2011 Lorca earthquake to AMF (Martínez-Díaz et al., 2012a) (Figure 2.10B). Some of these historical earthquakes are known to have ruptured the surface, as recently unveiled for the 1674 Lorca earthquake (Martínez-Díaz et al., 2018). Importantly, most of the instrumental seismicity in the EBSZ occurs relatively at shallow depths (<15 km) and focal mechanisms are consistent with the strike-slip and reverse character of the main faults (Stich et al., 2007, 2010).

Paleoseismic and geomorphological studies have demonstrated the capability of the system to generate large magnitude earthquakes ($M_w > 6.0$) and allowed to constrain critical seismic parameters (slip rate) in several of the main faults: AMF, CF, CAF or LTF. The current slip rate estimates range between 1.0 and 1.7 mm/yr for the central and southwestern segments of AMF, as summarized by Ferrater et al. (2017); 1.0 and 1.3 mm/yr for CF (Moreno, 2011); 0.37 ± 0.08 mm/yr for CAF (Martín-Banda et al., 2015) and 0.12 to 0.17 mm/yr for LTF (Insua-Arévalo et al., 2015). Conversely, PF, BSF and the northeastern termination of AMF have not been studied using detailed paleoseismic trenching analysis and their slip rate estimations are based mainly on long-term displacements of geological markers (e.g., Herrero-Barbero et al., 2020), which may be affected by larger uncertainties. See section 2.3.1 for details on the paleoseismic literature background developed in the EBSZ.

Continued tectonic activity in the EBSZ is also inferred from the current geodetic data, from the CuaTeNeo GPS network in the central and southwestern sectors of the system (Echeverria et al., 2013, 2015) and in the northeastern ones (Borque et al., 2019). The obtained velocities of AMF-PF combined (1.5 ± 0.3 ; Echeverria et al., 2013) are consistent with the paleoseismic and geomorphologic slip rates of AMF, suggesting a main role of this fault into the overall deformation. Similarly, geodetic velocities of CF (1.3 ± 0.2 mm/yr; Echeverria et al., 2015) are in agreement with its geological slip rates (1.1-1.3 mm/yr; Moreno, 2011). In the northeastern end of the EBSZ GPS data indicates a partitioning of the deformation into lateral and reverse components, and compatibility with the kinematics of CAF and BSF, respectively (Borque et al., 2019).

2.2.2 The Alhama de Murcia Fault

The Alhama de Murcia Fault (AMF) is a ~87 km long reverse-strike slip kinematics with a SW-NE orientation and it is one of the largest faults within the EBSZ (Montenat, 1973; Bousquet, 1979; Silva et al., 1993; Martínez-Díaz, 1998) (Figure 2.12). The AMF is an active and seismogenic fault with associated damaging historical earthquakes. According to Martínez-Díaz et al. (2018) at least eight earthquakes with intensities $I_{EMS} > VI$ have been located less than 10 km from the AMF since the sixteenth century, causing important damage in the nearby cities. Some of these are the 1908 and 1910 I_{EMS} VI earthquakes in Alcantarilla, the 1907 I_{EMS} VII in Totana or the 1579 I_{EMS} VII, 1818 I_{EMS} VI-VII and 1674 I_{EMS} VIII in Lorca (Martínez-Díaz et al., 2018) (Figure 2.12B). In more recent times, the AMF has caused several moderate magnitude earthquakes (e.g., 1977 M_w 4.2

earthquake near Lorca), among which the 2011 Mw 5.2 Lorca earthquake stands out. So far, it is the most damaging earthquake in Spain for the last 50 years, which caused nine deaths, extensive damage across the city of Lorca and losses over 1200 million euros (Martínez-Díaz et al., 2012b).

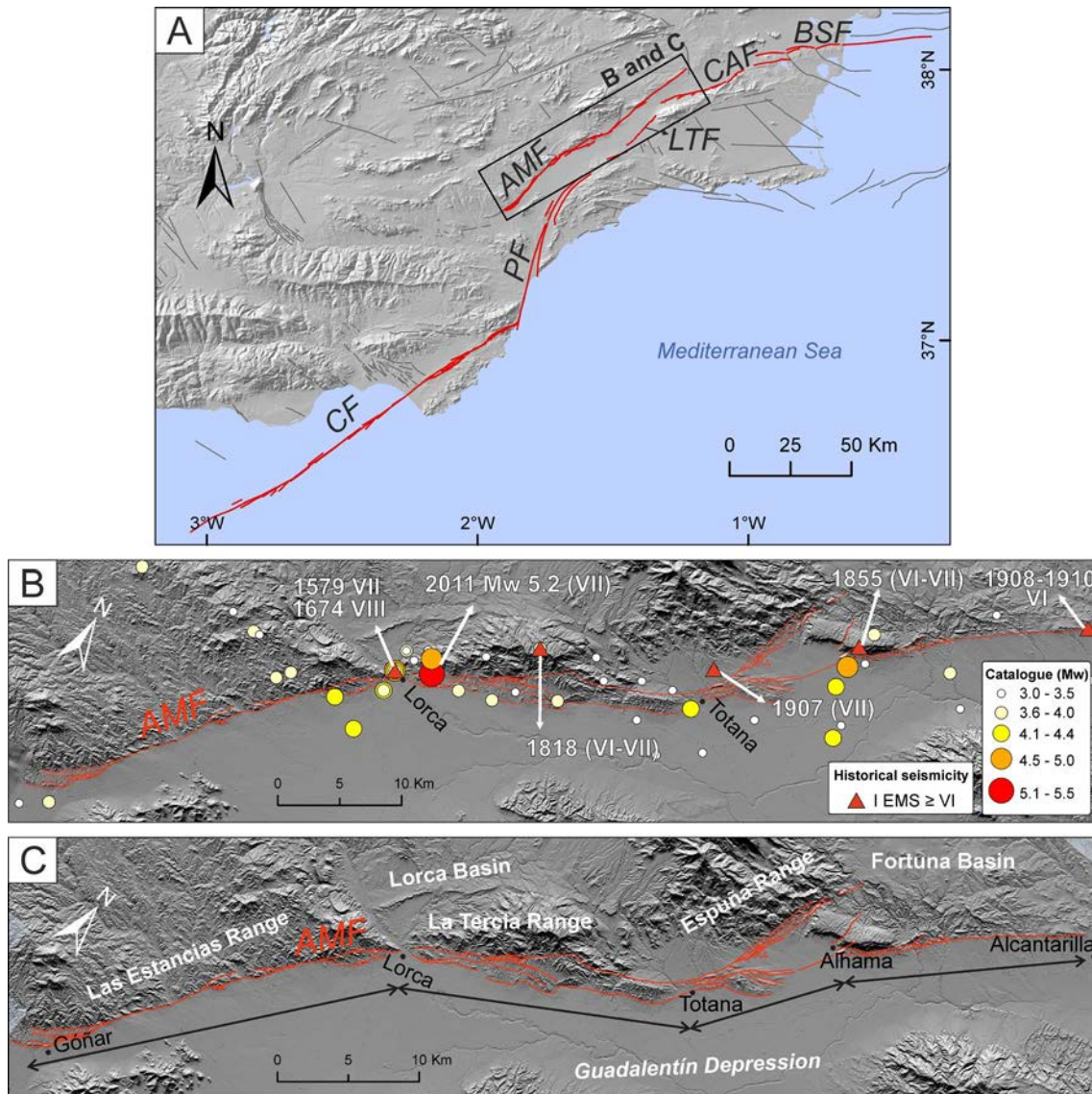


Figure 2.12. A) Main faults of the Eastern Betic Shear Zone (EBSZ). Acronyms defined in the footnote of Figure 2.10 and throughout the text. The area from figures B and C is indicated. B) Instrumental ($M_w \geq 3.0$) and historical ($I_{EMS} \geq VI$) seismicity around the Alhama de Murcia Fault (AMF). Main earthquakes referred in the text are pointed out by arrows. Seismicity extracted from the catalogue by IGN-UPM (2013). C) Main geological features along the AMF and main segments extracted from Martínez-Díaz et al (2012b). The hillshaded relief in figure A is from the WMS service by IGN (<https://servicios.idee.es/wmts/mdt>). The relief in figures B and C is obtained from the LiDAR-based 2 m DEM of the IGN agency (MDT02; <https://centrodedescargas.cnig.es>).

The AMF has been active under the current transpressive regime since the Late Miocene, when the onset of the Eurasia and Nubia convergence caused the tectonic inversion of the extensional structures limiting Neogene basins to the NW (e.g., Lorca and Fortuna basins). The AMF is interpreted as an inherited and re-activated structure from this extensional period (Montenat et al., 1987; Martínez-Díaz, 1998; Meijninger and Vissers, 2006; Herrero-Barbero et al., 2020). Nowadays, the materials of the Lorca and Fortuna basins are uplifted by the AMF in its hanging-wall (to the NW) forming a series of prominent ranges along the trace, i.e., Las Estancias, La Tercia and Espuña ranges (Figure 2.12C). These are formed by Paleozoic metamorphic rocks from the Internal Zones of the Betic Cordillera (Alpujarride and Maláguide complexes) and Neogene materials from the Lorca Basin. Conversely to the SE of the AMF (footwall), the pre-inversion relief that fed the northwestern basins is nowadays the Guadalentín Depression, where most part of the Quaternary sedimentation takes place (Silva et al., 1993; Martínez-Díaz, 1998).

The uplift of the ranges limited by the AMF enhanced the formation of alluvial and fluvio-alluvial deposits coming from the syn-tectonic denudation of the generated reliefs (Silva, 1994; Martínez-Díaz, 1998). These deposits are displayed in series of alluvial fan generations extending from the faulted mountain front towards the Guadalentín Depression, except for the southernmost part, in which the alluvial systems drain towards Almería. The alluvial fans range in age from the Middle Pleistocene to the Holocene whose disposition is affected by a combination of tectonic activity and climate (Silva, 1994; Martínez-Díaz et al., 2003). At least three alluvial fan generations and their inferred evolution are described in the Guadalentín Depression by Silva et al. (1992) and revised in Silva (2014) (Figure 2.13):

The first generation is from the Middle Pleistocene (dates from Ortuño et al., 2012; Sohbaty et al., 2012, in Silva, 2014) and formed by cemented debris-flow and sheet flow conglomerates with thick calcrete developments on top. This generation is deposited in proximal offlap, meaning that the strata is successively deposited towards the center of the basin, but still close to the mountain front. The second generation, Middle to Late Pleistocene in age, is formed by debris flow deposits as well as gravel and sands, forming a proximal onlap and backfilling, i.e., the apex of the sedimentation progressively migrates towards the mountain front (Figure 2.13). The third generation is from the Late Pleistocene to Early Holocene (based on paleoseismic data; e.g., Masana et al., 2004; Ortuño et al., 2012). It is composed by sheet flow deposits entrenched in the previous

generations and in a distal aggradation arrangement, meaning that the sedimentation is found further from the mountain front and towards the Guadalentín Depression.

According to Silva (2014), 85% of the uplift in the mountain fronts limited by the AMF in the Guadalentín Depression was accommodated during the Pliocene and Early Pleistocene, while the remaining 15% happened during the Middle Pleistocene in a dominantly strike-slip regime. From the late Pleistocene, the author proposes that the alluvial evolution was mainly controlled by climate, where the transition to arid conditions favored the entrenchment and progradation of fans towards the center of the basin. In addition, changes in the base level of the Guadalentín river during the Holocene might have also favored the entrenchment of the alluvial channels by headward erosion (Calmel-Avila, 2002).

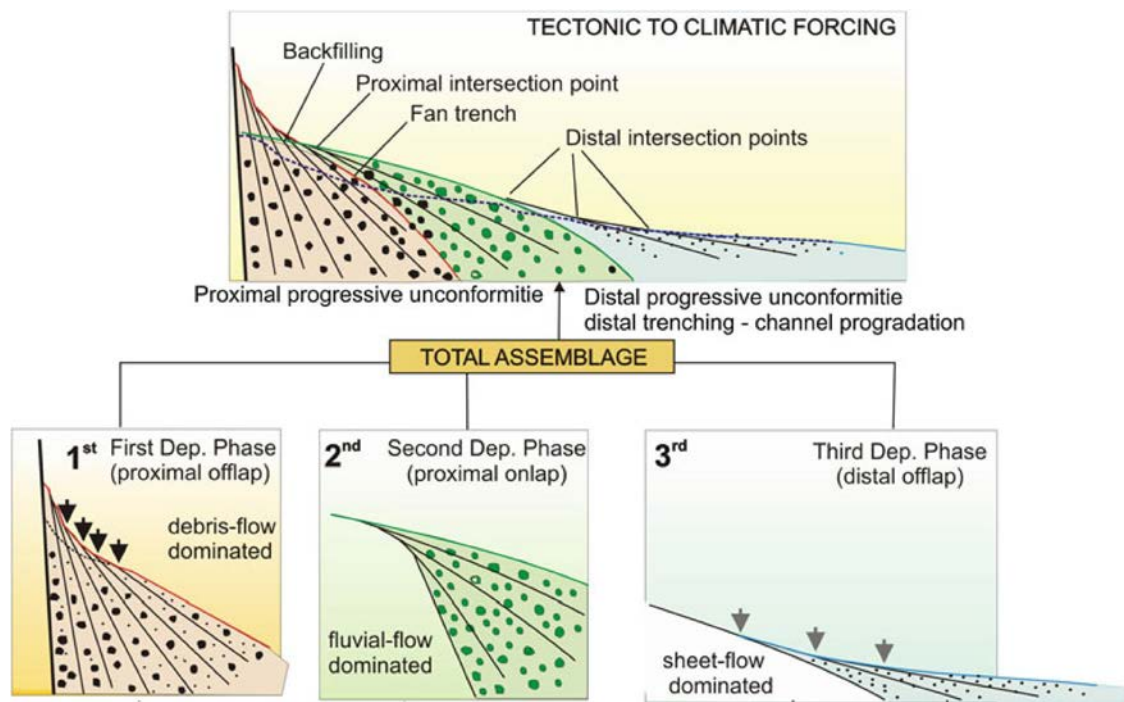


Figure 2.13. Alluvial fan phases or generations recognized along the margins of the Guadalentín Depression. Figure adapted from Silva (2014), used with permission from Springer.

2.2.2.1 Geomorphic expression and seismogenic nature

Along the trace of the AMF, many geomorphic and tectonic features can be identified, which allow to recognize its location and related deformation. Some of the main features are for instance fault lineations, scarps, drainage channel deflections (Figure 2.14), wind gaps (i.e., valleys disconnected from the drainage system by fault movement), among others (Martínez-Díaz et al., 2003; Masana et al., 2004; Ferrater et al., 2015a, 2015b). In

addition, paleoseismic and morphotectonic investigations in this fault, mentioned in section 2.3.1 and detailed in the introduction of section 5, have allowed to demonstrate i) the pre-historic seismic activity of the fault, ii) the recurrent occurrence of morphogenetic earthquakes, and to iii) constrain earthquake sequences and fault parameters. These studies prove that the AMF is one of the most active faults in the EBSZ.

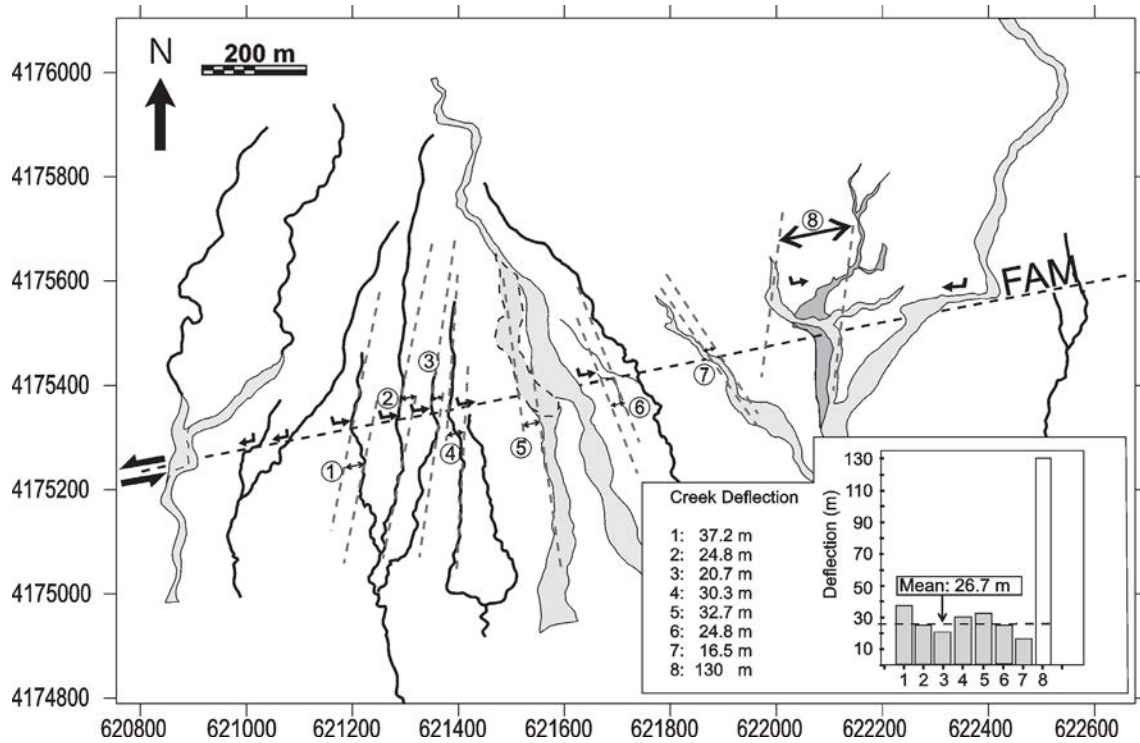


Figure 2.14. Left-lateral channel deflections generated by the Alhama de Murcia Fault (AMF) and measured through a morphotectonic analysis. The mean displacement of all the channels is 26.7 m, which is the mean values of the measurements 1 to 7 (grey bars in the histogram). Figure adapted from Martínez-Díaz et al. (2003), used with permission from the authors.

Based on the geomorphological expression, fault orientation and seismicity, among others, the AMF is divided in four segments (Silva, 1994; Martínez-Díaz et al., 2012b) named after the cities located in each end (Figure 2.12C). From SW to NE: Góñar-Lorca, Lorca-Totana, Totana-Alhama and Alhama-Alcantarilla. The two first segments are the ones with the most marked surface expression and, for this reason, have accumulated most part of the paleoseismic and morphotectonic studies (see section 2.3.1). The Góñar-Lorca segment is characterized by a rather narrow fault zone limiting the Las Estancias range to the NW and terminates with a horse-tail splay in the southwestern tip (Silva et al., 1992a; Ortuño et al., 2012). The Lorca-Totana segment limits the La Tercia range and is formed by several subparallel fault branches, at least three according to Ferrater (2016)

in a wider (>2km) deformation zone. The Totana-Alhama segment shows several subparallel branches and forming a splay with NNE-SSW oriented faults limiting the Espuña range (Martínez-Díaz et al., 2012b). The Alhama-Alcantarilla segment is characterized by a narrow fault zone with a decreasing geomorphological expression towards the NE. In this latter zone, the main deformation is interpreted to be transferred to the neighbouring Carrascoy Fault (Martínez-Díaz, 2002; Herrero-Barbero et al., 2020).

2.3 Background

This section summarizes the literature background of paleoseismic and seismic hazard studies focused in the EBSZ over the last years and the current state of the art upon which the present thesis is developed.

2.3.1 Paleoseismic studies of the Eastern Betics Shear Zone

Most part of the paleoseismic studies in Spain have focused on the faults of the southeastern margin of the Iberian Peninsula due to the relatively moderate seismicity compared to other regions of the country. In this context, the main studies have focused on the Eastern margin of the Betic Cordillera, in the Eastern Betics Shear Zone (EBSZ), with a marked increment since the 2011 Mw 5.2 Lorca earthquake. Figure 2.15 depicts the main paleoseismic studies in the different EBSZ faults during the last decades.

The first works on active tectonics started in the 1990s and were mainly focused on studying the main tectonic features and evolution of the central-eastern part of the Murcia region, mainly the Guadalentín Depression and also the southern part of Almería (Silva et al., 1993; Silva, 1994; Martínez-Díaz, 1998). In such studies, the main active faults of the region were recognized and characterized from a geomorphological and tectonic perspective, some of them even identifying evidence of paleoearthquakes (Silva et al., 1997 in the Palomares Fault). However, no direct characterization of fault parameters such as slip rates or recurrences was proposed until the start of the 2000s, where paleoseismic approaches started to be implemented in southeastern Spain, including trenching. The first study in this matter was in the Alhama de Murcia Fault (AMF), in which a structural folding analysis in the Carraclaca site (NE of Lorca city; see section 5) combined with U-Th dating, allowed to infer the first slip rates and recurrence intervals of the fault (Martínez-Díaz and Hernández-Enrile, 2001). In the following years Martínez-Díaz et al. (2003) and Masana et al. (2004) performed the first trenching surveys in Quaternary alluvial fan deposits affected by the AMF. Such studies allowed to identify

the first reliable paleoearthquake sequence of at least three paleoearthquakes for the last 27 ka with a recurrence of 14 kyr, and the first short-term net slip rates (0.07-0.6 mm/yr).

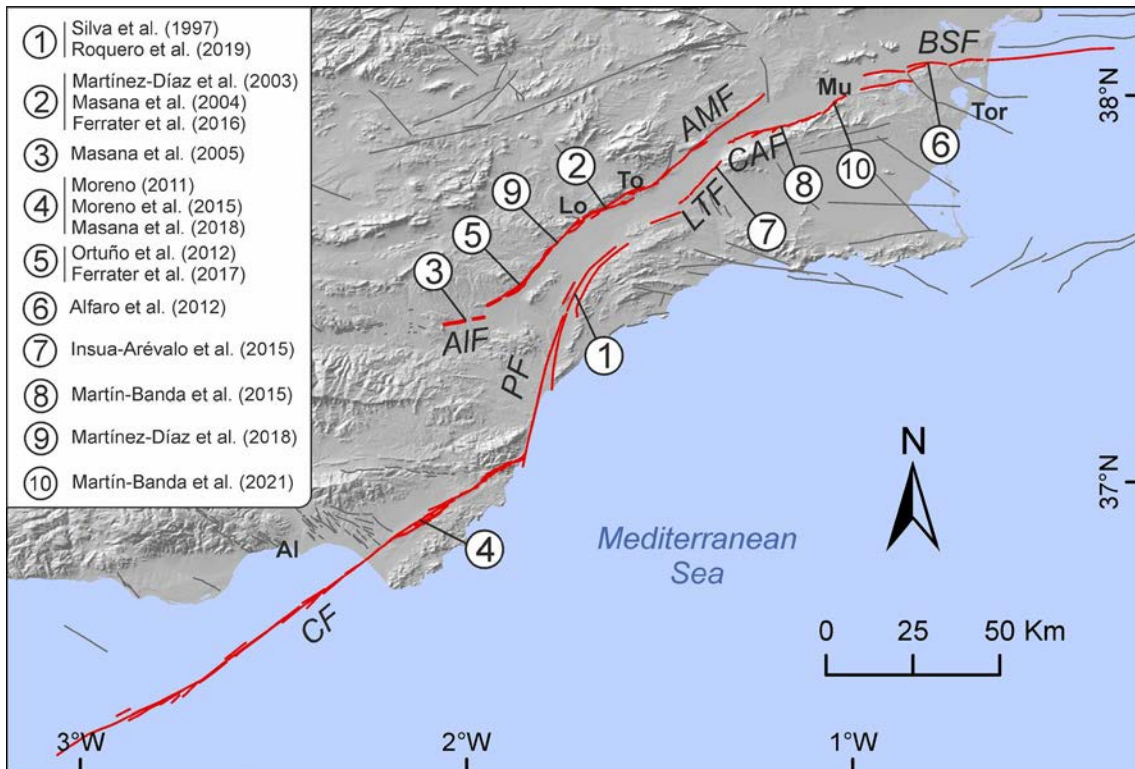


Figure 2.15. Location of all the paleoseismic studies developed within the Eastern Betic Shear Zone. Each number indicates the sites studied along a fault and in the legend the studies developed in that site. The numbers are ordered by the year of the first study developed per site. Al: Almería; Lo: Lorca; To: Totana; Mu: Murcia; Tor: Torreveja. Fault acronyms can be found in the footnote of Figure 2.10. The relief is from the WMS service by IGN (<https://servicios.idee.es/wmts/mdt>). Fault traces are from the QAFI database (IGME, 2015a).

The following years led to the development of more paleoseismic trench studies in the AMF, specifically in the southwestern termination and prolongation. The first one was located in the Albox Fault (Masana et al., 2005) (Figure 2.15) where two paleoearthquakes were identified, one previous to 650 AD and another one afterwards, and a slip rate of 0.01-0.04 mm/yr was inferred. Nearby, in the 2010s, Ortuño et al. (2012) applied a comprehensive paleoseismic study across different fault branches to obtain more representative fault parameters in the southwestern horse-tail termination of the AMF. A minimum of six paleoearthquakes were interpreted with a recurrence of 29 kyr, a net slip rate of 0.16-0.24 mm/yr (based on Late Pleistocene markers) and a strike-slip rate of 0.95-1.37 mm/yr (based in Quaternary geomorphological markers). Recently, in the same termination, Ferrater et al. (2017) applied a morphotectonic analysis in deflected drainage channels to obtain long-term slip rates. A slip rate of 1.6-1.7 mm/yr was obtained

for the past 200 ka, which is the highest slip rate for a fault in southeastern Spain to date. At the opposite tip of this segment, at La Torrecilla site (site 9 in Figure 2.15, Martínez-Díaz et al. (2018)), identified a historical surface rupture, attributed to the 1674 Lorca earthquake. This is the only evidence of a historical surface rupture in the EBSZ.

The latest paleoseismic study in the AMF was done in a fault branch of the Lorca-Totana segment by Ferrater et al. (2016). A 3D trenching approach was carried out in the same site than the trenches by Masana et al. (2004) to obtain reliable lateral slip rate estimations. A lateral and net slip rate of 0.9 ± 0.1 mm/yr for the last 20 ka was inferred, additionally to a long paleoearthquake sequence of at least ten events with a maximum recurrence of 5.1 kyr for the last 25 ka. The geological slip rate of this segment of AMF is consistent with the geodetic strike-slip rates (1.5 ± 0.3 mm/yr) inferred for the AMF and PF together in a transect near Lorca city (Echeverria et al., 2013) and suggests that the former might be absorbing most part of the deformation nowadays. More recent studies in the AMF have focused in a structural restoration analysis of the Alhama-Alcantarilla segment from seismic profiles to obtain long-term slip rates (maximum of $0.32^{+0.18}/_{-0.13}$ mm/yr for the last 4.8-7.6 Ma) (Herrero-Barbero et al., 2020).

In other faults of the EBSZ, the first paleoseismic studies focused on the CF, where 3D trenching along with geomorphological analysis onshore and offshore allowed to infer slip rates of ~ 1.1 - 1.3 mm/yr since 110.3 ka (Moreno, 2011; Moreno et al., 2015) and seven paleoearthquakes since 191 ka, inferring a maximum recurrence of 27.3 kyr. More recent studies in this fault (Masana et al., 2018) allowed to characterize the paleoearthquake sequence in other sites. The geological slip rates of the CF are almost identical to the geodetic strike slip rates (Echeverria et al., 2015), suggesting a constant slip behavior at least since ~ 110.3 ka.

Throughout the rest of the EBSZ, several paleoseismic studies developed after the 2011 Mw 5.2 Lorca earthquake (Figure 2.15) because the underestimation of the previous hazard assessments evidenced by this earthquake made clear the need to better characterize active faults, not only in the AMF. Martín-Banda et al. (2015) studied the southwestern segment of the CAF inferring a slip rate of 0.37 ± 0.08 mm/yr and identifying nine to eleven paleoearthquakes since 30.2 ka with a recurrence of 3.3 ± 0.7 kyr. In this same fault, in the northeastern segment, Martín-Banda et al. (2021) obtained a slip rate of 0.49 ± 0.02 mm/yr for the last ~ 125 ka and characterize the slip rate variations of the last 210 ka with the presence of super-cycles. Contemporarily, Insua-Arévalo et al. (2015)

characterize LTF in the connexion zone between the PF and CAF as a lately formed structure within the EBSZ, inferring slip rates of 0.12-0.17 mm/yr and a recurrence of 2.2-6.9 kyr. In this connexion zone other compressive active structures have been identified, although their detailed paleoseismic characterization is pending (Insua-Arévalo et al., 2018). Recently, Roquero et al. (2019) focused their study on the paleoearthquake identification in the northern part of the PF, one of the less studied ones in the EBSZ, although the lack of numerical dates prevented a precise age constraining and obtention of parameters for the hazard assessments (slip rates and recurrences).

To northeastern end of the EBSZ, in the BSF, Alfaro et al. (2012) integrate geological, geomorphological and geodetic data to calculate slip rates between 0.2-0.4 mm/yr and recurrence intervals between 4.5 and 21.5 kyr, while Perea et al., (2012) characterize the active tectonics structures of this fault offshore. The onshore data is in agreement with geodetic slip rates for the BSF: 0.2-0.7 (± 0.2) mm/yr (Borque et al., 2019).

2.3.2 Seismic hazard studies of southeastern Spain

The seismic hazard studies in the Iberian Peninsula have traditionally put emphasis in the SE given the known seismic activity and the occurrence of several damaging earthquakes, explained in the previous section, although no specific ones have focused on the study of the EBSZ alone. The first probabilistic (PSHA) studies considering the SE of Spain, applied either the Gumbel distribution (e.g., Martín-Martín, 1983; Roca et al., 1984) or considered the poissonian zonified models of Cornell (1968) based on the McGuire (1976) approach (e.g., Martín-Martín, 1983, 1989; Muñoz et al., 1984).

To this latter group belongs the 1991 Spanish seismic hazard map (IGN, 1991), upon which the NCSE-94 building code was based on (cf. García-Mayordomo, 2005). The same zonification model and methodology was used for the last building code (NCSE-02, 2002), only updating the seismic catalogue. In these studies, the seismic zonifications were based on the seismicity from the catalogue but mainly using intensity because it was the most reliable parameter for the historical earthquakes. From the 1990s, zoned approaches became extensively used to model the sources in seismic hazard studies in southeastern Spain, each of them proposing different zonification models (e.g., López-Casado et al., 1995; Jiménez and García-Fernández, 1999; Giner et al., 2002; Gaspar-Escribano et al., 2008; Benito et al., 2010). Contemporarily, other methodologies were explored in southeastern Spain, mainly using seismicity smoothing and modelling in terms of Arias intensisty (e.g., Peláez and López-Casado, 2002; Peláez et al., 2005,

respectively). This latter measures the earthquake intensity from instrumental records, and reduces the limitations of using empirical intensity scales (Arias, 1970).

Neither of the previous studies considered faults or fault properties for the definition of the seismogenic sources. Therefore, the resulting seismic hazard maps were, in general, highly influenced by the distribution of the previous seismicity. For instance, in the study by Peláez et al. (2005), the hazard maps show the highest hazard values in the regions where the largest historical earthquakes have occurred, even though the authors recognize that the catalogue shows important completeness issues (Figure 2.16 and Figure 2.17).

The first studies including fault data in the SE of Spain appeared in the mid-late 2000s with the publication of the first paleoseismic studies in the EBSZ. Then, the first PSHA studies in this matter incorporated faults of southeastern Spain as sets of independent segments considering either a characteristic earthquake model or a Gutenberg-Richter distribution using the fault dimensions and slip rates (García-Mayordomo, 2005; García-Mayordomo et al., 2007). Despite these studies, for the update of the 2013 Spanish seismic hazard map (Figure 2.18) faults were not included as seismogenic sources because the available fault data was neither representative nor complete for the whole territory, even in the SE (IGN-UPM, 2013). For this reason, several zonification and smoothed source models were applied and explored in a logic tree. One of these models was the one defined by García-Mayordomo et al. (2012) (GM12) and updated in García-Mayordomo (2015) (ZESIS), which considered the EBSZ as an independent source zone defined by the faults traces and their fault plane surface projections.

From the mentioned context it can be stated that the inclusion of faults into PSHA has not been a common practice in southeastern Spain even in recent times. The 2011 Lorca earthquake, however, evidenced the lack of accuracy of the seismic hazard estimations in the area. The earthquake reached PGA values of 0.377g (Alguacil et al., 2014), when the building code (NCSE-02) predicted PGA values of $\sim 0.12g$ for Lorca for the ~ 500 years return period. The earthquake evidenced to the modellers that the inclusion of faults into the hazard estimations was necessary. Thereby, Rivas-Medina (2014) and later Rivas-Medina et al. (2018) performed a comprehensive fault-based PSHA in southeastern Spain, in which proposed a hybrid approach for distributing seismic moment between faults and zones and ensuring that this distribution of seismic potential was not double counted. Their results showed clear control of the faults in the hazard and higher hazard estimations than the previously anticipated (see section 7.6). In such study however, faults were

included as independent sources, able to rupture only within their pre-imposed cartographic limits. So far, no studies in Spain have attempted to relax segmentation to model the occurrence of linked fault ruptures (multi-fault ruptures), despite it has demonstrated to provide more reliable hazard estimations in other regions such as California (Field et al., 2014) or central Italy (Valentini, 2021).

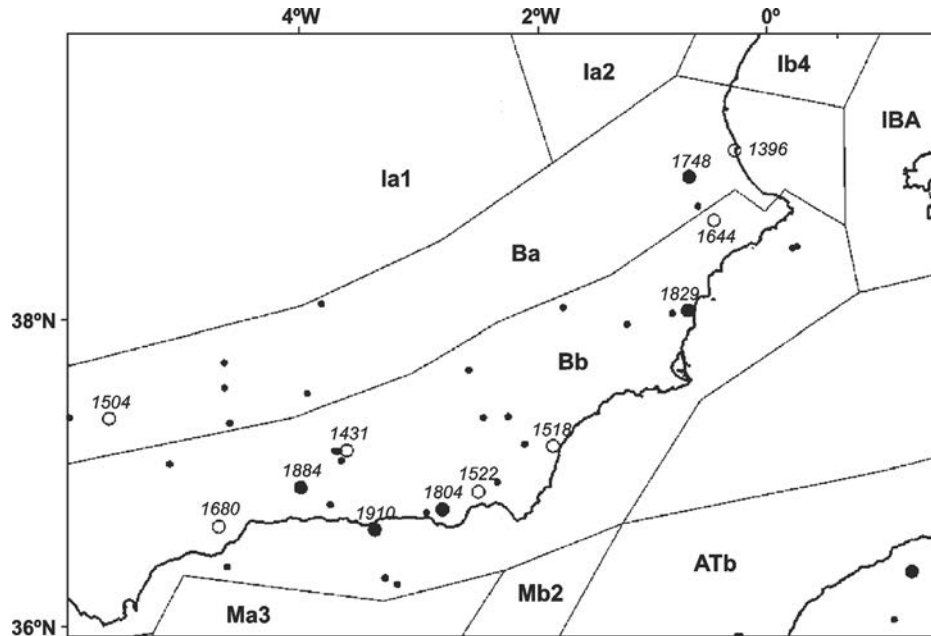


Figure 2.16. Example of seismogenic zoning model of southeastern Spain based on seismicity data. Filled circles represent seismicity since year 1700 AD: small are for M_s 4.5 -5.5 and larger for $M_s \geq 5.5$. Empty circles represent $M \geq 5.5$ since year 1300 AD. Figure from Peláez et al. (2005), used with permission from Elsevier under the STM Permissions Guidelines.

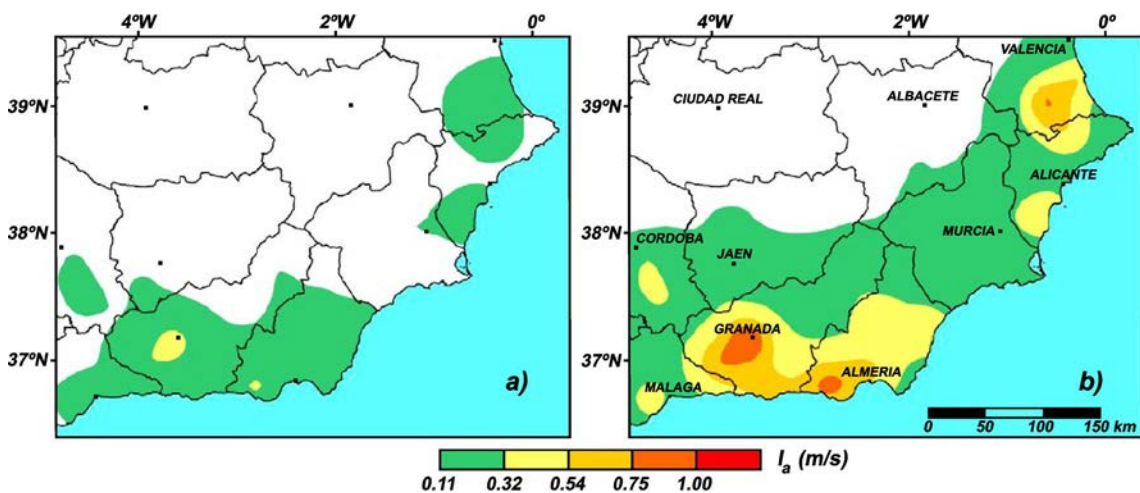


Figure 2.17. Seismic hazard maps in terms of Arias intensity for southeastern Spain in shallow soils and for the 475-year return period. Map **a**) represents the mean value of the attenuation curve, while **b**) represents the mean plus a standard deviation. Note that the highest hazard values are found where the largest earthquakes in the catalogue from Figure 2.16 happened (Granada, Almería or Alicante). Figure from Peláez et al. (2005), used with permission from Elsevier under the STM Permissions Guidelines.

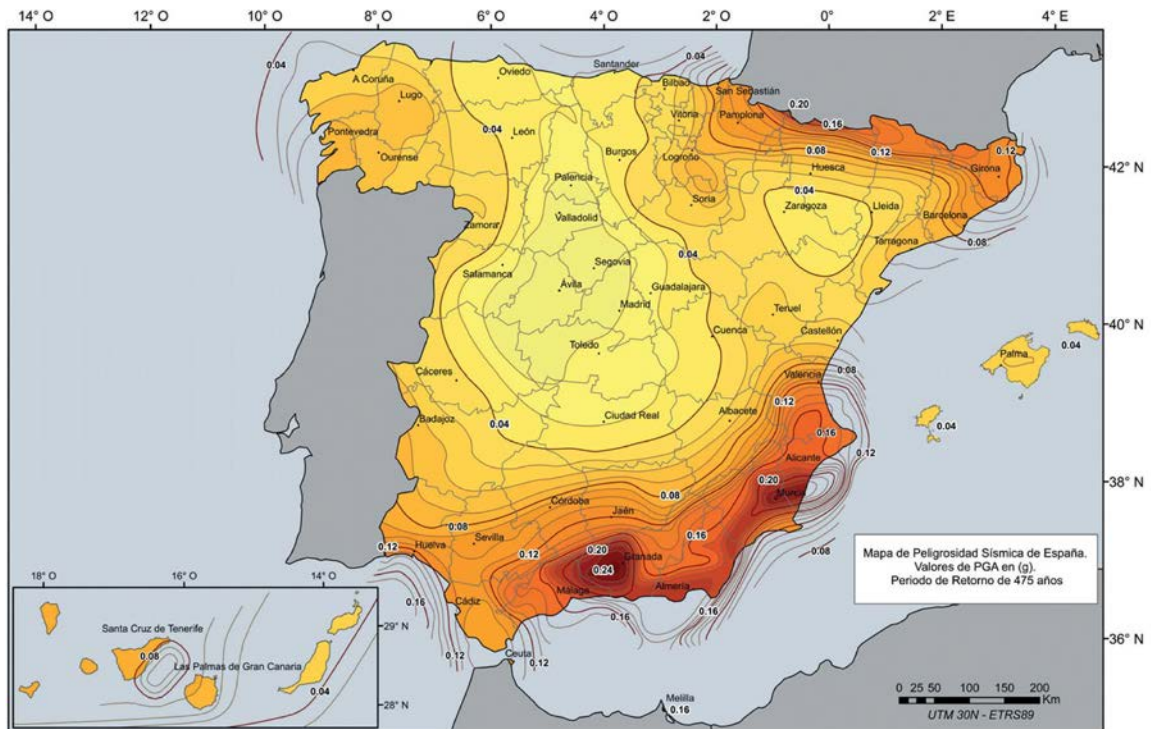


Figure 2.18. Seismic hazard map of Spain in terms of peak ground acceleration (PGA) for the 475-year return period. Figure from IGN-UPM (2013).

II. METHODS

This chapter explains the methods used for the paleoseismic study in the Alhama de Murcia Fault and for the probabilistic seismic hazard assessment of the Eastern Betics Shear Zone using faults as inputs.



View of the Guadalentín Depression from El Roser site.

3 Methods for paleoseismic characterization of the Alhama de Murcia Fault

In this section we explain the main tools used to characterize the different structures related to the Alhama de Murcia Fault (AMF) in the Lorca-Totana segment, quantify their deformation degree, its age and the seismic parameters of the different fault branches: recurrence, slip rates and slip per event. The main steps taken are: a) geomorphological and structural mapping of the central segments of the fault, b) trenching survey, c) modelling of the observed structures and fault displacement measurements, d) numerical dating of the sedimentary units in the trenches, and e) data integration to obtain paleoseismic parameters.

3.1 Geomorphological mapping

A detailed geomorphological and structural mapping was carried out in the Lorca-Totana segment to select the sites for the paleoseismological trenching survey and to recognize the main tectonic structures affecting Quaternary alluvial fans in the area. We also performed a geomorphological mapping in the Totana-Alhama segment of the fault to find potential future sites for paleoseismic studies (section 6 of this thesis). To do so we recognized the landform features related to the activity of faults, based on the descriptions in strike-slip faults by Burbank and Anderson (2011), first described by Wesson et al. (1975) in California. (Figure 2.3 of section 2.1.1). These features refer mainly to fault lineaments, fault scarps, folds, deflected/offset or beheaded drainage channels or sudden changes in drainage incision. We also mapped the different alluvial fan generations affected by the fault's deformation. For the mapping we used:

- 1956-57 USAF aerial photographs (scale 1:33000) for stereographic analysis with a mirror stereoscope.
- Recent orto-images from the PNOA plan (Plan Nacional de Ortofotografía Aérea) of the IGN agency (Instituto Geográfico Nacional) and old orto-images created from the 1956-57 USAF aerial photographs (available at: centrodedescargas.cnig.es).
- A high resolution digital elevation model (DEM) of 0.5 m grid spacing and point densities of 4-8 points/m². This DEM was obtained from airborne LiDAR in a previous project, funded by the Spanish government (SHAKE project: CGL2011-30005-C02-01), especially designed for fault trace cartography. In the areas not covered by the 0.5 m

model, we used a 2m resolution DEM retrieved from the Instituto Geográfico Nacional (IGN) Spanish agency (available at: centrodedescargas.cnig.es) (Figure 3.1). See Annex II (A) for the 0.5 m DEM in the studied regions.

- Spanish Geological Map (GEODE series) and Spanish Geomorphological map, both scale 1:50000, from the Instituto Geológico y Minero de España (IGME agency). The former corresponds to zone 2100 (Marín-Lechado et al., 2011). The latter corresponds to the sheet number 253 (25-38) of the geomorphological map series (Silva et al., 2004).

The fault strands have been classified in three main categories depending on the confidence of its position/location: a) Observed, where the fault has been directly observed or characterized (outcrops, trenches); b) Interpreted, where the fault is interpreted based on strong evidence such as surface scarps, lineaments, facets, etc.; c) Supposed, where the fault is inferred based on the position of other faults from the previous categories or where the context suggests so (e.g., mountain front limits).

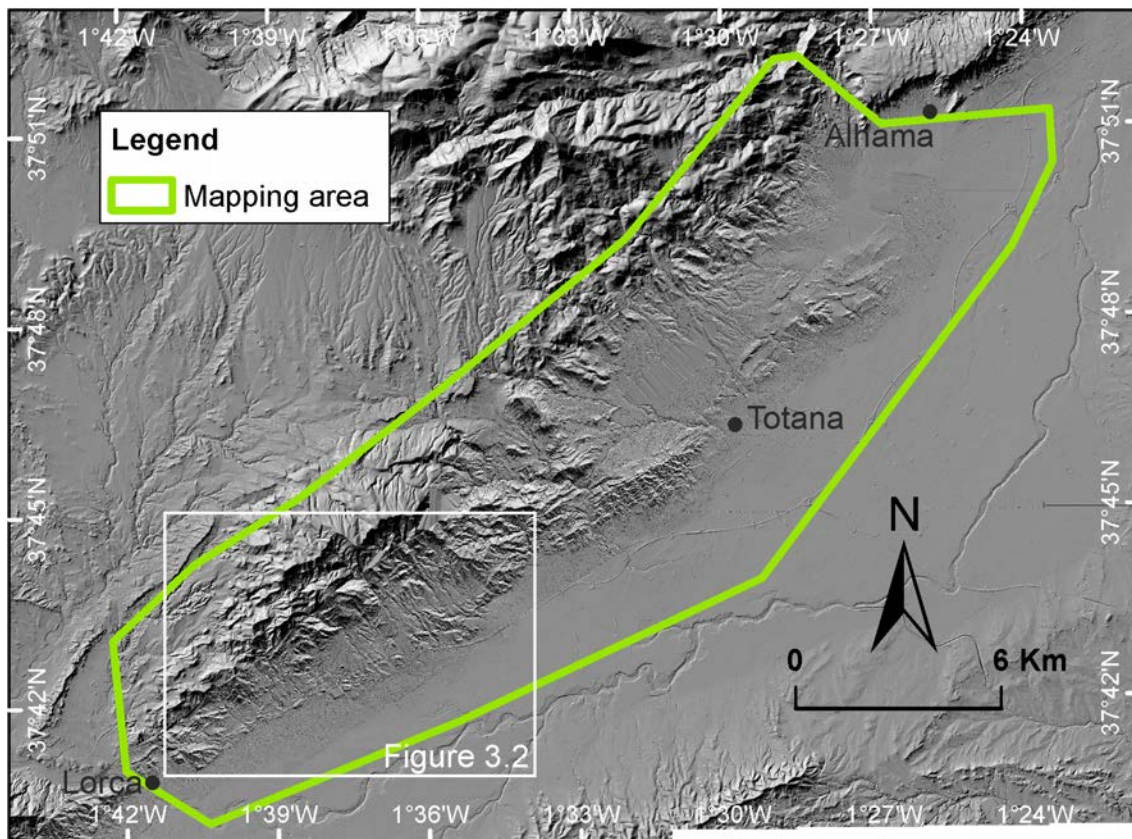


Figure 3.1. Mapping area used in this study. The paleoseismic study has focused in the sector between Lorca and Totana towns (Figure 3.2). Relief is obtained from the LiDAR-based 2m resolution DEM from IGN agency (centrodedescargas.cnig.es).

The alluvial fan generations are classified using relative ages based on their characteristics, only to identify and relate the units present in the studied sites. Three main criteria are used to differentiate the generations: a) location of the fans with respect to the actual base level (Guadalentín Depression in this case). The rationale “the higher with respect to this level, the older” was followed; b) geometry and overall degradation. Younger fans tend to have clear telescopic geometries with defined apexes and almost no degradation/erosion. Abundant small and shallow channels are developed in the surfaces of such fans. On the other hand, older fans tend to show less clear telescopic geometries and usually have well developed drainage systems on its surface, with less abundant but deeper channels, often abandoned, resulting from the evolved degradation of the fan; c) relationships between fans. In tectonically active mountain fronts with important uplift, younger fans tend to entrench and dissect older fans by erosion. Therefore, the older generations are usually found as remnants in higher relative levels with respect to the younger fan sedimentation level (Bull, 1977).

The mapping area covers $\sim 255 \text{ km}^2$ of the Lorca-Totana and Totana-Alhama segments of the fault (Figure 3.1). Special attention has been paid into the cartography of the studied Lorca-Totana segment to precisely locate the different fault strands and the extent of the identified alluvial units, which were exposed in the paleoseismic trenching.

3.2 Trenching survey

The sites are selected based on the presence of clear fault deformation in recent Quaternary alluvial deposits, which allows characterizing the activity and seismogenic character of the selected fault. Upon this analysis, a transect of the Lorca-Totana segment of the AMF has been selected to perform the paleoseismic study in the different fault branches. Eight paleoseismic trenches have been dug in four sites along four fault branches in the transect (Figure 3.2 and Figure 3.3).

From N to S the trenches dug are: two trenches at La Tercia site (T-2 and T-6), one trench at El Roser site (T-1), one trench at El Saltador site (T-16) and four trenches at La Hoya site (T-0, T-3, T-4 and T-5). In the last site, relevant paleoseismic information has only been obtained in T-3. T-16 is dug as an enlargement of a previous trench (TR-7; Ferrater, 2016; Ferrater et al., 2016). Remarkably, one of the identified branches could not be trenched due to the uncertainty in fault location.

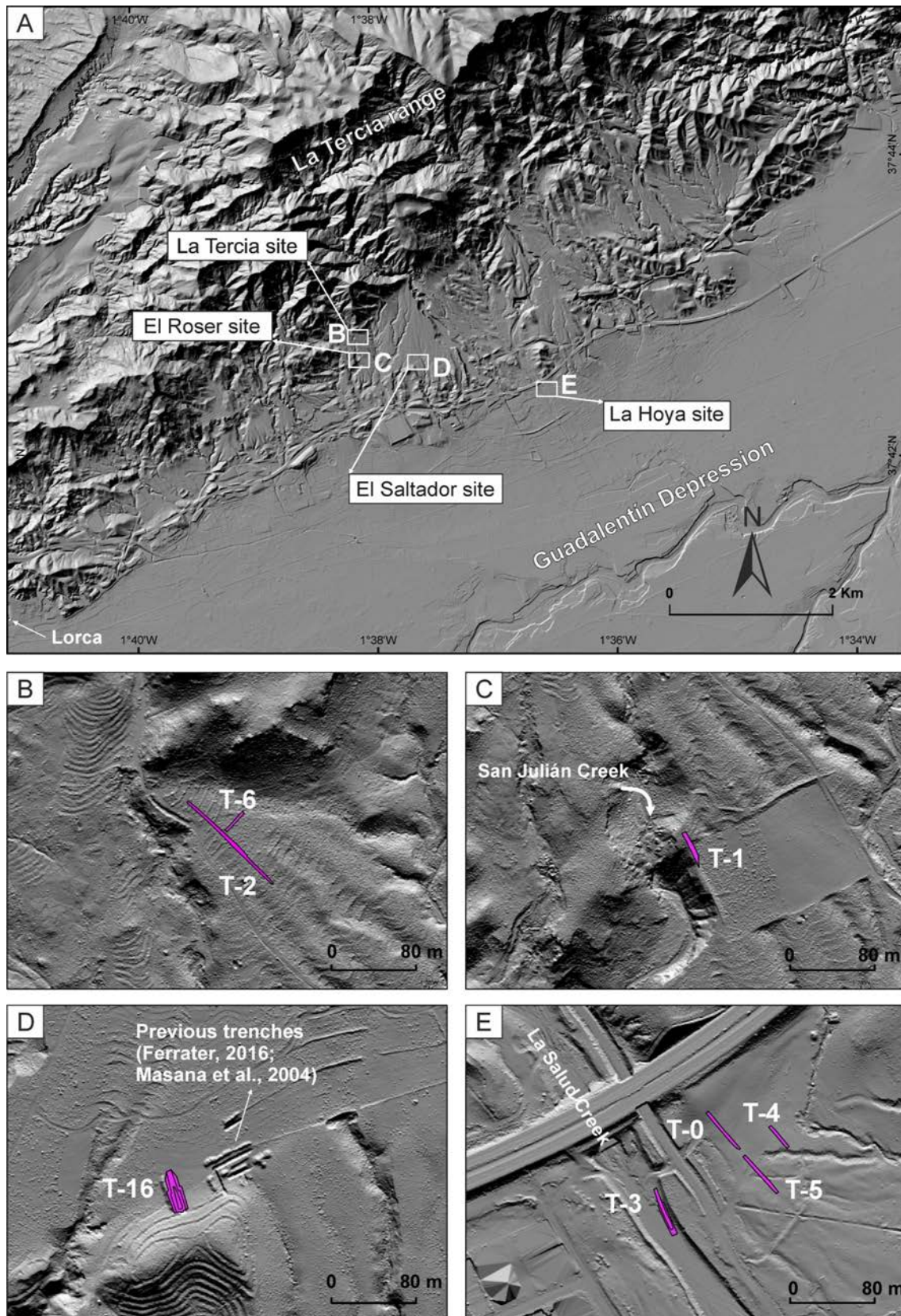


Figure 3.2. A) Location of the sites and trenches within the study area (Lorca-Totana segment), NE of Lorca city. Relief is obtained from the LiDAR-based 2m DEM from IGN agency (centrodedescargas.cnig.es). B) La Tercia site. C) El Roser site. D) El Saltador site, with the location of previous works indicated. E) La Hoya site. Relief from B) to E) is from the 0.5 m resolution DEM obtained in a previous project (SHAKE project).



Figure 3.3 General images of the paleoseismic trenches dug in this study. **A)** Overview landscape of La Tercia and El Roser sites; **B)** Overview of El Saltador site. **C)** Trench 1 (T-1) of El Roser site. **D)** Trench 2 (T-2) of La Tercia site. **E)** Trench 16 (T-16) of El Saltador site. **F)** Overview of the La Hoya site. Note that the photograph is a panoramic and distances appear distorted at the edges. **G)** Trench 3 (T-3) of La Hoya site, at the bottom of La Salud Creek.

All trenches are displayed perpendicular to the fault traces to demonstrate recent Quaternary seismic activity in non-studied branches and enlarge the paleoseismic record at El Saltador site, with the exception of T-6, which is parallel to the fault in order to infer the lateral displacement. Trench lengths range from 36 to 112 m and depths from 2 to 7m (Figure 3.3). Trench walls are systematically photographed to generate 1:20 scale photomosaics (Figure 3.4) with the Agisoft Metashape software (<https://www.agisoft.com>), following the workflow by Reitman et al. (2015). Upon these photomosaics, we draw and interpret the main trench features in the field. In the trenches, first the sedimentary sequences are interpreted, including the identification of erosive relationships and paleosoil developments that might indicate periods without deposition.



Figure 3.4 Examples of trench wall photomosaics obtained using the Agisoft Methashape software and following the workflow by Reitman et al. (2015). The upper mosaic corresponds to the SW wall of T-16 and the lower to the SW wall of T-4. Orientation is SE-NW in both.

Second, the deformation and faults activity are characterized by a) identifying the different type of structures (faults, folds, etc.) and the overall style of deformation and, b) identifying evidence of paleoearthquakes or deformation events such as differential deformation between units, colluvial wedges (e.g., McCalpin, 2009; Kondo and Owen, 2013). The main evidence of paleoearthquakes used in this thesis can be grouped in five (Figure 3.5):

- i) Fault truncations at the base of a sedimentary unit. The deformation of a fault or strand terminates at the base of a unit deposited after the earthquake generated by this fault. The horizon truncating the fault is the event horizon.
- ii) Differential deformation between units. The deformation of the successive younger units of a sedimentary sequence is lower, which indicates that it has been affected by less repeated paleoearthquakes. The first horizon marking the difference in deformation corresponds to the event horizon.
- iii) Angular unconformities related to differential deformation. A folded sequence is eroded by the overlying and less deformed sequence, generating an unconformity (i.e., event horizon).
- iv) Angular unconformity by onlap. A folded sequence is onlapped by a less deformed sequence. This generates wedging geometries of the onlapping unit towards the paleorelief generated by the underlying. The deformation is recognized because the internal stratifications of both units show different deformation degrees (tilting).

- v) Coseismic deposits related to earthquake shaking. In some localities worldwide (e.g., Argentina; Rockwell et al., 2014), paleoearthquakes are interpreted solely from sedimentary evidence. Earthquake shaking produces large amounts of dust that accumulate on the surface and that are washed out as mudflows by the e after the earthquakes. Such deposits can pond on coseismic fault scarps forming massive orange and fine-grained bodies, that are anomalous to the stratigraphy of typical alluvial fans. The presence of such sedimentary bodies in a fault zone is thus interpreted as a coseismic evidence.

Main paleoearthquake evidence used in this thesis

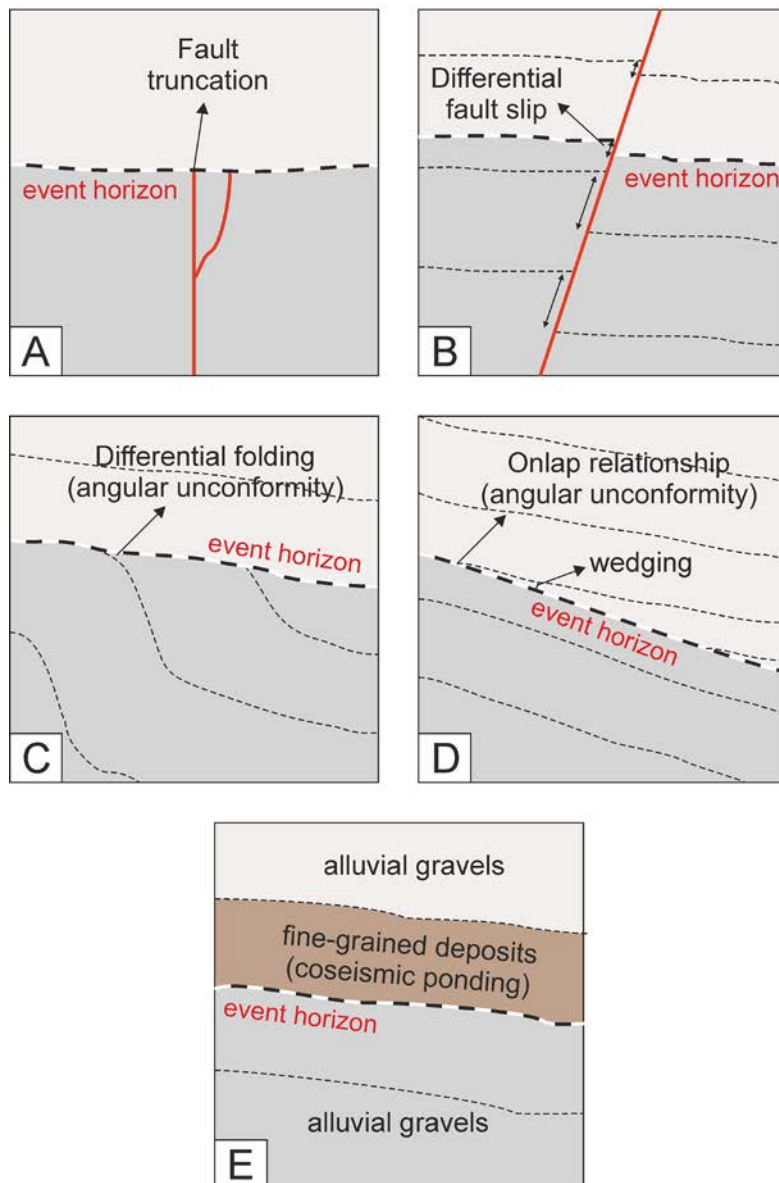


Figure 3.5. Sedimentary evidence of paleoearthquakes. **A)** Fault truncation. **B)** Differential deformation between units. **C)** Angular unconformity. **D)** Angular unconformity by onlap. **E)** Fine grained coseismic ponded deposits from earthquake shaking. Details of each case are provided throughout the text.

3.3 Dating of stratigraphic units

The age control of the deformation linked to the different fault branches investigated in this study is crucial to understand and characterize their recent tectonic activity by means of earthquake recurrence and seismic parameters such as slip rates. For this reason, we sampled several stratigraphic units for radiocarbon and Optically Stimulated Luminescence (OSL) numerical dating. The distribution of the samples along the sedimentary sequences and the dating method depends on the availability of datable material. A total of 21 samples have been dated in this study: 12 using OSL and 9 using radiocarbon. For El Saltador site (T-16), we use 14 dates obtained in previous trenching studies in that same site by Masana et al. (2004) and Ferrater (2016), given that the stratigraphic units are correlatable. These dates are from three different dating methods, including radiocarbon, OSL and Thermoluminescence (TL).

3.3.1 Optical Stimulated Luminescence (OSL)

The OSL method is a numerical dating procedure that allows to provide an age estimation for the last exposure to sunlight of a certain sediment and is based on the principle that certain minerals (quartz and feldspars) have the capacity to trap electrons from natural ionizing radiations (alpha, beta and gamma) into their crystalline lattice flaws (Medialdea, 2012). This ionizing radiation is defined per unit of time as the dose rate (Dr; in grays/1000 years or Gy/ka) and results from the disintegration of the radioactive elements of the rocks in the environment and the cosmic radiation.

The exposure of the sediment to sunlight causes the emptying of the crystalline positions, i.e., bleaching, generating a luminescence signal that allows to infer the absorbed or equivalent dose (De; in Gy). The absorbed dose is proportional to the time exposure of the sample to the environmental dose (dose rate) and both define the luminescence age (ka) as the De/Dr quotient. The luminescence age can be assumed as equivalent to the age of the sediment deposition if this sediment is exposed to the sunlight before deposition to ensure complete bleaching of the minerals and buried afterwards. In this sense, sediments that are transported (fluvial, eolian, etc.) are usually the best candidates for OSL because presumably are well exposed to sunlight during transportation (e.g., Lancaster, 2008; Schmidt et al., 2010; Medialdea, 2012).

The absorbed dose is quantified in the laboratory by applying luminescence protocols in which the signal of the sample is measured by stimulating the sample with a constant

radiation. In addition, the natural OSL signal of the sediment is artificially reproduced by irradiation of the sample to calibrate the measurements and to obtain the final De estimation. The dose rate of alpha, beta, gamma and cosmic radiation is estimated by chemical analysis and dosimetry measurements both the field (gamma spectrometry) and in the laboratory.

Important limitations are found in the methodology primarily related to the moisture of the sediment and the presence of carbonate such as carbonate cementation. These can affect importantly the dose rate of the sediment by reducing it because they attenuate the natural radiation and its subsequent mineral absorption. This could cause an overestimation of the age of the sample and for this reason, corrections need to be applied (e.g., Nathan & Mauz, 2008). Another important limitation relies on the fact that some minerals could have inherited luminescence signal due to non-complete bleaching. This is common in alluvial and fluvial systems with rapid transportation in turbulent fluxes and high sediment load (e.g. debris flows, mud flows) that are not exposed enough to the light and lead to an overestimation of the luminescence age (Smedley and Skirrow, 2020).

To capture and quantify the mentioned uncertainties, each sample is divided in different parts (aliquots) which are formed by several mineral grains. Each aliquot is measured separately, and the results further plotted so the effects of water content, carbonate or inherited signal can be traced and discarded from the resulting age distribution if necessary.

3.3.1.1 Dated samples and dating procedure

Fine-grained sediments, typically mud and fine sand layers embedded within gravel alluvial deposits, are sampled with opaque metallic tubes (~4 cm diameter) and used for OSL dating (Figure 3.6). The OSL samples from T-1 and T-2 (6 samples) were pre-treated and dated at CENIEH (Burgos, Spain) while the ones from T-3 (5 samples) at Instituto Superior Técnico (Lisboa, Portugal). An additional OSL sample from T-16 (T16-OSL-3) was dated at the University of Cologne (Germany). Each laboratory analyzes the samples using slightly different protocol specifications for luminescence dating:

- i. The samples dated at the Instituto Superior Técnico have been dated using 24 quartz multi-grain aliquots per each sample with granulometries of 160-250 μm . The burial moisture of the samples has been estimated between 7% and 15% and its influence to the absorption of the radiation is corrected using conventional

factors (Zimmerman, 1971). The carbonate content ranges from 21% to 48 % and is mainly dolomite, while feldspar concentrations are minor (4-13%). The luminescence measurements have been performed following the SAR-OSL protocol (e.g., Murray & Wintle, 2000, 2003) and using Risø readers DA-20. The resulting measurements have been analyzed in order to discard outliers using the Luminescence Analyst software (Duller, 2015) and the absorbed dose has been calculated using the robust mean and the respective uncertainty. Dose rate estimations are inferred based on K, Rb, Th and U concentrations from sample chemical analysis and in situ gamma spectrometry. Cosmic radiation has also been considered from the density of the materials (e.g., Prescott & Hutton, 1988).

- ii. The samples dated at the CENIEH have used 29-34 quartz multi-grain aliquots with granulometries of 90-125 μm and following the SAR-OSL protocol. The carbonate concentration of the samples ranges from 14 to 40% and moisture is estimated $\sim 4\text{-}9\% \pm 4\%$. Absorbed dose measurements have been done using a Risø TL/OSL DA-20 reader. Dose rate measurements have been obtained by determining the humidity content of each sample in the laboratory, in situ gamma spectrometry and gamma spectrometry of U, Th and U isotopes at the Radioisotope Service of the University of Sevilla. The statistical model for calculating the luminescence ages is the Central Age Model (CAM; Galbraith & Roberts, 2012), excluding the outliers (20-28% of values from the distribution).
- iii. The sample dated at the University of Cologne has been dated using 72 quartz multi-grain aliquots with granulometries of 150-250 μm and following the SAR-OSL protocol. The sample moisture has been estimated at $5 \pm 3\%$ and corrections are applied to account for its related attenuation and also the one from grain size. Absorbed dose has been estimated using the CAM with the outliers excluded (14% of the values from the distribution). The dose rate is based on high-resolution gamma spectrometry measurements of bulk sediment material ($\sim 100\text{g}$) from the surrounding of the sample and cosmic radiation estimations from burial depth. Gamma spectrometry measurements have been carried out at the Radioisotope Service of the University of Sevilla.

OSL dates are provided in calendar years referenced to the year of sampling (2019 in T-3 and 2020 in the rest), which we correct to years before present (BP). The individual reports of OSL dating from each laboratory are available in the Annex II (B).

3.3.2 Radiocarbon

The radiocarbon method is a numerical dating technique of materials containing organic carbon, such as charcoal and carbonated shells (snails, gastropods, etc.) (Figure 3.6) and allows to estimate the age elapsed from the death of the organism in question. The technique is based on the phenomena of disintegration of the radioactive ^{14}C isotope in nature and the resulting $^{14}\text{C}/^{12}\text{C}$ ratio of the materials suitable to date. The $^{14}\text{C}/^{12}\text{C}$ ratio in the living organisms is transferred from the CO_2 absorption of the plants through the food chain and it is maintained during their life cycles because the decayed ^{14}C is replaced by ingestion of plants or tissue. However, upon death, the ^{14}C of the organism starts to disintegrate without replacement, causing a time-dependent variation of the $^{14}\text{C}/^{12}\text{C}$ ratio that is used to estimate the elapsed time since this death (Taylor, 1997).

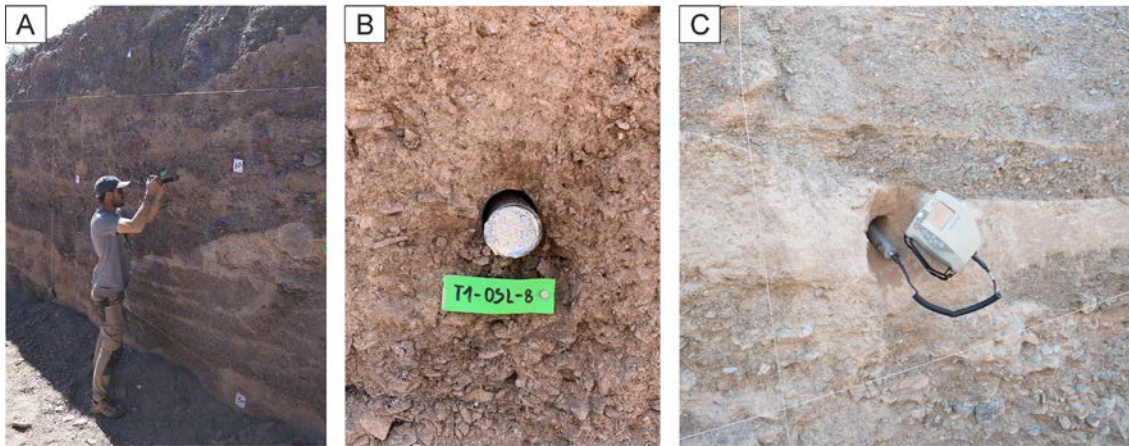
The radiocarbon age can be assumed, after proper calibration, as contemporary to the sediment deposition because to be preserved, organisms are buried shortly after its death. However, a few limitations need to be acknowledged as they can lead to errors or inaccurate dating results. The first one is that the datable materials might have suffered re-working and re-sedimentation during its evolution, leading to estimated ages older than the expected (e.g., Heier-Nielsen et al., 1995). Second, upon burial shell samples can suffer external contaminations by incorporating younger carbon from lixiviation of younger materials, leading to a variation in the $^{14}\text{C}/^{12}\text{C}$ ratio of the sample and resulting in a younger age (e.g., Colhoun, 1986). Third, snail shells can experience the so-called “old shell problem”, referring to the incorporation of old carbon from carbonate rocks (limestones) during life that causes an overestimation of the estimated ages (e.g., Goodfriend & Stipp, 1983; Rick et al., 2005). With this, charcoal usually constitutes the best option for radiocarbon dating because it is less susceptible to the mentioned sources of error, but its scarcity compared to snail shells in the study area requires the combined use of both materials in our case. Therefore, all these problems should be considered when analyzing numerical dates of stratigraphic units and subsequent interpretations.

3.3.2.1 Dated samples and dating procedure

Three charcoal fragments of 1-5 mm of diameter and six snail shell fragments of 1-2 cm have been sampled in younger sediments of the trenches because they are expected to be in the range of the dating method. Samples have been extracted from the sediment using a spatula, then folded with aluminum foil and saved in airtight plastic bags. Charcoals have been pre-treated and dated at the KCCAMS facility at the University of California,

Irvine (USA). Snail shell fragments have been pre-treated and measured in the DirectAMS Laboratory in Bothell (USA). Pre-treatment consisted of applying an acid-base-acid process prior to combustion with 1N HCl and 1N NaOH at 75°C. Radiocarbon concentrations, radiocarbon age and correction for isotopic fractionation of the results are provided following Stuiver & Polach (1977). $\delta^{13}\text{C}$ values have been measured on prepared graphite with an AMS spectrometer. The resulting radiocarbon ages are calibrated to years before present (BP) using the OxCal v.4.3.2 software (Bronk Ramsey, 2017) and the IntCal20 atmospheric curve (Reimer et al., 2020).

OSL sampling



Radiocarbon sampling



Figure 3.6. Examples of sampling of the two main dating methods used in this study. **A)** Optical Stimulated Luminescence (OSL) sampling process by extraction of sediment in metallic tubes **(B).** **C)** Gamma spectrometry performed in situ in the field. **D)** and **E)** Examples of snail shell fragments sampled for radiocarbon dating in this study.

3.4 Deformation quantification

Vertical separations are systematically measured to quantify the deformation related to uplift affecting the different units of the trenches where the dip slip component is dominant (T-1 and T-3) or represents a relevant part of the overall deformation

(e.g., T-16). Although the points measured are not actually piercing points, in the trenches where the vertical component is the predominant, we assume the vertical separations to be the same as the vertical slip and we refer to them as vertical slips henceforth. In T-16 we use the same nomenclature to ensure consistency throughout the text, although it should be noted that lateral component could imply part of these vertical slips to be apparent. Contrarily, predominant strike-slip motion and lack of relevant folding structures with marked vertical component prevent this procedure in T-2.

The lateral slips could not be precisely quantified in any of the trenches of this study because no 3D paleoseismic trenching has been carried out. Instead, indicative lateral slips estimated are inferred in La Tercia site from the displacement of a channel margin observed in T-6 with respect to an actual creek. In El Saltador site, the lateral component of the corresponding fault has been already estimated in previous 3D trenching studies (Ferrater, 2016), which we use here.

3.4.1 Vertical slip estimation

For the vertical slip measurements several methodological steps have been done which include the definition of the deformation limits and geological structure simplifications.

3.4.1.1 Limits of the deformation

To measure the vertical slips in the trenches, the limits of the deformation need to be defined. In all cases we have assumed that the deformation ends within the trench limits, thus, the units recover their depositional slopes outside the trench. The depositional slopes are estimated from topographic profiles parallel to the trenches along the corresponding alluvial fan surfaces (Figure 3.7). Once the topographic profiles are set, a linear regression line is adjusted in each of them to obtain the mean slope value. For each site, the slope value selected corresponds to the mean of one or several topographic profiles, depending on the variability.

For the profiles of El Roser site, the profile with the lowest slope (4.4°) is considered because it is the one with better fit with the stratigraphy in the trenches (profile 2 of El Roser site; Figure 3.7). This method provides a minimum estimation of the vertical slips because part of the deformation may extend out of the exposed limits, being T-16 the most relevant case.

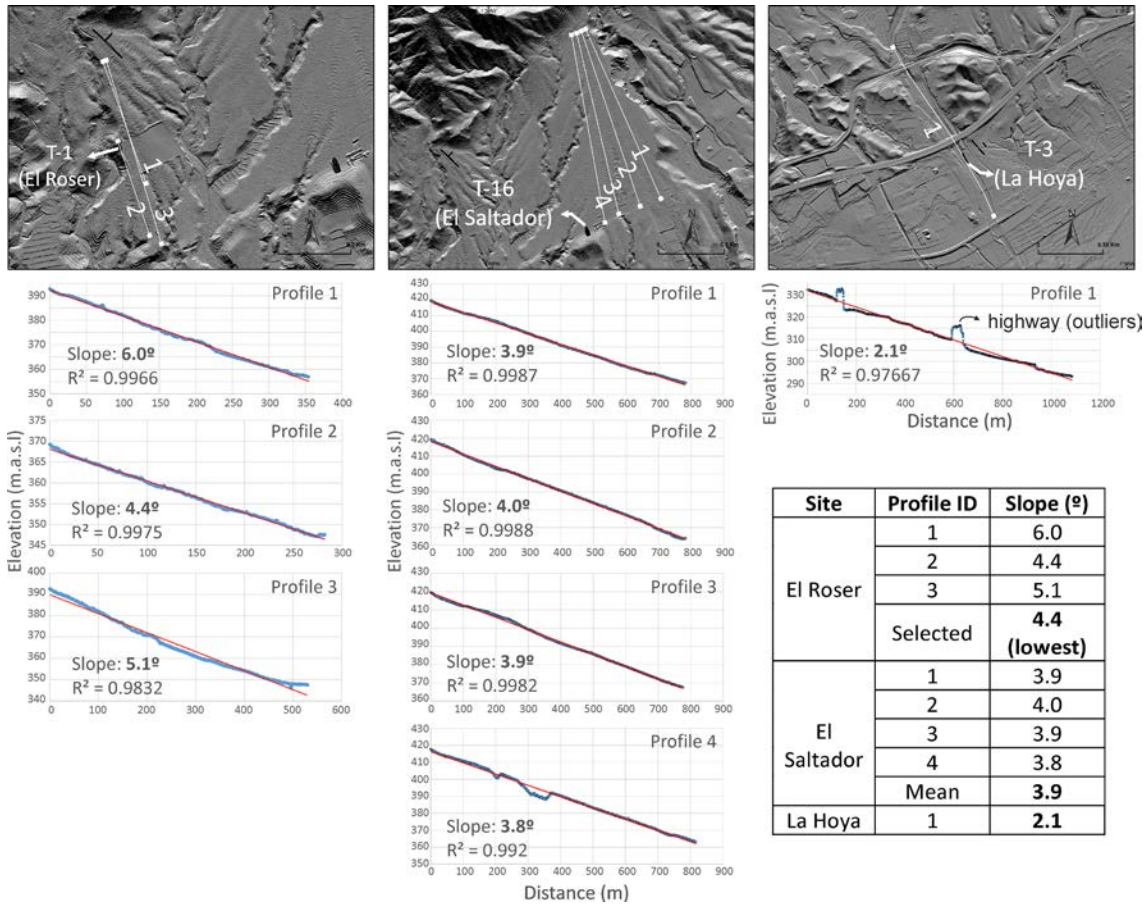


Figure 3.7. Slope analysis from topographic profiles performed in each site where the vertical slips are estimated. Slopes are obtained by adjusting a linear regression and their fit is expressed by the R^2 parameter. From left to right: El Roser, El Saltador and La Hoya sites. The table summarizes the slopes from each topographic profile and the selected slope for the slip analysis.

3.4.1.2 Structure simplification

We model the observed structure of each trench by simplifying the digitalized trench log in a graphics design software (CorelDraw). Only the unit contacts representing paleoseismic event-horizons are used for the structure modelling, namely surfaces that separate units with different degrees of deformation and that represent the occurrence of one or more paleoearthquakes (see Figure 3.5). In an alluvial fan context such as the one of the study area, this implies sedimentary bodies with, sometimes, channelized geometries and irregular/erosive contacts. Therefore, and to accommodate this epistemic uncertainty in the measurements, we considered a maximum and minimum position of the horizons in each wall, corresponding to the lowest and highest altitude points of an irregular contact, respectively (Figure 3.8). Using this method, the real slip can be overestimated in channelized units whose basal contact shows a higher dip than the depositional. In such cases we used the dip of the internal stratification/lamination of the unit as the marker for approaching the real tectonic dip of the unit (Figure 3.8).

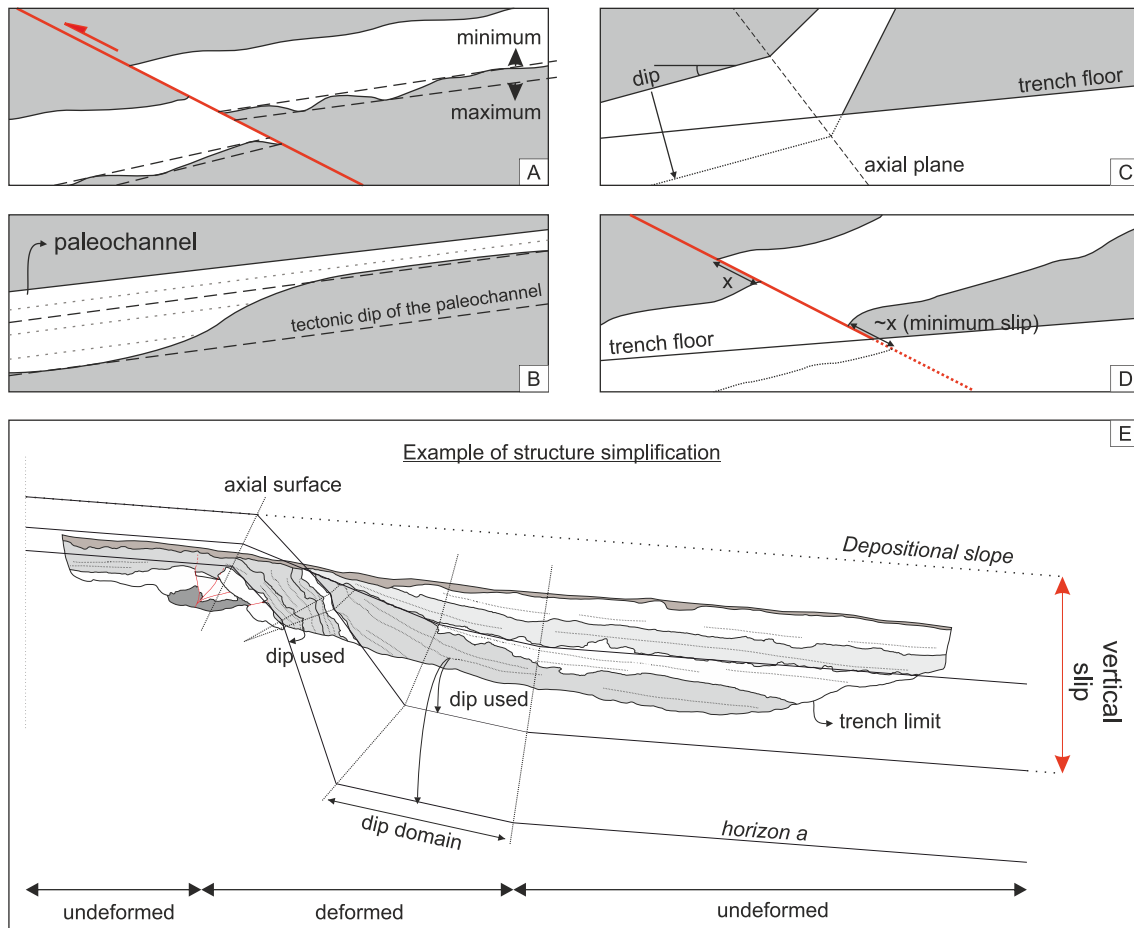


Figure 3.8. Graphical structure simplification performed in the trench walls of this study to obtain vertical slips of the different units. Note that this simplification provides minimum slip values. **A)** Simplification of irregular contacts using a minimum and maximum position. **B)** Simplification of channelized geometries to avoid overestimation of slips. **C)** Extrapolation of unit dips out of the trench limits using the dip of the immediate upper visible layer. **D)** Extrapolation of the fault slips out of the trench limits using the slip of the immediate upper visible unit. **E)** Example of structure simplification in a trench wall using the features in windows A to D to model different horizons (e.g., horizon a).

Folded structures are modelled using dip domains separated by axial lines defining the overall geometry of the structure. Faults are simplified to a line with a dip as much uniform as possible. Given the limited dimensions of the trench walls (at depth and laterally), the structure can hardly be inferred from the geometry of the exposed horizons (Figure 3.8). Therefore, the geometry outside the trench needs to be extrapolated to complete the structure and to measure the slips. This can be a problem for the horizons that cross several dip domains without data exposed in the trench (as horizon a in Figure 3.8). In these situations, and as a simplification, we assign the dip and fault slips of the immediate upper visible horizon to the non-visible part of the horizon. Also, the recovery of the depositional slopes of the units in the trench limits is made assuming unit

thickness preservation. These assumptions provide a minimum deformation for such horizons but reduce randomness on the structure simplification and avoid overestimation of the deformation.

3.4.1.3 Measurements

The slip measurements are carried out on the simplified structure from the trench logs. Cumulative vertical slips are measured for each horizon from the highest point in the uplifted part of the structure to the lower point. Each horizon has four slip measurements, two per wall (minimum and maximum positions of each contact). Thus, we provide the mean value ± 1 standard deviation (1σ) considering a symmetric normal distribution to depict the variability linked to the irregularity of the sedimentary contacts.

3.4.2 Lateral slip estimation

In this study, lateral slips are only inferred in La Tercia site from an actual channel and paleochannel cropping out in T-6. Because channels are usually sinuous, we follow the method proposed by Gold et al. (2011) adapted by Ferrater (2016) in the AMF (Figure 3.9). In this approach, lines are approximated to define the tendency of the channel features, i.e., margins and thalweg, and are projected onto the fault trace at both sides of it to measure slips. To account for the uncertainty of sinuosity, several lines are defined for each feature, either considering their orientation in the area near the fault, farther or the overall tendency. In our case, the slips are measured between the actual channel features and their homologous in a paleochannel of T-6 (see details in section 5.5.5.2). The measurements have been carried out using the 0.5 m resolution MDT in the ArcGIS software. The uncertainty of each measurement is considered to be ± 1 m, which is the minimum measure unit of the projected coordinates (UTM) used in the GIS project of this work. Additionally, for the thalweg measurements we consider a larger uncertainty of ± 5 m because the bottom of the actual creek is wide and thus difficult to define with a single discrete line. For the lateral slip estimation, a total of nine measurements are obtained and computed using the MATLAB software by Zechar & Frankel (2009) and expressed as probability density functions (PDFs) using a Gaussian distribution.

In the case of El Saltador site, lateral slips were estimated in previous studies through 3D paleoseismic trenching (Ferrater, 2016). We use the results from that study to yield the rake of the fault and the net slips of the site (see next section).

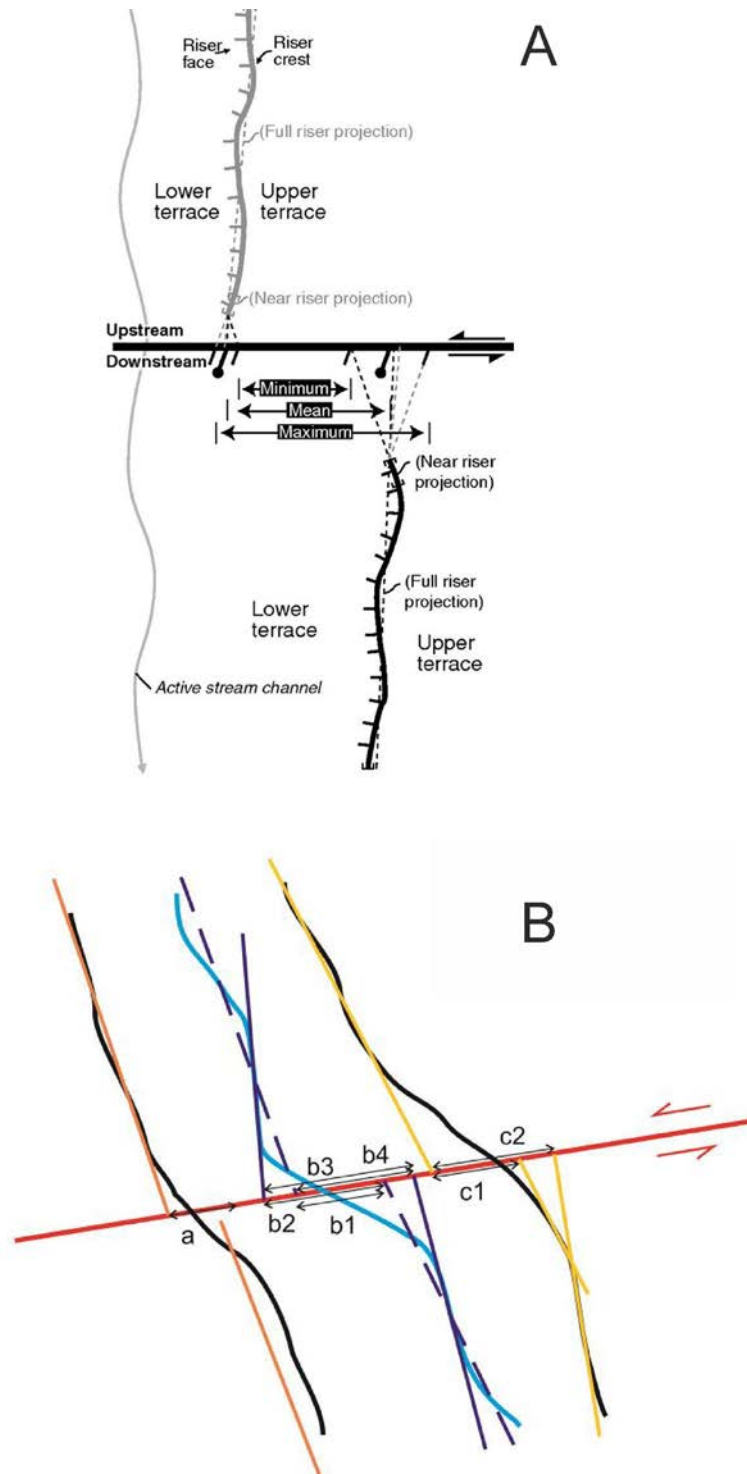


Figure 3.9. Methodology followed to infer the lateral slip of a offset channels in strike slip fault branches. **A)** Scheme of the method used to measure lateral slip in terrace risers affected by the Altyn Tagh fault in the northwestern Tibet. Note how the displacements are calculated based on the approximation of different hypothesis of tendency lines to the faulted feature. Figure by Gold et al. (2011). **B)** Method used to define and measure displacements of homologous lines in the margins and thalweg of active streams affected by the Alhama de Murcia Fault (AMF). Black lines represent the margins of the creek and the blue line, the thalweg. The piercing lines are projected onto the fault trace considering the orientation of the features farther and closer to the fault. The slips are measured independently (e.g., a, b1, b2) and a mean value \pm standard deviation is computed to calculate the mean lateral slip. Figure modified from Ferrater (2016).

3.4.3 Net slip estimation

The net slips are calculated for the faults with significant lateral component and dip slip faults with low angle dips. In dip slip faults with dips $\sim 90^\circ$, the net slip is assumed to be equal to the vertical (throw). In La Tercia site we use the measured lateral slip to infer the net slip following Equation 3.1. In T-16, the net slips are inferred using the fault rake following Equation 3.2, which is inferred from vertical slip measured in this work and lateral slip from Ferrater (2016) at El Saltador site following Equation 3.3.

$$NS = \frac{LS}{\cos(|\text{rake}|)} \quad \text{Equation 3.1}$$

$$NS = \frac{\frac{VS}{\sin(\text{dip})}}{\sin(|\text{rake}|)} \quad \text{Equation 3.2}$$

$$\text{Rake}(\text{°}) = \arctan \frac{VS}{LS} \quad \text{Equation 3.3}$$

Where VS, LS and NS correspond to vertical, lateral, and net slip, respectively. Note that Equation 3.3 is only valid for vertical-dipping faults.

3.4.4 Shortening estimation

Shortenings are inferred from the trench wall restoration of the vertical slips, which corresponds to the shortening registered along the direction of the trenches ($\sim N160^\circ$) and perpendicular to the fault traces, not necessarily the regional geodynamic shortening. To do so we retro-deformed the different deformation events identified in each trench and measured the total shortening of each one. This restoration is only done in the trenches of faults with important vertical component and does not account for strike-slip shortening, which needs to be particularly accounted in El Saltador site. This analysis is done for each of the horizons used for the vertical slip measurement and thus the shortenings are expressed as the mean value $\pm 1\sigma$ of four measurements per horizon.

3.5 Seismic and paleoseismic parameters

The results of the vertical slips analysis in the trenches and the numerical dating of the sedimentary units, allow inferring the seismic and paleoseismic parameters of the fault that are critical for its characterization, for the refinement of its seismic potential and to evaluate their repercussion into seismic hazard assessment.

3.5.1 Earthquake chronosequences and recurrence

Earthquake chronosequences are established for the groups of events in each trench using the OxCal v.4.3.2 software (Bronk Ramsey, 2017). This software uses Bayesian probability to calculate the probability density functions (PDFs) of dates, events or other chronological features. In paleoseismology this tool is used to constrain the occurrence of paleoearthquakes based on the provided dating constraints (OSL, radiocarbon, etc) and to calculate recurrence intervals (RI) (e.g., Lienkaemper and Ramsey, 2009). The resulting event dates are expressed as PDFs to account for the most probable dates and its uncertainties. Here, we use three types of commands from OxCal, alone or combined, to constrain the paleoevent ages. Each of them provides different probability constraints to the target the datable features: *Date*, *Boundary* and *Zero Boundary* (Figure 3.10).

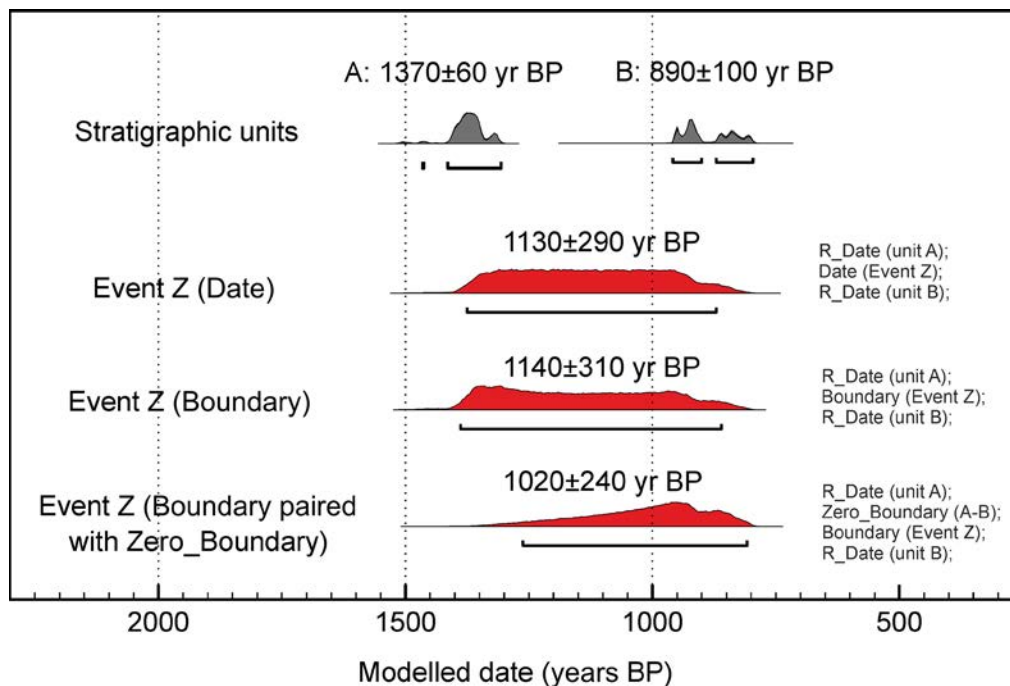


Figure 3.10. Examples of PDFs modelling a theoretical earthquake Z using the commands *Date*, *Boundary* or *Zero Boundary*. Uncertainty ranges refer to 2σ . The *Date* function generates a uniform distribution. The *Boundary* generates a skewed distribution towards the age of A. The *Boundary* paired with *Zero Boundary* clearly skews the distribution towards unit B because it is assumed that earthquake Z happened closer to the age of the unit B than A. Note that it also reduces the uncertainty range. Figure inspired by figures in DuRoss et al. (2011).

The first (*Date*) provides a uniform earthquake-time distribution between dates and in our case is applied where robust age constraint for an earthquake or group of earthquakes is lacking; for instance, a large period without sedimentary record in which an earthquake could have happened. The *Boundary* command provides a non-uniform earthquake-time

distribution and should be when the earthquake represents a changes/breaks in the depositional sequence (e.g., large earthquake deformation differences) or differences in the sample densities for pre- and post-faulting deposits (DuRoss et al., 2011). The *Zero Boundary* strongly skews the distribution towards a desired age in the sequence. Based on the recommendations by DuRoss et al. (2011), we pair the *Zero Boundary* with a *Boundary* in two situations. First, to skew an earthquake PDF towards the age of a unit, when we are confident that such earthquake happened shortly before its deposition. In this case, the *Zero Boundary* represents the time elapsed between the limiting units and the earthquake is modelled with a *Boundary* (Figure 3.10). Second, to model individual earthquake PDFs when there is a lack of numerical dates between two or more consecutive events. In this case the *Zero Boundary* represents the elapsed time between the unbracketed events and allows to model their individual PDFs without a numerical date in between. If there are more than two events lacking time brackets, the *Zero Boundary* is interpreted as the PDF of the event or events in the middle of the unbracketed sequence. The combination of two commands is advantageous because it prevents from having to set an arbitrary time gap and does not produce over-skewed or unrealistically constrained PDFs (DuRoss et al., 2011). See section 5.6.1 for the application of these OxCal specifications.

We also use the OxCal software to calculate the mean RI in each branch and the inter-event times. Upon them, we evaluate the fault recurrence model by computing the coefficient of variation (CV), which is defined by Equation 3.4. Based on Salditch et al. (2020), $CV < 0.5$ unveil a strongly-periodic behavior, $1 > CV > 0.5$ a weakly-periodic behavior, $CV = 1$ a random or Poissonian behavior and $CV > 1$ a clustered behavior.

$$CV = \frac{\sigma}{RI} \quad \text{Equation 3.4}$$

Where σ is the standard deviation of the inter-event times.

3.5.2 Slip rates and shortening rates

The vertical and lateral slip rates of the fault branches are inferred from the vertical and lateral slip analysis using the numerical ages of the sedimentary units. Similarly, the net slip rates for individual fault branches are calculated using the net slip estimations in each branch. Horizontal shortening rates are inferred from shortening estimations. All these

rates are computed using the MATLAB software by Zechar & Frankel (2009) and expressed as Gaussian probability density functions (PDFs). Trench slips are considered as Gaussian distributions based on the trench wall measurements ($\text{mean} \pm 1\sigma$). Unit age PDFs of OSL dates are represented with a Gaussian distribution following the provided lab age distributions ($\text{mean} \pm 1\sigma$) or Boxcar in case of radiocarbon dates which provide a range of ages (2σ range). We calculate slip rates for different periods of time to capture variations over the Quaternary, including periods of increased or decreased activity. In order to obtain the total slip rate of the Lorca-Totana segment of the AMF we integrate the slip rate values of each branch for a common time period of the last 18 ka. Total vertical and lateral slip rates are obtained by adding the respective values for each branch, assuming that all them merge at depth in a single fault plane. The total net slip rate is then computed following Equation 3.5.

$$\text{NSR} = \sqrt{\text{LSR}^2 + \left(\frac{\text{VSR}}{\sin(\text{dip})}\right)^2} \quad \text{Equation 3.5}$$

Where VSR, LSR and NSR correspond to the vertical, lateral, and net slip rate, respectively.

3.5.3 Slip per event and single event displacement

We calculate the slip per event (SPE) as the average of the total net slip of the different horizons in the trenches divided by the number of earthquakes affecting that marker ($\pm 1\sigma$). In addition, we calculate the slips generated by each single paleoevent (event displacement; ED) identified in the trenches from the differential slip between pairs of successive units. This is done to check the variability of this parameter with respect to the SPE and to estimate different earthquake sizes generated by the fault.

4 Methods for fault-based probabilistic seismic hazard assessment

In this section we present the approach, methodological specifications and requirements used for the source modelling and seismic hazard calculations performed in this thesis. To do so we first define different explorative fault and multi-fault rupture hypothesis of the Eastern Betics Shear Zone faults to be tested in the source modelling for the hazard, using a novel methodology developed in the frame of the ESC Fault2SHA working group (<https://fault2sha.net>). Multi-fault ruptures (relaxed segmentation) are considered here to model the fault system more realistically according to observations during earthquakes in nature (e.g., Wei et al., 2011; Zhang et al., 2012). This modelling implied a thorough compilation and revision of the available geological, geomorphological and geodetical fault data to include into the modelization as well as to check their resulting outputs. Secondly, we set two different seismogenic source models based on the fault rupture models explored and build their respective logic trees to compute the seismic hazard. This part contains some verbatim portions of text from the methodological sections of the two JCR publications that concern this part of the thesis. Section 4.1 is mainly based on Gómez-Novell et al. (2020a) and section 4.2 on Gómez-Novell et al. (2020b).

4.1 Data and methods to compute fault rupture hypotheses in the Eastern Betics Shear Zone

As a first step of the probabilistic seismic hazard assessment (PSHA) and to perform a qualitative analysis of the feasibility of multi-fault ruptures in the Eastern Betics Shear Zone, we set up possible multi-fault rupture scenarios or hypotheses in the study area and selected the fault slip rate data from published studies following a critical revision in specific cases. Then we used the SHERIFS code (Chartier et al., 2019) to model magnitude-frequency distributions (MFDs) at the whole EBSZ fault system scale for each multi-fault hypothesis, and analyzed the consistency or performance of the different models with data from the catalogue and paleoseismic studies.

4.1.1 Definition of fault rupture hypotheses

In this modelling we exclusively considered the main active major faults of the area because they are the ones absorbing most of the plate convergence motion in southeastern Spain (Bousquet, 1979; Silva et al., 1993), and because they show the best geological and paleoseismic data available in the region for seismogenic source modelling. From SW to NE these faults are (Figure 4.1): Carboneras Fault (CF), Palomares Fault (PF), Alhama

de Murcia Fault (AMF), Los Tollos Fault (LTF), Carrascoy Fault (CAF) and Bajo Segura Fault (BSF) (e.g., Bousquet, 1979; De Larouzière et al., 1988; Silva et al., 1993; Masana et al., 2004; Alfaro et al., 2012; Insua-Arévalo et al., 2015). Faults outside of the EBSZ or secondary faults have not been considered mainly due to lack of enough quality data (e.g. Crevillente Fault, Torrevieja Fault, San Miguel de Salinas Fault, El Andarax Valley Fault, El Alquían Fault System, among others; Figure 4.2A).

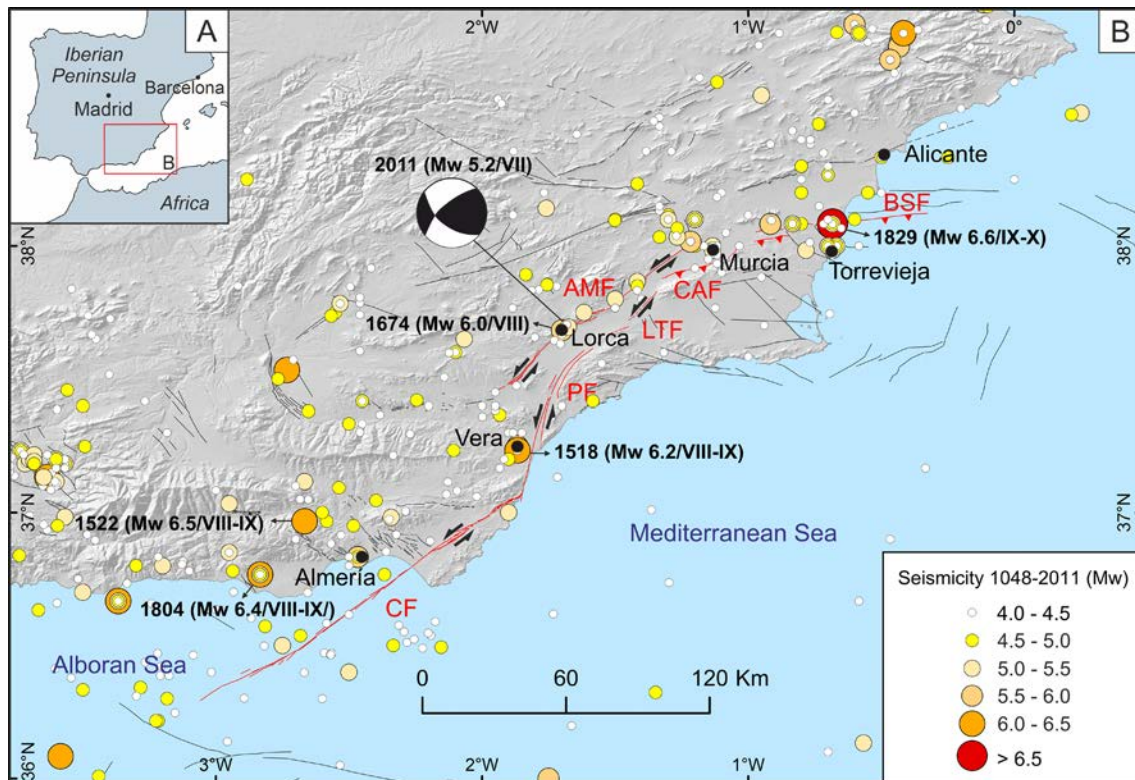


Figure 4.1. A) Location of the study region within the Iberian Peninsula. **B)** Seismotectonic context of SE Spain with the seismicity of $M_w \geq 4.0$ from the 1048-2011 period (IGN-UPM, 2013), including the most damaging historical earthquakes of the region. The focal mechanism of the 2011 Mw 5.2 is extracted from the Instituto Geográfico Nacional agency (IGN, 2011). Intensity scale is European Macroseismic Scale (EMS98). The fault traces are extracted from QAFI v.3. database (IGME, 2015a; García-Mayordomo et al., 2017) and the main faults used in this study are depicted in red. CF: Carboneras Fault; PF: Palomares Fault; LTF: Los Tollos Fault; CAF: Carrascoy Fault; BSF: Bajo Segura Fault; AMF: Alhama de Murcia Fault.

We defined four possible fault and multi-fault rupture scenarios for the EBSZ system as sets of incremental fault rupture lengths starting from minimal fault sections or segments. These scenarios represent plausible rupture possibilities according to our criteria and the available data, but other could be tested. The different hypotheses are thus explorative and the length of ruptures in the different scenarios is defined by imposing selected fault characteristics as barriers for rupture propagation. In our case, only geometry (mainly

sense of dip) and kinematic changes between major faults or groups of faults are used as criteria to explore multi-fault rupture propagation in the different hypotheses. In the case of AMF though, it is considered that the fault cannot rupture together with any other fault of the system in any hypothesis, since it dips towards the NE (Martínez-Díaz et al., 2012b) and this difficults the compatibility of a combined rupture with the rest of faults of the system. Other fault parameters frequently used as barriers for fault rupture propagation (e.g., Boncio et al., 2004; Wesnousky, 2008; Field et al., 2014) are not contemplated in this study as we explain below.

Changes in strike and distance between faults (gaps, stepovers) are not considered as a limiting factor for rupture propagation, because they are not significant enough considering, for instance, the criteria applied in California for strike slip faults (UCERF-3; Field et al., 2014). Neither slip rate variations along strike are used as barriers, even if these are important. This is consistent with observations on earthquakes such as the 2016 Mw 7.8 Kaikoura earthquake where more than 20 faults ruptured together, some of them with extremely different slip rates (e.g. 1-2 mm/yr for the Papatea fault and 24 ± 12 mm/yr for the Kekerengu fault; Langridge et al., 2018 and Little et al., 2018, respectively). Finally, the aspect ratios between fault length and width are not taken as a limiting factor for the occurrence of long fault ruptures in our models, since there is not a clear threshold for these parameters in large or extreme events, especially for strike-slip regimes. For instance, the 1906 Mw 7.9 San Francisco earthquake or the 1958 Mw 7.77 Alaska earthquake implied rupture lengths of 470 km and 260 km, respectively (Schwartz, 2018) with seismogenic widths of 12 km (Wells and Coppersmith, 1994) comparable to the EBSZ (Table 4.1). Also, it can be observed from the regressions in Leonard (2010) that, in strike-slip faults, for rupture lengths > 50 km the width becomes constant at a mean of 17 km but the dataset shows large dispersion in this range and a significant amount of large ruptures (> 100 km long) are found for widths similar to the EBSZ.

4.1.1.1 Fault rupture hypotheses

The major faults considered are divided in shorter sections based on their geometry, geomorphic expression and seismicity in the literature, as well as on their kinematics and activity evidence (Figure 4.2). Offshore segmentation of CF is adopted from Moreno (2011), while onshore is based on García-Mayordomo (2005), same as for PF. Segmentation of CAF is adopted from Martín-Banda et al. (2015), BSF from Alfaro et al. (2012) and AMF from Martínez-Díaz et al. (2012b).

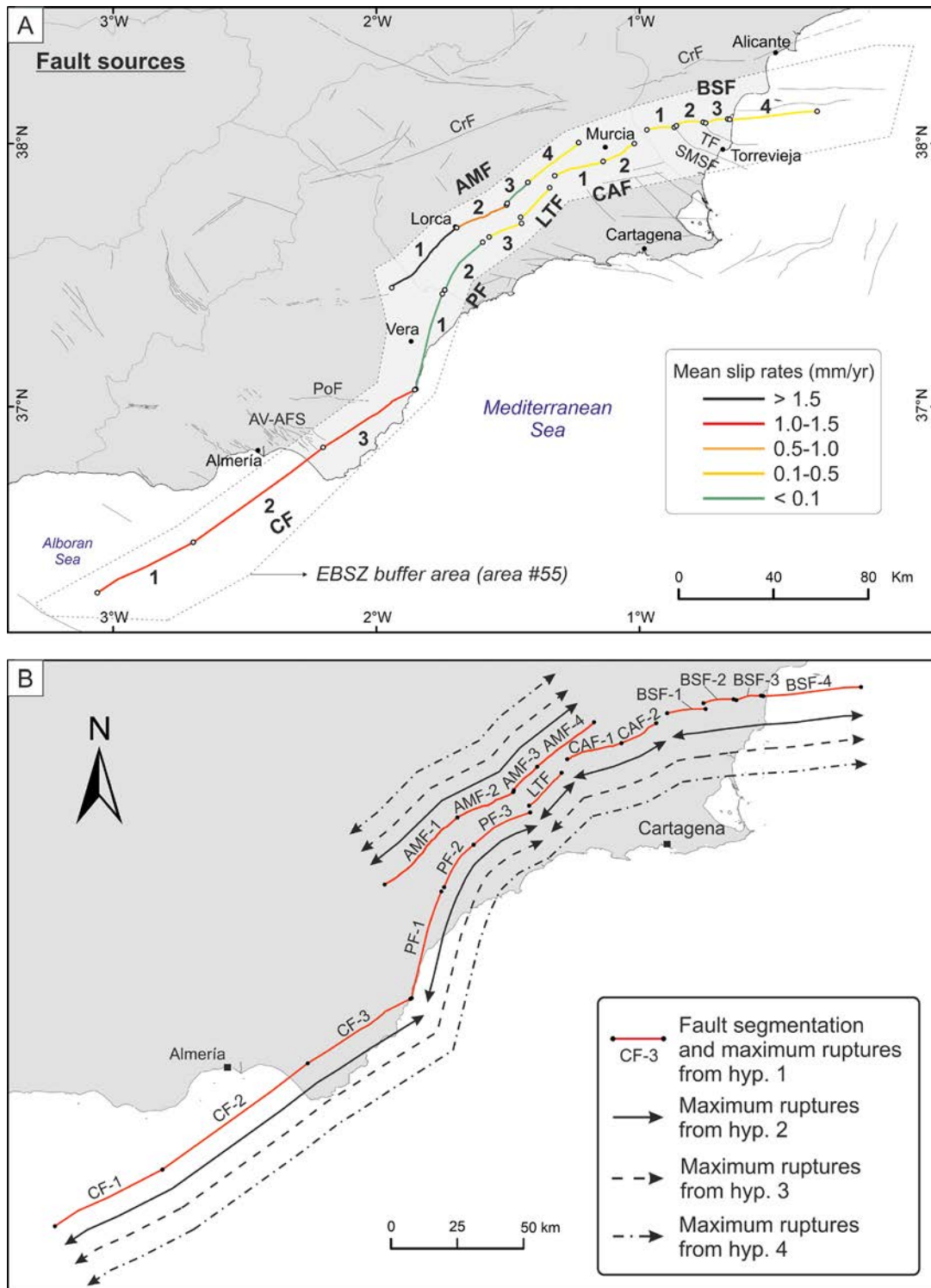


Figure 4.2. **A)** Simplified traces of the major faults of the EBSZ considered in the fault source modelling of this study. Each fault is marked by an abbreviation (see footnote of Figure 4.1B) and each section or segment of the respective fault has a number assigned (ID). The parameters of each fault ID are indicated in Table 4.1. The fault traces are presented following a colored scale according to their estimated mean slip rate values. Relevant secondary faults not included in the fault source modelling are also indicated. CrF: Crevillente Fault; SMSF: San Miguel de Salinas Fault; TF: Torrevieja Fault; AV-AFS: Andarax Valley and El Alquíán Fault System; PoF: Polopos Fault. The buffer area of the EBSZ is indicated around the faults by a dotted line. **B)** Extension of the maximum multi-fault ruptures allowed in each hypothesis considering the different fault sections or segments in which each major fault is divided.

Fault name	Fault section ID	Dip (°)	Main kinematics	Seismogenic depth range (km)	Fault length (km)	Net slip rate (mm/yr)			Type of information used to infer slip rate (references) and time frame covered
						Min.	Mean	Max.	
Carboneras (CF)	CF-1	90	Strike-slip	0 - 11	39.1	1.1	1.2	1.3	Displaced fluvial channels, trench offsets and GPS data (Moreno, 2011; Echeverría et al., 2015); since Pliocene - Holocene.
	CF-2	90	Strike-slip	0 - 11	59.6	1.1	1.2	1.3	
	CF-3	90	Strike-slip	0 - 11	39.5	1.1	1.2	1.3	
Palomares (PF)	PF-1	90	Strike-slip	0 - 8	41.1	0.01	0.04	0.08	Tectonic uplift of terraces and alluvial fans (García-Mayordomo, 2005 and references); since lower-middle Pleistocene.
	PF-2	90	Strike-slip	0 - 8	24.0	0.01	0.04	0.08	
	PF-3	90	Strike-slip	0 - 8	12.0	0.04	0.1	0.16	
Los Tollos (LTF)	LTF	85	Strike-slip	0 - 8	16.0	0.06	0.16	0.25	Analogy with LTF and PF-2 (expert opinion). Recurrence intervals in paleoseismic trenches (Insua-Arévalo et al., 2015); since 12 ka.
	CAF-1	70	Reverse	0 - 12	18.2	0.29	0.37	0.45	Restoration of deformed units, consistent with offsets in trenches (Martin-Banda et al., 2015); since 209.1 ka.
Carrascoy (CAF)	CAF-2	85	Strike-slip	0 - 12	13.1	0.48	0.53	0.58	Tectonic uplift (unpublished research by Martin-Banda et al.); since 160 ka.
	BSF-1	60	Reverse	1.0 - 12	11.6	0.25	0.33	0.41	Tectonic uplift (Alfaro et al., 2012); since 2-3 ka.
BSF-2	60	Reverse	1.0 - 12	9.2	0.25	0.33	0.41		
Segura (BSF)	BSF-3	60	Reverse	1.0 - 12	7.7	0.12	0.2	0.3	
Alhama de Murcia (AMF)	BSF-4	60	Reverse	1.0 - 12	29.3	0.12	0.2	0.3	Assigned by analogy to BSF-3 section (expert opinion). Consistent with GPS data (Borque et al., 2019).
	AMF-1	70	Strike-slip	0 - 12	34.1	1.6	1.65	1.7	Displaced fluvial channels (Ferrater, 2016; Ferrater et al., 2017); since 200 ka for AMF-1, 30 ka for AMF-2.
	AMF-2	70	Strike-slip	0 - 12	19.7	0.8	1.0	1.2	
	AMF-3	70	Strike-slip	0 - 12	11.3	0.01	0.07	0.1	Based on expert opinion from QAFI database (IGME, 2015a).
AMF-4	45	Strike-slip	0 - 12	23.9	0.07	0.2	0.37	Tectonic uplift (Herrero-Barbero, 2016); since late Miocene-Pliocene.	

Table 4.1. Fault input data used to calculate the earthquake rates of the EBSZ fault system with the SHERIFS approach in the fault source modelling. The sources of information and references from where fault slip rate data are extracted are summarized. Other fault parameters are extracted from the QAFI v.3. database (IGME, 2015a; García-Mayordomo et al., 2017). Note that the slip rate data from this table, used in the articles, has been further actualized due to the publication of new research and for some sections might be not up to date. The updated data is used to discuss the hazard results in section 7.6.5; see Table 7.1.

The segmentation for each of these faults is applied to define the minimal sections (hypothesis 1) that in the subsequent hypotheses are linked to generate larger ruptures; ‘multi-fault ruptures’ henceforth. The fault system geometry considered is shown in Figure 4.2A. For AMF-1, AMF-2, CF and PF we simplified fault sections with several parallel traces or splays to a single trace representative of the overall geometry. This is done because it is assumed that fault branches likely link at depth, as suggested by Moreno (2011) for CF or Martínez-Díaz et al. (2012b) for AMF. Also, the fault parameters of the simplified fault traces result from the merging of the individual fault branches’ parameters in some cases; the slip rates of CF, AMF-1 or PF are inferred from geomorphological estimations accounting for all branches. Moreover, in CF they are consistent with geodetic data (Table 4.1).

The main difference between the hypotheses considered is the length of the maximum fault ruptures allowed. One hypothesis considers only single-section fault ruptures and the other three allow multi-fault ruptures at different extents (Figure 4.2B):

- Hypothesis 1 (hyp. 1): The length of the segments in the segmentation from the literature set the maximum length of ruptures and multi-fault ruptures with the neighboring sections are not allowed. This follows the classical segmentation model in which is considered that maximum earthquakes are usually confined within specific fault segments and caused by its whole rupture (Schwartz and Coppersmith, 1984).
- Hypothesis 2 (hyp. 2): The maximum length of ruptures allowed in this hypothesis is that of complete major faults. Neighboring fault sections can rupture together within a same major fault, but complex ruptures between different major faults are not envisaged. For example, the whole CF can rupture at a time, but it cannot rupture with its adjacent section of PF (Figure 4.2B). In this case we assumed that geometry and kinematic characteristics that lead to define the limits between major faults in the literature act as barriers for fault rupture propagation.
- Hypothesis 3 (hyp. 3): This hypothesis allows linked ruptures between selected major faults with similar geometries and kinematics, while these are excluded between faults with less similarities on these parameters. This leads to the definition of three sub-systems, within which multi-fault ruptures are allowed, but not between them. We propose a CF-PF sub-system, a LTF-CAF-BSF sub-system and an AMF sub-system. The first one is characterized by vertical dipping left-lateral strike-slip faults (Table 4.1). The second one is formed by predominantly high angle S-SE dipping

faults with mainly reverse components (CAF and BSF). LTF, although being classified as mainly strike-slip, it has been considered within this sub-system because it limits the southern part of the mountain range uplifted by CAF suggesting its relationship with this fault. In addition, in the area, fault branches related to LTF with strong reverse components have been recently identified (Insua-Arévalo et al., 2018). The third sub-system is formed by AMF, a NW-dipping strike slip fault.

- Hypothesis 4 (hyp. 4): No restrictions are made in this hypothesis from CF to BSF. We considered that given a particular extraordinary event, a rupture could propagate across both systems. Conversely and as for hyp. 3, AMF is considered apart due to its contrastingly opposite dip direction compared to the rest of the faults.

4.1.2 Geological fault parameters as inputs for the calculations

A current challenge in the EBSZ is the difficulty to have a complete and reliable dataset of fault geological parameters for all its major faults, such as slip rates and rates of large earthquakes. Most paleoseismological studies have typically focused on specific branches of major faults while some of the faults remain poorly studied to date. This causes heterogeneity on how the knowledge on active faults is distributed. Accordingly, constraining the geological parameters for some of the faults considered is a difficult task and, for our modelling purposes, it requires taking a number of assumptions and extrapolating data among different fault sections. For this reason, we carried out a revision of the current geological data available on the EBSZ faults that are critical as inputs for the seismic hazard, mainly slip rates and geometrical parameters, after discussion in the frame of the Fault2SHA-Betics working group (García-Mayordomo et al., 2018). Special emphasis is put on the less studied structures of the system.

With posteriority to the publication of the articles that compose this part of the thesis, the slip rate data used for the seismic hazard calculations (Table 4.1), some of which has been estimated using unpublished work or expert criteria, has been further revised and updated for some fault sections due to the availability of new research in them. This includes the new data obtained in this thesis for the Lorca-Totana segment (AMF-2) (section 5) and other EBSZ faults. We therefore clarify that the slip rates in such fault sections should be treated as provisional and the reader is referred to Table 7.1 in section 7.6.5 for the updated values, where they are used to discuss the seismic hazard results.

4.1.2.1 Slip rates

The slip rates and uncertainties of the faults are directly obtained from published geological and paleoseismological studies (Table 4.1). Geological slip rates on faults have been assumed to be seismic slip rates in this study. We are aware that part of the slip rates considered may result partially from aseismic slip and it is one of the uncertainties. However, we do not estimate that the contribution of the aseismic slip in the EBSZ faults is that relevant because: i) creeping is usually associated with high levels of microseismicity (Scholz, 1990; Malservisi et al., 2005), which are not found at the EBSZ. ii) Creep tends to be highly localized at the surface and creeping faults tend to lack large brittle-deformation structures and lack deposits resulting from coseismic deformation (colluvial wedges, etc.) (McCalpin, 2009). Contrarily, the EBSZ faults show many evidences of brittle deformation that splay upwards to the free surface, indicating rapid deformation (e.g. as seen in trenches by Martín-Banda et al., 2015; Ferrater et al., 2016; Martínez-Díaz et al., 2018 or in section 5 of the present thesis). iii) There is no evidence of historical offsets, even small, in anthropic structures (walls, roads, etc.) that may be hundreds of years old and cross the traces of the faster faults (i.e. AMF, CF). They should be displaced if creep was dominant or even half of the total slip rate.

Stich et al. (2007) suggest that only ~24% of the total slip rate in the Betic-Alboran-Rif area is explained by the instrumental catalogue seismicity over a 21-year period, and that the remaining 76% might be generated in either aseismic processes or being accumulated as elastic deformation, but there is no way to distinguish among these two processes. We think that an important part of that 76% might be released as large seismic events, considering that the EBSZ is a low-strain region and that the last large events occurred previous to the 20th century (e.g. 1829 Torrevieja and 1674 Lorca earthquakes). Paleoseismic results in the area evidence that faults have much larger recurrence intervals (RI) than the time window of the seismic catalogue.

The compilation of slip rate values for each of the faults considered is done after the revision of the published data. In the fault sections or segments where there is available paleoseismic research, slip rate values are used without any modification. Conversely, in faults or fault segments where paleoseismic research is lacking (PF-3, CAF-2, BSF-4 and AMF-3) we inferred the slip rate values using expert criteria. Below, we detail the sources of information and expert criteria followed to assign the slip rate values from Table 4.1

in each fault section, as they are important to understand the further limitations of the results.

Faults whose slip rate data are directly extracted from published studies:

- CF: The lateral slip rate is inferred from geomorphological analysis onshore (CF-2, 3) and offshore (CF-1, 2), 3D paleoseismological studies (CF-3; Moreno, 2011; Moreno et al., 2015) and geodetic studies (CF-3; Echeverria et al., 2015). All three methods are coincident in the predicted slip rate values (1.2 ± 0.1 mm/yr) and valid since the Pliocene but also for the Holocene. Net and lateral slip rates show similar values because 1) the vertical slip rate for this fault is one to two orders of magnitude lower than the lateral (0.01-0.3 mm/yr; Moreno, 2011) and 2) the differences in the slip rate values are within the uncertainty range.
- PF-1 and 2: The net slip rates used are the lower and upper values of the long-term uplift rates of lower-middle Pleistocene terraces and alluvial fan surfaces (see discussion in García-Mayordomo, 2005). This study considers this fault as mainly dip-slip, but new recent data on PF (Roquero et al., 2019) suggest strike slip kinematics, which could change the net slip rate values significantly; the actual values are a minimum. There are no published paleoseismic studies available for this fault to date.
- LTF: The net slip rate of this fault is inferred from recurrence estimations of at least two paleoearthquakes observed in paleoseismic trenches and their respective offsets (Insua-Arévalo et al., 2015). The slip rate estimations refer to the last 12 ka.
- CAF-1: For this fault, the net slip rate is calculated from restoring the deformation of the top of a distinctive sedimentary unit exposed in trenches and cropping out in the mountain slope (Red Unit; Martín-Banda et al., 2015). This is a long-term slip rate for the last 209.1 ± 6.2 ka, which is the age of the Red Unit, but the slip rate value is consistent with the one obtained from offsets in younger units in the trenches for the last 6.9 ± 1.8 ka (Martín-Banda et al., 2015).
- BSF-1 to 3: The net slip rates of these fault sections are inferred from the uplift of 2-3 ka continental sedimentary units (Alfaro et al., 2012). No paleoseismic trench studies are available for these faults to date.
- AMF-1: The lateral slip rate in this section is inferred by summing up offsets in fluvial channels of the fault zone (Ferrater, 2016; Ferrater et al., 2017). Vertical slip rate estimations in this section are subject to a larger uncertainty and the values are about

- one order of magnitude lower (0.16-0.22 mm/yr; Ortuño et al., 2012), hence strike-slip is the predominant kinematics of the fault. The slip rate data is for the last 200 ka.
- AMF-2: The lateral slip rate (1.0 ± 0.2 mm/yr) is inferred from offsets in fluvial channels for the last 30 ka (Ferrater, 2016; Ferrater et al., 2017). Paleoseismic 3D trenching inferred net slip rate values in the same range (0.9 ± 0.1 mm/yr for the last 20 ka; Ferrater, 2016), hence, vertical slip rate is negligible (0.1 ± 0.0 mm/yr).
 - AMF-4: The net slip rate in this section is estimated from long term (since late Miocene-Pliocene) uplift through geological structural analysis in the mountain ranges limited by this fault section. These methods imply large uncertainties for the slip rate estimation, because factors such as sediment compaction need to be considered. Although the latest studies in this section infer better constrained values (0.13-0.18 mm/yr; Herrero-Barbero et al., 2017) we used the wider range estimated in Herrero-Barbero (2016) (0.07-0.37 mm/yr) to ensure a conservative margin of uncertainty.

Faults whose slip rate data are either inferred by expert criteria or based on unpublished work:

- PF-3: Slip rate estimations for this fault section are not available since there are no studies in this area. According to the values assigned, the slip rate increases from PF-1 and 2 to LTF. Thus, it is feasible that, to accommodate this difference, PF-3 has an intermediate slip rate. For this reason, we assigned to PF-3 a slip rate which is the median between the values of PF-2 and LTF. The uncertainty range assigned is also an intermediate value between the uncertainties of these two faults (Table 4.1).
- CAF-2: For this fault section there is a published net slip rate value of 0.54 mm/yr (García-Mayordomo, 2005 and references), based on geomorphological offsets and tectonic uplift (at minimum since the last 160 ka). However, ongoing research on this fault (Martín-Banda, personal communication) yields new slip rate values: 0.48-0.54 mm/yr, which we use.
- BSF-4: This section of BSF is offshore and only a few studies have focused on that part of the fault (Perea et al., 2012), hence not enough data is available to do estimations of the slip rate of this section. Although some authors (Alfaro et al., 2012) suggest that the deformation associated to the BSF decreases towards the east, from a conservative perspective we assigned the same slip rate range as for BSF-3 (0.12-0.3 mm/yr), which is consistent with new GPS results in that sector (Borque et al., 2019).

- AMF-3: There are no slip rate estimations for this section. In fact, the geomorphological expression of this fault is subtle, hence, its slip rate is probably much lower than the other sections. Since it is our only source of information, we used the net slip rate estimated in the QAFI database (0.042-0.097 mm/yr) for AMF-3, rounding the upper uncertainty value and enlarging considerably the lower bound uncertainty, obtaining a net slip rate range of 0.01-0.1 mm/yr. From our perspective, enlarging the uncertainties accounts for a more conservative way to express the lack of knowledge of this fault.

From the slip rate values compiled in Table 4.1 and Figure 4.2A, it is observable that slip rate values are remarkably different from one source to another. The faults that have higher slip rate values are those that have been the object of most paleoseismological, geomorphological and geodetic studies during the last decades (i.e. AMF-1 and 2, CF) and thus have better constrained geological parameters with lower uncertainty intervals. Conversely, faults that have been the object of very few or no paleoseismological nor geodetic studies have systematically lower estimated slip rate values. This has to do with the fact that their slip rates are mainly based on the long-term uplift of mountain fronts and sedimentary units (i.e. PF-1 and 2, BSF-1 to 3, CAF-2, AMF-4) and as a result, the net slip rate is inferred from the vertical slip rate (Table 4.1). The time frame of this data is much longer than that of the other faults, and the kinematics of some sections are not clear, thus their rake estimations are more uncertain.

4.1.2.2 Other parameters

Geological parameters of the faults such as dip, kinematics, fault traces, length and seismogenic depth are extracted from the Quaternary Active Faults of Iberia database (QAFI) (García-Mayordomo et al., 2017, 2012; IGME, 2015a), which compiles the data on the literature from each fault. Exceptionally, for PF we used the recent kinematics proposed by Roquero et al. (2019), although the net slip rate estimations are based on García-Mayordomo (2005) (Table 4.1) considering the fault as a dip slip fault. These slip rates, therefore, should be accounted as a minimum. Despite these discrepancies, the modelling process with SHERIFS does not rely on the kinematics of the fault since the scaling law is valid for all types (see section 4.2.1).

4.1.3 SHERIFS method

SHERIFS, standing for Seismic Hazard Earthquake Rates In Fault Systems (Chartier et al., 2019), is an open-source Python-based method of fault source modelling that uses

geological fault data as inputs to calculate fault earthquake rates. Among its advantages, a) it allows to model earthquake occurrence in fault systems as a whole and considering sets of multi-fault ruptures; b) is well adapted for regions, such as the EBSZ, where geological data is the prime source of information for characterizing faults because seismological and geodetic data are insufficient for such characterization.

To work, SHERIFS requires: i) a 3D geometry of the fault system, ii) slip rate of each fault source, iii) a target magnitude-frequency distribution (MFD) shape of the fault system (distribution type and b value), which may be based on published studies or seismic databases, iv) a scaling relationship to estimate the upper bound of the MFD distribution (M_{\max}), and v) a set of fault and multi-fault rupture hypotheses to be explored. The slip rate of each fault is treated as a budget that is consumed by an iterative loop process and converted into earthquake rates assuming a given shape of a target MFD set at the fault system level. A typical MFD shape would be a Gutenberg-Richter or GR (Gutenberg and Richter, 1944), but SHERIFS also allows to explore other distributions for the target such as Youngs and Coppersmith (1985) or YC. In this iterative process, SHERIFS randomly picks a magnitude according to the target MFD set and picks a rupture whose size corresponds to this magnitude based on the scaling law. Then, an increment of the slip-rate budget of the faults involved in this rupture is converted into earthquake rate. The iterative process goes on until the slip-rate budget of limiting faults is exhausted and the target MFD is fulfilled. The resulting output MFDs are specific of each rupture hypothesis that has been envisaged by the modeler and representative of the whole fault system. At this point the reader is referred to Chartier et al. (2019) for more details on the SHERIFS workflow.

In the process of reaching the target MFD, sometimes not all the slip rate can be converted into seismic moment rate and remains unmodelled. This remaining slip rate budget (i.e., moment rate), referred to as Non-Main-Shock slip or NMS (Chartier et al., 2019), actually results from the configuration of multi-fault ruptures and target MFD set in each hypothesis and, depending on its proportion, can be interpreted in very different ways. High NMS proportions, typically over 30% in a whole hypothesis (sensu Chartier et al., 2019) likely suggest a modelling error due to an incompatibility between data, target MFD and fault ruptures of that particular hypothesis. This means that the slip-rate value of some fault cannot be converted into seismicity rates with a given set of rupture hypotheses while respecting the target MFD shape. Such issues might appear, for

instance, in multi-fault ruptures involving faults with very different slip rates: faster faults have an important proportion of remaining slip rate that cannot be consumed because slower sources have rapidly exhausted their budget. Nonetheless, NMS proportions different than zero (<30%) do not necessarily imply modelling incompatibilities but might be interpreted as the possibility of some faults to accommodate part of their slip rate budget in non-seismic processes such as post-seismic slip or creep.

The method also allows to explore the epistemic uncertainties of the parameters involved in the calculations (e.g., fault slip rate, maximum magnitude of rupture, b-value of the MFD target shape, etc.) by selecting n random samples within the uncertainty ranges provided of these parameters to compute n models of annual earthquake rates for each multi-fault rupture hypothesis considered. Finally, each modelled MFD of each rupture hypothesis is compared to the seismicity rates from the regional catalogue and the paleorates deduced from paleoseismological studies to test their reliability (Figure 7.1 to Figure 7.3; section 7.2). Based on the outcome of this check, SHERIFS allows to incorporate a weight to each resulting model for the branches of a logic tree to be incorporated into PSHA, as we describe in section 4.2.5. It is important to remark that SHERIFS' outputs are automatically formatted to be used for seismic hazard calculations in the OpenQuake Engine (Pagani et al., 2014). SHERIFS is an open-source code available for download and use at <https://github.com/tomchartier/SHERIFS>.

4.1.4 Seismic and paleoseismic data to check the results

4.1.4.1 Seismicity rates from the regional catalogue

The earthquake catalogue used to check the synthetic MFDs is the one used in the frame of the update of the Spanish national seismic hazard map (see details in IGN-UPM, 2013), but without de-clustering and clearing of foreshocks and aftershocks. Moment rate budgets used in SHERIFS are based on geological slip rates, which in fact, integrate the main shocks as well as foreshocks, aftershocks, clusters, aseismic slip, etc. The resulting catalogue includes 2839 earthquakes of $M_w \geq 4.0$ from year 1048 AD to June 2011. In the EBSZ, the maximum magnitude (M_{max}) corresponds to the $M_w 6.6 \pm 0.2$, 1829 Torre Vieja earthquake, however, larger earthquakes could have happened given the large uncertainties in magnitude estimation of some historical earthquakes. For example, the 1518 Vera earthquake has an estimated magnitude of $M_w 6.2 \pm 0.8$, meaning that the event could have reached magnitudes up to $M_w 7.0$ with a 34.1% of probability. The completeness years of the catalogue are shown in Table 4.2.

Earthquake catalogue	
Magnitude range	Year of completeness
3.0-3.4	1978
3.5-3.9	1975
4.0-4.4	1908
4.5-4.9	1883
5.0-5.4	1800
5.5-5.9	1520
≥ 6.0	1048

Table 4.2. Completeness years of the earthquake catalogue in southeastern Spain (IGN-UPM, 2013).

To better compare the MFDs of each scenario, only catalogue earthquakes occurring within the seismogenic crust of the EBSZ are considered, which is assumed to have thicknesses ranging from 8 to 12 km depending on the area (García-Mayordomo, 2005; Table 4.1). This tries to ensure that earthquakes located in this depth range are more likely produced by the faults in our study and not by deeper unidentified sources. The buffer area used to extract the seismicity corresponds to area source #55 from the ZESIS national scale area source model (García-Mayordomo, 2015), available at the ZESIS database (IGME, 2015b). This area was delineated as the envelope of the surface projection of the EBSZ fault planes and characterized by the seismic record within it (IGN-UPM, 2013).

4.1.4.2 Paleoearthquake rates

Annual rates of large earthquakes out of the historical period or paleoearthquakes (paleorates) are inferred from minimum and maximum RI published in the available paleoseismic literature from trench data. This concerns studies developed in CF-3, LTF, CAF-1, AMF-1 and AMF-2 as compiled in Table 4.3. Mean values have been calculated for each different recurrence distribution or range. Such paleorates are used to compare with the synthetic MFDs obtained with SHERIFS and their significance within the geological information is discussed in section 7.5.1.

The sources of information to infer the paleorates of Table 4.3 in each fault are explained below.

- CF-3: Paleorates are estimated from trenching results (Moreno, 2011; Masana et al., 2018) in the N branch of the two parallel strands that compose CF-3. In these studies, at least seven paleoearthquakes since 191 ka were identified. However, we considered the recurrence of the three last earthquakes since 41.5 ka (Moreno, 2011), because the earthquake rates are increased for this time period.

- LTF: Paleorate estimations are inferred from the RI of the last two earthquakes identified in paleoseismic trenches since ~12 ka (Insua-Arévalo et al., 2015).
- CAF-1: The paleorates are from Martín-Banda et al. (2015). In that study these are calculated from the slip rate and seismic moment considering the rupture of the whole segment. However, these paleorates are consistent with the ones estimated from two paleoevents for the last 6.0 ka in trenches from that same study.
- AMF-1: The two paleorate estimations in this segment are from recent paleoseismological studies in the southwestern tip (Ortuño et al., 2012) and the northeastern tip (Martínez-Díaz et al., 2018). The paleorates in the first are representative for the last 116 ka and the second are calculated using the maximum magnitude model (Wesnousky, 1986).
- AMF-2: Paleoseismological studies in this section identified a minimum of ten paleoearthquakes for the last 59 ka, although the inferred paleorates in Table 4.3 correspond to the last eight events provided by Ferrater (2016) because are the ones better constrained in time.

Studies	Paleoearthquake rate estimations					Fault section ID	Type of information used to infer recurrence
	Recurrence interval (kyr)		Cumulative paleoearthquake rate (eq/yr)				
	Min.	Max.	Min.	Mean	Max.		
Ferrater (2016)	2.0	5.3	1.89E-04	3.44E-04	5.00E-04	AMF-2	Age constraints of paleoevents in trenches.
Insua-Arévalo et al. (2015)	2.2	6.86	1.46E-04	2.44E-04	4.55E-04	LTF	
Martín-Banda et al. (2015)	2.6	4.0	2.50E-04	3.08E-04	3.85E-04	CAF-1	
Moreno (2011)	1.15	13.8	7.25E-05	1.96E-04	8.70E-04	CF-3	
Ortuño et al. (2012)	15.0	29.0	3.45E-05	4.71E-05	6.67E-05	AMF-1	
Martínez-Díaz et al. (2018)	0.34	3.12	3.21E-04	7.97E-04	2.96E-03	AMF-1	Maximum magnitude model

Table 4.3. Recurrence intervals (RI) extracted from the paleoseismological studies and cumulative annual rates of paleoearthquakes ($M_w \geq 6.25 \pm 0.25$) inferred from these studies. The types of information used for the calculation of the recurrence values in each study are indicated as well as the fault sections where these studies developed; see Figure 4.2A for map location. Values are rounded to two decimal digits.

For all cases, the magnitude of the paleorates for all faults is assumed to be a minimum of $M_w 6.25 \pm 0.25$. This threshold is selected because statistically, earthquakes of $M_w < 6.0$ are less than 50% likely to rupture the surface (Biasi and Weldon, 2006) and hence to be recorded as fault ruptures in the paleoseismic record. Data by Bonilla (1982),

McCalpin (2009) or the Unified Database of Surface Ruptures (SURE; Baize et al., 2019) support this selection. Additionally, very shallow earthquakes in the EBSZ such as the Mw 5.1 ± 0.1 2011 Lorca earthquake (IGN-UPM, 2013) have not ruptured the surface, and the paleoearthquakes identified in trenches, despite the uncertainties of these estimations, infer slips per event consistent with Mw > 6.0 (e.g. Moreno, 2011; Ferrater, 2016; section 4.8 of this thesis).

4.2 Source models for the seismic hazard calculations

The source models for the PSHA calculations are built using fault earthquake rates from SHERIFS within the EBSZ, and area sources to model earthquake occurrence outside of it. This is done due to the lack of enough quality data on faults to carry a fault-based approach in the whole SE of Spain. It is noteworthy that the resulting composite source models for PSHA are not a classical hybrid approach where faults accommodate earthquakes from a cutoff magnitude and area sources accommodate background seismicity (e.g., García-Mayordomo et al., 2007); instead, in our model both fault and area sources are modelled for all the magnitude range (Mw ≥ 4.0), as we explain in the following sections. The seismic hazard is further computed using the OpenQuake engine (Pagani et al., 2014) (v.3.7.1; GEM, 2019).

4.2.1 Fault sources

The fault-system source model considered is spatially constrained to the limits of area source #55 of the ZESIS model (García-Mayordomo, 2015) (Figure 4.2A). In this present approach, earthquake occurrence in this area (hereinafter called EBSZ buffer area) is completely modelled on faults from the geological fault data shown in Table 4.1 and using SHERIFS. Because this is an important assumption and to accommodate the possibility that a portion of the seismic moment release in the EBSZ is due to unknown faults (e.g. blind, unmapped) different from the considered ones, we also model background seismicity in one of our models. Although the EBSZ buffer area is narrow and constrained to the surface projection of well-known faults, implying that likely most of the seismicity within it is related to them, it cannot be precluded that some activity may occur on unknown active faults not considered in this study. Therefore, two alternative fault source models are envisaged within the EBSZ buffer area, one exclusively considering the faults' activity (FM model) and another one considering a fraction of background seismic activity overlapped with the faults (FM_bg model).

For the faults earthquake rates we considered an MFD target shape that follows a Gutenberg-Richter distribution (GR; Gutenberg and Richter, 1944) with a b-value in the range of 0.8-1.2, whose central value is coincident with the b-value of 1.03 assigned to the EBSZ buffer area (IGN-UPM, 2013; IGME, 2015b). This wide b-value range is explored in order to prevent the resulting MFDs of our hypotheses from being limited or biased by such value or imposed shape of the MFD. To calculate the M_{\max} of the faults MFDs we used the regressions by Wells and Coppersmith (1994) for rupture area and ‘all type of kinematics’. A shear modulus of 30 GPa is assumed representative for the calculation of seismic moment in the area. In order to incorporate the epistemic uncertainty in the input data, the GR of each four hypotheses is composed by 20 GR curves (a total of 80 GR) resulting from 20 samples or computations exploring random values of input parameters, i.e., fault slip rates, b-values and M_{\max} of GR distribution per 0.1 magnitude bin. Minimum magnitude (M_{\min}) is set at Mw 4.0, since below that magnitude earthquakes are not likely to be damaging and therefore not of interest for a hazard model.

4.2.1.1 FM model

For this model, earthquake rates in the EBSZ buffer area are modelled only on the EBSZ fault system, assuming that all seismicity over Mw 4.0 occurring within its limits is related to these faults due to the narrowness of this buffer around them. This source model uses the GR earthquake rates or distributions computed with SHERIFS for each of the multi-fault rupture hypotheses set in the present study (section 4.1.1), which are representative of the whole fault system. The resulting earthquake occurrences of each scenario (80 GR curves for all four scenarios) are expressed as the seismicity rates of each fault-rupture involved in that scenario.

4.2.1.2 Fault sources with background: FM_bg model

A modification respect to the FM model is introduced by modelling a background to consider that part of the seismic moment release in the EBSZ buffer could be due to unknown active faults apart from the main ones. The rest of the input parameters are the same as for the FM model.

The background is a parameter from SHERIFS that allows sharing a fraction or ratio (percentage) of the seismicity rate of a given magnitude between the faults and the background or the area directly surrounding the faults. For instance, a background ratio of 70% for Mw 4.0 means that 70% of the total seismicity rate of Mw 4.0 is modelled on

faults and 30% as background seismicity. This is achieved by subtracting the proportional part of the seismic moment release of the GR from the faults (FM model in this case) (Figure 4.3) and assigning it to the background according to i) the ratios considered in the affected magnitude range and ii) respecting the GR distribution (see Chartier et al., 2019 for details on the background ratio). On the one hand, this avoids truncating the distributions at a given magnitude to distribute seismic potential between faults and background, and on the other hand, it avoids double counting of seismicity. Here the background area corresponds to the EBSZ buffer, whose seismic potential is not only defined by the faults contained but also by the background seismicity as an area source.

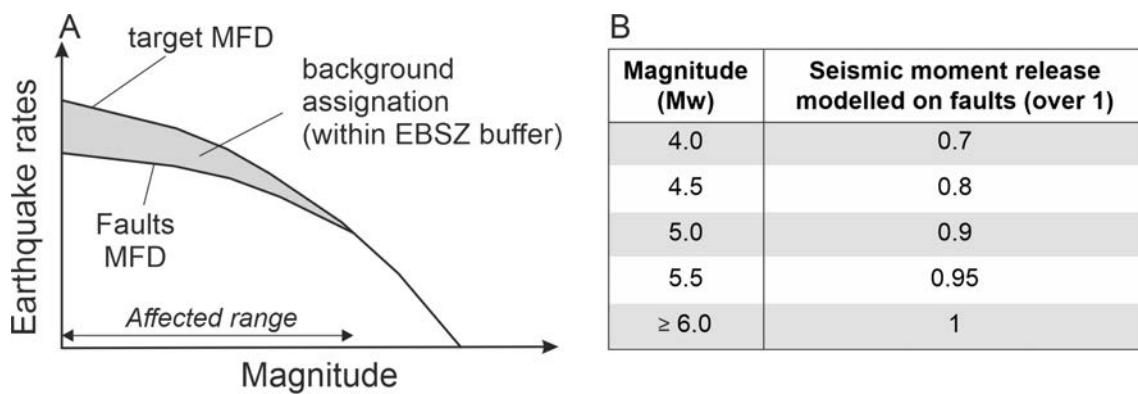


Figure 4.3. **A)** Schematic representation of the seismic moment release assignation to the background from a GR MFD. SHERIFS subtracts part of the seismic moment from the target MFD of the faults to assign it to the background in the affected magnitude range selected by the user. Background ratios are magnitude dependent, hence higher magnitudes have progressively lower percentages of assignation to the background. Out of the magnitude range affected, the earthquake rates of the faults are the same as the target MFD, meaning that all moment is modelled on such faults. The background is modelled in the buffer area defined around the faults; EBSZ buffer in this case. **B)** Background ratios used in this study for each 0.5 magnitude bin.

Setting background ratios might be a difficult task, especially given the novelty of the approach. Chartier et al. (2019) recognize that the user may rely on expert opinion to set this ratio, but propose to use the distance between earthquake epicenters and faults as possible criteria to set it. We cannot follow this approach due to large location errors of the seismicity within the EBSZ: 67% of the $M_w \geq 4.0$ earthquakes are previous to year 1962 (IGN-UPM, 2013) and hence show epicentral errors larger than 10 km or even 20 km (García-Mayordomo, 2005). We then set the background ratios following expert opinion but based on criteria from seismicity data of the region as we explain below. These ratios represent the percentage of the total EBSZ seismic moment that is actually modelled on faults for each 0.5 magnitude bin (Figure 4.3). The remaining is modelled as background in the area of about 10 km around the faults. The selected percentages are

consistent with the fact that most of the instrumental earthquakes of $M_w \geq 4.0$ in the EBSZ have occurred in the modelled faults. This is supported by the location of recent moderate earthquakes (e.g., 2011 Lorca seismic series related to AMF; Martínez-Díaz et al., 2012b) and by the fact that focal mechanisms of seismicity are in agreement with the main faults of the region (Stich et al., 2007, 2010). We select ratios that do not modify significantly the GR distributions from the FM model, so the same logic tree weighting can be applied and comparison can be directly done between both models.

Exclusively the range of M_w 4.0-5.5 is affected by the background ratio in our study because earthquakes this size rarely cause surface rupture (Biasi and Weldon, 2006) and thus, they may occur in unrecognized faults and unadvertised by the paleoseismic studies. $M_w > 6.0$ earthquakes though, are considered to be produced in larger faults with geomorphic expression so they are modelled exclusively on the known EBSZ faults.

4.2.2 Area sources

Outside the bounds of the EBSZ buffer area we consider the area sources of ZESIS model (García-Mayordomo, 2015). The area sources considered here are (Figure 4.4): #29, #30, #31, #34, #35, #36, #37, #38, #39, #40, #41, #43, #44, #45 and, for the FM_bg model only, #55. These areas are all located within a radius of 50 km from the external boundary of the mapping area to account for the influence of seismogenic sources adjacent to the EBSZ buffer area (#55). The potential influence of farther sources is considered negligible for the purposes of this study. The earthquake occurrence in these areas is modelled according to GR distributions obtained in the frame of the project to update the national seismic hazard map of Spain (IGN-UPM, 2013), and their parameters (a and b-value, M_{\min} , M_{\max} ; Table 4.4) are adopted here from the ZESIS database (IGME, 2015b). In the case of area #55, earthquake occurrence is controlled by the seismic moment assigned by the background ratios in each source model and following the target MFD of the faults. The area sources are added to the fault sources modelled with SHERIFS to build the different source models for the hazard calculations.

The characterization of the area sources is further completed defining a distribution of nodal planes and hypocentral depths in each area (OpenQuake manual v.3.7.1; GEM, 2019). The former controls the strike, dip and rake of earthquake ruptures inside the zone, while the latter controls the depth of the center of the ruptures. Nodal planes in each area are defined based on the predominant fault orientations from the QAFI v.3 database (IGME, 2015a), as well as by the distribution of focal mechanisms available in

southeastern Spain and North Africa (Stich et al., 2010), and the Alboran Sea (Gràcia et al., 2019) (Table 4.4). Eventually, a set of different nodal planes is defined for each area source having each one the same probability of occurrence. Similarly, two equally probable hypocentral depths are defined for each source area (Table 4.4): the upper is set at 5 km and the lower between 8 to 10 km depending on the minimum common seismogenic depth of all faults contained in the area. The maximum seismogenic depth of the faults in the QAFI database defines the seismogenic depth for each area source.

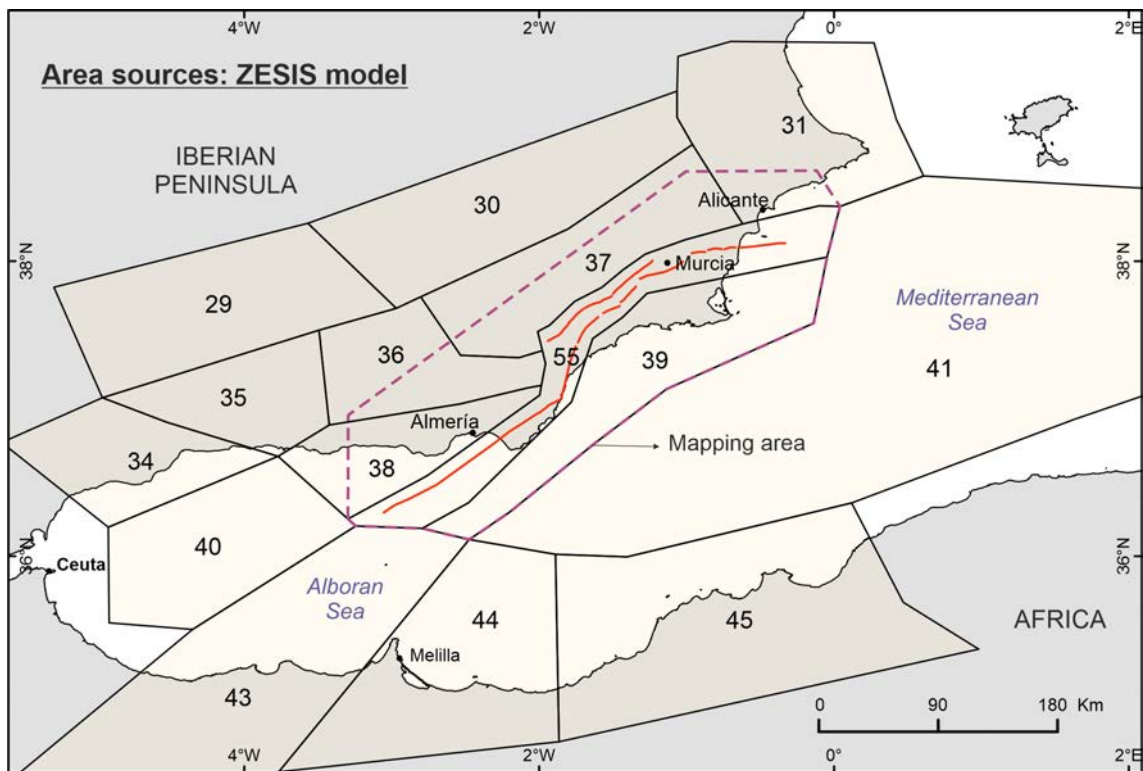


Figure 4.4. Seismogenic area sources considered in this study from the ZESIS model (García-Mayordomo, 2015; IGME, 2015b), whose parameters are indicated in Table 4.4. A dashed purple line delineates the mapping area where the seismic hazard is computed. The location of the main faults of the EBSZ from Figure 4.2 within its buffer area (#55) are indicated.

ZESIS parameters				OpenQuake parameters					Reference
Area source	Mw range (Mw)	GR parameters		Seismogenic depth (km)	Hypocentral depths (km)		Nodal planes		
		a	b		Depth (km)	Probability	Dip/rake/strike (°)	Probability	
29	4.0-6.6	3.36	1.02	20	a) 5 b) 10	a) 0.5 b) 0.5	a) 90/180/060	a) 1.0	
30	4.0-5.0	3.84	1.26	11	a) 5 b) 10	a) 0.5 b) 0.5	a) 85/-140/125 b) 90/-140/040	a) 0.5 b) 0.5	Mean fault orientations inferred from the QAFI database (IGME, 2015a)
31	4.0-6.6	2.99	0.89	15	a) 5 b) 10	a) 0.5 b) 0.5	a) 90/30/065 b) 60/-90/330	a) 0.5 b) 0.5	
34	4.0-6.6	3.30	1.0	8	a) 5 b) 8	a) 0.5 b) 0.5	a) 70/5/151 b) 85/160/060 c) 88/-170/243 d) 80/-2/152	a) 0.25 b) 0.25 c) 0.25 d) 0.25	Focal mechanisms by Stich et al. (2010)
35	4.0-6.8	4.24	1.12	9	a) 5 b) 9	a) 0.5 b) 0.5	a) 60/-90/150 b) 60/-90/330	a) 0.5 b) 0.5	
36	4.0-6.5	3.08	0.98	9	a) 5 b) 9	a) 0.5 b) 0.5	a) 60/-90/150 b) 60/-90/330	a) 0.5 b) 0.5	
37	4.0-6.8	4.23	1.16	11	a) 5 b) 10	a) 0.5 b) 0.5	a) 90/30/240 b) 90/-135/325	a) 0.5 b) 0.5	Mean fault orientations (QAFI)
38	4.0-6.7	3.34	0.96	8	a) 5 b) 8	a) 0.5 b) 0.5	a) 60/-135/150	a) 1.0	
39	4.0-6.7	4.29	1.34	8	a) 5 b) 8	a) 0.5 b) 0.5	a) 90/180/100 b) 60/-90/140	a) 0.5 b) 0.5	
40	4.0-6.5	2.88	0.94	10	a) 5 b) 10	a) 0.5 b) 0.5	a) 23/135/120 b) 85/5/214	a) 0.5 b) 0.5	Fault orientations from QAFI database and focal mechanisms by Gràcia et al. (2019)
41	4.0-6.5	4.5	1.35	8	a) 5 b) 8	a) 0.5 b) 0.5	a) 90/180/120 b) 90/0/014	a) 0.5 b) 0.5	Mean fault orientations (QAFI)
43	4.0-7.0	4.23	1.07	11	a) 5 b) 10	a) 0.5 b) 0.5	a) 85/5/214 b) 84/175/124 c) 90/0/210 d) 45/85/070	a) 0.25 b) 0.25 c) 0.25 d) 0.25	Focal mechanisms by Stich et al., (2010) and Gràcia et al. (2019)
44	4.0-6.4	3.08	0.9	11	a) 5 b) 10	a) 0.5 b) 0.5	a) 90/170/104 b) 90/170/001	a) 0.5 b) 0.5	Mean fault orientations (QAFI)
45	4.0-7.3	2.96	0.8	11	a) 5 b) 10	a) 0.5 b) 0.5	a) 18/102/59 b) 73/86/226	a) 0.5 b) 0.5	Focal mechanisms by Stich et al. (2010)
55	Earthquake occurrence is modelled with SHERIFS for Mw 4.0-5.5 considering the seismic rates assigned by the background ratios and following the target MFD shape (b-value) of the EBSZ faults.			12	a) 5 b) 8	a) 0.5 b) 0.5	a) 90/20/050 b) 60/90/080	a) 0.5 b) 0.5	Mean fault orientations (QAFI)

Table 4.4. Parameters of the area sources used for the area source model in this study. M_{\min} , M_{\max} (Mw range), a and b-values of the GR distribution are extracted from the ZESIS area source model (García-Mayordomo, 2015; IGME, 2015b). OpenQuake required parameters such as nodal planes are inferred from main fault orientations of the QAFI v.3. database (IGME, 2015a; García-Mayordomo et al., 2017) or focal mechanisms of the studies indicated in the table. Seismogenic depths are based on fault data compiled in the QAFI database.

4.2.3 Final composite seismogenic source models for the hazard calculations

Two resulting composite source models are used for the calculations: FM+area sources and FM_bg + area sources. The “composite” term is used here to remark that each source model is composed by a fault source model and an area source model. The former sets the occurrence rates of all the fault ruptures envisaged in each fault rupture hypothesis modelled with SHERIFS within the EBSZ buffer area. The latter sets the occurrence rates of the different area sources considered outside the EBSZ buffer area and the background seismicity in the case of FM_bg model. The final models are referred by the distinctive fault source model name henceforth (i.e., FM and FM_bg). Because each of the four multi-fault rupture scenarios is composed of 20 different GR curves, a total of 80 input source models for OpenQuake compose both FM and FM_bg source models. The fault source part (e.g., earthquake rates, M_{\max}) is different for each 80 models because it depends on a) on the rupture scenario considered and b) the values of the input parameters explored randomly during the SHERIFS calculation. Each FM and FM_bg are computed separately in a different hazard calculation to better test and highlight the influence of including a background ratio, and to compare results more directly.

4.2.4 Ground motion prediction equation

We selected the ground motion prediction equation (GMPE) derived by Campbell and Bozorgnia (2014) from the PEER NGA project (Power et al., 2008). This equation is well adapted for fault-based PSHAs since it accounts for near-fault features such as fault geometry, style of faulting, depth of rupture and hanging wall effects. For the fault-based approach that we propose, this equation is then suitable to show the sensibility of the seismic hazard results to the fault source models. Additionally this equation is the one that Rivas-Medina et al. (2018) selected for a fault-based PSHA in southeastern Spain after an analysis of several GMPEs. According to the authors, this equation allowed better estimations of the expected accelerations in the study region considering the characteristics of the sources and the available data.

We acknowledge that considering a set of GMPEs is a normal practice in PSHA in the attempt to capture the epistemic uncertainty related to ground motion. However, we consider just one GMPE to facilitate the detection of the impact of fault incorporation into PSHA and to be able to perform direct comparisons with previous studies. In order to quantify the influence of the GMPE on the results related to the fault source model and compared to other GMPEs not sensible to near-fault effects, we perform a sensibility

analysis to the FM model by using the Akkar et al. (2014) equation. This is the latest GMPE derived from pan-European databases and does not include fault parameters in its functional form apart from style of faulting as a dummy variable. The implications of this analysis are discussed in section 7.6.3.

4.2.5 Rupture model weighting and logic trees explored

Because each source model is computed separately, two logic trees are explored in this study. For each logic tree (Figure 4.5), the four different hypotheses of multi-fault ruptures are considered to incorporate the epistemic uncertainty of earthquake rates on faults. Each rupture hypothesis constitutes a branch of the logic tree and their weights are based on i) overall performance of the models in terms of NMS and ii) the agreement of the different GR distributions with the seismicity rates of the regional seismic catalogue and paleoearthquake rates. Concerning the NMS, models are weighted based on the overall percentage; lower percentages (<30% based on Chartier et al., 2019) show better performances than higher percentages. In terms of the catalogue and paleorates, we visually analyze their fit with the modelled GR curves and weight them based on the results. Good fits imply that the models allow to describe these datasets better. Those hypotheses, i.e. logic tree branches, that perform better in all the mentioned tests are weighted higher in the logic tree. Because each rupture hypothesis is composed by 20 GR curves, hence 20 input source models for OpenQuake that include a fault source model and an area sources model, the weight of each of the 20 branches or models that form a hypothesis equals 1/20 of the weight of the whole branch.

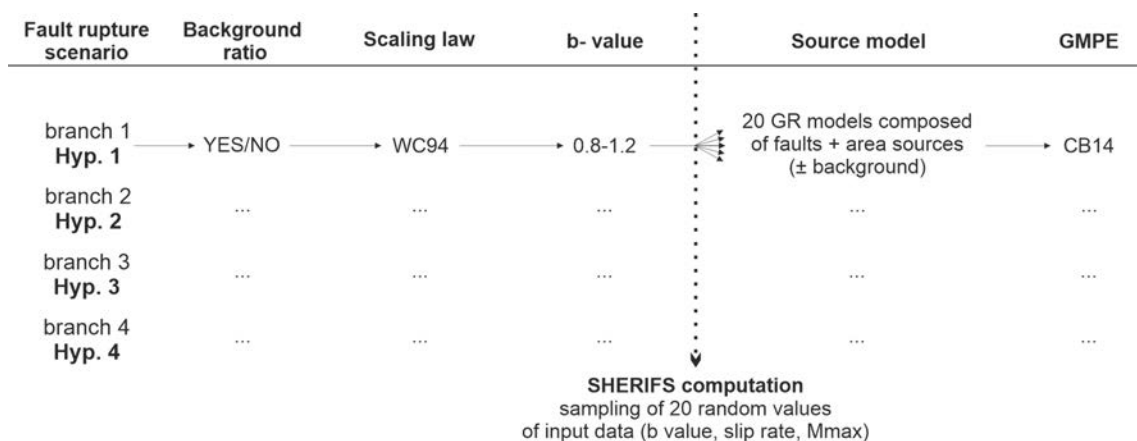


Figure 4.5. Scheme of the logic trees used in this study. Hyp.: hypothesis; WC94: Wells and Coppersmith (1994); CB14: Campbell and Bozorgnia (2014).

4.2.6 Hazard calculations

The hazard calculations are performed using the OpenQuake engine v.3.7.1 (Pagani et al., 2014; GEM, 2019). We compute mean hazard maps in terms of Peak Ground Acceleration (PGA) as function of probabilities of exceedance of 10, 5, 2 and 1% in a time window of 50 years, corresponding to return periods (RPs) of 475-, 975-, 2475- and 4975-yr, respectively (Figure 7.5 and Figure 7.6; section 7.4). The region considered is depicted in Figure 4.4 and follows a 2x2 km grid, accounting for 10,556 calculation points per return period. This region is defined to comprise completely the EBSZ buffer area and include important cities of the region (Murcia, Lorca, Almería, Vera, Torre Vieja, Alicante and Cartagena). To analyze fault influence, in the cities adjacent to the EBSZ faults we produce hazard disaggregation plots for the distance-magnitude relationship (Figure 7.7) and mean hazard curves in terms of PGA (Figure 7.8). Soil conditions are always considered to be rock or hard soil ($V_{s30} = 760$ m/s). The maximum distance considered for the hazard calculations is 100 km to better reproduce the near-fault related hazard of the EBSZ and because farther sources have negligible impact in the study area. Source input files of the hazard calculations including source models, GMPE, logic tree and calculation specifications can be found in:

- Mendeley Data repository corresponding to the data of the first article (source modelling with SHERIFS): Gómez-Novell et al. (2019).
- Supplementary material of the second article (seismic hazard results): Gómez-Novell et al. (2020b).

III. RESULTS AND PARTIAL DISCUSSIONS

This chapter presents the main results of the thesis: a structural and paleoseismic characterization of the Alhama de Murcia Fault and a fault-based probabilistic seismic hazard assessment for the Eastern Betics Shear Zone.

View of El Salvador site from the San Julián Creek.

5 Structural and paleoseismic characterization of a multi-branch transect of the Lorca-Totana segment of the Alhama de Murcia Fault

5.1 Introduction

In this section we present the main results obtained from the structural and paleoseismic characterization of multiple fault branches in the Lorca-Totana segment of the Alhama de Murcia Fault (AMF). The Lorca-Totana segment of the AMF extends for about 23 km of length and shows a change of orientation with respect to the other segments of the fault (Figure 5.1A): striking from NNE-SSW in the Góñar-Lorca, Totana-Alhama and Alhama-Alcantarilla segments to NE-SW in the Lorca-Totana one. Such strike variation implies a more perpendicular orientation of the fault with respect to the Africa Eurasia convergence vector (NNW-SSE). This causes the fault to i) have a higher reverse component evidenced by the presence of steeper scarps and important uplift (~950 m) of Miocene materials at La Tercia range (Ferrater, 2016), and ii) to splay into several subparallel branches as opposed to the other segments of the fault. This segment shows one of the most marked surface expressions of the whole fault, which motivated the development of most of the paleoseismic studies available thus far in the fault and of the Eastern Betics Shear Zone (e.g., Silva et al., 1997; Martínez-Díaz et al., 2003; Masana et al., 2004; Canora et al., 2016; Ferrater, 2016; Ferrater et al., 2016).

To date, paleoseismic studies in the AMF have mainly focused in one of the central branches of the Lorca-Totana segment (SAMF) (Martínez-Díaz et al., 2003; Masana et al., 2004; Ferrater et al., 2016; Ferrater, 2016) and have successfully been able to characterize its recent paleoearthquake record and slip rates. In the early 2000s, Martínez-Díaz et al. (2003) and Masana et al. (2004) performed the first paleoseismic studies in the fault, specifically in the central branch (SAMF), and excavated trenches in the sediments of El Saltador and El Colmenar alluvial fans (Figure 5.1B). From these studies the authors estimated a vertical slip rate of 0.04-0.35 mm/yr and inferred lateral and net slip rates of 0.06-0.53 mm/yr and 0.07-0.66 mm/yr, respectively, based on striae measurements in the fault zone. Also, they recognized at least three paleoearthquakes in the last 27 ka allowing to estimate an average recurrence period of ~14 kyr, with a likely clustering for the last two events.

In the 2010s, in the same branch at El Saltador fan, new techniques for slow moving faults such as detailed paleoseismic 3D trenching and morphotectonic analysis were applied to directly quantify lateral slip rates for this segment: 1.0 ± 0.2 mm/yr for the last 28 ka and 0.9 ± 0.1 mm/yr for the last 20 ka, respectively (Ferrater, 2016). The vertical slip rate is estimated at ~ 0.1 mm/yr, although it is probably underestimated because it does not account for folding-related deformation and is only measured directly on the fault plane. This study also identified the longest paleoearthquake record thus far with 10 events, yielding a mean RI of 3.5-5.3 kyr for the last 59 ka with a possible acceleration in the last 30 ka. Such new data allowed for a significant reassessment of the seismic potential of this fault, unveiling higher seismic parameters than anticipated in the previous years.

Because the Lorca-Totana segment is composed by more than one active branch absorbing the deformation the need to investigate all the branches is crucial to get a complete and integral characterization of the whole fault zone. Integrating the results of different sites has demonstrated to be a turning point in the characterization of a fault and, hence, for its implications in the seismic hazard assessment of the area (e.g., DuRoss et al., 2011). Single-site studies can cause an underestimation of the overall seismic potential of the fault and ultimately of its associated hazard. The first attempt of an integral analysis in the AMF was presented by Ortuño et al. (2012) in the southwestern termination of the fault (Góñar-Lorca segment; Figure 5.1). In this study, six paleoseismic trenches were dug across several fault branches in the horse-tail structure at the fault termination. The integration of seismic parameters from the different fault branches led to different values depending on the approach: estimations of the strike slip rate between 0.95 and 1.37 mm/yr when considering the longer-term geomorphological markers (channels) and to a total slip rate of 0.16-0.24 mm/yr for one of the transects by just extrapolating the observations on a single paleoseismological trench. A minimum of six paleoearthquakes with a maximum RI of 15-29 kyr for the last 59-116 ka.

Ferrater (2016) also integrated data from deflected channels along different fault traces. This allowed to refine the previous values of slip rates at 1.6-1.7 mm/yr for the Góñar segment since the Middle Pleistocene, which are remarkably higher than the ones obtained in the Lorca-Totana segment by paleoseismic trenching for shorter and more recent periods. Because fault displacement usually decreases at the fault tip regions (e.g., Roberts, 1996; Manighetti et al., 2005), this result might suggest that in the Lorca-Totana

segment the available values are underestimated, more so because are obtained for a single branch.

This context motivates the results presented in this part of the thesis. Three new paleoseismic sites are carried out in previously unstudied fault branches in order to characterize their Quaternary activity. This includes a thorough trenching analysis including the identification of the number and timing of paleoseismic events, their RI and the constraining of fault slip rates over different time periods. We also enlarge a previous trench from an already studied branch (SAMF) at El Saltador site to enhance the resolution and completeness of the paleoearthquake history of the fault, to re-evaluate the likely underestimated vertical component of the deformation and to re-assess the seismic parameters already estimated for that fault branch. With all this, the final aim is to integrate all the results (structural, morphological and paleoseismological) that characterize the activity of the whole fault segment, allowing a more detailed discussion of the implications for the seismic hazard assessment.

The results presented herein comprise: i) a geomorphological and structural characterization of the segment with special focus on a transect near La Hoya town (Figure 5.1), ii) a paleoseismological trenching analysis of four paleoseismic sites in this area and iii) an integration of the results to characterize the fault segment with key paleoseismic parameters. We recognize several evidence of paleoearthquakes in the trenches and establish an event chronosequence with the numerical dates available, we measure the vertical, lateral slips and shortenings of the different stratigraphic units in the trenches, and infer the net slips using the available kinematic field data (fault rakes). We then calculate the vertical slip rates, net slip rates and shortening rates for each fault branch and for the complete segment.

5.2 Geological setting of the Lorca-Totana segment

The activity of the AMF since the onset of the neotectonic period around Late Miocene, is related to a transpressive tectonic inversion of NW-dipping normal faults limiting sedimentary basins formed during the Neogene, such as the Lorca and Fortuna basins (Montenat et al., 1987; Meijninger and Vissers, 2006) (Figure 5.1A). This transpressive reactivation caused the basins inversion and uplift of mountain ranges in the northwestern block of the fault, enhancing the syn-tectonic formation of alluvial fan and fluvial environments in the frontal parts of these reliefs, especially since the Middle Pleistocene up to the present day (Silva, 1994; Martínez-Díaz, 1998). In the Lorca-Totana segment,

III. Results and partial discussions

the most prominent relief is La Tercia range (~1000 m.a.s.l.), formed by Neogene sedimentary rocks from the Lorca basin and Paleozoic rocks from the Betic range basement (Marín-Lechado et al., 2011), exhumated during the uplift.

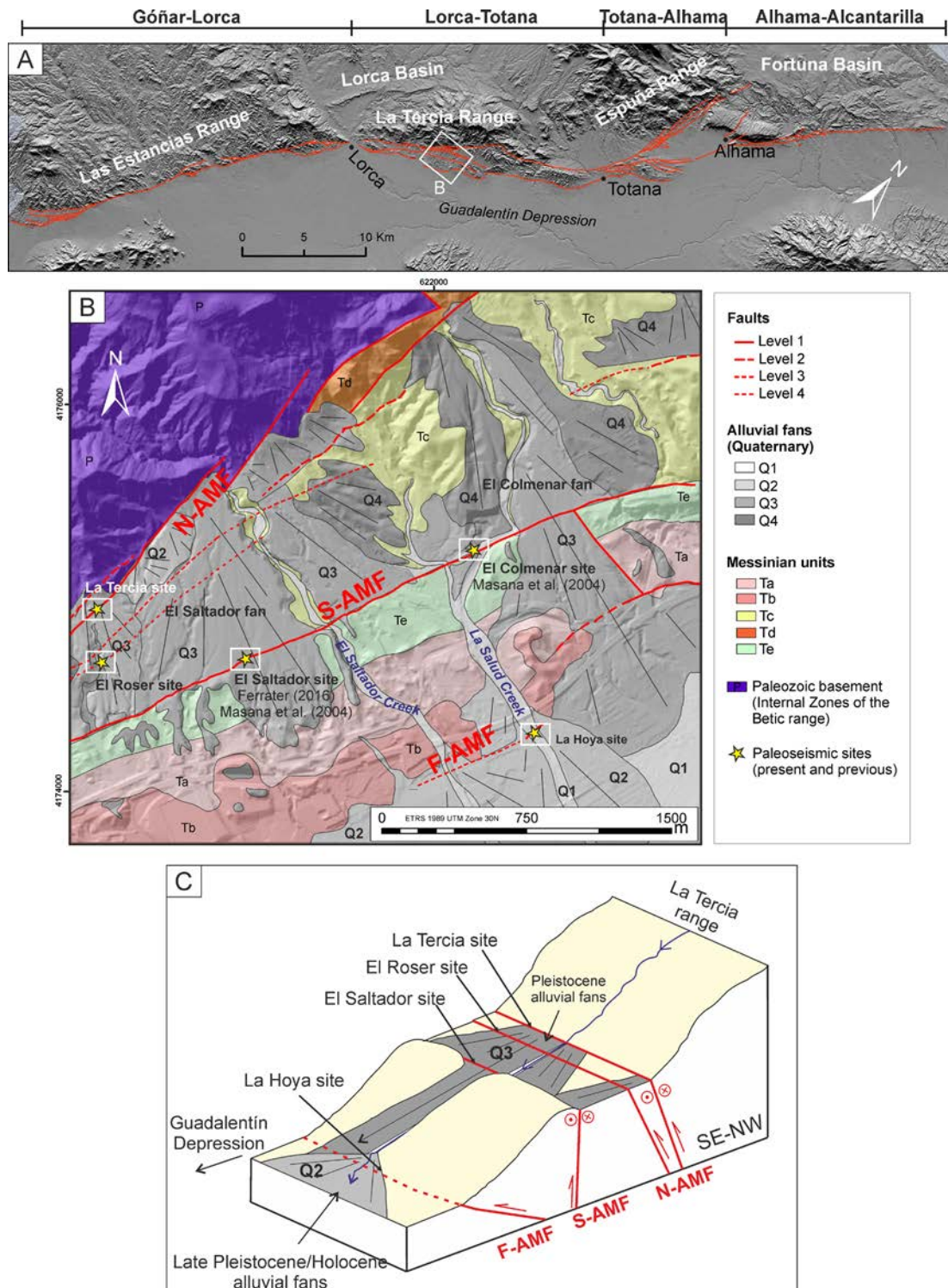


Figure 5.1. **A)** Location of the studied area within the segments of the Alhama de Murcia Fault (AMF). **B)** Geological map of the transect studied with the main geological units. The location of the current sites and previous studies in this sector are highlighted by white rectangles. Modified from Ferrater (2016). **C)** Block diagram of the geological context of the Lorca-Totana segment with the studied sites highlighted and the alluvial fans. Modified from Ferrater (2016).

The studied sites of the Lorca-Totana segment of the AMF are located in a NW-SE transect of about ~2 km long, whose characteristics make it suitable for the development of paleoseismic studies such as the ones presented in this document. These are displayed in different fault branches that affect Quaternary alluvial materials coming from La Tercia range to the NW, well-preserved and prevented from excessive erosion or sedimentation. Three of the sites (La Tercia, El Roser and El Saltador sites; Figure 5.1) are located in the surface of an alluvial fan with a well-defined telescopic geometry, which has been previously referred as El Saltador fan. This alluvial fan is limited by two fault strands, classically referred to as N-AMF and S-AMF (Martínez-Díaz et al., 2003; Ferrater, 2016). The N-AMF, limits the fan to the N, and controls the NE-SW orientation of the La Tercia range, which is a range formed mainly by Paleozoic rocks from the Alpujarride and Maláguide complexes of internal zones of the Betic Cordillera (Silva, 1994; Martínez-Díaz et al., 2003). The uplift of this range caused the onset of the alluvial sedimentation in the region, providing sediments for the formation of El Saltador alluvial fan during the Middle-Late Pleistocene (Martínez-Díaz et al., 2003).

The S-AMF limits, for the most part, the fan to the S by generating a scarp that consistently acted as a tectonic barrier blocking the sediments coming from La Tercia and affected the morphology of the fan. This special context allowed the preservation of the sediments and is the reason that paleoseismic studies at El Saltador and El Colmenar sites (e.g., Masana et al., 2004; Ferrater, 2016; Ferrater et al., 2016). The sedimentation of El Saltador fan is mainly dominated by debris flow units alternated with mud flow sediments that in the upper parts of the sequence show abundant alluvial channel sediments incised (Martínez-Díaz et al., 2003).

The reduction of the activity in the N-AMF branch during the Late Pleistocene-Holocene, caused the migration or distal offlap of the alluvial sedimentation towards the S in the more frontal parts of the fault uplifted reliefs (Silva, 1994; Martínez-Díaz et al., 2003). In these frontal parts, the alluvial sediments are affected by the frontal branch of the AMF (F-AMF; Ferrater, 2016) which limits the relief towards the S and constitutes the northern border of the Guadalentín basin. La Hoya site is located in this region of the fault system which records the most recent history of the fault (Figure 5.1).

The nowadays alluvial sedimentation is found towards the central parts of the Guadalentín basin conforming a distal offlap with respect to the previous deposits, more attached to the reliefs (Silva, 1994, 2014). These alluvial fans dissect the previous ones attached to

the frontal branch of the AMF, showing wide geometries and low slopes. The position and geometry of these fans, according to Silva (1994) responds to a decrease in the tectonic activity.

5.3 Mapping of the Lorca-Totana segment

At least five branches have been recognized in the Lorca-Totana segment of the fault, most of which have been previously recognized by other authors (e.g., Martínez-Díaz, 1998; Martínez-Díaz & Hernández-Enrile, 2001), but they have never been properly described or characterized through paleoseismic studies. Also, a more detailed mapping of the fault traces is provided for the first time. We propose a specific nomenclature for each one of the fault branches, which we use henceforth (Figure 5.2): N_1 - and $N_{2a,b}$ -AMF for the branches that conform the northernmost sector of the fault (N-AMF), S-AMF for the previously studied branch located in the middle of the transversal section of the fault system, and F-AMF for the southernmost or frontal branch of the pressure ridge. These nomenclatures are based on the ones previously proposed by Martínez-Díaz et al. (2003) and Ferrater (2016): N-AMF, S-AMF and F-AMF. All the fault branches show geomorphic evidence of recent activity supported by the presence of features such as fault scarps, lineaments or deflected drainage channels. This evidence is clearer in the Lorca-Zarcico creek sector of the segment, where the subparallel branches form a 2 km-wide deformation zone, which can be identified and distinguishable on the alluvial fan surfaces displayed in the area (Figure 5.2). Towards the NE of the Zarcico creek, the fault branches concentrate in a narrower fault zone whose geomorphological expression is less evident. This fact could reflect an actual decrease of complexity, but it might also be the result of the area having less geomorphological markers; there is a lack of alluvial surfaces and well-developed channels. Instead, erosive processes dominate and have exposed Miocene basement showing subvertical stratification.

The branches of this segment of the AMF affect differently the Quaternary alluvial fan generations. Four main generations have been identified in this study, which we name as Q4, Q3, Q2 and Q1. The alluvial generations have been previously identified by other authors, but our classification slightly differs from them as shown in Table 5.1. These comprise ages between Middle Pleistocene and the present. Older generations (Q4 and Q3) are generally spatially limited between the north-westernmost fault branch (N_1 -AMF), where the main mountain front is located, and the northwestern branch of the pressure ridge of this segment (S-AMF). These fans are adjacent to the mountain front

and in a much higher position than the base level of the Guadalentín river, which suggest that they are older and affected by a period of high tectonic activity (uplift), which implies a low deposition/tectonic activity relationship. One of the main examples is El Saltador fan, where the La Tercia, El Roser and El Saltador sites are located. Q2 fans are incised in the Q3 and Q4 generations and develop further away from the mountain fronts, closer to the frontal parts of the reliefs uplifted by the fault in the northern border of the Guadalentín Depression. Locally, selected deposits at El Saltador alluvial fan site, are developed on top of the older units rather than incised in them, which we interpret as an early Q2 sub-generation (Q2a) developed previous to the incision of the drainage and extensive migration towards the Guadalentín Depression. This sub-generation is found mainly at La Tercia and El Roser sites (Figure 5.2). Q2 deposits in the frontal parts of the relief are not currently active but also not completely disconnected from the drainage system, because channels have incisions no deeper than ~5m, which suggests that this generation is recent and its alluvial fans were active not a long time ago.

This study	Ferrater (2016)	Martínez-Díaz et al. (2003)	Silva et al. (2014)
Q4	Q4	B-C	1 st phase
Q3	Q3	D	2 nd phase
Q2 _a	Not identified	E	2 nd -3 rd phase
Q2	Q2	E	transition
Q1	Q1	F	3 rd phase

Table 5.1. Alluvial fan generations defined in this study compared to the ones identified in the main previous studies in the region.

The active alluvial and fluvial systems of the area are represented by the Q1 generation. These comprise the areas located within the incised creeks and in the distal parts of the mountain front up to the Guadalentín Depression. Due to the very low slope in this lowland area and the extensive agriculture, it is difficult to recognize original landforms and, in consequence, to delimitate the fan shapes. For this reason, we mostly represent this generation as a colored area that includes the alluvial fans and also flood areas of the river, depositional glaciais and active channels (Figure 5.2).

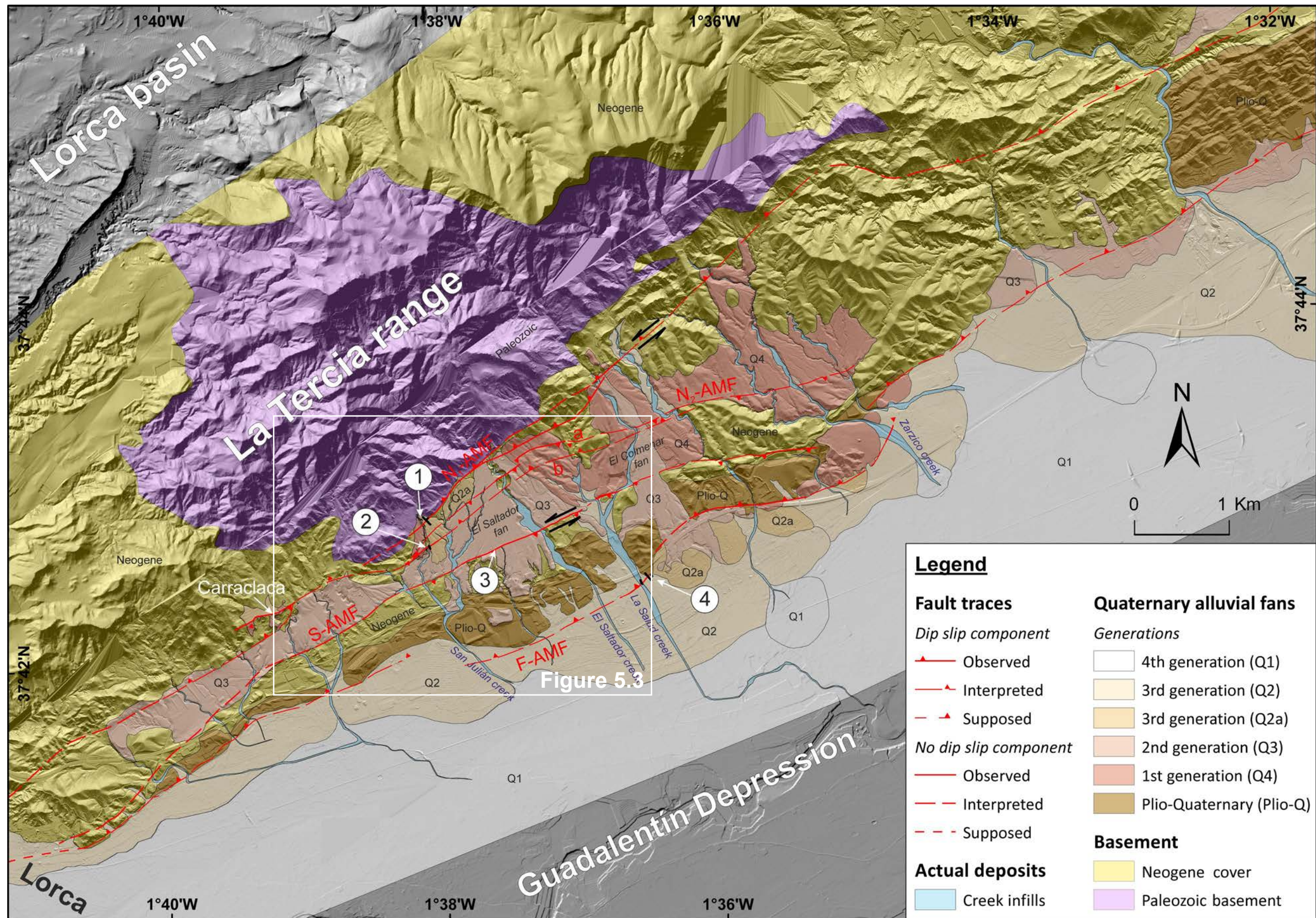


Figure 5.2. Geological map of the Lorca-Totana segment of the Alhama de Murcia Fault (AMF) done in this study, centered in the studied transect. The locations mentioned throughout the text of the present section are indicated, including fault strands and paleoseismic sites. 1: La Tercia site; 2: El Roser site; 3: El Saltador site; 4: La Hoya site. Relief is based on the 0.5 m resolution MDT in the fault zone (SHAKE project) and on the LiDAR-based 2m resolution DEM from IGN agency (centrodedescargas.cnig.es) outside of it. See Annex II (A) for the uninterpreted 0.5 m DEM of this map. Basement cartography is based on the Spanish Geological Map (1:50000) zone 2100 (Marín-Lechado et al., 2011).

5.4 Structure of the Lorca-Totana segment

In the study area, the Lorca-Totana segment shows a wide deformation zone of ~2 km, distributed into at least five different fault branches that cause deformation in the basement rocks and reach the different generations of Quaternary alluvial fans preserved (Figure 5.2). In this section we describe the main morphological and structural features of each of the branches recognized, including their related deformation and inferred kinematics. We combine observations from field reconnaissance, mapping and photointerpretation.

5.4.1 Fault branches

The five main branches recognized in the Lorca-Totana segment are displayed subparallel, following a predominant NE-SW orientation, consistent with the overall orientation of the fault segment (Figure 5.2). They can be distinguished as three main fault branches (N₁-, N₂- and S-F-AMF), being two of them split on two other branches limiting two parallel pressure ridges: The central one, limited by N_{2a}- and N_{2b}-AMF, and the southern one, limited by S- and F-AMF branches (Figure 5.3). These are described in order, from NW to SE.

5.4.1.1 N-AMF

- N₁-AMF

The N₁-AMF fault branch constitutes the northernmost branch of the Lorca-Totana segment and bounds the mountain front of La Tercia range to the south. This fault branch shows a ~N55° orientation, that in the study area of El Saltador fan changes slightly to N35°-N41° (Figure 5.2). The fault displays mainly sub-vertical or strongly dipping to the NW (70-90°), although the appearance and deformation of the fault zone is variable depending on the affected materials. In metamorphic materials from La Tercia range, the fault generates relatively wide (>10 m) shear zones or bands with associated fault gauges where mineral alteration processes take place. These characteristics evidence a long-term history of activity and deformation on this fault strand, capable to generate these kind of deformation features and studied in detail by Rodríguez-Escudero (2017). One example of this kind of N₁-AMF zone is the outcrop recognized at El Saltador creek or near at the base of the La Tercia range mountain front (Figure 5.4). In younger Quaternary sedimentary deposits, the lower compaction and shallow conditions of these materials cause refraction of the fault. Therefore, the fault displays as vertical planes mainly recognized by clast lineations and incipient calcification along these fracturing zones. The

III. Results and partial discussions

fault zones are also narrower (<5 m) and do not present shear structures such as the gauges in older units, evidencing less amount of repeated deformation and consistent with the younger age of the materials (Figure 5.4).

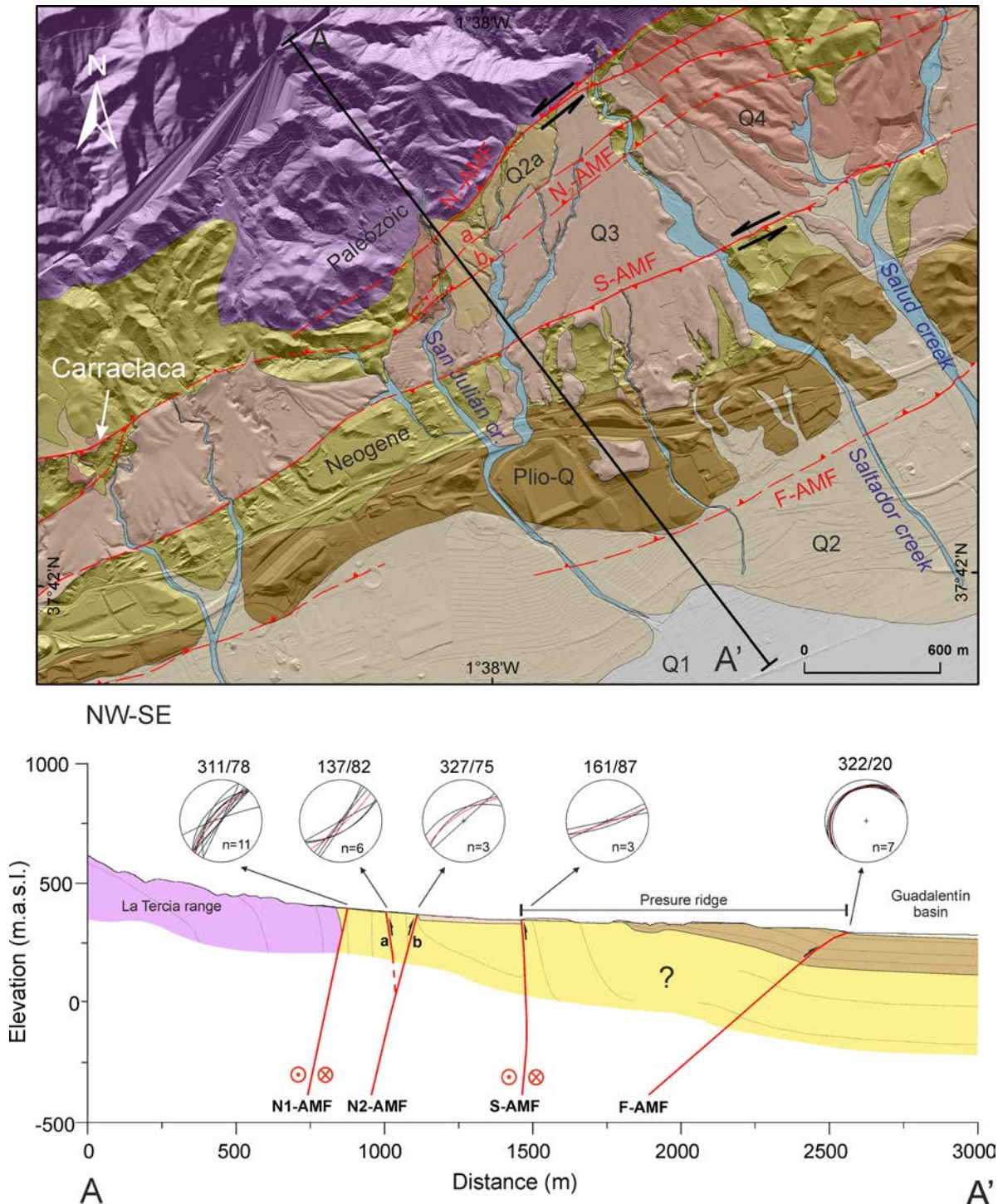


Figure 5.3. Detail of the geological map in Figure 5.2 and cross section of the transect studied depicting the recognized fault branches and the main structural features. Stereographic plots are made from field measurements of fault structures. The structure of the basement materials is inferred from field observations and based on the cross sections proposed by Martínez-Díaz et al., 2012b). The structure of the Miocene between S-AMF and F-AMF is uncertain due to the lack of outcrops in this area. The legend of geological units and faults are described in Figure 5.2.

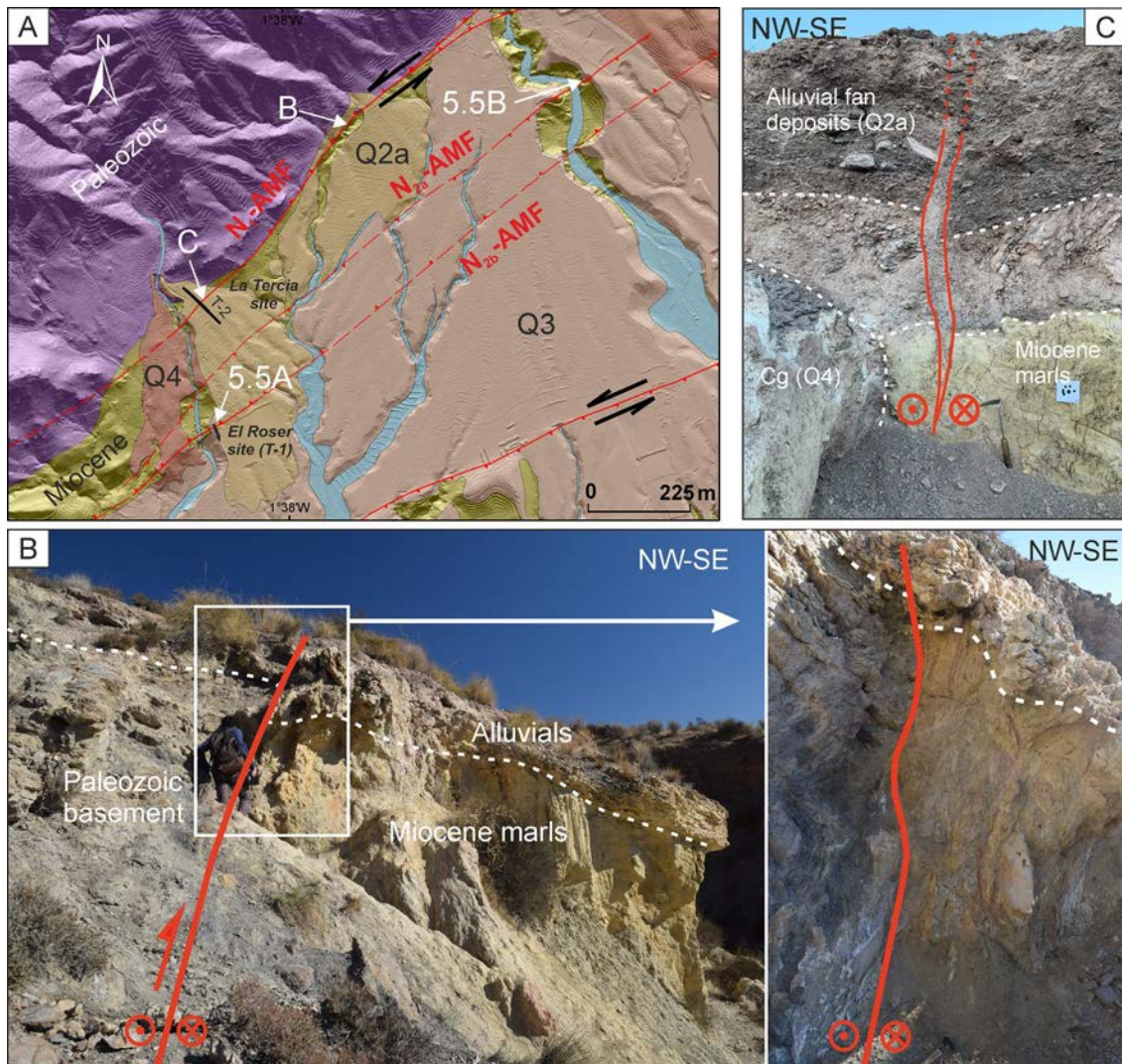


Figure 5.4. Appearance of the N_1 -AMF branch in different outcrops. **A)** Location of the different outcrops of windows B and C near La Tercia site. The location of the images from Figure 5.5 of El Roser site is also depicted. The geological units are the same as Figure 5.2. **B)** NW-dipping fault zone in basement materials, with highly tectonized shear bands. Notice that in this area the fault puts in contact Paleozoic and Miocene materials. **C)** Appearance of this fault strand in young Q2 materials in the walls of T-2. See Annex II (C) for the uninterpreted images.

- N_2 -AMF

The N_2 -AMF is composed of two subparallel branches that define a push-up structure. The corresponding synthetic fault is named N_{2b} -AMF and it dips 70 - 80° towards the NW. The antithetic fault is named N_{2a} -AMF and it dips similarly but towards the SE. Both faults show a general mean orientation of $N55$ - $N58^\circ$ in the study area with a local $\sim N36^\circ$ bending in San Julián creek, where both faults merge, and a major $\sim N75^\circ$ bend more towards the NE (Figure 5.3). Similar surface unions of the two branches are found towards the SW in Carralaca (Figure 5.2), suggesting that both strands join at depth. The footprint of these faults in the surface geomorphology throughout the study area is in general less

marked, but their extension can be inferred from surface scarps, selected channel deflections, and can be directly observed in a few outcrops in the San Julián and El Saltador creeks (Figure 5.5).

In the studied transect of El Saltador fan, the N_{2b} -AMF is the principal fault of this push-up extending clearly from of El Saltador creek to the SW up to Lorca city (Figure 5.2). Conversely, the antithetic N_{2a} -AMF shows less surface expression and mainly appears where the N_{2b} -AMF shows a change of orientation along-strike, such as in Carraclaca (described by Martínez-Díaz & Hernández-Enrile, 2001). Towards the NE however, the principal fault seems to be N_{2a} -AMF as its surface expression is more marked with a clear fault scarp, while the N_{2b} -AMF is less identifiable, especially NE of El Saltador creek (Figure 5.2 and Figure 5.3).

Both fault strands have similar associated deformation patterns mainly controlled by monoclinical propagation folds affecting the Tortonian marls of the basement up to the Quaternary alluvial covers. In the study area, the folding geometry is mainly controlled by the flank verticalization of a distinctive cemented alluvial unit in the N_{2b} -AMF, where nearly 20 m vertical displacements can be observed in the San Julián creek (Figure 5.5B). This unit, referred to as “Cg” henceforth, has a defined tabular geometry and is placed discordant on top the Tortonian basement defining the base of the Quaternary deposits in some parts of the study area. It is interpreted as a glaciais that covered the previous paleorelief and its age is estimated to be Middle Pleistocene according to Martínez-Díaz & Hernández-Enrile (2001).

The rest of the alluvial sequence upwards in the N_{2b} -AMF (mainly Q3 generations; Figure 5.5B) defines a progressive disconformity, with attenuation of the deformation towards the surface, suggesting repeated deformation over the Quaternary. The deformation of this branch is not identified at the bank sides of El Saltador creek, consistent with its less surface expression towards the NE. Conversely, the N_{2a} -AMF shows smaller amount of vertical separation in San Julián creek, where the cemented unit is slightly folded, while it is up to 10 m at El Saltador creek (Figure 5.5A), also consistent with its increased surface expression to the NE.

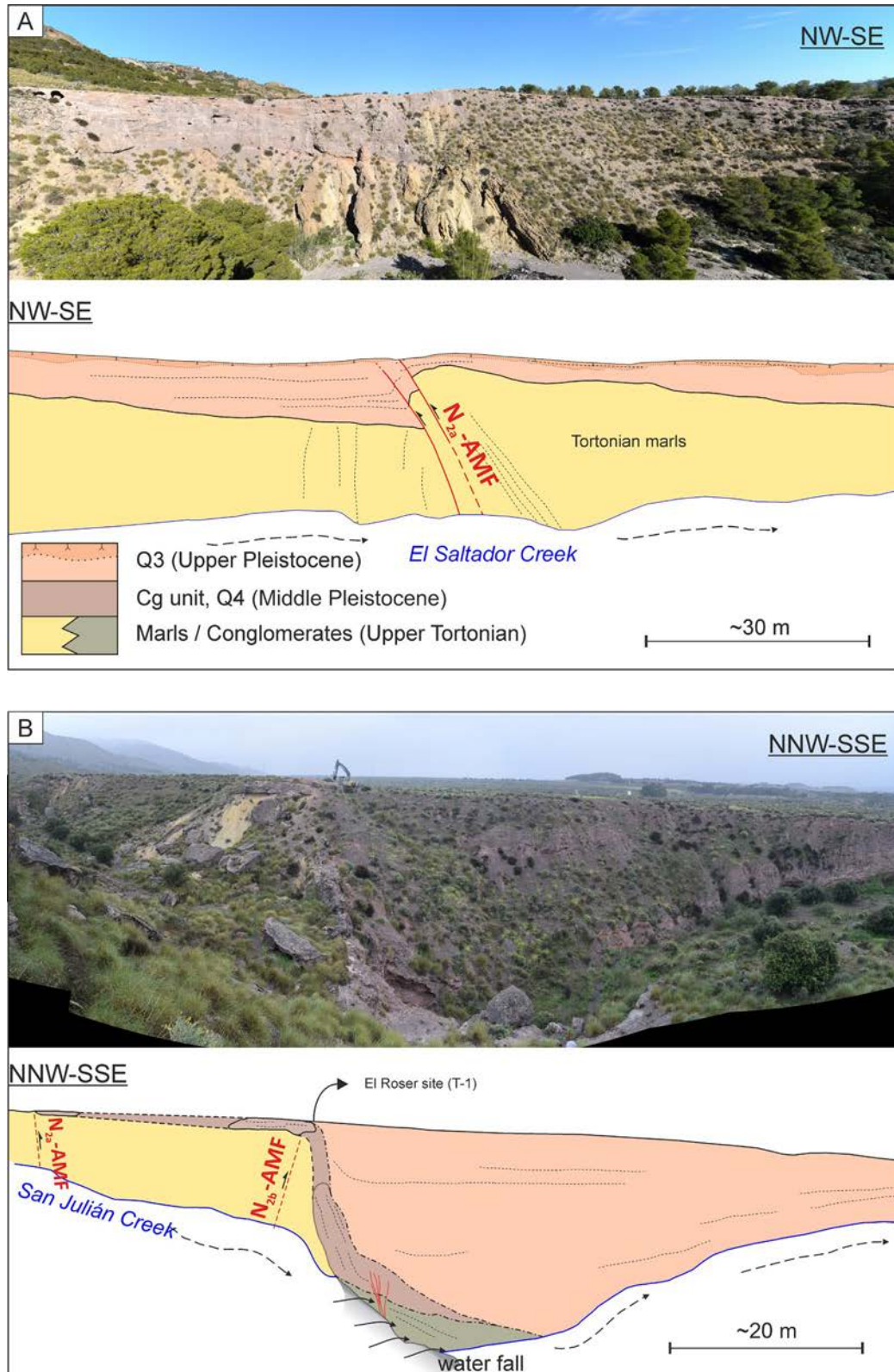


Figure 5.5. **A)** Outcrop of the N_{2a} -AMF in the northeastern margin of the El Saltador Creek where the fault is affecting the whole exposed sequence and generating a geomorphological bump on the surface. **B)** Outcrop of the N_{2b} -AMF in the NE margin of the San Julián Creek where the fault generates a pronounced monoclinical fold in the Q4 (Cg unit) materials. The location of both outcrops is located in Figure 5.4A. See Annex II (C) for the uninterpreted images.

5.4.1.2 S-AMF

The S-AMF branch shows one of the most marked geomorphological expressions out of all the studied branches, but also of all the AMF. Clear fault scarps, lineations, channel deflections or wind gaps can be observed in the DEMs and in the aerial photographs evidencing the recent activity of this fault (Figure 5.6A and B), previously identified in many studies (e.g., Martínez-Díaz et al., 2003; Masana et al., 2004; Ferrater et al., 2017). This context explains why most paleoseismic studies in the Lorca-Totana segment have focused in this specific branch to estimate the seismic and paleoseismic parameters of the AMF.

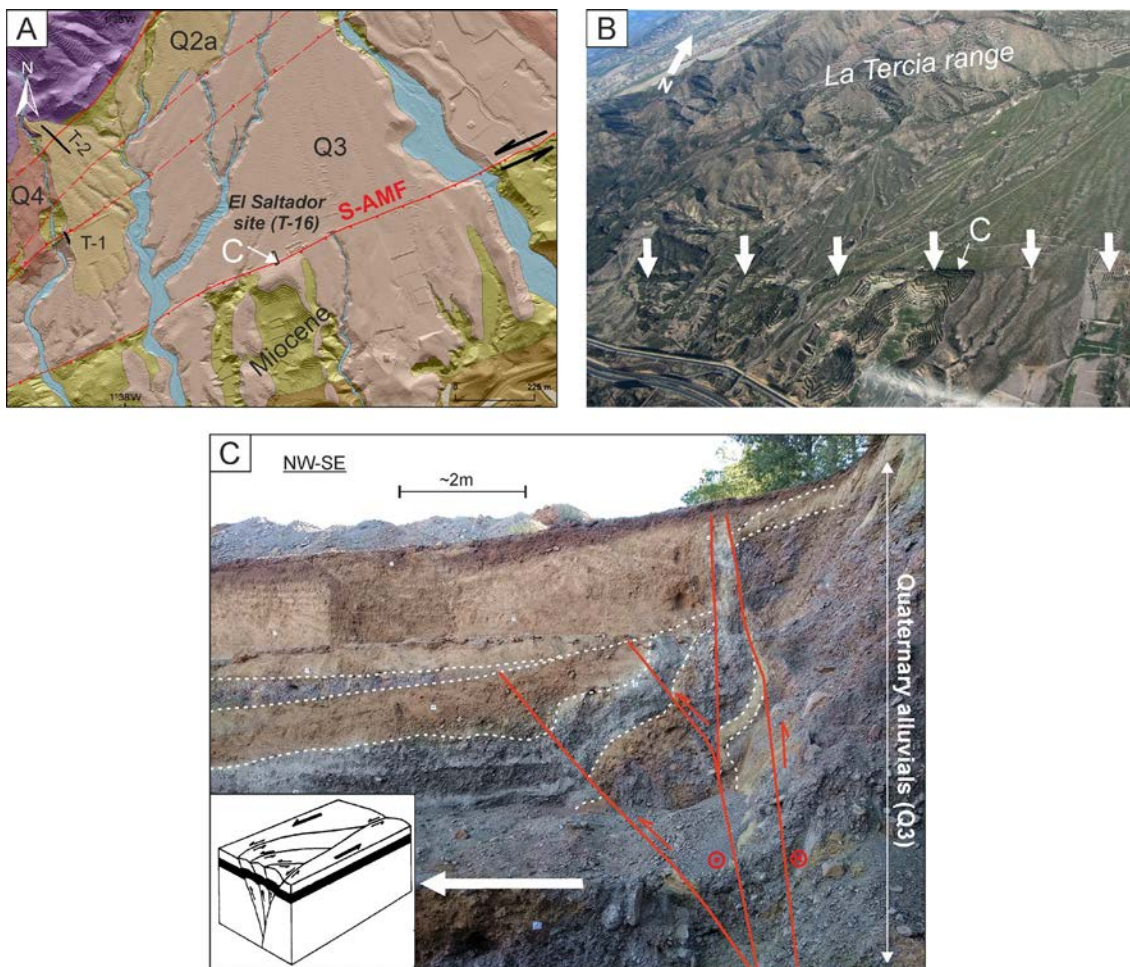


Figure 5.6. **A)** Situation of the S-AMF in the studied transect within the geological map obtained in this study (Figure 5.2). The location of window C is indicated. **B)** Photograph of the zone depicted in window A obtained from a microlight aircraft. Courtesy of José J. Martínez-Díaz. Arrows depict the counter-slope scarp generated by S-AMF. The location of image C is indicated. **C)** Detail image of the S-AMF fault zone in El Saltador site (T-16) affecting Q3 alluvial materials. The structure shows a flower geometry with verticalized strata indicative of shear deformation typically found in strike-slip systems. Flower structure diagram is modified from Twiss and Moores (1992), in McCalpin (2009). Used with permission from John Wiley and Sons. See Annex II (C) for the uninterpreted images.

The S-AMF fault branch shows a mean $\sim N65^\circ$ orientation in the study area, but it changes to $\sim N84^\circ$ in the NE, near La Hoya site (Figure 5.2). The fault dips strongly (subvertical) to the SE, uplifting the southern block and generating a SW-NE elongated relief that constitutes a pressure ridge bounded by the F-AMF to the SW. This S-AMF, together with the N_1 -AMF, define a sunken block that might have acted as a sedimentary trap for most part of the deposition of El Saltador alluvial fan, blocking the drainage of the system during morphogenetic earthquakes (Ferrater et al., 2016).

The S-AMF fault zone is defined by shear deformation that causes verticalization of the Quaternary sedimentary units pinched within the fault zone (Figure 5.6C). In older basement materials, mainly Tortonian marls, the fault shows a highly deformed zone with the presence of fault gauges, similar to the N_1 -AMF branch. In the paleoseismic trenches of El Saltador site (including T-16), minor synthetic SE-dipping fault strands emerge from the main verticalized fault forming a flower structure geometry and generating northwestern verging propagation folds (footwall; Figure 5.6C). These accommodate an important part of the vertical uplift associated with this fault branch, especially in the lower alluvial units of the studied sequence.

5.4.1.3 F-AMF

The F-AMF constitutes the frontal branch of the Lorca-Totana segment and the southernmost branch known so far. This fault strand bounds the southeastern flank of the pressure ridge limited by the S-AMF to the NW and separates the relief generated by the AMF system from the Guadalentín Depression (Figure 5.2 and Figure 5.3). It displays subparallel to the S-AMF, although its trace is more irregular, with relay zones such as the one present NW of La Hoya site. The F-AMF is a low angle-dipping fault with a dip $\sim 20^\circ$ towards the NW, which might also explain the lateral irregularity of the fault trace, conditioned to the topography (Figure 5.7).

The surface expression of this fault is not very marked since no clear fault scarps, channel deflections or other related features are observed. This might be due to the fact that the alluvial materials affected by this branch are from younger generations (Q2) and thus have suffered less tectonic activity. More so, the intense anthropization of this zone hampers the detection of such morphological features. In this context, the presence of the fault trace is mainly interpreted as the geomorphological limit of the pressure ridge uplifted at the northwestern edge of the Guadalentín Depression. Direct surface

III. Results and partial discussions

observations from this fault in the segment are mainly from a road cut located ~1 km NE from it (Figure 5.7B) and from the paleoseismic survey at La Hoya site (see section 5.5).

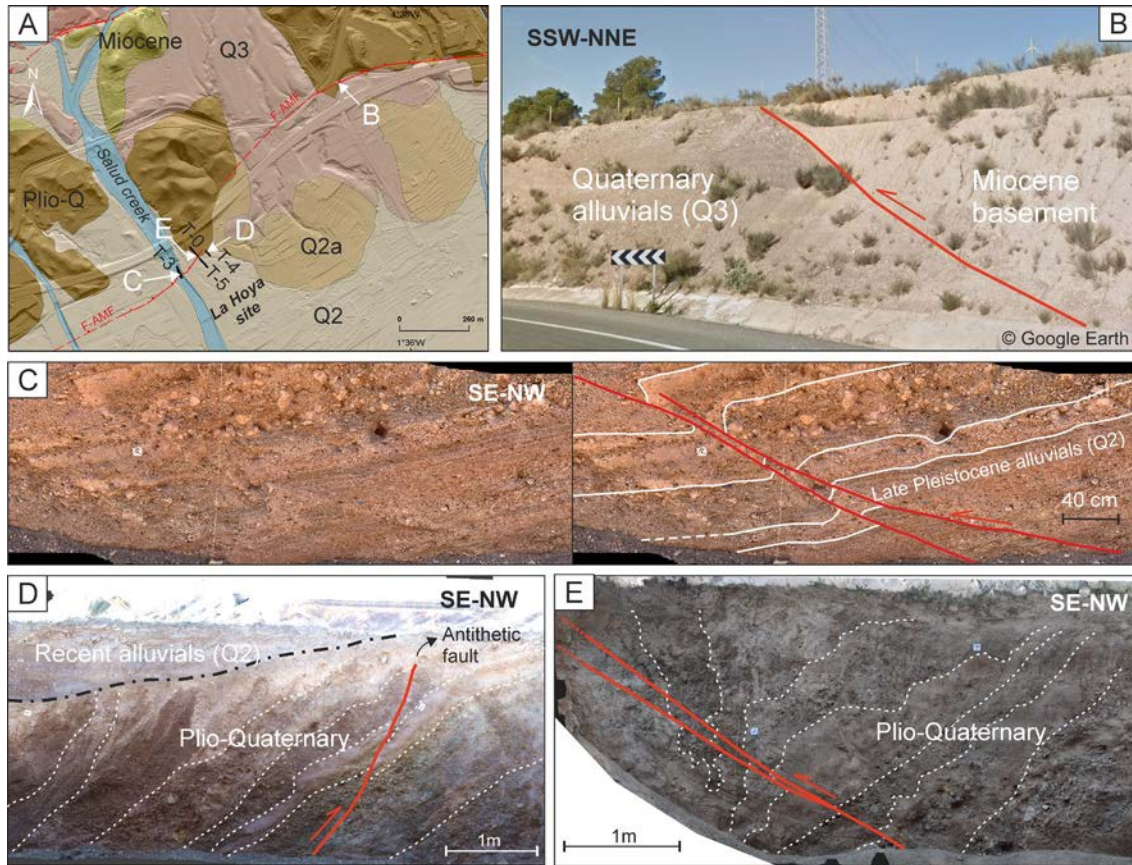


Figure 5.7. A) Location of the F-AMF in the vicinity of La Hoya site (trenches T-0, T-3, T-4 and T-5) and images B to E. B) Exposure of the F-AMF in a road cut near La Hoya site where the Miocene basement rocks are thrusting the Q3 alluvials. Image retrieved from Google Street View C) Detail of the F-AMF and associated displacements in Q2 alluvials within T-3. D) Deformation associated with the F-AMF in Plio-Quaternary alluvial materials of T-4. They show intense shear zones, strong tilting depicting a flank of a monoclinial fold and SE dipping faulting. These faults are antithetic to the F-AMF. E) F-AMF in old Plio-Quaternary materials generating intense tilting and shear of the units. See Annex II (C) for the uninterpreted images.

In Quaternary alluvial materials from the Q2 generation, the deformation is more subtle and restricted to the individual fault plane than compared to the previously described fault branches, which commonly have wider deformation zones. This again is because these alluvial deposits affected are younger and so have had less time to be deformed by tectonic activity. The affected deposits are cut by the fault generating small decimeter scale on-fault slips and most part of the deformation is accommodated through a low angle monoclinial propagation fold, as recognized in T-3 (Figure 5.7C).

In older Plio-Quaternary materials, tilting, folding and localized shear zones are identified (Figure 5.7D and E), suggesting the existence of this branch at least during the whole

Quaternary. In these materials, several SE-dipping high angle faults are observed that might be interpreted as antithetic faults rooted to the low angle NW-dipping fault (Figure 5.7E) observed in T-3 or in the southeastern end of T-0 (Figure 5.7A).

5.4.2 Kinematic distribution

The main kinematics of the Lorca-Totana segment of the AMF is strike slip with important reverse component (oblique-reverse), which is the responsible for the uplift of La Tercia range. The strong reverse component of this fault segment has been interpreted due to its ENE-WSW orientation with respect to the regional NNW-SSE compression field (e.g., Martínez-Díaz et al., 2012b). Despite this, when the focus is put on local observations, the associated deformation of each fault branch suggests different kinematics and thus, a partitioning in the deformation between strike-slip and reverse components over the different branches. We describe the kinematics of each branch based on field observations and geomorphological reconnaissance.

5.4.2.1 N-AMF

- N₁-AMF

The strike slip kinematics appears as the dominant component in this fault branch and it is mainly evidenced by:

- i) Fault zones containing striae with pitches varying from 2° to 20° consistent with a predominant strike slip faulting (Figure 5.8C).
- ii) No significant vertical slip displacements, scarps or any other morphological evidence are identified in the surface of the Q2 alluvial deposits affected by the fault in La Tercia site, which are observed in other branches with vertical displacement.
- iii) Lack of displacement correlation between outcrops, suggesting major role of the lateral component. For instance, in the San Julián creek, this fault causes an apparent uplift of the Cg unit in the southern block (Figure 5.8A). However, towards the NE, in outcrops at the base of La Tercia range towards this unit shows apparent uplift of the northern block.
- iv) Deflection of the channel margins of San Julián creek and El Salvador creek at the base of the La Tercia range, consistent with a left-lateral movement (Figure 5.8B and C).

This fault branch is limiting the relief from La Tercia range, which means that the vertical component has played an important role throughout its evolution to cause such uplift.

III. Results and partial discussions

However, the kinematic evidence in the recent materials suggests that the fault has been acting mainly as a strike-slip fault at least during the end of the Quaternary period.

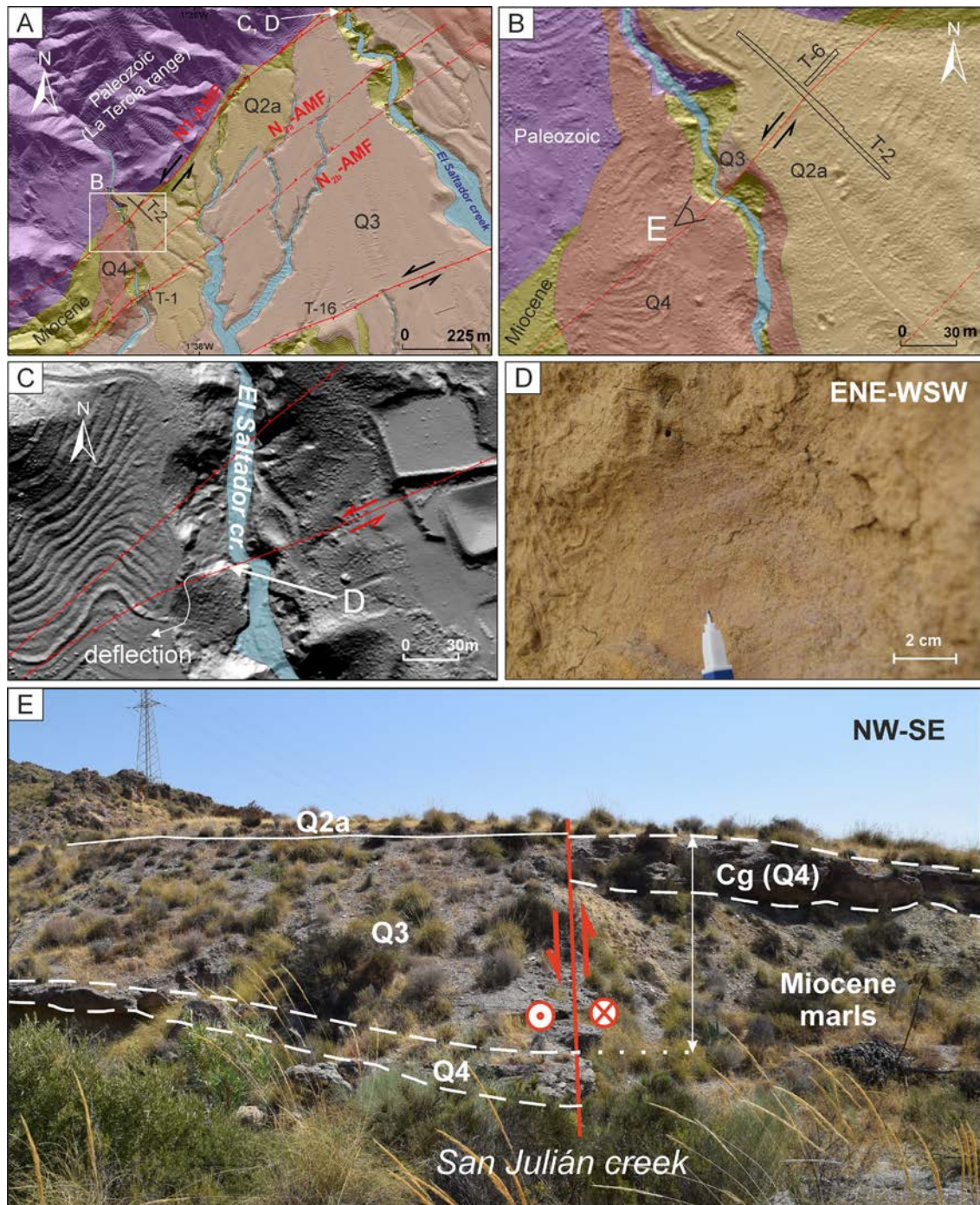


Figure 5.8. **A)** Map of the situation of the windows B to D in the context of the N_1 -AMF branch. **B)** Left lateral channel deflection of the San Julián Creek, recognized by the displacement of the alluvial units in the creek margins caused by the N_1 -AMF. The location of the image in window E is indicated. **C)** Deflection linked to N_1 -AMF in El Saltador Creek. The location of image C is indicated. **D)** Fault plane striae in fine-grained Miocene marls in El Saltador creek indicating strike-slip kinematics. **E)** Apparent vertical separation of the Q4 (Cg) materials in the San Julián Creek, a few meters SW of La Tercia site. The location of the site is indicated in window B.

- **N₂-AMF**

The two ramifications that conform the push-up structure of this branch evidence a main vertical slip component, supported by:

i) Presence of monoclinial fault-propagation folds that generate significant vertical displacements up to ~20 m, as observed at the Cg unit in San Julián creek (Figure 5.5).

No lateral component evidence, such as thickness changes in the units throughout the fold geometry, verticalized shear zones or strike-slip striae are identified.

ii) Consistency in the fault apparent deformation and inferred kinematics across different outcrops along the fault branch. For instance, the monoclinial folds at San Julián or El Saltador creeks are concordant to the ones in Carralaca site, both in style and geometry of the deformation.

iii) Presence of fault scarps associated with the cartographic trace of the two strands composing this branch, consistent with upthrown movements of the faults.

Along the interpreted fault traces of this branch a few dextral channel deflections can be identified, the most significant one found on the surface of El Saltador alluvial fan by N_{2a}-AMF (Figure 5.3). Even though the AMF is left-lateral, a right-lateral component cannot be ruled out in N₂-AMF because of the possible relative movements between the blocks separated by the different branches. However, these deflections could also be explained as a result of the re-adaptation of the drainage system to the generation of relief from vertical displacement. Further research is needed to unveil the lateral component in both branches of N₂-AMF.

5.4.2.2 S-AMF

This fault branch has predominant strike slip kinematics and it has been characterized in previous paleoseismic studies at El Saltador site. According to the slip rate estimations by Ferrater et al. (2016) the vertical slip rate of the branch (~0.1 mm/yr) is 8-10 times smaller than the strike slip rate (0.9 ± 0.1 mm/yr). Two main evidence support a predominant role of the lateral component:

i) Geomorphological elements suggesting lateral movement such as offset or deflected drainage channels (Martínez-Díaz et al., 2012b; Ferrater et al., 2015a).

ii) Geological elements such as offset paleochannels in 3D paleoseismic trenches (Ferrater, 2016).

Despite the predominant lateral motion of S-AMF, this fault also shows clear evidence of vertical slip component that suggest a non-negligible role of the uplift in this branch:

i) The existence of a ~5-7 m high north-facing scarp along the trace of the fault that consistently shows uplift of the southern block of the fault.

ii) Fault propagation folds in the northern block of the fault with important vertical displacements (e.g., Figure 5.6C). This is observable in the trenches dug along this branch in El Salvador site in previous studies and in the present study (T-16). The vertical displacements of these propagation folds in its whole length are unaccounted in previous studies, which imply higher vertical deformation values than anticipated.

5.4.2.3 F-AMF

This fault branch shows a predominant reverse kinematics based on three main evidence:

i) The fault shows a low dipping angle ($\sim 20^\circ$), which is a rare feature for strike-slip faults, unless in bend areas as it is the case of the segment. Strike-slip faults usually show high angle or subvertical dips (Sylvester, 1988).

ii) The vertical uplift generated by this fault in the relief is more prominent than the one generated by the S-AMF on the northern bound of the pressure ridge: ~10-20 m as measured from the height difference between La Hoya site and the top of the ridge to the N. This supports a predominant role of the dip slip component of this fault.

iii) Absence of laterally offset features throughout the trace of this branch such as deflected drainage.

iv) The main deformation of this branch is a monoclinial propagation fault that shows no evidence of lateral movement. This is clearly observed in T-3 (Figure 5.7C), where the sedimentary units can be correlated at both sides of the fault and the fault slips are consistent with the stratigraphic level with more displacement in the lower units. The strong tilting of the Plio-Quaternary materials supports this (Figure 5.7D and E).

Based on this evidence, we suggest that this fault branch is the frontal part of the AMF system, absorbing an important part of the vertical slip of the pressure ridge nowadays.

5.5 Paleoseismic study

5.5.1 Site selection

The paleoseismic sites have been strategically chosen in order to ensure the presence of Quaternary materials without being affected by excessive sedimentation or erosion rates. From N to S, La Tercia site (trenches T-2 and T-6), has been placed in an area where the N_1 -AMF, which is typically affecting the basement, cuts the apical sediments of El Saltador fan right at the base of La Tercia range front. This site is actually disconnected from the drainage (San Julián creek), preventing enhanced erosion. El Roser site (T-1) is located in alluvial sediments on top of the fault scarp generated by N_{2b} -AMF and next to the left margin of the San Julián creek, which is highly incised (>20 m) in this location and isolates it from erosion. El Saltador site (trench T-16) is located in the tectonic barrier generated by the counter-slope uplift of the S-AMF, which creates a trap for the sediments of El Saltador fan and creates a unique environment for their preservation. La Hoya site (trench T-3) is located at the bottom of La Salud/El Colmenar creek. Aerial photographs from year 1929 show that the creek was practically filled with sediments at that time (Figure 5.9), which means that a significant thickness of unaffected creek sediments has been eroded since then (possibly near 3-5 m in La Salud creek; T-3). The excavation of T-3 at the bottom of the creek ensured less thickness of these unaffected materials and shallower position of the affected materials compared to other possible sites at the margins of the creek. It is important to note that the N_{2a} -AMF has not been included in the paleoseismic study because the uncertainty in the fault location has prioritized the other branches.

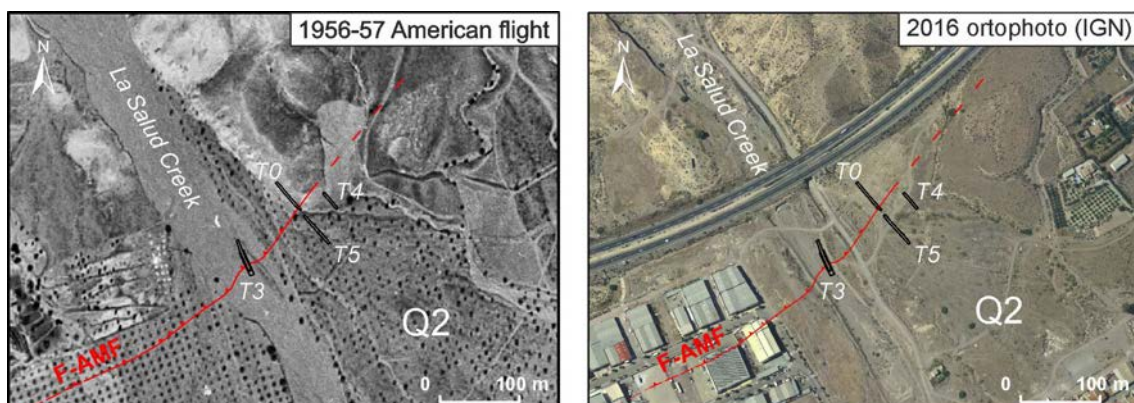


Figure 5.9. Comparison of La Salud Creek in La Hoya site between the 1956-57 aerial image (left) and the 2016 ortophoto from IGN agency (right) (centrodedescargas.cnig.es). Note the amount of sediments present in the former compared to the latter, evidencing recent erosion of the creek infills.

5.5.2 Sedimentary units of the trenches

The paleoseismic trenches exposed a series of sedimentary units (Figure 5.10) that are crucial to understand the sedimentary setting of each site, as well as their linkage with the tectonic activity of the faults that affect them. Details of the sedimentary description of each unit are given in the legends of Figure 5.11 to Figure 5.14. See Annex II (D) for the high-quality photologs and sedimentary unit interpretations of each trench.

The sedimentary sequences cropping out in the different trenches belong to the Q3 and Q2 alluvial fan generations, conformed mainly by proximal alluvial and fluvial deposits from La Tercia range. The nomenclature used for the different studied sites is singular for each one and coincident names do not imply unit correlation, except for the Cg unit. In El Salvador site we adopted the nomenclature used for the trenches by Ferrater (2016) to define the units in T-16 because are the same. The deepening of a previous trench (TR-7) to excavate T-16 allowed to enhance the sedimentary resolution for some units, therefore we define sub-unit names based on the previous ones (e.g., units N1, N2, N3 for unit N; Figure 5.13).

The base of the Quaternary deposition of the studied area in El Salvador fan is the Cg unit, corresponding to the Q4 alluvial fan generation. This unit is deposited over the Tortonian basement (yellow marls and calcarenites) and is found locally in the trenches at La Tercia and El Roser sites. On top of Cg, the stratigraphy of the trenches is divided into two main sequences related to the Late Pleistocene evolution of the sedimentary environment:

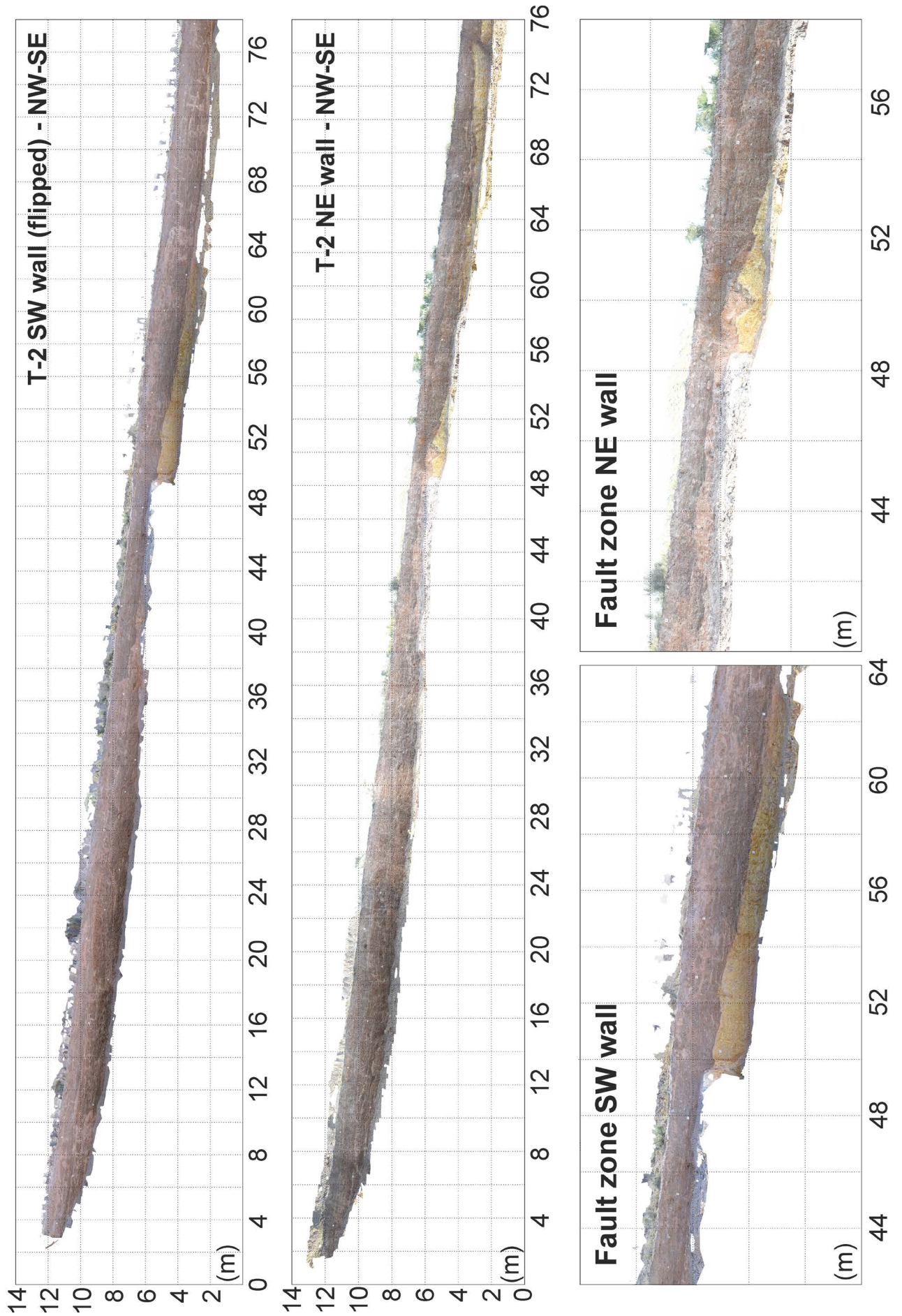
The first (older) Quaternary sequence is mainly formed by clast supported coarse to medium heterometric and subangular gravels related to turbulent fluxes such as debris flows. These correspond to the Q3 alluvial fan generation and are related to the dynamics of the alluvial fan activity in its proximal areas, typically sheet flow and debris flow deposits. In the study area, they are represented by unit Rg in T-2 and T-6 (Figure 5.11), units 6 to 3 in T-1 (Figure 5.12), units S to I in T-16 (Figure 5.13) and units W to I1 in T-3 (Figure 5.14). The Q3 alluvial sequence is also characterized by the presence of several paleosoil levels indicating episodes with no sedimentary deposition, also evidenced by the available numerical datings (section 5.5.3). One of the most distinctive cases is unit 5 in T-1 (Figure 5.12), which corresponds to a paleosoil developed on top of unit 6 or the actual soil formations of unit Z in T-16 (Figure 5.13).

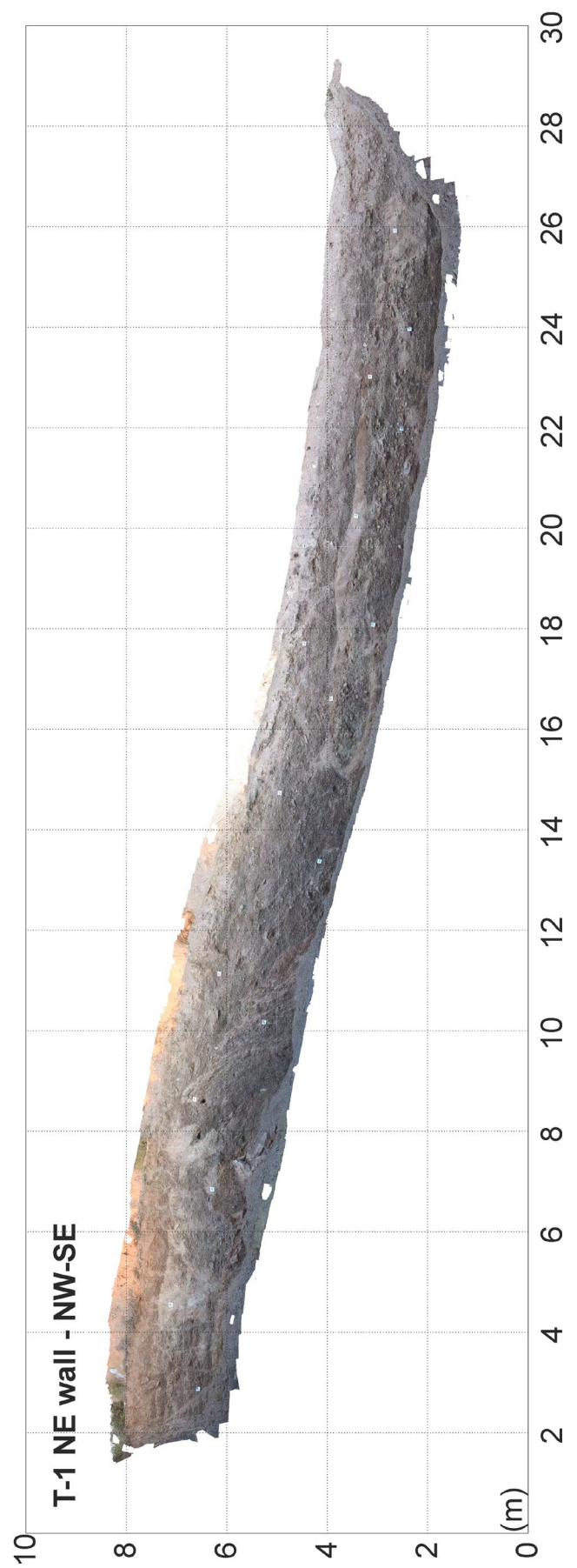
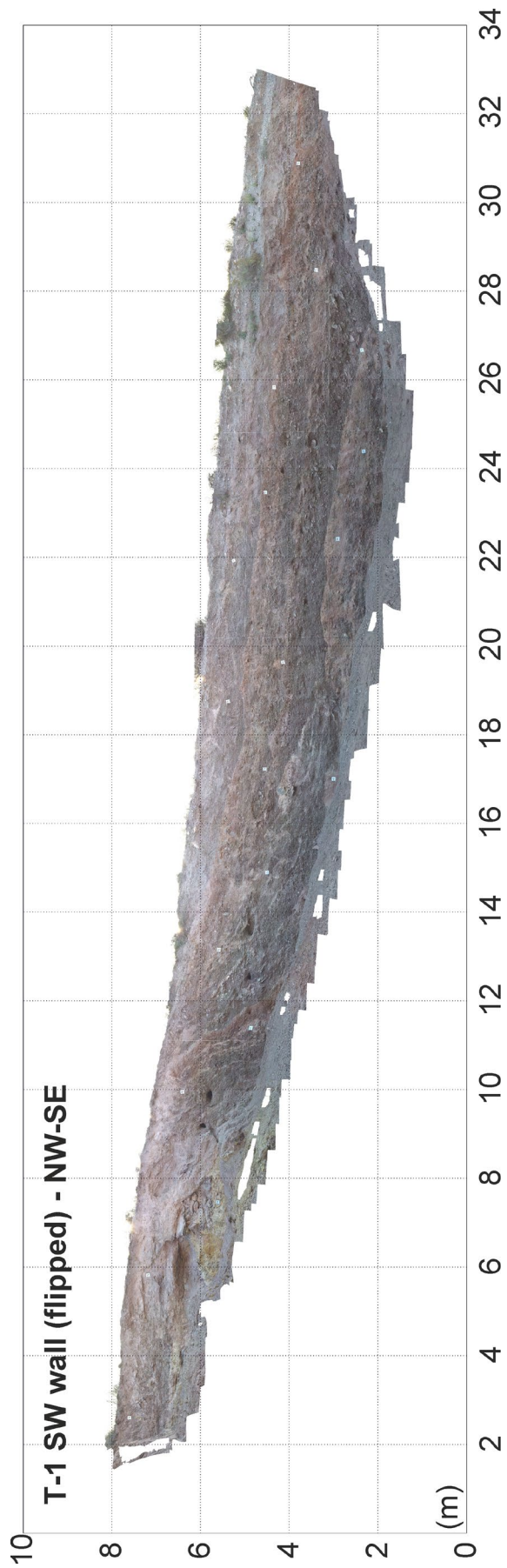
Another characteristic sedimentary feature of this first sequence is the presence of embedded fine sands and yellow-orange matrix supported silts with floating clasts, typically indicative of mud flows. These are mainly found at El Saltador site and show important thicknesses that can reach up to ~1 m (e.g., unit J in T-16; Figure 5.13) closer to the fault zone. The lithology of these deposits is unusual in a proximal alluvial fan context and have been interpreted to be coseismic evidence in this area (Martínez-Díaz et al., 2003; Masana et al., 2004; Ferrater, 2016), based on previous observations in regions such as La Laja fault in Argentina (Rockwell et al., 2014) or during the 2010 Mw 7.2 El Mayor Cucapah earthquake (Fletcher et al., 2014). A possible explanation to these deposits is the seismic shaking, which is known to generate large amounts of dust, and facilitates the accumulation of fine particles (dust) on the surface. These could be easily washed off by the rainfalls shortly after an event and hence, generate mud flows. The S-AMF in El Saltador site could have acted as a tectonic barrier ponding these sediments. In T-16 these materials are interpreted to be units C, E, G, J, L1, N4c, N5 and P.

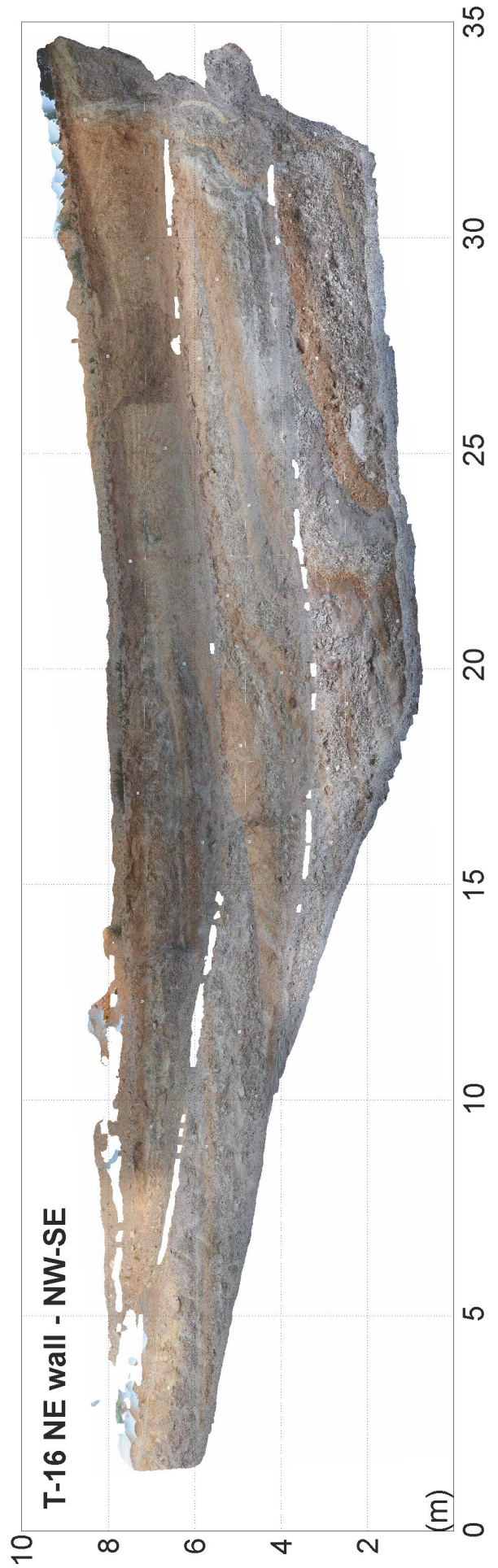
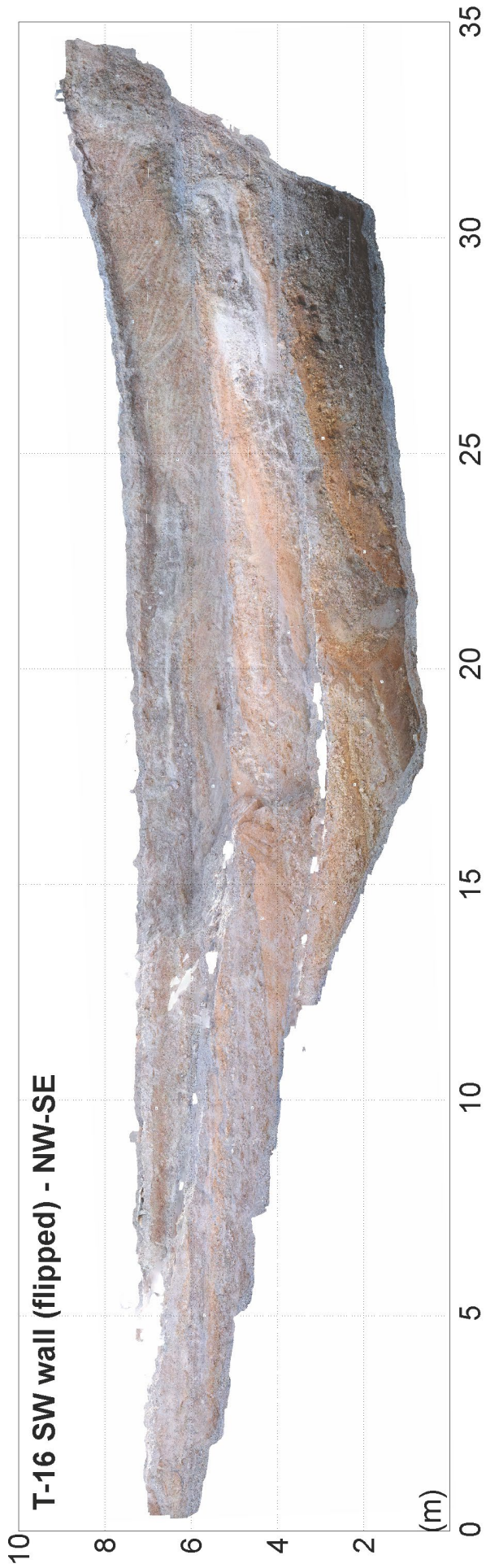
On top of the Q3 alluvial sequence, there is a change to channelized clast supported gravel units with planar and localized crossed bedding, which are incised into the underlying alluvial sequence. This second (younger) sequence corresponds to the Q2 and Q2a alluvial generation. It implies a transition to a channelized alluvial regime, corresponding to the abandonment or decreasing activity of the alluvial fans and corresponding erosion with the development of incision channels (Martínez-Díaz et al., 2003; Ferrater, 2016). This sequence is represented by units D3 to C1 in T-2, unit D in T-6, units 2 and 1 in T-1, units H to Z in T-16 (Figure 5.11 to Figure 5.14). The change of regime probably marks the start of the migration of the principal alluvial sedimentation to the S and incision of El Saltador, La Salud and San Julián creeks (Martínez-Díaz et al., 2003).

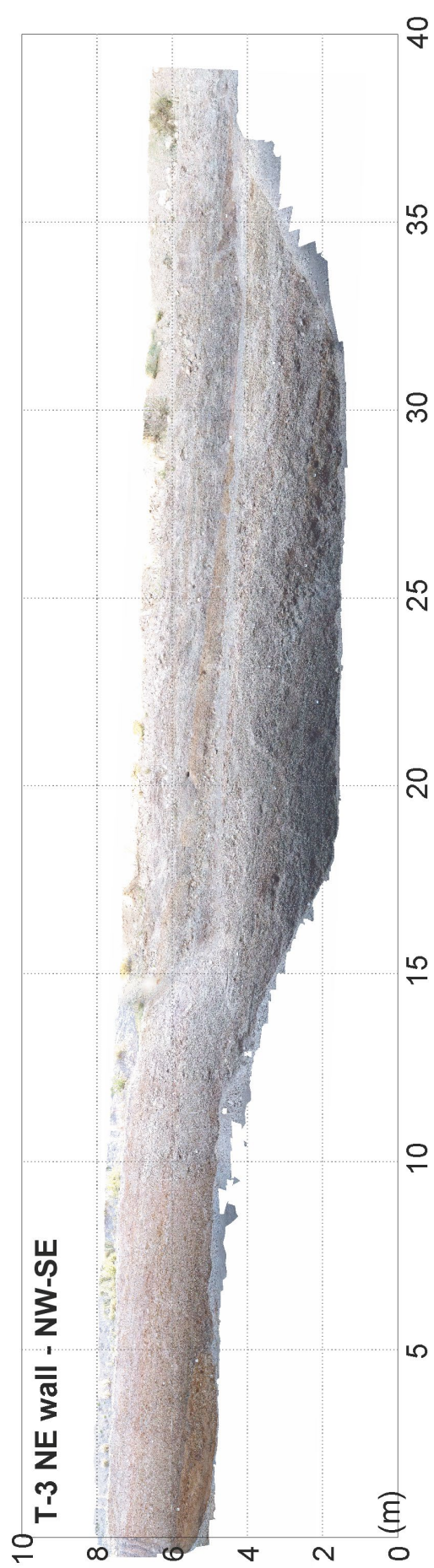
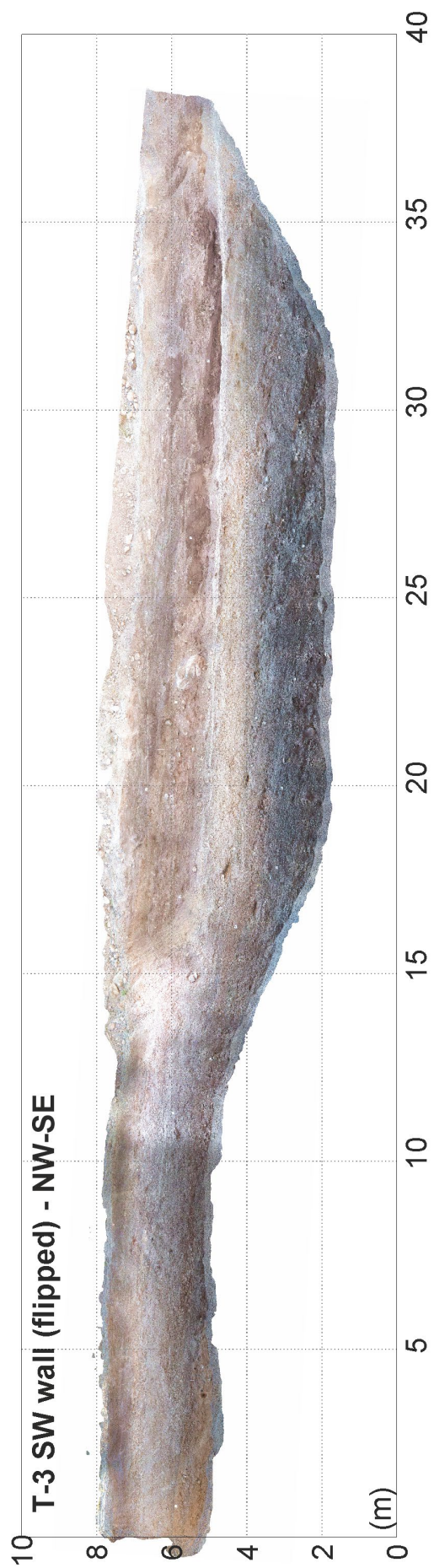
The trenches of La Hoya site are the only ones located in this younger zone of deposition (Q2); hence, the recent alluvial sedimentation is posterior than the other sites (section 5.5.3). At La Hoya site, this sequence is represented by units W to I1 (T-3) and culminates with unit B (T-3, T-4 and T-5) (Figure 5.14), which corresponds to channelized alluvial deposits (creek deposits) with presence of crossed bedding and erosive bases. On top, unit A corresponds to creek deposits of channels incised within the alluvial fan, one of them being La Salud creek, which feeds the alluvial deposition at the central parts of the Guadalentín basin. The whole sequence of La Hoya site is deposited on top of old Pliocene-Quaternary alluvial gravels and embedded massive silts, with strong

cementation and paleosoil developments (unit X; Figure 5.14). This approximate age of these units is inferred from regional cartography in this area (e.g., Martínez-Díaz, 1998).









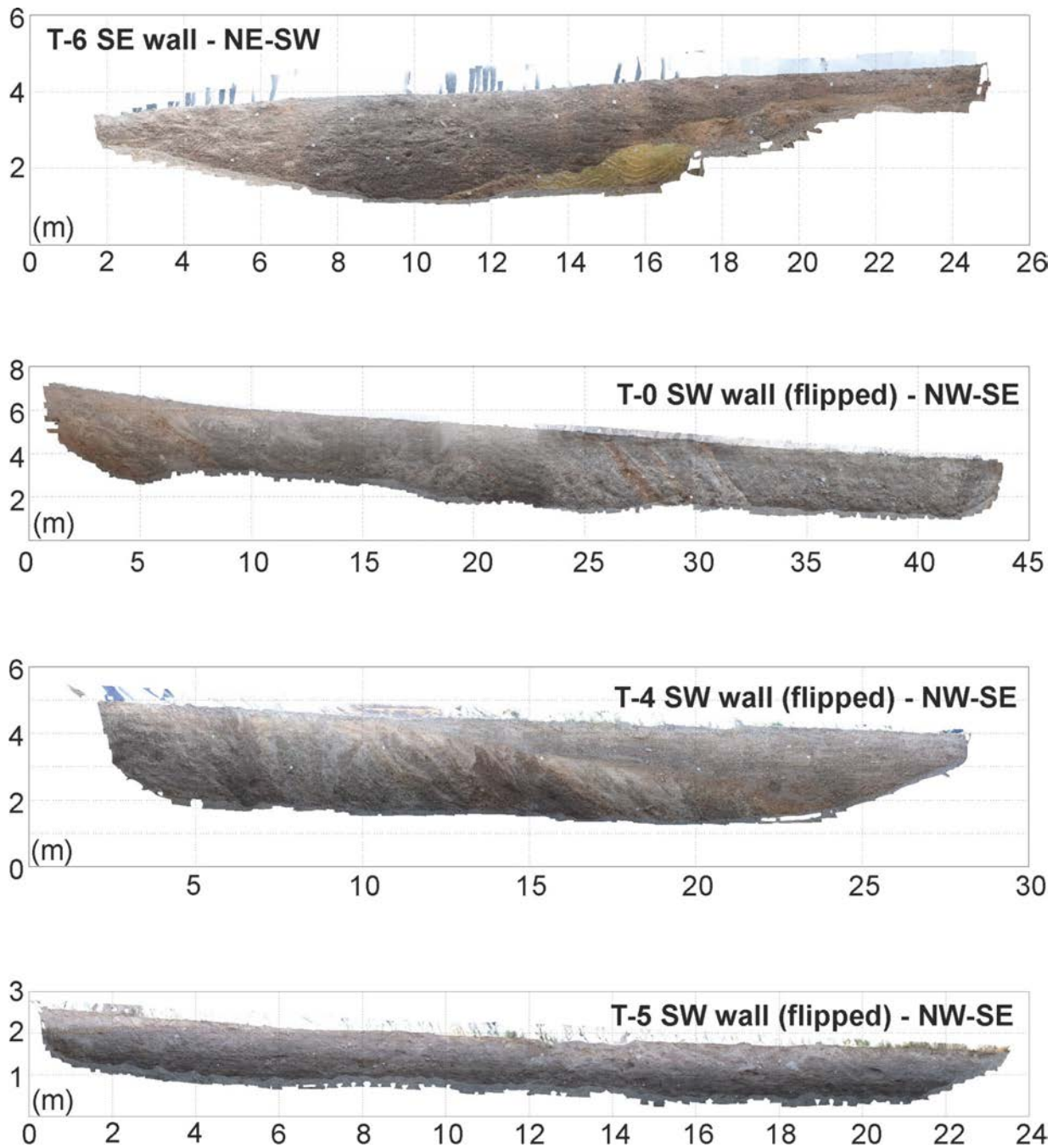
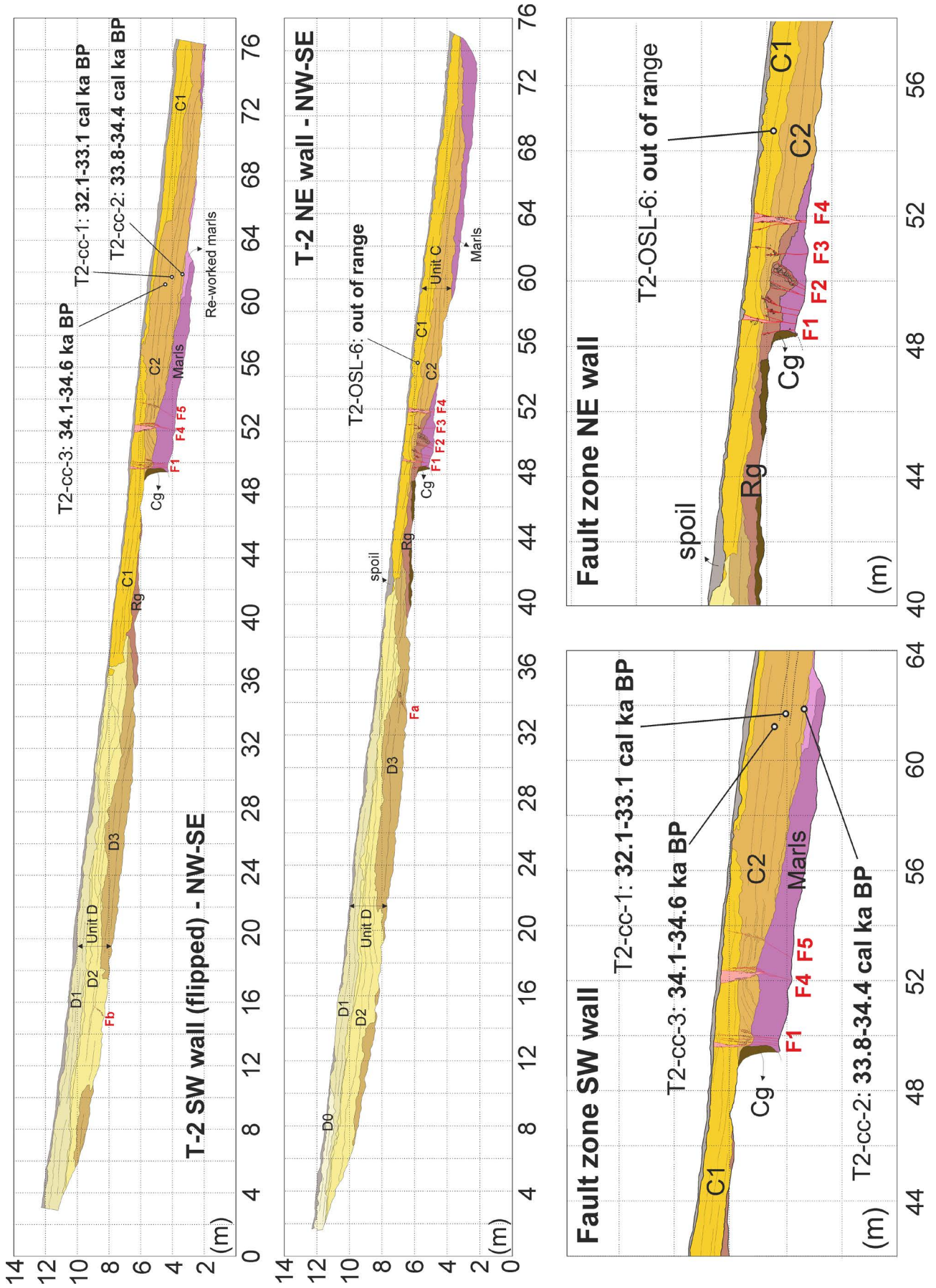
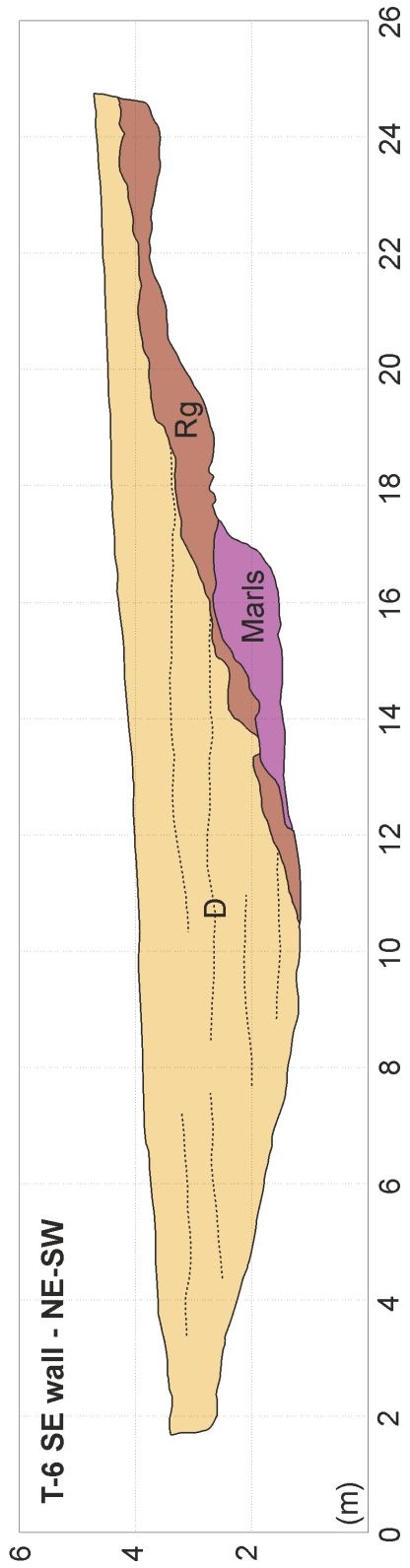


Figure 5.10 Photomosaics of all the trenches performed in this study. For trenches T-6, T-0, T-4 and T-5 only one trench wall is analyzed because the paleoseismic information obtained from them is poorer than the other trenches. See Annex II (D) for the high-quality photologs.

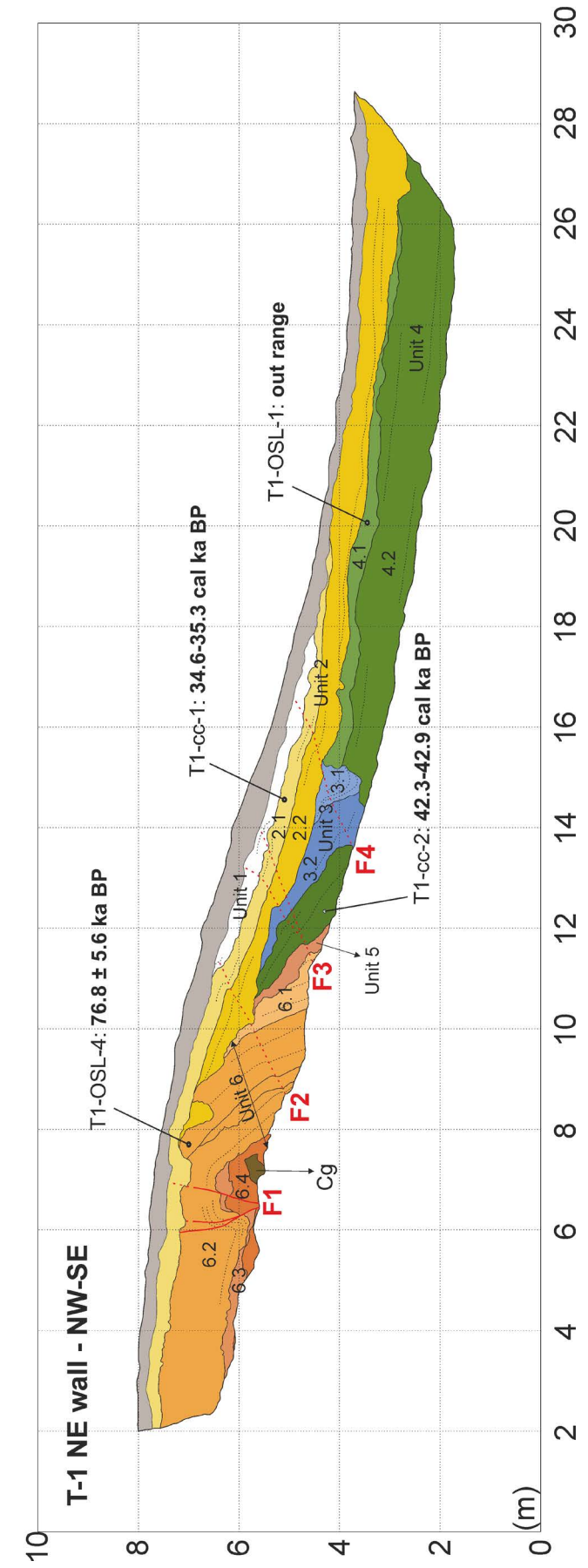
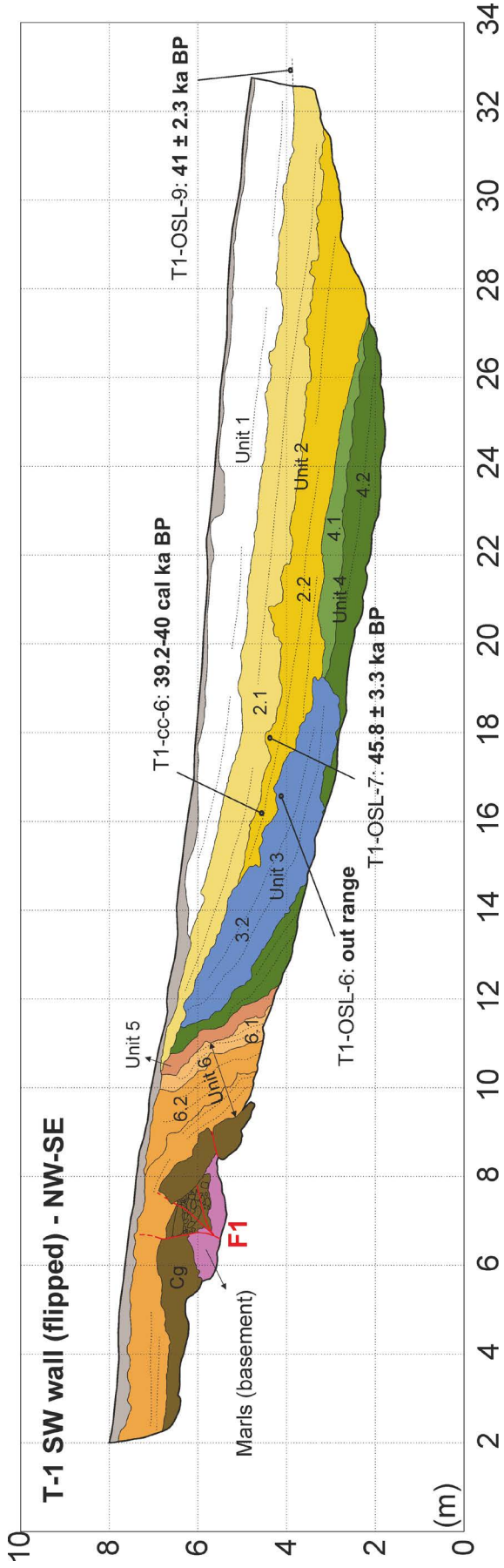




Stratigraphic units of La Tercia site (T-2 and T-6)

Unit	Description
C1	Clast-supported fine to medium gravels, well sorted and laminated. The unit shows 5-20 cm thick silty layers embedded with poor lateral continuity.
C2	Clast-supported fine to medium gravels with localized coarsening and silty layers. The unit is well sorted and laminated, although poorer than C1.
D0	Detritic sequences formed mainly by clast-supported medium to coarse gravels forming paleochannel geometries. The sorting is generally poor although lamination is observed in some paleochannels. Each sequence shows embedded silty layers and a 20-30 cm red colored silty paleosoil development on top that marks the limits to the different sub-units (D0 to D3).
D1	
D2	
D3	
Rg	Regolith of the underlying unit. Red silts with weathered conglomerate blocks embedded in the silty matrix
Cg	Coarse and highly cemented conglomerates forming a 1-2 m thick slab. In the fractures of fault zones this unit shows travertine growths.
Marls	Yellow marls and gypsum veins with localized embedded layers (~10-20 cm) of conglomerates and fine-medium sands.

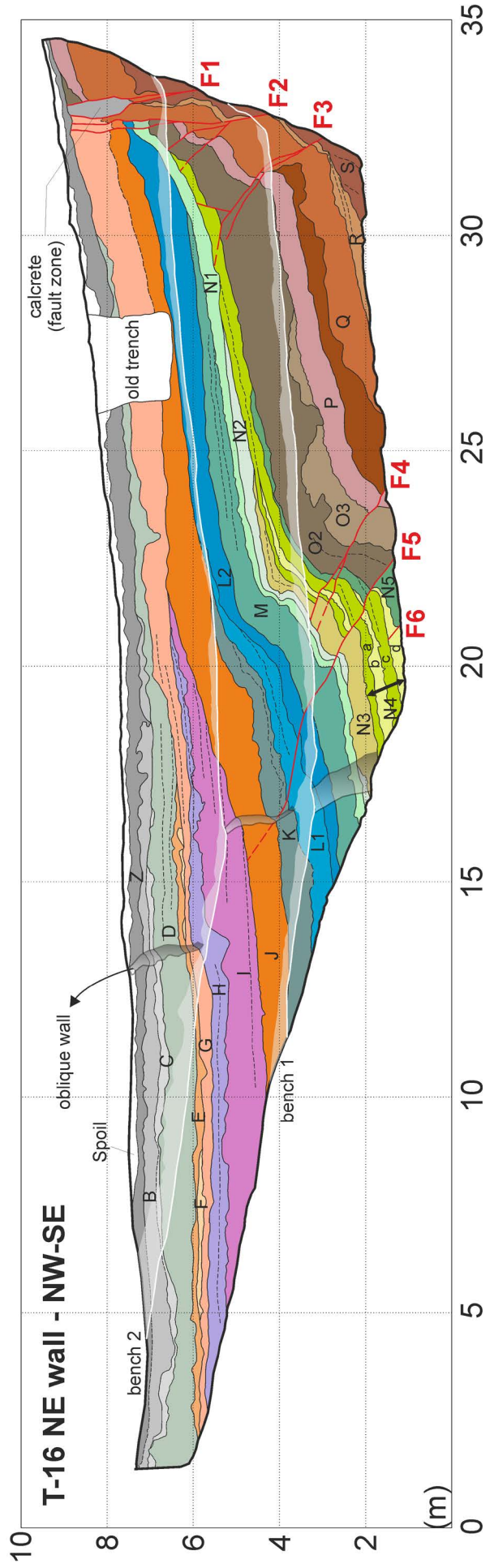
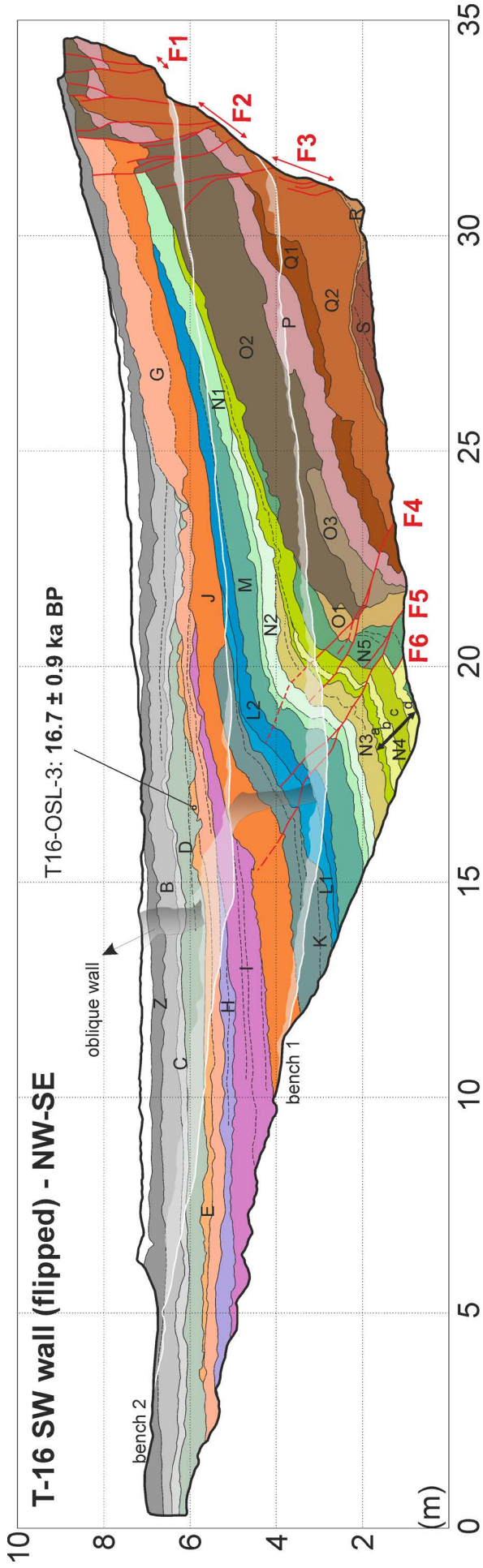
Figure 5.11. Interpreted logs of T-2 and T-6 in La Tercia site and respective stratigraphic unit descriptions. Numerical dating results are indicated in the logs. See Annex II (D) for high-quality interpreted trench logs.



Stratigraphic units of El Roser site (T-1)

Unit	Description
1	Clast-supported fine to medium well sorted gravels with embedded 10-20 cm thick silty layers. Silty matrix is abundant throughout the unit.
2.1	This unit is composed by two sequences of 40-60 cm thick layers of poorly sorted clast-supported gravels culminating with 20-30 cm thick red silty layers indicating paleosoil developments.
2.2	
3.1	Sequence formed by clast-supported medium to coarse gravels with paleochannel geometries and erosive bases, being sub-unit 3.1 the most distinctive paleochannel. The unit is poorly sorted and shows localized planar lamination.
3.2	
4.1	Very fine and well sorted layer of pure silts with a thickness up to 45-50 cm.
4.2	Clast supported coarse gravels, poorly sorted and with variable clast sizes (10-20 cm diameter). The sequence shows coarsening upwards.
5	Paleosoil developed on top of unit 6.1. Clast supported medium gravels with a distinctive red colored silty matrix and carbonatic cementation.
6.1	Clast supported medium gravels with very abundant silty matrix and incipient cementation. This unit marks the transition to unit 5.
6.2	Well stratified clast supported medium gravels with abundant silty matrix, alternated with centimetric (~5cm) silty layers.
6.3	Paleosoil developed on top of unit 6.4. Clast supported gravels with carbonatic cementation and distinctive red coloration.
6.4	Clast-supported coarse gravels (10-20 cm diameter) with abundant silty matrix. The base of the unit shows re-sedimented Tortonian marls.
Middle Pleistocene alluvials	Coarse and highly cemented conglomerates forming a 1-2 m thick slab. In the fractures of fault zones this unit shows travertine growths.
Tortonian	Yellow marls and gypsum veins with localized embedded layers (~10-20 cm) of conglomerates and fine-medium sands.
Marls	

Figure 5.12. Interpreted logs of T-1 in El Roser site and respective stratigraphic unit descriptions. Numerical dating results are indicated in the logs. See Annex II (D) for high-quality interpreted trench logs.



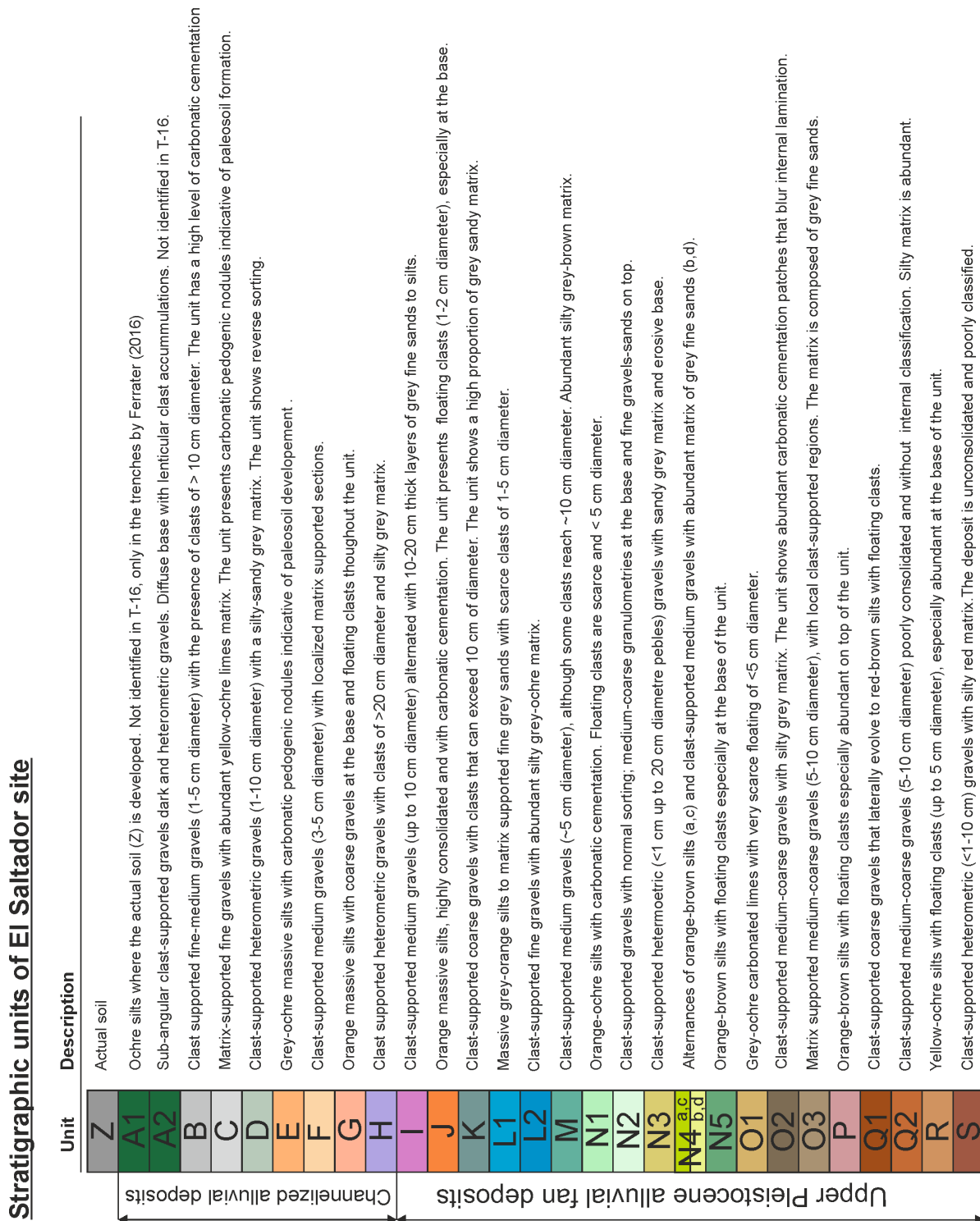
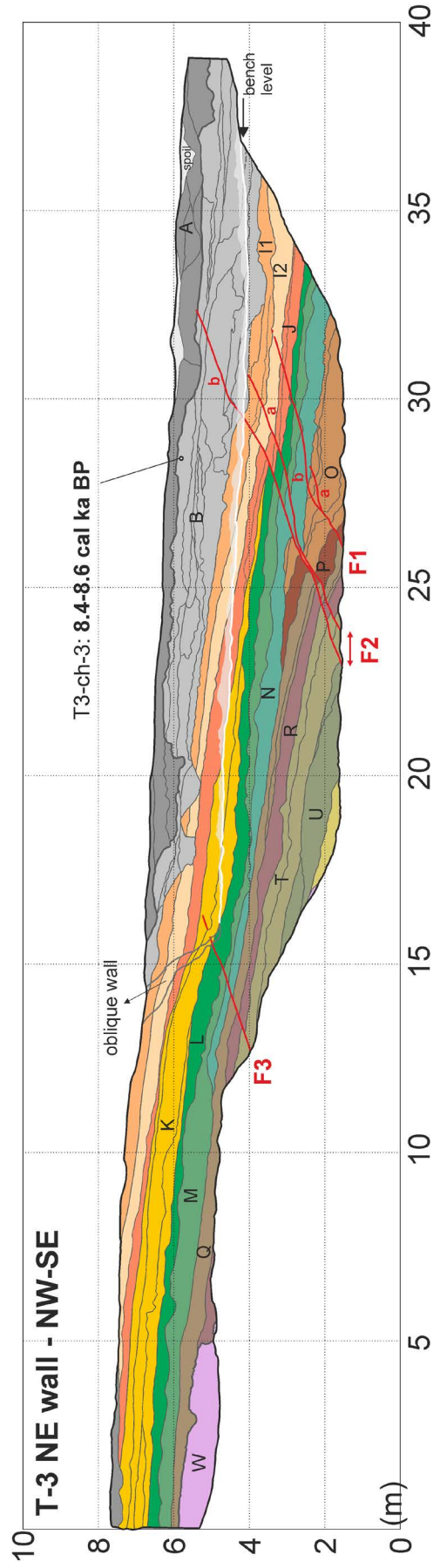
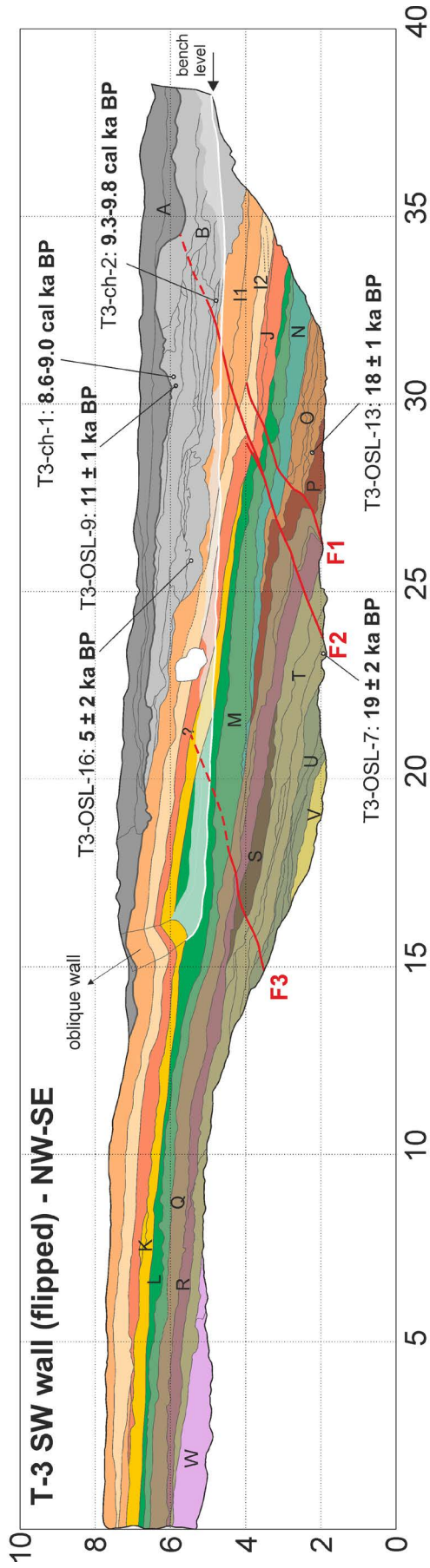
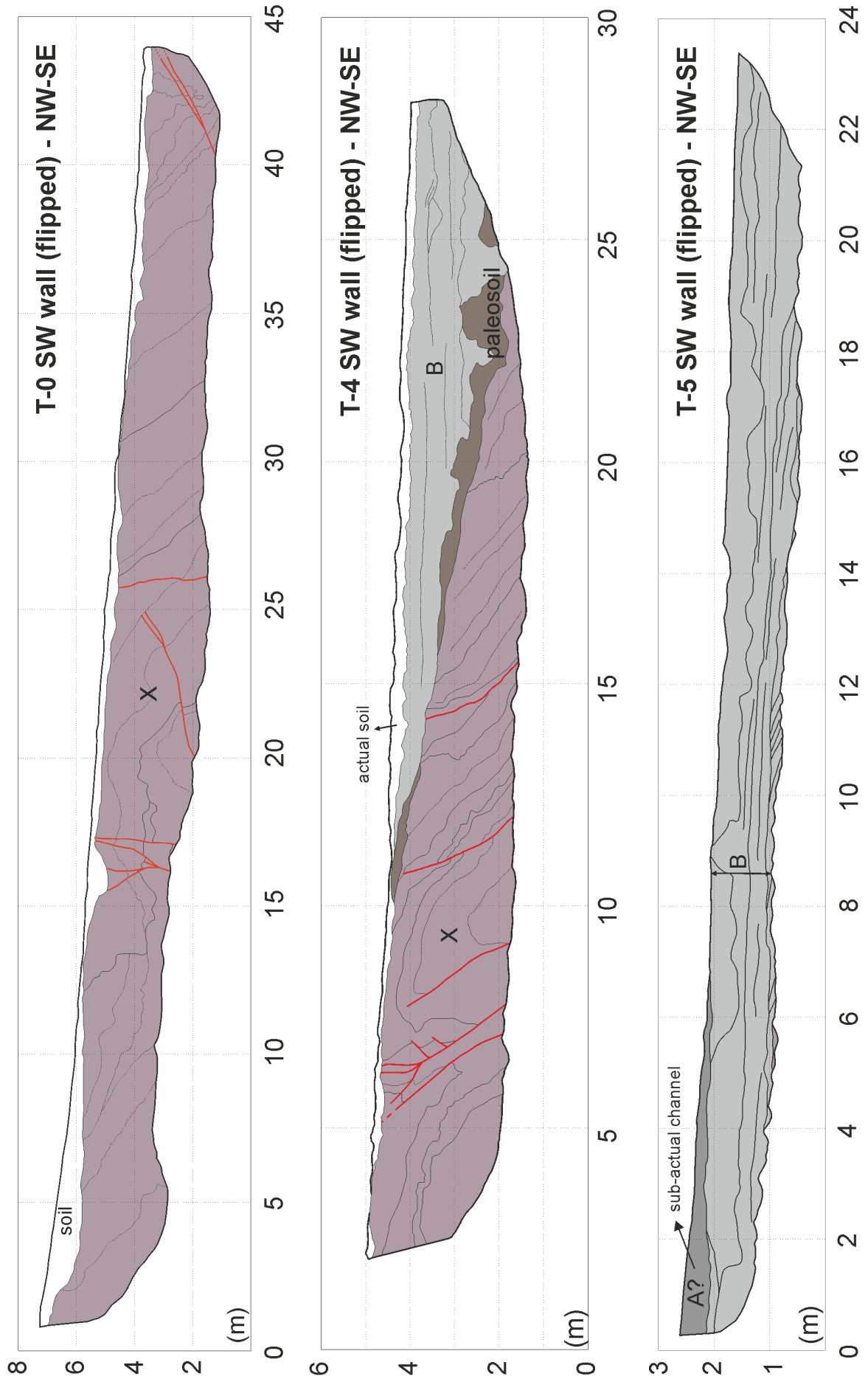


Figure 5.13. Interpreted logs of T-16 in El Saltador site and respective stratigraphic unit descriptions. Note that the numerical dating results and bench levels of the trench and spoil are depicted in the logs. See Annex II (D) for high-quality interpreted trench logs.





Stratigraphic units of La Hoya site (T-0, T-3, T-4 and T-5)

Unit	Description
A	Clast-supported medium well laminated gravels with erosive base forming paleochannels. These are recent creek fluvial deposits.
B	Clast supported medium well laminated gravels with embedded brown silty layers (20-30 cm thick) forming different paleochannel bodies.
I1	Clast-supported medium well laminated gravels. The unit shows a distinctive ochre coloration due to paleosoil development.
I2	Clast-supported medium well laminated gravels with the presence of big clasts (up to 20 cm diameter) and eventually boulders.
J	Clast-supported coarse gravels that can reach up to ~20 cm of diameter. The unit has a distinct red coloration due to the sandy matrix.
K	Clast-supported medium-coarse gravels (5-10 cm diameter). On top, the unit shows yellow color due to paleosoil development.
L	Clast-supported fine-medium gravels (1-5 cm diameter). The unit has an erosive base forming paleochannel-type shapes.
M	Clast-supported fine-medium gravels (1-5 cm diameter) with a brown matrix composed of fine sands.
N	Clast-supported fine-medium gravels (1-5 cm diameter) with local clasts of ~10 cm diameter. The unit has a sandy ochre-grey matrix.
O	Fine sands and limes with floating clasts (~5 cm diameter) embedded with paleochannels of clast-supported unconsolidated coarse gravels.
P	Clast-supported coarse gravels (10 cm diameter or more) The unit has an important fraction of sandy brown matrix.
Q	Clast-supported and poorly consolidated coarse gravels alternated with layers (~10 cm thick) of fine-medium gravels. Erosive base.
R	Clast-supported medium-coarse gravels (5-10 cm diameter). The unit has a distinctive red color from its silty matrix.
S	Clast-supported coarse gravels (up to 10 cm diameter) with a chaotic fabric and erosive channel-shape base.
T	Clast-supported and well laminated fine-medium gravels that alternate coarser levels with clasts of diameters up to > 20 cm.
U	Clast-supported gravels that alternate levels of fine-medium granulometry with coarse levels of clasts exceeding 20 cm of diameter.
V	Clast-supported coarse gravels (up to 10 cm diameter) without clear internal structure.
W	Fine brown silts with floating heterometric clasts, especially on top of the unit
X	Highly cemented clast supported coarse gravels (>10 cm diameter) alternated with massive silty layers. The unit shows several paleosoil developments.

Creek deposits

← Holocene alluvial fan deposits

← Late Pleistocene

Quaternary alluvials

Figure 5.14. Interpreted logs of T-3, T-0, T4 and T-5 in La Hoya site and respective stratigraphic unit descriptions. Note that the numerical dating results and bench levels of T-3 are depicted in the logs. See Annex II (D) for high-quality interpreted trench logs.

5.5.3 Geochronology of the stratigraphic units: sedimentary interpretation

In this section we present the results from the numerical datings performed on the different stratigraphic units cropping out in the trenches. These were used to establish event chronosequences and to calculate different seismic and paleoseismic parameters.

A total of 21 samples have been dated. From these, 12 are sediment samples that have been dated by OSL, 6 are snail shell fragments and 3 are charcoals both of which have been dated by AMS radiocarbon. In addition, for T-16 we use previous dates obtained by Ferrater (2016) and Masana et al. (2004) at El Saltador site and recently revised by Ortuño et al. (2021; in preparation), which are from OSL, TL and radiocarbon. Table 5.2 and Table 5.3 group the dating results obtained in this study for each trench and technique. We also group the previous dates used for the analysis of El Saltador (Table 5.4 and Figure 5.15) and provide a table with the selected results used in this work (Table 5.5). The plots of the OSL dose distributions are also shown in Figure 5.16 for discussion. The stratigraphic sequences extend from the Upper Pleistocene to Early Holocene.

Trench	Unit	Sample ID	Depth (m)	Moisture (%)	Dose rate (Gy/ka)	Absorbed dose (Gy)	Age $\pm 1\sigma$ (ka BP)
T-2	C1	T2-OSL-6*	0.5	8 \pm 4	3.76 \pm 0.18	X \pm X	Out of range
T-1	4.1	T1-OSL-1*	0.9	9 \pm 4	3.65 \pm 0.18	X \pm X	Out of range
	6.2	T1-OSL-4*	0.6	4 \pm 4	3.01 \pm 0.16	230.9 \pm 11.7	76.8 \pm 5.6
	3.2	T1-OSL-6*	2.0	4 \pm 4	3.08 \pm 0.16	X \pm X	Out of range
	2.2	T1-OSL-7*	1.7	4 \pm 4	3.48 \pm 0.17	159.3 \pm 8.2	45.8 \pm 3.3
	1	T1-OSL-9*	0.9	9 \pm 4	3.78 \pm 0.18	155.3 \pm 4.4	41.0 \pm 2.3
T-16	E	T16-OSL-3 ^x	1.2	5 \pm 3	2.45 \pm 0.08	40.8 \pm 1.6	16.7 \pm 0.9
T-3	T	T3-OSL-7 [†]	5.2	11	2.4 \pm 0.1	46 \pm 4	19 \pm 2
	B	T3-OSL-9 [†]	1.0	15	3 \pm 0.1	34 \pm 4	11 \pm 1
	O	T3-OSL-13 [†]	4.6	7	2.02 \pm 0.04	49 \pm 5	24 \pm 3 Re-analyzed: 18 \pm 1
	B	T3-OSL-16 [†]	1.4	12	2.6 \pm 0.05	14 \pm 4	5 \pm 2

Table 5.2. Dating results of the sedimentary units of the different trenches using the Optical Stimulated Luminescence technique (OSL). All uncertainties refer to 1 sigma (σ). The position of each sample can be found in Figure 5.11 to Figure 5.14. *Samples dated at CENIEH (Burgos, Spain); ^x Sample dated at the University of Cologne (Germany); [†]Samples dated at the Instituto Tecnico Superior (Lisboa, Portugal). For more details, check the full reports of the OSL dating results from the respective laboratories in the Annex II (B). These are included with permission from the authors.

Trench	Unit	Sample ID	Sample type	Fraction of modern	Radiocarbon age (years BP)	Calibrated age (years BP)
T2	C2	T2-cc-1 ^a	Snail shell	2.906±0.042	28424±116	32051-33092
		T2-cc-2 ^a		2.541±0.039	29502±123	33781-34376
		T2-cc-3 ^a		2.434±0.038	29848±125	34123-34581
T-1	2.1	T1-cc-1 ^a		2.209±0.040	30627±145	34630-35336
	4.2	T1-cc-2 ^a		0.779±0.028	39000±289	42384-42907
	2.2	T1-cc-6 ^a		1.377±0.033	34424±193	39205-39996
T-3	B	T3-ch-1 ^b	Charcoal	0.3724±0.0012	7935±30	8638-8985
	B	T3-ch-2 ^b		0.3453±0.0037	8540±90	9306-9759
	B	T3-ch-3 ^b		0.3803±0.0013	7765±30	8449-8600

Table 5.3. Dating results of the sedimentary units of the different trenches using the radiocarbon technique. All uncertainties refer to 1 sigma (σ) except the calibrated age, which refers to 2 sigma (2σ). Calibration of radiocarbon ages has been done using the IntCal20 curve (Reimer et al., 2020) and the OxCal software (Ramsey and Lee, 2013). The position of each sample can be found in Figure 5.11, Figure 5.12 and Figure 5.14. ^a Samples dated at the DirectAMS Laboratory (Bothell, USA). ^b Samples dated at the KCCAMS facility, University of California (Irvine, USA).

5.5.3.1 T-2 (La Tercia site)

In this trench, usable dating results have been exclusively obtained from three radiocarbon samples in C2 providing ages all around 32-34.5 ka BP (Table 5.3), which indicates a very brief period of deposition of this unit, probably related to few episodes. Conversely, the remaining OSL sample from unit C1 (T2-OSL-6) did not provide any results as the resulting absorbed dose is out of the range of detection of the method (Table 5.2). This is likely due to poor bleaching of the minerals during the transportation, and it can be a common effect in very proximal alluvial environments such as the one of the site. Also, these alluvial materials might have incorporated older alluvial deposits previously accumulated in the uplifted La Tercia range, now almost completely eroded. Because of this short distance to the source area and the inherent turbulence of the fluxes generating the deposits (e.g., debris or mud flows), the complete bleaching of the sample minerals is hampered and therefore, the mineral grains have inherited luminescence signals that cause the sample to have an absorbed dose out of the range of detection. Given the lack of numerical dates in the stratigraphic units especially below unit C2, the lower age bound of the stratigraphic sequence cannot be constrained confidently.

The age of the Cg unit cropping out in this trench is adopted from the minimum age provided by Martínez-Díaz & Hernández-Enrile (2001): $\sim 198 \pm 6.5$ ka. According to these dates, we identify a large gap (~ 160 kyr) between this unit and unit C. This evidences a large time window for the sedimentation of units Rg and D, implying that the sedimentation is most likely discontinuous. In addition, unit D is similar to unit C2 from the sedimentary perspective, which means that its age is likely closer to the latter than to Cg. The deposition in La Tercia site ceased not much later than ~ 32 - 34.5 ka, implying another depositional gap since this age and the present.

5.5.3.2 T-1 (El Roser site)

In this trench, the presence of datable fine-grained material throughout the sequence allowed to perform a sampling process of different units to constrain the different paleoseismic events. A total of five OSL samples and three radiocarbons from snail shells have been dated. Two out of the five OSL samples (T1-OSL-1 and T1-OSL-6) could not provide usable dates due to the same effect as the one explained in T-2 (poor bleaching).

The Quaternary sequence of this trench is deposited on top of the Cg unit and comprises ages (BP) from ~ 77 ka (T1-OSL-4) to ~ 35 - 41 ka (T1-cc-1, T1-OSL-9, respectively) (Table 5.2 and Table 5.3). Dates from radiocarbon, although are very similar to the OSL, provide slightly younger ages for the same units and lower uncertainty ranges (< 1 ka in all cases). These differences might be attributed to a non-complete bleaching of all the electrons of the sample minerals, compatible with the proximal context and leading to older ages for the OSL samples. Also, the effect of sediment parameters such as variations of moisture or carbonate content can affect importantly the resulting age, especially for the carbonates as no corrections have been applied during the dating process. For this reason, and to maintain a stratigraphic coherency between the dates, in the units 4.2 to 1 we selected the radiocarbon results as preferred dates to calculate the seismic parameters of this fault branch. Also, the radiocarbon ages show smaller uncertainty ranges than the OSL (Table 5.3).

The younger ages in T-1 are consistent with unit C2 in T-2, which might suggest that are contemporary. With these observations and considering the close location of both T-1 and T-2, the age of unit 2.2 in T-1 might be assumed as a minimum age for the base of unit D (D3) in T-2 as they both constitute the lower part of the channelized alluvial sequence of

each respective site. In addition, they share similar sedimentary characteristics and overall deposit fabric: channelized clast-supported gravels with internal planar laminations.

In this trench a large depositional gap is identified (~120 kyr) between the Cg unit (198 ± 6.5 ka) and the overlying unit 6, and between unit 6 and unit 4.2 (~35 ka). This latter gap is also recognized by the presence of unit 5, which is a paleosoil development. The deposition in this site ceased ~35 ka, which implies another gap between the said date and the present.

5.5.3.3 T-16 (El Saltador site)

The dates from this trench, except for T-16-OSL-3 (Table 5.2), are adopted from the different studies performed at El Saltador site (Table 5.4). Dates from units I, G and A1 are assigned using the radiocarbon dates obtained by Ferrater (2016), and the same OSL dates for units H and P. The rest of the samples from that study were dated using both single-grain for K-feldspar IRSL (Infrared Stimulated Luminescence) and multiple quartz aliquots for OSL, although only the IRSL was included due to their generally younger age estimations (Figure 5.15). In this work, we prefer the OSL dates over the IRSL for two main reasons that diminish the reliability of the latter estimations (Alicia Medialdea, personal communication). The first is that the feldspar signal decays over time, i.e., anomalous fading, affecting its natural luminescence signal. The absorbed dose measured in the laboratory corresponds to the one generated in laboratory times, not in real geological time, implying that the measured signal does not show the real decay that the sample has experimented in nature and ultimately affects its estimated age. Although methods can be applied to minimize the anomalous fading or correct the estimated age, this limitation is a source of error. The second is that the potassium within the feldspar structure contributes to the dose rate and its concentration varies from grain to grain. This concentration cannot be quantified in the grains that are measured and requires the incorporation of a theoretical correction value to account for the potassium contribution. The use of this correction value for multi-grain aliquots can be assumed as representative for the many grains measured, but for single-grain analysis such as the one used in the study by Ferrater (2016) it is more arbitrary and represents another important source of uncertainty. This selection of OSL vs IRSL dates implies a change in the estimated ages of several units with respect to Ferrater (2016): samples SAL-23, 24, 25, 26, 27 and 28 for units J, L2, N1, B and A2, respectively (Table 5.4).

Trench	Unit	Sample ID	Method	Age and uncertainty (ka BP)	Study/Source		
TR-6	I	SAL2	Radiocarbon	25.2-25.8	Datings in El Saltador site from Ferrater (2016)		
TR-10	A1	SAL5		1390-1443 AD			
		SAL6		1426-1521 AD			
TR-5	G	SAL20		21.9-22.3			
TR-7	H	SAL10	OSL	21.7±1.6	Datings in El Saltador site from Ferrater (2016). We use OSL results instead of the IRSL used in that work.		
	P	SAL 11		>101 ka			
TR-10	J	SAL23		31.7±3.7			
TR-7		SAL24		31.2±2.6			
TR-7	L (L2)	SAL25		45.9±3.5			
	N (N1)	SAL26		73.4±7.0			
TR-10	B	SAL27		15.2±1.1			
TR-11	A2	SAL28		0.66±0.03			
TR-3	C	TRM27		TL		17.2±2.1	Datings in El Saltador site from Masana et al. (2004)
		TRM43				17.2±2.3	

Table 5.4. Dates of the sedimentary units in el Saltador site from trenches in previous studies and adopted in the present. OSL and Thermoluminescence (TL) uncertainties refer to 1σ and radiocarbon ages to the 2σ range. The position of the samples can be found in Figure 5.15.

When different dating techniques are available for a same unit, radiocarbon dates are selected over OSL because of their smaller uncertainties. This is the case of unit G (SAL-20) and unit I (SAL-2). Finally, two Thermoluminescence (TL) dates (TRM27 and TRM43) from Masana et al. (2004) have been used for unit C instead of the dates in Ferrater (2016) because they are more coherent with the ages of the rest of the sequence.

The base of the alluvial sequence is estimated ~ 101 -130 ka, based on the SAL-11 sample on unit P, which provides a minimum age of 101 ka. The 130 ka bound is an indicative (rounded) age value selected to coincide with the base of the Upper Pleistocene, which is the age of most of the alluvial deposits of the fan (Ferrater, 2016). The oldest age used in this study is ~ 73 ka BP for unit N (sample SAL-26; Table 5.4). The top of the alluvial sequence culminates at ~ 25.5 ka BP with unit I (SAL-2; Table 5.4), marking the transition to a channelized alluvial system (units H-B). The top of the channelized sequence in

T-16 is unit B with an age estimated of 15.2 ka (SAL-27), while in other parts of El Saltador site, two additional units A1 and A2 are found on top, which correspond to near-present sediments of channels in the alluvial fan surface (SAL-6 and SAL-28, respectively; Table 5.4). The stratigraphic sequence also shows depositional gaps in the site, although these are smaller than in the previous sites: between units P and N1 (~27.6 kyr), between N1 and L2 (~27.5 kyr), and the most recent from 15.2 ka up until historical sediments. The two former gaps represent very condensed sequences of deposition for unit O between P and N1, and for unit M between N1 and L2, respectively. The latter gap corresponds to the horizon between unit B and unit A2 or younger (Figure 5.15).

Site	Units	Sample ID	Age and uncertainty (ka)	Method	
La Tercia (T-2)	C2	T2-cc-1	32.1-33.1	Radiocarbon	
		T2-cc-2	33.8-34.4		
		T2-cc-3	34.1-34.6		
El Roser (T-1)	2.1	T1-cc-1	34.6-35.3		
	2.2	T1-cc-6	39.2-40.0		
	4.2	T1-cc-2	42.4-42.9		
	6.2	T1-OSL-4	76.8±5.6	OSL	
El Saltador (T-16 and previous trenches)	A1	SAL5	1390-1443 AD	Radiocarbon	
		SAL6	1426-1521 AD		
	A2	SAL28	0.66±0.03	OSL	
	B	SAL27	15.2±1.1	TL	
	C	TRM27	17.2±2.1		
		TRM43	17.2±2.3		
	E	T16-OSL-3	16.7±0.9	OSL	
	G	SAL20	21.9-22.3	Radiocarbon	
	H	SAL10	21.7±1.6	OSL	
	I	SAL2	25.2-25.8	Radiocarbon	
	J	SAL23	SAL23	31.7±3.7	OSL
			SAL24	31.2±2.6	
		L2	SAL25	45.9±3.5	
N1		SAL26	73.4±7.0		
P	SAL 11	>101 ka			
La Hoya (T-3)	B	T3-ch-3	8.5-8.6	Radiocarbon	
	B	T3-ch-1	8.6-9.0		
	B	T3-ch-2	9.3-9.8		
	O	T3-OSL-13	18±1	OSL	

Table 5.5 Selected ages in each site and used for the paleoseismic study of this work. OSL uncertainties refer to 1σ and radiocarbon dates correspond to the 2σ range. The position of the samples can be found in Figure 5.11 to Figure 5.15

5. Structural and paleoseismic characterization of the Lorca-Totana segment

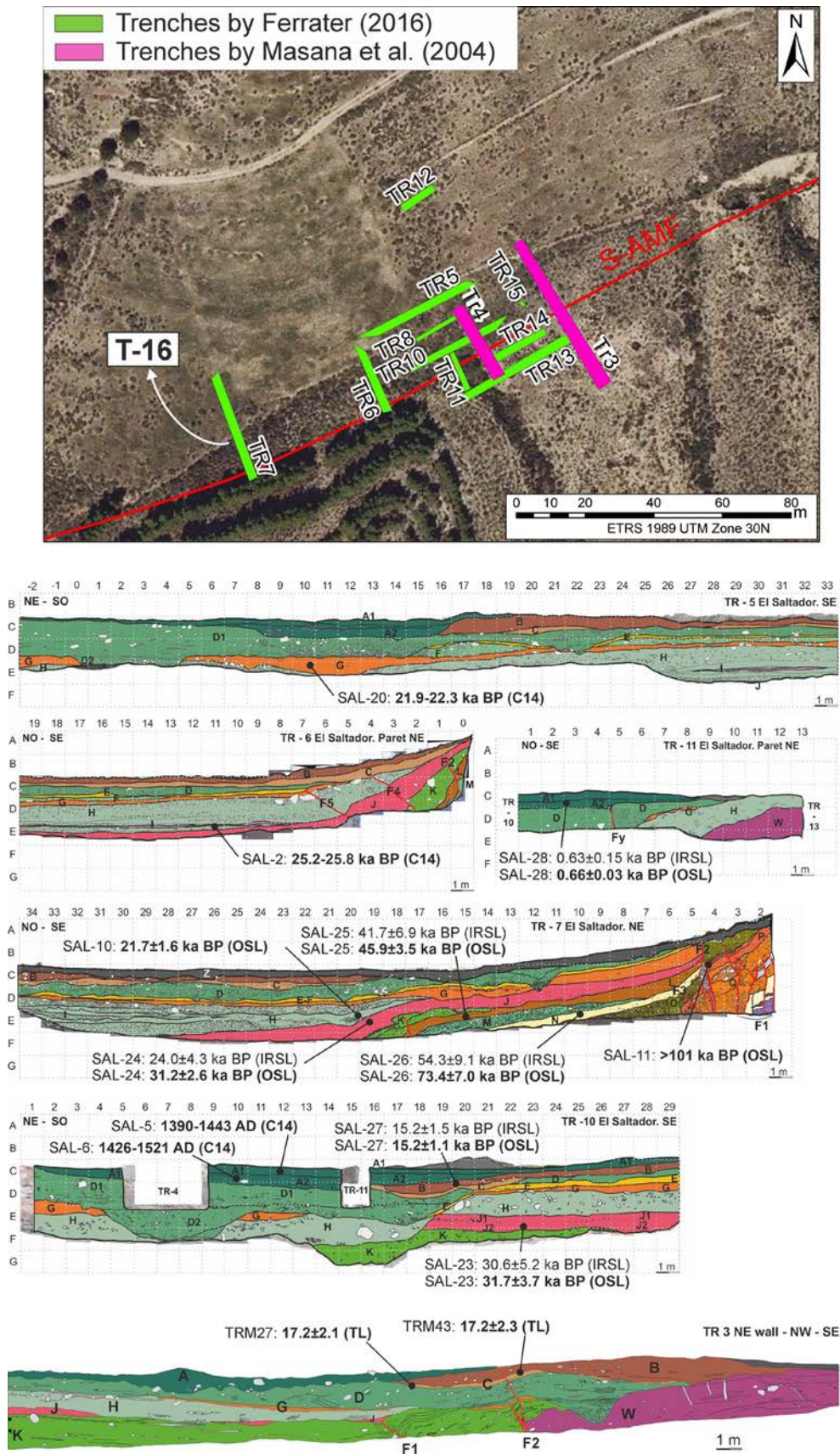


Figure 5.15. Placement of the dates from previous studies in El Saltador site used in the present one. Modified from Masana et al. (2004) and Ferrater (2016). Dates used are highlighted in bold. The unit nomenclature by Masana et al. (2004) is modified to make it equivalent to our study.

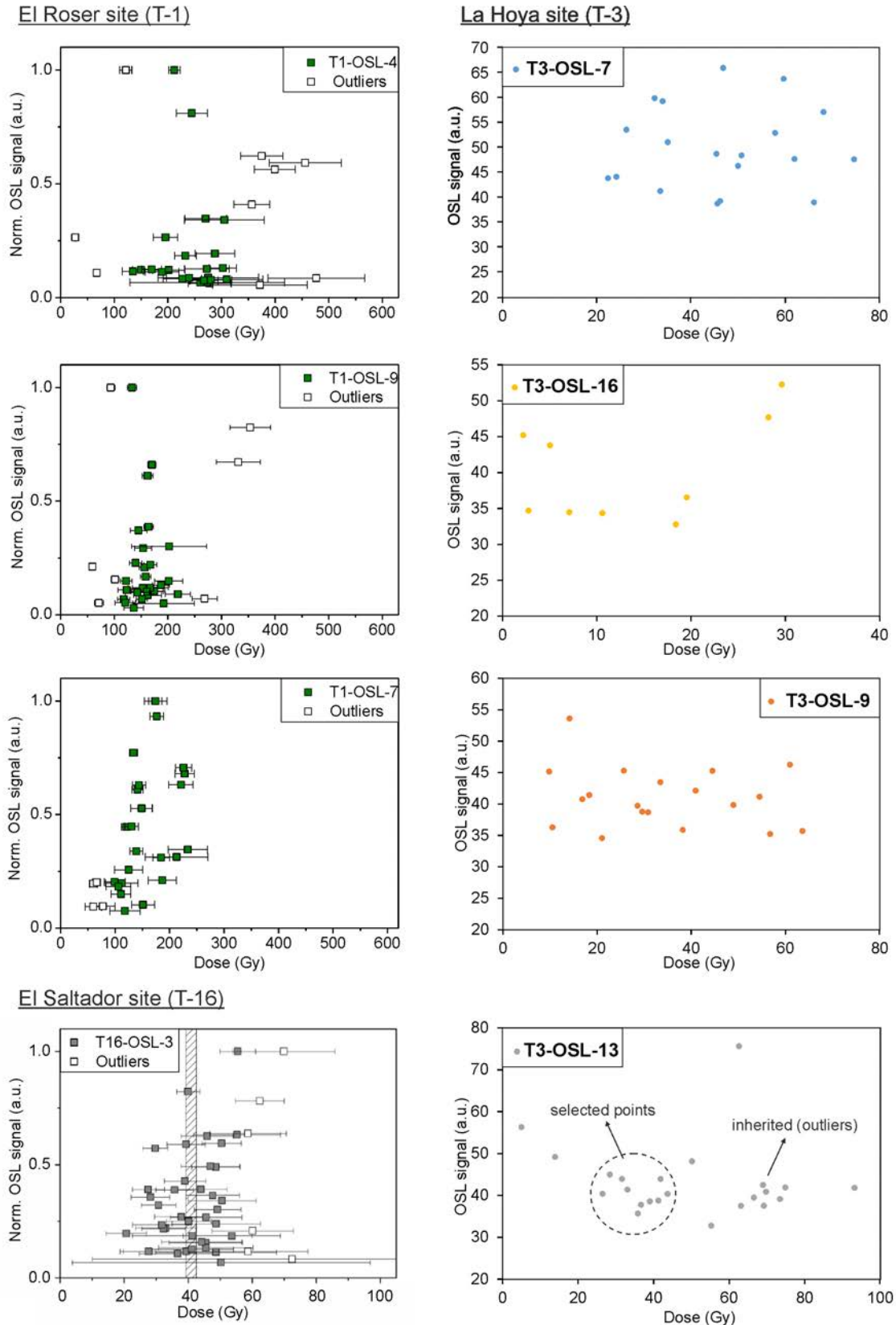


Figure 5.16. Dose distributions derived from OSL measurements of multi-grain quartz aliquots of the samples analyzed in the trenches and provided by the laboratories. Each plot represents the mean with one standard error and outliers with inherited luminescence signal are highlighted. For the sample T3-OSL-13 the group of points selected for the re-calculation of the age is indicated. Figures modified from the laboratory reports and reproduced with permission from the respective authors. Full reports of OSL dating results are available in the Annex II (B).

5.5.3.4 T-3 (La Hoya site)

The heterogeneous distribution of the samples within the stratigraphic sequence of this trench is due to the lack of datable material. The resulting dates are mainly from the lower units in the sequence (units O and T) and from the upper unit B. The ages obtained in this trench are the youngest of all the sites and cover a relatively short time window of ~10 kyr; from ~20 to 8-9 ka BP.

Samples T3-OSL-7 (unit T) and T3-OSL-13 (unit O) have both ages around ~20 ka, however the mean values of the age distribution are not coherent with the stratigraphy. This is because sample T3-OSL-13 has a very high carbonate concentration in the sample matrix, which hampers the dose rate of the sample and leads to an age older than the real. Furthermore, for this sample the luminescence plots obtained for each of the 23 aliquots are concentrated in two groups, one with lower absorbed dose values and therefore younger luminescence ages, more coherent with the stratigraphy (Figure 5.16). This suggests that part of the aliquots might have an inherited luminescence signal due to a non-complete bleaching during deposition and thus that the mean luminescence age is biased by these aliquots. For this reason, we re-calculated the luminescence age considering only the younger aliquot aggrupation and obtained a mean age of 18 ± 1 ka, coherent with the stratigraphy of the trench (Table 5.2).

The rest of the samples are from unit B and provide different values depending on the method used. Radiocarbon dates from charcoals provide an age of the unit ranging from 9.3-9.7 ka near the base of the unit (T3-ch-2) to 8.4-8.5 ka on top of the unit (T3-ch-3). Conversely, OSL dates provide non-coherent results with the stratigraphy nor the radiocarbon dates. Sample T3-OSL-16 provides a luminescence age of 5 ± 2 ka, which appears too young compared to the radiocarbon dates. This can be explained considering that the age of this sample has been determined using only 9/24 aliquots and shows the highest uncertainty percentage (29%) of all samples. Also, a possible contamination during sampling cannot be discarded and hence this age is only an indicative minimum and cannot be used for paleoseismic purposes. Sample T3-OSL-9 has an age (11 ± 1 ka) closer to the ones from the radiocarbon, but slightly older. This might be due to inherited geological signal in some aliquots, evidenced by the fact that a significant part of these aliquots (10/19) show ages < 20 ka in the distribution (Figure 5.16). The age of unit B therefore seems to be better represented by the radiocarbon dates than the OSL, as they are more coherent with the stratigraphy and consistent with each other. Moreover,

charcoal is less susceptible to present inheritance effects from older carbon and thus constitutes a more reliable source in this case. The selected ages for the paleoseismic parameters in this study are shown in Table 5.5.

A sedimentary gap is identified in this trench between unit B (~8-9 ka BP) and unit A, which corresponds to the actual La Salud creek deposits and hence could be only a few tens of years old. The lack of numerical dates between unit B and unit O prevents from the identification of other gaps in the sequence.

5.5.3.5 Sedimentary evolution

The dating results in the different paleoseismic trenches support the evolution model of the sedimentary environment of the area with the migration of younger deposits towards the Guadalentín basin to the S. The Quaternary alluvial sequences at El Saltador alluvial fan comprise ages from ~101 ka up to ~ 25 ka (Q3). During this period, the alluvial sedimentation was active within the area between the N₁-AMF and S-AMF fault branches, as revealed by the spatial constraining of El Saltador fan, although the deposition reached to the Guadalentín Depression (Figure 5.2). In the upper parts of the fan (La Tercia and El Roser sites), the ceasing of the alluvial deposition and incision of alluvial channels (Q2a) started at ~ 40 ka BP (unit 2.2 in T-1) and extended into at least 35-32 ka BP (units 2.1 and C2 in T-1 and T-2, respectively). In the lower parts of the fan the channelized alluvial sequence started at ~25 ka BP (unit I in T-16) and lasted up to ~15 ka BP (unit B in T-16). Upon this age the fan activity was practically abandoned and only a few channels developed in the recent years (e.g., units A1 or A2 in El Saltador site; Ferrater, 2016). During this transition, the migration of the alluvial systems towards the frontal parts of the range formed new deposits, consistent with the dates of the lower units in T-3 (~19 ka for unit T). In these frontal parts the Q2 alluvial deposition lasted up until ~9 ka, when the alluvial fans were abandoned and incised by creeks up until nowadays. These channels feed the active alluvial fans (Q1) that are found more towards the central parts of the Guadalentín basin (Figure 5.2).

The tectonic activity in all the different studied sites, affects the display and deposition of the sedimentary units, especially in those with folding and important vertical slip displacement. In El Roser and La Hoya sites, the folding grows towards the SE, in the same direction of the drainage of the alluvial fans coming from La Tercia range. This causes the erosion of the successive syn-tectonic units in the uplifted block. Conversely,

in El Salvador, the sedimentary model is different because the S-AMF folding grows towards the NE, generating a tectonic barrier of El Salvador alluvial fan. This implies that, in some parts of the alluvial fan, the sediment inflow coming from la Tercia range was prevented from directly crossing the fault to the S (e.g., Ferrater et al., 2016). The location of T-16 is one of these parts, where the north-facing scarp causes wedging and onlap of the sedimentary units towards the uplifted block. In other places of El Salvador site, 60-70 m NE of T-16, the smaller expression of this scarp, allows the sedimentary units to exceed the tectonic barrier, which are used as markers to measure fault slips (Masana et al., 2004; Ferrater, 2016).

5.5.4 Paleoearthquake evidence

We evaluate the paleoearthquake evidence in each trench corresponding to each fault branch of the studied transect. Because not all the paleoearthquakes are supported by the same amount or equally robust evidence, we classify each paleoearthquake in two categories depending on the confidence of their evidence:

- i) Strong: when the evidence can only be explained by tectonic processes such as fault deformation truncations or other clear geometric evidence such as differential deformation between units suggesting angular unconformities.
- ii) Weak: when there is a single or few evidence that are not clear or could be explained by non-tectonic processes. For instance, when there are slight differences in the deformation degree of successive layers that could be originated by depositional processes (e.g., paleochannel incisions or depositional onlaps).

From N to S, the paleoearthquake evidence of the excavated branches are described in the following sections. See Figure 3.5 in section 3.2 for details on the type of sedimentary evidence used to identify paleoearthquakes in this thesis. It is noteworthy that no trenches were dug in the N_{2a}-AMF, so the paleoseismic characterization of this branch remains undisclosed.

5.5.4.1 N₁-AMF

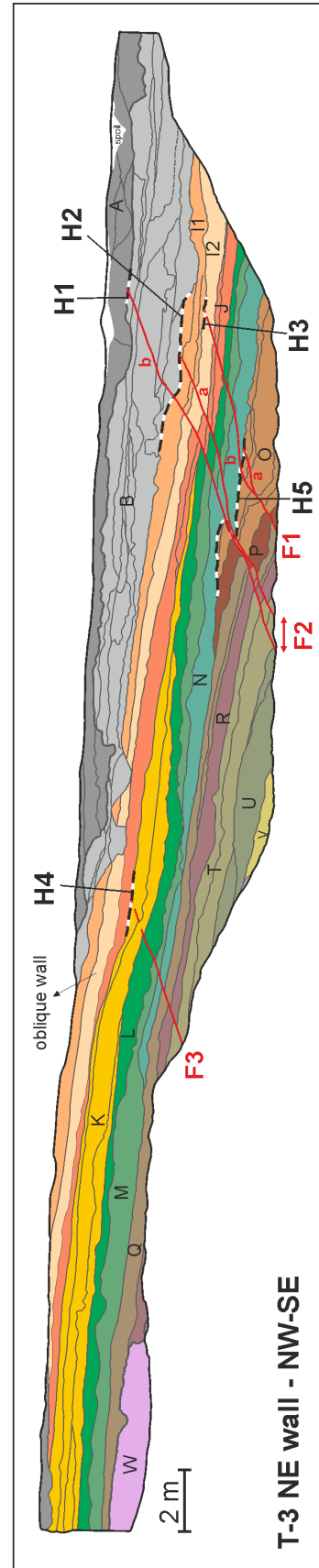
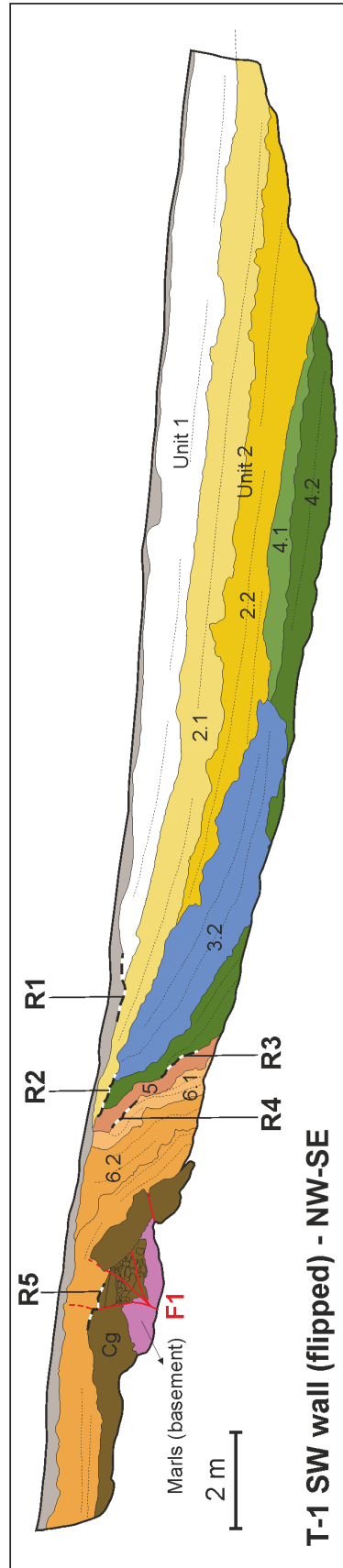
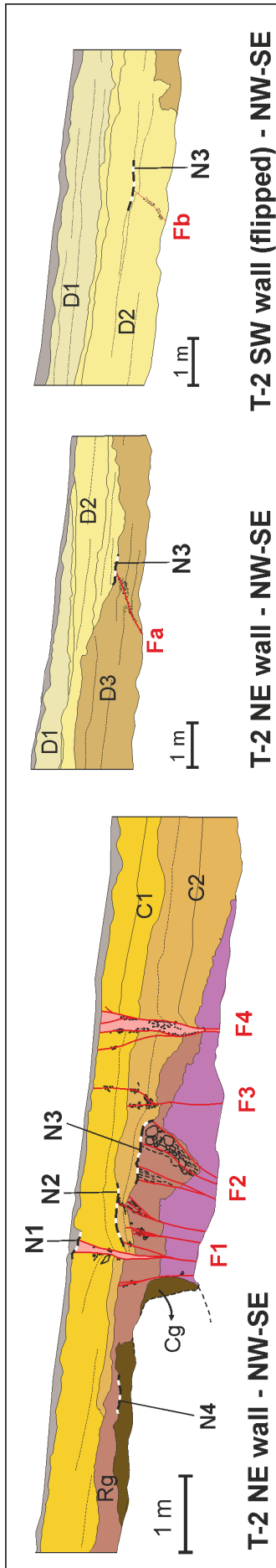
A minimum of four paleoearthquakes have been identified in T-2. The deformation in this trench is localized in a narrow 5 m fault zone, hence most of the evidence are restricted to this area of the trench. Table 5.6 compiles the supporting evidence and quality assigned to each paleoearthquake, and Figure 5.17 the location of the event horizons. Given the

strike-slip character of this fault, most of the evidence is based on fault strand truncations, as it is the case of events N3 to N1. In the case of N4, however, the supporting evidence is that the Cg unit is not present at both sides of the fault while the Rg unit is. This implies that the former had to be deformed and eroded before the latter was deposited. All paleoearthquakes are considered to have strong evidence, because fault truncations are robust.

The number of events identified is a minimum. The different ages between the Cg and alluvial units on top (event N4) implies a large depositional gap within which several earthquakes could have occurred. The event identified in the base of unit C2 in this zone is likely the same as event N3. However, it cannot be precluded that an additional event occurred before unit C2 deposition and different from N3. This is because in the fault zone of the trench, unit D is not preserved. It should also be recognized that it is feasible that event N3 could be two events if it is considered that the affected D2 in the SW wall corresponds to a younger incision than the unaffected D2 in the NE wall (Figure 5.17). However, we prefer the single-event hypothesis because, from the logs in Figure 5.11, it appears that the fault truncations in both walls are in similar stratigraphic levels and thus most likely correspond to a same event horizon.

Units	Evidence	Quality
Actual Soil		
Event N1	The whole outcropping stratigraphic sequence is faulted up to the base of the actual soil, which postdates several fractures from the fault strands F1, F3, F4 and F5.	Strong
Unit C1		
Event N2	The base of unit C1 postdates some fractures of the fault strands F1 and F3. Also, unit C1 postdates the folding observed in C2 between faults F1 and F4 in the SW wall, and the folding related to the faults F5 and F3 in the SW and NE wall, respectively.	Strong
Units C2-D2		
Event N3	An internal layer within unit D2 postdates the deformation produced by a minor fault strand Fb in the SW wall and by Fa in a similar stratigraphic level in the NE wall. This event might be the same one identified in the main fault zone of T-2, where unit C2 postdates several strands of F1 and F2.	Strong
Units D2-Rg		
Event N4	Unit Rg is deposited at both sides of the fault, on top of the Cg unit in the northern block and on top of the marls in the southern. On the contrary the cemented unit is only present in one block, implying at least an event previous to the deposition of the Rg unit.	Strong
Cg		

Table 5.6. Paleoearthquake evidence identified in T-2 for the N₁-AMF branch. The placement of these events in the trench logs can be found in Figure 5.17.



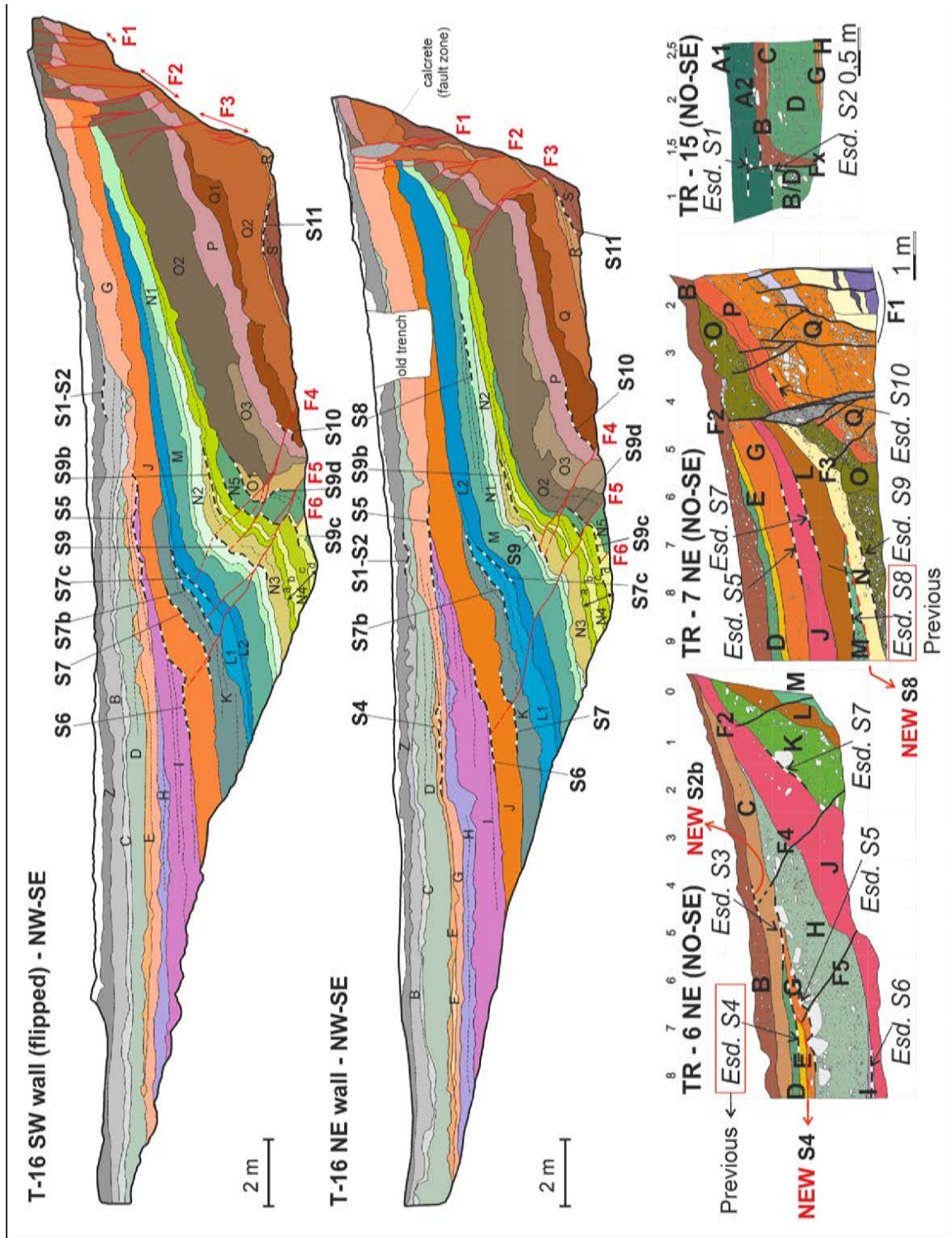


Figure 5.17. Paleoseismicity evidence in the different sites analyzed in this study. In the case of El Salvador site, the three sketches below T-16 are modified from Ferrater (2016) and indicate the events identified in that study coincident with ours, as well as the ones whose event horizon has been relocated here. Dashed black and white lines mark the position of the different event horizons.

5.5.4.2 N_{2b}-AMF

A minimum of five paleoearthquakes have been identified in T-1 for the N_{2b}-AMF branch (Table 5.7). In the trench, the main fault is barely observed, instead a fold scarp caused by the Cg unit is found (Figure 5.17). In this context, a propagation monoclinial fold is depicting the deformation related to this branch. Hence, paleoearthquakes are evidenced by the angular unconformities within the fold and subsequent sedimentary relationships between units. In addition, minor faults producing clast lineations and slips of a few centimeters reaching the surface are also identified in the NE wall (Figure 5.18) as evidence for the last event R1 (Figure 5.12). These are interpreted as internal readjustments of the deposits (clast rotation) during the fold growth.

Unit	Evidence	Quality
Actual Soil		
Event R1	Units 1 to 2.1 show higher slopes than the depositional one in the central part of the trench, which imply that they are folded by at least one last event. Also, lineations F2-F5 in the NE affect the whole sequence and are postdated by the current soil (see logs in Figure 5.12).	Strong
Units 1-2.2		
Event R2	The base of unit 2 forms an angular unconformity with the underlying units showing marked different degrees of deformation. In the flank zone of the fold, the internal layers from unit 2.2 and 2.1 are onlapping the ones from unit 6 and eroding the previous structure. The postdating of the fault F1 by unit 2.1 might correspond to this event, as well.	Strong
Units 3.1-4.2		
Event R3	Internal lamination from unit 4.2 is onlapping unit 5, which implies deformation before the deposition of unit 4.2. Also, the whole sequence of unit 4 to 3 shows lower dips than unit 5, which implies a lesser deformation degree.	Strong
Unit 5		
Event R4	The base of unit 5 shows an angular unconformity with the internal lamination of unit 6.1, especially recognizable in the NE wall. Unit 5 is a paleosol as evidenced by the red coloration and calcification present in the unit, which suggests that unit 6 was exposed to the surface and deformed in absence of deposition.	Strong
Unit 6		
Event R5	Fault F1 (SW wall) shows less displacement in unit 6 than in the Cg unit. This event is not actually observed in the trench because the sequence does not show the geometry of the Cg unit. In the cut of the left margin of the San Julián creek (Figure 5.5B) the Cg unit depicts a marked monoclinial fold with a verticalized flank producing a slip much larger than the ones observed in the alluvial fan units on top, which are onlapping the cemented unit. This difference in the deformation might suggest that R5 is actually the result of different events with a gap in the deposition.	Strong
Cg		

Table 5.7. Paleoseismic evidence identified in T-1 for the N_{2b}-AMF branch. The placement of these events in the trench logs can be found in Figure 5.17.

Table 5.7 compiles the main supporting evidence and quality for each identified paleoearthquake. The number of events identified, especially in this trench, is a minimum because there are important sedimentary gaps. The deformation of the Cg unit, ~17 m (detailed in section 5.5.5) below the bottom of the trench in the outcrop of San Julián creek (Figure 5.5B) is much larger than that of unit 6, which cannot be explained by a single event. This means that the event horizon of event R5 encompasses a period with several paleoseismic events, but without sedimentary record to distinguish them. More so, the lack of deposition in this site since ~35 ka, implies that the last event R1 could be more than one event. This has a clear impact on the recurrence periods as we discuss in section 5.6.1.

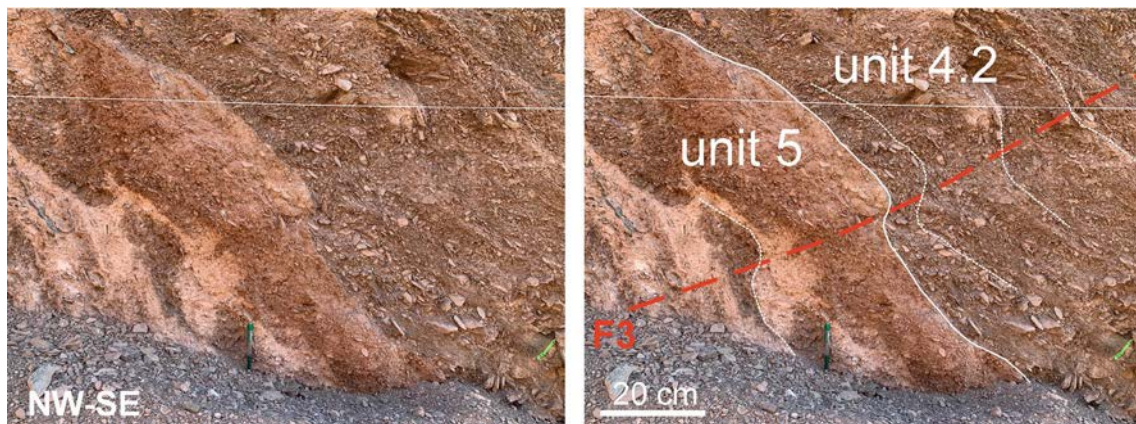


Figure 5.18. Folding and clast lineations linked to small fractures (F3) observed in the NE wall of T-1 (El Roser site). See Figure 5.12 for location of this fracture in the trench log.

5.5.4.3 S-AMF

For this branch we integrate the paleoearthquakes identified in T-16 with the ones from Ferrater (2016) in the other trenches at El Saltador site. A minimum of thirteen paleoearthquakes are identified in T-16, nine of which show strong evidence. Accounting for the other trenches in El Saltador site, not just the studied here, a total of seventeen paleoearthquakes are identified, ten with strong evidence. Table 5.8 compiles the evidence for all the identified paleoearthquakes at El Saltador site. The better sedimentary resolution of T-16 with respect to previous trenches allowed to enlarge the paleoearthquake record for the S-AMF, constituting the largest paleoearthquake record to date in the AMF and southeastern Spain.

We use the same nomenclature of events as the one by Ferrater (2016), revised afterwards by Ortuño et al., (2021; in preparation). This last work re-analyzes the El Saltador paleoseismic site, previous to the opening of T-16, and refines the paleoearthquake

catalogue by integrating observations from older trenches in that site (Masana et al., 2004; Ferrater, 2016) and new observations. Here, newly identified events in T-16 are added the terms “a”, “b”, “c”, etc. to avoid disrupting the numeric nomenclature from such previous studies (e.g., S7, S7b, etc.) (Figure 5.17). Due to lack of stratigraphic resolution in the upper units (units E-Z), events S1, S2, S2b and S3 are not directly observed in T-16 but in previous trenches in El Saltador site.

The presence of yellow-orange silt deposits embedded within the predominantly gravel materials of the sedimentary sequence in this trench (e.g., units C, E, G, J, L1, N4c, N5 and P) has been interpreted as ponded strata evidencing paleoearthquakes in previous studies (Ferrater, 2016). During earthquakes, the shaking of the surface can produce large amounts of dust that can generate mudflows shortly after the event. The tectonic uplift of the southern block in the S-AMF branch acts as a tectonic barrier for El Saltador fan (Martínez-Díaz et al., 2003) that might have contributed to the ponding of these sediments. In this sense, these bodies can be interpreted as coseismic sedimentary evidence as done in analogue environments in the American continent (Fletcher et al., 2014; Rockwell et al., 2014). Despite this, not enough research has developed yet around this matter to provide robust sedimentary evidence for the relationship between such deposits and its coseismic origin, especially because fine grained heterogeneous sediments can be found in alluvial fan environments. For this reason, in this study, the presence of these deposits alone is not considered as an evidence of paleoearthquakes if not combined with other evidence.

The sedimentary model of the site is crucial to interpret the paleoearthquakes in T-16 because, unlike the rest of the other sites, the propagation fold related to the fault grows against the depositional slope of the alluvial fan, uplifting the southern block. This blocks the drainage coming from the N and generates a set of thinning upslope (wedging) geometries in the sedimentary units that are used to support the paleoearthquakes. In the work by Ferrater (2016), some of these wedging geometries are considered to be result of tectonic angular unconformities with the overlying units (e.g., base of unit D), which places the respective event horizons at these unconformities (e.g., situation in Figure 5.19A). According to this model, the geometries are explained by post-event erosion and subsequent deposition on top. Based on the observations in T-16, however, this model is not entirely accurate because the internal stratification of the units usually shows no deformation differences between the units bracketing the alleged unconformities

(Figure 5.17). We then state that these geometric features can be misinterpreted as a tectonic angular unconformity if the internal stratification is not accounted (e.g., contact between units D and E or L and M). Here, the wedging geometries are interpreted to have a depositional origin due to the presence of a preexisting counter-slope coseismic relief (barrier). This model places the event horizon before the deposition of the wedging unit, i.e., at its base (Figure 5.19B), which is consistent with the onlap relationships of such units towards the slope. This revised depositional model rules out some of the evidence identified to support two paleoearthquakes in Ferrater (2016) and displaces the position of their event horizons (Figure 5.17):

Event S4: according to Ferrater (2016) the angular unconformity between unit D and unit E in TR-6 caused by fault F5 is an evidence for this earthquake (Figure 5.17). In T-16 we recognize that both units are subparallel based on internal lamination and both onlapping unit G. This is consistent with the reassessment by Ortuño et al. (2021; in preparation) pointing that F5 in TR-6 is actually postdated by the base of unit E (e.g., situation in Figure 5.19A and B).

Event S8: in Ferrater (2016) this event is placed at the base of unit L in TR-7, previous name of the smaller size trench now enlarged in T-16 (L in TR-7 equals L2 in T-16). This was explained because unit L was interpreted as a coseismic ponded strata in the fault zone and because its base seemed not to be affected by fault F3 (Figure 5.17). In T-16, unit L2 shows the same deformation than the internal strata of the underlying unit M, both onlapping the unit N1. This would place the event horizon at the base of unit M, compatible with unit L postdating fault strand F3 in TR-7 because M is not preserved on top of this strand.

In T-16, most paleoseismic events are identified by the differential deformation of the different units in the propagation fold. In the uplifted block, the stratigraphic sequence from units O to Z is not present (Figure 5.17) either because it has been eroded or because these deposits were not able to exceed the fault relief. The latter option is the preferred given the mentioned sedimentary environment of this site and the fact that most units wedge towards the fault. However, this is not the case of units J and G, which are directly cut by the fault (F1-F2; Figure 5.17) and hence, were likely present in the uplifted block at some point.

Unit	Evidence	Quality
Units Z-A1		
Event S1	Local evidence in TR-15. Unit A2 is displaced ~12.5 cm by fault Fx, while unit A1 postdates the deformation of this fault (Ferrater, 2016). The progression of fault Fx across unit A1 cannot be discarded.	Weak
Unit A2		
Event S2	Unit B is more deformed than unit A2. The former shows a monoclinical fold with verticalization in the fault zone (Fx) of TR-15, generating a ~60 cm slip. The latter postdates this folding deformation. In T-16 this event cannot be distinguished from S1, unit B is tilted towards the NW, contrary to the depositional slope. The fine-grained A2 suggests coseismic origin of this unit related to ponding in the fault zone.	Strong
Unit B		
Event S2b	Local evidence in TR-6. The base of unit C shows a slight folding geometry coincident with the position of fault F4, while unit B is not displaced by this fault. However, the progression of this fault through unit C is not clear and the geometry of this unit base could be a depositional adaptation to a pre-existing lump caused by F4.	Weak
Unit C		
Event S3	In TR-6 the base of unit C is less deformed than the one from unit D, but in T-16 this relationship is not observed as both units appear subparallel, although it is probably due to lack of complete exposure of these units in this trench. Also, unit C is a fine-grained unit whose origin can be interpreted as coseismic ponding in the fault zone.	Weak
Units D-E		
Event S4	Units E-D are onlapping the underlying units. The internal lamination of unit G shows a higher dip than units E and D in the NE wall, which suggests a differential deformation. However, these variations are slight and units E-D are clearly paleochannels incised in the G unit, hence the observed onlap relationships could also be depositional. The fine-grained characteristics of unit E can be interpreted as coseismic origin.	Weak
Unit G		
Event S5	The base of unit G shows an angular unconformity with the underlying sequence. This is only observable in the NE wall of T-16, where the internal laminations of unit H are cut by the base of unit G. This dip difference is small, and the evidence is very localized; could likely be explained by a depositional overlay of unit G. The lithological characteristics of unit G (orange massive silts), suggest a coseismic origin.	Weak
Units H-I		
Event S6	Unit I is postdating the fault strand F5 and is also onlapping the underlying units with a marked angle because the dip of the internal lamination of unit I is lower than unit J.	Strong
Unit J		
Event S7	This event is mainly interpreted from the sedimentary characteristics of unit J, which is a massive silty orange unit, interpreted as a ponded coseismic deposit. In the NE wall this unit might be postdating one strand of F2, but it is not clear because the unit is very massive and the contact in this part of the trench is diffuse.	Weak
Unit K		
Event S7b	Unit K postdates a strand of F5 and part of the deformation from other F5 strands showing slightly less slip than the underlying units. Unit K is onlapping unit L depicted by the internal stratification.	Strong
Unit L1		
Event S7c	Unit L1 postdates one strand of the F4 fault in the SW wall. It also shows a slightly lower dip than the underlying unit L2, as evidenced by the onlap of the internal lamination in the limb zone of the fold. More so, the lithological characteristics of unit L1 (massive silts), might suggest a coseismic origin.	Strong
Units L2-M		
Event S8	Unit M is onlapping the underlying units with its internal stratification in the NE wall showing a lower dip than the N1-N2 contact.	Strong
Units N1-N2		
Event S9	Unit N2 is postdating the majority of the F4 strands and its base is also less displaced by the F5 than the underlying units. In the NE wall the thickness of unit N3 is smaller in the hanging wall of fault F4 than in the foot wall, which supports the existence of an event after N3. The postdating of fault F3 by unit N1 might be related to this event, although it could be event S10 as well because N2 and N3 are missing on top.	Strong
Unit N3		
Event S9b	Unit N3 shows a slightly lower dip than the underlying N4a and N4b units, causing an onlap in the limb area of the hanging-wall of strand F4 (NE wall). This relationship is local and slight, hence could be related to depositional features in a channel. The base of unit N3 appears less displaced by some strands of F4 in the SW wall than the underlying units. The postdating of fault F3 by unit N1 could also be from this event.	Weak
Units N4a-N4c		
Event S9c	Unit N5c postdates the fault F6 and two strands of F4 and F5, respectively in the SW wall. Unit N4c is also onlapping the underlying unit O near the main fault zone (between strands F2 and F3). The lithological characteristics of unit N4 (orange massive silts), might also support a coseismic origin of this unit related to sediments ponded in the fault zone.	Strong
Units N4d-N5		
Event S9d	Unit N5 is less deformed than the underlying O unit, and shows an onlapping relationship, especially observable in the fold hinge between faults strands F4 and F5 in the SW wall. In this zone, unit O1 shows a nearly vertical dip, while the internal stratification of unit N5 dips towards the NW. Additionally, the lithological characteristics of unit N5 (orange massive silts), might support a coseismic origin.	Strong
Units O1-P		
Event S10	The base of unit P shows less displacement than unit Q1 in the fault F4 of the SW of the fault, although this could be due to lateral component of the fault, especially considering that this fault causes higher slips in younger units such as N4c. Also, the lithological characteristics of unit P are compatible with a coseismic ponded sediment in the fault zone.	Weak
Units Q-R		
Event S11	Unit R shows less deformation than the underlying unit, as evidenced by the onlap of the former with respect to the higher dip of unit S.	Strong
Unit S		

Table 5.8. Paleearthquake evidence identified in El Salvador site (T-16) for the S-AMF branch. Note that the events S1, S2, S2b and S3 are not directly observed in T-16, and are described in other trenches in El Salvador site from previous studies (Ferrater, 2016; Ortuño et al., 2021; in preparation). The placement of these events in the trench logs can be found in Figure 5.17.

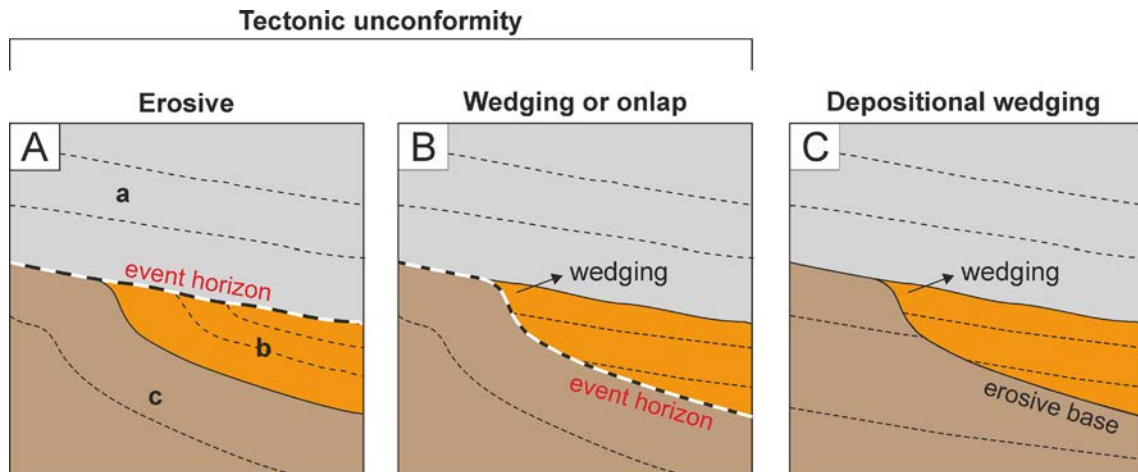


Figure 5.19. Different possible stratigraphic relationships that can mislead the placement of event horizons. **A)** Tectonic erosive unconformity. In this model, the overlying unit “a” is less deformed and erodes the strata of the underlying “b”. **B)** Tectonic unconformity, but in this case the overlying unit “a” is concordant with the unit “b”. Instead, the horizon event is placed at the base of “b”, which is less deformed and onlaps the underlying unit “c”. This happens when there is a previous tectonic relief that results in onlap and thus wedging geometries of the overlying unit upslope. **C)** Depositional wedging of the units exclusively due to sedimentary processes such as the incision of a paleochannel. Note that, without the internal stratification, all three situations would appear the same. We put focus on that to re-locate the events misinterpreted as situation A by Ferrater (2016) to situation B, as mentioned in the text.

5.5.4.4 F-AMF

A minimum of five paleoearthquakes are identified in T-3 for the F-AMF branch, all of them with strong evidence, as explained in Table 5.9. The truncations of the fault strands, cut by the erosion base of overlying units, the slip decrease of the progressively younger sedimentary units in the sequence and the angular disconformities related to the growth of the propagation fold, constitute the principal paleoearthquake evidence in this trench. Overall, the materials affected are much younger than in the previous trenches (Table 5.5) and therefore this trench depicts a more recent seismic history of the AMF system than the other branches.

Unit	Evidence	Quality
Unit A		
Event H1	Unit A postdates the fault F2b and shows a low-angle angular disconformity with the underlying B unit, especially recognizable in the SW wall, where the internal stratification of B is cut by the base of A in the uplifted block.	Strong
Unit B		
Event H2	Unit B shows an angular disconformity with the underlying units, as recognized by the higher dip of the internal stratification of unit I1. Also, this unit postdates F2a in the NE wall. The slip generated by this strand in unit B is smaller than the generated in the underlying I1.	Strong

Continues in the next page

Continued from the previous page

Unit I1		
Event H3	The base of unit I1 postdates the fault strand F1 and shows less slip by fault F2 than the underlying units.	Strong
Unit I2-J		
Event H4	The base of unit J is postdating the fault F3. This is clearer in the NE wall of T-3 because in the SW wall this horizon is in the bench area of the trench. The base of unit J is discordant with respect to the underlying units but shows a higher dip and incision towards the footwall, which might suggest that this relationship is sedimentary.	Strong
Units K-N		
Event H5	The base of unit N shows an angular unconformity with the underlying units, which are more deformed and show higher slips related to the faults F1 and F2 than the overlying units. This horizon also truncates strand F1a.	Strong
Units O-W		

Table 5.9. Paleoseismic evidence identified in T-3 for the F-AMF branch. The placement of these events in the trench logs can be found in Figure 5.17.

5.5.5 Fault slips

5.5.5.1 Vertical slips

Trench vertical slip measurement is performed in faults with evident important vertical component: N_{2b}-AMF (T-1), S-AMF (T-16) and F-AMF (T-3). In N₁-AMF (T-2), no vertical slip analysis is performed because the vertical separations are minor and probably apparent related to the predominant strike-slip kinematic observed for this fault.

Table 5.10 summarizes the slip values in each trench, which are provided for the event-horizons delimitating units with differential deformation. In T-16, only the event horizons that show strong evidence for seismic origin are considered because they are the ones with marked differential deformation. These delimitate units with the same degree of deformation. Note that the uncertainty ranges refer to 1σ (68.3% confidence interval) and correspond to the variability of four slip measurements per horizon in the graphics software (see section 3.4 for details on the slip quantification). These do not necessarily reflect the epistemic uncertainty of the measurements related to the assumptions or simplifications made when modelling the structures of the trenches. We have to acknowledge that the observed separation might differ from the real vertical displacement due to the possible lateral component and because the trench might not be excavated precisely parallel to the direction of fault displacement.

5. Structural and paleoseismic characterization of the Lorca-Totana segment

N₁-AMF				
Unit block	Age (ka)	Vertical slip ± 1σ (m)	Lateral slip ± 1σ (m)	Net slip ± 1σ (m)
Unit D	Minimum of 40	-	24.3 ^{+4.1} / _{-6.3}	24.3 ^{+4.1} / _{-6.3}
T-1 (N_{2b}-AMF)				
Cg	Min. 198±6.5	17.8±1.2	-	17.8±1.2
Unit 6	76.8±5.6	7.8±0.5	-	7.8±0.5
Unit 5	Not dated	6.2±0.7	-	6.2±0.7
Units 4.2 to 3.1	42.6±0.2 (4.2)	4.3±0.3	-	4.3±0.3
Units 2.2 to 1	39.6±0.3 (2.2) 35±0.2 (2.1)	2.6±0.2	-	2.6±0.2
T-16 (S-AMF)				
Unit S	Not dated	17.7±0.3	72.2±1.3	74.3±1.3
Units R to O2	Min. >101 ka (P)	15.6±0.5	63.6±2.0	65.5±2.1
Units N5 to N4d	Not dated	11.7±0.2	47.7±0.8	49.1±0.8
Units N4c to N3	Not dated	10.2±0.5	41.6±2.0	42.8±2.1
Units N1 to N2	Min. 73.4±7.0 (N1)	10.1±0.3	41.2±1.3	42.4±1.3
Units M to L2	Min. 45.9±3.5 (L2)	8.9±0.2	36.2±0.8	37.3±0.8
Unit L1	Not dated	8.2±0.2	33.4±0.8	34.4±0.8
Units K2 to J	Min. 31.2±2.6 (J)	6.8±0.3	27.7±1.3	28.5±1.3
Units I to B	25±0.3 (I) 15.2±1.1 (B)	4.0±0.2	16.3±0.8	16.8±0.8
T-3 (F-AMF)				
Units W to O	Min. 18±1 (O)	5.2±0.1	-	15.2±0.3
Units M to N	Not dated	3.2±0.1	-	9.4±0.3
Units J to I2	Not dated	3.1±0.1	-	9.1±0.3
Unit I2	Not dated	2.9±0.3	-	8.5±0.9
Unit B	9.5±0.1 (B base) 8.50±0.04 (B top)	2.2±0.2	-	6.4±0.6

Table 5.10. Vertical, lateral and net slips of the different deformed blocks obtained in this study for N₁-AMF, N_{2b}-AMF (T-1), S-AMF (T-16) and F-AMF (T-3). Age ranges of the blocks from the numerical dates (Table 5.5) are indicated. Note that the lateral slips from T-16 are indirectly inferred (analytically derived) from the rake and vertical slips. See text for details.

- N_{2b}-AMF

Five equally deformed blocks or units are considered: Cg unit, unit 6, unit 5, units 4.2 to 3.1 and units 2.2 to 1. The Cg unit is by far the most deformed one as inferred from the verticalization of the unit at the San Julián creek. The slip for this unit is based on topographic measurements performed on the DEM using the ArcGIS software. This slip

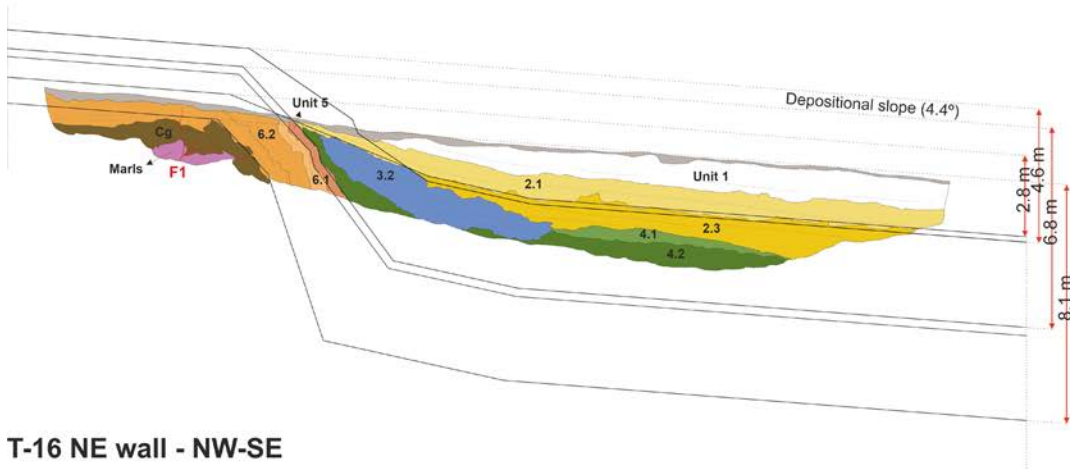
is particularly indicative of a minimum because not all the deformation of this unit is resolved in the outcrop of the creek as it extends towards the S (Figure 5.5). The other units' slips range from 7.8 ± 0.5 m in unit 6 to 2.6 ± 0.2 m in units 2.2-1 (Table 5.10). These values are also considered a minimum because the fold structure is extrapolated out of the T-1 limits using minimum dip values from the outcropping units directly on top, which are less deformed (see details in the methods section). This is especially important in lower units where more extrapolation is required (Figure 5.20). For instance, the base of unit 6 is only observed in the uplifted block and hinge zone of the fold. To extrapolate the dip of the unit at depth of the anticline limb, we use the dip observed in the upper sub-unit 6.1 on top. In the syncline part of the downthrown block, we use the outcropping dip of the upper units 3 and 4. Similarly, to extrapolate the dip of the top contact of the 4.2-3.1 sequence in the hinge zone of the anticline, which is eroded by units 2.2-1, we use the internal stratification of unit 3.2 (Figure 5.20).

- S-AMF

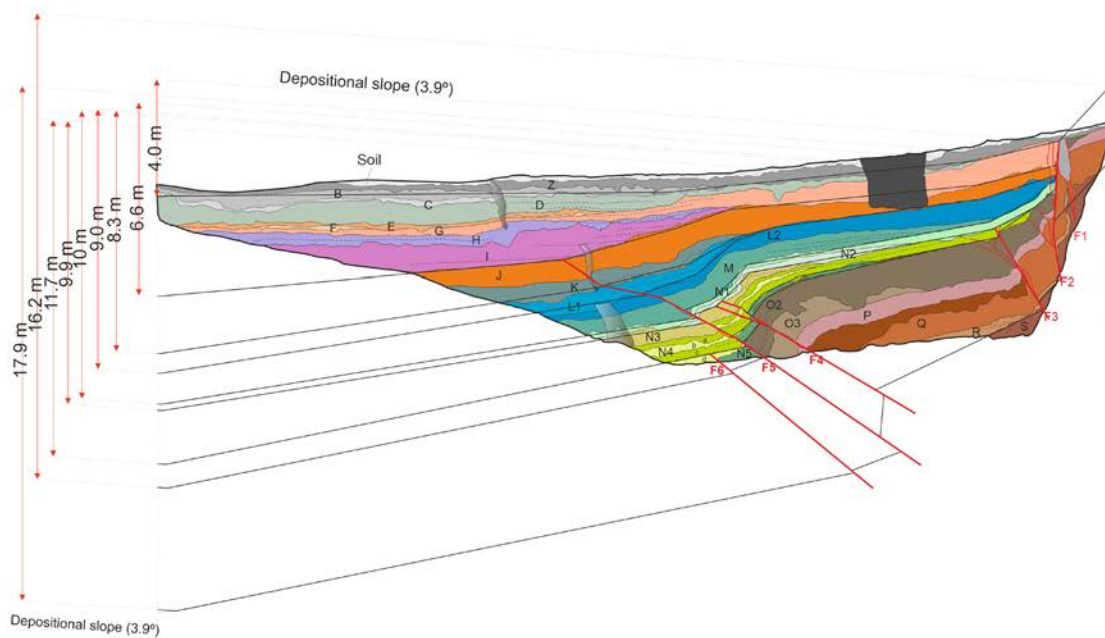
A total of nine equally deformed blocks are considered: unit S, units R-O2, units N5-N4d, units N4c-N3, units N1-N2, units M-L2, unit L1, units K2-J and units I-B. Maximum vertical slip values are 17.7 ± 0.3 m for unit S or 15.6 ± 0.5 m for the units R-O2 sequence, while the uppermost units I-B sequence shows a 4.0 ± 0.2 m slip, which corresponds to at least the last two earthquakes (S1 and S2) (Table 5.10). In T-16 especially, the measured slips are also a minimum, first due to the structure extrapolation simplifications already pointed out for T-1. This is more evident in the lower units, especially the unit S-R contact, because it is only exposed in a small part of the trench and its deformation is almost completely assumed from the upper contact (unit O2-N5). Similarly, all the contacts are extrapolated with a constant dip at the northwestern end of the trench (Figure 5.20). Although this is done because no significant dip changes are observed in the uppermost outcropping units, this could lead to an underestimation of the slip in the lower units because other structures could be present in this blind area of the trench. Second, the deformation related to S-AMF is simplified to end at the tips of the trench, although it clearly extends above those limits, especially in the southeastern block of the fault which is barely exposed (Figure 5.20). Thus, it cannot be discarded that some units were present in the uplifted block and have been eroded later. Third, the S-AMF is predominantly strike-slip and, in consequence, the vertical slips in this trench could be in

part apparent related to the lateral motion, even more considering that the unit contacts are laterally irregular.

T-1 SW wall (flipped) - NW-SE



T-16 NE wall - NW-SE



T-3 SW wall (flipped) - NW-SE

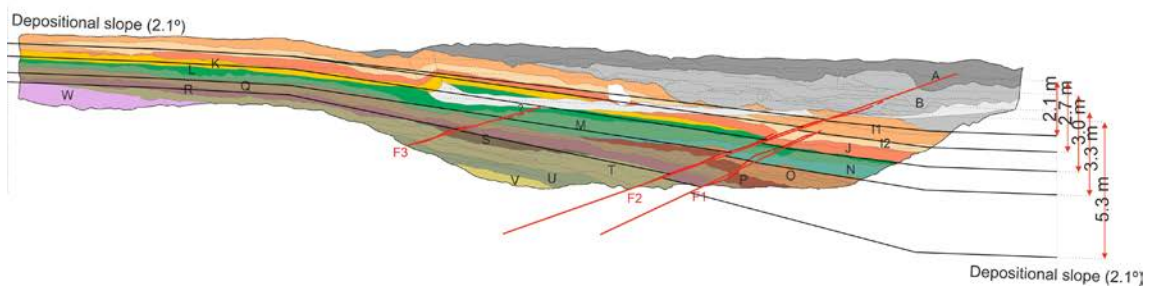


Figure 5.20. Structure simplification to calculate vertical slips carried out in T-1, T-16 and T-3. Note that this corresponds to an example from one trench wall and a single position of the unit contact. See details of the simplification method in section 3.4. Note that the measured slips are a minimum, especially for lower units where important extrapolations have been considered.

- **F-AMF**

A total of five blocks are defined: units W-O, units M-N, units J-I2, unit I2 and unit B. The slip range is smaller than the other faults because the age of the sequence is younger. Vertical slips range from 5.2 ± 0.1 m for the lower W-O units, up to 2.2 ± 0.2 m in unit B, while unit A is undeformed (Table 5.10). In this trench, the limits of the deformation are better defined than in the other trenches because most of the deformation is resumed within the exposed walls. The limit of the deformation is clear for all of the units in the hanging wall of the F-AMF, while in the footwall it is observed in the unit I1 base, which acquires the depositional slope ($\sim 2.1^\circ$) and is used as a reference for the older units (Figure 5.20). In the upper units, the irregular and incisive geometry of the base of channelized unit B could lead to overestimated slip values because the unit incises towards the SE. To avoid this, the dip of the internal stratification of unit B is considered as a deformation marker instead of its real base to estimate the deformation of the unit towards the NW. This is also applied for unit J, which shows a higher dip than its lower units in the fold limb, indicating incision.

5.5.5.2 Lateral slips

- **N₁-AMF**

Lateral slips are inferred in the N₁-AMF branch from analysis of a paleochannel buried in T-6 (parallel to the fault) in relationship with an actual drainage channel a few meters to the NE, which we assume that were previously aligned (Figure 5.21).

We related both features because: i) the width, depth and geometry of the paleochannel incision (Figure 5.22B) is similar to the dimensions of the actual drainage system (Figure 5.21A); ii) the inferred kinematics from this displacement is consistent with the left-lateral kinematics of the N₁-AMF; iii) the paleochannel unit is not found in the southern block of the fault in T-2, which supports the possibility of it being displaced to the E.

For the actual creek both the thalweg and right margin of the channel are used to do the measurements using the method proposed by Gold et al. (2011) and adapted by Ferrater (2016) (Figure 5.21A) explained in the chapter II (section 3.4.2). The left margin is not considered in this analysis because its position in the buried paleochannel is not observed. This analysis is done exclusively downstream of the fault because the homologous points upstream are not in the actual channel but buried in T-6.

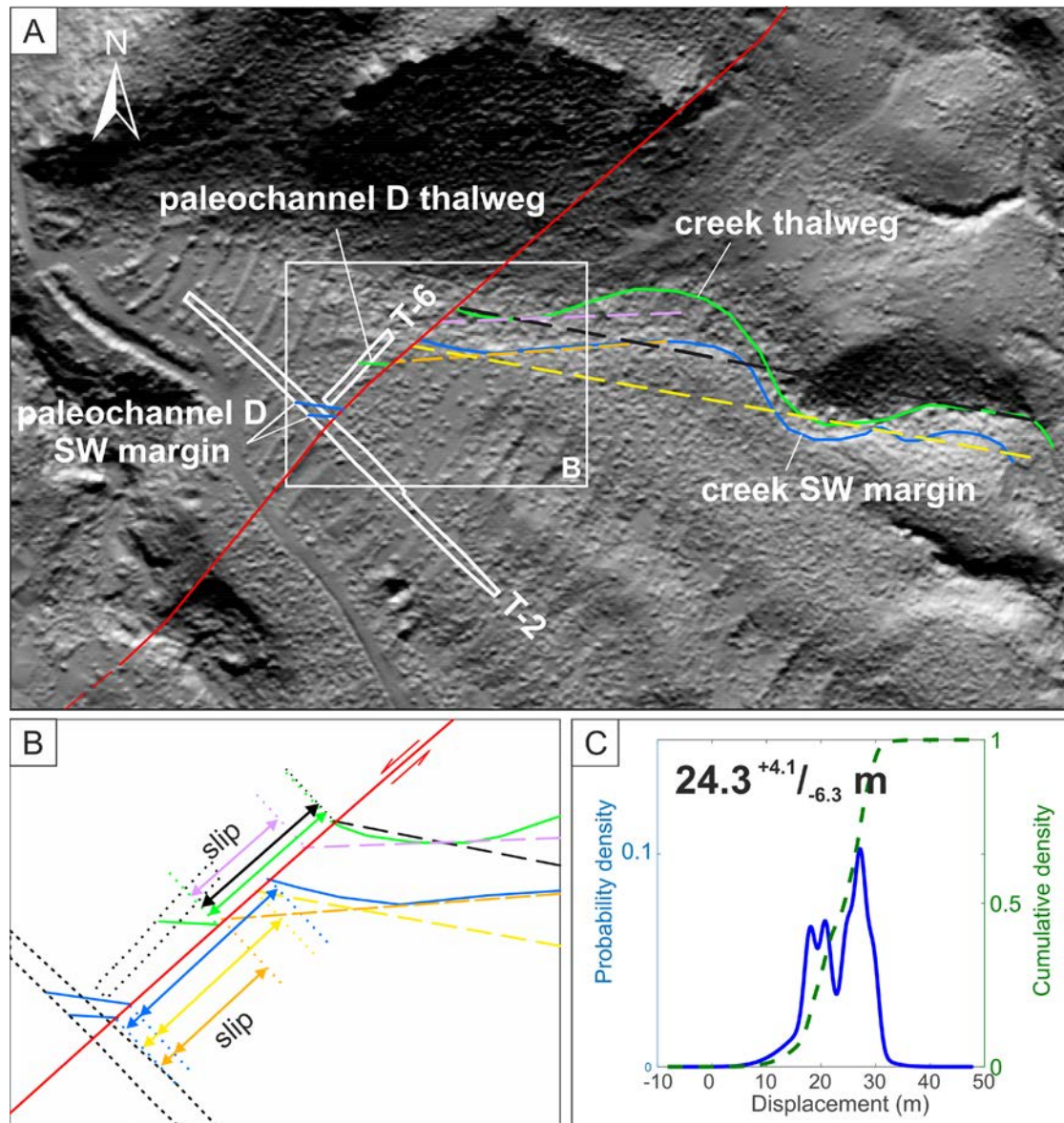


Figure 5.21. Estimation of the lateral slip of the paleochannel in the N_1 -AMF following the method in Gold et al. (2011) and Ferrater (2016). **A)** Floor plan view of the displaced channel and paleochannel D right margin (blue) and thalweg (green) in each side of the fault. Downstream of the fault, the actual channel features are simplified and projected to the fault with tendency lines accounting for their orientation closer (orange and purple dashed lines for the margin and thalweg respectively) and farther from the fault (yellow and black dashed lines for the margin and thalweg respectively). Upstream these are projected using the orientation observed in the trench walls. Relief based on the 0.5 m DEM from the SHAKE project. **B)** All nine possible slip measurements from the line projections of the channel and paleochannel features in window A. **C)** Lateral slip PDF of paleochannel D from the integration of the measurements in window B. The slip value refers to the median and 68.27% confidence interval computed with the code by Zechar and Frankel (2009).

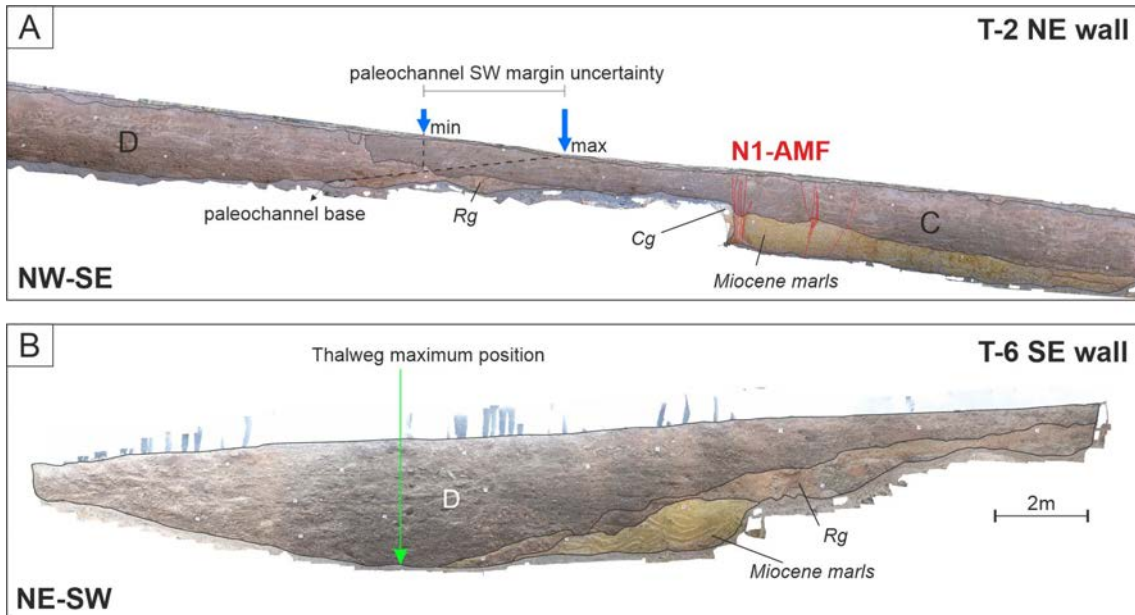


Figure 5.22. **A)** Minimum and maximum position hypotheses of the paleochannel D right margin in T-2. Its orientation inferred from both trench walls is projected onto the fault (N_1 -AMF). **B)** Geometry of the paleochannel D in the photomosaic of T-6. Note that a creek geometry and size of the incision is similar to the actual channel NE of the trench (Figure 5.21A). Note also that the position of the thalweg is a maximum and could be more towards the NE.

For the buried paleochannel the orientation and of its right margin and thalweg is inferred from its intersection with the trench walls and projected into the fault to perform the measurements. The paleochannel incision identified in T-6 likely corresponds to unit D in T-2, because their sedimentary characteristics are similar and the right margin of the paleochannel of unit D can be inferred in both walls of the T-2. Because part of this margin in this trench is eroded, we consider two positions of it in the surface (Figure 5.22A): i) the vertical surface projection of its truncation by unit C and ii) the extrapolation of the channel base following its mean inclination. Due to the left-lateral strike-slip motion of the fault, unit D could have been displaced and disconnected from the drainage in the southeastern block of the fault. Then, the posterior headward erosion could have formed a new active channel in the northwestern block, and the old one remained buried. Given that no fault parallel trenches have been dug in the southern block of N_1 -AMF, the measured lateral slip is a maximum because the paleochannel might not correspond to the position of the current incision. Higher slips than the measured are not envisaged as that the actual creek is limited by a hill of basement rocks of La Tercia range.

A mean lateral slip of $24.3^{+4.1}_{-6.3}$ m (68.27% confidence) has been inferred for the channel of unit D based on nine different displacement values accounting from different options of channel margin and thalweg position (Figure 5.21). These significant lateral

displacements contrast with the very minor vertical displacements observed in T-2, supporting the field observations of this fault having a major lateral component.

- **S-AMF**

In the S-AMF, lateral slips have been previously estimated by Ferrater (2016) using 3D trenching in the paleochannel from units B (4.3 ± 1.1 m) and D ($16.3^{+2.3}/_{-0.3}$ m). According to the authors, the slip of unit B is a minimum due to the lack of preservation in the southeastern block of the fault and may possibly be equal to unit D. This is consistent with the fact that unit B shows the same vertical deformation as unit D in T-16, which is why in our slip measurements these units are interpreted as part of the same deformational block I-B (Table 5.10). The lateral slips of the remaining units in T-16 are calculated indirectly using the vertical slips from the present study and the fault rake ($\sim 14^\circ$; see next section).

5.5.5.3 Net slips

The net slips are indirectly inferred from the measured vertical or lateral slips in each corresponding fault branch. In the N_{2b}-AMF the net slip is assumed to be the vertical because the fault is subvertical, while for F-AMF the net slip is computed using a 20° dip of the fault and considering a pure dip slip motion (Equation 3.1). However, because no 3D paleoseismic analysis has been done, the presence of a certain lateral component in these faults should not be completely disregarded and therefore the associated net slips should be regarded as minimum. In the branches with predominant lateral component, the net slips are similar to the lateral and much larger than the vertical in S-AMF (Table 5.10).

In the N₁-AMF, the field rake measurements (2 - 20°) imply similar net slips to the lateral ones for unit D especially if the lower bound rake of 2° is considered: $24.3^{+4.1}/_{-6.3}$ m (2° rake) and $25.9^{+4.4}/_{-6.7}$ m (20° rake). From these rake measurements vertical slips between $0.7^{+0.1}/_{-0.2}$ and $8.5^{+1.4}/_{-2.2}$ m are computed, respectively. The roughly 20 cm of apparent vertical slip of unit Rg in T-2 (Figure 5.11) suggest that a vertical slip ~ 8.5 m is not feasible for unit D and thus that rake measurements are probably closer to a pure-strike slip rake. For this reason, the slip data from the 2° rake is the preferred (Table 5.10).

In El Saltador site, the net slips are inferred using the fault rake. This parameter is estimated from the lateral slip of unit D by Ferrater (2016) and the vertical slip measured here considering a $\sim 90^\circ$ dip (Equation 3.3). A mean rake of $\sim 14^\circ$ is inferred, which differs significantly from the 5° rake inferred from vertical and lateral slips by Ferrater (2016).

In that study, vertical slips are likely underestimated because the vertical deformation of propagation folds outside of the fault plane was not accounted. The resulting net slips are the largest out of all the analyzed sites, which is consistent with the marked geomorphological evidence and expression of the S-AMF branch respect to the others.

Regardless of the obtained values, it should be noted that net estimations are affected by uncertainties related mainly to the rake values. Rake values from field measurements may not be representative of the whole fault because they might reflect surface fault motions that do not correspond with the ones at depth or at greater scale. In addition, the extrapolation of the rake values for long periods of time (e.g., for all the stratigraphic sequence in T-16) might be undermining possible variations of this parameter over time. To test these variations, we inferred the rake from older units in T-16 (R-O1) by estimating their lateral slip. This slip corresponds to the distance between this trench and the drainage channel of El Saltador site (Figure 5.23) and it is a minimum because it is assumed that i) the depocenter of these units is located in T-16 and ii) the actual channel is the piercing point of these units. The minimum lateral displacement obtained is ~66 m, which combined with the vertical slip (15.6 ± 0.5 m; Table 5.10), yield a rake of $13 \pm 0.5^\circ$, coherent with the 14° used in this study. Despite the assumptions, the coincident values might suggest that the rake has not varied significantly since the Upper Pleistocene.

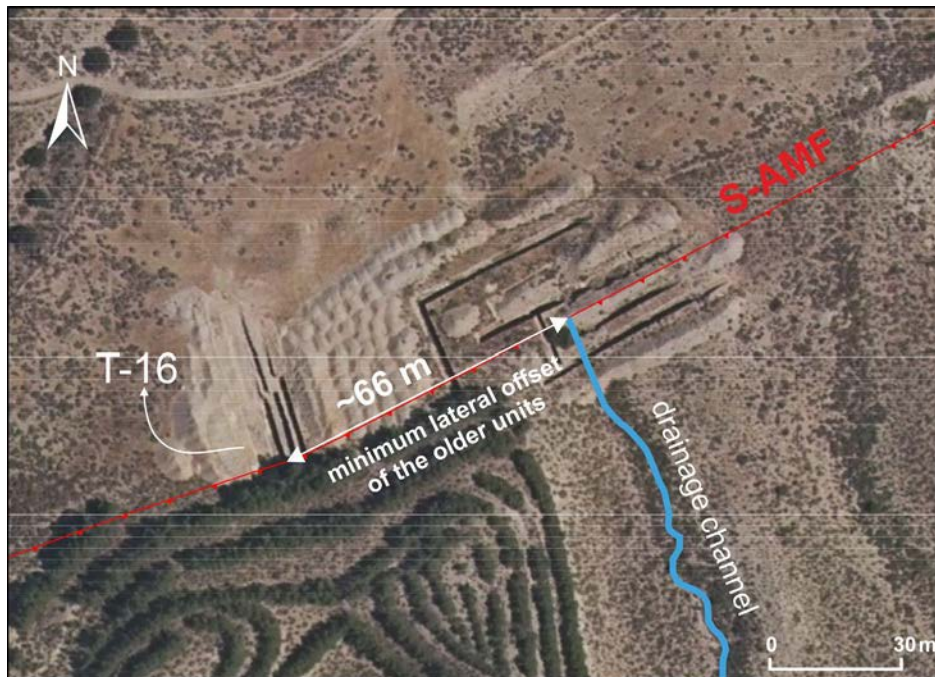


Figure 5.23. Minimum lateral displacement of the older units in T-16 (R-O1) assuming that these units are channelized, and that the actual drainage channel (blue line) has constituted a fixed exit point of the sediments in El Saltador site.

5.5.5.4 Shortenings

Shortening values are inferred from the restoration of trench walls (Figure 5.24 to Figure 5.26). This is done in the trenches with vertical slip component (T-1, T-16 and T-3) and the units considered are the same as for the vertical and net slips. The restoration is performed in steps corresponding to different seismic events or deformation phase with assigned strong evidence. Table 5.11 shows the shortening values obtained. Given that the vertical slips in the trenches are considered a minimum, the shortening values are too since both are dependent. From the results, it is remarkable that the shortenings from T-16 are considerably smaller than the ones from T-1 (Table 5.11), despite the vertical slips from the former are for the most part higher. This is interpreted to be due to the lack of exposure of the whole deformation caused by the S-AMF, leading to underestimated displacements, especially in the units above O not found in the uplifted block. Also, in S-AMF the lateral component is predominant, which means that the real shortening is oblique to the trench walls and likely higher. This, however, has not been included in the restorations due to lack of 3D modelization.

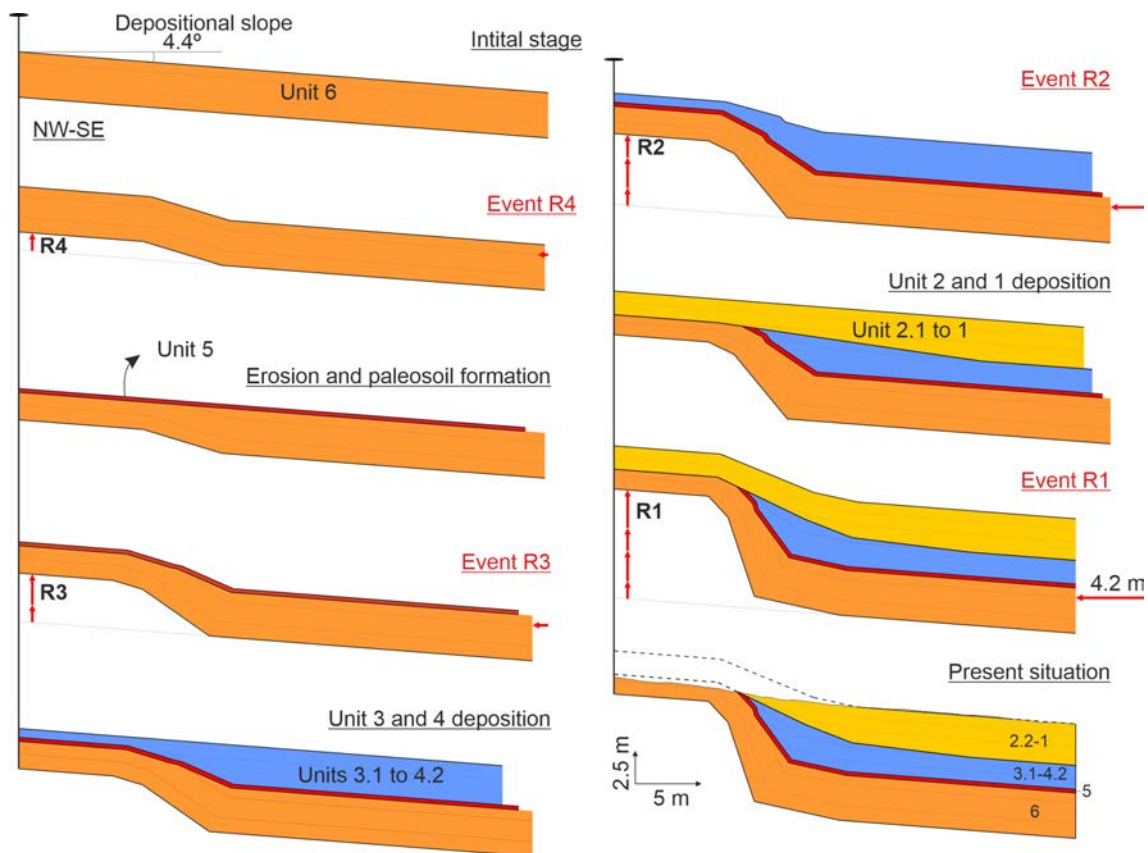


Figure 5.24. Evolutive restoration of equally deformed units in T-1 comprising event R4 to R1. Total shortening of the oldest unit in this restoration (unit 6) is highlighted with a red arrow together with the uplift generated by each paleoearthquake. The present situation marks the erosion of the fold.

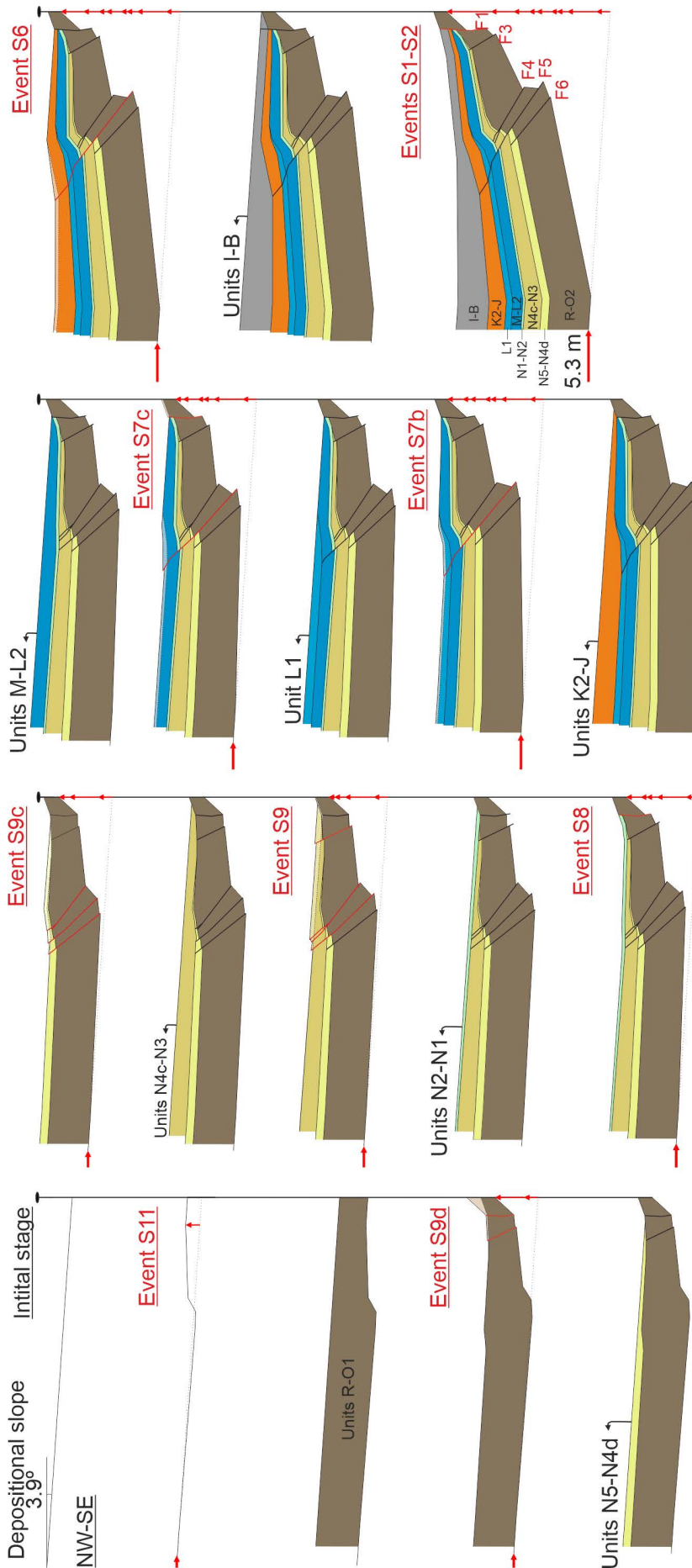


Figure 5.25. Evolutive restoration of equally deformed units of T-16 (NE wall) comprising events S11 to S1. The simplified contacts in Figure 5.20 are used for this restoration. Exclusively events with strong evidence are considered because are the ones causing substantial vertical slips for this analysis. Note that events S1 and S2 cannot be differentiated in T-16. Total shortening of the oldest units in this restoration (R-O1) is highlighted with a red arrow together with the uplift generated by each paleoearthquake. Translucid polygons indicate eroded parts of the sequence during the fold growth. The southeastern block of the fault F1 is moved in each stage to generate the necessary relief to avoid units above O2 from trespassing, accordingly with the sedimentary environment (sedimentary trap) interpreted for El Salvador site.

5. Structural and paleoseismic characterization of the Lorca-Totana segment

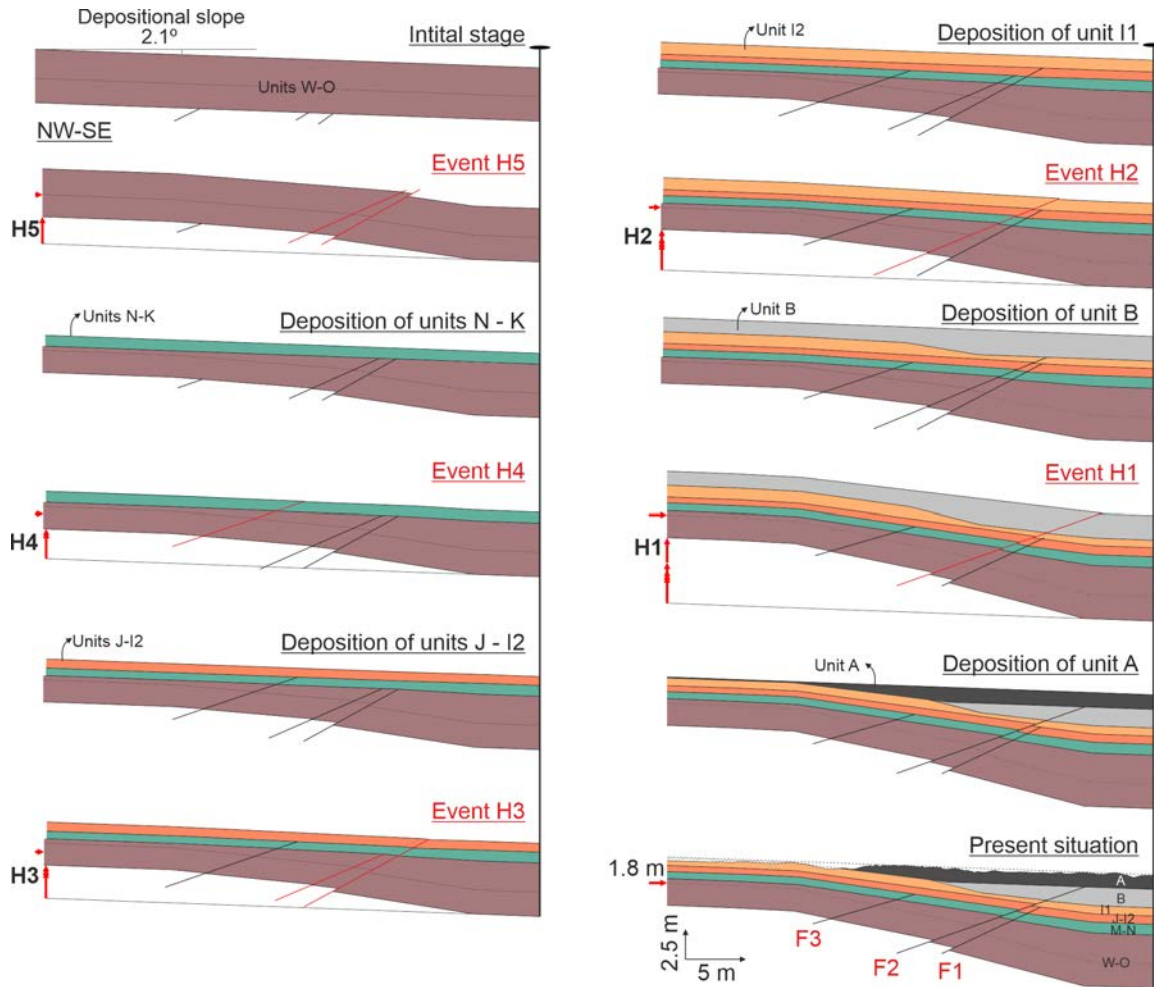


Figure 5.26. Evolutive restoration of equally deformed units in T-3 comprising event H5 to H1. Total shortening of the oldest units in this restoration (units W-O) is highlighted with a red arrow together with the uplift generated by each paleoearthquake.

T-1 (N _{2b} -AMF)		T-16 (S-AMF)		T-3 (F-AMF)	
Unit blocks	Shortening (m)	Unit blocks	Shortening (m)	Unit blocks	Shortening (m)
6	4.2±0.7	S	5.3±0.1	W to O	1.8±0.3
5	2.8±0.7	R to O2	3.1±0.1	M to N	0.9±0.1
4.2 to 3.1	1.4±0.3	N5 to N4d	3.0±0.1	J to I2	0.8±0.2
2.2 to 1	0.5±0.1	N4c to N3	2.2±0.1	I1	0.6±0.0
		N1 to N2	1.8±0.1	B	0.3±0.0
		M to L2	1.1±0.0		
		L1	0.7±0.0		
		K2 to J	0.7±0.0		
		I to B	0.1±0.0		

Table 5.11. Shortening values for each equally deformed block in T-1, T-16 and T-3. Note that the shortening of the Cg unit is not estimated here because its vertical slip is not inferred in the T-1 and thus could not be included in the restoration. All uncertainties refer to 1σ. Zero values are due to numerical rounding to the first decimal.

5.6 Seismic and paleoseismic parameters of the Lorca-Totana segment

5.6.1 Event chronosequence and recurrence intervals

The event chronosequences are strictly conditioned by the position of the available numerical dating results within the sedimentary sequence. Because these dates are heterogeneously distributed, in some cases individual event dates cannot be constrained and instead groups of two events are dated within a same PDF.

Event dating with the OxCal software (Ramsey and Lee, 2013) has been performed using three commands depending on the requirement of each sequence: *Date*, *Boundary* and *Zero Boundary*, as discussed by DuRoss et al. (2011). Uniform distributions (*Date* command) are used for events whose limiting units are very spaced in time and imply large periods of time in which the event could have occurred. This is done to avoid over-constraining and bias of the PDF towards a limiting age, especially if the period of occurrence of such earthquakes within a time span is unknown. Conversely, non-uniform distributions (*Boundary* and *Zero Boundary* commands) are used to date those events that are located in horizons that represent a change or a “break” in the stratigraphic sequence (e.g., angular unconformity, change in sedimentology suggesting coseismic origin). These distributions, especially the *Boundary* paired with *Zero Boundary* are used to skew the distribution towards a desired horizon considered to be closer to the date of an event. Both allow to reduce the uncertainty of the event PDFs with respect to the *Date* but can imply over-constraining of the distributions if the age is very uncertain (see Figure 3.10 in section 3.5 for details on the three types of distributions mentioned).

For the event sequence, in all trenches the upper age limit of the last event is assumed to be the 1674 AD Lorca earthquake, because is the only one in the historical period with evidence of surface rupturing (Martínez-Díaz et al., 2018). Although, certainly, previous historical large earthquakes could have ruptured the surface as well, their consideration for the upper limit instead of the 1674 event would imply negligible changes in the OxCal models because the time windows analyzed here extend thousands of years, contrary to the few hundreds of the historical record. Moreover, the historical record is considered complete since 1674 and no potentially morphogenetic earthquakes have occurred since.

The recurrences are provided as mean RI for each trench as well as inter-event times. The latter is the PDF of the time in between the modelled event PDFs with OxCal, while mean RI are calculated subtracting the age of the oldest and youngest event PDFs of a time

window and dividing it by the number of event intervals. We also calculate the coefficient of variation (CV) to evaluate the variability of the RI and recurrence model of earthquakes, based on the classification in Salditch et al. (2020): $CV < 0.5$ imply a strongly-periodic behavior; $1 > CV > 0.5$ a weakly-periodic behavior; $CV = 1$ imply random or Poissonian behavior; $CV > 1$ imply clustered behavior. The CV analysis is only done for S-AMF (El Saltador site) as it is where the paleoearthquake record is the most complete of all the sites and because the variability and reliability of the parameters is highly linked to the number of paleoseismic events identified. Usually, < 10 events imply large uncertainties and under-estimation of the CV (Cowie et al., 2012 and references).

The CV is calculated using the mean and standard deviation of the inter-event times (Table 5.12), which inform of the time between individual events. Figure 5.27 to Figure 5.30 summarize the chronosequence models of each site, including the age PDFs of the numerical dates. We also indicate the type of OxCal command used to constrain each event. Table 5.12 summarizes the RI in each branch. The OxCal scripts used are available in the Annex II (E). For each fault branch the events are explained from older to younger. They have been constrained using the numerical dates from Table 5.5. The event ages mentioned in the text correspond to the mean and 2σ uncertainties of the earthquake PDFs, while the age ranges correspond to limits of the 95.4% confidence interval.

5.6.1.1 N₁-AMF

The lack of numerical dates throughout the sequence and the fact that the geological record is very condensed and presents large gaps (T-2; Figure 5.11) leads to a poorly established chronosequence in this site. The ages of units C2 and the Cg unit are known, and the age of the base of unit D (D3) is assumed to be similar to unit 2.2 in T-1 (~40 ka), as both represent the start of the channelized alluvial drift of the sequence in the area. Based on these data we date the four paleoearthquakes recognized (Figure 5.27).

Event N4 is estimated at 159.2 ± 74.6 ka. The distribution is skewed towards the age of the Cg using *Zero Boundary* (Figure 5.27) because Rg comes from the alteration of this unit and it is expected to be closer to its age than to the upper sedimentary sequence (units D and C). The upper sequence corresponds to the channelized alluvial phase that is incised into the Rg, Cg and basement marls in T-6, indicating that it is from a younger stage.

The large time span covered by N4 in the models (85.9-206.8 ka; 95.4% confidence), implies that it corresponds likely to more than one event. Also, between events N4 and N3, other earthquakes might have occurred given the gap between Rg and D units. In this trench, however they cannot be determined because these units lack direct contact in the fault zone. Event N3 (36.1±2.9 ka) affects the lower part of unit D (D2) (Figure 5.17) and thus probably occurred closer to its estimated minimum age (~40 ka).

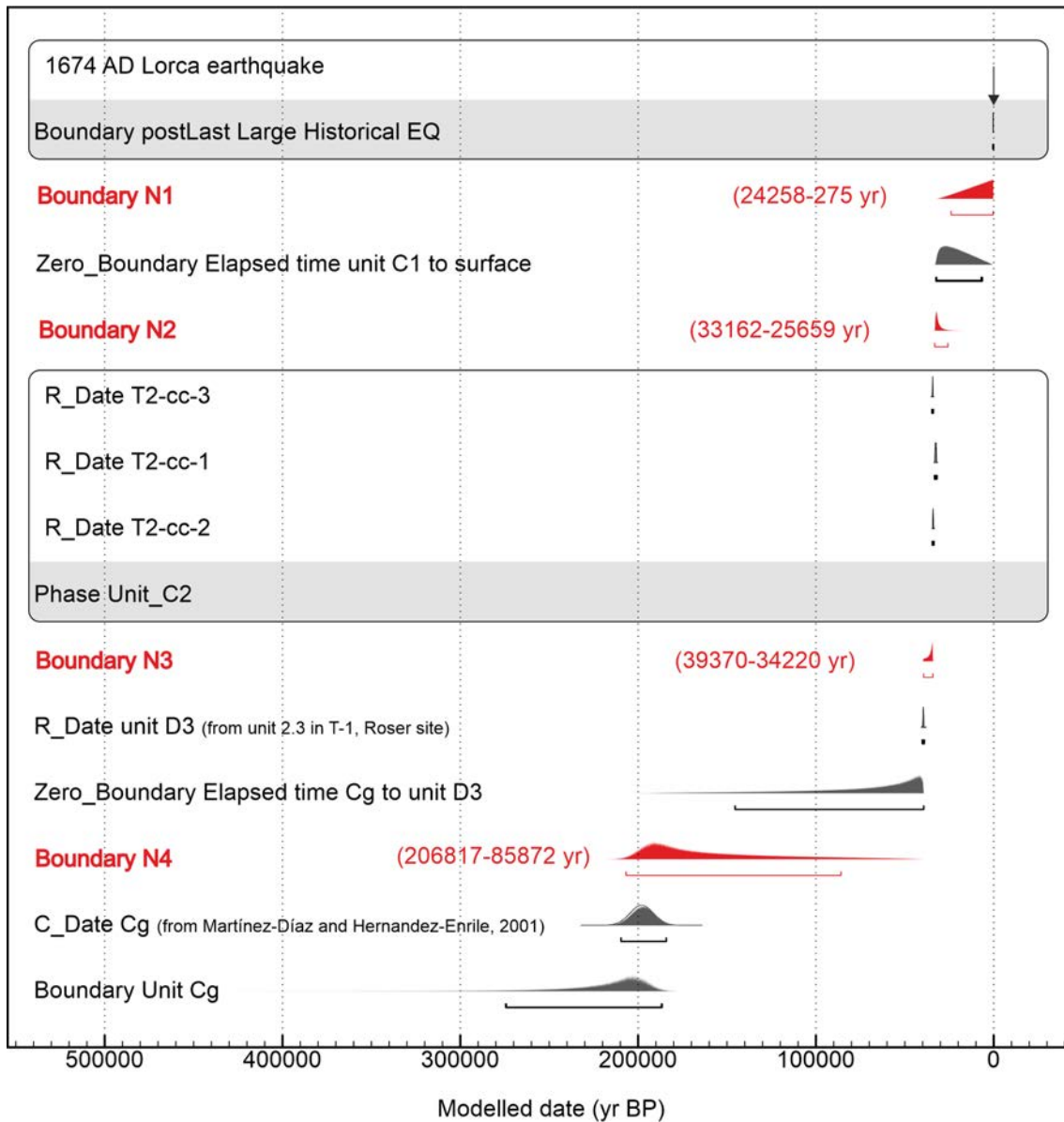


Figure 5.27. Event chronosequence of La Tercia site (N₁-AMF) using the OxCal software. Age ranges specified for each event PDF refer to the 95.4% confidence. The commands used are indicated as well as the samples (numerical date PDFs) used to constrain the different events. Note that R_Date is used for the radiocarbon dates and C_Date for all other dates (e.g., OSL).

To date events N2 and N1 we use the configuration of commands *Boundary* paired with a *Zero_Boundary* (Figure 5.27) based on the case explained in DuRoss et al. (2011) (see methods; section 3.5.1). Numerical dates are not available in unit C1. To solve this, its age is modelled as the elapsed time between the deposition of unit C2 and the upper sequence limit (1674 AD) (Figure 5.27). This allows to i) skew the N1 and N2 PDFs towards the ages of the respective bracketing levels (C2 and surface), and ii) reflect the elapsed time between events without having to set a fixed time gap, which reduces the arbitrariness according to DuRoss et al. (2011).

Event N2 (30.7 ± 5.0 ka) is skewed towards the age of unit C2 because this and unit C1 are probably very close in time, considering that the abandonment of deposition in this part of the fan is around 32-35 ka BP as observed in T-1. Conversely, event N1 (10.4 ± 14.5 ka or 0.3-24.3 ka; 95.4% confidence), is skewed towards the upper limit of the sequence (1674 AD). The large uncertainty of this last event is caused by the lack of sedimentary record since the abandonment of the fan (C1) and permits to account for the probability of this event either happening close to event N2 or corresponding to more than one.

Given that event N4 likely represents more than a single event, we excluded it from the RI computation. Considering only the last three events (N3-N1) since ~ 40 ka, the inter-event times obtained range from 1.3-11.6 kyr (Table 5.12) with a mean RI of 12.8 ± 7.4 kyr. The uncertainty of the RI, along with the wide inter-event times (Table 5.12) reflect the poor time constraining of the events in this trench, especially of the last event N1 (Figure 5.27). Also, the small number of events used to compute the RI (three) and the lack of sedimentary record since ~ 32 ka compromise its reliability. In all cases the obtained RI should be regarded as a maximum.

5.6.1.2 N_{2b}-AMF

The oldest event identified in this branch in T-1 is R5, which, as explained before probably constitutes more than one event due to the large difference of deformation and time gap between the Cg unit and unit 6. Thus, we modelled this event using the *Date* function to allow a multi-event scenario in this time span. A large age uncertainty is thus inferred: 138 ± 68.7 ka (Figure 5.28). Events R4 (69.5 ± 17.2 ka) and R3 (47 ± 11 ka) are dated using *Boundary* functions paired with a *Zero Boundary* to account for the elapsed time between events, given that there are no numerical ages available in between. Unit 5, a paleosol, represents this elapsed time indicating the presence of a depositional gap and reinforces the decision of skewing R4 towards the age of unit 6 and R3 towards unit 4.2.

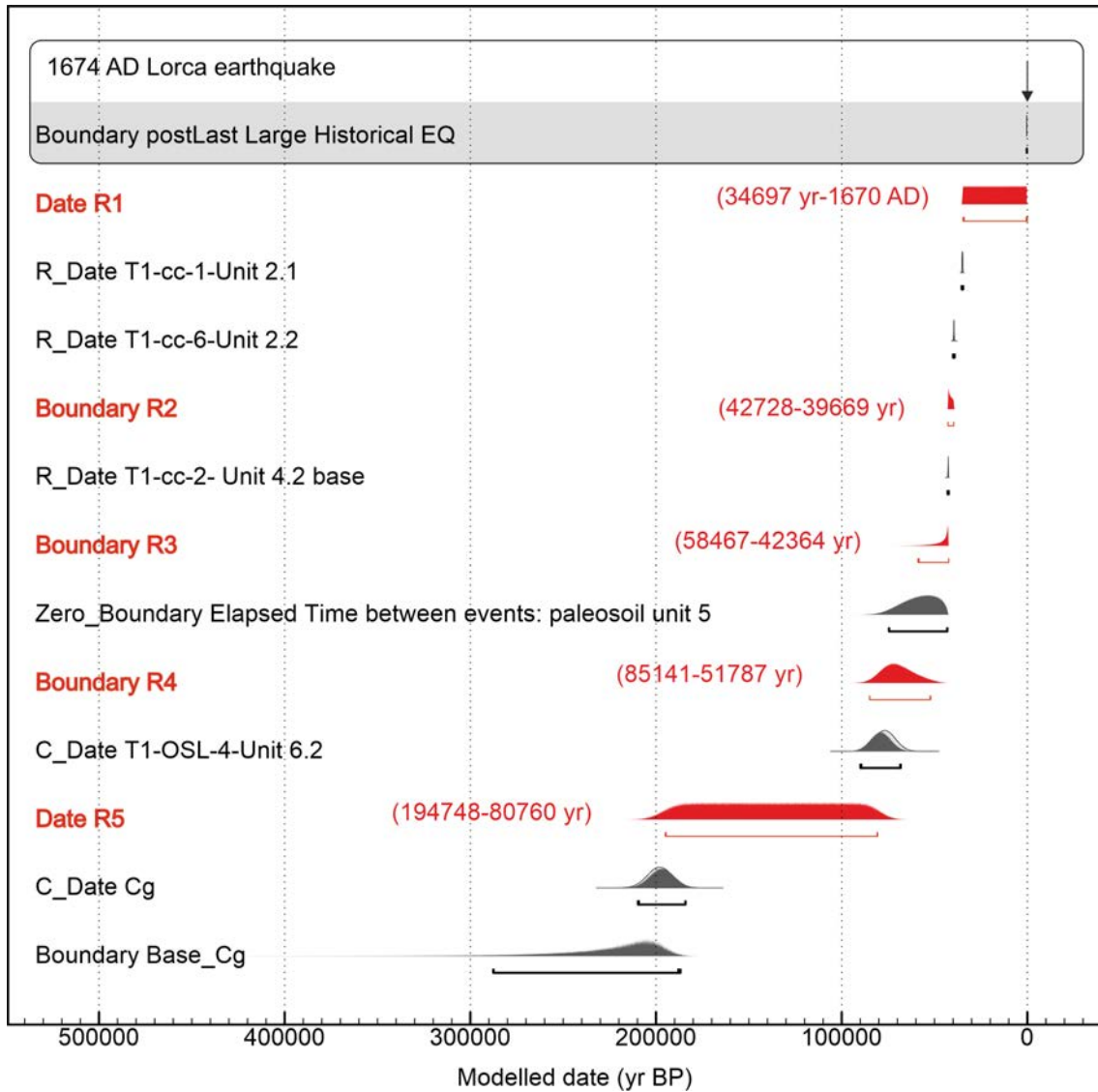


Figure 5.28. Event chronosequence of El Roser site (N_{2b} -AMF) using the OxCal software. Age ranges specified for each event PDF refer to the 95.4% confidence. The commands used are indicated as well as the samples (numerical date PDFs) used to constrain the different events. Note that *R_Date* is used for the radiocarbon dates and *C_Date* for all other dates (e.g., OSL).

Event R2 (41.3 ± 1.8 ka) is dated using *Boundary* and shows a very well constrained age due to the radiocarbon dates of the limiting units (Figure 5.28). Event R1 (17.6 ± 20.0 ka) uses the *Date* function because there are no clear criteria to skew the distribution and because it could represent more than one earthquake; in the time span between 35 ka (Unit 2.1) and 1674 AD two earthquakes are identified in the N_1 -AMF (T-2). This lack of age control since ~ 35 ka explains the large uncertainty of this event.

Similar to T-2, because the R5 event horizon represents a large gap with more than one event, we excluded it from the recurrence analysis. Considering the last identified four events (R4-R1), inter-event times range from 2 to 40.5 kyr with a mean RI of

17.3±8.8 kyr for the last 77 ka (Table 5.12). This RI is a maximum value because the number of events observed in this trench is a minimum considering that there is a sedimentary gap between 77 and 35 ka, and no sedimentary record since ~35 ka. In addition, the wide ranges of the inter-event times reflect, like in T-2, the poor age constraining of the events.

5.6.1.3 S-AMF

Event dating in El Saltador site is performed using *Boundary* functions, sometimes paired with *Zero Boundary*. The pairing is done to: i) skew the distributions towards the estimated age of fine grained/silty units that are assumed to be coseismic (ponded strata), and ii) model individual PDFs of more than two earthquakes than are not bracketed by numerical dates. In these latter cases, the central earthquake is modeled as a *Zero Boundary* representing the elapsed time between the two limiting earthquakes (events S7 to S7c and S9 to S9d; Figure 5.29). This configuration, based on DuRoss et al. (2011), allows for less skewed distributions of the limiting earthquakes, preventing from over-constraining (see section 3.5.1 for details on this command configuration).

The first group corresponds to events S2, S3, S4, S5 and S7, which are defined at the base of fine-grained silty units interpreted to be sediments ponded in the fault zone shortly after a morphogenetic event. Therefore, the PDFs in this case are skewed towards the age of these units (units A2, C, E, G and J respectively) (Figure 5.29). The second group corresponds to events S7b, S7c or S9-S9d, because the lack of numerical dates does not allow differentiating for each event and, therefore, they are inferred indirectly. Event S7b is modelled as a *Zero Boundary* representing the elapsed time between S7 and S7c, which at the same time skews the distribution of S7 towards the age of the coseismic ponding unit J. Similarly, S9b-S9c are all modelled in a same distribution as the elapsed time between S9 and S9d. This configuration allows to differentiate between events instead of providing a single PDF for all of them but preventing from over-constraining the distributions (Figure 5.29). Events S1, S2b, S6 and S8 are modelled as *Boundary* because the event horizons are well constrained by available numerical ages and represent changes in the type of sedimentation (e.g., gravels vs. silts) and/or geometry (angular disconformities).

III. Results and partial discussions

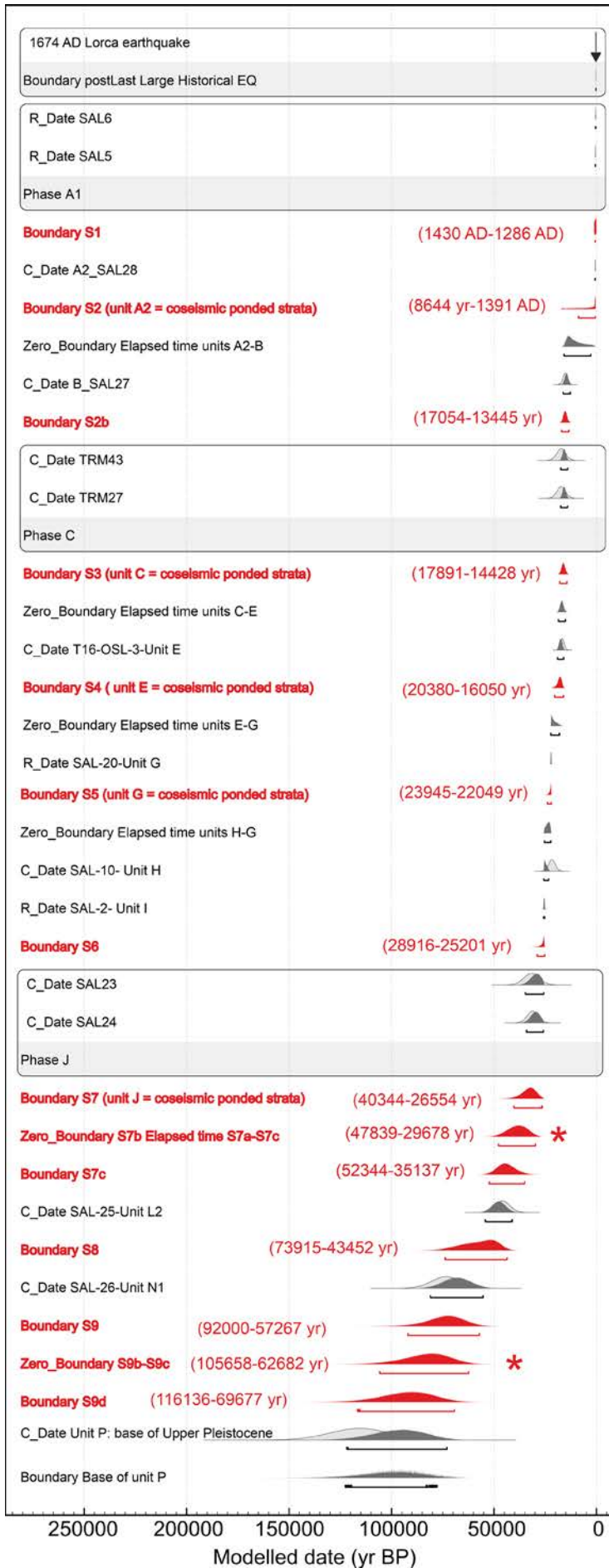


Figure 5.29. Event chronosequence of El Saltador site (S-AMF) using the OxCal software. Age ranges specified for each event PDF refer to the 95.4% confidence. The commands used are indicated as well as the samples (numerical date PDFs) used to constrain the different events. Note that R_Date is used for the radiocarbon dates and C_Date for all other dates (e.g., OSL). Events marked with a (*) correspond to the ones inferred indirectly from the age of other bracketing events using the *Zero Boundary* command paired with a *Boundary*. In the case of S9b and S9c, the PDF is for both events together.

The modelled event sequence shows two differentiated parts, one with well constrained distributions from event S6 to S1 (last 31 ka), and another one with wider and more uncertain distributions from event S9d to S7, mainly due to the lack of precise age control. Accounting for S1 to S8, the calculated inter-event times of El Saltador site imply wide ranges (e.g., 2 to 30.9 kyr between S7c-S8; Table 5.12). However, these become narrower if only the last seven events (S6-S1) are accounted, meaning that the event distributions of this last group are better constrained in time. The mean RI for the S1-S8 (last ~73 ka) is 5.7 ± 1.6 kyr and for the S1-S6 sequence (last ~31 ka) is 4.3 ± 0.4 kyr (Table 5.12). In this case, the uncertainties linked to these RI, especially the shorter-term, are reasonably small compared to the other branches, evidencing that the events at El Saltador site are much well-constrained. This, together with the long paleoearthquake record makes the analysis of the recurrence and CV more adequate than the other sites.

The CV computed provides values of 0.8 for the last ~74 ka and 1.0 for the last ~31 ka. Although the former implies a weakly periodic behavior and the latter a Poissonian behavior, both values are similar, meaning that the value is stable in time. In this case, our preferred value is the one for the last 31 ka because, although the number of events is smaller, the recurrence estimation has a much smaller uncertainty. In addition, all events from S6 to S1 are constrained by bracketing numerical dates, which is more reliable than constraining them indirectly using combinations of OxCal commands (i.e., S7 to S7c).

5.6.1.4 F-AMF

The placement of numerical datings in T-3 difficults the constraining of events between H2 and H5. Because the age of the limiting units is known (units B and O, respectively), a *Boundary* paired with a *Zero Boundary* is used to define the age of events H5 (16.8 ± 3.1 ka) and H2 (11.1 ± 2.9 ka), and the age range of H3 and H4 in a single distribution representing the elapsed time between both events (14.0 ± 4.2 ka) (Figure 5.30). This allows constraining the individual H5 and H2 distributions, skewed towards the age of their underlying and overlying units (O and B, respectively), but still overlap with the wider PDF of H3-H4 to reflect the uncertainty in the occurrence of all four events. The last event H1 (8.5 ka – 1670 AD) is modelled using a uniform *Date* distribution because the age of the postdating unit A is unknown (Figure 5.30). This unit conforms the last ~1 m of the sedimentary sequence and could have formed in historical or even during the 20th century, especially considering that La Salud creek is active and that during the 1950s, the amount of sediment in the creek was more important than

nowadays (Figure 5.9). Therefore, the age of event H1 is highly unknown and could equally have happened just after the deposition of unit B or in fact correspond to the historical 1674 AD earthquake.

The mean RI in this trench is 3.1 ± 1.4 kyr for the last ~ 18 ka (events H5-H1) (Table 5.12), being the smallest in all the trenches analyzed. Although the age control is limited in this site, the age gaps in this trench are smaller than the ones identified in other trenches and therefore a have smaller impact in overestimating the recurrences. Inter-event times can only be inferred for pairs of PDFs representing single events. In this respect, only one wide interval is defined for events H1-H2 (1.5-11.6 kyr; Table 5.12).

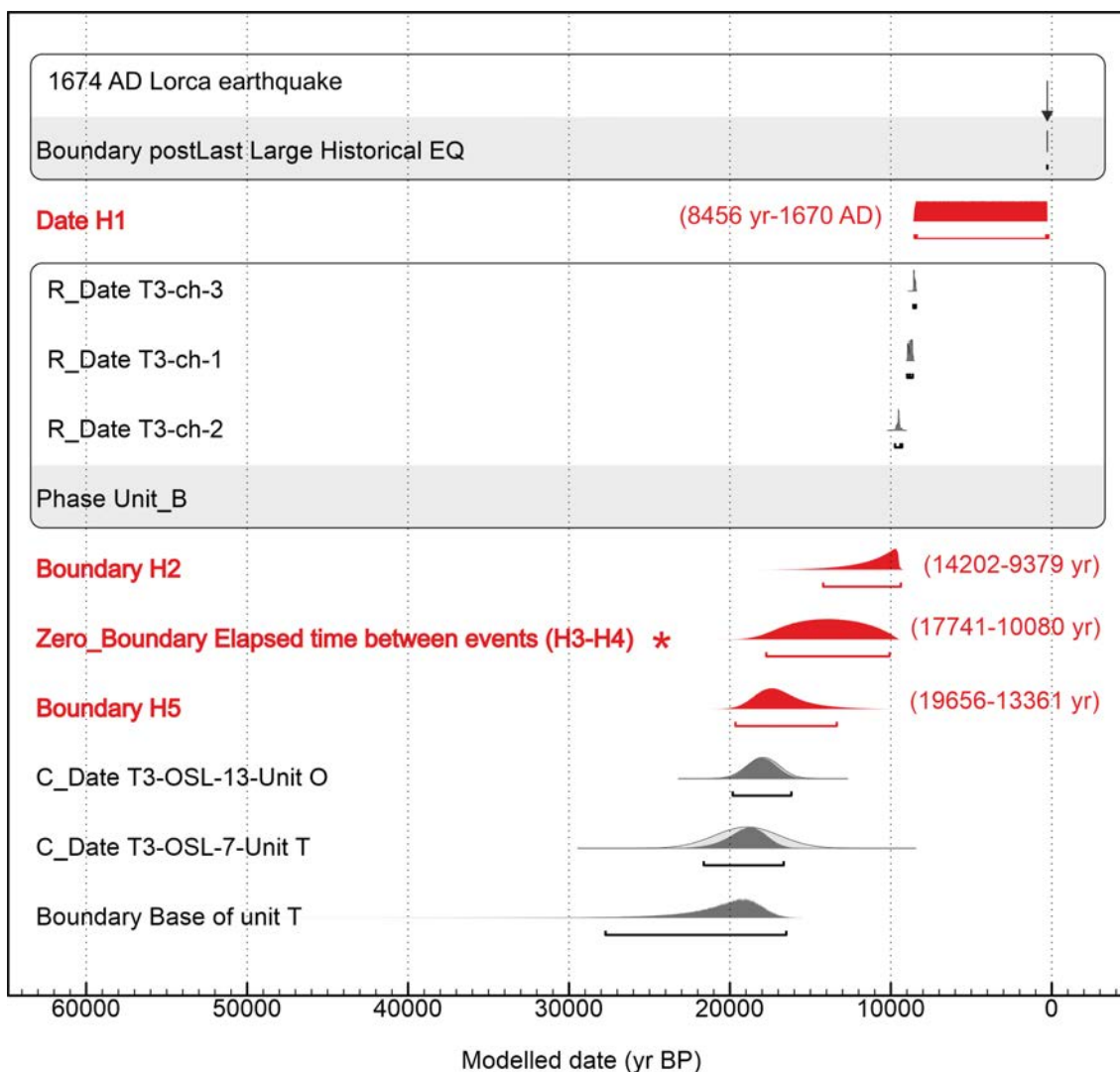


Figure 5.30. Event chronosequence of La Hoya site (F-AMF) using the OxCal software. Age ranges specified for each event PDF refer to the 95.4% confidence. The commands used are indicated as well as the samples (numerical date PDFs) used to constrain the different events. Note that R_Date is used for the radiocarbon dates and C_Date for all other dates (e.g., OSL). Events marked with a (*) correspond to the ones inferred indirectly from the age of other bracketing events using the *Zero Boundary* command paired with a *Boundary*.

5. Structural and paleoseismic characterization of the Lorca-Totana segment

Events	Inter-event time (yr)	σ of inter-event times (kyr)	Mean recurrence interval (kyr)	CV
N₁-AMF (La Tercia site)				
N1-N2	6445-32023	-	12.8±7.4 (3 events since ~40 ka)	-
N2-N3	1344-11646	-	-	-
N_{2b}-AMF (El Roser site)				
R1-R2	7125-40496	-	17.3±8.8 (4 events since ~77 ka)	-
R2-R3	2-17493	-	-	-
R3-R4	4523-38704	-	-	-
S-AMF (El Salvador site)				
S1-S2	2-8132	-	-	-
S2-S2b	6139-16557	-	-	-
S2b-S3	3-2494	4.4	-	-
S3-S4	72-4270	(11 events since ~73 ka)	5.7±1.6 (11 events)	0.8 (11 events)
S4-S5	1953-7119	-	-	-
S5-S6	1107-6767	4.4	4.3±0.4 (7 events)	1.0 (7 events)
S6-S7	3-13759	(7 events since ~31 ka)	-	-
S7-S7b	3-13659	-	-	-
S7b-S7c	3-13639	-	-	-
S7c-S8	2-30855	-	-	-
F-AMF (La Hoya site)				
H1-H2	1453-11607	-	3.1±1.4 (5 events since ~18 ka)	-

Table 5.12. Earthquake inter-event times (95.4% confidence) and mean recurrence intervals (RI) $\pm 2\sigma$ of the four fault branches studied in the Lorca-Totana segment and for different time periods obtained with the OxCal software. Standard deviation (σ) of the mean inter-event times and CV are provided only for the S-AMF, as it is where the paleoearthquake record is long enough to evaluate the CV reliably.

5.6.2 Slip rates

We use the slip values inferred from the trenches (Table 5.10) and the available numerical dates to compute the slip rate PDFs (as defined by Zechar and Frankel, 2009) for the vertical, lateral and net components (see Annex II (F) for complete PDF functions). Based on the guidelines by these authors, slip rates are provided as the median value of the distribution and 68.3% confidence interval and we do it for different time periods from a given age to the present, based on the numerical dates available (section 5.5.3) (Table 5.13).

We calculate the slip rate variations for defined time periods throughout the complete time sequence covered in each trench to detect variations that are not represented by these averages (Table 5.13). The time periods used are conditioned to the availability of numerical dates in the sedimentary sequences in the trenches. Each period is defined by the age of sedimentary markers in Table 5.10, although here we round these ages to the units and avoid the uncertainties to ease the readability text (Table 5.13).

The units that have a numerical date available and whose slip has been quantified in section 5.5.5, are used to compute the slip rates. The time variability of slip rate is computed using the slips of different dated deformed blocks (Table 5.10). The slips of consecutive deformed blocks are subtracted to calculate the slip rate for the time span between these blocks. In the case where more than one numerical date is available for an equally deformed block, we only considered the younger to prevent an underestimation of the slip rate (e.g., units 2.2 to 1 in T-1 (Table 5.10)). Finally, we integrate the results from all the branches to obtain total slip rates for different time periods that are representative of the Lorca-Totana segment (Table 5.14). We excluded the unit Cg in T-1 and unit S in T-16 from the slip rate analysis because their estimated ages are very uncertain. In the former, the age is adopted from another site (198.0 ± 6.5 ka; Martínez-Díaz and Hernández-Enrile, 2001) and in the latter, the age is a minimum. In addition, these ages provide a long-term estimation not correlatable with the rest of the branches. We also compute shortening rates based on trench wall restoration (Table 5.15) and the numerical ages as mentioned for the slip rates. Later in this chapter, the variations of these values are discussed (5.7.1).

Time period	Marker used	Vertical slip (m)	Vertical slip rate (mm/yr)	Lateral slip (m)	Lateral slip rate (mm/yr)	Net slip (m)	Net slip rate (mm/yr)	N. of events
N₁-AMF								
40 ka - present	Unit D3 (paleochannel)	negligible	-	24.3 ^{+4.1} / _{-6.3}	0.65 ^{+0.12} / _{-0.17}	24.3 ^{+4.1} / _{-6.3}	0.65 ^{+0.12} / _{-0.17}	3 (N1-N3)
N_{2b}-AMF								
77 ka - present	Unit 6.2	7.8±0.5	0.10±0.01	-	-	~7.8±0.5	~0.10±0.01	4 (R1-R4)
43 ka - present	Unit 4.2	4.3±0.3	0.10±0.01	-	-	~4.3±0.3	~0.10±0.01	2 (R2-R1)
35 ka - present	Unit 2.1	2.6±0.2	0.07±0.01	-	-	~2.6±0.2	~0.07±0.01	1 (R1)
77 ka - 43 ka	Unit 6 to 4.2	3.5±0.6	0.10±0.02	-	-	~3.5±0.6	~0.10±0.02	2 (R4 + R3)
43 ka - 40 ka	Unit 4.2 to 2.2	1.7±0.4	0.56 ^{+0.16} / _{-0.14}	-	-	~1.7±0.4	~0.56 ^{+0.16} / _{-0.14}	1 (R2)
S-AMF								
73 ka-present	Unit N1	10.1±0.3	0.14 ^{+0.02} / _{-0.01}	41.2±1.3	0.56 ^{+0.06} / _{-0.05}	42.4±1.3	0.58 ^{+0.06} / _{-0.05}	11 (S8-S1)
46 ka-present	Unit L2	8.9±0.2	0.19 ^{+0.02} / _{-0.01}	36.2±0.8	0.79 ^{+0.07} / _{-0.06}	37.3±0.8	0.81 ^{+0.07} / _{-0.06}	10 (S1-S7c)
31 ka-present	Unit J	6.8±0.3	0.22±0.02	27.7±1.3	0.89 ^{+0.09} / _{-0.08}	28.5±1.3	0.91 ^{+0.09} / _{-0.08}	7 (S1-S6)
15 ka-present	Unit B	4.0±0.2	0.26±0.02	16.3±0.8	1.07 ^{+0.1} / _{-0.09}	16.8±0.8	1.11 ^{+0.1} / _{-0.09}	2 (S1 + S2)
73 ka - 46 ka	Unit N1 to L2	1.2±0.4	0.04±0.02	5.0±1.5	0.18 ^{+0.09} / _{-0.06}	5.1±1.5	0.19 ^{+0.09} / _{-0.06}	1 (S8)
46 ka - 31 ka	Unit L2 to J	2.1±0.4	0.14 ^{+0.04} / _{-0.03}	8.5±1.5	0.58 ^{+0.15} / _{-0.12}	8.8±1.5	0.60 ^{+0.16} / _{-0.12}	3 (S7-S7c)
31 ka - 25 ka	Unit J to I	2.8±0.4	0.49 ^{+0.27} / _{-0.13}	11.4±1.5	2.01 ^{+1.09} / _{-0.54}	11.7±1.5	2.06 ^{+1.12} / _{-0.56}	1 (S6)
F-AMF								
18 ka-present	Unit O	5.2±0.1	0.29±0.02	-	-	15.2±0.3	0.84±0.05	5 (H1-H5)
8.5 ka-present	Unit B (top)	2.2±0.2	0.26±0.02	-	-	6.4±0.6	0.76±0.08	1 (H1)
18 ka-9.5 ka	Unit O to B (base)	3.0±0.2	0.35±0.04	-	-	8.8±0.7	1.03±0.14	4 (H1-H4)

Table 5.13. Vertical, lateral, and net slip rates for different time periods up to the present of N₁-AMF, N_{2b}-AMF (T-1), S-AMF (T-16) and F-AMF (T-3). The markers used and their slips are indicated. All values correspond to the median and 68.3% confidence intervals. The time periods used are marked by the rounded numerical ages of the bracketing marker units (second column). See Table 5.5 for un-rounded ages and uncertainties of each marker. Note that some slip rate values in S-AMF show larger uncertainties due to the error propagation of the slip. Probability density function (PDF) figures of each slip rate value are available in the Annex II (F).

5.6.2.1 Vertical slip rates

- N_{2b}-AMF

In T-1 (N_{2b}-AMF) unit 6 (76.8±5.6 ka BP; accumulated throw 7.8±0.5 m) is used as a long-term marker, while units 4.2 (42.6 ± 0.2 ka; 4.2±0.2 m) and 2.1 (35±0.2 ka BP; 2.6±0.2 m) are used for the shorter-term. The Cg unit is not considered for the slip rates because it covers a time period much older than the other branches. As shown in Table 5.13, long term vertical slip rates (last 77 ka; 0.10±0.01 mm/yr) are higher than short-term, especially for the last 35 ka (0.07±0.01 mm/yr), where the values highlight a ~30% decrease in the uplift towards recent times. When looking at the particular slip rate variations between time periods in the sequence, it can be seen that this decrease is not progressive but is preceded by a drastic increase in the vertical slip rate to 0.56^{+0.16}/_{-0.14} mm/yr between 43 and 40 ka (units 4.2-2.2) (Table 5.13). This increase corresponds to a single event (R2) and indicates that this event caused a high fault slip, compared to the other events in longer periods.

Because units 2.2 and 2.1 are equally deformed, a cease in the deformation is identified between ~40 and 35 ka. This is evidence of an inter-seismic period and thus that the fault deformation is achieved by seismic events rather than by constant slipping or creep.

- S-AMF

In T-16 (S-AMF), four age markers are used for slip rate estimations: unit N1 (73.4±7.0 ka BP; 10.2±0.5 m) is selected for the longer-term, while units L2 (45.9±3.5 ka; 8.9±0.2 m), J (31.2±2.6 ka; 6.8±0.3 m) and B (15.2±1.1 ka BP; 4.0±0.2 m) are selected for the short-term. Vertical slip rates are higher if shorter periods of time are considered, showing a maximum slip rate for the last 15 ka (0.26±0.02 mm/yr) (Table 5.13), which is approximately two times the slip rate for the last 73 ka (0.14^{+0.02}/_{-0.01} mm/yr). This progressive increase in the vertical slip rates is achieved in two pulses, one smaller (0.14^{+0.04}/_{-0.03} mm/yr) in the period between 46 and 31 ka, a larger one (0.49^{+0.27}/_{-0.13} mm/yr) in the period between 31 and 25 ka, followed by a deceleration at 25 ka. Same as in N_{2b}-AMF, the large increase between 31 and 25 ka corresponds to a single event (S6; Table 5.13), which generates an important differential deformation between units J and I in T-16 (Figure 5.17). Although the large negative uncertainty should be considered when evaluating this peak value, these single-event pulses imply

the occurrence of large fault slips in short periods as opposed to smaller slips in longer periods.

Between 25 and 15 ka no notable vertical deformation is recorded in T-16 because units I and B, respectively, show the same vertical slips. However, there is sedimentary evidence for four paleoearthquakes (S2b-S5; Table 5.8) between these ages, not only in T-16 but also in other parts of El Saltador site. This implies that the fault did not cease activity within this period but did not generate significant vertical slips.

- **F-AMF**

In T-3, unit O (18 ± 1 ka BP) and the upper level of unit B (8.5 ± 0.0 ka BP) are selected as markers, which compared to the other trenches both represent the short-term given the recent sedimentation of T-3. Similar slip rate values are obtained for both periods (~ 0.26 - 0.29 mm/yr), although for the period between 18 and 9.5 ka the slip rate is higher (0.35 ± 0.04 mm/yr) (Table 5.13). This might suggest that this fault has slightly decreased its activity since 8.5 ka. Despite this, it is noteworthy that the vertical slip rates of this fault branch for the 18-9.5 ka and 8.5 ka-present periods are both within the uncertainty range of the ones for the 31-25 ka and 15 ka-present periods in S-AMF, respectively ($0.49^{+0.27}_{-0.13}$ mm/yr and 0.26 ± 0.02 mm/yr). This highlights the possibility of a joint uplift for both branches, which is consistent with them being the limits of a pressure ridge. Between 9.5 and 8.5 ka, which is the time span of deposition of the whole unit B, no deformation is recorded. This evidences an inter-seismic period and thus a seismogenic behavior of the fault.

- **Summed values**

The total vertical slip rate of the AMF can be assumed as the summatory of all its active branches, except for S-AMF and F-AMF. In this case, because both branches have opposed dips and are assumed to join at depth forming a pressure ridge, the vertical slip rates of S-AMF must be subtracted from the F-AMF to derive the total vertical slip rate of this ridge with respect to the Guadalentín Depression. The paleoseismic record in each site is not available for the same time span, thus, the most reliable total slip rate estimations are for the periods where all branches have available information. In the studied case this corresponds to the period between 18 ka and the present, controlled by the shortest record in F-AMF. The slip rates selected for the other branches to be representative of the 18 ka, are the ones for the last 35 ka in N_{2b}-AMF and the last 31 ka

in S-AMF. In the latter, we prefer to use a longer-term marker of 31 ka rather than the younger ~15 ka (unit B) because we estimate it to be more representative and less likely to be influenced by the effect of fluctuations over time. Conversely, for younger periods analyzed (last 8.5 ka controlled by F-AMF), the slip rates of the last 15 ka are used for the S-AMF to depict short-term variations (Table 5.13).

A mean total vertical slip rate of 0.14 ± 0.03 mm/yr is obtained for the last 18 ka by considering the mentioned periods in each branch (Table 5.14). For the last 8.5 ka, this value shows a marked decrease to 0.07 ± 0.03 mm/yr, which evidences fluctuations of this parameter since ~18 ka. This is because both F-AMF and S-AMF show equal vertical slip rates in this period (8.5-15 ka), which implies that the total contribution of the frontal pressure ridge to the uplift is almost null. Hereby, the uplift of the AMF for the last 8.5-15 ka seems to be only absorbed by N_{2b}-AMF. Despite this, negligible uplift contribution does not mean inactivity. In fact, the individual vertical slip rates of these two branches are almost four times the ones for the N_{2b}-AMF. This evidences that, regardless of the uplift, their activity is higher, and reveals that the fault responsible for the pressure ridge, at depth, is more active than the N_{2b}-AMF.

Based on this analysis, we prefer the total vertical slip rates for the last 18 ka as reference because they are likely less influenced by the identified shorter-term variations. For this common period, ~50% of the vertical slip rate is absorbed by both S-AMF and F-AMF in the frontal pressure ridge, while the remaining 50% is accommodated by N_{2b}-AMF, despite the higher activity is registered in the two former.

5.6.2.2 Lateral slip rates

- N₁-AMF

Lateral slip rates are estimated for the N₁-AMF from the offset channel D (24.3^{+4.1}/_{-6.3} m). The obtained slip rate is $0.65^{+0.12}/_{-0.17}$ mm/yr, for the last 34-40 ka (Table 5.13). The age range is the estimated for the unit D formation, which itself is a minimum because it is assigned from the maximum ages of unit C2 (34.4 ka BP) and unit 2.2 in T-1 (40 ka BP). Therefore, the lateral slip rate is a maximum.

- S-AMF

In this site, lateral slip rates are estimated from the vertical slip rates of T-16 using the rake of the fault (14°). Both rake (~14°) and lateral slip rates are conditioned to the vertical

slips, which are minimum values. The lateral slip rate for the last 31 or 15 ka in T-16 ($0.89^{+0.09}/_{-0.08}$ mm/yr; $1.07^{+0.1}/_{-0.09}$ mm/yr, respectively), are both in the range the ones by Ferrater (2016) for the last 28 and 20 ka: 1.0 ± 0.2 and 0.9 ± 0.1 mm/yr, respectively. The pattern of lateral slip rate variations is the same as the one explained for the vertical slips in this fault branch, with a maximum peak of lateral slip rate between 31 and 25 ka at $2.01^{+1.09}/_{-0.54}$ mm/yr and a large uncertainty range (Table 5.13).

- Summed values

The total lateral slip rate is inferred from the summatory of the N₁-AMF and S-AMF branches. For these branches, the common paleoseismic record is longer (last ~40 ka), which allows to estimate $1.44^{+0.13}/_{-0.18}$ mm/yr (Table 5.14). For the last 31 ka, the lateral slip rate increases to $1.54^{+0.14}/_{-0.18}$ mm/yr, and up to $1.72^{+0.16}/_{-0.19}$ mm/yr for the last 15 ka. The higher values for the shorter-term are related to a higher activity controlled by S-AMF (Table 5.13). This, together with the decrease of the vertical slip rate identified for the AMF since ~8.5-15 ka, might suggest that the lateral component becomes more relevant over time. This lateral component is controlled by the S-AMF, absorbing ~58-62% of the lateral slip rate since ~15-31 ka. This is consistent with its stronger geomorphological expression. Despite this, the fluctuations for the N₁-AMF branch should be also considered yet cannot be disclosed since are based on a single age marker.

5.6.2.3 Net slip rates

In S-AMF, net slip rates for the last 46, 31 or 15 ka (Table 5.13) are all in the range of the 0.9 ± 0.1 mm/yr net slip obtained by Ferrater (2016) for the last 20 ka, especially the one for the last 31 ka ($0.91^{+0.09}/_{-0.08}$ mm/yr). Slip rate time variations show the same variation pattern as the lateral and vertical slip rates with a peak between 31 and 25 ka corresponding to event S6 ($2.06^{+1.12}/_{-0.56}$ mm/yr; Table 5.13). However, this peak estimation has a large negative uncertainty, meaning that the slip rate could be lower. In the N₁-AMF, the net slips are inferred considering a preferred 2° rake based on field measurements, which yields a value coincident with the lateral slip rate of this branch, considering the uncertainties: $0.65^{+0.12}/_{-0.17}$ mm/yr for the last 30-40 ka. The high net slip rates of the F-AMF indicate the resolution of the shortening needed to generate the vertical slip rate in a low-angle fault plane. In this case thus, only the vertical slip rate might be used to characterize the total slip rate of the fault (Figure 5.31), especially because the whole AMF is characterized as a subvertical structure at depth (see below).

- **Summed values**

The total net slip rate of the Lorca-Totana segment is calculated from the vectorial summatory of the total vertical and lateral slip rates in Table 5.14 for the common last 18 ka (Figure 5.31). Since the net slip vector is different for each fault, the total net slip rate for all the branches must be computed following Equation 3.5 (see section 3.5.2). We assume that all branches link at depth in a same fault plane with a general 70° dip, which is in agreement with surface observations and geophysical data from magnetotelluric (Martí et al., 2020) and well studies (Rodríguez-Escudero et al., 2014).

The estimated total net slip rate of the Lorca-Totana segment for the last 18 ka is $1.55^{+0.14}/_{-0.18}$ mm/yr while it increases to $1.72^{+0.16}/_{-0.19}$ mm/yr for the last 8.5 ka (Table 5.14). This increase in the net slip for recent times is due to a decrease in the uplift generated by the frontal pressure ridge: S-AMF and F-AMF have almost equal vertical slip rates in this period, which translate into null uplift contribution to the AMF. This implies, as mentioned, a more important role of the lateral component. Hereby, the values for the last 18 ka are the preferred, as they are likely more representative and less influenced by shorter-term fluctuations.

For the last ~18 ka, the values obtained for the vertical and lateral components of the slip rate in the previous sections determine that, in the Lorca-Totana segment, the vertical slip rate is much smaller than the lateral (~eleven times). Using such relationship between the vertical and lateral slip rates, a rake of 5-9° is obtained for the studied transect of AMF following Equation 5.1.

$$\text{Rake}(\text{°}) = \arctan \frac{\text{VSR}/\sin(\text{dip})}{\text{LSR}} \quad \text{Equation 5.1}$$

Where VSR and LSR are the vertical and lateral slip rates, respectively, and the dip = 70°.

The inferred rake suggests an overall predominance of the lateral component for the Lorca-Totana segment, regardless of the slip partitioning observed between branches. This is consistent with the predominantly strike-slip character attributed to this fault in previous studies (e.g., Masana et al., 2004; Ferrater et al., 2016), although it contrasts with the 20-40° rakes inferred from the focal mechanisms of the 2011 Lorca earthquake series (López-Comino et al., 2012). This might be because the earthquake happened in an intersegment zone and did not involve the whole fault segment as we do here.

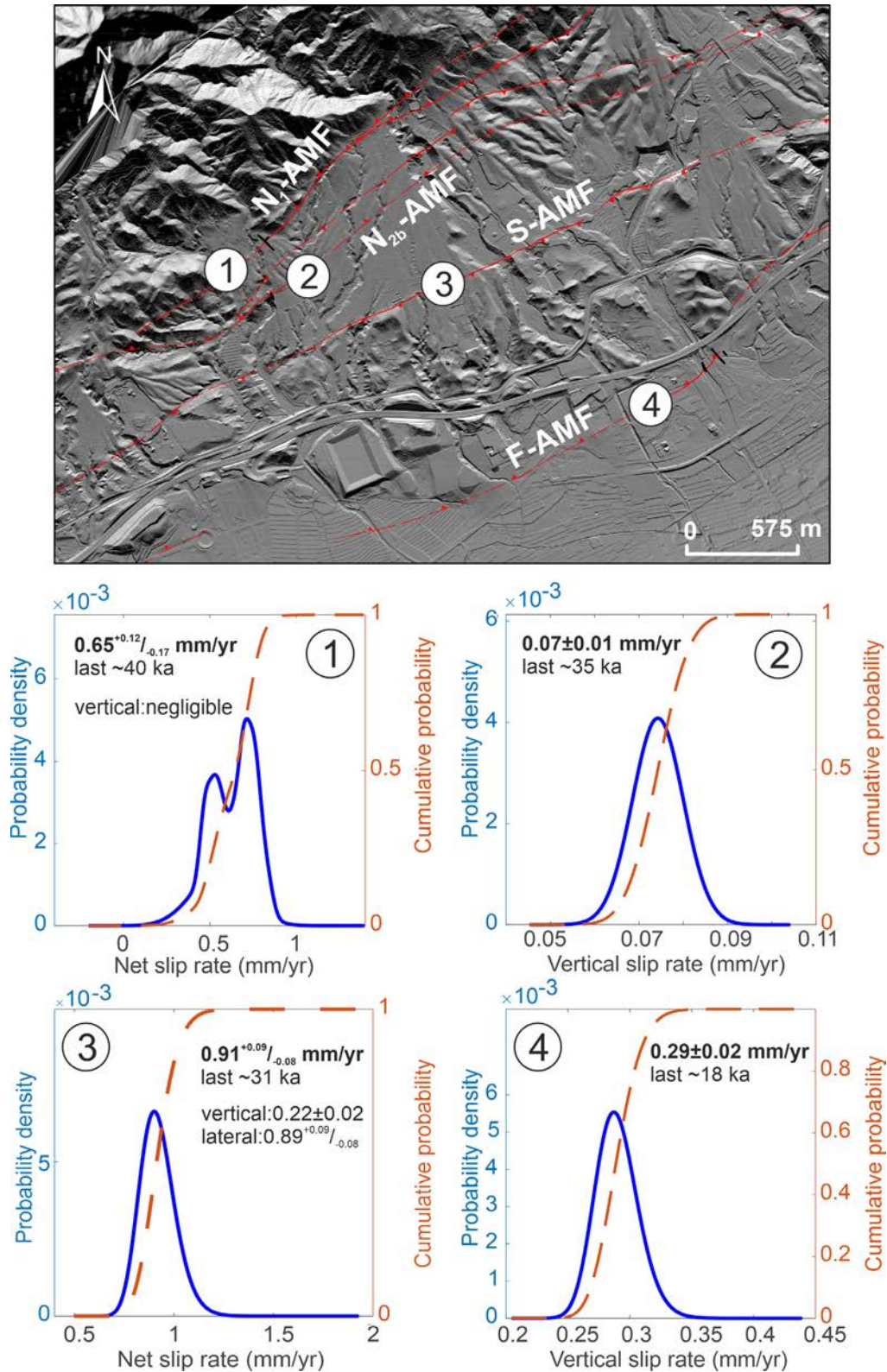


Figure 5.31. Summary figure of the slip rate PDFs of each branch, whose vertical and lateral components have been used to compute the total net slip rate for the last ~18 ka. Note that for the N_{2b}-AMF and the F-AMF only the vertical slip rates are used for the total net slip rate calculation because the faults are mainly dip-slip and assumed to join at depth in a single ~70° structure. The PDFs are obtained following the approach and code proposed by Zechar and Frankel (2009). 1: La Tercia site; 2: El Roser site; 3: El Saltador site; 4: La Hoya site. Slip rate data for other time periods is available in Table 5.10 and PDF figures in the Annex II (F).

All four branches of the Lorca-Totana segment			
Time period	Vertical slip rate (mm/yr)	Lateral slip rate (mm/yr)	Net slip rate (mm/yr)
40 ka - present	-	$1.44^{+0.13}/_{-0.18}$	-
31 ka - present	-	$1.54^{+0.14}/_{-0.18}$	-
18 ka - present	0.14 ± 0.03	$1.54^{+0.14}/_{-0.18}$	$1.55^{+0.14}/_{-0.18}$
8.5 ka - present	0.07 ± 0.03	$1.72^{+0.16}/_{-0.19}$	$1.72^{+0.16}/_{-0.19}$

Table 5.14. Summed vertical, lateral and net slip rates for all four fault branches explored in this study and for different time periods. The values correspond to the median and 68.3% confidence intervals. For the last ~40 and 31 ka, only the lateral slip rates are depicted because are the ones available for all branches with lateral component (N₁-AMF and S-AMF). Conversely, for the vertical and thus net slip rate, data for all branches is only available since 18 ka. Note that the total slip rates for the past 18 ka are computed using the slip rates for the time periods in Figure 5.31. For the past 8.5 ka instead, in S-AMF and F-AMF the periods used are the last 15 and 8.5 ka, respectively.

5.6.3 Shortening rates

Shortening rates are calculated using the same age markers as for the slip rates in each trench. Values are expressed as the median with uncertainties representing a 68.3% confidence interval (Table 5.15). For the long-term in N_{2b}-AMF, the shortening rate estimated is 0.05 ± 0.01 mm/yr for the last 77 ka. Conversely, for the short-term these show a pronounced decrease to 0.03 ± 0.01 mm/yr for the last 43 ka and to 0.01 ± 0.00 mm/yr for the last 35 ka. Between these periods, the shortening rates show variations, especially between 43 and 40 ka, where these increase up to $0.29^{+0.11}/_{-0.10}$ mm/yr (Table 5.15). This value shows a large uncertainty mostly related to the uncertainty of the shortening in this period (0.8 ± 0.3 m).

In S-AMF for the last 73, 46 and 31 ka, shortening rates remain constant at 0.02 ± 0.00 mm/yr, while for the last 15 ka the values decrease to 0.01 ± 0.00 mm/yr. Between 73 and 31 ka, these shortening rates are slightly higher at 0.03 ± 0.01 mm/yr, with a short substantial increase to $0.11^{+0.06}/_{-0.03}$ mm/yr between 31 and 25 ka. All these variations are not in agreement with the observed slip rate increase for shorter-term periods, which might be because in this trench especially, an important part of the deformation of the uplifted block is not captured. Also, the lateral component might be playing an important role by creating shortening not parallel to the T-16 direction.

In F-AMF, the shortening rate values are different for both periods explored, despite the vertical slip rate values are similar: a shortening rate of 0.09 ± 0.02 mm/yr is obtained for the last 18 ka, while it is 0.10 ± 0.02 mm/yr for the last 8.5 ka. A significant increase to

0.18±0.04 mm/yr is found between 18 and 9.5 ka. The important shortening variations contrast with the smaller vertical slip rate variations and are attributed to the low angle dip of the fault. Low angle faults require more shortening to generate a given vertical displacement than high angle faults do, thus small variations in the vertical component are caused by considerable variations in the horizontal component. This is evidenced by the large net slip rates (dip-slip) of this fault compared to the vertical.

N_{2b}-AMF	
Time period	Horizontal shortening rate (mm/yr)
77 ka - present	0.05±0.01
43 ka - present	0.03±0.01
35 ka - present	0.01±0.00
77 ka - 43 ka	0.08 ^{+0.03} / _{-0.02}
43 ka – 40 ka	0.29 ^{+0.11} / _{-0.10}
S-AMF	
73 ka-present	0.02±0.00
46 ka-present	0.02±0.00
31 ka-present	0.02±0.00
15 ka-present	0.01±0.00
73 ka – 46 ka	0.03±0.01
46 ka – 31 ka	0.03±0.01
31 ka - 25 ka	0.11 ^{+0.06} / _{-0.03}
F-AMF	
18 ka-present	0.09±0.02
8.5 ka-present	0.10±0.02
18 ka-9.5 ka	0.18±0.04
All three branches	
18 ka - present	0.11±0.02
8.5 ka - present	0.12±0.02

Table 5.15. Horizontal shortening rates inferred from restoration of trench walls in T-1 (N_{2b}-AMF), T-16 (S-AMF) and T-3 (F-AMF) for different time periods. Integrated rates for all three branches since 18 and 8.5 ka are included. The values correspond to the median and 68.3% confidence interval. Zero uncertainties are due to rounding to the second decimal. Probability density function (PDF) figures of each shortening rate value are available in the Annex II (F).

A total shortening rate of 0.11±0.02 mm/yr is inferred for all three branches for the last 18 ka with a slight increase since 8.5 ka (0.12±0.02 mm/yr) These similar values suggest

that the shortening has remained constant for the last 18 ka. All these estimations should be especially regarded as minimum because the shortenings measured are perpendicular to the fault traces and not necessarily parallel to the maximum regional shortening vector. Moreover, the vertical slips upon which the restoration is based on are a minimum.

5.6.4 Mean slips per event and event displacements

We average the mean slips per event (SPE) based on the net slips estimated in the units at each site divided by the number of paleoearthquakes affecting such unit (Table 5.16). We also measure the event displacements (ED), which are the net slips generated by each individual paleoseismic event. This is done by subtracting the net slips between consecutive deformed units (Table 5.10) and allows to evaluate the rupture slip variability of the fault, as opposed to the averages provided by the SPE. We compare the results obtained. Long and short-term periods in each trench are analyzed to depict variations.

5.6.4.1 Slip per event (SPE)

In N₁-AMF, the net displacement of the unit D (Table 5.10) affected by a minimum of three events (N3-N1), yield a SPE of $8.1^{+1.4}/_{-2.1}$ m. This value is a maximum because i) the displacement is a maximum, ii) the age considered for unit D is a minimum and iii) the number of events is a minimum, especially considering the age gap between unit C1 and the present-day soil.

In N_{2b}-AMF, we select three markers for the SPE. For the long-term, the minimum of four events (R1 to R4) since ~77 ka displacing unit 6 (7.8 ± 0.5 m) yield a mean SPE of 2.0 ± 0.1 m. This value is similar to the shorter-term SPE of 2.2 ± 0.2 m obtained for the last two events (R1 and R2) since ~43 ka affecting unit 4.2 (4.3 ± 0.3 m) (Table 5.16). Conversely, when only the last event is considered (R1), the SPE increases slightly to 2.6 ± 0.2 m for the last 35 ka, which corresponds to the slip of units 2.2 to 1.

In the S-AMF, for the long-term, a SPE of 3.9 ± 0.1 m is computed from the 42.4 ± 1.3 m net slip of unit N1, affected by eleven events (S1-S8) since ~73 ka. A similar SPE value of 4.1 ± 0.2 m is calculated from the 28.5 ± 1.3 m slip of unit J, affected by the last seven events since ~31 ka (S1-S6). Conversely, for a short-term of the last ~15 ka, the SPE is strongly increased to 8.4 ± 0.4 m considering the 16.8 ± 0.8 m slip of unit B, affected by the last two events (S1 and S2). In this latter case especially, the SPE is a maximum because, for the last ~15 ka, the deposition in El Saltador site is notably scarce, likely hampering the correct detection of paleoseismic events.

5. Structural and paleoseismic characterization of the Lorca-Totana segment

Time period	SPE (m)	N. of paleoevents	Paleoseismic event	Bracketing units	ED (m)
N₁-AMF					
40 ka - present	8.1 ^{+1.4} / _{-2.1}	3 (N1-N3)	-	-	-
N_{2b}-AMF					
43 ka - present	2.0±0.1	2 (R1 and R2)	R1	2.2 to soil	2.6±0.2
			R2	4.2 to 2.2	1.5±0.2
77 ka - present	2.0±0.1	4 (R1 to R4)	R3	5 to 4.2	2.1±0.7
			R4	6.2 to 5	1.6±0.9
S-AMF					
15 ka - present	8.4±0.4	2 (S1 and S2)	<i>S2/S1 to S5</i>	Z to I	16.8±0.8
			S6 to S7	I to K	11.7±1.5
			S7b	K to L1	5.9±1.5
31 ka - present	4.1±0.2	7 (S1 to S6)	S7c	L1 to L2	2.9±1.1
			S8	M to N1	5.1±1.5
			S9	N2 to N3	0.4±2.5
73 ka - present	3.9±0.1	11 (S1 to S8)	<i>S9c to S9b</i>	N3 to N4d	6.3±2.2
			S9d to S10	N5 to Q	16.4±2.2
			S11	R to S	8.8±2.5
F-AMF					
18 ka - present	3.0±0.1	5 (H1 to H5)	H1	A to B	6.4±0.6
			H2	B to I1	2.0±1.1
			H3	I1 to I2	0.6±0.9
			H4	J to K	0.3±0.4
			H5	N to O	5.8±0.4

Table 5.16. Mean net slips per event (SPE) and event displacements (ED) in T-2 (N₁-AMF), T-1 (N_{2b}-AMF), T-16 (S-AMF) and T-3 (F-AMF). All values refer to the mean and 68.3% confidence interval. For the ED, the units bracketing the paleoseismic events and whose differential slip has been used to calculate the parameter are included. Note that in S-AMF several ED represent more than one event, although only the event horizons with strong paleoseismic evidence are accounted because are the ones producing significant slip differences between units. Events with weak evidence are marked in italics (see Table 5.8 for event classification in this trench). The high uncertainties in some of these ED are due to error propagation when subtracting values of different deformational blocks. Net slips upon which the SPE and ED are calculated are in Table 5.10.

The SPEs herein are, in all cases, likely overestimated because the observed number of earthquakes in the trenches is always a minimum. This is more noticeable in the short-term SPEs, consistently higher than the ones averaged for longer periods. This is because in all the trenches, especially the ones in El Saltador alluvial fan, the deposition has not been active since ~15 ka (T-16) to ~32-35 ka (T-1 and T-2), hampering the detection of the paleoseismic events occurred since. Thus, when shorter-term periods are analyzed,

the influence of such gaps is amplified, leading to overestimated SPEs. In this respect, the SPEs averaged for long-term periods are more reliable and thus preferred.

5.6.4.2 Event displacement (ED)

The EDs are measured from the slip difference between bracketing units of paleoseismic events in each trench (Table 5.16).

In T-1 (N_{2b}-AMF), the ED is similar for all the events R4 to R1, considering the uncertainty ranges, although slightly higher for the event R1 (Table 5.16). This last slip might be affected by the sedimentary gap from ~35 ka to the present, as also identified in the SPE, that could be preventing the detection of additional events. However, the slip difference is not significant enough to clearly estimate this and thus could be simply related to fault slip distribution variability along the fault.

In T-16, the ED values show a high variability, even excluding those slips that represent more than one event (Table 5.16). Events S1-S5 and S9d-S10 are the ones that show higher values compared to the rest. The first value might be simply because the slip represents many events (six events), although i) all events except S2 show weak evidence (Table 5.8) and ii) no clear vertical slip differences have been identified between units B to I, which could be due to the lack of exposure of part of the deformation in T-16. The second value could be because this event represents the moment when the fault started acting as a permanent tectonic barrier, blocking units above O1 from crossing the fault zone (Figure 5.17). This could explain why these units are not found in the uplifted block of the fault in T-16.

In T-3, the first and last events (H1 and H5) show similar ED around 6 m, while the intermediate events all show much smaller slips. These large differences could suggest an underestimated number of earthquakes in these horizons, especially considering the wide time window of occurrence for event H1 (Figure 5.30).

For some horizons, the variability of ED in the trenches can be interpreted as indicative of the occurrence of earthquakes with different slips rather than a multi-event. This is supported by the slip rate variability that shows short periods with larger single-event slips (i.e., S6 in T-16 or R2 in T-1; Table 5.13) and longer periods with multiple events and smaller slips. Despite this, such variability cannot be directly interpreted as different earthquake magnitudes because earthquake ruptures do not always nucleate in the same region. Fault slip is a highly variable parameter along strike (e.g., Kearsse et al., 2018) and

the different ED could just be depicting different distributions of the slip along the fault in equally sized earthquakes. Conversely and as mentioned for the SPE, in some other cases the ED variability can also be interpreted as a result of an incomplete paleoearthquake record, which leads to interpret multiple earthquakes as a single one. This could be the situation of the earthquake horizons located on top of the sequences in the apical parts of El Saltador fan (e.g., R1 in T-1; El Roser site), marked by long periods without deposition, or the last event H1 at La Hoya site.

5.7 Discussion on the paleoseismic parameters of the Lorca-Totana segment

In this section, the paleoseismic parameters presented in the results section are analyzed to: i) discuss the slip rate estimations within the AMF and the EBSZ contexts and their evolution over time, ii) evaluate recurrent and possible synchronic ruptures in different branches by correlation of the different earthquake chronosequences and iii) characterize the seismic potential of the Lorca-Totana segment and the implications of the new data presented for the AMF and EBSZ settings.

5.7.1 Slip rates

The slip rate estimations presented in this work constitute a step forward to better characterize the Lorca-Totana segment of the AMF with respect to previous studies, the most recent one by Ferrater (2016). In that study, the slip rate of the segment was characterized exclusively for the S-AMF, which constitutes the most prominent fault branch in the segment. The study of three additional fault branches to S-AMF in this segment, allowed to obtain their slip rate values for different periods and to integrate them to obtain a slip rate for the whole segment. In this respect, this work focuses on solving the data gaps highlighted in the previous studies concerning the multi-branch configuration of this fault segment. Remarkably, the obtained values constitute, in general, minimum estimations because i) they are based on minimum slips observed in the trenches, ii) do not include data from other identified branches such as N_{2a}-AMF that might be absorbing deformation and iii) the lateral component of the vertical slip branches cannot be completely disregarded without 3D paleoseismic trenching.

A net slip rate of $1.55^{+0.14}/_{-0.18}$ mm/yr is obtained for the last 18 ka in the Lorca-Totana segment accounting for the four fault branches studied (Table 5.14). The value is around two times higher than the 0.9 ± 0.1 mm/yr previously published by Ferrater (2016), which is expected given that only the S-AMF was studied, and reinforces that integral paleoseismic studies allow to improve and complete the seismic parameters of a fault. The decomposition of the net slip rate for the last ~18 ka reveals that, in the Lorca-Totana segment, the vertical component is very small compared to the lateral (0.14 ± 0.03 mm/yr vs. $1.54^{+0.14}/_{-0.18}$ mm/yr; Table 5.14). This is consistent with the results from previous studies in this segment (Masana et al., 2004; Ferrater, 2016).

Specifically, in this segment, both S-AMF and F-AMF (pressure ridge) accommodate half of the recent vertical slip rate (~50%) of the transect (Table 5.13). The similar vertical slip rates of both branches for the last ~18 ka suggest a joint uplift that is consistent with

a pressure ridge context in which the central block is extruded by the motion of both limiting faults rather than by the pure vertical movement of the joining fault at depth. Despite the similar vertical rates, for the last 18 ka the F-AMF shows slightly higher values than S-AMF (Table 5.13), which suggest that the former dominates the uplift in this frontal part. In this way, the cumulative effect of higher rates in the F-AMF since long before 18 ka would explain why El Saltador fan is uplifted respect to the Guadalentín basin nowadays. The vertical slip rate of S-AMF provided here is around two to three times higher than the inferred by Ferrater (2016) (0.1 mm/yr) (Table 5.13). The 3D trenching methodology applied in that study allowed to precisely measure the lateral slips of paleochannels but underestimated the vertical slips because these were measured exclusively on the fault plane. From the observations in T-16, we detected that most part of the vertical deformation of the units is caused by fault propagation folds in the downthrown block and forming a positive flower structure. These structures appear a were not considered for the slip measurements in the previous 3D trenching. We then conclude that this revised vertical slip rate is more reliable.

The N_{2b}-AMF accommodates the remaining half of the uplift of the segment for the last ~35 ka. Average slip rate values show a slight decrease in the slip rates for this period compared to previous (0.07±0.01 mm/yr; Table 5.13), which can be interpreted as a slowdown of the fault branch. However, given that the time occurrence of the last event R1 is very uncertain (34.7 ka-1670 AD; Figure 5.28), it cannot be discarded that the fault branch is inactive or in a long inter-seismic period should the last event have happened close to the age of the last unit. In this scenario, the Lorca-Totana segment would not be generating relevant uplift respect to the Guadalentín level, especially since 15-8.5 ka. The slip rates of N_{2b}-AMF agree with the 0.087^{+0.003}/_{-0.009} mm/yr (198-26 ka) inferred for the same fault at the Carralaca site (Martínez-Díaz and Hernández-Enrile, 2001). This reinforces the results obtained here and supports the continuity of the activity to the SW.

Concerning the lateral slip rate, in the segment it is basically accommodated by the S-AMF (~60%) and to a lesser extent by the N₁-AMF (~40%). The lateral slip rates of the S-AMF for the last 31 and 15 ka (Table 5.13) are in agreement with the 1.0±0.2 mm/yr and 0.9±0.1 mm/yr by Ferrater (2016) for the last 28 ka and 20 ka, respectively. However, it is acknowledged that the coincidence in the lateral values is not completely independent because we used the lateral slip of unit D from Ferrater (2016) (El Saltador site) to calculate the fault rake and to indirectly obtain all the lateral slips from our vertical

measurements. For the N₁-AMF the lateral slip rate obtained ($0.65^{+0.12}/_{-0.17}$ mm/yr) is a maximum because the age of the unit D in T-2 (La Tercia site) is a minimum (~40 ka). Moreover, the lateral displacement used should be checked with 3D trenching.

5.7.1.1 Slip rate variability over time

The analysis of the slip rates for different periods of time in each branch, allowed evaluating variations of the slip rate over the Quaternary. We discuss these variations in terms of slip rate evolution in the Lorca-Totana segment for the N_{2b}-, S- and F-AMF branches. Slip rate variations of N₁-AMF cannot be discussed due to the lack of detailed age markers within the stratigraphic sequence.

We identify that the S-AMF is the controlling fault in the system, while the other branches have minor influence either because they accommodate vertical component, much lower than the lateral, or because their lateral slip rate is lower (N₁-AMF). Also, in the case of F-AMF, the time window is restricted to the last ~18 ka, which hampers the correct characterization of its role in the system in older periods (Figure 5.32). For the Upper Pleistocene-Holocene period (last ~77 ka), the slip rates of the three analyzed branches show significant variations over time, depicting periods of low activity and, consequently, lower slip rates, alternated with periods of increased activity and slip rates (Figure 5.32). Lower slip rates cover wider time periods than the higher slip rates, which usually show short peaks of acceleration of 3-9 kyr (high slopes; Figure 5.32). After these peak values, drastic slip rate drops are identified, followed by less marked rises to the current slip rate values (lower slopes). The pattern of alternating low and higher slip rates is defined as a super-cycle in the sense of Sieh et al. (2008).

Two supercycles are identified in the net slip dominated mainly by the S-AMF (Figure 5.32A). The other branches show generally poorer time resolution preventing a proper analysis of the overall variations (e.g., N₁-AMF). Conversely, the vertical slip rates depict three super-cycles due to the influence of the N_{2b}-AMF as well. In this case, the individual vertical slip rates in S-AMF and F-AMF since ~18 ka are higher than the northern sector of the system (N_{2b}-AMF), which depicts increased activity in the former respect to the latter for this period (Figure 5.32B). Because the two former branches are limits of a pressure ridge likely joining at depth, their vertical slip rates probably reflect the extrusion of the block in-between rather than the actual vertical slip rate of the deep fault. However, the rate of this extrusion is likely proportional to the net slip rate of the single fault at depth. Hence, increased vertical slip rates in these two branches likely reflect an increase

on the activity of the deep fault responsible for the pressure ridge. This also points out a potential abandonment of the N_{2b} -AMF, consistent with the detected decrease in the activity of La Tercia range front since Late Pleistocene, as suggested by Silva (1994) based on the alluvial fan generations. Nonetheless, the lack of sedimentary record since 35 ka in the N_{2b} -AMF, does not allow discarding minor variations in younger periods.

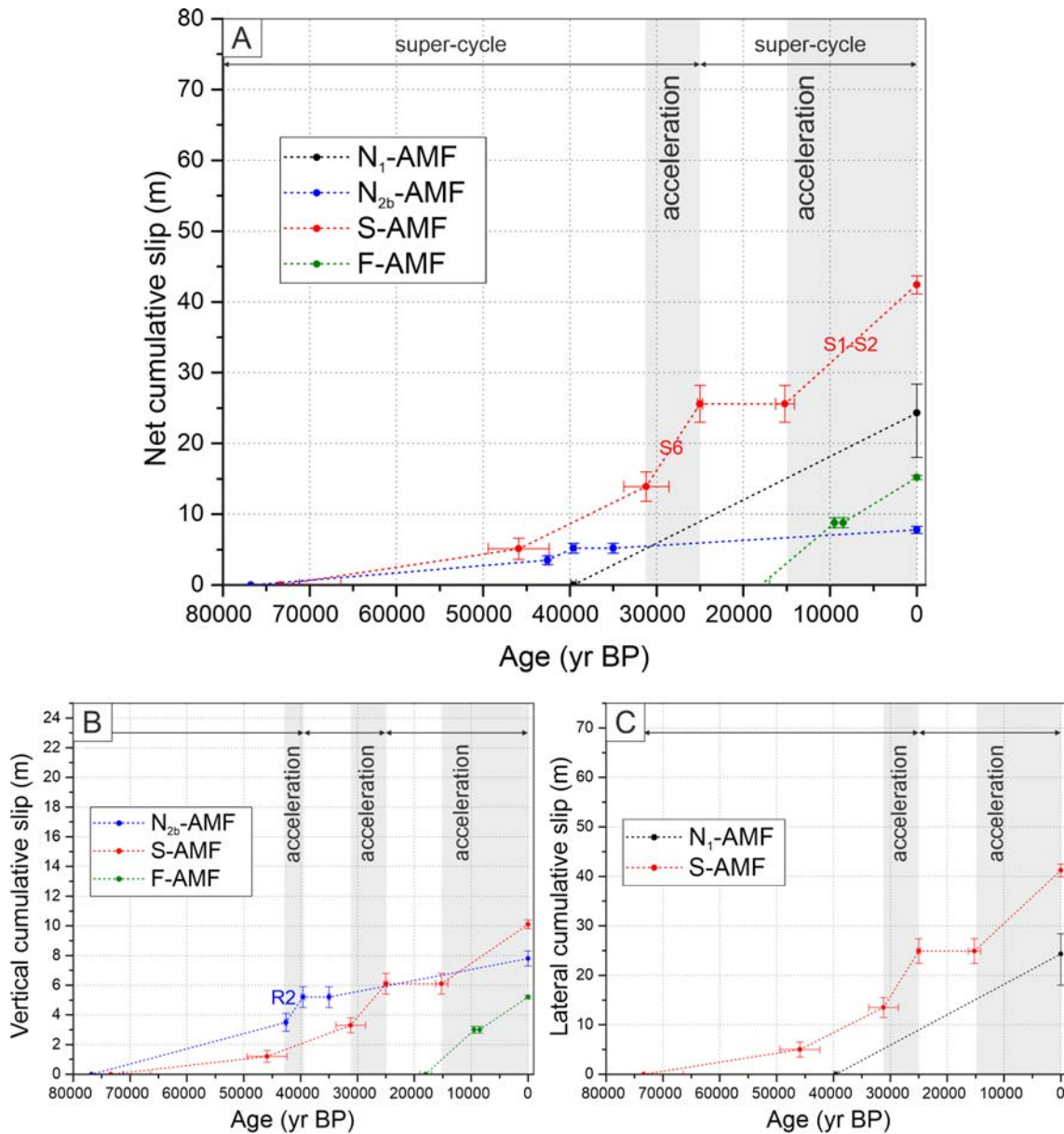


Figure 5.32. Cumulative slips as a function of time for the A) net, B) vertical and C) lateral components for each of the fault branches studied. For the net and vertical slip the comparison between branches is only reliable for the last ~18 ka because it is controlled by the record available in the F-AMF. For the lateral, it is reliable for the last ~40 ka controlled by N_1 -AMF. The slope of the curves that link the different data points in each branch represents the slip rate between time periods (Table 5.13), with higher slopes representing higher slip rates. Ages are extracted from numerical ages of the units in the trenches (Table 5.5) and cumulative slips are inferred from the values in Table 5.10. Grey bands represent periods of slip rate acceleration with respect to periods of decreased slip rates (white bands). The paleoseismic events coincident in time with an acceleration phase are also indicated (see Table 5.13 for correlation of all periods with events).

A pattern of higher activity in S-AMF and F-AMF is also observed in the net slip rate (Figure 5.32A). In this case, however, the role of the N₁-AMF could be important should the slip rate since 40 ka be representative of recent times, although it might be regarded as a maximum because the age of the marker used is a minimum (see section 5.6.2.2).

Super-cycle patterns have also been identified by Martín-Banda et al. (2021) in the northeastern segment of the Carrascoy Fault (Figure 5.33), one of the prominent tectonic structures in the EBSZ. According to the authors, short and high slip rate increases may be explained by the effect of fault interaction, particularly stress transfer from earthquakes occurring on adjacent faults although they could also be due to interaction between branches of the segment.

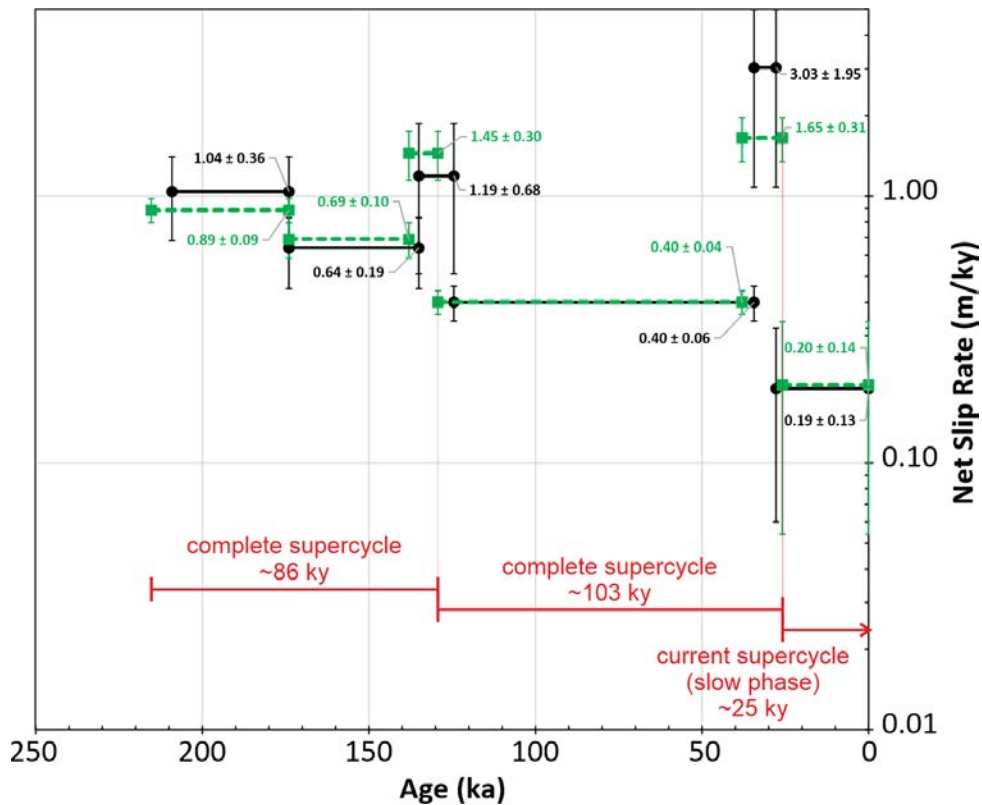


Figure 5.33. Variation of the net slip rate on the northeastern segment of the Carrascoy Fault for the last ~210 ka with supercycles identified by red horizontal lines. Black lines represent the slip rates computed using the average age of the sediments, while the green lines represent those calculated using the minimum ages (or maximum calcrete ages). Modified from Martín-Banda et al. (2021).

We estimate that such short accelerations are either due to the occurrence of large paleoearthquakes with higher slips than the average or to the occurrence of a surface rupture with maximum displacement in the studied site. The fact that some of these prominent accelerations correspond in time to a single and well age-constrained

paleoseismic event (i.e., event R2 to N_{2b}-AMF or event S6 in S-AMF; Table 5.16) support this idea. The chances of overestimating the ED are greater for longer periods than for smaller because the number of paleoseismic events is always a minimum. This means that EDs bracketed in shorter time spans are more reliable and that the accelerations here hardly correspond to event clusters but to larger fault displacements, at least based on the paleoseismic resolution.

5.7.1.2 Shortening rate evaluation and variability over time

The restoration of the trench walls provided minimum shortening values for all the branches with a total of 0.11 ± 0.02 to 0.12 ± 0.02 mm/yr for the last 18 ka and 8.5 ka, respectively (Table 5.15). In each trench the shortening measured is parallel to the trench direction, which in all cases is $\sim N160^\circ$, perpendicular to the fault. It should be considered that the total values obtained in this thesis are an underestimation because i) not all the branches are included, ii) not all the deformation could be quantified in some branches, especially S-AMF being the most prominent in the segment and iii) the maximum shortening vector might not be parallel to the orientation of the trenches restored.

Individual shortening values of the different fault branches can be compared with previous studies. In the N_{2b}-AMF branch at the Carraclaca site, Alonso-Henar et al., (2018) have inferred shortening rates of 0.029-0.098 mm/yr for the last 300 ka, which are in the range of the values obtained here for the last 77 ka; 0.05 ± 0.01 mm/yr. In the S-AMF, Masana et al. (2004) obtain a shortening of 0.05-0.48 mm/yr for the last 17.2-29 ka, higher than the 0.01-0.02 mm/yr obtained here for the last 15-31 ka (Table 5.15). This disagreement could be because i) the maximum shortening vector is not parallel to the walls of T-16 and ii) such vector may present along-strike changes of orientation related to the asperities in the trace combined with the left-lateral component.

Variations of the total shortening rate for different time periods follow similar patterns as for the slip rates in the different branches (Table 5.15), which is expected given that both parameters are related. Nowadays, the F-AMF is the one accommodating most part of the fault-perpendicular shortening (0.12 ± 0.02 for the last ~ 8.5 ka) in the Lorca-Totana segment at $\sim 80\%$, despite having the same vertical slip rates than S-AMF. This is attributed to the low angle of the former, which requires a higher shortening amount to generate the same uplift values. These higher values for F-AMF are consistent with the detected increased activity towards the southernmost branches (Figure 5.32B) and reinforce the important role of this frontal fault in the shortening.

5.7.1.3 Implications of the slip rates within the Eastern Betics Shear Zone

In this section, the slip rate values and variability for the Lorca-Totana segment are compared and discussed with regional geodetic data and slip rates of neighboring segments of AMF. We also contextualize our findings with the slip rates of the main EBSZ faults and discuss their main implications for the tectonic setting of the system.

- Contribution to the convergence and local geodetic rates

The obtained slip rate values in this thesis provide further evidence that the AMF is one of the most prominent faults in the EBSZ, with a major role in the deformation rates caused by the convergence between the Eurasia and Nubia plates (4-6 mm/yr; DeMets et al., 2015). According to Serpelloni et al. (2007), the EBSZ accommodates 1.6-2.7 mm/yr of convergence, highlighting that the AMF could be currently absorbing most part of the deformation caused by this convergence in the eastern part of the Betic Cordillera (up to ~1.5-1.6 mm/yr based on our estimations). Considering the slip rate evolution of the fault during the last ~77 ka, we propose that the current slip rate values of the Lorca-Totana segment are in an acceleration phase in reference to previous periods (Figure 5.32).

Local geodetic data also gives insight on the role of the AMF within the Guadalentín Depression. The short-term lateral slip rate value obtained in this thesis for the last ~18 ka ($1.54^{+0.14}/_{-0.18}$ mm/yr) is in agreement with the geodetic 1.5 ± 0.3 mm/yr strike slip rate in the transect between the Lorca-Totana segment and the Palomares Fault (PF) (Echeverría et al., 2013). Such agreement suggests that the AMF is absorbing most of the left-lateral deformation in this sector of the Guadalentín Depression. In terms of shortening, the geodetic compression rates obtained for a perpendicular transect (N164°) between AMF and PF (0.8 ± 0.4 mm/yr; Echeverría et al., 2013) are considerably higher than the short-term shortening rates obtained in this thesis ($0.11-0.12\pm 0.02$ for the last 8.5-18 ka). This disagreement is reasonable because i) our paleoseismic study does not include all the fault branches of the AMF system nor the PF, and ii) the shortening vector of the whole AMF-PF transect might not have the same orientation as the local vectors driving the motion in each AMF branch.

- Variations of the slip rate along the segments of the Alhama de Murcia Fault

In the southwestern segment of the AMF (Góñar-Lorca), the lateral slip rate values (1.6-1.7 mm/yr, last 200 ka; Ferrater, 2016) agree with the obtained in this thesis ($1.54^{+0.14}/_{-0.18}$ mm/yr; last ~18 ka), suggesting that the segmentation might not affect the

way that the lateral deformation is accommodated in this sector of the fault. Despite this, such values do not allow to clarify if both fault segments move at similar slip rates nowadays because the time periods analyzed are very different for each segment. Conversely, short-term lateral slip rates resulting from summing all the branches in the horse-tail termination of the Góñar-Lorca segment (0.97-1.37 mm/yr; Ortuño et al., 2012) are slightly lower. This is concordant with the location of the segment (Goñar-Lorca) in the fault tip, where generally the slip decreases compared to the central parts of a fault (i.e., Lorca-Totana) (e.g., Roberts, 1996; Manighetti et al., 2005). In terms of vertical slip rates, the values obtained here (0.14 ± 0.03 mm/yr for the last 18 ka), agree with the ones at the Góñar-Lorca segment (0.16-0.22 mm/yr since 47-63 ka; Ortuño et al., 2012). However, the latter values are likely not accurate to the vertical slip rate of the fault, but to re-adjustments of a pressure ridge. The context in the horse-tail termination of the Góñar-Lorca segment is very similar to the one in the Lorca-Totana, where several faults accommodate the deformation in a wide transect and likely link at depth into a same fault. In the study by Ortuño et al. (2012), the vertical slip rates were measured in fault branches within a pressure ridge, without accounting for the major branches limiting it. It is from these latter ones where the actual vertical component of the fault at depth can be inferred, while the others only depict tectonic readjustments of the block comprised in between. In the present study, we have accounted for that by considering that the uplift recorded in the northern limit of the ridge (S-AMF) needs to be subtracted from the southern (F-AMF) to obtain the vertical slip rate representative of the single fault at depth.

In the other AMF segments towards the NE (Totana-Alhama and Alhama-Alcantarilla), paleoseismic data is not available so far. In the Alhama-Alcantarilla segment, Herrero-Barbero et al. (2020), based on cross section restoration and GPS data, infer a maximum long-term (last 4.8-7.6 Ma) slip rate of $0.32^{+0.18}/_{-0.13}$ mm/yr in the southeastern sector of the segment and $0.05^{+0.03}/_{-0.02}$ mm/yr for the northeastern. These values are considerably lower than the ones inferred here for the Lorca-Totana segment and highlight how the slip rate decreases towards the northeastern tip of the AMF. This decrease, consistent with a fault tip context, is explained by the authors due to the transference of deformation between this sector of the AMF and the nearby Carrascoy Fault. Concerning the Totana-Alhama segment, no paleoseismic studies have focused there to date and thus, research is needed to better characterize how the slip rates of the Lorca-Totana segment link and are

resolved towards the NE. In section 6 we present preliminary field observations to propose potential future paleoseismic sites there.

- **Comparison with other faults in the Eastern Betics Shear Zone**

In the Guadalentín Depression, the Carrascoy Fault (CAF) is one of the most prominent tectonic features of the EBSZ. There, recent studies (Martín-Banda, 2020; Martín-Banda et al., 2021) have estimated a net slip rate of 0.49 ± 0.02 mm/yr for the northeastern segment of the fault since ~ 124 ka and 0.37 ± 0.08 mm/yr for the southwestern segment in the last 210 ka. These values are considerably smaller than the net slip rates inferred for the Lorca-Totana segment ($1.55^{+0.14}/_{-0.18}$ mm/yr). Because the CAF is mainly a reverse fault its net slip rate is more comparable to the vertical slip rate in the Lorca-Totana segment of AMF (0.14 ± 0.03 mm/yr).

In the CAF, several slip rate variations are recognized for the last 210 ka in the northeastern segment (Martín-Banda, 2020; Martín-Banda et al., 2021). The variation patterns of the slip rate, interpreted by the authors as super-cycles (three super-cycles), are similar to the ones observed for the AMF, especially in the vertical slip rates: long periods of lower tectonic activity or quiescence followed by short periods of increased slip rates (Figure 5.33). Nowadays, the CAF is in a period of lower slip rates, which contrasts with the actual regime in the AMF showing an increase since ~ 15 ka controlled by the S-AMF. The maximum peak of increase in the northeastern segment of the CAF happens between 34 and 28 ka, which is coincident with the peak of the S-AMF in the Lorca-Totana segment between ~ 31 and 25 ka (Figure 5.32). In both faults, this increase corresponds to a single paleoseismic event (Sx in the CAF and S6 in S-AMF) and, together with their tight time window of occurrence, suggests that the acceleration is due to a large coseismic fault slip in both sites. Despite this, the lack of paleoseismic resolution between 31 and 25 ka still does not allow to completely discard the occurrence several events (clustering) in this period.

From our perspective, the time coincidence of paleoearthquakes between CAF (Sx) and S-AMF (S6) is compatible with a synchronicity of ruptures in both faults that could suggest an earthquake triggering behavior due to stress transfer between these segments. However, a preliminary Coulomb stress transfer analysis by Álvarez-Gómez et al., (2018) suggests that triggering between these fault segments seems unlikely, but it should not be

ruled out. The study is a theoretical exercise subject to uncertainties in the fault kinematics and geometry of the faults, as acknowledged by the authors.

Other active faults in the Guadalentín corridor are Los Tollos Fault (LTF) and Palomares Fault (PF). The former is interpreted as a lately formed tectonic feature, with an estimated slip rate of 0.12-0.17 mm/yr, which is much lower than the AMF (Insua-Arévalo et al., 2015). The latter is a poorly studied fault from the paleoseismological view, and its slip rate is very low compared to the other faults of the system: 0.01-0.08 mm/yr of vertical slip rate since Middle-Late Pleistocene (García-Mayordomo, 2005) for the central and southern segments, while for the northern it remains unknown. The poor knowledge of the PF is hence a critical problem for its slip rate characterization and, in this respect, ongoing geodetic research might shed light on its characterization. Preliminary data by Khazaradze et al. (2020) suggests that the PF could be slipping laterally $\sim 0.4 \pm 0.2$ mm/yr in the transect between the Lorca-Totana segment and PF fault. Accounting for the respective uncertainty ranges, this preliminary value of the PF fits in this setting since the geodetic lateral slip rate (AMF+PF) is 1.5 ± 0.3 mm/yr (Echeverría et al., 2013) and our estimation for the Lorca-Totana segment is $1.54^{+0.14}_{-0.18}$ mm/yr.

Concerning the tips of the EBSZ system, to the south, the Carboneras Fault (CF) is the most important active fault with an estimated lateral slip rate of 1.1-1.3 mm/yr, coincident for the geodetic, paleoseismic and geomorphological approaches in different time periods since the Pliocene (Moreno, 2011; Echeverría et al., 2015). The similarity of this lateral slip rate to the ones of the Lorca-Totana segment ($1.54^{+0.14}_{-0.18}$ mm/yr) and long-term of the Góñar-Lorca (1.6-1.7 mm/yr), suggests continuity of the lateral component towards the south. Conversely, the vertical slip rate, the fault shows much lower values (0.1-0.15 mm/yr for the last 130 ka; Moreno, 2011), similar to the ones from the southwestern tip of the AMF (0.16- 0.22 mm/yr since 47-63 ka; Ortuño et al., 2012).

To the northeastern end of the system, the Bajo Segura Fault (BSF) is the northernmost major fault of the system, regarded as a blind reverse fault (Alfaro et al., 2012). The E-W orientation of this fault enhances the predominance of dip-slip component due to the perpendicular orientation to the convergence vector. Its geological vertical slip rates of 0.1-0.3 mm/yr (Alfaro et al., 2012) contrast with the 0.2-0.7 (± 0.2) mm/yr of geodetic shortening estimated for this fault (Borque et al., 2019). However, in this latter case, the authors estimate that the geodetic shortening is not completely absorbed by the BSF.

To sum up, the slip rate evolution of the AMF during the Upper Pleistocene and the synchronicity of larger fault displacements with the CAF suggest that the EBSZ is a dynamic connected fault system. However, the cause of such synchronicities remains undisclosed so far and more research is needed in this field to unveil the relationships between the different faults composing the system. Moreover, the lack of detailed slip rate evaluations for most of the EBSZ faults prevents from doing this analysis further. In this respect, the results presented here evidence that the integration of paleoseismic data from multiple sites is a fine approach to characterize faults and their possible relationships more comprehensively.

5.7.2 Paleearthquakes in the Lorca-Totana segment

5.7.2.1 Event chronosequence and correlation

In this section we discuss the paleoearthquake record identified among the different branches of the studied transect in the AMF and evaluate possible synchronic ruptures in different sites from their time constraints. All the paleoseismic trenches excavated in this study record evidence of several paleoearthquakes for different time periods, proving the seismic activity of all four fault branches during the Upper Pleistocene and Holocene. For the newly excavated branches, i.e., in N₁-AMF (La Tercia site), N_{2b}-AMF (El Roser site) and F-AMF (La Hoya site) a minimum of four (N₁-AMF) to five paleoearthquakes (N_{2b}-AMF and F-AMF) have been recognized in each one, while the enlargement of a trench in S-AMF (T-16 in El Saltador site) allowed for the identification of at least seventeen paleoearthquakes, even more events than those identified in for a younger record in the site by Ferrater (2016). This constitutes one of the most complete paleoearthquake records identified in the Iberian Peninsula and in southern Europe.

Despite the number of numerical datings carried out in this study (Figure 5.34), the uncertainties in the age estimations of some events are significantly large, as it can be seen by the overlapping event age ranges in the chronosequences of the different branches and large uncertainty ranges of older events, mainly due to lack of density of numerical datings (e.g., T-2 or T-3; Figure 5.11 and Figure 5.14). This is most important for those events or groups of events that lack detailed age constraints in their respective limiting units, especially in S-AMF (e.g., S9-S9d; Figure 5.29). In such cases, the application of the OxCal software allowed to model PDFs for each individual event instead of event groups, significantly constraining their uncertainty and allowing to compute recurrence estimations, although their ranges still show large overlaps. This evidences that the

approach used to model these events cannot replace a more detailed sampling for numerical dates in the future.

Large uncertainties in age estimations are found for those events that represent more than one earthquake in a large sedimentary gap. Clear examples are events N4 and R5 for the N₁-AMF and N_{2b}-AMF branches, respectively, that cover >100 kyr periods (Figure 5.35) between the Cg unit and the respective overlying alluvial sequences. For this reason, they have been excluded for recurrence analysis. Other smaller sedimentary gaps are identified throughout the sequence and on top of it as very little to no sedimentation has occurred since ~35-32 ka in the La Tercia and Roser sites and since ~15 ka in El Saltador site (Figure 5.34). This indicates that the sedimentary sequences of the sites are mostly not continuous and therefore that the identified number of events is a minimum. In the two northernmost branches (N₁-AMF and N_{2b}-AMF) this lack of record is emphasized by their higher position in El Saltador fan, making deposition more difficult and erosion easier than in S-AMF, where the tectonic barrier acted as a sedimentation prone area.

The chronosequences of paleoearthquakes obtained in this study differ from one branch to another. The main reasons have to do with the age range of units exposed in the trenches and the resolution of the sedimentary sequences (condensed vs. non-condensed stratigraphy). For instance, age constraining of events is much more accurate in the S-AMF and F-AMF branches than in the N₁-AMF and N_{2b}-AMF (Figure 5.35). In S-AMF, the availability of many numerical datings allowed for a precise constraining of the paleoevents especially for the last 31 ka (S1-S6), while in the F-AMF the short time span exposed in the trench (last 18 ka), constrained the five events with considerably small uncertainties. This facilitates the event correlation between S-AMF and F-AMF where for the last ~18 ka five events are recognized in both branches.

Another issue is the completion of the paleoearthquake record. Often, two or more consecutive events could have been recorded as a single deformation event (multievent) due to the lack of depositional units between the earthquakes. When comparing different fault branches, a potential “multievent” can be suspected if two or more events are identified in another branch for the same time-period. Analyzing the ED and the accumulated slip of that time span might shed some light into this question. This comparison has been made in different correlations within the studied trenches.

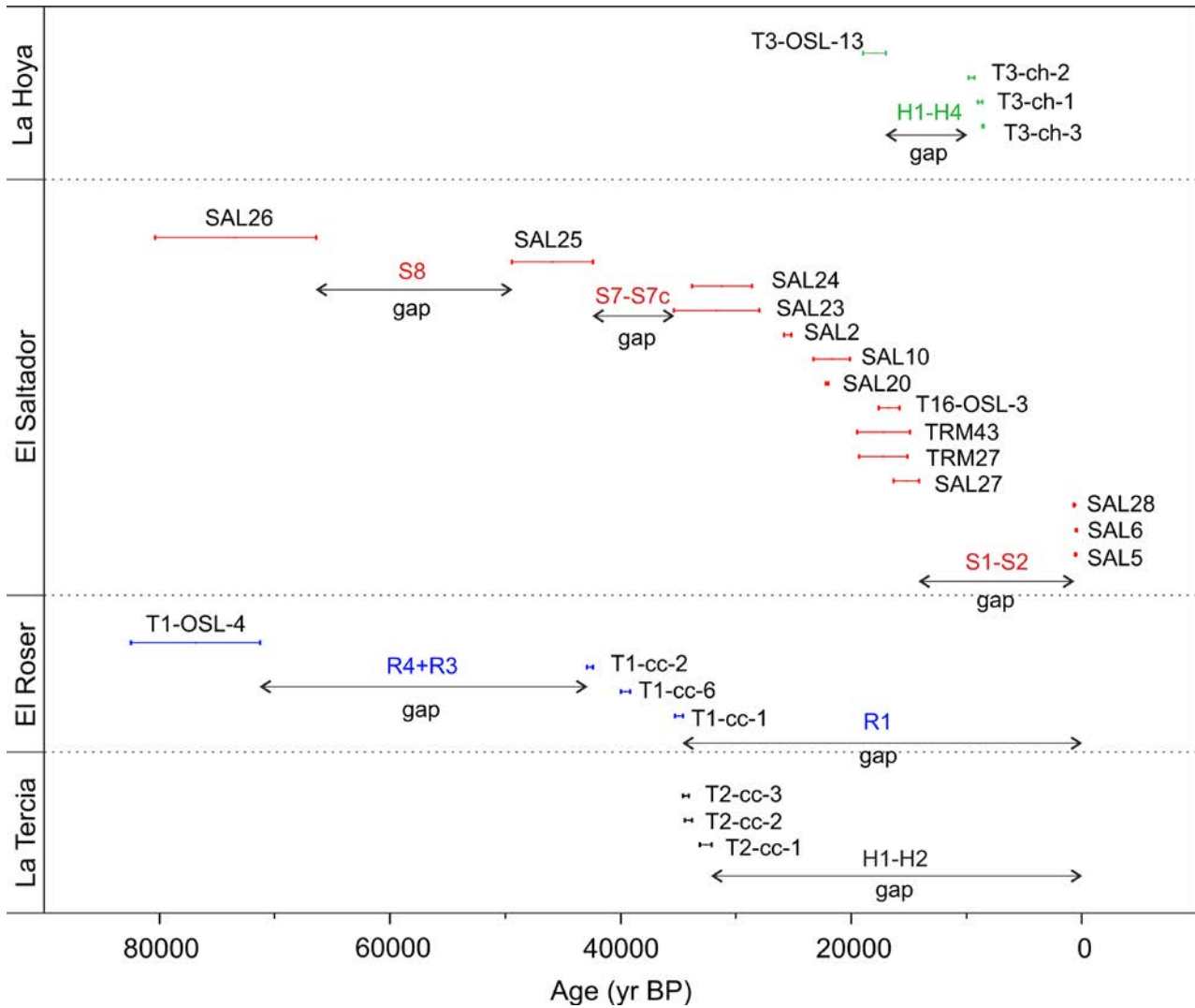


Figure 5.34. Numerical dates used in this study for all the branches with the main sedimentary gaps indicated as well as the events identified in such gaps. The location of each sample in the trench logs can be identified in Figure 5.11 to Figure 5.14 and the numerical dates in Table 5.5.

The time span of event H1 can be correlated with events S1 and S2 (Figure 5.35B), which could imply the under detection of an event in F-AMF. This is compatible with the slip (ED) of the last affected unit in T-3 (unit B) being larger than the EDs generated by events H2-H4 (Table 5.10). Based on the date of S1 (1286-1430 AD) and the skew of the S2 distribution (Figure 5.29), event H1 could likely be historical corresponding to either of these events. In the AMF, the only known historical earthquake to have caused surface rupture is the 1674 AD, identified in the Góñar-Lorca segment (Martínez-Díaz et al., 2018). Assuming H1 as this historical event, the related rupture would necessarily have affected both Góñar-Lorca and Lorca-Totana segments simultaneously, although more dates are needed to constrain the upper limit of this event (unit A in T-3).

The three events H3 to H5 in F-AMF are compatible in time with the three events S2b to S4 in S-AMF (Figure 5.35B). Although the individual event correlation is difficult due to overlap in F-AMF, it cannot be discarded that these earthquakes could be equivalent and ruptured on both sides of the pressure ridge: event H5 corresponding to S4, and H3 and H4 to S3 and S2b, respectively. For H3 and H4 the correlation is more uncertain because both events are dated within a single PDF due to the lack of constraining ages. Event H2 covers the time span without seismic record in S-AMF due to a large gap in the sedimentary record between 15 (unit B) and 0.6 ka (unit A2) (Figure 5.34 and Figure 5.35B) suggesting that an event may be underestimated in this branch. However, although the S2 distribution is skewed towards the age of unit A because it is considered as a coseismic unit (ponded strata), we cannot discard that this event could have happened anytime between ~15 and 0.6 ka, making the correlation with H2 feasible.

The considerably compatible correlation in time and number of events between S-AMF and F-AMF, suggests that these branches might have ruptured together in several occasions during, at least, the last 18 ka. This agrees with the ~0.26 mm/yr vertical slip rate of both branches for the last 15 ka (S-AMF) and 8.5 ka (F-AMF) that suggests a joint uplift of both branches. A joint uplift is compatible with the structural model interpreted for these faults, which infers that they are part of the pressure ridge structure. Despite this, the lack of exact correlation between individual events, does not rule out completely the possibility of these two branches rupturing separately during the last 18 ka.

For the N₁-AMF and N_{2b}-AMF branches the correlation is not as straightforward because the event ages are more uncertain. In the last ~35 ka, the time span of event R1 in N_{2b}-AMF is compatible with all the five events in F-AMF and nine events in S-AMF (S1-S7b) (Figure 5.35A). However, the ED generated by R1 in T-1 (2.6±0.2 m; Table 5.16) does not seem consistent with the occurrence of such a number of events, as it would imply vertical slips per event ~0.3 m, which are considerably smaller than the other event slips in the same branch. Conversely, event R1 is compatible in time with the two events N1 and N2 in N₁-AMF. Although the sedimentary gap since ~35 ka in N_{2b}-AMF hampers the detection of more events, the ED of R1 is larger than other events R2-R4 (Table 5.16) and suggests that R1 could be the record of at least these two events (N1 and N2). The possibility of joint ruptures between N₁-AMF and N_{2b}-AMF is pointed out, although it cannot be proved.

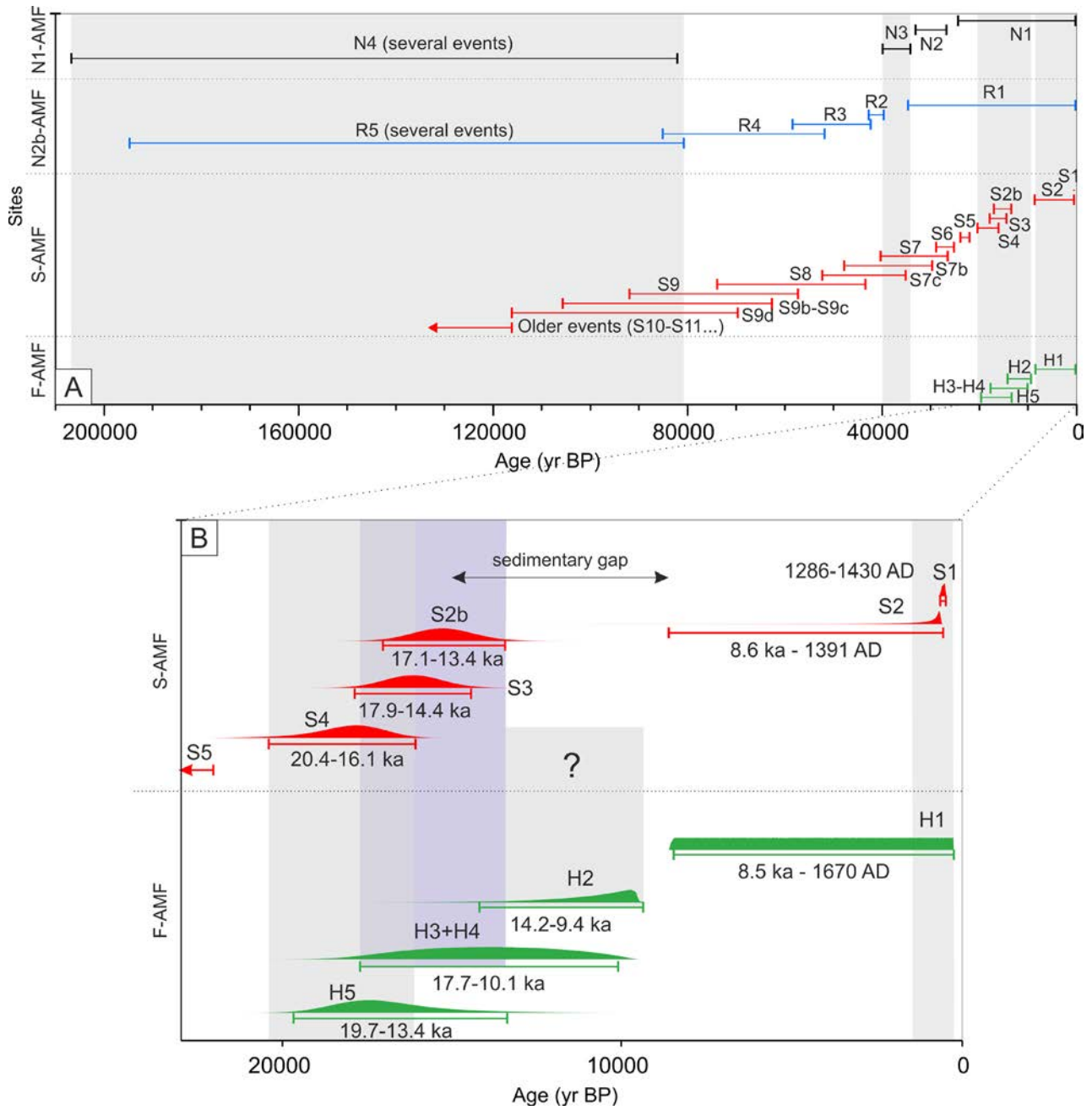


Figure 5.35. A) Earthquake chronosequences of the different fault branches studied. Individual chronosequences can be found in Figure 5.27 to Figure 5.30. Grey bands highlight possible correlations of events mentioned in the text. B) Detail of the chronosequences from S-AMF and F-AMF for the last ~20 ka with possible correlations between events (shaded bands). Note that the large uncertainty in the PDFs of events in F-AMF difficult the individual correlation with S-AMF. Age ranges and horizontal bars refer to the 95.4% confidence interval.

In older periods (>35 ka), event correlation becomes more difficult because the event dates show larger uncertainties. Between the northern branches (N₁-AMF and N_{2b}-AMF) and the S-AMF, the individual correlation is not possible because all events cover wide time spans and overlap in S-AMF. In terms of time compatibility, the eight events between ~35 and ~85 ka in T-16 (S7-S9d) could correspond to any of the two events that

are identified within the same period in N_1 -AMF (N2-N3) and the three in N_{2b} -AMF (R2-R4). In this period (> 35 ka), between the two northern branches, several observations can be done concerning the correlation; Event N3 in N_1 -AMF occur within a period of no deformation between 40 and 35 ka in N_{2b} -AMF, while events R2-R4 take place within a period of inactivity in the N_1 -AMF between 82 and 40 ka (Figure 5.35A). This observation suggests a possible behavior of alternation of the deformation between these two branches. Despite this, it should be noted that events N4 and N3 are dated using numerical dates from unit 2.2 in T-1 (39.2-40.0 ka; Table 5.3) to approximate the age of unit D (see section 5.5.3.2). Because this age is a minimum for unit D, the age of these events might be older and, thus, the behavior described above should be revised.

For periods older than ~ 80 ka, the oldest event horizons N4 and R5 coincide for the most part of their time windows (Figure 5.35A). Because these two likely represent multiple seismic events, a joint or alternative behavior of both branches cannot be approximated. In such case, the coincidence only evidences that both branches have been active at least since ~ 200 ka. In T-16 (S-AMF) these old events could correspond to either of the S9b-S9d and likely to older events S10-S11, which have not been included in the chronosequence due to lack of dates in older units. The presence of various events (minimum of five) older than 80 ka in S-AMF reinforces that N4 and R5 represent multievents.

This study constitutes the first one to integrate paleoearthquake data from branches in a nearly complete segment in the AMF and in the EBSZ. The transect analyzed by Ortuño et al.(2012) in the southwestern AMF lacked two of the four branches and the analysis by Martín-Banda (2020) in the CAF focused on several sites but on a single fault branch. Despite the uncertainties in the correlation made here, the time compatibility of some events suggests that the four studied branches of the Lorca-Totana segment are active and behave as a system, especially S-AMF and F-AMF, and supports that are part of the same seismogenic structure at depth. The complexity of this behavior needs to be characterized in further studies by i) improving and refining the age control of the stratigraphic units limiting the different events and ii) investigating the N_{2a} -AMF, not included here.

5.7.2.2 Recurrence intervals and seismic behavior

The use of OxCal to calculate earthquake chronosequences allowed to infer mean RI and inter-event times for the four fault branches analyzed, available in Table 5.12. Mean recurrences show important variations depending on the branch. In the N_1 -AMF branch,

the RI for the last 40 ka (12.8 ± 7.4 kyr) is a maximum because the sedimentary record of this branch is not available for approximately the last ~ 32 ka. Similarly, the RI of the N_{2b} -AMF for the last 77 ka (17.3 ± 8.8 kyr) constitutes the longest one out of all the trenches. Since the sequence shows a sedimentary gap between the 77 and 43 ka (paleosoil of unit 5) and between 35 ka and the present, this RI value is also likely to be a maximum related to missing the detection of paleoseismic events. In this same branch, Martínez-Díaz & Hernández-Enrile (2001) obtain a RI of 4.8 kyr in the Carraclaca site, which is a smaller value than ours. In that work, the authors use the cumulative vertical slip of the fault in the Cg unit (~ 15 m) and a SPE of 42 cm obtained from coseismic slip measurements. Their SPE value is much lower than our SPE in T-1 (2.0 ± 0.1 m for the last ~ 77 ka), which increases the number of theoretical events and thus reduces the RI. As commented before, our SPE is likely overestimated due to the lack of a complete paleoearthquake record. However, the study in the Carraclaca site is also likely underestimating the SPE (i.e., the RI) because the 42 cm are deduced from two events in an outcrop and not a complete earthquake sequence. In T-1 we observed how event R2 causes an ED of 1.7 ± 0.4 m in a short period of ~ 3 kyr, which suggests that larger SPEs than 42 cm happen in this fault branch. Also, even if more than one earthquake occurred within this 3 kyr time window, the SPE would still be considerably higher than the Carraclaca one.

In the S-AMF, mean RI vary depending on the time period considered: 5.7 ± 1.0 kyr for the last 73 ka and 4.3 ± 0.4 kyr for the last 31 ka, marking a possible increase in the fault activity as also recognized by Ferrater (2016) for the last ~ 30 ka. The shorter recurrence and smaller uncertainties of the last period are due to a better constraining of the events for the last 31 ka (events S1-S6) and is therefore preferred. The longer uncertainties in the long-term RI are due to the presence of unconstrained multievent horizons related to sedimentary gaps in older parts of the sequence, such as event S8 (43.4-73.9 ka) or events S7 to S7c (26.5-52.3 ka) (Figure 5.29). Our RI is in agreement with the 3.5-5.3 kyr for the last 59 ka obtained by Ferrater (2016), but shows a smaller uncertainty range due to the use of the *Zero Boundary* paired with *Boundary* commands in OxCal to constrain the event ages at the base of coseismic ponding units. These commands were not used in the previous study and, instead, events were dated using the *Date* command that provides a uniform and less constrained distribution. In the F-AMF, the mean RI for the last 18 ka

is the shortest out of all the branches (3.1 ± 1.4 kyr), but in the range of the uncertainty of the S-AMF for the last 31 ka (Table 5.12).

Despite the number of events recognized in the trenches, the uncertainty in the event age estimation of each chronosequence has an important repercussion in the mean RI estimations, with larger event uncertainties leading to larger mean recurrences. In the N_1 -AMF and N_{2b} -AMF branches, the recurrence periods are larger than in the other trenches but also show large uncertainties from poor constraining of the respective event chronosequences. Conversely, the better constraining of events in S-AMF and F-AMF leads to shorter RI with significantly smaller uncertainties. In this sense, the chronosequences of these two last branches are considered as more reliable.

- CV estimation

The calculation of the CV of the earthquake chronosequences provides insight on the recurrence behavior of the faults. As pointed out by Cowie et al (2012), paleoseismic studies usually provide poorly constrained CV estimations due to the intrinsically poor constraining of paleoseismic events in trenches. Here we only discuss the CV estimation of the S-AMF because it is where the paleoearthquake record is more complete (Figure 5.29) and hence more reliable. Oppositely, in the N_1 -AMF or the N_{2b} -AMF the detection of paleoearthquakes is hampered by the presence of large sedimentary gaps, which would likely influence the CV and compromise its reliability. The type of alluvial environment in southeastern Spain, dominated by uncontinuous sedimentation, is the main cause of such incomplete paleoearthquake records. In the N_1 -AMF and N_{2b} -AMF this is aggravated by their higher position within El Saltador fan, which makes erosion easier. Conversely, in the S-AMF, the tectonic barrier acts as a sedimentary prone area or “sedimentary trap”.

The CV of S-AMF varies between 1 and 0.8 depending on the number of paleoearthquakes considered (last seven since 31 ka or last eleven since 73 ka, respectively), inferring a random (Poissonian) to weakly periodic behavior (or strongly aperiodic; Salditch et al., 2020). These CV values agree with findings in other regions. For instance, Moernaut (2020) points out the link between slip rate and CV and observes from many studies worldwide (see references therein) that $CV > 0.85$ are exclusively found in faults systems characterized by low slip rates < 7 mm/yr. Conversely, periodic recurrences ($CV < 0.8$) usually occur on plate boundary regions, as suggested by Berryman

et al. (2012) in the Alpine Fault of New Zealand. Having said that, although both CV values in S-AMF are similar, the latter is probably less reliable because it is influenced by the poor age constraints of older events S7 to S8. This relates to the presence of sedimentary gaps providing unconstrained event PDFs for S7 to S7c and S8, and also to the lack of available dates, which forced the use of OxCal commands to artificially model individual event PDFs for S7 to S7c (Figure 5.29). In addition, the presence of a sedimentary gap in the sequence between the last ~15 ka and historical times (Figure 5.34), might also affect the CV in the better constrained sequence (last seven events), although in a lower degree since the gap is smaller. In this latter respect, further effort should be put in better constraining the earthquake history of this fault in recent times. One option could be the development of paleoseismic studies in creeks, where the most recent sedimentation is located. The successful results in F-AMF at La Hoya site (T-3) in this thesis or in the Góñar-Lorca segment (Martínez-Díaz et al., 2018), might serve as a precedent to that.

5.7.2.3 Implications of the constrained recurrences within the Eastern Betics Shear Zone setting

The event chronosequences identified in this thesis have contributed to complete the paleoearthquake record of the Lorca-Totana segment of the AMF, evidencing for the first time the time compatibility of simultaneous ruptures in two different fault branches of the segment (at least the last five events in S-AMF and F-AMF; Figure 5.35). So far, this record is the most complete within the EBSZ and the overall Iberian Peninsula, although this resolution is heterogeneous among the different branches. In this section, we compare the chronosequences obtained in this study with the ones from the latest paleoseismic studies developed in different faults of the EBSZ.

With exception of the S-AMF and F-AMF for the last ~18 ka, the earthquake chronosequences of the different branches in the Lorca-Totana segment are difficult to correlate due to the large time uncertainties of the events in most faults. If compared with other AMF segments (Figure 5.36), in the Góñar-Lorca segment (Ortuño et al., 2012) the chronosequences do not allow to establish linked ruptures with the Lorca-Totana segment, as most events overlap in time. For instance, event PE1 in Góñar-Lorca, could have been events N1 in N₁-AMF, R1 in N_{2b}-AMF or several events from S-AMF (S2-S5) and F-AMF (H1-H5). In any case, the large overlapping uncertainties do not allow to neither prove or reject the possibility of synchronic ruptures between both segments.

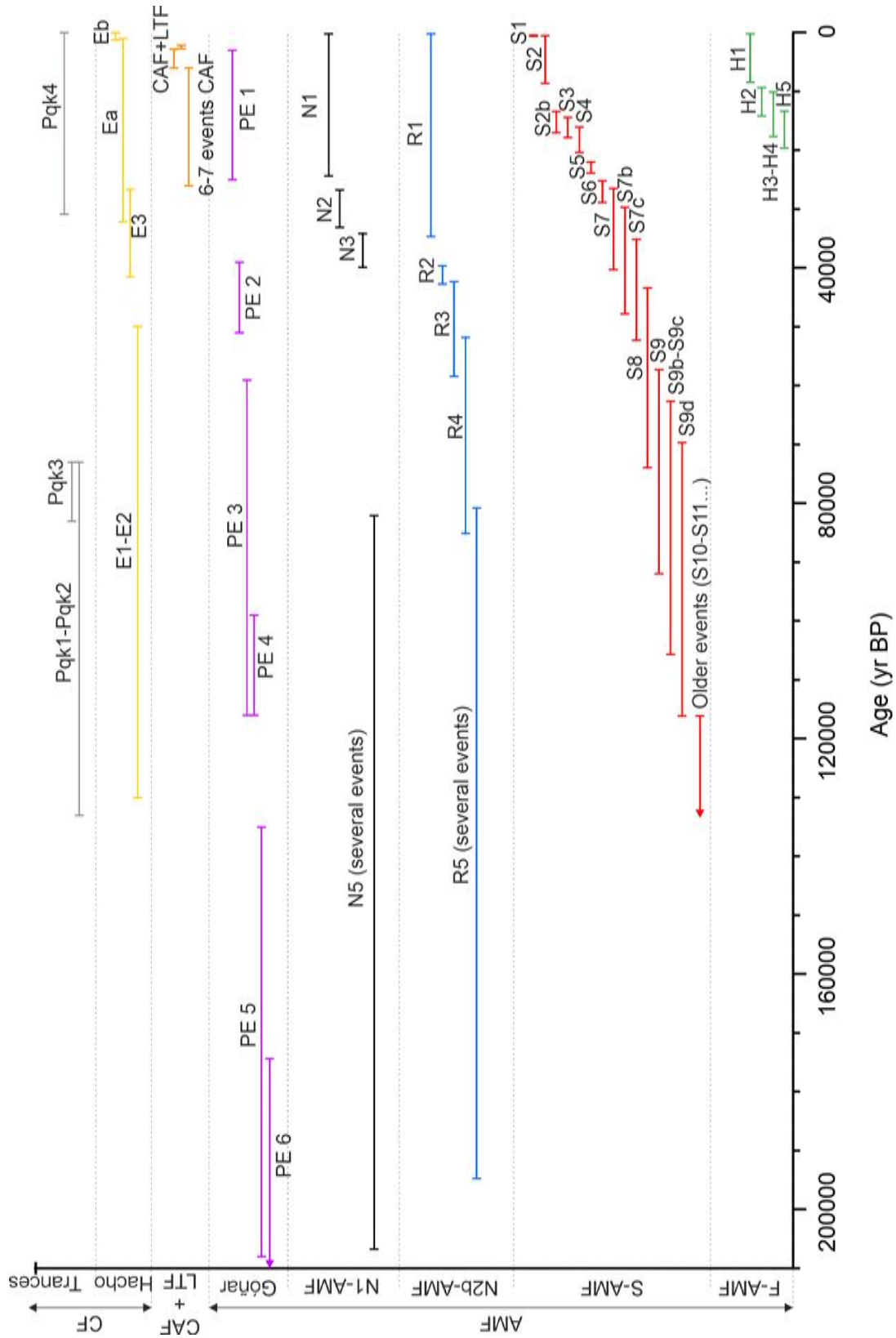


Figure 5.36. Earthquake chronosequences of the different fault branches studied plotted together with the chronosequences from different studies developed in other EBSZ faults. Event ages of the Carboneras Fault (CF) in El Hacho site are extracted from Moreno (2011), while in Los Trances site from Masana et al. (2018). Event ages of the Carrascoy Fault (CAF) and Los Tollos Fault (LTF) are extracted from Martín-Banda (2020) and event ages of the Góñar-Lorca segment of the Alhama de Murcia Fault (AMF) are extracted from Ortuño et al. (2012).

In the CF, two sites have been studied. At El Hacho site, a minimum of five paleoearthquakes are identified since ~ 130 ka, and the last event Eb could correspond to the 1522 Almería earthquake (Moreno, 2011). At Los Trances site (Masana et al., 2018), a minimum of four paleoearthquakes are identified since ~ 133 ka, although in this case the constraining of the events is too poor to be correlated with the events at El Hacho site (Figure 5.36).

In the CAF, at least eight to nine paleoearthquakes are identified for the last ~ 26 ka, the last two between 2-6 ka interpreted as joint ruptures with the LTF (Martín-Banda et al., 2015; Martín-Banda, 2020). The time span of these last two earthquakes is compatible in time with events S2 of S-AMF and H1 in F-AMF (Figure 5.36). The possibility of these events being part of the same rupture is small because both faults show opposite dips, different kinematics and are separated for more than 10 km, which according to segmentation rules from Boncio et al. (2004) or Field et al. (2014) is a large distance that would typically prevent a rupture from propagating. In this sense, in Gómez-Novell et al. (2020), the rupture scenarios regarded for the EBSZ do not consider AMF to rupture simultaneously with any other EBSZ due to these particularities. However, the possibility of a stress transfer triggering between both faults cannot be discarded in this case and should be explored in the future. The coincidence in slip rate accelerations between 25 and 34 ka in both faults reinforces this possibility.

In terms of recurrence, the estimated RI for other faults of the EBSZ are generally longer than the ones estimated for the AMF in this study, especially in the S-AMF and F-AMF branches. This is mainly related to the larger uncertainty ranges in the event estimation (e.g., Moreno, 2011) that contribute to enlarge these recurrence estimations. Also, the differences in the time periods considered for the recurrence calculations prevent from an accurate comparison. The recurrences in the Góñar-Lorca segment of the AMF are 15-29 kyr for the last 59-116 ka (Ortuño et al., 2012) and are similar to the ones obtained in the N_{2b}-AMF (17.3 ± 8.8 kyr for the last 77 ka). The similar uncertainty ranges in the events of both faults (Figure 5.36) suggest that in both cases these recurrences are a maximum and affected by the non-continuous deposition in both sites. In the CF, the recurrences inferred for both El Hacho and Los Trances sites (13.8 and 33 kyr for the last 41.5 and 133 ka, respectively; Moreno, 2011; Masana et al., 2018) are also a maximum, as suggested by the much shorter recurrence calculated numerically using the slip rate and slip per event (1.1 kyr; Moreno, 2011). In CF and LTF, the better constraining of the

last two events since ~ 6 ka, allows to infer shorter recurrence periods (2.2-6.9 kyr for LTF and 3.3 ± 0.7 kyr for CAF; Martín-Banda, 2020) that are in agreement with the RI for the S-AMF and F-AMF (4.3 ± 0.4 and 3.1 ± 1.4 kyr for the last 31 and 18 ka, respectively). These short and constrained values possibly approximate better the recurrence of large earthquakes in the EBSZ, although the periods analyzed in the CAF and LTF are considerably shorter (last 6 ka) and could be affected by clustering.

In conclusion, the earthquake chronosequences obtained in this thesis are difficult to correlate with the ones in other EBSZ faults because the paleoseismic records are discontinuous and because the uncertainties of event ages are generally too large to be correlated. In this context, the record of S-AMF shows the better constrained sequence, especially for the last ~ 31 ka (since event S6), and therefore it is the most reliable in the EBSZ so far.

5.8 Discussion on the seismic potential of the AMF

In this section, the seismic potential of the AMF is discussed in terms of maximum expected magnitude from SPE, ED and surface rupture length (SRL). We also discuss the implications of the use of each parameter into the seismic potential.

The SPEs inferred in this thesis (Table 5.16) range from 2 to 8.4 m. Although in some cases such estimations are a maximum (S-AMF or N_1 -AMF), the obtained magnitudes for the events range between M_w 7.1 and 7.7 based on the empirical relationship of maximum displacement for strike slip faults by Wells and Coppersmith, (1994). The largest magnitudes are obtained for the SPE of S-AMF and short periods because the scarcity of sedimentary record since ~ 15 ka probably hampers the identification of paleoearthquakes, highlighting that the inferred event magnitudes are overestimated. Similarly, the large 8.1 m SPE in the N_1 -AMF is a maximum affected by a sedimentary gap since ~ 32 ka.

The occurrence of a joint rupture between two or more fault branches within the Lorca-Totana segment should not be overruled considering the time compatibility of events between S-AMF and F-AMF. In this respect, a joint rupture of all four branches would imply the sum of SPE of each involved branch and larger magnitudes than considering single branch ruptures. Adding the vectorial components (vertical and lateral) of the long-term SPEs for all four branches (Table 5.16) in a general 70° fault plane, also subtracting the vertical component of the S-AMF from F-AMF, infers a total net SPE of ~ 12 m. This

would cause extraordinary magnitudes up to \sim Mw 7.8-7.9 (Wells and Coppersmith, 1994 for strike slip). Refining earthquake chronosequences is then necessary to evaluate the feasibility of such scenarios as the implications for the seismic hazard are evident.

Because the SPE is an average parameter, it might be masking the contribution of large fault slips. In this respect, the ED (Table 5.16) might help to estimate better the maximum magnitudes produced by each individual earthquake and their variability in time within the trench sequences. For this, we exclude the ED representing more than a single event and those located in sedimentary gaps because they might also represent multievent horizons (i.e., R3 to R5, S8 and S7 to S7c or H1 and H5). In this respect, the most reliable EDs are R2 in T-1 (mean of 1.5m) and H2 to H4 in T-3 (0.3 up to 2.0 m), which imply magnitudes of Mw 6.3-7.1 (Wells and Coppersmith, 1994 for strike-slip). The variability in these magnitudes depicts the variability on the fault slips during the consecutive events. However, because fault slip is a variable parameter along-strike (e.g., Kearse et al., 2018), the presence of slip dispersion alone does not allow to clearly identify if it is due to the occurrence of different magnitudes or to other causes such as the location within the surface fault rupture (central part or tips). Although this variability in fault slip data is inconclusive in terms of cause, from our perspective it seems unfeasible that all earthquakes in the AMF correspond to similar sized ruptures. The precedent of the 2011 Lorca earthquake sequence proved that moderate earthquakes are also produced by the AMF. In addition, the magnitude-frequency distributions from the modelling in section 7.2 of this thesis (Gómez-Novell et al. 2020a) suggest that a Gutenberg-Richter distribution in the AMF agrees with the regional seismic catalogue and paleoseismic data.

Generally, the use of fault displacements, whether it is the average SPE or individual ED, to infer earthquake magnitude is less reliable than the use of the surface rupture length. As commented, the fault slips might be overestimated due to poor paleoseismic resolution or can show contrasting values for a same SRL, as pointed by Wells and Coppersmith (1994). For this reason, here we use both relationships from Wells and Coppersmith (1994) and Stirling et al. (2013) for strike-slip faults to infer the M_{\max} from the SRL (considering a crustal width of 13 km; Martínez-Díaz et al., 2012b) (Table 5.17). The SRL of the complete Lorca-Totana segment (\sim 23 km) would imply magnitudes of Mw \sim 7.1. The rupture of both the Góñar-Lorca and Lorca-Totana segments (\sim 51 km) would cause magnitudes of Mw 7.1 -7.2 and the rupture of the complete fault (87 km), Mw 7.3-7.5. These values point out that the rupture of two segments or the complete fault

is required to achieve the magnitudes caused by the SPE and ED considering a single-branch rupture.

Rupture scenario	M _w ($\pm 1\sigma$)	Empirical relationship
Lorca-Totana segment (23 km)	6.7 \pm 0.2	(Wells and Coppersmith, 1994)
	6.7 \pm 0.1	(Stirling et al., 2013)
Lorca Totana + Góñar Lorca segments (51 km)	7.1 \pm 0.2	(Wells and Coppersmith, 1994)
	7.2 \pm 0.1	(Stirling et al., 2013)
Complete AMF rupture (87 km)	7.3 \pm 0.2	(Wells and Coppersmith, 1994)
	7.5 \pm 0.1	(Stirling et al., 2013)

Table 5.17. Maximum magnitude estimations of the AMF according to scaling relationships using the surface rupture length (SRL) of different rupture hypotheses.

Simultaneous ruptures of different branches within the Lorca-Totana segment are regarded as feasible, at least for the two S-AMF and F-AMF according to the coincident event chronosequences and almost identical similar vertical slip rates for the last 18 ka. This likely suggests that both branches rupture together in large earthquakes, more so being part of the same pressure ridge structure. In this respect, despite the variability of the parameter, to achieve the cumulative SPE of rupturing all the branches in the Lorca-Totana segment (~ 12 m), the SRL of at least the whole AMF is required, probably even more. So far, it is still unknown which rupture scenario within the AMF, i.e., single segment rupture, whole fault rupture, etc., favors the occurrence of such simultaneous ruptures or the possible frequency patterns. Furthermore, the feasibility of linked ruptures between AMF and other faults of the EBSZ remains undisclosed as more data is needed to characterize their possible linkage. Here, the 1980 Ms 7.3 El Asnam earthquake, which happened in a similar tectonic setting at the North African coast, might serve as a precedent since the fault rupture propagated through barriers between segments of the fault (King and Yielding, 1984). Having said that, the feasibility of complex ruptures between segments cannot be discarded in the AMF nor can the linked ruptures with other faults of the system. In favor of this, the recent modellings such as the one presented in section 7 or the physics-based approach by Herrero-Barbero et al. (2021) highlight the feasibility of linked ruptures in the EBSZ.

5.9 Overview: structure and tectonic evolution of the Lorca-Totana segment

In this section we evaluate the structural and tectonic evolution of the Lorca-Totana segment based on the observations and data obtained in this chapter. We also propose a deep structure model for the AMF based on our surface data (Figure 5.37).

The deformation features and structure characterized in the Lorca-Totana segment of the AMF lead to infer a partitioning of the deformation between the different five branches of the segment. The inferred decreased activity of the northern N_{2b}-AMF might have caused an increase of such activity towards the S in the pressure ridge limited by the S-AMF and F-AMF. This fact could also be the responsible for the abandonment of El Salvador alluvial fan and incision of channelized alluvial systems between 35 and 25 ka, as identified in T-1 and T-16, respectively. During this time, the decreased activity in the mountain front of La Tercia range, could have caused the migration of the alluvial deposition towards the S (e.g., Ferrater, 2016; Martínez-Díaz et al., 2003), at the base of the pressure ridge.

The frontal migration of the activity is characteristic of the evolution in mountain ranges, where younger activity is registered towards the foreland basins (e.g., Vergés et al., 2002), in this case, the Guadalentín basin. This evolutive model would suggest that the F-AMF is the youngest structure in the segment, however such statement cannot be proved nor rejected based on the data presented here. On the one hand, the fact that the thick Plio-Quaternary sequence in T-0 and T-4 (La Hoya site; Figure 5.14) shows the same degree of deformation (~45° tilting towards the SE) could support that they have been deformed long after their deposition. On the other hand, the onset of this deformation is not clear especially because the deformation caused by the F-AMF in the underlying Miocene materials is not cropping out. If the Miocene and Plio-Quaternary rocks were concordant as we propose (Figure 5.37), the deformation could in fact have started shortly after the deposition of the latter sequence. In either case, the deformation started long before ~19 ka, which is the oldest age of the materials in T-3, much less deformed than the Plio-Quaternary sequence.

Concerning the lateral deformation of the segment it is mainly absorbed by the S-AMF, which explains the numerous geomorphic features supporting left-lateral kinematics along this fault and large number of paleoearthquakes identified in El Salvador site (minimum of seventeen for the last ~100-130 ka). The N₁-AMF branch also absorbs lateral component of the fault, although its role is probably secondary due to the lower

inferred slip rates and less marked geomorphic footprint. This branch limits La Tercia range front, with an uplift of at least ~ 650 m (Ferrater, 2016), an observation that contrasts with the almost pure strike-slip kinematics inferred in Quaternary materials. The current strike-slip character of the N₁-AMF combined with the relief of the La Tercia range suggests a change in the kinematics, which could have started at least around 198 ka, marked by the age of the first Quaternary alluvial unit (Cg unit).

During the onset of the neotectonic period in the Late Miocene the AMF reactivated from a normal fault limiting Neogene basins to the NW to an oblique reverse fault in a transpressive context (Montenat, 1973; Meijninger and Vissers, 2006). We thus propose that the N₁-AMF branch could be one of such structures acting as a mainly reverse fault during the transpressive inversion, supported by the fact that the fault uplifts La Tercia range and limits the former Neogene Lorca basin to the NW. In this context, the other branches, mainly S-AMF and F-AMF, could have formed during the neotectonic period (since Late Miocene), and as a response to the orientation of the fault to the compressional regional stress field from the Africa-Nubia convergence.

The more perpendicular orientation of the Lorca-Totana segment ($\sim N80^\circ$; Figure 5.1A) to the NNW-SSE convergence vector ($\sim N150^\circ$; Martínez-Díaz et al., 2012b), probably enhanced a larger amount of shortening perpendicular to the faults and the consequent higher reverse component compared to the Góñar-Lorca segment. This situation could have favored the formation of the different branches to absorb the total amount of shortening, which N₁-AMF might not have been able to accommodate alone. The presence of the F-AMF in the frontal part of the segment supports this since low-angle faults can accommodate shortening more effectively than high angle faults. Tectonic inversion evidence has been found in the Alhama-Alcantarilla segment by Herrero-Barbero et al. (2020). These authors identify a decrease in the dip of the AMF to the surface in the Alhama-Alcantarilla segment, which is interpreted as a reverse-fault refraction from the compressional reactivation. Based on this, we suggest that the low-angle F-AMF could be one of these refraction structures from the reactivation created to accommodate the higher shortening of the convergence. Conversely, the strike slip component from the transpressive regime is absorbed by high angle faults (e.g., S-AMF). Having said that, it should be acknowledged that the kinematics observed in the surface might not necessarily reflect the fault's accommodation of the compression at depth. This means that it is also possible that the multi-branch character and slip partitioning observed

for the AMF here are just related to tectonic readjustments to accommodate the compression in the surface, where the confinement pressure is decreased. Geophysical data at depth is needed to further investigate the evolutive hypotheses proposed here.

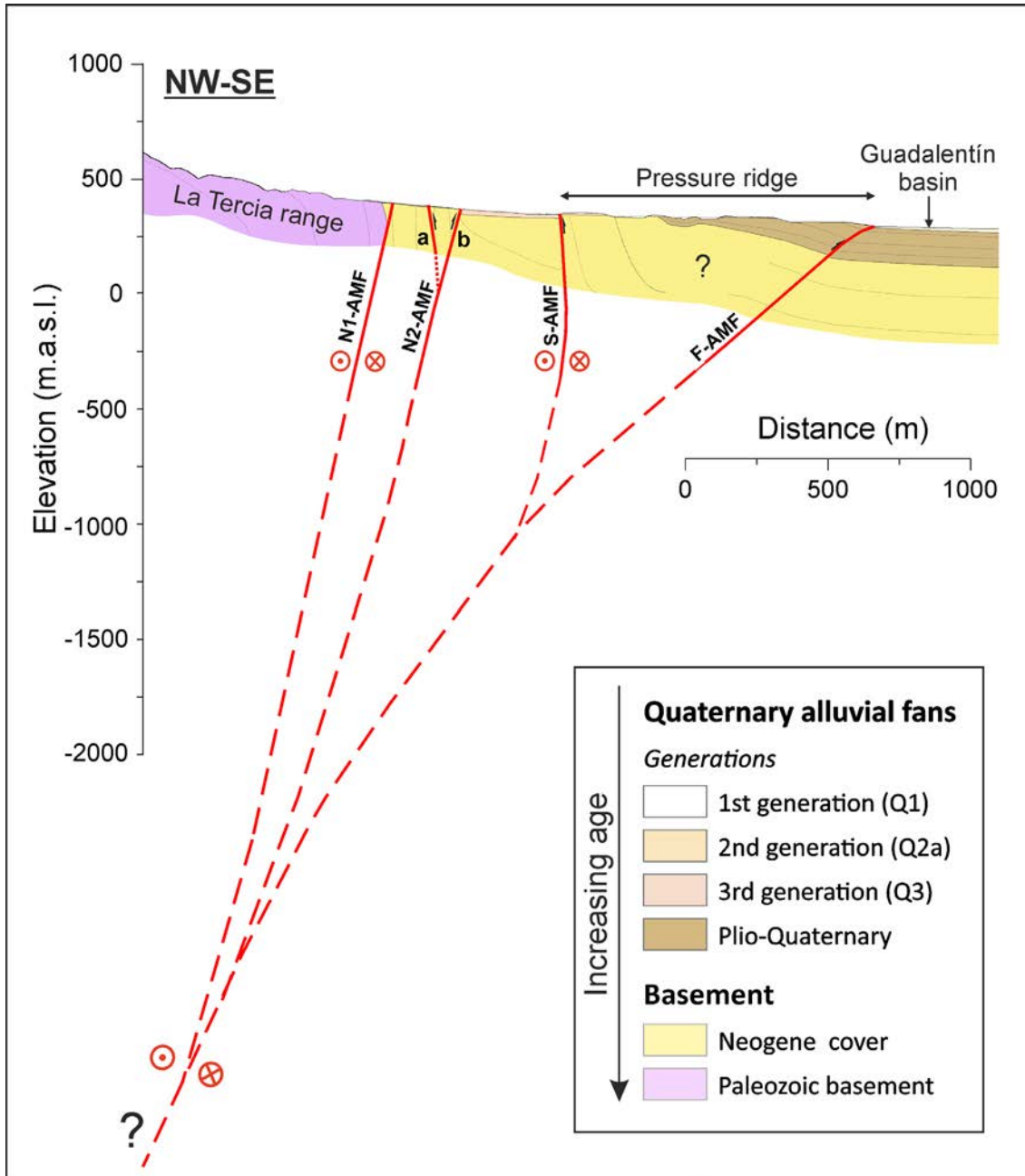


Figure 5.37. Proposal of deep structure of the Lorca-Totana segment of the Alhama de Murcia Fault (AMF) based on surface data obtained in this thesis. The geological section and its location is the same as the one depicted in Figure 5.3. Note that, according to this interpretation, the branches S-AMF and F-AMF form a pressure ridge that links at depth in a shallower position than the rest of the branches. In this model, N₁-AMF could correspond to a Neogene structure reactivated during the neotectonic period (since Late Miocene).

In the Góñar-Lorca segment (except for the horse tail termination), the less perpendicular strike (NNE-SSW) to the NNW-SSE convergence implied lower reverse component. This is consistent with the less prominent relief related to the AMF in this segment (Las Estancias range) and the long-term lateral slip rates comparable to the Lorca-Totana (1.6-1.7 mm/yr; Ferrater et al., 2017). The lower fault-convergence perpendicularity might have resulted in a narrower fault zone being able to absorb most part of the left-lateral deformation without partitioning in several branches. Geophysical data in La Torrecilla site is coherent with this: a 70° NW-dipping structure is identified with a fault zone narrower (<1 km) than the Lorca-Totana segment (>2 km) (Martí et al., 2020).

The proposed interpretation suggests that the studied branches of the Lorca-Totana segment link at depth because they are part of the same tectonic structure. We propose the model in Figure 5.37, in which all branches link at the northern part of the system, interpreted as the original structure upon which the current AMF is developed on. Remarkably, this interpretation only relies on surface data and no subsurface nor geophysical data are available to corroborate it. Furthermore, detailed structural studies in the region should focus on better characterizing the structure of the studied segment in the surface and at depth. It is crucial to better understand the role of each fault branch within the AMF system, their associated deformation, the tectonic relationships among them and their evolution.

6 Structural data for potential future paleoseismic sites in the Totana-Alhama segment of the Alhama de Murcia Fault

6.1 Introduction

The first steps of the paleoseismic research in the present thesis, implied carrying out explorative field surveys in different parts of the Alhama de Murcia Fault (AMF) to select the most suitable sites for a paleoseismic trench study. Originally and in addition to the Lorca-Totana segment, one of the targets for the development of this study was the Totana-Alhama segment of the fault mainly because of: i) the scarcity of available data compared to other segments of the fault as it had never been studied with paleoseismic approaches and ii) the presence of geomorphologic and structural evidence of tectonic activity such as fault scarps or deflections affecting Quaternary alluvial deposits (e.g., (Herrero-Gil, 2014; Ferrater et al., 2015c). This placed the interest in that segment as it could help to i) understand and characterize its paleoseismic activity during the Quaternary and ii) to unveil the role of the segment within the AMF system, especially given the loss of surface expression in this sector and towards the NE, compared to the southwestern segments (Figure 6.1). Despite the lack of paleoseismic studies there, evidence for at least one surface rupturing historical earthquake around 1550 BC has been revealed by the presence of earthquake archaeological effects in a Bronze Age settlement (Tira del Lienzo; Figure 6.2) (Ferrater et al., 2015c). This reinforces the seismogenic potential of the segment and highlights the need for paleoseismic research.

Three field surveys and detailed photointerpretation were carried out along the segment to perform a geomorphological mapping of faults and alluvial fans (see methods of section 3.1), and a preliminary structural analysis of their Quaternary deformation and activity. This eventually led to the selection of a site to perform a paleoseismic survey and planning for the opening paleoseismic trenches across the Amarguillo Fault (AF), named by Martínez-Díaz et al., (2012b) for the first time. In this work we have constrained the length of the AF in ~11 km long, being a NNE-SSW ramification of the AMF (Figure 6.1) and constituting one of the most geomorphologically prominent structures of the Totana-Alhama segment. This fault bounds the Espuña Range to the E and it is composed by several sub-parallel fault strands that generate scarps in the Quaternary alluvial deposits. Despite the scarcity of published works for this fault, the AF has been interpreted as a structure of the AMF with vertical component that generates the sinking of the western block (Martínez-Díaz et al., 2012b).

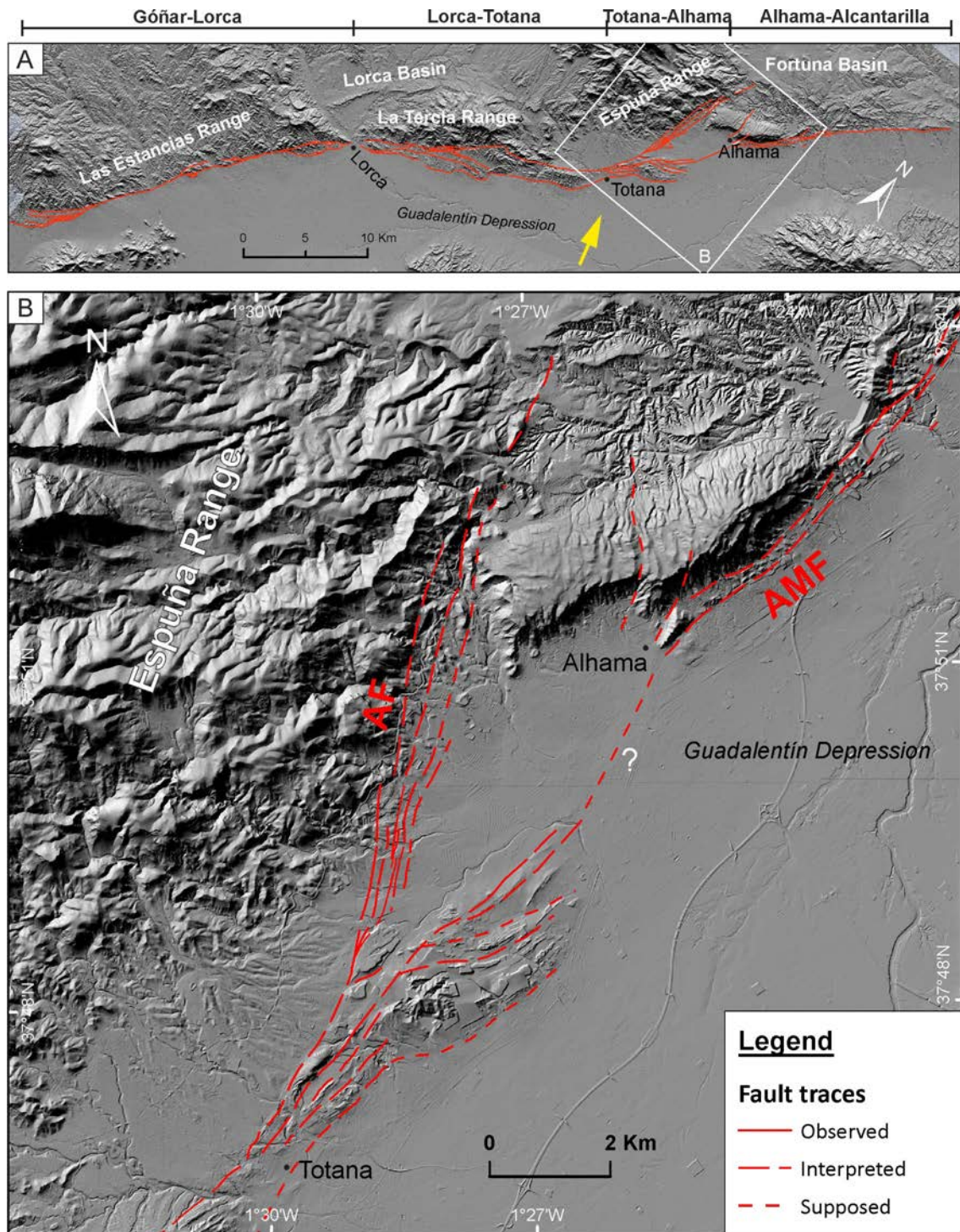


Figure 6.1. A) Location of the studied area within the segments of the Alhama de Murcia fault (AMF). Yellow arrow depicts the mean regional shortening vector $\sim N164^\circ$ from Echeverría et al. (2013). B) Cartography of the fault traces of the Totana-Alhama segment, classified in levels of confidence according to the legend. AF: Amarguillo Fault. Relief is obtained from the 2m resolution DEM from IGN agency (centrodedescargas.cnig.es).

Recently, a geomorphological study (Herrero-Gil, 2014) identified and quantifies the Quaternary expression of activity in the AF including scarps, lineaments and offset markers. The study presents a mapping and interpretation of the fault as a negative flower-

structure with oblique-sinistral kinematics, capable to generate magnitudes above Mw 6.0 and significant from the seismic hazard point of view. The use of these data for the detection and discussion of potential paleoseismic sites however was not the object of previous studies, which motivates our work there.

The paleoseismic study planned for the AF could not be developed during this thesis due to the continue delays during the obtention of permits from the land owner, which forced the re-configuration of the paleoseismic study and led to focus in the Lorca-Totana segment (section 5). Nonetheless and to serve as a preliminary basis for future paleoseismic works, all the relevant field observations, mapping and data for the site selection performed during this process are summarized in this section. We present i) a cartography of the Totana-Alhama segment of the AMF, refined with respect to the one from Herrero-Gil (2014) for the fault traces and alluvial fans, ii) the description of the main deformational features related to the AF including field observations and iii) the selection of a site and proposal for a potential future trenching survey.

6.2 Cartography and structure of the Totana-Alhama segment

The Totana-Alhama segment is a singular zone in which the AMF ramifies in two main structures NE of Totana city. One ramification shows a NE-SW orientation and constitutes the continuation of the AMF towards the Alhama de Murcia city in the Alhama-Alcantarilla segment. This forms a relatively wide (~1.5 km) deformation zone with several fault strands forming a horse-tail like structure and generating the uplift of a series of reliefs to the SE that limit the northwestern border of the Guadalentín Depression (Figure 6.2). These reliefs also act as a barrier for the alluvial drainage coming from the Espuña Range, especially near Totana. To the NE and towards Alhama city, the structure loses almost completely its geomorphic expression making its cartography very difficult. The other ramification is the Amarguillo fault (AF), which has a NNE-SSW (~N10°) orientation and a narrower deformation zone (~600-700m) composed by at least five subparallel fault branches (Figure 6.2). Contrary to the AMF, the AF shows a clear geomorphic expression towards the NE that extends up to the southern limits of the Fortuna basin (Figure 6.1A). The fault produces a series of fault scarps, lineations and left-lateral drainage channel deflections on the surfaces of the alluvial fans that evidence a clear activity of this fault during the Quaternary. Compared to the AMF, the AF shows a very clear vertical component, which might be suggesting that the latter is accommodating an important part of the vertical deformation.

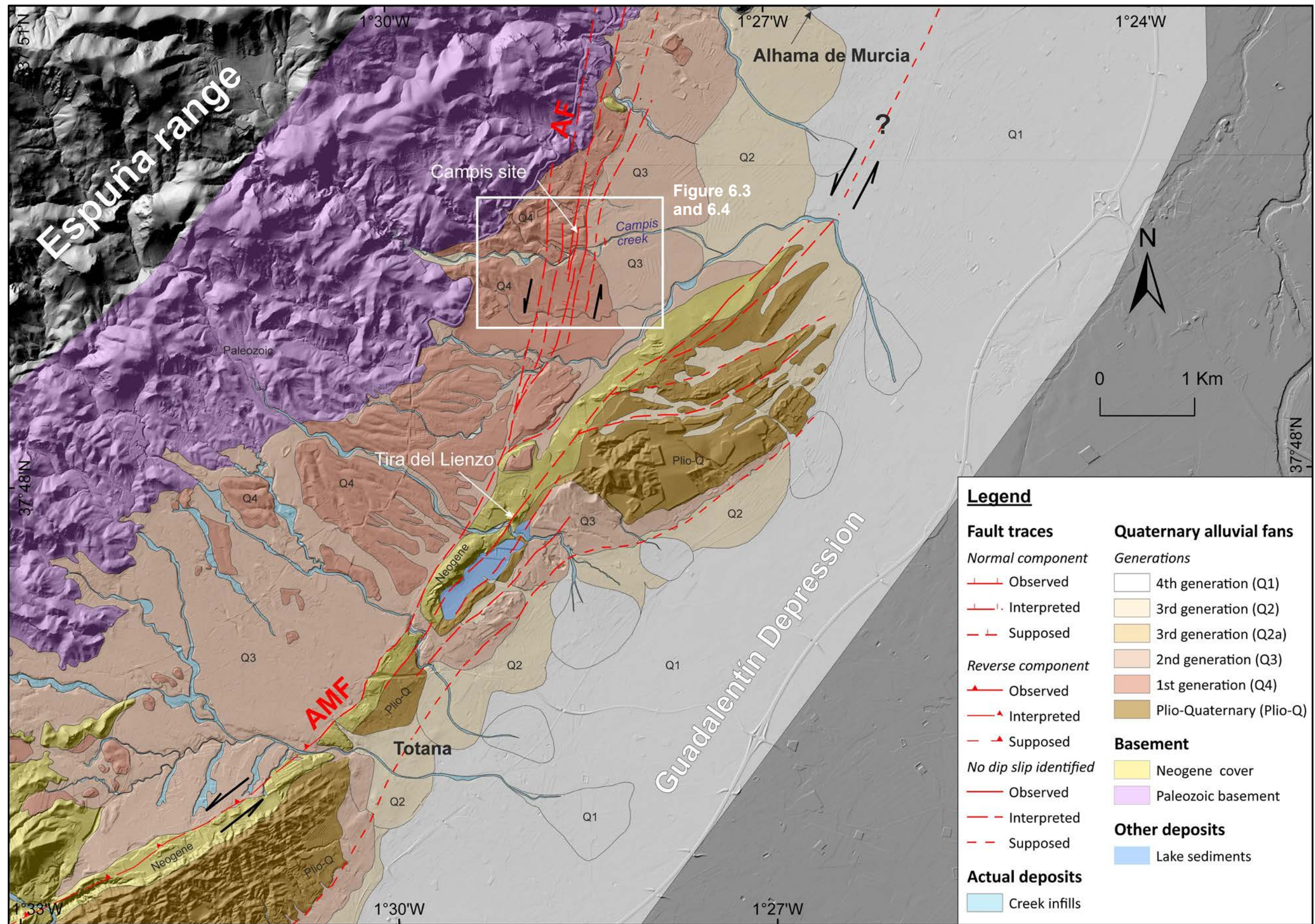


Figure 6.2. Geological map of the Totana Alhama segment of the Alhama de Murcia Fault (AMF) done in this study, including the Amarguillo Fault (AF). The locations mentioned throughout the text of the section are indicated: Campis creek, Campis site and Tira del Lienzo. Relief is obtained from the LiDAR-based 2m resolution DEM from IGN agency (centrodedescargas.cnig.es). See Annex II (A) for the uninterpreted DEM of this map. Basement cartography is based on the Spanish Geological Map (1:50000) zone 2100 (Marín-Lechado et al., 2011).

The alluvial materials affected by the faults in this segment are generally older than the ones from the Lorca-Totana segment. We use the same alluvial fan generation classification as for that segment, explained in section 5.3, which is based in the classifications by Silva et al. (1992b), in Silva (2014) and Martínez-Díaz et al. (2003). The AF mainly affects materials from the Q3 and especially Q4 alluvial generations that come from the drainages in the Espuña range (Figure 6.2). These show important calcrete developments on top, allowing for the preservation of fault scarps and other tectonic structures as we detail in section 6.3. The AMF conversely affects Miocene basement rocks (mainly marls and gypsums) and Plio-Quaternary alluvials that, in general, show a weaker geomorphological expression (Figure 6.2). This might be one of the reasons why an intense anthropization is found in this last location, making the identification and characterization of the fault zone in the field and DEMs even more difficult.

Like the Lorca-Totana segment, younger alluvial materials from the Q2 and Q1 generations are found towards the SE, in the frontal parts of the reliefs generated by the fault and bounding the Guadalentín Depression, although no clear geomorphological evidence of a frontal fault is recognized.

In this area, we have relied strongly on the aerial pictures from the 1956-57 American flight due to the intense anthropization that is present nowadays in this area. This anthropization causes the excavation of alluvial fan deposits or infilling of creeks for agricultural purposes, difficulting the identification of tectonic features. We refer the reader to the Annex II (A) for the aerial picture zoom in this zone.

6.3 Deformation related to the Amarguillo Fault

The Amarguillo Fault (AF) is the frontal fault of the Espuña range, limiting it to the E (Martínez-Díaz et al., 2012b). Similar to La Tercia range it is one of the main mountain ranges whose origin is related to the Miocene extensional period. The Espuña range is limited by the Lorca basin to the SW and by the Fortuna basin towards the NE (Figure 6.1A), both Neogene basins formed during the pre-inversion extensional period. The tectonic inversion during the Late Miocene, caused the the inversion of these basins and the uplift Espuña range by the activity of extensional faults in its footwall (Ferrater et al., 2015b), one of which is the AF.

The AF is composed by at least five subparallel fault branches that affect the alluvial fans from the Q3 and Q4 generations. The faults show subvertical dips (average $\sim 86^\circ$) and the

fault zone is displayed as a set of subparallel branches that form small horst-graben structures in the calcrete surfaces of the alluvial fans mainly by folding. In the DEM this is recognized as scarps, lineations and beheaded drainage channel incisions throughout the fan surfaces. One remarkable case is identified on the fan surface N of Campis creek, where the folding of the fan surfaces generating scarps is very clear, or S of this same creek, where small channel incisions are beheaded (Figure 6.3).

Although the faults show subvertical dips, we interpret them as mostly normal faults related to local transtension. The AF is more subparallel to the NNW-SSE maximum shortening vector in the Guadalupe basin ($N164\pm 7^\circ$; Echeverria et al. 2013) (Figure 6.1A) than any other AMF segment, which favours local extension and the development of a transtensional environment or bend (e.g., Sylvester, 1988). The horst and graben configuration of this fault is also consistent with a transtensional model and, in this respect, the several branches of the AF could correspond to a negative flower structure as previously suggested by Herrero-Gil (2014). Beside this, part of this horst and graben configuration might also be explained by tectonic re-adjustments linked to lateral displacement of the fault, as suggested by the presence of several deflected drainage channels showing consistent left-lateral kinematics (Figure 6.3). In the previous work by Herrero-Gil (2014) these deflected channels were consistently analyzed and lateral displacements of tens of meters (from ~ 20 up to ~ 80 m) were measured, indicating an important lateral component of this fault, in agreement with the kinematics of the AMF.

In the field, the faults cropping out are characterized by the presence of subvertical shear zones with intense fracturation, clast lineations, verticalized strata and local carbonate growths, probably related to fluid circulation in the fault zone (Figure 6.4). Vertical separations associated with these faults can reach up to 10 m produced by folding of the easternmost branches at the Campis creek (Figure 6.4E), although separations up to 28 ± 5 m are described by Herrero-Gil (2014) next to La Tira del Lienzo (Figure 6.2). Such separations should be assumed as partially apparent given the lateral component of the fault but indicate that the vertical component is also important in the AF.

The faults rupture the entire stratigraphic sequence of the alluvial fans, including the calcrete developments on top. This indicates that surface rupturing, i.e., paleoearthquakes, have occurred after the formation of these calcretes, which might be thousands of years after the deposition of the alluvial fan materials. According to Martínez-Díaz et al. (2003) and Silva (1994) the Q4-Q3 generations formed around Middle Pleistocene, thus the

maximum age of the calcretes deformation is from this period. More so, the dimensions of several meters for the vertical separations of these calcretes require the occurrence of several paleoearthquakes to achieve such deformations and might suggest recurrent activity in the AF since, at least, Middle Pleistocene.

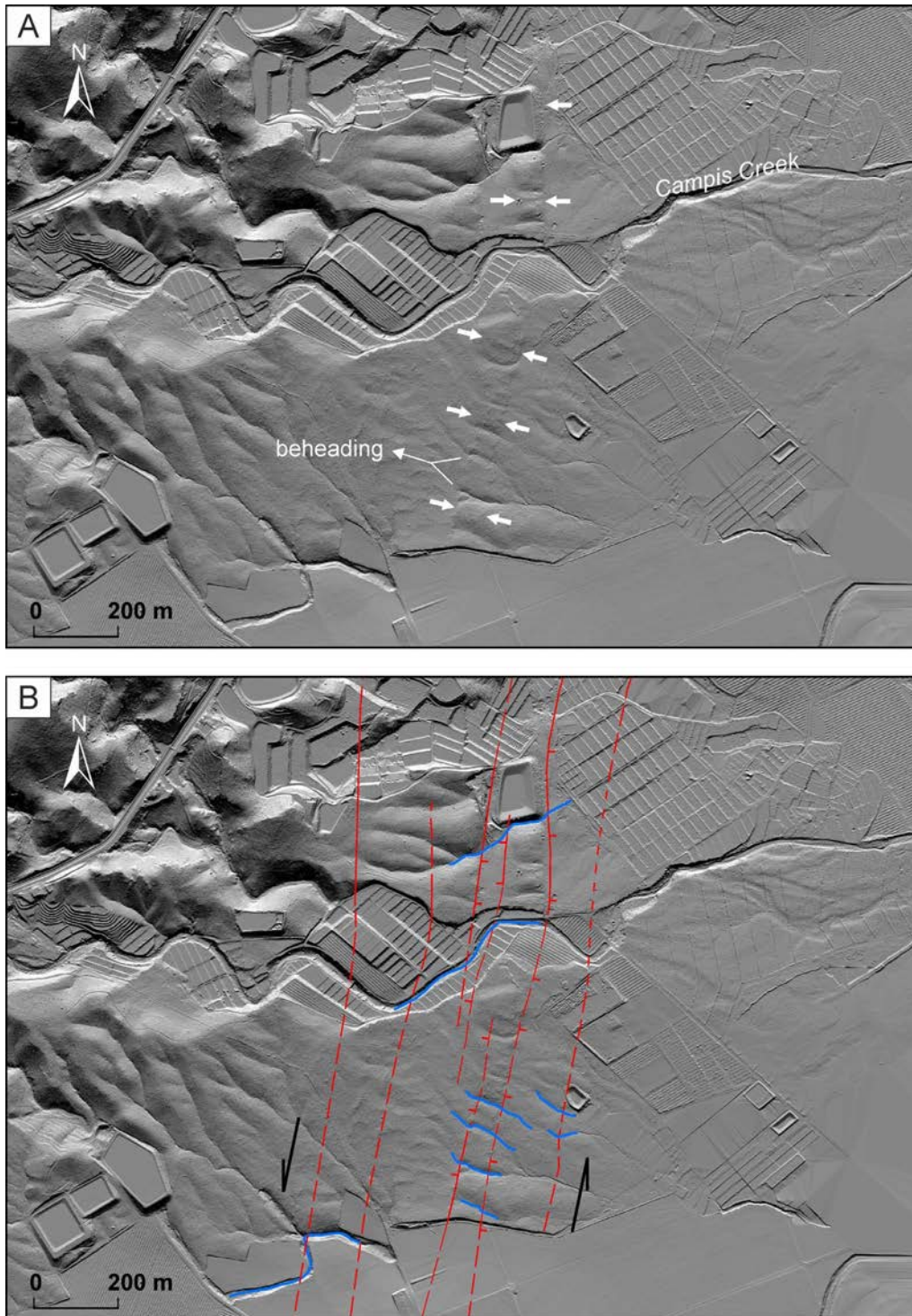


Figure 6.3. A) Fault lineations and drainage beheadings in the surface of the alluvial fans affected by the Amarguillo Fault (AF). B) Interpreted fault traces of the AF and channel left-lateral deflections in the drainages eroding the surfaces of the alluvial fans. Relief is based on the 0.5 m resolution MDT (SHAKE project). See Annex II (A) for the uninterpreted DEM.

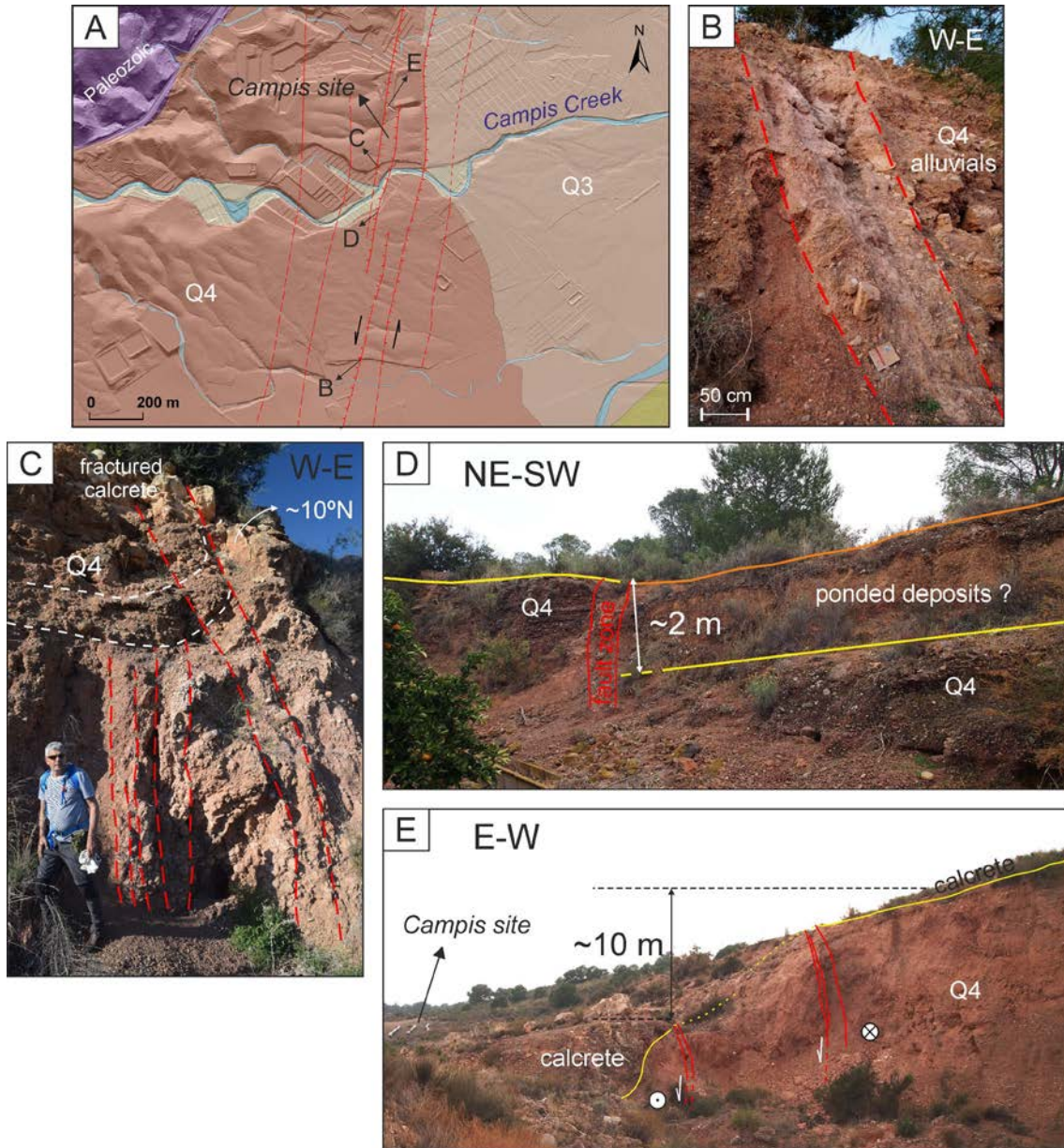


Figure 6.4. **A)** Map location of the Amarguillo Fault (AF) outcrops highlighted in windows B to E. Legend of the lithological units can be found in Figure 6.2. **B)** Outcrop of one of the AF branches in Q4 alluvial materials. Note that the materials between fault planes are “crushed” defining a band of shear deformation. **C)** Outcrop of one of the AF branches in Q4 materials, generating marked sub-vertical clast lineations, folding and calcrete fracturation. The orientation of the fracturation is $\sim 10^\circ\text{N}$, consistent with the mean orientation of the AF. **D)** Fault outcrop of the AF first described and interpreted by Herrero-Gil (2014) as an evidence for coseismic displacement and subsequent ponding of deposits onto the fault zone. **E)** Vertical separation generated by the AF in the calcrete surface of the Q4 alluvial fan. This separation is apparent as lateral displacement should be accounted. The Campis site (Figure 6.5) is indicated.

Precise paleoearthquake identification in the line of paleoseismic trench studies cannot be obtained from the present field work. Nonetheless, Herrero-Gil (2014) interpreted evidence of ponded deposits adjacent to a ~ 2 m fault slip in the southern margin of the Campis creek (Figure 6.4D), suggesting a coseismic origin. This reinforces the interest

of applying paleoseismological techniques to unveil the paleoearthquake history of the AF in future work.

6.4 Potential site for paleoseismic survey

Most part of the tectonic features in Quaternary materials of the AF are found in the vicinity of Campis creek (Figure 6.4), which is one of the active drainages of the region. This is mainly because the fan surfaces in this zone are less anthropized, whereas other zones are excavated for agricultural purposes or covered by greenhouses. This allows the precise positioning of fault traces from the observation of scarps and outcrops, crucial for the definition of paleoseismic sites. In this context we identify the Campis site, located 100-150 m N from Campis creek (Figure 6.5). This site is defined by the presence of at least three subparallel fault branches of the AF that generate a small double horst-graben relief in the surface of a Q4 alluvial fan. In the downthrown blocks, the Q4 materials are covered by unconsolidated colluvial deposits coming from the small drainage channels incised (Figure 6.5). These materials, although having a maximum thickness of ~1 m, cover the traces of the faults inferred in the Q4 materials and are potentially much younger, probably Late Pleistocene-Holocene given the lack of consolidation. This makes the site as suitable for a paleoseismic survey because the position of the faults is well constrained and there are younger materials that could be potentially affected.

The excavation of paleoseismic trenches in this site would allow to: i) estimate if this fault has been recently active or not, ii) characterize this activity in terms of paleoearthquakes, if identified, and earthquake chronosequences based on numerical datings and iii) estimate the slip rates from the displacements of the sedimentary units in the trenches. As a first explorative phase, we propose to excavate at least three fault-perpendicular paleoseismic trenches in the Campis site, one for each of the fault branches recognized (Figure 6.5A), to achieve the mentioned objectives. The study of the different branches will also permit to integrate the data to perform an integral characterization of the fault. As seen in the previous section 5, this allows to obtain more representative fault parameters for the whole fault, especially those that are critical for the seismic hazard assessment, such as slip rates. To estimate the lateral slip rate in trenches, we propose to start with a morphotectonic analysis of deflected channels similar to the one in Herrero-Gil (2014), but accompanied with numerical datings and refinement of the methodology based on Ferrater (2016). 3D trenching is more accurate, but its applicability to the site is

unknown because the thickness of the colluvium materials is small and the presence of suitable paleochannels is uncertain. It also requires more economic resources and time than perpendicular trenching. Hence, this is a possibility that might be considered after concluding the first trenching phase and once the sedimentary units and deformation of the site are well characterized.

6.5 Overview

The data from the Totana-Alhama segment of the AMF presented in this section highlights the importance of considering this fault segment as a seismogenic and capable source to be properly characterized in future paleoseismic studies.

The AF is a NNE-SSW ramification of the AMF that represents a transtensional bend with predominance of sub-vertical normal faults and local extension forming a horst and graben configuration. This is explained by the nearly subparallel orientation of the AF to the NNW-SSE maximum shortening vector inferred from GPS (Echeverria et al., 2013) and contrasts with the transpressive character of the AMF, which is more perpendicular (NE-SW), especially in the Lorca-Totana segment (Figure 6.1A). The slight obliquity of the AF with respect to the shortening vector, also explains its left-lateral component recognized by the presence of deflected features along its trace such as channels.

The strong geomorphic expression of the AF, compared to the diffuse eastern ramification of the AMF towards the city of Alhama, could be indicating that the AF is playing a major role in the uplift deformation of this sector bounding the España range. We then interpret a partitioning of the deformation between the AF and the AMF. The former might be absorbing most part of the vertical slip component in this sector, while the latter, the strike-slip. The less perpendicular orientation of the AMF to the shortening vector in the Totana-Alhama segment agrees with a predominantly strike-slip component, as opposed to the situation in the Lorca-Totana segment where the nearly perpendicular orientation results in a transpressive bend with important reverse component.

Our proposal for paleoseismic research in the future focuses on a site in the AF where several fault branches are located and aims to do a first characterization of these fault branches' Quaternary activity in terms of paleoearthquake identification and slip rates. If successful, this study would shed light on the paleoseismic activity of the Totana-Alhama segment. This is important because right now, the lack of precise and well constrained fault parameters such as slip rates and earthquake recurrences prevent from a proper

characterization of the segment. Such problems are critical limitations for the fault source modelling in seismic hazard that should be acknowledged, as explained in section 7.

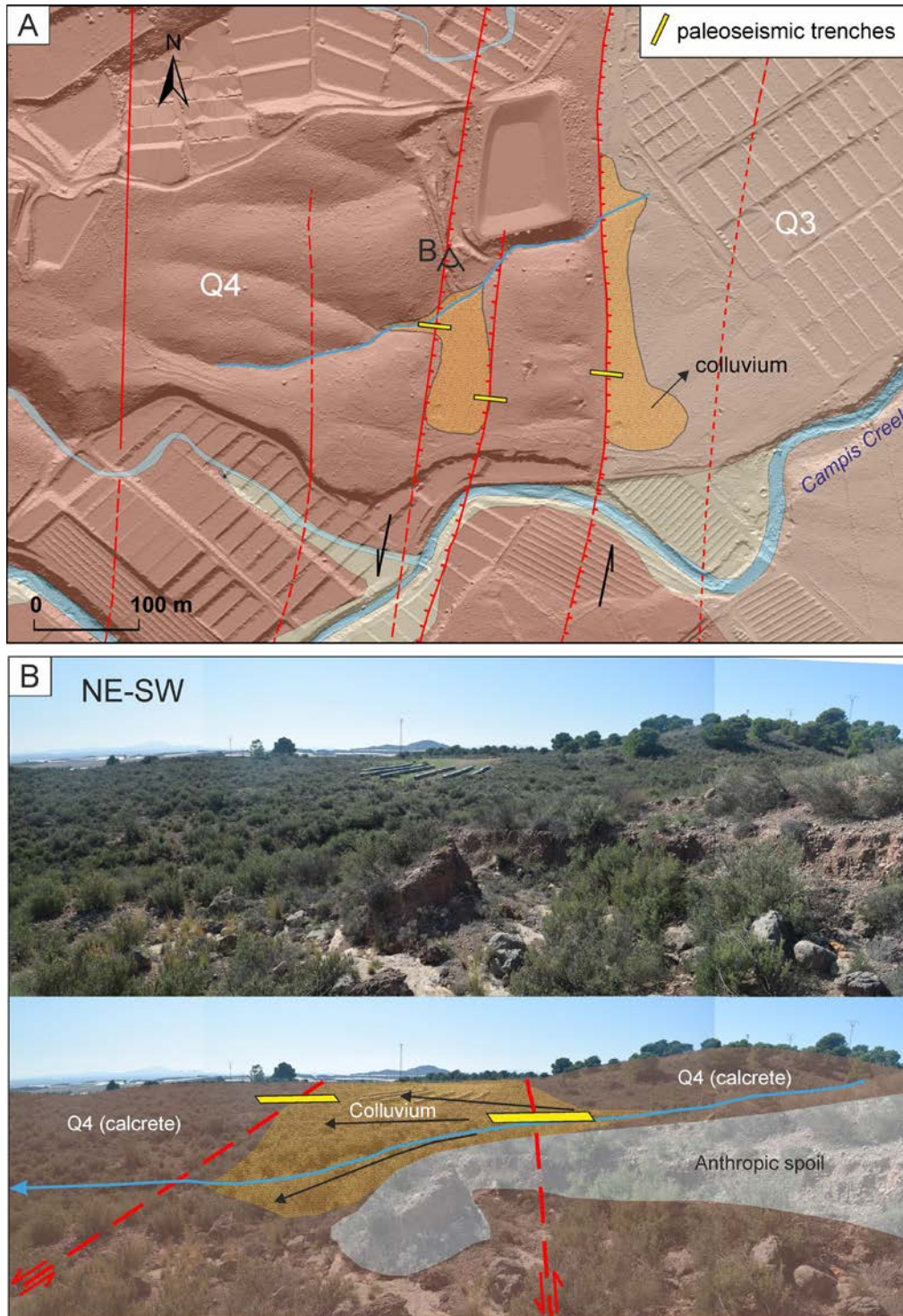


Figure 6.5. **A)** Map of the Campis site and location proposal for paleoseismic trenches. The colluvium deposits from small drainage systems on top of the Q4 deposits are indicated. Note that its location is restricted to the downthrown blocks between faults. Note also that the cartography of Q4 is inferred from the aerial photographs of the 1956-57 American flight (see Annex II (A)). Some of these areas are now excavated for agricultural plantations as the relief of this figure shows (0.5 m DEM; SHAKE project). **B)** Field picture and interpretation of the western part of the site, where the faults' positions are known.

7 Fault-based probabilistic seismic hazard assessment of the Eastern Betics Shear Zone

7.1 Introduction

In this section, we present the main results from the probabilistic seismic hazard assessment (PSHA) performed in the Eastern Betics Shear Zone (EBSZ) using a fault-based approach for the source modelling, as described in the chapter II (section 4). The data presented here includes the main results and discussions of two JCR articles published in the frame of the thesis, the first one presenting the source modelling approach (Gómez-Novell et al., 2020a) and the second the seismic hazard results (Gómez-Novell et al., 2020b). The text of this section, thus, contains verbatim portions from these articles.

Probabilistic seismic hazard approaches in Spain have classically modelled the hazard using area sources following the Cornell-McGuire methodology (Cornell, 1968; McGuire, 1976) by delineating the territory in different zones and obtaining the respective magnitude frequency distributions (MFDs) from the seismic catalogues (e.g., Gaspar-Escribano et al., 2008, 2015). This approach is also the one used for the current Spanish building code (NCSE-02, 2002). The development of few neotectonic and paleoseismic studies in southeastern Spain, especially in the EBSZ, during the late 1990s and early 2000s (e.g., Silva, 1994; Martínez-Díaz, 1998; Martínez-Díaz and Hernández-Enrile, 2001; Martínez-Díaz et al., 2003; Masana et al., 2004) motivated the inclusion of faults into PSHA as sets of independent sources considering either a characteristic earthquake model or an exponential MFD from fault dimensions and slip rate (García-Mayordomo, 2005; García-Mayordomo et al., 2007).

The use of geological data for seismic hazard assessments in southeastern Spain has not usually been a common practice due to the incompleteness of the paleoseismic, geomorphic and geodetic research on active faults over the territory to implement the required parameters in the hazard calculations. These parameters mainly concern the fault slip rates and recurrences that usually require many years of studies to obtain reliable estimations, especially in low-to-moderate active regions such as the one of interest here. This explains why in the 2013 updated version of the Spanish seismic hazard map, the seismic hazard was modelled following an areas model, even for the EBSZ. The occurrence of the 2011 Mw 5.2 Lorca earthquake reminded the population and institutions of the importance of understanding and characterizing the seismogenic faults in due to

their evidenced damaging potential. This context motivated the development of many paleoseismic and geodetic studies in the area that contributed to significantly improve the knowledge of the faults and allowed to constrain with higher precision and representativeness the fault parameters of interest for PSHA (e.g. Ortuño et al., 2012; Echeverria et al., 2013, 2015; Insua-Arévalo et al., 2015; Martín-Banda et al., 2015; Moreno et al., 2015; Ferrater et al., 2017; Martínez-Díaz et al., 2018).

In southeastern Spain, the inclusion of fault data into PSHA has become common very recently during the last few years, with approaches such as the one by Rivas-Medina et al. (2018) in which an hybrid approach is presented to set seismic potential between faults and background. Despite this, faults are considered as independent sources in this study and so far, no studies in Spain attempted to consider multi-fault rupture possibilities at a whole fault-system scale as an aleatory uncertainty for the source modelling. Therefore, the work presented here is the first one in this matter in which the inclusion of multi-fault ruptures, a widely observed phenomenon in nature, is seen as a step towards more realistic approximations of fault source modelling and seismic hazard for the EBSZ.

7.2 Evaluation of earthquake rupture models for the Eastern Betics Shear Zone

In this section we present and evaluate the results of the models performed with SHERIFS and their consistency with data from the seismic catalogue and paleoseismological studies. Note that the fault slip rates used for the models (Table 4.1) correspond to the ones available at the time of publication of the articles and that have been updated later on based on new published studies and the results of this thesis (see Table 7.1 in section 7.6.5). Similarly, the paleorates to check the models (Table 4.3) have been updated for the AMF-2 based on the results of the paleoseismic analysis of the thesis (section 5).

7.2.1 Modelled earthquake rates from SHERIFS

The modelling with SHERIFS was conducted as explained in chapter II (methods section 4.1). It provided four MFDs for each FM and FM_bg models which refer to the rupture hypotheses set and that are representative of the whole EBSZ system (Figure 7.1). Each of the four obtained GR MFDs is composed by a set of twenty samples per 0.1 magnitude increment, which form twenty different MFDs. These twenty distributions that result from the random sampling process of the input data (slip rate, M_{\max} and b-value) compose the overall curve of each hypothesis. As Figure 7.1 illustrates, the hypotheses that consider larger multi-fault rupture scenarios show larger M_{\max} . Annual rate values are similar for hyp. 1 to 3 in the range of Mw 4.0-6.5, while hyp. 4 shows much lower values for the

whole log-linear distribution. In this case, the results of the FM and FM_bg models are very similar because the background modelling concerns a small part of the magnitude range and for low magnitudes, which has small seismic potential compared with the one assigned to the faults. Only for hyp. 4, the rates of the FM_bg model show slightly higher values of the mean GR curve than the FM (Figure 7.1). The effect of the background is enhanced here allowing to increase the rates of the system due to the lower rates of the faults in this hypothesis, represented by the curve of the FM model.

7.2.1.1 Performance of the models

We analyze the performance of the different hypotheses in terms of the % of Non-Main-Shock slip (NMS). Its relationship with the seismic moment rate describes the performance of the hypotheses in SHERIFS. In both FM and FM_bg models, hyp. 1 to 3 have more than 70% of the slip rate converted into seismic moment rate, thus less than 30% of the slip is assumed as NMS for most of the samples (Figure 7.1). Conversely, in hyp. 4, only 10% of the slip rate (i.e. 90 % of NMS) is converted into seismic moment rate for the FM model and 20% for the FM_bg (i.e., 80-90% of NMS). This implies that the model from hyp. 4 shows a lower performance than the others.

The NMS percentage in the models is explained as a result of the configuration of ruptures of each hypothesis related to the slip rate variations between fault sections. This configuration affects how the slip rate budget is consumed in the different iterations of the modelling. The fact that large multi-fault ruptures involve slower sources, causes their slip rate budget to be rapidly exhausted in the highest magnitude ruptures, since they are the ones that consume most seismic moment rate. When this happens, the target MFD of the system is set and the rest of the calculation follows this imposed shape.

In the case of the EBSZ, the rates of very large ruptures (i.e. hyp. 4) are significantly low because they are limited by slow moving faults (e.g. PF, LTF, BSF; Figure 4.2A and Table 4.1, section 4.1). When the target is set in the high magnitudes, the rates of the whole distribution are therefore lowered. Consequently, for such large rupture scenarios the system has a lot of remaining slip rate budget not converted into seismic moment (i.e., NMS). This NMS is hosted by the faster faults, which are the ones whose budget is not exhausted.

Because NMS cannot be directly interpreted as a nature-related effect but as an artefact of the model linked to the rupture hypotheses, MFD target and input data set, we use it to

evaluate the adequacy of our hypotheses. In the line of Chartier et al. (2019), a threshold no higher than 30% of NMS for the overall system is an indicator of adequacy for the models. This value is in agreement with studies that estimate that post-seismic moment release reaches at most 30% of the total moment released in seismic events. The normal faulting Mw 5.9, 1999 Athens earthquake, for instance, was interpreted to have released aseismically 30% of the total moment (Baumont et al., 2004). The strike-slip faulting Mw 5.6 1979 Homestead and the Mw 7.5 1992 Landers earthquakes in California showed estimated post-seismic releases of about 10-15% (Shen et al., 1994; Stein and Lisowski, 1983). The NMS percentages of hyp.1 to 3 could therefore be interpreted as part of the slip rate that is not consumed seismically. Conversely, the high NMS values of hyp. 4 suggest that the fault rupture configuration is not adequate given the methodology and fault input data and hence, a modelling error is detected. This is also evidenced by the high dispersion of the log-linear GR curve of this model compared to the others.

7.2.2 Consistency check of the models

The consistency of the GR of each model is checked by their fit with the earthquake rates of the seismic catalogue and the paleoearthquake rates from paleoseismic research.

7.2.2.1 Seismicity rates from the regional earthquake catalogue

We visually analyze the fit between the MFDs modelled with SHERIFS and the annual seismicity rates obtained from the regional earthquake catalogue (IGN-UPM working group, 2013). Note that the GR curve from the catalogue covers a dispersed range of annual rates due to the exploration of the code within the magnitude uncertainty of the events in the catalogue (Figure 7.1). The dispersion is higher for the high magnitudes ($M_w \geq 6.0$) due to the large uncertainties related to the magnitude estimation of large historical events at the EBSZ. The MFDs from hyp. 2 and 3 show the best fits with the seismicity rates in both FM and FM_bg models, especially for Mw 4.0-6.0 as it is the range with smaller uncertainties in the catalogue (Figure 7.1). In detail, hyp. 2 shows a somewhat better fit than hyp. 3 because the mean GR values of the latter slightly underestimate part of the rates from the catalogue in the Mw 4.0-5.0 range. For hyp. 1 the consistency is poorer than the other two hypotheses as the model slightly overestimates the catalogue, although the fit is still acceptable for most part of the samples. Conversely, the GR from hyp. 4 shows a strong disagreement with the seismic catalogue in both models given that the rates modelled highly underestimate the seismicity and no overlap is observed whatsoever (Figure 7.1).

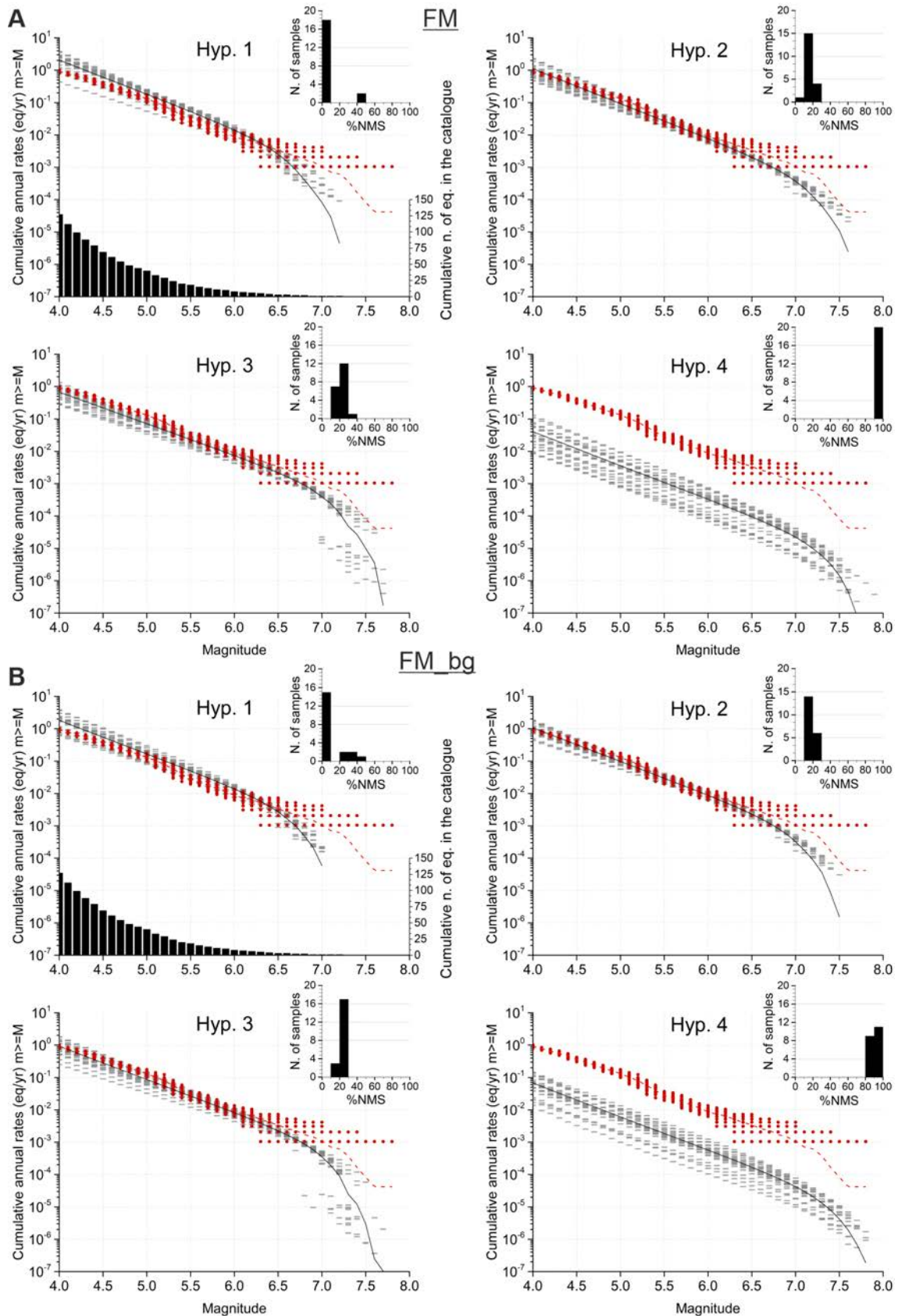


Figure 7.1. Comparison between the GR curves of each hypothesis (grey) and the earthquake rates from the catalogue (red) for the **A)** FM and **B)** FM_bg models. Mean GR curve modelled: solid black line; samples: short grey lines; catalogue mean GR curve: dashed line. The bottom of hyp. 1 graph shows the cumulative number of earthquakes of the catalogue per magnitude used to draw its MFD. Non-Main-Shock slip (NMS) histograms of the models are indicated.

7.2.2.2 Paleoearthquake rates from paleoseismic research

Annual earthquake rates from paleoseismological research at the EBSZ (Table 4.3) are compared with the modelled curves for the $M_w \geq 6.0$ range. The paleorates from each paleoseismological study are plotted with the participation rates of the corresponding fault section for each rupture hypothesis (Figure 7.2 and Figure 7.3). These GR curves show the participation rates resulting from considering all the ruptures hosted in each fault section per rupture scenario.

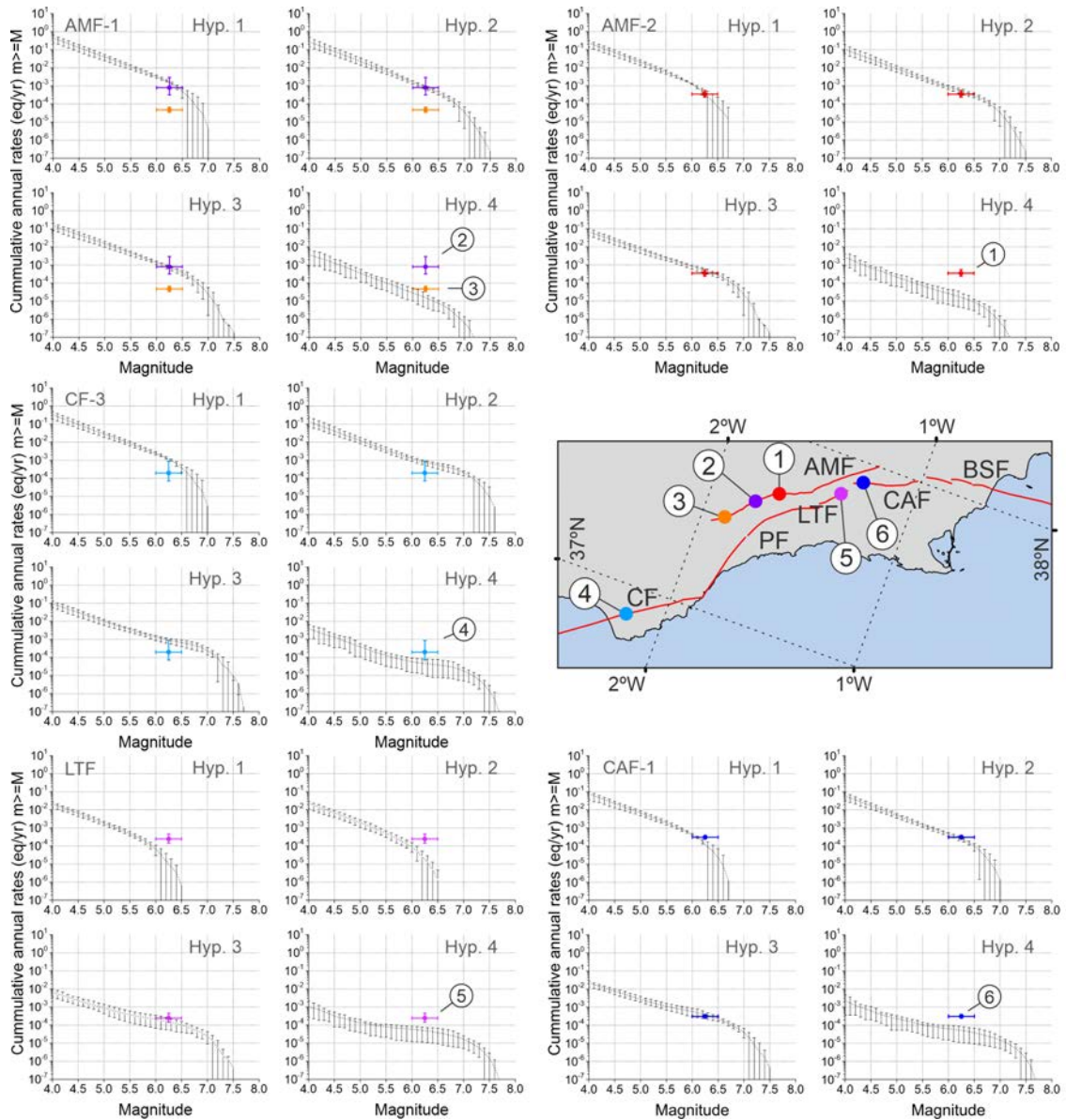


Figure 7.2. Annual rates of paleoearthquakes with their uncertainty ranges inferred from paleoseismological studies. These are plotted together with the FM model GR curves of their respective fault sections (participation rates) and for each rupture hypothesis. Participation rates are expressed as the mean (solid lines) and error bars. A fault map with the location of the paleoseismic studies (numbers) in each fault section is included. 1: Ferrater (2016); 2: Martínez-Díaz et al. (2018); 3: Ortuño et al. (2012); 4: Moreno (2011); 5: Insua-Arévalo et al. (2015); 6: Martín-Banda et al. (2015). Paleoearthquake rate values are available in Table 4.3.

Note that for the FM_bg model, and especially for hyp. 4, the rates of lower magnitudes in the range of Mw 4.0-6.0 are lowered with respect to the FM due to the effect of the background (Figure 7.3). This is because, contrary to the MFDs of the whole system in Figure 7.1, the curves exclusively depict the seismic moment rate modelled on faults.

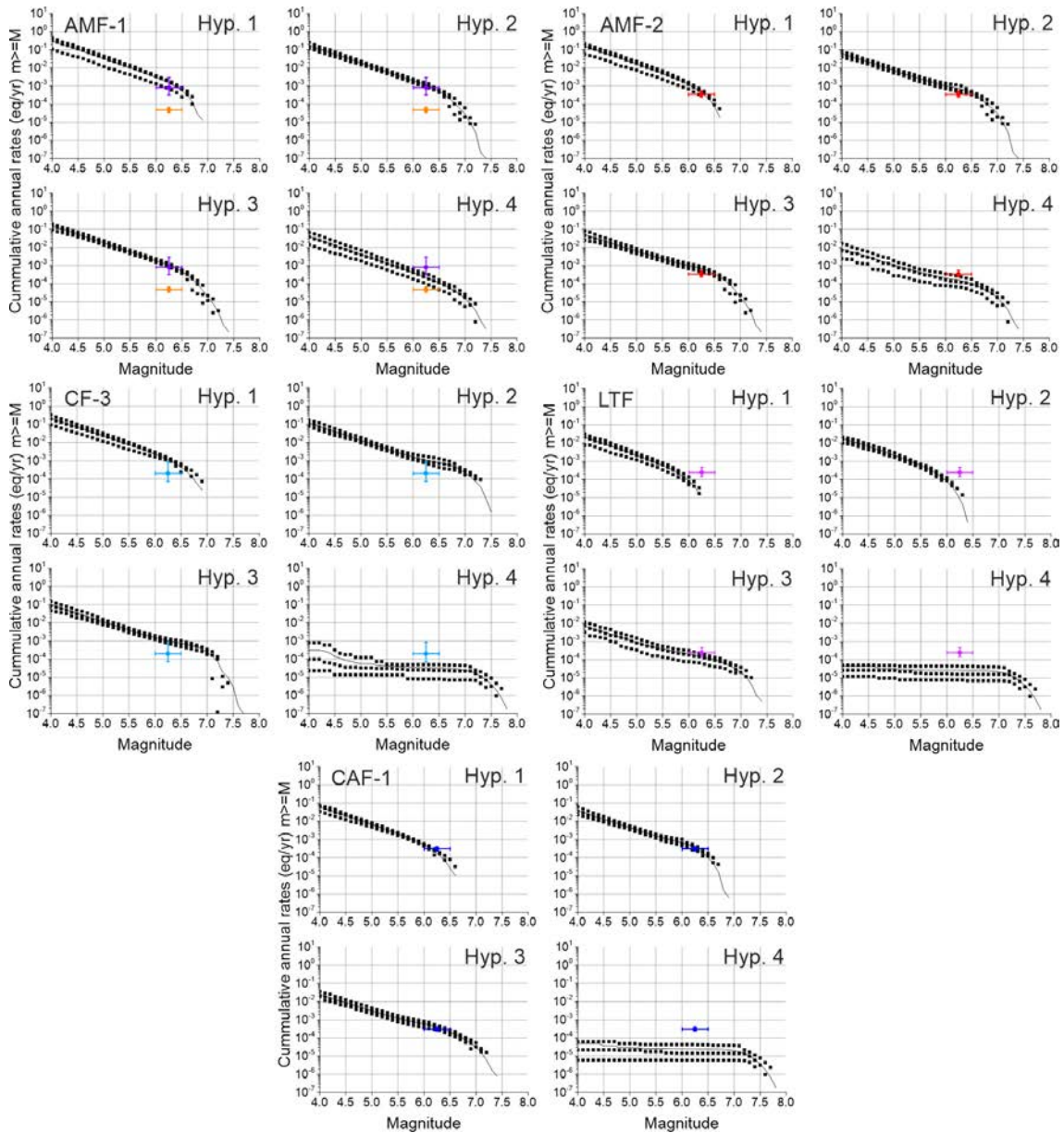


Figure 7.3. Annual rates of paleoearthquakes from paleoseismic studies plotted with the FM_bg model's GR participation rates of the fault section where the respective paleoseismic study is developed. The location of each paleoseismic site and studies are depicted in the map of Figure 7.2. In the participation rates the solid line represents the mean value and the squares represent the median, 16th and 84th percentiles of the distribution.

From this analysis it is obtained that hyp. 1 to 3 show all good fits with the paleoearthquake rate data. In both FM and FM_bg models, hyp. 2 and 3 are the ones with better results and, in fact, the differences between these two hypotheses are barely

noticeable in most fault sections. This is observable in the participation rate figures of the faults in each paleoseismic site in CF, AMF-2 and CAF-1, exceptuating LTF where hyp. 3 has the better fit because the rupture model of the fault is the same in hyp. 1 and 2 (Figure 7.2 and Figure 7.3). For both models, in hyp. 1 good fits with the paleorates are also found in some fault sections such as AMF-1 and 2 or CAF-1, however, their fit is not superior than it is for hyp. 2 and 3.

Oppositely, hyp. 4 shows very poor fits with the paleorates in the faults for both FM and FM_bg models. This reinforces the bad performance of the hypothesis also observed with the catalogue checks. Interestingly, for the FM_bg model the participation rates of hyp. 4 in AMF-1 and 2 fit better the paleorates in these sites than the FM model (Figure 7.3), which is attributed to the effect of the background. The slip rates of these faults are some of the highest in the system, implying that in large multi-fault rupture scenarios they show high NMS amounts because the neighbouring segments have contrastingly lower slip rates (AMF-3 and 4) and act as limiting for rupture propagation. The background subtracts part of the seismic potential from the faults allowing to reduce their NMS and increases the earthquake rates. Despite this, the overall fit of the whole hyp. 4 with the paleorates from all the sites is poor.

7.3 Logic tree weighting

A better fit of the GR with the data does not allow describing the manner in which the EBSZ system works, but shows that, given the methodology used, the input data and the rupture hypotheses explored, certain models are more consistent with the seismicity and paleorates than others. Therefore, no hypothesis should be ruled out, especially considering the epistemic uncertainties linked to some slip rate estimations. In this line, the consistency of these models can be used to guide their weight in a logic tree for PSHA, as we do (Figure 7.4). The models with better performance in terms of NMS and fit with both catalogue and paleoseismic datasets are the ones with higher weight in our logic tree.

For both FM and FM_bg models, hyp. 2 and 3 are the ones with higher weight because are the ones that perform better in all the categories used to check the models. First, concerning the NMS these hypotheses show percentages below 30% in the majority of their samples, indicating a good performance of the model in terms of how the slip rate budget is consumed by SHERIFS. Second and concerning the catalogue, both hypotheses show the best fits with the catalogue and very similar between them. Third, their fit with the paleorates is the best. Accordingly, the same weight of 0.35 (or 35%) is assigned to

each of the branches of hyp. 2 and 3 in the respective logic trees of the FM and FM_bg models (Figure 7.4).

Hyp. 1 is assigned a lower weight than the other hypothesis due to its lower consistency with the catalogue compared to hyp. 2 and 3. Even though hyp. 1 shows considerably good fits with the paleorates, it is important to recall that the most suitable hypothesis should agree not only with the rates of the higher magnitudes, but also with the rates of smaller magnitudes represented by the seismic catalogue. Hyp. 2 and hyp. 3 satisfy this requirement more correctly than hyp. 1. A weight of 0.2 (or 20%) is assigned to the branch of this hypothesis in the logic trees of both FM and FM_bg models (Figure 7.4).

Concerning hyp. 4, the smallest weight out of all the hypotheses is assigned because the consistency of this model is very low. First, the remarkably high NMS percentages highlight modelling issues with the data and rupture scenarios explored. Second, it does not allow describing the rates of the catalogue and paleoearthquakes because it shows generalized poor fits with these data. A weight of 0.1 (or 10%) is assigned to the branch of this hypothesis in both models (Figure 7.4).

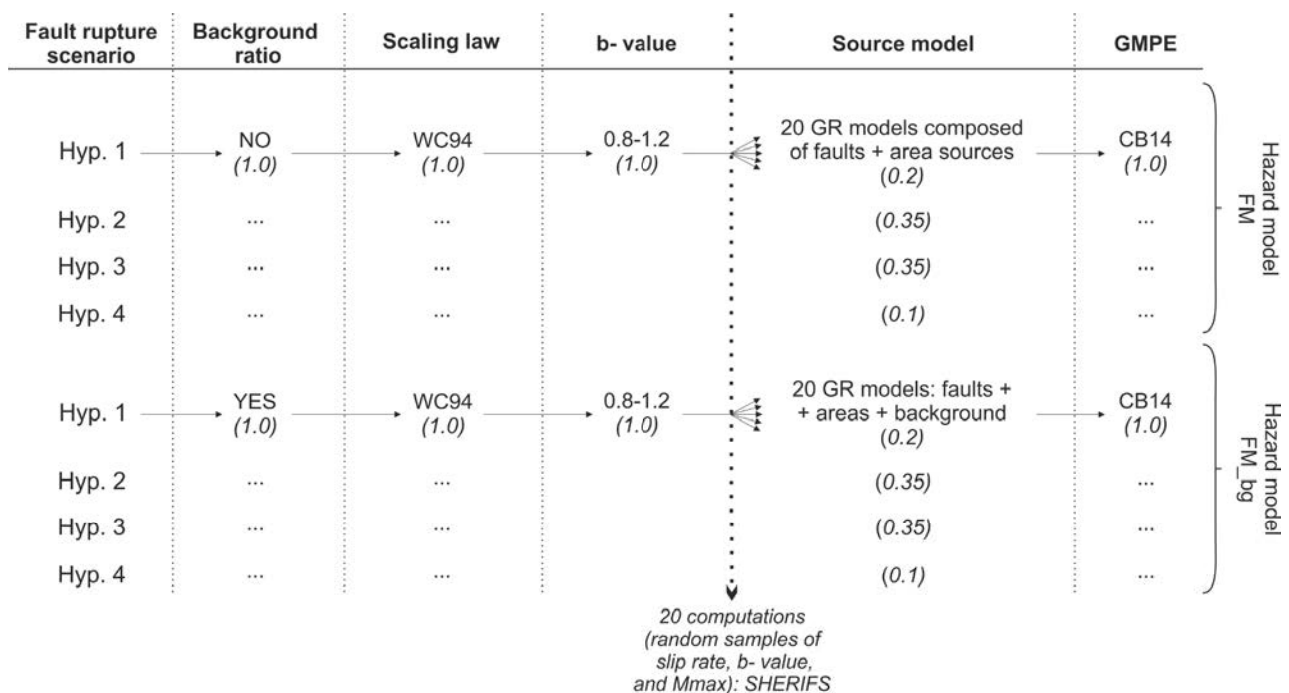


Figure 7.4. Logic tree schemes followed in this study for both FM and FM_bg source models. The weights (over 1) of each branch in the logic tree are indicated in brackets. Hyp.: hypothesis; WC94: Wells and Coppersmith (1994); CB14: Campbell and Bozorgnia (2014).

7.4 Probabilistic seismic hazard assessment results

Based on the earthquake rates from the different SHERIFS hypotheses that are part of the fault sources in the FM and FM_bg source models and the logic tree weighting in section 7.3, we present the results of the seismic hazard for each of these models and discuss their main implications for the seismic hazard of the Eastern Betics, also compared with previous PSHA studies in Spain. Details on the method followed are given in section 4.2.

The results of the calculations are presented in mean hazard maps (Figure 7.5 and Figure 7.6), hazard disaggregation (Figure 7.7) and mean hazard curves for five cities of the region: Murcia, Lorca, Almería, Vera, Torrevieja (Figure 7.8). Maps were obtained after interpolation using the natural neighbor approach from the OpenQuake outputs and depicted in terms of PGA. The hazard disaggregation is performed for the FM_bg model in the cities of Lorca, Almería, Vera and Murcia to test the influence of the different fault sources and seismic background in the hazard for the magnitude-distance relationship. Mean hazard curves for the cities are also depicted in terms of PGA on rock.

Briefly, the results show a clear control of the EBSZ faults over the seismic hazard of southeastern Spain for all return periods (RPs), especially in the vicinity of faults (10-20 km). Slip rate values directly affect fault influence into the hazard because highest accelerations are located around faults with higher slip rates of the system, while lower slip rate faults have much less influence. The impact of the background into the models is very limited given the similarity of results from both FM and FM_bg.

7.4.1 Mean hazard maps and magnitude-distance disaggregation

7.4.1.1 Fault influence

The mean hazard maps from both FM and FM_bg models (Figure 7.5 and Figure 7.6) produce very similar results in terms of absolute hazard levels and distribution, and increments between them are very low (Figure 7.9). The modelled EBSZ fault system exerts a clear control into the seismic hazard of southeastern Spain for all RPs, especially noticeable in the near-fault regions, where maximum PGA values are located.

In both models, the maximum acceleration values range from 0.5-0.6 g for the 475-yr RP to 1.2-1.3 g for the 4975-yr RP (Figure 7.5 and Figure 7.6) and are located along the faults with higher slip rates. That is the case of the southwestern termination of AMF, near Lorca (AMF-1 and 2) or CF near Almería, which have the highest slip rates of the system (> 1.0 mm/yr; Table 4.1). Conversely, lower slip rate faults have minor influence in the

hazard levels for all RPs, also depending on their slip rates. Mean hazard maps from both FM and FM_bg models (Figure 7.5 and Figure 7.6, respectively) show that PF is the fault with less footprint on the hazard for all RPs, which is consistent with its slip rate being the lowest of all the system according to the available estimations (<0.1 mm/yr; Table 4.1). Other faults such as the Eastern termination of BSF (BSF-3 and 4), AMF-4 or LTF, have higher slip rates (~ 0.1 - 0.4 mm/yr; Table 4.1) but their influence to the hazard is limited compared to AMF-1, 2 or CF.

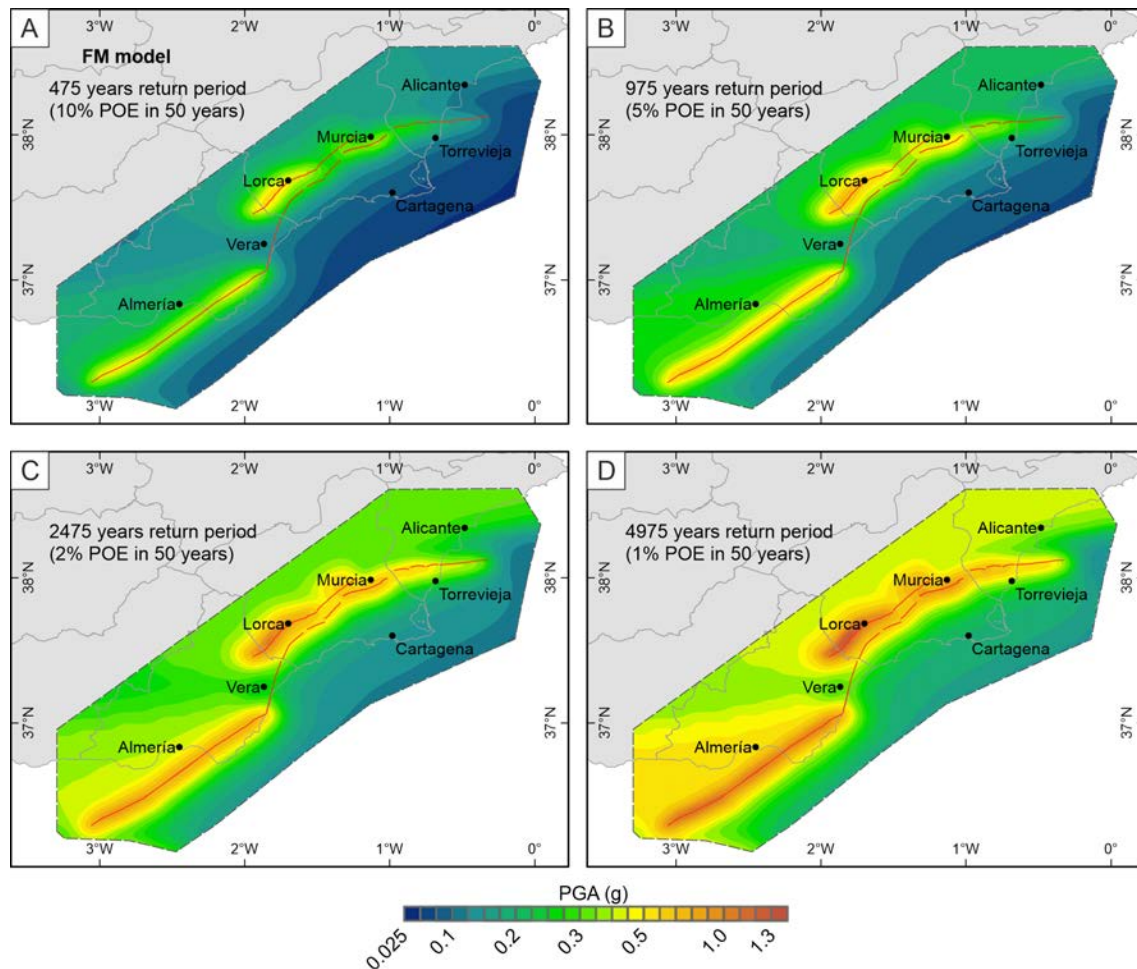


Figure 7.5. A) Mean hazard maps for PGA (g) of the FM model for the respective return periods (RPs) of 475 years, B) 975 years, C) 2475 years and D) 4975 years, equivalent to the probabilities of exceedance (POE) of 10%, 5%, 2% and 1%, respectively. A common color scale is set for all return periods. The main cities in the region are indicated, and the traces of the EBSZ faults considered are depicted in red. See Figure 4.2A for the names of each fault.

The hazard disaggregation of the FM_bg model (Figure 7.7) shows that all the contributions to the seismic hazard in a specific site are from sources located within a 20-30 km radius, suggesting that farther sources do not influence the hazard. Higher slip rate faults contribute the most to the seismic hazard values of the closer zones, while lower

III. Results and partial discussions

slip rate faults have very small contributions, even in the sites in their closest vicinity. In the cities of Lorca and Almería (Figure 7.7A to D), the magnitude-distance relationships that influence most the hazard coincide with the location of AMF-1 and 2, and CF-3, respectively, which are the fault sections with higher slip rates in the system (Table 4.1).

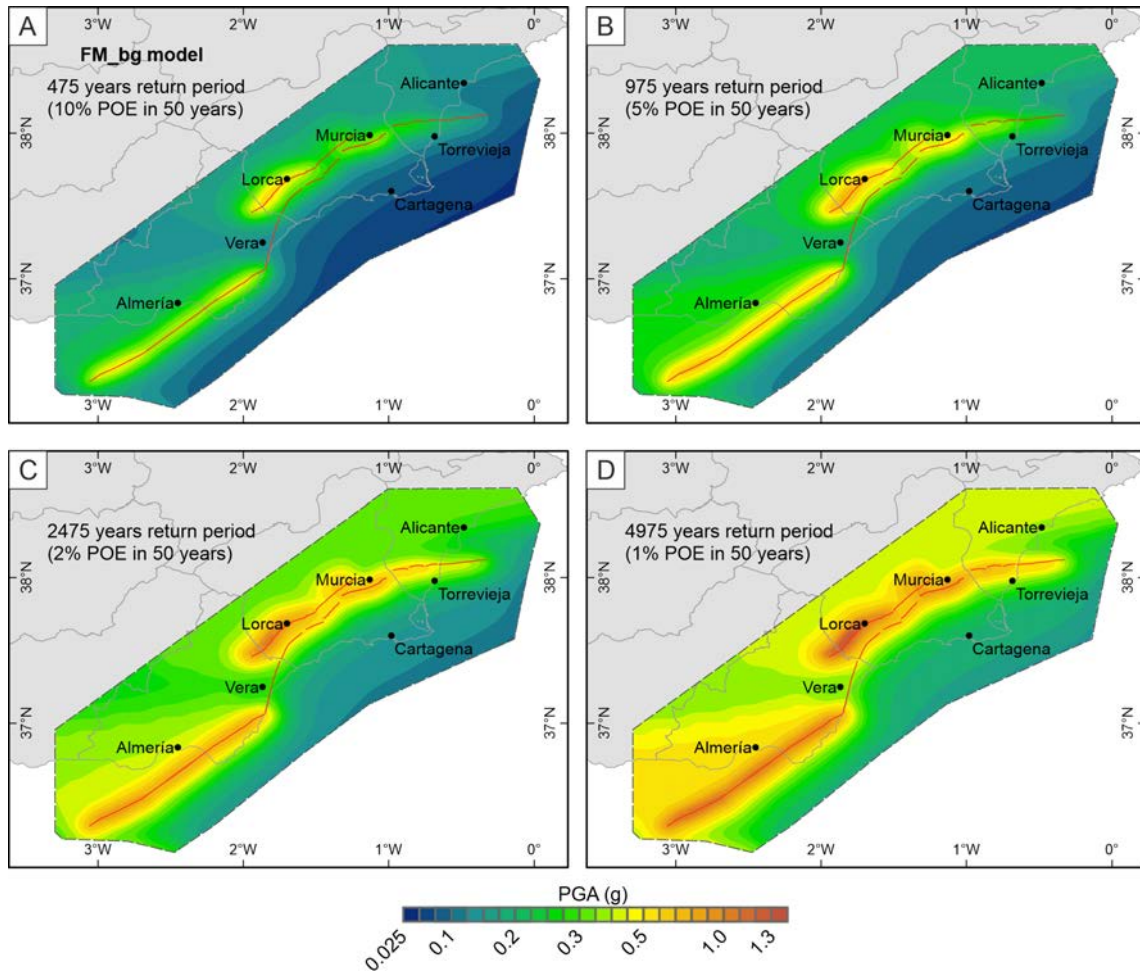


Figure 7.6. A) Mean hazard maps for PGA (g) of the FM_bg model for the return periods (RPs) of 475 years, B) 975 years, C) 2475 years and D) 4975 years, equivalent to the probabilities of exceedance (POE) of 10%, 5%, 2% and 1%, respectively. A common color scale is set for all return periods. The main cities in the region are indicated, and the traces of the EBSZ faults considered are depicted in red. See Figure 4.2A for the names of each fault.

Lorca is located < 1 km from AMF in the limit between AMF-1 and 2, which explains the maximum influence from sources located between 1-5 km. These maximum contributions are in a tight Mw 6.5-6.75 range for both RPs (Figure 7.7A and B), which might suggest the controlling earthquakes in this city. Almería is located at ~ 15 km from CF-3, consistent with the distance of the source's maximum contribution. The higher distance of the fault from the city causes its contribution to be considerably lower than AMF-1 and hence other non-fault sources influence the hazard as well (Figure 7.7C - D).

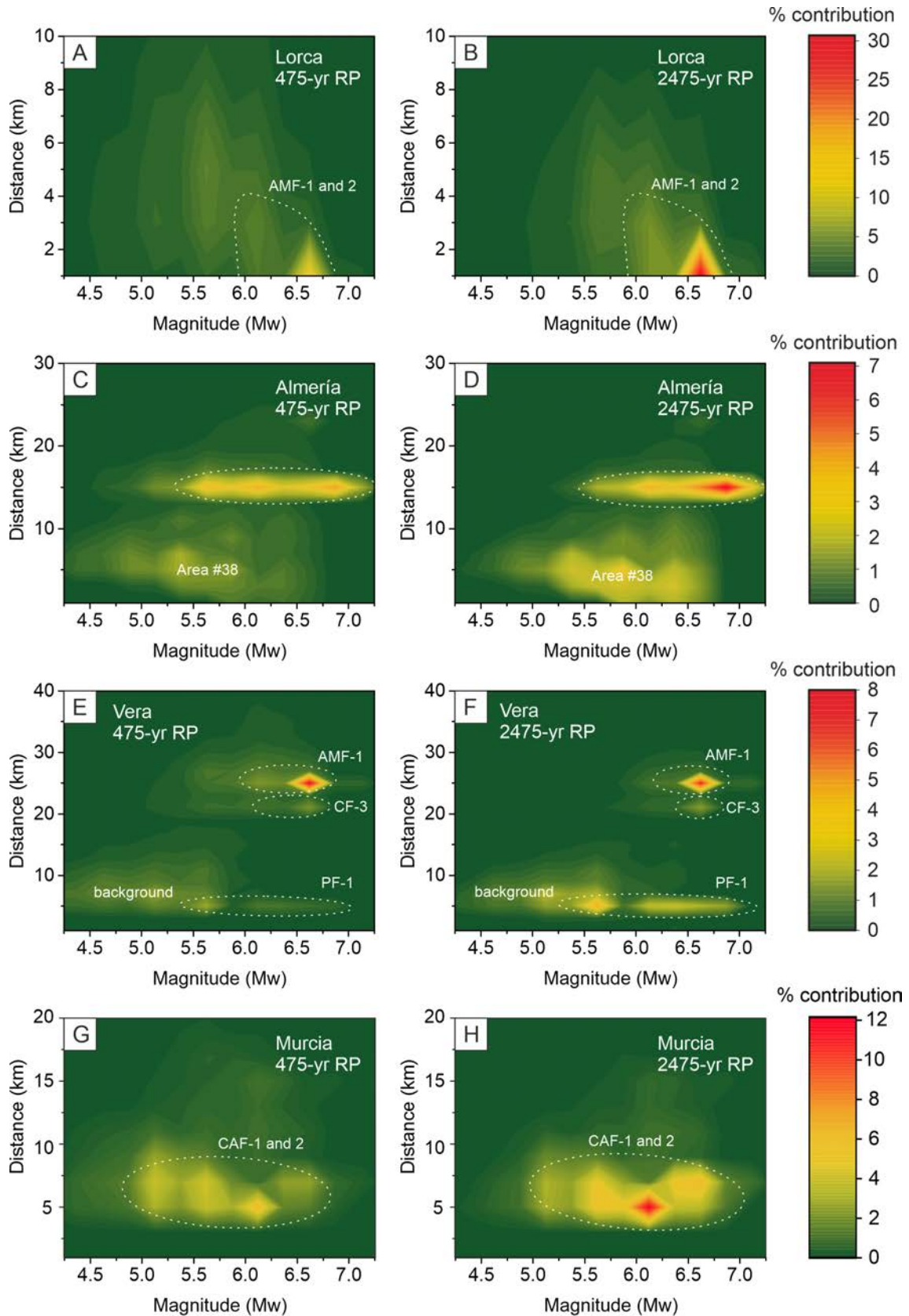


Figure 7.7. A) Hazard disaggregation for the magnitude-distance relationship of the FM_bg model in the cities of Lorca for the return periods of 475 years and B) 2475 years, C) Almería for 475 years and D) 2475 years, E) Vera for 475 years and F) 2475 years and G) Murcia for the 475-years and H) 2475-years. A common color scale is set for the two return periods representing each city. The main contributing sources of each city are highlighted.

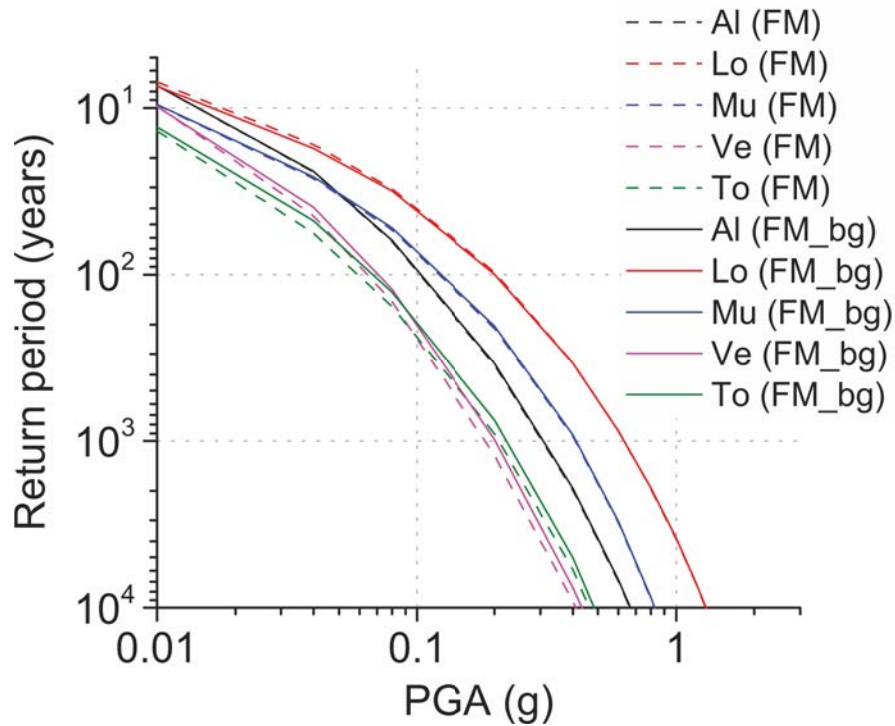


Figure 7.8. Mean hazard curves for PGA (g) of the FM and FM_bg models in the cities of Almería (Al), Lorca (Lo), Murcia (Mu), Vera (Ve) and Torrevieja (To).

The contributions of CF-3 comprise a wider magnitude range (Mw 5.0-7.0) in the 475-yr RP (Figure 7.7C), while they concentrate around Mw 6.5-7.0 in the 2475-yr RP (Figure 7.7D). Conversely, in zones like Vera, located next to very low slip rate faults (i.e., PF), the main contributions to the hazard are not from the closer faults, but from other farther faults (Figure 7.7E and F). In this city AMF-1 is the main contributor despite this fault being ~25 km farther, while PF is the least even for long RPs (Figure 7.7F). A hanging wall effect can be observed in non-vertical dipping faults such as AMF, CAF or BSF (Figure 7.5 and Figure 7.6). Such near-fault effect is more visible at longer RPs (i.e., 2475 and 4975 years), where PGAs for two selected sites at the same distance of a fault trace but on opposite sides, are higher on the hanging wall. A clear example is the transect perpendicular to AMF near the city of Lorca (Figure 7.10E). This is significant for seismic hazard assessment in near-fault zones as discussed in section 7.6.1.1.

7.4.1.2 Background influence

The similarities between the mean hazard maps from the FM and FM_bg models suggest that adding a seismic activity background ratio in the FM_bg model produces minor changes to the final hazard results within the EBSZ buffer for any RP (Figure 7.9). In general, the background contributes to raise the hazard values with respect to the FM

model, while the decreases are depreciable. PGA increments, especially for the shorter RPs, are mild (Figure 7.9A to C), but for the 4975-yr RP the hazard values are incremented up to a maximum of ~ 0.1 g in some zones (e.g., E of BSF; Figure 7.9D). For the faults, PGA values remain practically identical for all RPs, which means that earthquake occurrence on most faults is higher than the one generated by the background. However, the background contributes to slightly increment the hazard within the EBSZ buffer area in the zones farther from the traces and influence of the faults (e.g., E of BSF-4) or next to faults with slip rates much lower than the average of the system (~ 0.5 mm/yr; based on the mean values in Table 4.1); mainly PF. In these zones, the poor influence of faults allows the background of the FM_bg model to overcome the occurrence rates (i.e., probabilities of exceedance) of the hazard from the FM model, thus higher values are found in the FM_bg model within a same RP.

The maximum hazard increments caused by the background happen E of BSF-4 (Figure 7.9), where the Bajo Segura Fault terminates. This is because fault-related seismic hazard influence is larger and wider in the transversal sections across faults rather than in their longitudinal ends, as it can be seen in CF or the southwestern termination of AMF (Figure 7.5 and Figure 7.6). In addition, BSF-4 has a lower slip rate (~ 0.2 mm/yr) than the average of the faults in the system and the closest area sources in this zone, i.e., #31, #39 and especially #41 (Figure 4.4), have very low activity rates (IGME, 2015b). This situation causes low occurrence rates of the hazard from the FM model in this zone and allows the background (FM_bg) to overcome such rates more remarkably than any other zone.

All these observations are consistent with the disaggregation results of the FM_bg model as in general the background shows low contributions on the hazard, especially where faults dominate the hazard (Figure 7.7). Only in the case of Vera, the seismic background has a significant contribution due to the lower slip rates, hence activity rates, of the PF (Figure 7.7E and F). This causes the background to overcome the contribution of PF in the Mw 4.0-5.5 range and to contribute significantly to the seismic hazard levels of the city, especially in longer RPs (Figure 7.7F).

7.4.1.3 Area sources influence

From the mean hazard maps of both FM and FM_bg models it can be observed that the area sources have a much minor footprint in the seismic hazard distribution of the EBSZ than the faults. This is mainly because the activity rates of the area sources modelled are either very low (#31, #36, #39 or #41; IGME, 2015b) or are located too far (> 100 km) to

7.4.2 Mean hazard curves

Figure 7.8 shows the mean hazard curves obtained for five cities located close to the EBSZ faults (Almería, Lorca, Murcia, Vera and Torrevieja) for both the FM and FM_bg models. Setting a background ratio for the EBSZ buffer area does not imply dramatic changes in the hazard curves of these cities, which are all very close to active faults. In the case of the Almería, Lorca and Murcia, the respective hazard curves of both models predict practically identical PGA values for any RP. Conversely, in Torrevieja and, especially, in Vera, the FM_bg model predicts higher PGAs than the FM model, although these differences are very small: less than $< 0.1g$ for the $\sim 10,000$ -yr RP. The reason for these differences is the lower slip rates of the BSF and PF, respectively for Torrevieja and Vera, that allow the background to overcome these rates in the FM_bg model.

7.5 Discussion on earthquake rupture models in the Eastern Betics

This section discusses the main implications and limitations of the modelled earthquake rupture hypotheses with SHERIFS and the datasets used to weight them for the logic tree of the PSHA.

7.5.1 Analysis of the modelling results with the datasets (consistency check)

The results from the consistency check of the models obtained with SHERIFS suggest that multi-fault ruptures are feasible at the EBSZ because some of the hypotheses explored agree considerably well with the rates from the seismic catalogue and paleoearthquake research. In this context, the occurrence of simultaneous ruptures involving whole faults (hyp. 2) or groups of faults (hyp. 3) seem to be the most consistent, although the other hypotheses cannot be disregarded, nor it is the main goal of the modelling. These rupture configurations have important implications for the seismic potential of the EBSZ and for the hazard assessment in the near-fault areas, as discussed in section 7.6, but several limitations should be taken into account when analyzing the reliability of the modelled earthquake rates with the datasets.

7.5.1.1 Earthquake catalogue

The analysis of the fit with the earthquake catalogue of the modelled GR (Figure 7.1), as explained, insights on which models are more consistent and could allow to describe better the seismicity of the EBSZ. Nonetheless, the misfits of some of the hypotheses with this catalogue can also be cause of the rupture models' configurations. For instance, the overestimation of the catalogue seismicity rates by hyp. 1 could be caused by two factors: i) a non-adequate segmentation model for the faults that considers too short fault sections and hence, higher earthquake rates than the catalogue or ii) the already acknowledged uncertainties and poor reliability of some geological fault data affecting the modelization. Similarly, the slight underestimation of hyp. 3 to the catalogue in the FM_bg model could be due to the largest ruptures allowed in this model that may contribute to limit the annual rates in the lower magnitudes. We are not able to distinguish the contribution of each option, but further research should focus first on exploring the impact of new segmentation and rupture models in the modelling and second, on constraining critical fault parameters in some faults (i.e. slip rate; section 7.6.4).

The large dispersion of the seismicity rates of the catalogue for magnitudes above Mw 6.0 also contributes to the uncertainties in the fit analysis of the modelled GR curves and it is due to the lack of completeness of the catalogue in these high magnitudes. The work

by IGN-UPM (2013) for the updating of the Spanish seismic hazard map, evidences this issue because it is identified that from $M_w \geq 6.0$, the year of completeness is the same (year 1048; Table 4.2, section 4.1).

7.5.1.2 Paleoearthquake rates

Recent studies on active faults at the EBSZ allowed to infer slip rates in specific portions of such faults as well as to calculate rates of earthquakes. In this study, the rates inferred from paleoseismology are a qualitative way to analyze the prediction of the models in the high magnitude range, where the seismic catalogue is not well represented. Similar to the case of the catalogue, the agreement or disagreement of the paleorates with the modelled rates does not provide a way to accept or rule out any of our hypotheses, but to weight them for PSHA (section 7.3). Paleorates, though, have an additional problem related to the high uncertainties and low resolution of the paleoseismological data in the study area.

One of the problems applies mainly to the magnitude of the events inferred from geological observations. We considered that all the paleorates reflect earthquakes of $M_w \geq 6.25 \pm 0.25$. However, lower magnitude earthquakes can rupture the surface as well (i.e. the M_w 5.5 1975 Homestead Valley earthquake; Schwartz, 2018) implying that they could be observed in the EBSZ paleoseismic trench studies and incorporated to the paleorate estimations as larger. This uncertainty has a difficult assessment although our magnitude threshold selection is supported by statistical observations of fault ruptures (see section 4.1.4.2).

Another issue affects directly the paleoearthquake rate estimations and concerns the fact that paleoseismology always provides a minimum number of paleoearthquakes, hence maximum RI. There are two main causes for this, the first being that paleoseismic studies are local, limited to specific sites and branches of a fault and rarely account for the whole structure. Surface ruptures are usually not continuous along strike and do not always accommodate ruptures on the same branch. Recent examples such as the 2016 M_w 7.8 Kaikoura earthquake (New Zealand) support this observation, where a significant part of the deformation was accommodated off-fault (e.g. Kearse et al., 2018). This way, missing events in the paleoseismic record is likely and higher paleorate values should be expected. Following this reasoning, our hyp. 4 is not suitable, since increased paleorates would lead to even much stronger disagreement with the modelled curves of such hypothesis (e.g., Figure 7.2). This, together with its misfit with the catalogue and high NMS percentage suggesting modelling issues, lead us to estimate that this rupture

hypothesis treats unrealistically long multi-fault rupture possibilities considering the data used and the rupture hypotheses explored.

The second reason is linked to the lack of depositional continuity, highlighted by Ortuño et al. (2012) in AMF-1. The discontinuous geological record hinders the identification and time constraining of the number of paleoseismic events observed and might lead to erroneous paleorate estimations. In Figure 7.2 and Figure 7.3, the paleorate from Ortuño et al. (2012) in AMF-1 is underestimated due to this effect, resulting in a misfit with the modelled MFDs of hyp. 1-3 and the paleorate by Martínez-Díaz et al. (2018).

Similar to the analysis with the catalogue, the weaker agreement of hyp. 1 with the paleorates could mean that either or both the segmentation proposed for these faults is not adequate and larger ruptures should be expected (e.g. hyp. 2 and 3), and that paleoearthquake data is underestimated. Both epistemic uncertainties should be explored in further research, although the latter is more difficult to assess, since the issues are somehow inherent to the paleoseismic approaches. More paleoseismic research might help improve and better constrain paleoearthquake data at the EBSZ.

Finally, the method used to infer the paleorates in each study (Table 4.3, section 4.1) is conditioning the robustness of the results, because it affects the independence of the analysis. Martínez-Díaz et al. (2018) results are based in a single observed paleoevent in a trench. The paleorates are inferred using the geological moment rate from the fault slip rate and the seismic moment of the maximum expected rupture following the maximum magnitude model from Wesnousky (1986). Since SHERIFS uses slip rates as inputs, the models for this fault are somehow linked to the paleorates and the analysis cannot be claimed as completely independent. Martín-Banda et al. (2015) infer the paleorate for CAF-1 similarly, but the value is consistent with the one inferred independently from age constraints of paleoevents in trenches. Insua-Arévalo et al. (2015) for LTF, infer the slip rate of the fault from the paleorates and the slips in the trenches. This dependence between models and data to weight them does not invalidate the analysis, though; the modelled MFDs are not build relying only on the exploration of slip rates but also on fault rupture scenarios (M_{max}) and the b value, which in this case are independent variables.

In the other faults explored, the paleorate estimations (Table 4.3) are inferred from dividing the number of paleoevents in trenches over their observational time period, thus they are independent data to compare with the modelled earthquake rates.

7.5.2 Considerations of the fault sources modelling and perspectives

The present study raised several critical questions concerning the modelling that may be of interest for other low-strain regions similar to the EBSZ and for PSHA modelers. SHERIFS constitutes a useful tool to discuss the epistemic uncertainties affecting a given fault system for fault source modelling in PSHA, including geological input parameters and identifying which fault rupture models are more coherent given the input data. The method is also seen as a good tool to determine the weights that different fault source models should have in PSHA according to their consistency with the seismic catalogues and paleoseismic studies, even if the limitations are important.

In the particular case of the EBSZ, as in most low-strain regions, the main epistemic uncertainties are related to the geological fault input data used, especially affecting slip rate and paleoearthquake rate estimations, and the definition of fault rupture scenarios to be explored. In this sense, the results of this study, far from precisely determining the EBSZ behavior, have shown to be a practical tool to highlight where these uncertainties are more important and limiting. A clear example is PF, one of the less studied faults of the system in terms of paleoseismological research and that shows remarkably low slip rates compared to the other faults (Table 4.1). Such slip rates affect the performance of the modelling in large multi-fault scenarios by increasing drastically the NMS and abnormally lowering the resulting GR distributions, especially of hyp. 4. This helps to highlight in which areas of the EBSZ there is a need for more research in the future, especially to verify the current slip rate estimations that cause such problems during the modelling. Knowing and assessing these uncertainties in the fault slip rates is critical for fault-based PSHA, as we explain later on in sections 7.6.4 and 7.6.5.

It is critical that researchers challenge classical segmentation models and consider faults as systems of geological structures that can interact. The main point is that multi-fault ruptures are regarded as a frequent phenomenon, demonstrated by numerous morphogenetic earthquakes in the last decades (e.g., Choi et al., 2012; Hamling et al., 2017; Villani et al., 2018) and might allow to model earthquake occurrence on faults in a more realistic way. This is especially relevant in regions of distributed deformation along complex fault systems (e.g. Berryman et al., 2012) as it could be the case of the EBSZ, where the rupture models selected may have important repercussions on PSHA. Further work needs to be focused towards reducing the uncertainties raised, especially from the geological and paleoseismic records and also on exploring new fault and multi-fault

rupture hypotheses, complementary to the ones presented here. In addition to this, the approach might serve as an example for similar seismo-tectonic contexts, as well as for defining deterministic earthquake-scenarios for engineering applications.

The models presented follow a GR distribution, because it is the one used for the Spanish seismic hazard map (IGN-UPM, 2013). Considering the data available from the catalogue and paleoseismic studies, we do not have clear criteria to dismiss it. However, other studies in other regions, for instance New Zealand (Stirling and Gerstenberger, 2018), have proved that GR distributions do not always describe annual rates of the high magnitudes derived from paleoseismic data. Exploring other MFD options in the EBSZ is therefore another interesting topic for further research due to its repercussions on earthquake frequencies and hence, seismic hazard assessments.

7.6 Discussion on the seismic hazard results

This section discusses the seismic hazard results (section 7.4) compared to previous PSHA studies in southeastern Spain, its implications related to moderate-magnitude earthquakes, GMPE, fault slip rate knowledge and limitations.

7.6.1 Comparison with previous probabilistic seismic hazard assessments in southeastern Spain: implications on the modelling

The results presented highlight a clear influence of the faults of the EBSZ in the seismic hazard of southeastern Spain, as shown in Figure 7.5 to Figure 7.7. Both FM and FM_bg source models applied show very similar results, meaning that the application of a background ratio has minor influence on the hazard, especially in zones closer to faults (Figure 7.9). Hence, for the comparison analysis that follows we will focus on results of the FM model, though practically all the observations are applicable to the FM_bg model. In the same way and due to the low impact of the background on the hazard, the fault influence observations from the disaggregation of the FM_bg model are valid for the FM model. We compare our results with a PSHA produced only considering the ZESIS area sources model, and with a recent fault-based PSHA done in southeastern Spain (Rivas-Medina et al., 2018).

7.6.1.1 Comparison with a hazard assessment using the ZESIS areal model

The PSHA results of our FM model are compared with a PSHA reached here by using exclusively the area sources of the ZESIS model (Figure 4.4) and the same GMPE as our calculations (Campbell and Bozorgnia, 2014). Significant changes in PGA are found

between both models within the limits of the EBSZ, where the faults are modelled (Figure 7.10A to D); outside these limits, the hazard values do not experience any change since all use the same area sources model.

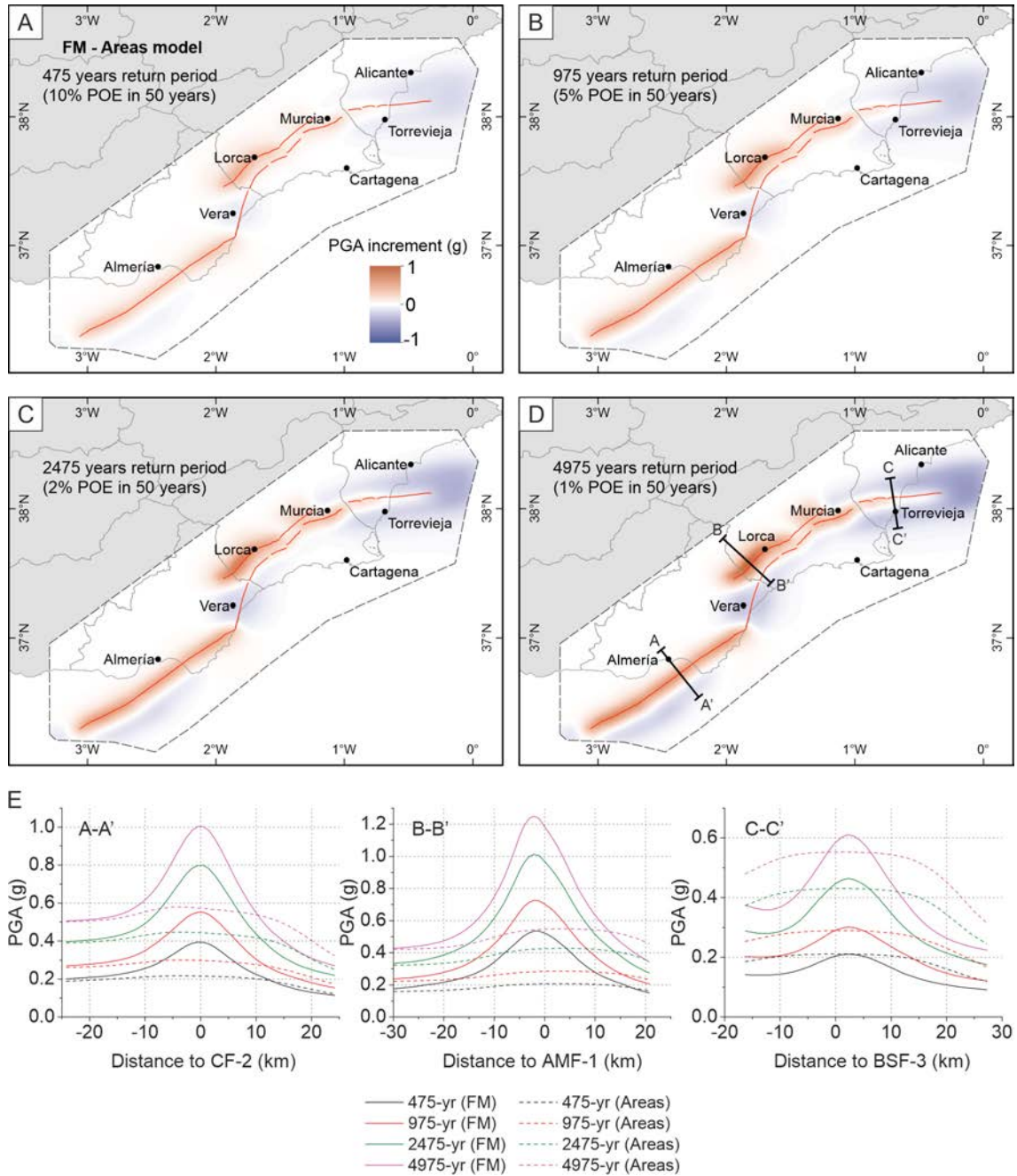


Figure 7.10. A) Difference (in g) of the mean hazard map from the FM model (Figure 7.5) respective to the mean hazard map using exclusively the ZESIS area source model (Areas model) and for the return periods of 475 years, B) 975 years, C) 2475 years and D) 4975 years. The traces of the EBSZ faults considered are depicted in red. A common color scale is set for all return periods. E) Cross sections representing PGA values of both FM model (solid line) and Areas model (dashed line) as a function of distance to the surface fault trace and for the same return periods as the maps. The locations of the cross sections are depicted in figure D.

The FM model increases the PGA with respect to the areas approach in the zones strictly around the faults. Hence, faults concentrate the hazard highlighting the controlling effect of the faults on the hazard levels. The curves in Figure 7.11A depict this effect as Lorca, which is located nearly on top of AMF (Figure 4.2A), shows the highest increment in the FM model. Next, Murcia and Almería show progressively lower PGA increments with respect to the areas model as the distance to the fault increases. These hazard increments in the near-fault zones are achieved by reducing the hazard in the zones farther from the faults with respect to the areas approach and are more visible in longer RPs (975-yr RP or larger; Figure 7.10B to D), where the faults have more influence.

The influence of faults on the hazard (net PGA and areal extension) respect to the areas approach, strongly depend on the fault slip rates. The cross sections A-A' and B-B' (Figure 7.10E), show that higher slip rate faults in the system such as CF or AMF-1, respectively (1-2 mm/yr; Table 4.1) influence the hazard up to 10-20 km far from the fault trace for all return periods. This causes significant increments in the PGA values within 20-40 km-wide influence zones of ~70-80% for all RPs in CF-3 and ~130-150% for all RPs in AMF-1 (Figure 7.10E). Such increments are slip rate dependent, thus higher for AMF-1 because it has the highest slip rate. Despite this, the disaggregation results of the FM_bg model show that faults can control the hazard in regions farther than the influence zone of the faults (20-30 km away), as it is the case of AMF-1 in Vera (Figure 7.7E and F). Farther than this distance limit however, no source has significant influence in any part of the studied area. Fault influence zones are also dependent on the dip direction in non-vertical dipping faults (AMF, BSF), wider in the hanging wall (Figure 7.10E), implying a hanging wall effect.

Contrarily, lower slip rate faults have much less impact on the hazard with respect to the areas approach. Although no exhaustive slip rate analysis has been performed, it can be observed that the faults that have slip rates < 0.1 mm/yr do not increase the seismic hazard and it is overcome by the areas approach, as it is the clear case of PF (Figure 7.10 and Figure 7.11A in Vera). Even so, faults with slightly higher slip rates (~0.1-0.4 mm/yr; AMF-4, LTF or BSF) do influence the hazard, but their impact is more limited than AMF-1, 2 or CF, even for long RPs. The cross section in BSF-3 (C-C'; Figure 7.10E) depicts one of these latter examples. This fault section has a slip rate range 4 to 14 times smaller than AMF-1 and CF (0.12-0.3 mm/yr; Table 4.1), which causes its influence zone to be over 2-3 times smaller (< 10 km wide). In this case the near-fault PGA increments are

negligible for short RPs of 475- and 975-yrs and very small ($<0.1g$) for longer RPs (Figure 7.10E). The small influence of the fault causes the FM's PGA values to be overcome by the areas approach in less than 5 km from the peak of maximum fault influence. This is also depicted by the Torrevieja curves (Figure 7.11A) and the maps of Figure 7.10. The implications of lower slip rate faults on the hazard are discussed in section 7.6.4.

The consideration of near-fault hazard in the vicinity of the EBSZ faults as both FM and FM_bg models do, including effects such as the hanging wall, provides more realistic estimations of the seismic hazard. This is relevant because during earthquakes, zones close to active faults are exposed to higher accelerations due to these near-source effects (e.g., 2011 Lorca earthquake; Alguacil et al., 2014). Their location respect to the dip direction of the fault is also relevant for the ground motion, usually higher in the hanging wall (e.g., Yu and Gao, 2001). Conversely, area source approaches do not reproduce these effects, but uniform PGA distributions within an area, as depicted by the nearly identical mean hazard curves of the cities within the EBSZ buffer area (Figure 7.11A). A detailed and representative analysis of the relationship between PGA, distance to the fault and influence of fault slip rate is a necessary step to be taken in further hazard studies in the region, as it could be useful to define amplification coefficients in earthquake resistant provisions to account for near-fault effects in sites located next to active faults.

7.6.1.2 Comparison with Rivas-Medina et al. (2018) fault-based approach

We compare the results from the FM model with the fault-based study of Rivas-Medina (2014), recently published in Rivas-Medina et al. (2018). In that study a PSHA of southern Spain is performed considering faults as independent, non-interacting sources, following a hybrid methodology (HM model) that avoids setting an arbitrary cutoff magnitude for modelling seismicity in the background (see details in Rivas-Medina et al., 2018). The PSHA was performed for a larger territory of southeastern Spain than the present study and for all the active faults of the region as compiled in the old QAFI v.2 database back in 2012. The areal model for this study (GM10) is different from the ZESIS model (aka GM12; IGN-UPM, 2013) as it does not identify the EBSZ buffer area (area #55; Figure 4.4). The GMPE used is the same as in our study. We compare the mean hazard curves of the FM model with the HM model, including Alicante (Figure 7.11B and C). The hazard curves for the cities of Lorca, Vera and Torrevieja were not computed specifically by the authors, hence we inferred visually the PGA values at these cities from pixel screening of the hazard maps for each of the four RPs calculated (Figure 7.11C).

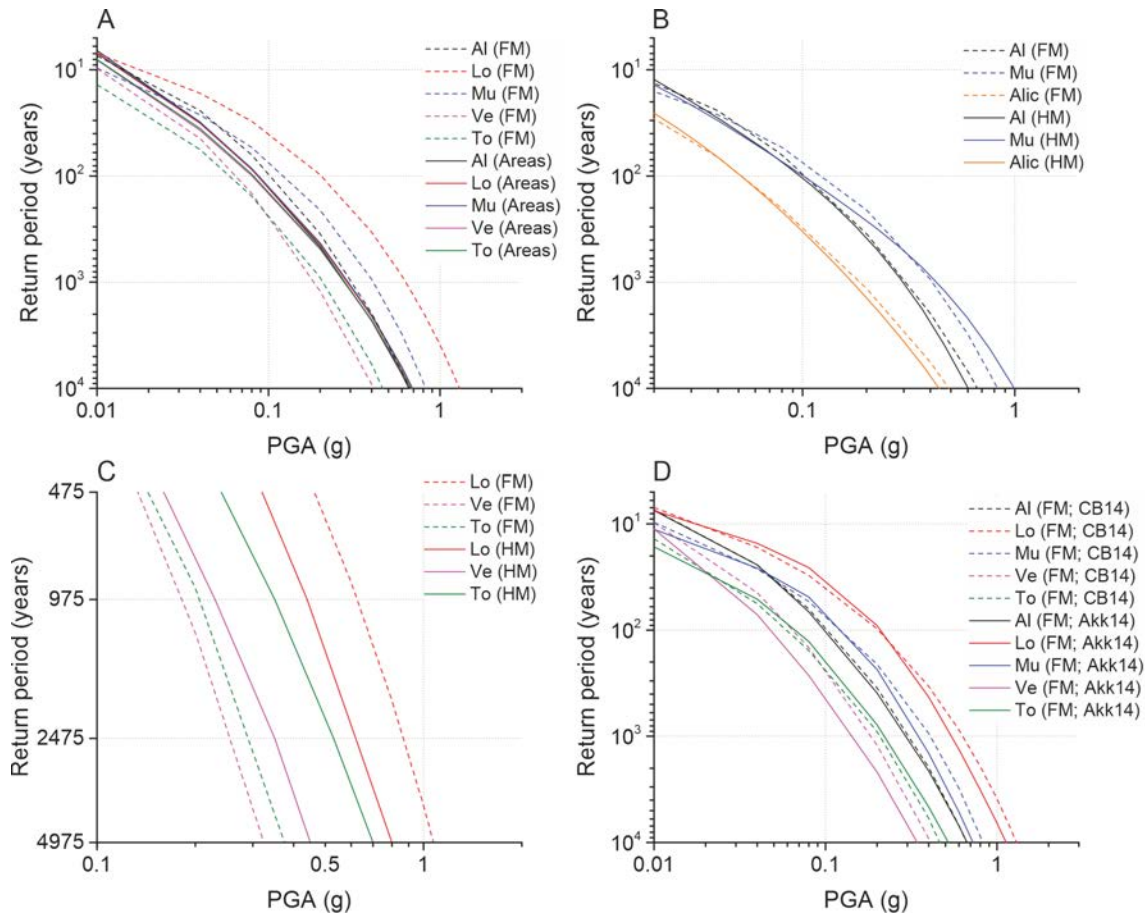


Figure 7.11. **A)** Mean hazard curves for PGA (g) of the FM model plotted with the ones of the ZESIS areas model for the cities of Almería (Al), Lorca (Lo), Murcia (Mu), Vera (Ve) and Torre Vieja (To). **B)** Mean hazard curves for PGA (g) of the FM model and the HM model from Rivas-Medina et al., (2018) for the cities of Almería, Alicante (Alic) and Murcia and **C)** for the cities of Lorca, Vera and Torre Vieja. In these last three cities, the results are visually inferred from pixels of the maps from this publication, hence the curves are exclusively plotted for the return periods of 475, 975, 2475 and 4975 years. **D)** Mean hazard curves for PGA (g) of the FM model using the CB14 (Campbell and Bozorgnia, 2014) and Akk14 (Akkar et al., 2014) GMPEs and for the same cities as figure A.

The main contribution of our work with respect to Rivas-Medina et al. (2018) is the consideration of multi-fault ruptures in the source modelling, which causes differences in the hazard estimations mainly for long RPs. Regarding the EBSZ as a whole in PSHA and accounting for such rupture possibilities is a novelty in Spain and might constitute a more realistic approach to model the seismic hazard.

In general, the study by Rivas-Medina et al. (2018) provides hazard levels in the range of the ones obtained by the FM model, however there are noteworthy differences. These are mainly due to a) the consideration of multi-fault ruptures in the FM model, b) differences in the fault data used in each source modelling, c) the background seismicity of the HM

model and d) the number of faults considered. The FM model treats the fault system as a whole by allowing the possibility for faults to rupture simultaneously in multi-fault ruptures including large rupturing scenarios. This consideration allows a larger number of fault rupture possibilities to host a certain magnitude and therefore hazard values are generally higher for this model, as shown by the curves of Lorca, Almería and Alicante (Figure 7.11B and C). These differences are more notable in RPs over ~1000 years because multi-fault ruptures produce higher magnitudes that control the longer RPs. Moreover, the discrepancies in the slip rate values and segmentation between both FM and HM models are also responsible for the hazard differences. For instance, the higher values of the FM in Lorca are because updated slip rate data for AMF-1 and AMF-2 are used (1.65 and 1.0 mm/yr, respectively; Table 4.1), contrary to the HM model (0.3 and 0.5 mm/yr). The higher values in Almería, on the other hand, are because CF is divided in three segments with a mean slip rate of 1.1 mm/yr in the FM model, while in the HM it is divided in two segments, one of which uses an outdated slip rate (0.04 mm/yr).

In the cities of Murcia, Vera and Torre Vieja, the curves of the HM model predict higher values than the FM model (Figure 7.11B and C). In Murcia this is only for RPs over ~500 years, as for lower RPs the tendency is the same as the mentioned for Almería and Lorca. We attribute this to the fact that CAF, which controls the hazard of this city (Figure 7.7G and H), is considered as a single-segment fault in the HM model (CAF; 0.54 mm/yr), while in the FM as two segments with different and lower mean slip rates (0.37 and 0.53 mm/yr for CAF-1 and 2, respectively; Table 4.1). In RPs over 500 years this implies that probably a big part of the magnitudes that in the HM model are achieved independently by CAF, in the FM model are achieved by multi-fault ruptures involving CAF-1 and 2. As the slip rates of CAF-1 are lower than CAF-2, the occurrence rates of these multi-fault ruptures are limited by the former (see slip rate treatment in SHERIFS on section 4.1.3) and hence are lower than the HM model in this area. On the other hand, the fact that the fault is divided in two segments increases the earthquake rates of lower magnitudes and consequently the PGA values for low RPs (<500 years) in this city with respect to the HM model (Figure 7.11B). As such, linked ruptures between segments, i.e., higher magnitudes, are less frequent in low RPs.

In Vera and especially Torre Vieja the higher values of the HM model are visible in all RPs represented (Figure 7.11C). In the former, the hazard is not controlled by the nearest faults due to the low activity rates of PF, so the background seismicity of the HM model

overcomes the ones from the FM. Remarkably, performing this comparison with the curves from the FM_bg model would produce practically the same results, as the background seismicity of the HM model is modelled for a larger magnitude range (Mw 4.0-6.9) and implies higher seismicity rates. In the latter, the higher HM values are because in this area, additional fault sources apart from the BSF are considered in the modelling (Torrevieja and San Miguel de Salinas faults; Figure 4.2A). While the incorporation of more fault sources on the hazard might suggest that the results from the HM model in the Torrevieja zone are more accurate than the FM, it should be noted that including more faults on the hazard does not necessarily imply more accurate results. These additional faults are not included in our models because are secondary faults to the BSF system (Alfaro et al., 2012) and hence are not part of the main structures in the EBSZ. Moreover, neither their relationship with the EBSZ system and their geological parameters have been studied in detail. The inclusion of such faults on the hazard should account for these uncertainties as they could imply misguided hazard estimations.

7.6.2 Implications for moderate magnitude earthquakes

The hazard results from the disaggregation show that moderate magnitudes in the Mw 4.5-6.0 range, although not being the most remarkable, have a non-depreciable contribution to the final hazard in the selected studied sites even in long RPs (e.g. Almería and Vera; Figure 7.7D and F, respectively). Moreover, according to Gaspar-Escribano et al. (2008), in southeastern Spain, low-to-moderate magnitude earthquakes between Mw 4.0 and 5.5 control seismic hazard for the 475-yr RP. Such kind of earthquakes are relatively frequent in southeastern Spain and have demonstrated to be quite destructive. The 1999 Mw 4.8 Mula, 2002 Mw 5.0 Bullas and 2005 Mw 4.8 La Peca earthquake series are some recent examples (Benito et al., 2007), being the 2011 Mw 5.2 Lorca earthquake the latest one (Martínez-Díaz et al., 2012a).

The near-source effects of the 2011 Mw 5.2 Lorca earthquake produced exceptionally high accelerations around 0.37g in the city of Lorca (Cabañas et al., 2011) due to: a) the proximity of the epicenter to the city, b) the shallow depth of the earthquake and c) the directivity of the rupture propagation towards Lorca (Alguacil et al., 2014). The hazard map of the current Spanish Building Code (NCSE-02, 2002) for the 500-yr RP and the updated national seismic hazard map for the 475-yr RP (IGN-UPM, 2013) predict PGA values in Lorca (0.12g and 0.19g, respectively) that underestimate the PGA reached in the Lorca earthquake. Conversely, the results of the FM and FM_bg models predict values

that differ less than 0.1g from the ones reached in the 2011 Lorca earthquake: $\sim 0.45g$ for the 475-yr RP. Rivas-Medina et al. (2018) predict slightly lower values of 0.3g in Lorca for the same RP, but that are also close to the measured ones.

The fact that fault-based PSHAs in southeastern Spain predict PGA values for the 475-yr RP coherent to the ones of the Lorca earthquake, whose moderate magnitude produced severe damage, may suggest that fault-based approaches perform more realistic hazard predictions than classical area source approaches, particularly for sites located on top of faults or in their vicinity. The PSHA such as the one presented in this study or the one from Rivas-Medina et al. (2018) approximate better the hazard for short RPs due to the effect of faults. However, other site effects such as topography, directivity and changes in soil properties should be incorporated for a more accurate hazard estimation, especially in seismic microzonation.

7.6.3 Implications of the Ground Motion Prediction Equation selection (GMPE)

The selection of GMPEs for PSHA is also a difficult task as it has a great influence on the hazard results obtained for a particular study region and, sometimes, can mask or exaggerate the influence of a seismic source. In this study, we selected a NGA GMPE that is well adapted for fault-based PSHA (Campbell and Bozorgnia, 2014) as it is sensitive to near-fault effects. Therefore, the strong contribution of the faults into our hazard models could be seen as a result of applying such equation. To test the sensitivity of the hazard models to the GMPEs we performed the hazard calculation of the FM model using the equation by Akkar et al. (2014) (henceforth Akk14). We used this equation because is not as specifically designed for near-fault effects as the one by Campbell and Bozorgnia (2014) (henceforth CB14) and the source characteristics of earthquakes are exclusively represented by magnitude and style of faulting. The mean hazard maps of the FM model using Akk14 are shown in Figure 7.12A and B for the 475- and 4975-yr RPs. The differences with the CB14 equation are depicted in the maps of Figure 7.12C and D and the cross sections of Figure 7.12E for the same RPs. Only these two extreme RPs are shown to point out the maximum variations with the CB14 equation.

The sensitivity test performed with the Akk14 equation evidences that the influence of the EBSZ faults on the hazard results performed in this study is independent of the GMPE used. Therefore, the marked influence of the faults into the PSHA is not a consequence

III. Results and partial discussions

of the GMPE. The resulting mean hazard maps of Akk14 are very similar to the ones obtained with the CB14 equation (Figure 7.5) showing a similar hazard distribution.

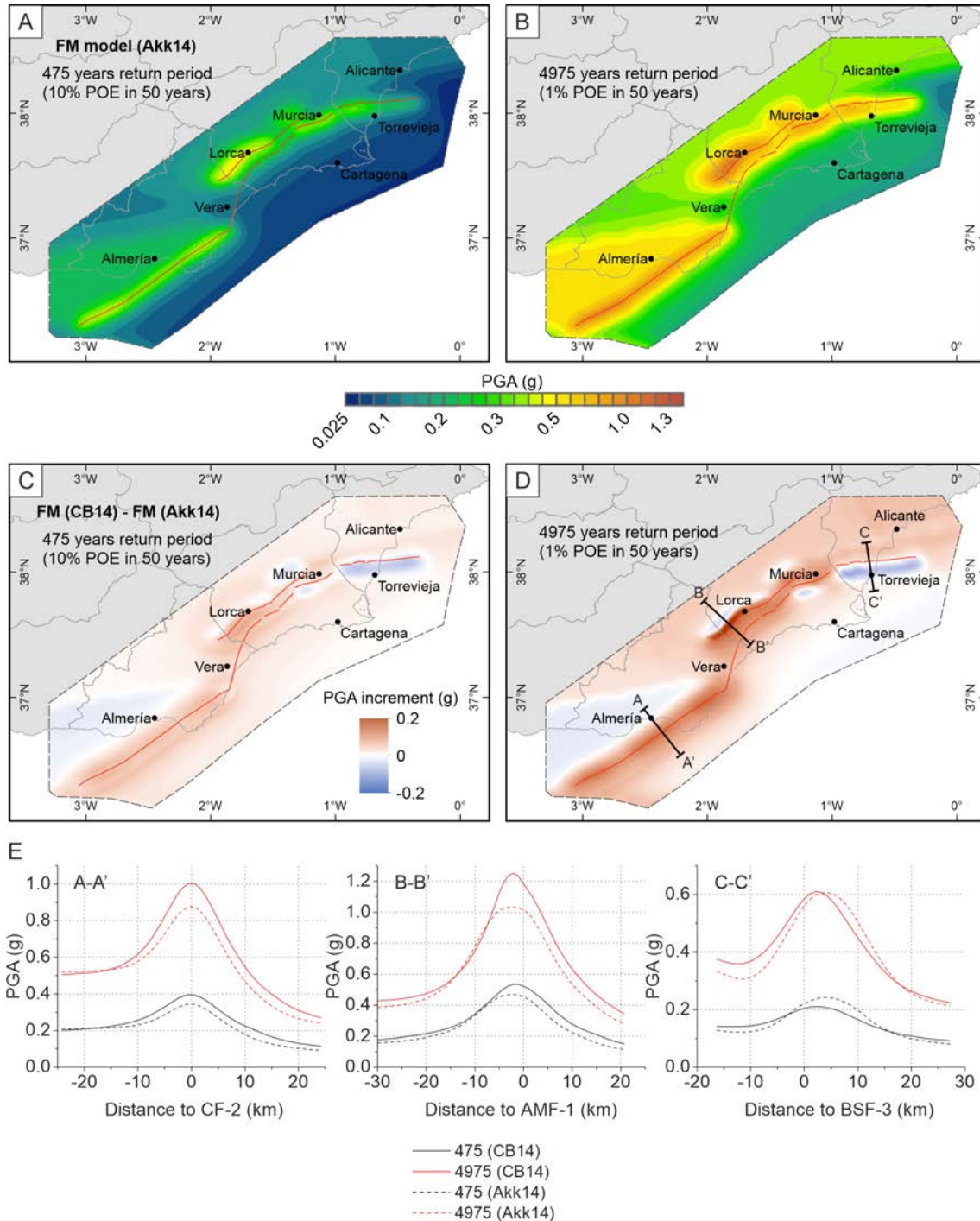


Figure 7.12. A) Mean hazard maps for PGA (g) of the FM model using the Akk14 GMPE (Akkar et al., 2014) for the return periods of 475 years and B) 4975 years. The color scale is common for both return periods. C) Difference (in g) of the mean hazard maps from the FM model using the CB14 equation with respect to using Akk14 for the return periods of 475 years and D) 4975 years. The color scale is common for both return periods. The traces of the EBSZ faults considered are depicted in red in all panels. E) Cross sections representing PGA (g) values of the FM model using the CB14 (solid line) and Akk14 (dashed line) GMPEs as a function of distance to the surface fault trace and for the same return periods as the maps. The locations of the cross sections are indicated in figure D.

Faults have a clear influence on the hazard for both RPs explored in the near-fault zones and the highest PGA values are found along the traces of the faults, especially the most active according to their slip rates (e.g., AMF-1 and CF). Hanging wall effects are also recognized in the map using Akk14 for non-vertical dipping faults (AMF, CAF and BSF; Figure 7.12A and B). Despite this, due to its less sensitivity to near-fault hazard estimations, Akk14 computes a more diffuse hazard estimation around the faults, with lower PGA values in general and lower PGA increments as a function of distance to the fault trace (Figure 7.12E). Therefore, CB14 produces higher PGA values than Akk14 for most of the mapped area and especially around faults, accentuating near-fault effects on the hazard levels. Maximum variations are located close to the traces of faults with higher slip rates, importantly around CF or AMF-1, where these are up to 0.1g and 0.2g, respectively for the 4975-yr RP and <0.1g for the 475-yr RP (A-A' and B-B', respectively; Figure 7.12E). The mean hazard curves from Lorca, Almería, Murcia and Vera also depict PGA increments for the CB14 equation in RPs over ~100 years (Figure 7.11D). In other lower slip rate faults such as BSF, the use of different GMPEs implies practically negligible PGA variations for all RPs (C-C' cross section along BSF-3; Figure 7.12E). In this case, for the 475-yr RP, the use of Akk14 provides slightly higher PGA values (~0.05g) due to the less sensitivity of the equation to the fault slip rates, up to one order of magnitude lower than AMF-1 or CF (Table 4.1).

In non-vertical dipping faults, hanging wall effects are more accentuated with the CB14 equation (Figure 7.12C to E). In the zones further away from the fault trace on the hanging wall, hazard decreases more abruptly with CB14, especially in long RPs. The higher PGA gradient around the fault trace causes a rapid drop on the hazard values with respect to the lower gradient of Akk14 as distance to the fault increases. AMF, CAF and BSF are clear examples of this effect and, in particular, BSF is the one affected by highest reductions on the hanging wall for all RPs, because its dip is lower (Table 4.1) and the surface projection of its fault plane is larger (Figure 7.12C and D). The curve of Torre Vieja represents this effect related to the BSF as well (Figure 7.11D).

7.6.4 Implications of the fault slip rates

Fault slip rates are a controlling factor in the hazard values obtained in this study as they have a direct impact on the probabilities of exceedance in a given observational period. Higher slip rate faults (e.g., AMF-1 and 2 or CF) imply higher PGA values and influence

than lower slip rate faults, some of which have slip rate values so low (<0.1 mm/yr; PF) that are not able to influence significantly the hazard at any RP. This is also observable in the slip rate values used by the source models that compose each branch of the logic tree in relationship with the resulting PGA for each model (Figure 7.13). Each source model is built by picking random slip rate values from the fault uncertainty ranges provided as inputs (Table 4.1). Thus, aside from the fault rupture hypotheses considered, the models that use higher slip rate values within the uncertainty range show an overall tendency to produce higher PGA estimations at closer sites within the same hypothesis (e.g. AMF-1 in Lorca; Figure 7.13A and B). Nevertheless, the data in the plots show high dispersion, which suggests that the slip rate uncertainty is not the only parameter affecting seismic hazard variability. In fact, the proximity of the fault to the analyzed site, the rupture hypothesis in question or the RP might control the slope of the mentioned tendency for each hypothesis. Closer sites, i.e., Lorca, result in steeper slopes, similarly to higher RPs (Figure 7.13A and B).

Another important observation is that PGA variations as a function of slip rate uncertainty are more remarkable in higher slip rate faults (Figure 7.13A and B), despite their uncertainties being smaller than for lower slip rate faults (Figure 7.13 C and D). AMF-1 has an uncertainty that represents only the $\sim 3\%$ of the mean, while it is $\sim 100\%$ for PF-1, however the hazard variations linked to the slip rate variations are considerably higher for the former in Lorca than the latter in Vera. This is because lower slip rates have less impact on the return periods studied than higher slip rate faults, which is consistent with the low influence of PF in our hazard calculations (Figure 7.7E and F).

The identification of the method and source of information upon which slip rate data is based on for each individual fault (section 4.1.2) is a crucial step, as it affects the reliability of such data and ultimately the hazard results. At the EBSZ, this is one of the main challenges today as most paleoseismic studies focus only on specific fault sections or single strands of faults with multiple branches, while others remain poorly studied. The faults that concentrate most part of these studies and thus have a better characterization are AMF-1 and 2, CAF and CF. Although most of these focus only on the major fault branches, their slip rate estimations are robust and consistent with overall geodetic data. Conversely, PF, AMF-3 and 4 or BSF have not yet been the object of detailed paleoseismic research and fault data is inferred based on qualitative geomorphological indicators and from geodetic data. These less studied faults at the EBSZ are the ones that

have lower slip rate estimations (Table 4.1) and contribute poorly to the hazard, which could imply a bias of such hazard towards the well-studied ones.

Considering the clear sensitivity of the seismic hazard to the fault slip rates, the acquisition of new data in the less studied faults is critical to increase the quality and reliability of the current available data compared to other faults in the EBSZ. Updated parameters can have important implications in the hazard results around them, especially PF, as we explain in the following section 7.6.5.

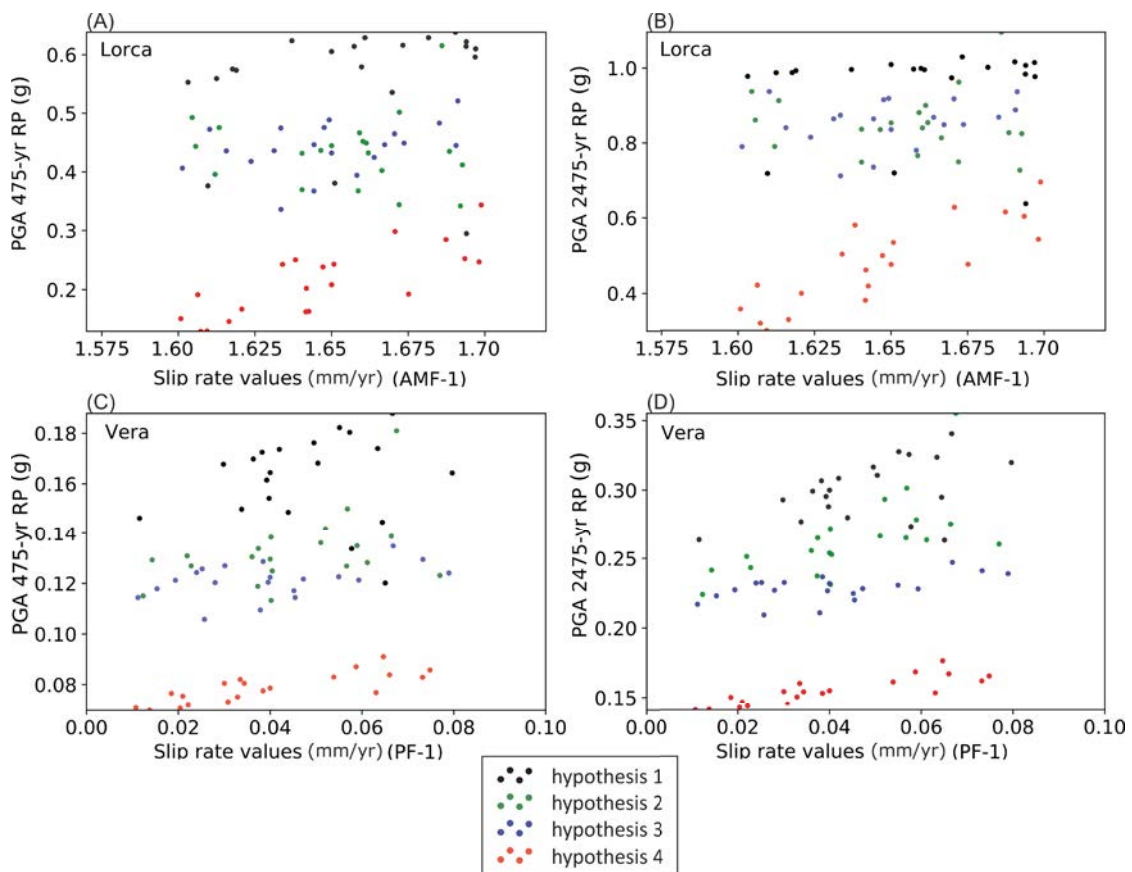


Figure 7.13. A) Relationship between the slip rate values of AMF-1 used in each 80 source models that compose the logic tree of this study and the respective PGA (g) values obtained in the city of Lorca for the return periods of 475 years and B) 2475 years. C) Same relationship for PF-1 and the PGA (g) obtained in the city of Vera for the return periods of 475 years and D) 2475 years. Note that, in order to highlight better this effect, the faults considered here are the closest to the cities analyzed.

7.6.5 Testing the impact of updated slip rate data into the seismic hazard

From the date of completion of the hazard results presented in this section and subsequent publication in JCR journals (Gómez-Novell et al., 2020a, 2020b) to the date of redaction of the present thesis, new paleoseismic results of the EBSZ faults have been published, including new slip rate estimations. Given the acknowledged sensitivity of the hazard

models to fault slip rate data, we found it pertinent to perform, as a test, a seismic hazard calculation using these updated data, including the values obtained in this thesis for the Lorca-Totana segment of AMF (AMF-2). This analysis allows to identify and discuss possible variations with the published results and their relevance.

To do so, we first modelled the earthquake rates of the EBSZ fault system with SHERIFS using the same four hypotheses of fault ruptures and the same modelling parameters for the FM model explained in the methods (section 4), but considering the updated fault data for the inputs. Additionally, for each hypothesis 10 samples instead of 20 have been explored to simplify the computations. The new model is henceforth referred as FM_updated and no background ratios are included to better test the influence of faults into the hazard. The new published data, compiled in Table 7.1, concern updated slip rates for some of the faults in the system (AMF-2, AMF-4, CAF-2) or kinematic observations that can imply changes in the previous values (PF-1 to PF-3). The new data also motivate the revision of the values assigned to AMF-3, previously inferred using expert opinion (section 4.1.2). We detail them below for each case:

- PF-1 to 3: The recent study by Roquero et al. (2019) highlights that PF is mainly a strike slip fault with a pitch of 10-11° based on fault plane striae. This contrasts with previous slip rate data in these fault segments that referred to uplift rates of the mountain fronts (Table 4.1; section 4.1.2.1) and considered the fault mainly as a dip-slip structure. We have then calculated the net slip rate of the three segments of PF by applying the new kinematic information to the previously estimated uplift rates (Equation 3.1; section 3.4.3). The net slip rate of PF-1 and 2 (0.05-0.42 mm/yr; Table 7.1) is calculated from the uplift rates in García-Mayordomo (2005) (0.01-0.08 mm/yr) while for PF-3 (0.17-0.40 mm/yr), instead of using expert opinion as before, we relied on the uplift rates in Silva et al. (2003) (0.03-0.07 mm/yr).
- CAF-2: New published data in this segment from Martín-Banda et al. (2021) estimate a slip rate of 0.49 ± 0.02 mm/yr for the last ~125 ka
- AMF-4: New published data in this segment from Herrero-Barbero et al. (2020) infer a maximum long term net slip rate of $0.32^{+0.18}/_{-0.13}$ mm/yr for the last 4.8-7.6 Ma. The maximum estimate is used because it provides a more conservative assessment.
- AMF-2: The new data in this segment is the one obtained in this thesis (section 5): a net slip rate of $1.55^{+0.14}/_{-0.18}$ mm/yr for the last 18 ka, which is the longest time period where there is record available for all the fault branches considered.

- AMF-3: This segment remains unstudied to date, but we estimate that the previously assigned values of Table 4.1 are, at our criterion, too small in the context of the surrounding segments, more so considering that these values were inferred mainly based on expert criteria. Thus, a median value between the AMF-2 and AMF-4 segments is assigned to AMF-3: 0.9 ± 0.2 mm/yr. This guarantees a triangular model of slip rate distribution for the AMF in which the slip rate is lower at the tip sections (AMF-4) and increases towards the central segments (AMF-3 to AMF-2), as observed in nature (e.g., Manighetti et al., 2005).

Fault name	Fault section ID	Net slip rate (mm/yr)		
		Min.	Mean	Max.
Carboneras (CF)	CF-1	1.1	1.2	1.3
	CF-2	1.1	1.2	1.3
	CF-3	1.1	1.2	1.3
Palomares (PF)	PF-1*	0.05	0.24	0.42
	PF-2*	0.05	0.24	0.42
	PF-3*	0.16	0.28	0.4
Los Tollos (LTF)	LTF	0.06	0.16	0.25
Carrascoy (CAF)	CAF-1	0.29	0.37	0.45
	CAF-2*	0.47	0.49	0.51
Bajo Segura (BSF)	BSF-1	0.25	0.33	0.41
	BSF-2	0.25	0.33	0.41
	BSF-3	0.12	0.2	0.3
	BSF-4	0.12	0.2	0.3
Alhama de Murcia (AMF)	AMF-1	1.6	1.65	1.7
	AMF-2*	1.37	1.55	1.69
	AMF-3*	0.7	0.9	1.1
	AMF-4*	0.19	0.32	0.5

Table 7.1. Fault slip rate data used for the FM_updated model in each fault section. The fault sections affected by the new values are marked with (*). References for the new values with respect to the FM model are explained in the text of this section. See Table 4.1 in section 4.1.2 to consult the previous values assigned to each fault and upon which the hazard calculations of the thesis are based on.

7.6.5.1 Model performance and consistency check

The resulting fault GRs from the FM_updated model have been analyzed both with the seismicity rates from the earthquake catalogue and paleorates (Figure 7.14 and Figure 7.15), like in the FM model in section 7.2.2. In this case we use the new RI obtained in this thesis for the S-AMF and F-AMF (section 5.6.1) to check the models in AMF-2.

The GR curves from the new model show that hyp. 2 and 3 are still the ones with the best fits with the regional seismic catalogue and even better than for the FM model because the modelled curves show less dispersion (Figure 7.14). This, together with the NMS

III. Results and partial discussions

percentages below 30% indicate a good performance of these two hypotheses and reinforce their robustness and suitability for the EBSZ. Remarkably, hyp. 4 shows a considerably better performance than in the FM model with some of the samples overlapping the catalogue (Figure 7.14). This highlights the importance of slip rate data into the modelling with SHERIFS because the better results of this hypothesis are direct consequence of such data. In the FM model, the lower performance of hyp. 4 was related to the lower slip rates of some faults, mainly PF, that acted as a limiting factor for the exhaustion of the slip rate budget and, hence, contributed to i) lower significantly the earthquake rates and ii) increase the NMS up to 80-90%. The updated slip rate values for these faults are higher, a fact that allows easing the modelling issues related to the NMS. The new models have lower NMS percentages, now between 40 and 85% (Figure 7.14), which contrasts with the FM model values. This implies an overall better performance of the rupture model from hyp. 4, although it is still the poorest (>30-40%). We then interpret that the rupture scenarios in this hypothesis are not the most suitable for the EBSZ.

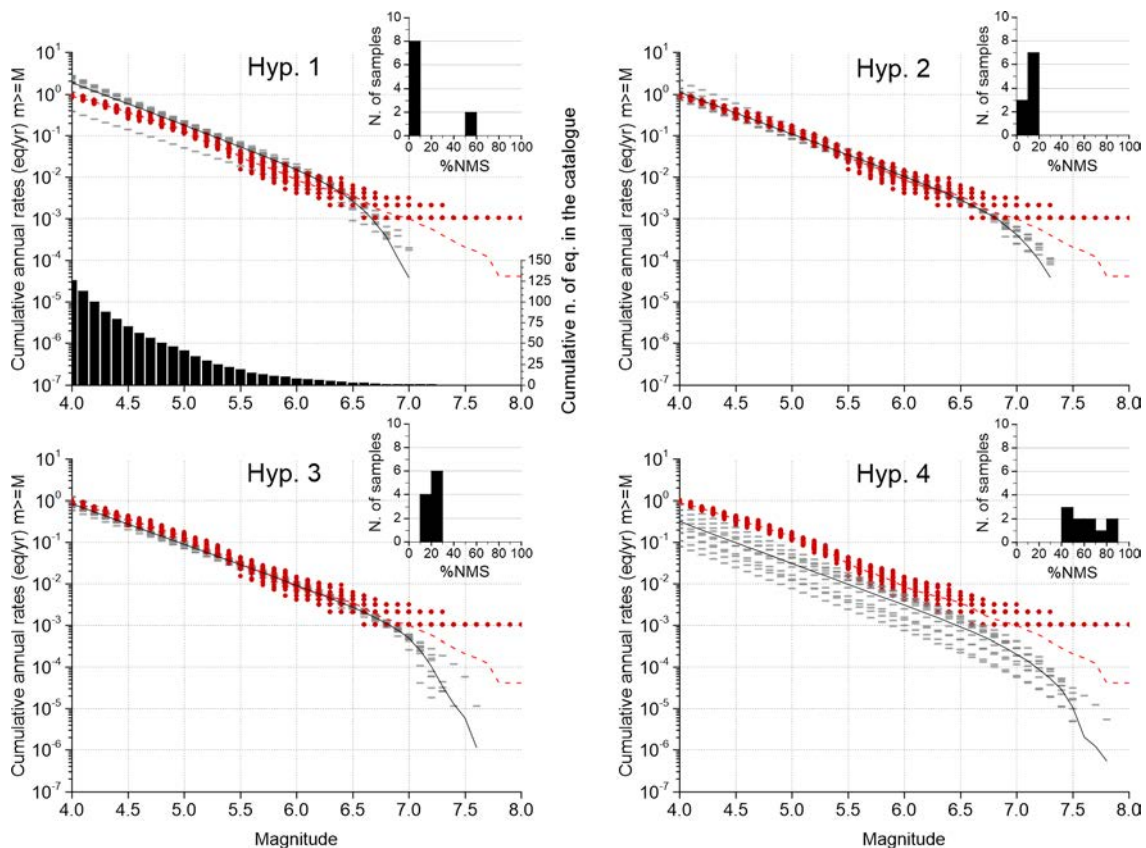


Figure 7.14. Comparison between the GR curves of each hypothesis (grey lines) and the earthquake rates from the catalogue (red dots) for the FM_updated model. Mean GR curve modelled: solid black line; samples: short grey lines; catalogue mean GR curve: dashed line. The bottom of hyp. 1 graph shows the cumulative number of earthquakes of the catalogue per magnitude used to draw its MFD. Non-Main-Shock slip (NMS) histograms of the models are indicated.

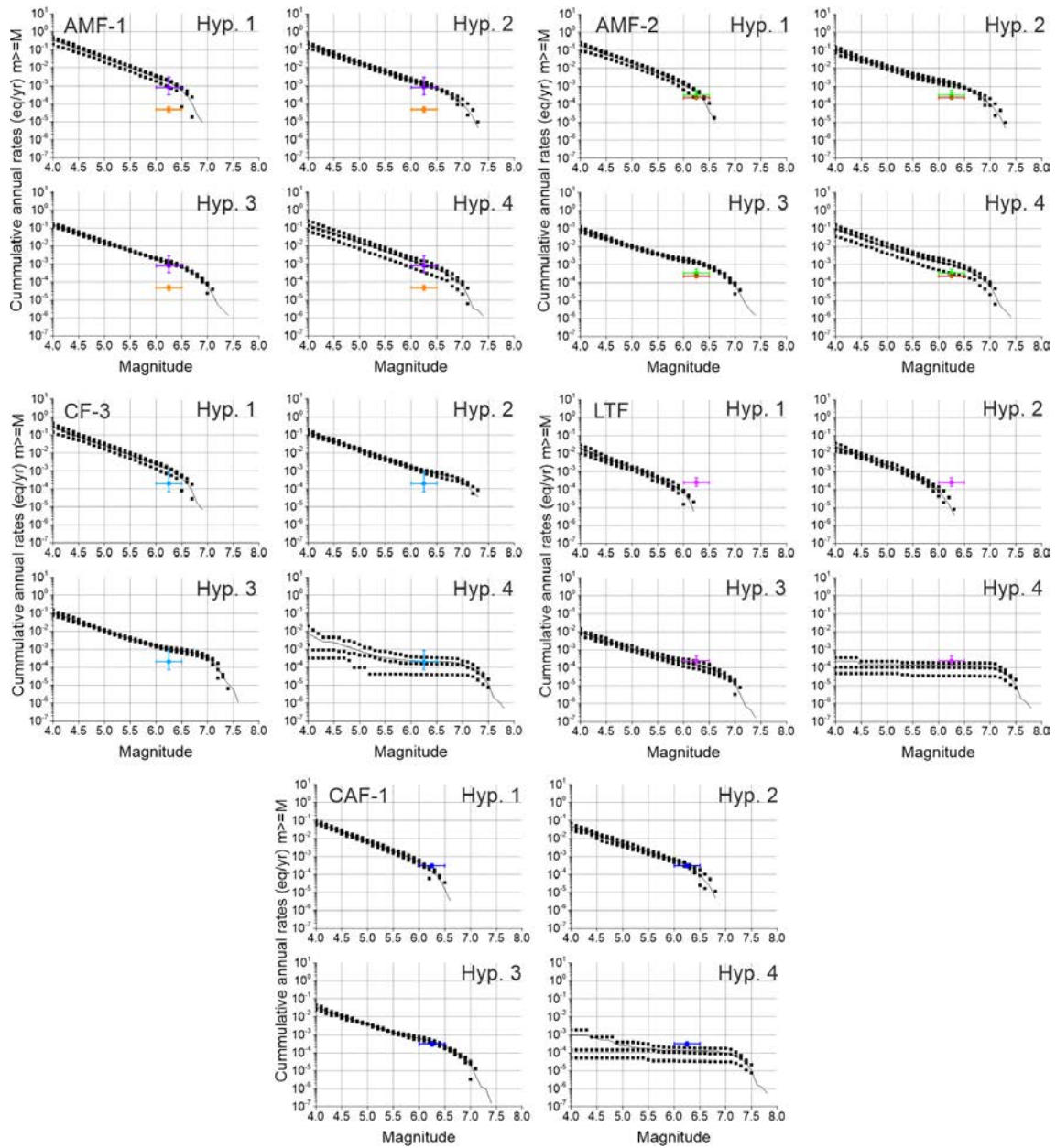


Figure 7.15. Annual rates of paleoearthquakes from paleoseismic studies plotted with the FM_updated participation rates of the fault section where paleoseismic studies are developed. The location of each paleoseismic site and studies are depicted in the map of Figure 7.2, except for the paleorates in AMF-2 that are based on the recurrences of S-AMF (red) and F-AMF (green) obtained in this thesis (Table 5.12). In the participation rates the solid line represents the mean value and the squares represent the median, 16th and 84th percentiles of the distribution.

In terms of the paleorates, the fit of the new FM_updated model is similar to the FM for hyp. 1 to 3 in most of the sites, with generally good fits especially for hyp. 2 and 3 in CAF-1 or hyp. 3 in LTF (Figure 7.15). The main differences arise for hyp. 4 as the modelled GR curves show good agreement in the paleoseismic sites of AMF-1 and 2 or CF-3. Similar to the fit with the catalogue, the updated slip rate values contribute to change significantly the earthquake rates of the faults especially in scenarios where large

multi-fault ruptures are involved (i.e., hyp 4) and where the modelling becomes more sensitive to slip rate variations. Despite these good fits, the fact that hyp. 4 shows still poor agreement with the catalogue and overall bad performance in terms of NMS, does not allow to rank it better than the other three hypotheses. In addition, and as seen in section 7.5.1.2, the paleorate analysis is affected by uncertainties larger than the earthquake catalogue ones that concern mainly their completeness, especially in the EBSZ, and may not be used as a main dataset to check the models presented. Interestingly, the paleorates that show good fits with hyp. 4 in the FM_updated model are the ones with larger uncertainty ranges, e.g., AMF-1 or CF-3, and the modelled curves also show the highest dispersion. Thus, the reliability of the analysis for this hypothesis is lower. Regarding the logic tree weights, the same weights as the FM model have been used because the fits of the hypotheses with the datasets provide similar rankings (section 7.3).

7.6.5.2 New hazard results and implications for the Eastern Betics Shear Zone

The hazard calculations have been performed using the same specifications explained in section 4.2.6. We present seismic hazard maps for the four calculated RPs (Figure 7.16) as well as hazard disaggregation plots for the cities of Lorca, Almería, Vera and Murcia for the 475- and 2475-yr RPs (Figure 7.17). The seismic hazard maps, like in the FM model, show a clear influence of the modelled faults: highest PGA values are localized around the faults with higher slip rates in the system (i.e., AMF or CF). Conversely, the consideration of the new slip rate values causes significant differences that concern the seismic hazard around the affected faults (AMF-2 to 4, PF and CAF-2) and especially for long RPs (2475- and 4975-yr). The most remarkable change is observed around PF's trace, whose spatial distribution depicts the influence of this fault into the PGA, especially for the two longer RPs (Figure 7.16). This is also observed in the disaggregation plot of the city of Vera as well (Figure 7.17) because the PF controls the seismic hazard for almost all the magnitude range (M_w 4.5-6.8), even for the 475-yr RP. This contrasts with the FM model in which PF had a minor contribution.

Other significant changes are observed for AMF, where the updated values in the segments AMF-2 to 4 contribute to increase the hazard around them in all RPs, especially in AMF-2. The AMF contribution to the seismic hazard of the Lorca city is thus underpinned compared to the FM model (Figure 7.17). The range of magnitudes contributing to the hazard is expanded towards lower magnitudes due to the higher expected rates. Similarly, CAF-2 shows a slightly higher contribution to the hazard in the

disaggregation plot than for the FM model due to the reduction of the uncertainty range in the new slip rates (Table 7.1).

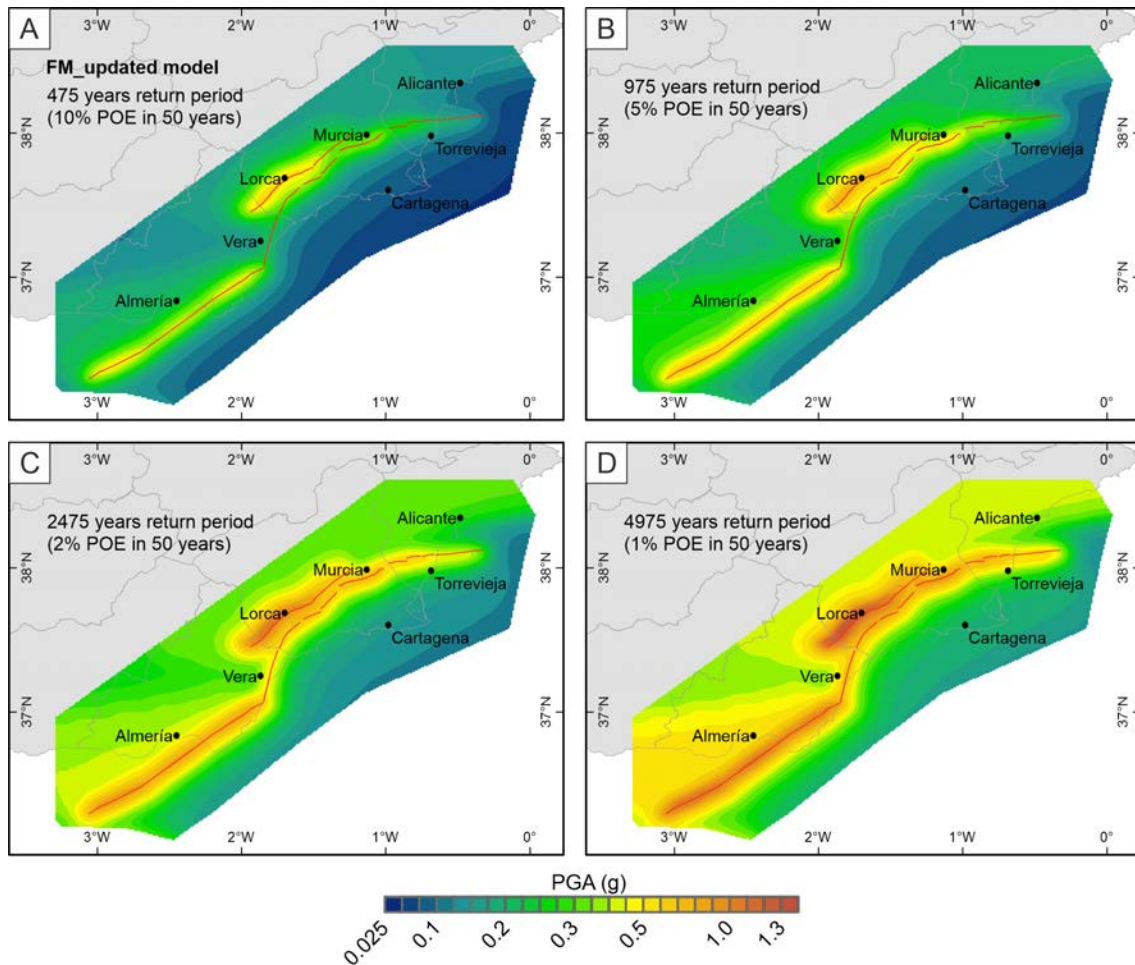


Figure 7.16. A) Mean hazard maps for PGA (g) of the FM_updated model for the return periods (RPs) of 475 years, B) 975 years, C) 2475 years and D) 4975 years, equivalent to the probabilities of exceedance (POE) of 10%, 5%, 2% and 1%, respectively.

The results of the test performed in the FM_updated model remark how crucial fault slip rates are for the seismic hazard assessment because they can imply very important variations in the hazard estimations of some sites even for short return periods. This is even more important when the affected sites are highly populated (Lorca, Almería or Alicante) and where the occurrence of an earthquake can have devastating consequences in terms of human and economic costs, as seen with the 2011 Lorca earthquake. First, the hazard values for the AMF-2 in this updated analysis are seen as more representative and reliable than the previously published (FM model) because the slip rate is based on a more complete transect of the fault. Second, the contrasting results found mainly around PF are a direct consequence of the updated slip rate values and highlight, again, the urgent need for the development of detailed paleoseismic studies in this fault. The PF values are just

an approximation based on local kinematic data and should not replace nor exempt doing paleoseismic research. At our criterion, future studies should focus on the recent Quaternary activity of the unstudied faults (PF, AMF-3) to ensure that the current long-term estimations are correct and that reflect the current fault behavior.

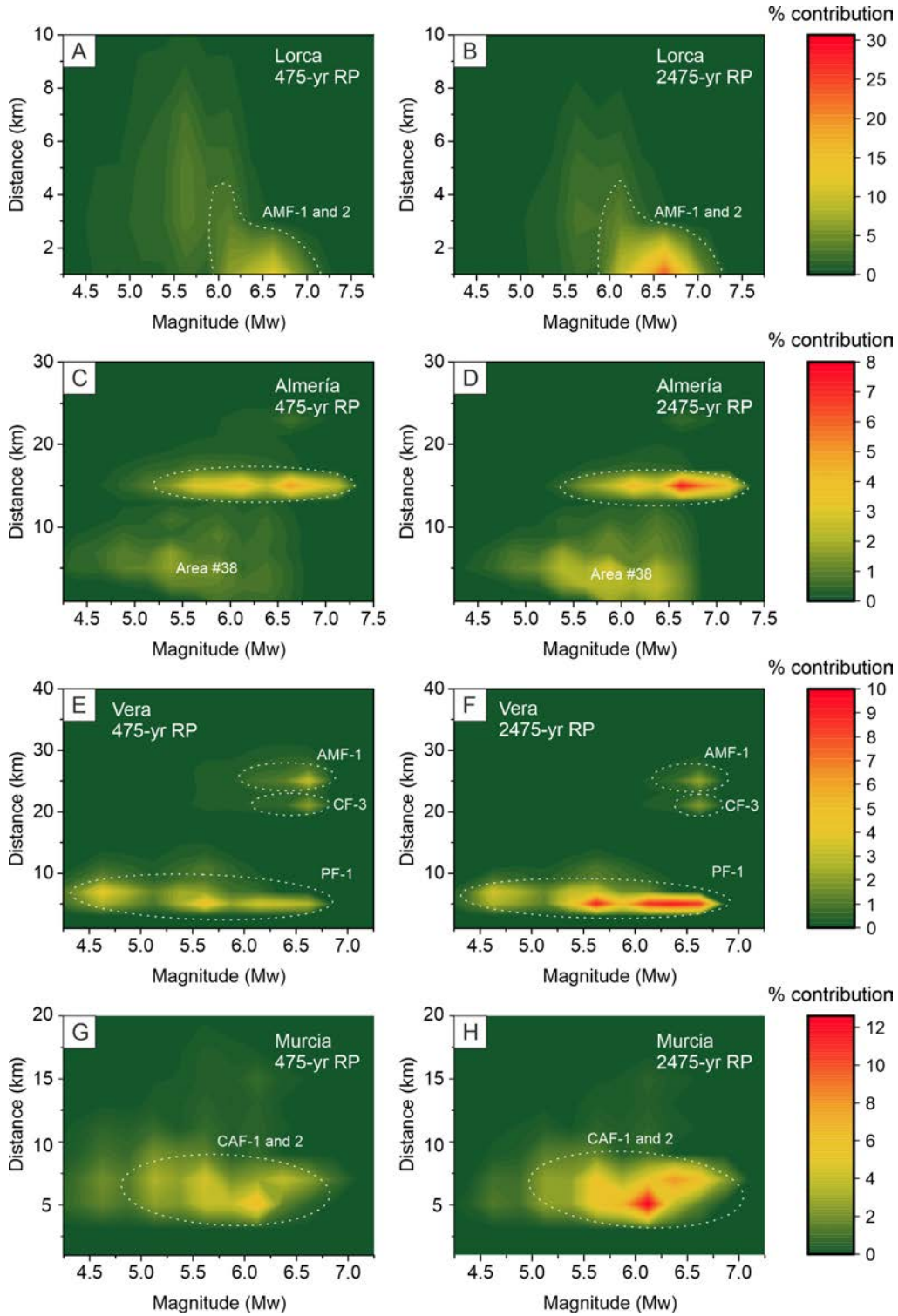


Figure 7.17. A) Hazard disaggregation for the magnitude-distance relationship of the FM_updated model in the cities of Lorca for the return periods of 475 years and B) 2475 years, C) Almería for 475 years and D) 2475 years, E) Vera for 475 years and F) 2475 years and G) Murcia for the 475-years and H) 2475-years. The main contributing sources are highlighted.

7.6.6 Overview: limitations and perspectives

The high hazard values in the near-fault zones, the large contribution of faults on the sites' hazard and the agreement of the 475-yr RP PGA values with the 2011 Lorca earthquake represent more coherent results with the observed values than classical area source methods. Examples of these classical methods are the current Spanish Building Code (NCSE, 2002) and the updated national seismic hazard map (IGN-UPM, 2013). The inclusion of multi-fault ruptures into fault-based PSHA is a novelty for Spain and yet unusual in other low-to-moderate seismicity regions worldwide. Generally, the lack of fault data prevents such kind of analysis in these regions, but as seen, it can imply very important hazard (PGA) changes respect to classical approaches. Moreover, considering multi-fault ruptures is a step forward towards a more realistic seismic hazard assessment, as the occurrence of multi-fault ruptures in nature is becoming an increasingly identified phenomena (e.g., Langridge et al., 2018; Quigley et al., 2019). We therefore aim that our work in the EBSZ could serve as a case example for other studies focused in low-to-moderate seismicity regions.

It is necessary however to assess the uncertainties of the study that affect the hazard results presented and need to be considered when interpreting them. One remarkable topic is the background ratio selection of our study. The ratios modelled are an assumption that is established following expert opinion, based on available geological and seismological data from earthquakes in the region. This means that the ratios are not necessarily defining of the study area but just a preliminary assumption. The option selected here considers that a large part of the earthquakes in the Mw 4.0-5.5 range are related to the faults modelled because it is consistent with observations (section 4.2.1.2). However, we acknowledge the existent implicit epistemic uncertainties within this assumption, as exemplified by the main shocks of the 2019 Ridgecrest sequence (Mw 6.4 and 7.1), which occurred in non-previously mapped faults (Ross et al., 2019). In this sense, different background ratios could and should be explored in a logic tree in further research to account for the epistemic uncertainty of earthquakes happening outside of known faults, even the larger ones. In the line of Chartier et al. (2019), we also recognize the difficulty of setting this parameter and encourage the discussion among researchers on what parameters could help its determination. This is a key issue in southeastern Spain considering the large uncertainties affecting the seismicity epicenter locations of most $M_w \geq 4.0$ earthquakes.

Another limitation of our results is the fact that the present hazard calculations may be underestimating the contribution of other fault sources in southeastern Spain outside of the EBSZ fault system. There are several Quaternary-active faults within the mapping area selected that have not been considered in the source modelling mainly because of a lack of quality data, contrary to the faults within the EBSZ. Fault systems such as El Alquíán and Andarax Valley, Polopos or San Miguel de Salinas (Figure 4.2A) are some examples of active faults in the area with evidence of related seismicity (QAFI database; IGME, 2015a). These faults could also contribute to the seismic hazard, especially outside the EBSZ buffer area, although none of them have the dimensions, i.e., length, of the ones in the EBSZ considered in our study and thus their contribution should not be expected to be that relevant.

Further research is then encouraged to focus on incorporating such uncertainties in the light of a complete and more accurate PSHA analysis. As such, in the zones where there is a lack of paleoseismological studies (i.e., PF or AMF-3), obtaining well-constrained, short-term and updated fault parameters, especially slip rate values, is critical because they can compromise the reliability or bias of the hazard results. This is not only important for the EBSZ faults but also for the ones outside of it and not included here. Updated paleoseismic and geodetic data on faults and the inclusion of more faults as sources would necessarily lead to a reassessment of the source modelling and the hazard in the region. Because paleoseismic research usually requires time, in the meanwhile and given the need of updated and more realistic hazard assessments, it would be useful to consider the near-fault hazard estimations in our models. They could help to set near-fault amplification coefficients to be applied at sites located on top of active faults or in close vicinity.

Further research should also focus on exploring the use of other parameters rather than PGA to quantify the seismic hazard such as the spectral acceleration or peak ground velocity and displacement. These parameters are usually more indicative of the damage generated by an earthquake than PGA as they highlight possible amplification effects in buildings and structures at a given site that ultimately are of interest for seismic engineering purposes. In this sense, and additionally to the use of GMPEs, exploring approaches of spatially correlated ground motion intensity measures (e.g., Park et al., 2007) could be interesting for further research in order to better characterize expected ground motion, damage and loss estimates for seismic hazard and risk assessment

IV. GLOBAL DISCUSSIONS

This chapter discusses globally the results from this thesis, mainly related to evaluate the impact that paleoseismic data has in the seismic hazard assessments of the Eastern Betics Shear Zone. It also discusses the role that geologists and hazard practitioners have on improving the reliability of such assessments.



View of Sierra de la Almenara from El Colmenar.

8 Connection between paleoseismic data and seismic hazard assessment at the Eastern Betics Shear Zone; forward look

The results presented and discussed in this thesis comprise two main topics of the earthquake geology and seismic hazard disciplines that are very different from each other and that use different methodologies. The first topic concerns the seismic source characterization of the Alhama de Murcia Fault (AMF) in a complete cross section from a geological, structural and paleoseismic perspective (section 5), with the aim to obtain more reliable and representative fault parameters of one of the fault's segment. The second one presents a source modelling and probabilistic seismic hazard assessment (PSHA) of the Eastern Betics Shear Zone (EBSZ) using fault data and complex fault rupture scenarios to obtain more reliable hazard estimations (section 7). Despite the differences, both topics comprehend vital steps for the PSHA and influence each other in a way that allows to detect and address the main implications, limitations and uncertainties of the data and results. The global discussion of this thesis is then focused on the implications that the fault data from paleoseismic studies have on the fault-based PSHA. We also discuss the role of both earthquake geologists (data collectors) and hazard modellers on the development of seismic hazard assessments and how, from expert judgement, the collaboration bridge between them is important.

8.1 The impact of paleoseismic data in fault-based approaches in the EBSZ

Fault-based PSHAs strongly rely on the fault data that serve as inputs for the source modellings, as observed in section 7. Therefore, obtaining reliable, well-constrained and representative data of the faults is crucial for the seismic hazard because faults control the earthquake rates and maximum expected magnitudes upon which the hazard models are further based on. In this matter, Faure Walker et al. (2019) identify and characterize the importance of having detailed slip rate profiles along the fault traces and their geometries for the hazard assessment. They can drastically change fault parameters such as recurrence and ground-shaking intensity levels at specific sites that can lead to improved fault-based seismic hazard calculations. Here, the main implications of incorporating the obtained fault parameters (slip rates, recurrences and fault rupture geometry) into PSHA are discussed, along with the implications of slip rate variability and recurrence models for such PSHA in the EBSZ.

8.1.1 Slip rates

In the present study, the most important parameter for the characterization of a fault's activity and hence, for the hazard assessment, is the fault slip rate because it controls the rates of earthquakes in the EBSZ system and ultimately the hazard values around faults. In our PSHA, peak ground accelerations (PGA) are strongly dependent and proportional to the fault slip rates, meaning that higher values locate around the faults with higher slip rates and vice-versa. This is important because, if a certain fault has a slip rate value that is not well constrained, PGA could be misleading to underestimate or overestimate the actual hazard of the nearby region. Clear cases in study area are the Palomares Fault (PF) or the Totana-Alhama segment of the AMF (AMF-3; Figure 8.1), both of them lacking detailed paleoseismic studies to date and previously conceived as very slow faults or fault segments.

The important role of well-constrained and representative slip rates in the reliability of PSHA motivates the paleoseismic study that we have developed in the Lorca-Totana segment of the AMF (section 5). Even though the previous slip rate values were reliable and obtained from paleoseismic 3D trenching data, they were estimated from a single fault branch (S-AMF), meaning that the seismic potential of other branches was undermined. In this respect, the slip rates obtained in this thesis ($1.55^{+0.14}/_{-0.18}$ mm/yr for the last 18 ka) account for four main branches of the segment and hence are likely more representative than the previous ones. However, they should still be regarded as a minimum because there is at least one branch not accounted (N_{2a}-AMF) and the lateral component of vertical-slip branches has not been characterized through 3D trenching.

For the seismic hazard assessment, the inclusion of updated and more representative slip rates translates into different and likely more reliable hazard estimations in the near-fault zones. The test performed in section 7.6.5 with updated slip rate values for selected EBSZ faults highlights such hazard changes with PGA increases around the AMF or PF respect to the previous model and evidences the relevance of slip rates in the calculations as well as the strong dependency on this parameter alone (Figure 8.1).

The dependency on slip rates is relevant yet can be problematic because in those areas where fault slip rates are poorly constrained or unreliable, the hazard might be misleading and the whole assessment can appear biased towards the most reliable ones, as we have seen in our assessment. In this manner, the SHERIFS methodology applied to the EBSZ has been revealed as a good tool to highlight where these poor reliable slip rate

estimations in some faults act as a limitation for the hazard modelling. Consequently, this is useful to identify where future paleoseismic studies should be prioritized to i) fill the knowledge gaps in the EBSZ fault system in terms of slip rate characterization and ii) homogenize this knowledge over the territory to reduce possible bias in the hazard. In faults such as the PF or AMF-3 (Figure 8.1), the need for detailed paleoseismic research to unveil slip rates is urgent for the sake of PSHA studies and especially because the areas nearby are very populated (Murcia city, near 450,000 inhabitants or Lorca city, near 94,000 inhabitants). In this sense, the results from the SHERIFS modelling depict that these faults limited the performance of the hazard models, which justifies the initial geomorphic and structural investigations made in the Totana-Alhama segment (AMF-3) and Amarguillo Fault to explore potential future paleoseismic sites (section 6). The future development of paleoseismic studies in these critical faults will allow assessing whether if their current slip rate values are acceptable or underestimated due to the poor knowledge on them. This might also increase the reliability of the source modellings performed with SHERIFS in this thesis and ultimately of the seismic hazard results around them.

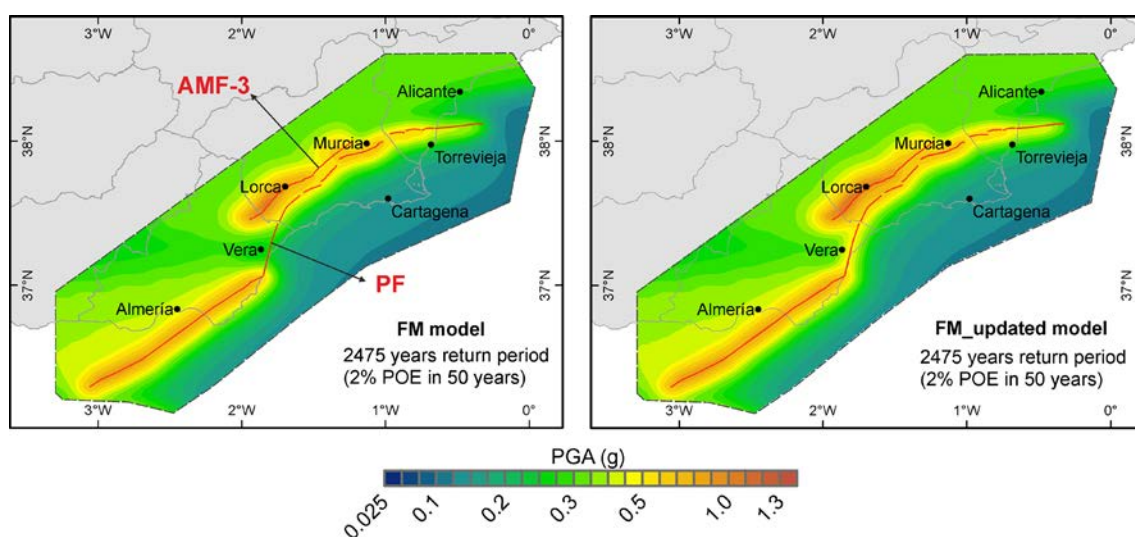


Figure 8.1. Comparison of seismic hazard maps of the FM and FM_updated models in the Eastern Betic Shear Zone (EBSZ). Note that the seismic hazard values in PF and AMF-3 vary significantly between models. Considering the high sensitivity of the hazard to slip rates, and that these faults are poorly studied, the acquisition of reliable slip rate constraints there is vital to improve PSHA.

8.1.2 Earthquake recurrences (Paleorates)

Another important parameter for the characterization of a fault's activity is the earthquake recurrence. It expresses the frequency of large earthquakes ($M_w > 6.0-6.5$ from paleoseismic studies) happening on the studied faults, which in paleoseismology are generally calculated from time constraints of paleoseismic events in trenches. For PSHA,

paleoseismic recurrences are important because they complete the rates of large magnitude earthquakes in the magnitude-frequency distributions (MFDs) provided by seismicity (e.g., Youngs and Coppersmith, 1985).

In this thesis, the paleoseismic recurrences from faults are converted into paleoearthquake rates (paleorates) to check the reliability or consistency of the modelled MFDs of each hypothesis in the large magnitudes ($M_w \geq 6.0 \pm 0.25$). In the EBSZ, as in other low-to-moderate seismicity regions, this is relevant because the seismic catalogue for these magnitudes is not complete and thus paleoseismic data is the only source of information. These paleorates, however, have important limitations mainly related to: i) the lack of continuous sedimentary deposition in alluvial fan environments that may hamper the differentiation between an individual or multiple paleoearthquakes; and ii) the local character of paleoseismic approaches, which sometimes leads to focus only on single segments of complex systems and often missing part of the paleoearthquake history (see details in section 7.5.1.2). These limitations hinder having a complete picture of the paleoearthquake record of a fault, especially those that have more than one branch accumulating deformation. Thus, they tend to overestimate the recurrences (i.e., underestimate paleorates) and enlarge their uncertainties. The large uncertainties in some paleorate estimations in the EBSZ (Figure 8.2) can difficult the performance of a precise check of the modelled hypotheses MFDs for a logic tree weighting, as the Góñar-Lorca segment (AMF-1) or Carboneras Fault (CF-3) (e.g., Figure 7.2; section 7.2.2).

Additional problems contributing to inaccurate recurrence periods in the AMF are related to the difficulty of obtaining precise numerical dates. This is caused by: i) the scarcity of materials suitable for dating with ^{14}C as alluvial fans in arid environments are mainly formed by clast-supported gravels and lack sufficient organic material (e.g., charcoal); ii) the need to study longer paleoearthquake sequences in slow-moving faults, which require the use of techniques extending beyond age the limits of ^{14}C (>40 ka) but that imply larger uncertainties (i.e., OSL); iii) the non-complete bleaching of the quartz minerals in some sediments that prevent the correct dating of the units with OSL. This latter problem is related to the proximity of the materials to the source areas, which implies short transport distances and therefore less susceptibility to a complete bleaching. Often, the recycling of materials from older alluvial units adds complexity to the age distributions (i.e., OSL aliquots presenting disparity of ages). In the studied transect the northern branches (N_1 -AMF and N_{2b} -AMF) are the most affected by the non-complete

bleaching (see section 5.5.3), likely because they are the closest to the mountain front of La Tercia range (source area of El Salvador alluvial fan).

In the AMF, the mentioned problems compromising the detection of complete paleoearthquake sequences and estimating recurrence have been previously identified by Ortuño et al. (2012) or Ferrater (2016). The distribution of the deformation among several branches, especially in the Lorca-Totana segment, contributes to this problem because previous studies only focused on the central branch (S-AMF) potentially missing events recorded in the other branches. The integral study performed in the Lorca-Totana segment in this thesis aimed to mitigate this problem by obtaining RI for each branch. The mean RI obtained, varies significantly from branch to branch: 12.8 ± 7.4 kyr in the N₁-AMF, 17.3 ± 8.8 kyr in the N_{2b}-AMF, 4.3 ± 0.4 kyr in the S-AMF and 3.1 ± 1.4 kyr in the F-AMF. These important differences may be the result of the lack of synchronicity among the branches but also, most probably, are result of differences in completeness of the paleoearthquake records due to large depositional gaps. This is the case of the two northern branches (N₁-AMF and N_{2b}-AMF), where the erosion is predominant compared to the other sites. Conversely, the S-AMF and F-AMF have shorter recurrences because the respective sites show smaller gaps and therefore the paleoseismic record is completer. These two latter recurrence periods might therefore be more robust and approximate better the recurrence of the Lorca-Totana segment than the other branches. Additionally, in the case of S-AMF our study allowed to reduce better the recurrence uncertainties with respect to Ferrater (2016) (Figure 8.2): 0.4 kyr uncertainty here (last 31 ka) and ~ 1 kyr in Ferrater (2016) (last 59 ka), both referring to the 95.4% confidence interval.

For the hazard assessments performed here, larger uncertainties in the paleorate estimations imply less clear and more subjective weighting of the different hypotheses for PSHA (e.g., Figure 7.2). One example in the EBSZ are the uncertainties of the paleorate from the Carboneras Fault as opposed to the well-constrained ones of Los Tollos (LTF) or Carrascoy faults (CAF) (Figure 8.2). Based on this, future paleoseismic studies in the EBSZ should aim to better constrain the paleoearthquake chronologies of all the fault segments. In this line, multi-site integral paleoseismic studies have demonstrated to be crucial in constraining this parameter (e.g. DuRoss et al., 2011 in the Wasatch Fault Zone) and are, at our criterion, the best method to obtain more reliable recurrence estimations of a fault.

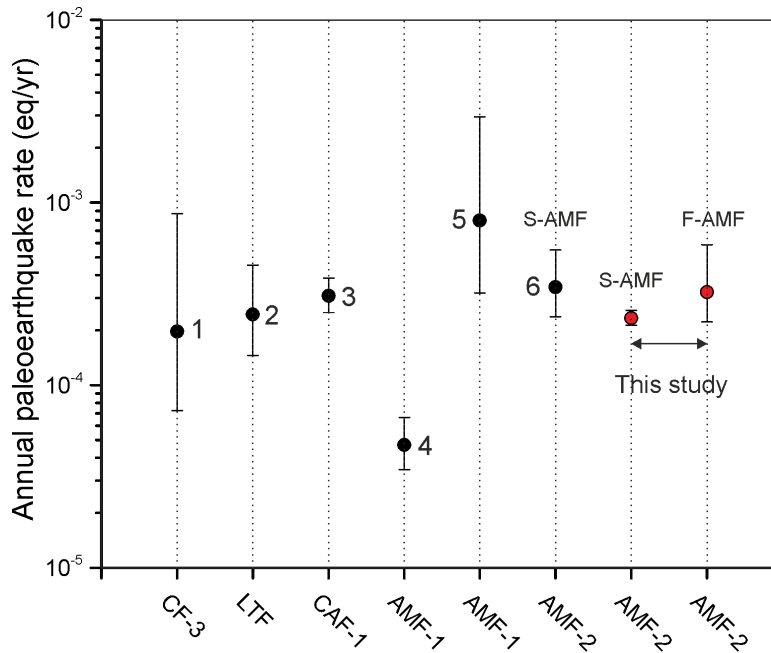


Figure 8.2. Annual paleoearthquake rate estimations of the different fault sections (horizontal axis) in the Eastern Betics Shear Zone (EBSZ) and for each paleoseismic study (numbers). Note the differences in the uncertainty ranges depending on the study, and the considerably smaller uncertainty in S-AMF obtained from this thesis. 1: Moreno (2011); 2: Insua-Arévalo et al. (2015); 3: Martín-Banda et al. (2015); 4: Ortuño et al. (2012); 5: Martínez-Díaz et al. (2018); 6: Ferrater (2016). The location of the fault sections can be found in Figure 4.2, section 4.1.

8.1.3 Fault rupture complexity and fault geometry

The extent of earthquake ruptures within a certain fault or fault system is one of the critical parameters often discussed in both paleoseismic and hazard studies because it controls the maximum magnitude (M_{\max}) that can be expected in a given period. The evidence of many damaging earthquakes with fault ruptures involving several faults simultaneously has put emphasis on the inclusion of such kind of multi-fault scenarios into the source modellings for PSHA (e.g., UCERF-3 in California). Furthermore, a key issue concerns to the characterization of the fault ruptures in fault systems.

In the EBSZ and other low-to-moderate seismicity regions, the lack of surface rupture descriptions in the instrumental and historical period, combined with incomplete/heterogeneous fault cartographies and poor paleoseismic resolution prevent the characterization of fault ruptures. The use of either explorative or expert opinion-based rules to define hypotheses of fault and multi-fault rupture lengths is the first and most affordable option that can be explored for PSHA and it has been done in this thesis for the source modelling (see section 4.1). Nonetheless, the development of studies aiming to reduce the subjectivity and randomness in the definition of the hypotheses is further needed for a more reliable evaluation.

Given the intrinsic limitations of the seismic catalogue in southeastern Spain, i.e., lack of completeness for magnitudes over M_w 6.0 and the large uncertainty of epicenter location for events older than 1962 (67% of the catalogue; IGN-UPM, 2013), paleoseismic approaches become one of the most important sources of information to estimate the seismogenic potential of active faults. The results obtained for the Lorca-Totana segment in this thesis are important in this matter because they allowed demonstrating time compatibility between events in S-AMF and F-AMF that could indicate simultaneous ruptures at least for the last five events since 18 ka. However, the lack of precise age constraining of some events, especially in the northern branches, prevents from a direct event correlation to unveil possible synchronic ruptures of the whole fault segment. Similarly, the poor age brackets of paleoseismic events in other EBSZ faults, does not allow to establish clear correlations, hence, possible fault interactions between them (e.g., Coulomb stress triggering).

The analysis of the slip rate time evolution has shown cyclic patterns of acceleration in the AMF that have also been observed in the CAF (Martín-Banda et al., 2021) and that coincide in time (between 34 and 25 ka). This observation suggests a possible rupture synchronicity or fault interaction between faults of the EBSZ and, although it cannot be concluded, sets a basis for further studies in the area. A recent example is the study in the Teton Fault in Wyoming (DuRoss et al., 2021) that allowed to unveil the rupture of the whole fault at least once during the Holocene. Such integrative paleoseismic studies in other faults of the EBSZ could help to define better the rupture hypotheses explored for the source modelling with SHERIFS.

In this line, physics-based approaches could be used to define fault and multi-fault rupture scenarios in the EBSZ. These approaches could be useful to explore more objectively earthquake ruptures in the EBSZ. The recent study by Herrero-Barbero et al. (2021) reproduces a 100 ka-long synthetic earthquake catalogue of the EBSZ by computing earthquake simulations with the RSQSim code (Dieterich and Richards-Dinger, 2010) and considering fault data as inputs (slip rates, kinematics and 3D geometry). Upon this modelling, they conclude that multi-fault ruptures are possible within the EBSZ, especially in predominantly strike-slip structures. Their seismicity curves show an agreement with the seismicity rates (MFDs) obtained from SHERIFS in this thesis (Figure 8.3). Specifically, their synthetic catalogue agrees with the Gutenberg-Richter curves (GR) from hypotheses 1 to 3 and strongly disagrees with hypothesis 4 for the FM model.

Such results are coincident with the consistency check performed here with the regional seismic catalogue and thus reinforces that i) multi-fault ruptures are feasible in the EBSZ and ii) the complete rupture of the whole EBSZ system seems unfeasible considering the fault data available so far. Using RSQSim, the authors further manage to provide more information about the geometry of the ruptures and rupture behavior, and suggest that propagation between AMF and LTF is possible. This statement is relevant because, since the LTF connects with the CAF (Martín-Banda, 2020), it might help to explain the coincidences in slip rate acceleration patterns between the AMF and CAF.

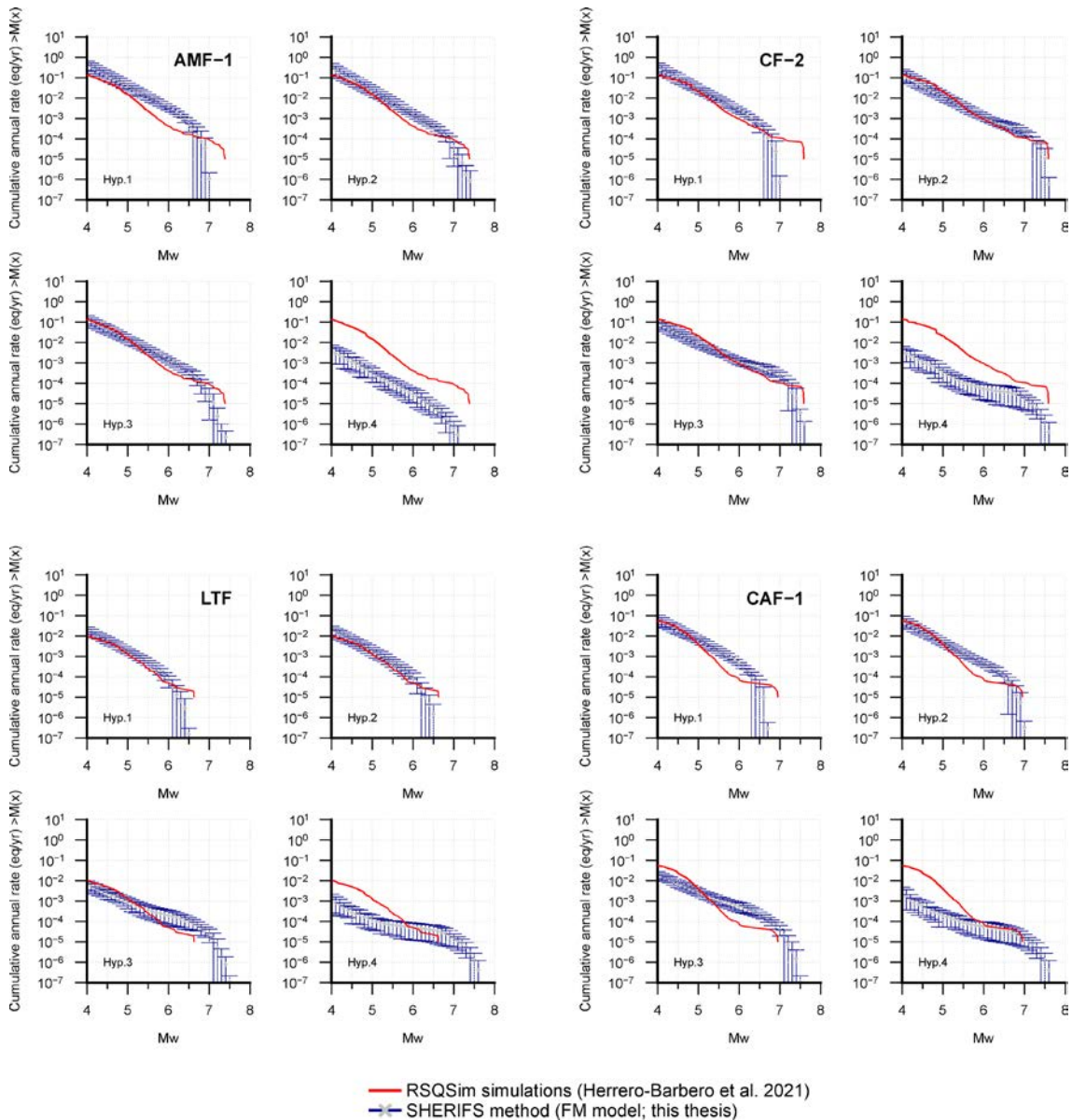


Figure 8.3. Comparison of the magnitude frequency distributions (MFD) obtained using the RSQSim code by Herrero-Barbero et al. (2021) with the ones obtained in this thesis using SHERIFS. The RSQSim synthetic catalogue is compared with the earthquake participation rates of different EBSZ fault sections and for each of the four rupture hypothesis explored. The location of the fault sections can be found in Figure 4.2, section 4.1. Modified from Herrero-Barbero et al. (2021). Used with permission from John Wiley and Sons, and the authors.

Other frequently used physics-based approaches are the ones related to the Coulomb stress transfer. In these modellings, the along-strike fault geometry is a key parameter as it can imply significant changes in the calculations (Mildon et al., 2016; Faure Walker et al., 2019). Accordingly, in the light of the source modellings it may be beneficial to develop detailed fault mappings that are consistent throughout the study area of interest and that reflect the detailed knowledge of faults. One example is the Fault2SHA Central Appenines database (Faure Walker et al., 2021) in which fault traces and parameters are compiled and organized according to common classifications and criteria especially designed for hazard modellers.

In Spain, the only available database is the QAFI (IGME, 2015a), which compiles the fault data, including their fault traces and geometry based on the available research at the moment. Unfortunately, detailed fault mappings are not available for all the EBSZ, generally only in the fault segments where paleoseismic research has developed extensively. Sections of the Carboneras, Alhama de Murcia or Carrascoy faults have very detailed mappings, while in others such as the Palomares Fault, the traces are commonly inferred exclusively from photointerpretation. Based on the potential repercussions in physics-based source modellings, it is then interesting to focus on homogenizing the detail of fault mappings in the future, including along-strike changes of orientation, kinematics or dip, among others. Introducing this level of detail may be considered for detailed or site-specific PSHAs, such as the performed for critical infrastructures. The availability of high-resolution topographic models derived from LiDAR data and the photogrametry using old aerial photographs might help in the field mapping, leading to refine the fault cartographies. This thesis might be an example of the improved cartography of an already previously study area by the use of those approaches, allowing to detect five fault branches in a sector where previously only three branches were mapped (i.e., Martínez-Díaz et al., 2003; Masana et al., 2004). Also, these techniques have allowed the cartography of more recent tectonic geomorphic features in EBSZ areas of less topographic expression such as fault relay zones (e.g., Insua-Arévalo et al., 2015).

Finally, the characterization of fault geometries at depth is critical for the source modelling in PSHA, as it controls the seismogenic depth, fault width and potential rupture area that ultimately have a great impact on the overall seismic potential of a fault (M_{\max}). The geometry at depth also has an impact on the superficial distribution of ground motion levels, which have been identified, for instance, in the areas surrounding the Bajo Segura

Fault (e.g., Figure 7.5) where the higher PGAs are found on the hanging wall. To date, in the EBSZ this is one of the main disadvantages as very few geophysical studies have focused on characterizing fault structures at depth. In the Góñar-Lorca segment of the AMF, the studies by Martí et al. (2020) (magnetotellurics) and Rodríguez-Escudero (2017) (well data) allowed to characterize the fault as a 70-65° NW-dipping structure. In the Alhama-Alcantarilla segment, Herrero-Barbero et al. (2020) infer a ~59° dip for the fault from the interpretation of 2D seismic reflection profiles. It is then important that future studies characterize the deep geometry of the fault, especially in the Lorca-Totana segment. This segment records most part of the AMF activity and presents several branches accommodating deformation, most likely linking into a single structure at depth.

8.1.4 Time variability of slip rates and earthquake recurrence model

The PSHA performed in this thesis assumes a Poissonian model, which implies that the earthquake occurrence is assumed to be independent in time. However, in nature, the existence of foreshocks, aftershocks and earthquake triggering sequences suggests that earthquakes can be, in fact, time dependent. Coulomb stress transfer models have allowed to propose earthquake triggering relationships in earthquake sequences such as the 1994 Northridge earthquake (Stein et al., 1994) or the 2019 Ridgecrest sequence (Toda and Stein, 2020), and even allowed to explain an important part of earthquake occurrence in Central Italy since historical times (Verdecchia et al., 2018; Mildon et al., 2019). In this sense, the elapsed time from the last earthquake influences on the earthquake probabilities, evidencing a time dependent relationship (Figure 8.4). In addition, stress changes over-time can cause faults to experience variations in their slip rate and recurrences, as we have identified in the AMF (section 5). To accommodate this, time-dependent approaches or renewal models, have been discussed and developed during the recent decades to incorporate earthquake probability as a time-dependent variable linked to the elapsed time since the last earthquake (Allin Cornell and Winterstein, 1988; Sornette and Knopoff, 1997; Matthews et al., 2002; Salditch et al., 2020). Despite this, renewal models imply assuming the characteristic earthquake model because require setting a reference earthquake upon which the elapsed time is measured. In the source modelling performed here we considered a Poissonian model in which the seismicity rates of the EBSZ follow an exponential (non-characteristic) distribution, consistent with the regional catalogue.

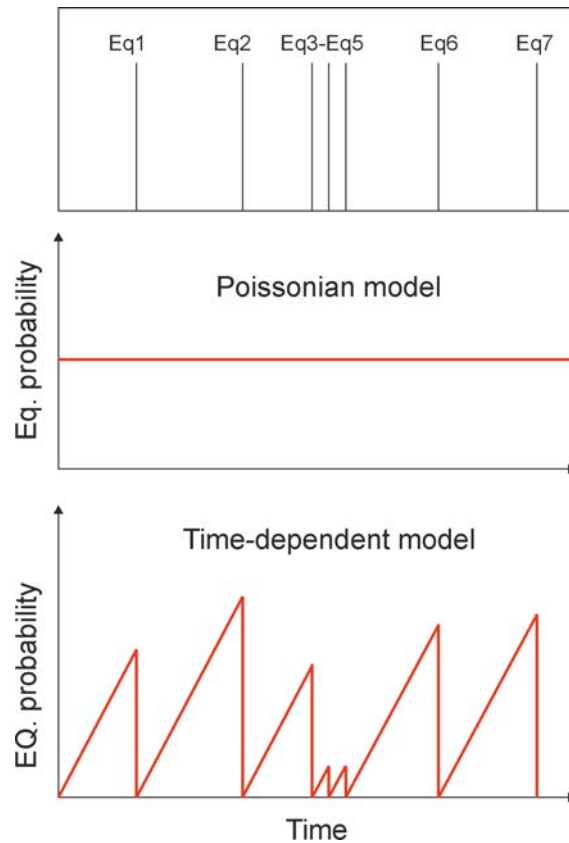


Figure 8.4. Earthquake recurrence models. The Poissonian model assumes constant earthquake probability over time (time-independent). The time-dependent or renewal model assumes that the probability increases proportionally with the elapsed time since the last earthquake. Note that there is a cluster between earthquakes (eq) 3 and 5. Figure inspired by Salditch et al. (2020).

8.1.4.1 Slip rates

The slip rate and recurrence parameters obtained from the Lorca-Totana segment of the AMF show time variations that support a non-steady behavior of the fault. In terms of slip rate, the AMF has shown variations at least since ~ 77 ka with at least two cycles formed by slow phases followed by shorter acceleration phases (Figure 5.32). Similarly, the slip rate in the Carrascoy Fault shows noticeable variations for the last ~ 210 ka (Martín-Banda et al., 2021). This has important implications for the hazard assessment of the EBSZ because depending on the analyzed period the average slip rates and thus, earthquake probabilities can have significantly different values. A paleoseismic approach such as the one performed here, despite the limitations in age control, stands out over single-site approximations because it allows to better observe slip rate variations, detect how these variations evolve among different sites and explore which time windows should be considered more appropriate for the hazard assessments.

Given the strong dependence of seismic hazard on the slip rate, we find relevant to reach consensus on the representative time windows for the slip rate estimations among the different faults of the EBSZ. Based on this, some questions arise that need to be agreed upon in the future: What is the best time interval to define as representative for the fault slip rate? Are long-term slip rates representative of the current fault motions? Are the rapid slip rate accelerations skewing the average slip rate distributions and causing an overestimation in the short-term especially? Right now, the available slip rates in the EBSZ are representative for contrasting intervals. Long-term windows are used in faults with scarce paleoseismic data because slip rates are based on older geomorphic or structural markers (e.g., PF), while short-term intervals are available in faults with paleoseismic research (e.g., Lorca-Totana segment). On the one hand, long-term slip rates may not match the current values. Short-term slip rates, on the other hand, are more susceptible to be influenced by fast slip rate accelerations (i.e., larger fault slips than average; S6 in S-AMF; Table 5.13) or earthquake clusterings. Both cases can mislead the hazard estimations and should be studied in the future.

8.1.4.2 Earthquake recurrence model

In terms of paleoseismic recurrence models, these usually assume that earthquake occurrence is periodic, which implies that earthquakes happen with the same frequency, but this assumption does not reflect other patterns of earthquake cyclicity also observed (e.g., clustering; Salditch et al., 2020) (Figure 8.4). Importantly, in low strain regions of intra-plate tectonic settings, such as the EBSZ, earthquake occurrence is usually clustered as a result of many faults accommodating deformation and interacting with each other (Li et al., 2009; Salditch et al., 2020). The earthquake recurrence model of a fault system is typically characterized by the coefficient of variation (CV; Equation 3.4; section 3.5.1) (e.g., Berryman et al., 2012; Salditch et al., 2020). For the AMF in this thesis, the CV is only reliable for the S-AMF because it is where the paleoearthquake record is more complete and well time-constrained. The values, ranging from 0.8 to 1.0 (last 73 and 31 ka, respectively), indicate a weakly periodic to random or Poissonian behavior, consistent with the Poissonian earthquake occurrence modelling considered for the hazard assessment of the EBSZ. These CV values are also in agreement with the expected in low slip rate faults, as suggested by Moernaut (2020) ($CV > 0.85$). However, several limitations should be considered when evaluating the CV.

First, to infer the recurrence model of the AMF, all the branches should be accounted for. Right now, the lack of precise age constraints for the events in the N-AMF and F-AMF, and the important depositional gaps in the former, prevent to have a complete and well time-constrained paleoearthquake record. Generally, the CV is systematically underestimated when the number of earthquakes considered is less than ten (Ellsworth et al., 1999; Console et al., 2008; Parsons, 2008, in Cowie et al. 2012), which invalidates this analysis outside of the S-AMF. Second, although the record in the S-AMF is relatively long and well constrained, especially for the last 31 ka (7 events), the sequence also presents depositional gaps (i.e., between 73 and 46 ka or between ~15 ka and historical times; Figure 5.34) that most likely imply missing of paleoseismic events and could modify the CV. According to Cowie et al. (2012), small CV variations can imply important differences in the probabilistic earthquake forecasts and resulting hazard.

Paleoseismic approaches should put effort towards better constraining and completing earthquake chronosequences in active faults for them to be representative to characterize the RI and CV, and to be useful for PSHA. In this thesis, two main steps have been taken that have allowed to improve the paleoearthquake record compared to previous studies: i) performing a multi-site paleoseismic survey, including the excavation of a deep trench (S-AMF) to enlarge the record, and ii) carry out more numerical dates to constrain the ages of the events. Despite this, improvements should be made to solve the incompleteness of the paleoearthquake record, especially in the branches where the CV could not be computed. One improvement may come with the use of hyperspectral imaging in the paleoseismic trench walls to increase resolution in the detection of sedimentary layers. A better resolution might allow to guide better the sampling for numerical dates and thus to improve the age control. Another improvement may be the study of new paleoseismic sites in the future. Specifically, the exploration of creek infills has demonstrated here to be fruitful (F-AMF in La Hoya) for the characterization of the most recent seismic activity, not recorded in the Pleistocene alluvial fans of the area (e.g., El Saltador alluvial fan). Furthermore, in the light of future fault-based PSHAs, performing multi-site paleoseismic studies in other EBSZ faults to improve their paleoearthquake record might help unveiling their recurrence behavior. Upon these challenges, exploring renewal time-dependent distributions is an interesting approach for the near future research to test the fit of the EBSZ to alternative earthquake probability distributions.

9 Strengthening the bridge between data collectors and hazard practitioners

Seismic hazard assessments should be regarded as dynamic and always provisional documents, subject to periodic updates made in accordance with the availability of new and more reliable fault data. Many experiences of damaging earthquakes happening in zones previously thought to have low hazard support this (e.g., 2011 Tohoku earthquake in Japan; Mulargia et al., 2017). In this aspect, it is fundamental that both data collectors (earthquake geologists, paleoseismologists) and hazard modelers share and understand the limitations and uncertainties of the data that each other deal with. In the end, hazard assessments are the documents provided to the institutions, whose decisions have a direct impact on the safety of the society and infrastructures. In California, institutions such as the Southern California Earthquake Center (SCEC) (<https://www.scec.org/>) are focused on the collaboration between researchers studying earthquakes and their related hazards, as well as on the dissemination and discussion of this research. To do so, working groups, workshops and meetings are carried out regularly to enhance such synergies between disciplines, including governments, administrations and decision-makers. In Europe, initiatives such as the Fault2SHA Working Group (<http://fault2sha.net/>) have been created to set a common basis for both data collectors and hazard modelers in the understanding of the fault data and its uncertainties, in the incorporation of faults into PSHA and to work together to fill the gaps of knowledge between (Scotti and Peruzza, 2016; Pace et al., 2018). The Working Group had a crucial role in the development of this thesis and permitted to improve the collective awareness on the importance of reliable and detailed fault data for PSHA among the EBSZ researchers.

One of the main issues is the, sometimes excessive, division of work by the involved parties during the development of a hazard assessment and the, sometimes, scarce collaboration between them. On the one hand, data collectors typically focus on specific sites of a fault to perform detailed paleoseismic studies and obtain parameters that allow describing the fault in question (slip rates, recurrence, elapsed time, slip per event, etc.). However, these parameters are usually too local to be extrapolated to a whole fault or fault segment, especially in contexts such as the AMF where more than one branch is actively absorbing deformation. In addition, sometimes the epistemic uncertainties linked to the obtention of these parameters are not properly acknowledged nor represented in the final publications or databases. This can generate confusion for hazard modelers and a

non-appropriate propagation of such uncertainties into the hazard calculations. For instance, in this thesis, acknowledging the quality of the slip rate data in each fault has been crucial to understand the hazard results and to critically evaluate their reliability. Not doing so, could have misled the hazard interpretations. On the other hand, hazard modelers do not usually analyze in detail the fault data coming from field paleoseismic studies nor the real uncertainties linked to them, often because the results are not presented in “friendly” or clear formats, and also because of the generally engineering-physics background of the users. In addition, modellers tend to simplify fault parameters such as their surface traces, 3D geometry, and slip rate changes that can be vital for the source modelling and hazard (e.g., Faure Walker et al., 2019; Mildon et al., 2019b).

Based on the mentioned issues, as data collectors we should in all cases acknowledge and explain properly the uncertainties linked to their estimated parameters and, if possible, provide quality or reliability rankings for each of them in a way that can be incorporated or weighted in a logic tree. This can be found in the QAFI database (IGME, 2015a), which classifies the reliability of the seismic parameters (M_{\max} and recurrence) based on the strength of the Quaternary evidence and accuracy of the slip rates in the Iberian Peninsula (García-Mayordomo et al., 2017). Furthermore, the ongoing update of the database (QAFI v.4) will contribute to improve this as well. Having said that, we also propose the development of an EBSZ database, specifically designed for detailed fault-based PSHAs of southeastern Spain, in which local field observations, paleoseismic sites and, if available, along-strike fault parameter changes (slip rates, rake, etc.) are included and documented. The database in the Central Appenines (Faure Walker et al., 2021) can serve as an inspiration to that. It should be aimed to characterize faults as a whole, avoiding single-site studies; otherwise, the estimated parameters might not be accurate to the actual fault behavior. A clear example of this is the evolution of the knowledge for the slip rate values in the Lorca-Totana segment over the last decades, as more sites in different branches have been studied; from 0.07-0.66 mm/yr (Masana et al., 2004) to ~1.5-1.6 mm/yr in this thesis.

Complementarily, as hazard modelers, we should focus on understanding how the data on faults is collected, what assumptions are made by the geologists to infer fault parameters and their main limitations. This means understanding the real epistemic uncertainties affecting the data beyond the uncertainty ranges provided. It is critical to be aware of the reliability of the parameters in each fault, the method used to infer them or

whether if they are a minimum or a maximum. It is also important to understand if the fault data is valid for the long-term or the short-term and the implications of mixing both into a same hazard calculation. In this sense, the cooperation with data collectors is necessary to reach consensus on the time periods representative for the PSHA of parameters such as the slip rate. In this thesis, we have seen that not all the data has the same reliability nor coverage over the EBSZ territory depending on the method used (paleoseismic trenches vs geomorphic markers) or the time frame covered (long or short term). These limitations need to be accounted for when building the source models in the future and could be assessed, for instance, by considering different fault parameter hypotheses in a logic tree.

This thesis presents a study that encompasses the whole process of estimating the seismic hazard of a region, from the data collection, exemplified by a multi-site paleoseismic study in the AMF, to the use of the obtained parameters to perform a fault-based probabilistic seismic hazard assessment in the EBSZ. This thesis has allowed, on the one hand, to better understand the issues and uncertainties affecting the paleoseismic data mentioned in the previous lines. On the other hand, it has allowed to directly observe i) which fault parameters have more influence on the seismic hazard and thus should be estimated with priority, ii) how the inclusion of fault data impacts the hazard results and iii) how the fault data uncertainties and reliability issues propagate and ultimately compromise the reliability of the hazard estimations. Such ability to observe the bigger picture is, at our criterion, crucial to perform more critical and overall, better seismic hazard assessments.

To conclude and focusing in southeastern Spain, we find important that both data collectors and hazard modelers keep working together in the light of more reliable hazard assessments. Fruitful precedents to that are the Iberfault meetings (Insua-Arévalo and Martín-González, 2010; Álvarez-Gómez and Martín-González, 2014; Canora et al., 2018), created to share data between researchers working on active faults and seismic hazard in Iberia, and the Fault2SHA Betics group (e.g., García-Mayordomo et al., 2018; Ortuño et al., 2018), devoted to apply the aims and methods of the Fault2SHA to the Eastern Betics. In this respect, the creation of workshops, meetings and projects targeted for both audiences is strongly encouraged to i) understand each other's work, ii) define and use common terminologies, iii) reach consensus in topics such as representative time frames for slip rates, and iv) create accessible fault databases for both parties.

v. CONCLUSIONS

This chapter presents the main conclusions of this thesis concerning the structural and paleoseismic study of the Alhama de Murcia Fault, and the probabilistic seismic hazard assessment for the Eastern Betics. It includes the global conclusions of the thesis concerning both topics, their relationships, and their implications for the study area.

View of Lorca city and Sierra de las Estancias from El Saltador.

Conclusions on the structural and paleoseismic characterization of the Alhama de Murcia Fault

The structural and paleoseismic characterization of the Alhama de Murcia Fault (AMF) has required i) a geomorphological and structural analysis in the two central segments (Lorca-Totana and Totana-Alhama), and ii) an integral paleoseismic survey across different branches of the Lorca-Totana segment. The main conclusions reached in this study for each segment are outlined below:

A) On the Lorca-Totana segment

Structural analysis

The Lorca-Totana segment is composed by, at least, five subparallel active branches in a 2-3 km wide transect. The deformation is partitioned among them, which from N to S have been designated as N₁-AMF, N_{2(a and b)}-AMF, S-AMF, and F-AMF. The N₁-AMF and S-AMF accommodate mostly the strike-slip component, while the N_{2(a and b)}-AMF and F-AMF are mainly dip slip faults. The S-AMF and F-AMF limit a pressure ridge structure in which the latter conforms the frontal thrust of the AMF system. The partitioned deformation suggests a complex resolution of the compression at the surface, which we infer it could be due to the subperpendicular orientation of the segment (N50-65°) respect to regional maximum shortening (~N150°), and to the generation of new fault branches that merge at depth with the inherited structure.

Paleoearthquake record and recurrence

Paleoseismic trenching in a NW-SE transect has revealed evidence of recurrent paleoearthquakes in four fault branches. The S-AMF at El Saltador site shows the most complete paleoearthquake record in Spain with, at least, seventeen events recorded since ~100 ka, seven more than ones the identified previously in a shallower exposure at this site. We calculated mean recurrence intervals (RI) of 5.7 ± 1.7 to 4.3 ± 0.4 kyr for the last 73 and 31 ka, respectively. This infers a weakly periodic to Poissonian model (CV = 0.8 - 1.0). The F-AMF has experienced similarly frequent earthquakes for the last 18 ka with a RI of 3.1 ± 1.4 kyr for five events. Conversely, in the N₁-AMF and N_{2b}-AMF the paleoearthquake record is more incomplete probably due to the presence of important depositional gaps in the sedimentary sequences. Hence, their RI are most likely overestimated: 12.8 ± 7.4 (last 40 ka) and 17.3 ± 8.8 kyr (last 77 ka), respectively.

Slip rates

We obtain a total net slip rate (summed for four branches) of $1.55^{+0.14}/_{-0.18}$ mm/yr for the last ~ 18 ka, derived from a lateral one of $1.54^{+0.14}/_{-0.18}$ and a vertical one of 0.14 ± 0.03 mm/yr. These can be considered a minimum because the N_{2a}-AMF has not been analyzed nor has the lateral component of the dip slip branches. The lateral slip rates suggest that the AMF accommodates most part of the left-lateral motion in this sector, based on geodetic data summed for the AMF and Palomares fault (PF) (1.5 ± 0.3 mm/yr).

The S-AMF is the principal fault of the system showing the clearest slip rate fluctuations over time. At least two patterns of short slip rate accelerations followed by longer periods of quiescence are identified since ~ 73 ka and interpreted as super-cycles. The coincidence in time and duration of an acceleration period between the AMF (31-25 ka) and Carrascoy Fault (34-28 ka) suggests, for the first time in the EBSZ, a potential pattern of activity synchronicity. This could be the result of fault interaction (e.g., triggered ruptures) that should be further investigated in detail.

The vertical slip rate evolution suggests an increase of the activity in the southern branches of the segment (S-AMF and F-AMF) since ~ 18 ka with respect to the northern N_{2b}-AMF. This agrees with the southeastern migration of the alluvial deposition since 25 ka. In this context, the F-AMF dominates the uplift of the frontal pressure ridge respect to the Guadalentín Depression and accommodates $\sim 80\%$ of the shortening since 18 ka.

Event correlation and seismic potential

Simultaneous ruptures are feasible in the two branches of the frontal pressure ridge (S-AMF and F-AMF), as suggested by the time compatibility of the last five events in both branches for the last 18 ka. Moreover, their very similar vertical slip rates since 18 ka (~ 0.26 mm/yr) support their joint uplift. Synchronic ruptures with other branches, segments of the AMF or faults of the EBSZ cannot be concluded due to the larger uncertainties in the event dates, related to the poor resolution of the sedimentary record (age control).

The maximum estimated magnitudes (M_{\max}), from the surface rupture length and empirical relationships range from $M_w 6.7 \pm 0.2$ for the Lorca-Totana segment rupture to $M_w 7.5 \pm 0.2$ considering the complete fault rupture, which we cannot rule out. Considering the slips per event identified here (2.0-8.4 m), the M_{\max} reaches $M_w 7.1-7.7$,

although this parameter is more unreliable because, in some cases, the lack of paleoseismic resolution can lead to interpret the cumulative slip of several events as one.

B) On the Totana-Alhama segment

The Totana-Alhama segment is an area of diffuse deformation over a wide transect (3-4 km). The most prominent structure is the Amarguillo Fault (AF), a NNE-SSW ($\sim N10^\circ$) fault composed by, at least, five parallel branches displaying a small horst and graben structure with left-lateral component. This sector corresponds to a transtensional bend, likely caused by its nearly parallel orientation to the regional shortening vector ($\sim N150^\circ$). In this framework, the AF could be absorbing most part of the vertical component in the segment as suggested by its marked geomorphic expression.

The Quaternary activity of the AF is evidenced by faulting of Middle to Late Pleistocene alluvial fans and by the presence of tectonic geomorphic features such as scarps and deflected channels. This spotlights the importance of developing paleoseismic studies in this fault to constrain its paleoseismic parameters (slip rates and recurrences). Given the difficulties of finding recent faulted sediments in the area, we propose a suitable site with potentially young materials across the AF for future paleoseismic studies.

Conclusions on the probabilistic seismic hazard assessment in the Eastern Betics Shear Zone

The fault-based probabilistic seismic hazard assessment (PSHA) of the EBSZ has been conducted by considering the main faults of the system as the principal sources, and a relaxed segmentation approach. Four hypotheses of fault and multi-fault ruptures have been conceived in two separate source models (FM and FM_bg). Their respective earthquake magnitude-frequency distributions (MFD) have been computed with the SHERIFS code. The main conclusions from this PSHA are outlined below:

Fault-based source modelling

The source modelling performed with SHERIFS suggests that multi-fault ruptures are feasible in the EBSZ, based on the fits with the seismic catalogue and paleoearthquake record. Particularly, ruptures extending longer than the classic segments defined in the literature and involving individual to several whole faults (hyp. 2 and 3, respectively) are the most consistent with the datasets. Conversely, the rupture of the whole system (hyp. 4) is unlikely based on the poor fit with such data.

Considering multi-fault ruptures in the source modelling is a step forward to account for a complexity observed in nature. The use of this approach for the first in the western Mediterranean might serve as a case example for other low-to-moderate seismicity regions worldwide.

Seismic hazard assessment

In both FM and FM_bg models, the EBSZ faults dominate the seismic hazard in the areas around them and up to 20-30 km away. This is remarkable for southeastern Spain, as most of the important populations are commonly found on top or very close to active faults (e.g. Alicante, Lorca, Murcia). Contrarily, modelling a portion of the Mw 4.0-5.5 seismicity rate as background (FM_bg) has a minor impact in the EBSZ.

Faults increase peak ground accelerations (PGA) compared to previous area source-based PSHAs. However, their influence zone is strongly dependent on the slip rates. Faults with the higher slip rates (>1 mm/yr; Carboneras Fault or southwestern segments of AMF) increase up to 150% the PGA respect to area source models. Conversely, faults with the lowest estimated slip rates (<0.1 mm/yr; PF) have no significant impact in the hazard.

For the 475-year return period, our fault-based hazard models in near-fault sites provide more accurate estimations than the building code (NCSE-02) or the updated national seismic hazard map (area source approaches). This is supported, for instance, by the better agreement of our results with the PGA values recorded in Lorca during the 2011 Mw 5.2 earthquake.

Fault input data

The lack of detailed paleoseismic studies in some faults of the EBSZ, mainly those with lower slip rate assignments (PF and northeastern segments of AMF), can compromise the reliability of our models. These faults might cause underestimation of the seismic hazard around them because they limit the earthquake rates of higher slip rate faults in long rupture scenarios. These issues have allowed to highlight which knowledge gaps of fault data are critical in the models and require more attention in future studies.

The performance of a new hazard model (FM_updated) using updated slip rates for the AMF (this thesis) and PF (literature) has allowed to reduce the modelling issues found in the first models. This shows the impact of the fault slip rates on the seismic hazard in the region, especially in those poorly studied faults.

Global conclusions

The results of this thesis are a step forward for a more reliable characterization of the seismic hazard in the EBSZ in terms of i) improving the representativeness of fault parameters in one of the main faults (AMF) and ii) evaluating the importance and impact of such parameters for PSHA. The general conclusions are:

- Fault slip rate is the most important parameter controlling earthquake occurrence and, hence, seismic hazard in the EBSZ. Disposing of representative and reliable slip rates for the faults is key for a proper source modelling characterization and seismic hazard assessment. This is especially important in the EBSZ because most faults accommodate deformation in several fault branches across wide transects, and seismic parameters from a single branch might lead to hazard underestimation.

- Performing multi-site and integral paleoseismic surveys improves the characterization of faults with respect to single-site studies. The comprehensive paleoseismic survey carried out in the AMF allowed for more representative slip rate estimations than previous studies. The new and higher values obtained here ($1.55^{+0.14}/_{-0.18}$ mm/yr) increase the hazard around the AMF and are an example of how necessary the integral paleoseismic studies in the EBSZ are.

- The current slip rates assigned to some faults of the EBSZ (mainly PF and northeastern segments of the AMF) are contrastingly lower than other surrounding and more well-studied faults. It is strongly recommended that further research prioritizes obtaining new paleoseismic-derived slip rate data in these poorly studied faults to detect possible underestimation in the current values.

- The feasibility of synchronic ruptures among branches of the AMF (S-AMF and F-AMF) can help to add criteria and reduce the subjectivity on the definition of fault rupture scenarios for PSHA in the EBSZ. Further research in this matter can also help to identify possible patterns of activity synchronicity and interaction between faults. All these might serve as input data to improve future source modellings (e.g., physics-based).

- The Poissonian model considered for the PSHA of the EBSZ agrees with the recurrence model inferred for the paleoearthquake record in the S-AMF. The suitability of this model is reinforced because this branch is the principal in the Lorca-Totana

segment. However, it does not allow to exclude the adequacy of time-dependent models for the EBSZ as well, which should be further explored.

- This thesis presents a study that encompasses the whole process of estimating the seismic hazard of a region, from the paleoseismic data collection to PSHA. Acknowledging and prioritizing the impact of geological data and its issues on PSHA is fundamental to improve the seismic hazard knowledge and thus the social preparedness to the effects of earthquakes. In the EBSZ, the issues concerning fault data are: lack of age control of the paleoearthquake record, lack of common time periods for the slip rates in different sites, and the existence of poorly constrained faults. This integral view allows performing more critical and overall, better interpretations of the outcomes from fault-based PSHAs in complex systems.

REFERENCES

- Akkar, S., Sandikkaya, M.A., and Bommer, J.J., 2014, Empirical ground-motion models for point- and extended-source crustal earthquake scenarios in Europe and the Middle East: *Bulletin of Earthquake Engineering*, v. 12, p. 359–387, doi:10.1007/s10518-013-9461-4.
- Aldaya, F., 1970, Pliegues triásicos en la Sierra de Lujar, zona Bética, provincia de Granada (Nota preliminar): *Boletín Geológico y Minero de España*, v. 81, p. 593–600.
- Alfaro, P., Bartolomé, R., Borque, M.J., Estévez, A., García-Mayordomo, J., García-Tortosa, F.J., Gil, A.J., Gràcia, E., Lo Iacono, C., and Perea, H., 2012, The Bajo Segura Fault Zone: Active blind thrusting in the Eastern Betic Cordillera (SE Spain): *Journal of Iberian Geology*, v. 38, doi:10.5209/rev_JIGE.2012.v38.n1.39217.
- Alguacil, G., Vidal, F., Navarro, M., García-Jerez, A., and Pérez-Muelas, J., 2014, Characterization of earthquake shaking severity in the town of Lorca during the May 11, 2011 event: *Bulletin of Earthquake Engineering*, v. 12, p. 1889–1908, doi:10.1007/s10518-013-9475-y.
- Allen, C.R., 1986, Seismological and paleoseismological techniques of research in active tectonics, *in* Wallace Chairman, R.E. ed., *Active Tectonics: Studies in Geophysics*, Washington, D.C., National Academy Press.
- Allin Cornell, C., and Winterstein, S.R., 1988, Temporal and magnitude dependence in earthquake recurrence models: *Bulletin of the Seismological Society of America*, v. 78, p. 1522–1537.
- Alonso-Henar, J., Herrero-Barbero, P., Martínez-Díaz, J.J., Álvarez-Gómez, J.A., Canora, C., and Insua-Arévalo, J.M., 2018, Local shortening rates at the Carraclaca Outcrop. Lorca-Totana Segment, Alhama de Murcia Fault, *in* Canora, C. ed., *Resúmenes de la 3ª Reunión Ibérica sobre Fallas Activas y Paleosismología*, Alicante, Spain, Universitat d'Alacant, p. 11–14.
- Álvarez-Gómez, J.A., Insua-Arévalo, J.M., Herrero-Barbero, P., Martínez-Díaz, J.J., Canora, C., Alonso-Henar, J., and García-Mayordomo, J., 2018, Potencial de encadenamiento de roturas sísmicas en la Zona de Cizalla de las Béticas Orientales por transferencia de esfuerzos de Coulomb, *in* Canora, C. ed., *Resúmenes de la 3ª Reunión Ibérica sobre Fallas Activas y Paleosismología*, Alicante, Spain, Universitat d'Alacant, p. 157–160.
- Álvarez-Gómez, J.A., and Martín-González, F., 2014, Una aproximación multidisciplinar al estudio de las fallas activas, los terremotos y el riesgo sísmico. *Resúmenes de la 2ª Reunión Ibérica sobre fallas activas y paleosismología: Lorca, Spain, Instituto Geológico y Minero de España*, 251 p.
- Archuleta, R.J., 1984, Faulting Model for the 1979 Imperial Valley Earthquake.: *Journal of Geophysical Research*, v. 89, p. 4559–4585, doi:10.1029/JB089iB06p04559.
- Arias, A., 1970, Measure of earthquake intensity, *in* Hansen, R. ed., *Seismic Design for Nuclear Power Plants*, Cambridge, Massachusetts, Massachusetts Institute of

- Technology Press, p. 438–483.
- Azañón, J.M., and Goffé, B., 1997, Ferro- and magnesiocarpholite assemblages as record of high-P, low- Γ metamorphism in the Central Alpujarrides, Betic Cordillera (SE Spain): *European Journal of Mineralogy*, v. 9, p. 1035–1052, doi:10.1127/ejm/9/5/1035.
- Baize, S. et al., 2019, A Worldwide and Unified Database of Surface Ruptures (SURE) for Fault Displacement Hazard Analyses: *Seismological Research Letters*, doi:10.1785/0220190144.
- Baize, S., Audin, L., Winter, T., Alvarado, A., Pilatasig Moreno, L., Taipei, M., Reyes, P., Kauffmann, P., and Yepes, H., 2015, Paleoseismology and tectonic geomorphology of the Pallatanga fault (Central Ecuador), a major structure of the South-American crust: *Geomorphology*, v. 237, p. 14–28, doi:10.1016/j.geomorph.2014.02.030.
- Basili, R., Valensise, G., Vannoli, P., Burrato, P., Fracassi, U., Mariano, S., Tiberti, M.M., and Boschi, E., 2008, The Database of Individual Seismogenic Sources (DISS), version 3: Summarizing 20 years of research on Italy's earthquake geology: *Tectonophysics*, v. 453, p. 20–43, doi:10.1016/j.tecto.2007.04.014.
- Baumont, D., Scotti, O., Courboux, F., and Melis, N., 2004, Complex kinematic rupture of the Mw 5.9, 1999 Athens earthquake as revealed by the joint inversion of regional seismological and SAR data: *Geophysical Journal International*, v. 158, p. 1078–1087, doi:10.1111/j.1365-246X.2004.02374.x.
- Bazzurro, P., and Cornell, C.A., 1999, Disaggregation of seismic hazard: *Bulletin of the Seismological Society of America*, v. 89, p. 501–520.
- Benedetti, L., Manighetti, I., Gaudemer, Y., Finkel, R., Malavieille, J., Pou, K., Arnold, M., Aumaître, G., Bourlès, D., and Keddadouche, K., 2013, Earthquake synchrony and clustering on Fucino faults (Central Italy) as revealed from in situ ^{36}Cl exposure dating: *Journal of Geophysical Research: Solid Earth*, v. 118, p. 4948–4974, doi:10.1002/jgrb.50299.
- Benedetti, L.C., and Van Der Woerd, J., 2014, Cosmogenic nuclide dating of earthquakes, faults, and toppled blocks: *Elements*, v. 10, p. 357–361, doi:10.2113/gselements.10.5.357.
- Benito, B. et al., 2007, An overview of the damaging and low magnitude Mw 4.8 La Paca earthquake on 29 January 2005: Context, seismotectonics, and seismic risk implications for southeast Spain: *Bulletin of the Seismological Society of America*, v. 97, p. 671–690, doi:10.1785/0120050150.
- Benito, B., and Jimenez, M.E., 1999, Peligrosidad sísmica: *Física de la Tierra*, p. 13–47.
- Benito, M.B., Navarro, M., Vidal, F., Gaspar-Escribano, J., García-Rodríguez, M.J., and Martínez-Solares, J.M., 2010, A new seismic hazard assessment in the region of Andalusia (Southern Spain): *Bulletin of Earthquake Engineering*, v. 8, p. 739–766, doi:10.1007/s10518-010-9175-9.
- Berberian, M., 1979, Earthquake faulting and bedding thrust associated with the Tabas-e-Golshan (Iran) earthquake of September 16, 1978: *Bulletin of the Seismological Society of America*, v. 69, p. 1861–1887.

- Berryman, K.R., Cochran, U.A., Clark, K.J., Biasi, G.P., Langridge, R.M., and Villamor, P., 2012, Major Earthquakes Occur Regularly on an Isolated Plate Boundary Fault: *Science*, v. 336, p. 1690 LP – 1693, doi:10.1126/science.1218959.
- Biasi, G.P., and Weldon, R.J., 2006, Estimating surface rupture length and magnitude of paleoearthquakes from point measurements of rupture displacement: *Bulletin of the Seismological Society of America*, v. 96, p. 1612–1623, doi:10.1785/0120040172.
- Bommer, J.J., Scherbaum, F., Bungum, H., Cotton, F., Sabetta, F., and Abrahamson, N.A., 2005, On the use of logic trees for ground-motion prediction equations in seismic-hazard analysis: *Bulletin of the Seismological Society of America*, v. 95, p. 377–389, doi:10.1785/0120040073.
- Boncio, P., Lavecchia, G., and Pace, B., 2004, Defining a model of 3D seismogenic sources for Seismic Hazard Assessment applications: The case of central Apennines (Italy): *Journal of Seismology*, v. 8, p. 407–425, doi:10.1023/B:JOSE.0000038449.78801.05.
- Bonilla, M.G., 1982, Evaluation of Potential Surface Faulting and Other Tectonic Deformation: USGS Open-File Report 82-732.
- Borque, M.J. et al., 2019, How Much Nubia-Eurasia Convergence Is Accommodated by the NE End of the Eastern Betic Shear Zone (SE Spain)? Constraints From GPS Velocities: *Tectonics*, v. 38, p. 1824–1839, doi:10.1029/2018TC004970.
- Bousquet, J.C., 1979, Quaternary Strike-Slip Faults in Southeastern Spain: *Tectonophysics*, v. 52, p. 277–286, doi:10.1016/B978-0-444-41783-1.50044-1.
- Bronk Ramsey, C., 2017, Methods for Summarising Radiocarbon Datasets: *Radiocarbon*, v. 59, p. 1809–1833.
- Bull, W.B., 1996, Dating San Andreas fault earthquakes with lichenometry: *Geology*, v. 24, p. 111–114, doi:10.1130/0091-7613(1996)024<0111:DSAFEW>2.3.CO;2.
- Bull, W.B., 2003, Lichenometry dating of coseismic changes to a New Zealand landslide complex: *Annals of Geophysics*, v. 46, p. 1155–1168, doi:10.4401/ag-3451.
- Bull, W.B., 1977, The alluvial-fan environment: *Progress in Physical Geography*, v. 1, p. 222–270, doi:10.1177/030913337700100202.
- Bungum, H., 2007, Numerical modelling of fault activities: *Computers and Geosciences*, v. 33, p. 808–820, doi:10.1016/j.cageo.2006.10.011.
- Burbank, D.W., and Anderson, R.S., 2011, *Tectonic Geomorphology*: Wiley-Blackwell, 460 p., doi:10.1002/9781444345063.
- Cabañas, L. et al., 2011, Informe del sismo de Lorca del 11 de Mayo de 2011: Instituto Geográfico Nacional, Madrid, Spain, <http://hdl.handle.net/10261/62381>.
- Calais, E., DeMets, C., and Nocquet, J.-M., 2003, Evidence for a post-3.16-Ma change in Nubia–Eurasia–North America plate motions? *Earth and Planetary Science Letters*, v. 216, p. 81–92, doi:10.1016/S0012-821X(03)00482-5.
- Calmel-Avila, M., 2002, The Librilla “rambla”, an example of morphogenetic crisis in the Holocene (Murcia, Spain): *Quaternary International*, v. 93–94, p. 101–108, doi:10.1016/S1040-6182(02)00009-5.

- Camelbeeck, T., Alexandre, P., Vanneste, K., and Meghraoui, M., 2000, Long-term seismicity in regions of present day low seismic activity: The example of western Europe: *Soil Dynamics and Earthquake Engineering*, v. 20, p. 405–414, doi:10.1016/S0267-7261(00)00080-4.
- Campbell, K.W., and Bozorgnia, Y., 2014, NGA-West2 ground motion model for the average horizontal components of PGA, PGV, and 5% damped linear acceleration response spectra: *Earthquake Spectra*, v. 30, p. 1087–1114, doi:10.1193/062913EQS175M.
- Canora, C. et al., 2016, Nuevos datos de actividad paleosísmica de la falla de Alhama de Murcia en el abanico de La Salud (segmento Lorca-Totana de la Falla de Alhama de Murcia), Béticas Orientales, *in IX Congreso Geológico de España*, Huelva, Spain.
- Canora, C., Martín-González, F., Masana, E., Pérez-López, R., and Ortuño, M., 2018, Avances en el estudio de fallas activas, terremotos y peligrosidad sísmica de Iberia. Resúmenes de la 3ª Reunión Ibérica sobre Fallas Activas y Paleosismología: Alicante, Spain, Universitat d'Alacant, 324 p.
- Chartier, T., Scotti, O., and Lyon-Caen, H., 2019, SHERIFS: Open-Source Code for Computing Earthquake Rates in Fault Systems and Constructing Hazard Models: *Seismological Research Letters*, v. 90, p. 1678–1688, doi:10.1785/0220180332.
- Choi, J.H., Jin, K., Enkhbayar, D., Davvasambuu, B., Bayasgalan, A., and Kim, Y.S., 2012, Rupture propagation inferred from damage patterns, slip distribution, and segmentation of the 1957 MW 8.1 Gobi-Altay earthquake rupture along the Bogd fault, Mongolia: *Journal of Geophysical Research B: Solid Earth*, v. 117, p. 1–24, doi:10.1029/2011JB008676.
- Colhoun, E.A., 1986, Field problems of radiocarbon dating in Tasmania.: *Papers & Proceedings - Royal Society of Tasmania*, v. 120, p. 1–6, doi:10.26749/rstpp.120.1.
- Console, R., Murru, M., Falcone, G., and Catalli, F., 2008, Stress interaction effect on the occurrence probability of characteristic earthquakes in Central Apennines: *Journal of Geophysical Research: Solid Earth*, v. 113, doi:10.1029/2007JB005418.
- Cornell, C.A., 1968, Engineering seismic risk analysis: *Bulletin of the Seismological Society of America*, v. 58, p. 1583–1606.
- Do Couto, D., Gorini, C., Jolivet, L., Le Bret, N., Augier, R., Gumiaux, C., D'Acremont, E., Ammar, A., Jabour, H., and Auxietre, J.-L., 2016, Tectonic and stratigraphic evolution of the Western Alboran Sea Basin in the last 25 Myrs: *Tectonophysics*, v. 677–678, p. 280–311, doi:10.1016/j.tecto.2016.03.020.
- Cowie, P.A., Roberts, G.P., Bull, J.M., and Visini, F., 2012, Relationships between fault geometry, slip rate variability and earthquake recurrence in extensional settings: *Geophysical Journal International*, v. 189, p. 143–160, doi:10.1111/j.1365-246X.2012.05378.x.
- DeMets, C., Iaffaldano, G., and Merkouriev, S., 2015, High-resolution Neogene and Quaternary estimates of Nubia-Eurasia-North America Plate motion: *Geophysical Journal International*, v. 203, p. 416–427, doi:10.1093/gji/ggv277.
- Dercourt, J. et al., 1986, Geological evolution of the tethys belt from the atlantic to the pamirs since the LIAS: *Tectonophysics*, v. 123, p. 241–315, doi:10.1016/0040-

- 1951(86)90199-X.
- Dewey, J.F., Helman, M.L., Knott, S.D., Turco, E., and Hutton, D.H.W., 1989, Kinematics of the western Mediterranean: Geological Society, London, Special Publications, v. 45, p. 265–283, doi:10.1144/GSL.SP.1989.045.01.15.
- Dhakal, Y.P., 2021, Strong-Motions From Damaging Moderate Magnitude ($5.9 \geq M_w$) Earthquakes in Japan Recorded by K-NET and KiK-net: *Frontiers in Earth Science*, v. 9, p. 1–20, doi:10.3389/feart.2021.618400.
- Dieterich, J.H., and Richards-Dinger, K.B., 2010, Earthquake Recurrence in Simulated Fault Systems: Pure and Applied Geophysics, v. 167, p. 1087–1104, doi:10.1007/s00024-010-0094-0.
- Dikbaş, A., Akyüz, H.S., Meghraoui, M., Ferry, M., Altunel, E., Zabcı, C., Langridge, R., and Yalçiner, C.Ç., 2018, Paleoseismic history and slip rate along the Sapanca-Akyazı segment of the 1999 İzmit earthquake rupture ($M_w = 7.4$) of the North Anatolian Fault (Turkey): *Tectonophysics*, v. 738–739, p. 92–111, doi:10.1016/j.tecto.2018.04.019.
- Duller, G., 2015, The Analyst software package for luminescence data: overview and recent improvements: *Ancient TL*, v. 33, p. 1–8.
- DuRoss, C.B., Personius, S.F., Crone, A.J., Olig, S.S., and Lund, W.R., 2011, Integration of paleoseismic data from multiple sites to develop an objective earthquake chronology: Application to the Weber segment of the Wasatch fault zone, Utah: *Bulletin of the Seismological Society of America*, v. 101, p. 2765–2781, doi:10.1785/0120110102.
- DuRoss, C.B., Zellman, M.S., Thackray, G.D., Briggs, R.W., Gold, R.D., and Mahan, S.A., 2021, Holocene paleoseismology of the steamboat mountain site: Evidence for full-length rupture of the teton fault, wyoming: *Bulletin of the Seismological Society of America*, v. 111, p. 439–465, doi:10.1785/0120200212.
- Echeverria, A., Khazaradze, G., Asensio, E., Gárate, J., Dávila, J.M., and Suriñach, E., 2013, Crustal deformation in eastern Betics from CuaTeNeo GPS network: *Tectonophysics*, v. 608, p. 600–612, doi:10.1016/j.tecto.2013.08.020.
- Echeverria, A., Khazaradze, G., Asensio, E., and Masana, E., 2015, Geodetic evidence for continuing tectonic activity of the Carboneras fault (SE Spain): *Tectonophysics*, v. 663, p. 302–309, doi:10.1016/J.TECTO.2015.08.009.
- Egeler, C.G., and Simon, O.J., 1969, Orogenic evolution of the Betic Zone (Betic Cordilleras, Spain), with emphasis on the nappe structures: *Geologie en Mijnbouw*, v. 48, p. 296–305.
- Ellsworth, W.L., Matthews, M., and Nadeau, R., 1999, A physically based earthquake recurrence model for estimation of long-term earthquake probabilities, *in* *Earthquake Recurrence: State of the Art and Directions for the Future*, Rome, Italy, Istituto Nazionale de Geofisica, p. 22–25, <http://geopubs.wr.usgs.gov/openfile/of99-522/of99-522.pdf>.
- Faccenna, C., Piromallo, C., Crespo-Blanc, A., Jolivet, L., and Rossetti, F., 2004, Lateral slab deformation and the origin of the western Mediterranean arcs: *Tectonics*, v. 23, p. n/a-n/a, doi:10.1029/2002TC001488.

- Faure Walker, J., Boncio, P., Pace, B., Roberts, G., Benedetti, L., Scotti, O., Visini, F., and Peruzza, L., 2021, Fault2SHA Central Apennines database and structuring active fault data for seismic hazard assessment: *Scientific Data*, v. 8, p. 1–20, doi:10.1038/s41597-021-00868-0.
- Faure Walker, J.P., Visini, F., Roberts, G., Galasso, C., McCaffrey, K., and Mildon, Z., 2019, Variable fault geometry suggests detailed fault-slip-rate profiles and geometries are needed for fault-based probabilistic seismic hazard assessment (PSHA): *Bulletin of the Seismological Society of America*, v. 109, p. 110–123, doi:10.1785/0120180137.
- Ferrater, M. et al., 2017, Lateral slip rate of Alhama de Murcia fault (SE Iberian Peninsula) based on a morphotectonic analysis: Comparison with paleoseismological data: *Quaternary International*, v. 451, p. 87–100, doi:10.1016/j.quaint.2017.02.018.
- Ferrater, M. et al., 2016, Refining seismic parameters in low seismicity areas by 3D trenching: The Alhama de Murcia fault, SE Iberia: *Tectonophysics*, v. 680, p. 122–128, doi:10.1016/j.tecto.2016.05.020.
- Ferrater, M., 2016, Velocitat de desplaçament de la falla d'Alhama de Murcia (Bètiques Orientals); implicacions en el seu potencial sísmic: PhD thesis, Universitat de Barcelona, Barcelona, Spain, 282 p.
- Ferrater, M., Arrowsmith, R., and Masana, E., 2015a, Lateral offset quality rating along low slip rate faults: Application to the Alhama de Murcia Fault (SE Iberian Peninsula): *Remote Sensing*, v. 7, p. 14827–14852, doi:10.3390/rs71114827.
- Ferrater, M., Booth-Rea, G., Pérez-Peña, J.V., Azañón, J.M., Giaconia, F., and Masana, E., 2015b, From extension to transpression: Quaternary reorganization of an extensional-related drainage network by the Alhama de Murcia strike-slip fault (eastern Betics): *Tectonophysics*, v. 663, p. 33–47, doi:10.1016/j.tecto.2015.06.011.
- Ferrater, M., Silva, P.G., Ortuño, M., Rodríguez-Pascua, M.Á., and Masana, E., 2015c, Archaeoseismological Analysis of a Late Bronze Age Site on the Alhama de Murcia Fault, SE Spain: *Geoarchaeology*, v. 30, p. 151–164, doi:10.1002/gea.21505.
- Field, E. et al., 2014, The Uniform California Earthquake Rupture Forecast, Version 3 (UCERF3): *Bulletin of the Seismological Society of America*, v. 3, p. 1122–1180, doi:10.3133/ofr20131165.
- Fletcher, J.M. et al., 2014, Assembly of a large earthquake from a complex fault system: Surface rupture kinematics of the 4 April 2010 El Mayor-Cucapah (Mexico) M w 7.2 earthquake: *Geosphere*, v. 10, p. 797–827, doi:10.1130/GES00933.1.
- Frankel, A., 1995, Mapping Seismic Hazard in the Central and Eastern United States: *Seismological Research Letters*, v. 66, p. 8–21, doi:10.1785/gssrl.66.4.8.
- Galbraith, R.F., and Roberts, R.G., 2012, Statistical aspects of equivalent dose and error calculation and display in OSL dating: An overview and some recommendations: *Quaternary Geochronology*, v. 11, p. 1–27, doi:10.1016/j.quageo.2012.04.020.
- García-Hernández, M., López-Garrido, A., Rivas, P., Sanz de Galdeano, C., and Vera, J., 1980, Mesozoic palaeogeographic evolution of the External Zones of the Betic Cordillera: *Geologie en Mijnbouw*, v. 59, p. 155–168.

- García-Mayordomo, J., 2005, Caracterización y análisis de la peligrosidad sísmica en el sureste de España: PhD Thesis. Universidad Complutense de Madrid, Madrid, Spain, 373 p.
- García-Mayordomo, J., 2015, Creación de un modelo de zonas sísmogénicas para el cálculo del mapa de peligrosidad sísmica de España: Instituto Geológico y Minero de España, Madrid, Spain, <http://igmpublicaciones.blogspot.com.es/2014/10/riesgos-geologicosgeotecnia.html>.
- García-Mayordomo, J. et al., 2012, Modelo de Zonas Sísmogénicas para el Cálculo de la Peligrosidad Sísmica en España, *in* 7^a Asamblea Hispano-Portuguesa de Geodesia y Geofísica, Donostia, Spain, doi:10.13140/RG.2.1.4536.5608.
- García-Mayordomo, J., Gaspar-Escribano, J.M., and Benito, B., 2007, Seismic hazard assessment of the Province of Murcia (SE Spain): Analysis of source contribution to hazard: *Journal of Seismology*, v. 11, p. 453–471, doi:10.1007/s10950-007-9064-0.
- García-Mayordomo, J., Martín-Banda, R., Insua-Arévalo, J.M., Álvarez-Gómez, J.A., Martínez-Díaz, J.J., and Cabral, J., 2017, Active fault databases: Building a bridge between earthquake geologists and seismic hazard practitioners, the case of the QAFI v.3 database: *Natural Hazards and Earth System Sciences*, v. 17, p. 1447–1459, doi:10.5194/nhess-17-1447-2017.
- García-Mayordomo, J., Ortuño, M., Insua-Arévalo, J.M., Scotti, O., Visini, F., and Fault2SHA-Betics Working Group, 2018, The Fault2SHA-Betics Working Group: Promoting knowledge interchange between earthquake geologists and seismic hazard modellers in the Eastern Betics (SE Spain), *in* Canora, C. ed., Resúmenes de la 3^a Reunión Ibérica sobre Fallas Activas y Paleosismología, Alicante, Spain, Universitat d'Alacant, p. 243–246.
- García-Mayordomo, J., Peruzza, L., Ortuño, M., and Pace, B., 2019, Fault Complex Interaction: Characterization and Integration into Seismic Hazard Assessment (SHA). *Proceedings of the Fault2SHA - 4th Workshop: Barcelona, Spain*, 42 p.
- Gaspar-Escribano, J.M., Benito, B., and García-Mayordomo, J., 2008, Hazard-consistent response spectra in the Region of Murcia (Southeast Spain): comparison to earthquake-resistant provisions: *Bulletin of Earthquake Engineering*, v. 6, p. 179–196, doi:10.1007/s10518-007-9051-4.
- Gaspar-Escribano, J.M., Rivas-Medina, A., Parra, H., Cabañas, L., Benito, B., Ruiz Barajas, S., and Martínez Solares, J.M., 2015, Uncertainty assessment for the seismic hazard map of Spain: *Engineering Geology*, v. 199, p. 62–73, doi:10.1016/j.enggeo.2015.10.001.
- GEM, 2019, The OpenQuake-engine User Manual: Global Earthquake Model (GEM). OpenQuake Manual for Engine version 3.7.1, doi:10.13117/GEM.OPENQUAKE.MAN.ENGINE.3.7.1.
- Giner, J.J., Molina, S., and Jauregui, P., 2002, Advantages of using sensitivity analysis in seismic hazard assessment: A case study of sites in Southern and Eastern Spain: *Bulletin of the Seismological Society of America*, v. 92, p. 543–554, doi:10.1785/0120000299.
- Goffe, B., Michard, A., Garcia-Deñenas, V., González-Lodeiro, F., Monie, P., Campos, J.,

- Galindo-Zaldívar, J., Jabaloy, A., Martínez-Martínez, J.M., and Simancas, J.F., 1989, First evidence of high-pressure, low-temperature metamorphism in the Alpujarride nappes, Betic Cordilleras (S. E. Spain): *European Journal of Mineralogy*, v. 1, p. 139–142.
- Gold, R.D., Cowgill, E., Arrowsmith, J.R., Chen, X., Sharp, W.D., Cooper, K.M., and Wang, X.-F., 2011, Faulted terrace risers place new constraints on the late Quaternary slip rate for the central Altyn Tagh fault, northwest Tibet: *Geological Society of America Bulletin*, v. 123, p. 958–978, doi:10.1130/B30207.1.
- Gold, R.D., Cowgill, E., Arrowsmith, J.R., Gosse, J., Chen, X., and Wang, X.F., 2009, Riser diachroneity, lateral erosion, and uncertainty in rates of strikeslip faulting: A case study from Tuzidun along the Altyn Tagh Fault, NW China: *Journal of Geophysical Research: Solid Earth*, v. 114, p. 1–24, doi:10.1029/2008JB005913.
- Gómez-Novell, O., Chartier, T., García-Mayordomo, J., Ortuño, M., Masana, E., Insua-Arévalo, J.M., and Scotti, O., 2019, Modelling earthquake multi-fault ruptures across complex fault systems for probabilistic seismic hazard assessment: the Eastern Betics Shear Zone: *Mendeley Data*, v1, doi:10.17632/pt32rrncdm.1.
- Gómez-Novell, O., Chartier, T., García-Mayordomo, J., Ortuño, M., Masana, E., Insua-Arévalo, J.M., and Scotti, O., 2020a, Modelling earthquake rupture rates in fault systems for seismic hazard assessment: the Eastern Betics Shear Zone: *Engineering Geology*, v. 265, doi:10.1016/j.enggeo.2019.105452.
- Gómez-Novell, O., García-Mayordomo, J., Ortuño, M., Masana, E., and Chartier, T., 2020b, Fault System-Based Probabilistic Seismic Hazard Assessment of a Moderate Seismicity Region: The Eastern Betics Shear Zone (SE Spain): *Frontiers in Earth Science*, v. 8, doi:10.3389/feart.2020.579398.
- Goodfriend, G.A., and Stipp, J.J., 1983, Limestone and the problem of radiocarbon dating of land-snail shell carbonate: *Geology*, v. 11, p. 575, doi:10.1130/0091-7613(1983)11<575:LATPOR>2.0.CO;2.
- Gràcia, E. et al., 2019, Earthquake crisis unveils the growth of an incipient continental fault system: *Nature Communications*, v. 10, p. 1–12, doi:10.1038/s41467-019-11064-5.
- Grützner, C., Fischer, P., and Reicherter, K., 2016, Holocene surface ruptures of the Rurrand Fault, Germany—insights from palaeoseismology, remote sensing and shallow geophysics: *Geophysical Journal International*, v. 204, p. 1662–1677, doi:10.1093/gji/ggv558.
- De Guidi, G., Brighenti, F., Carnemolla, F., Cataldo, D., and Piro, A.G., 2019, New dating of rapid vertical deformation of Santa Tecla Fault scarps (Mt. Etna volcano, Sicily) by lichenometry method: *Quaternary International*, v. 525, p. 78–88, doi:10.1016/j.quaint.2019.07.031.
- Gutenberg, B., and Richter, C.F., 1944, Frequency of earthquakes in California: *Bulletin of the Seismological Society of America*, v. 34, p. 185–188.
- Hamling, I.J. et al., 2017, Complex multifault rupture during the 2016 Mw 7.8 Kaikōura earthquake, New Zealand: *Science*, v. 356, doi:10.1126/science.aam7194.
- Heier-Nielsen, S., Conradsen, K., Heinemeier, J., Knudsen, K.L., Nielsen, H.L., Rud, N.,

- and Sveinbjörnsdóttir, Á.E., 1995, Radiocarbon Dating of Shells and Foraminifera from the Skagen Core, Denmark: Evidence of Reworking: *Radiocarbon*, v. 37, p. 119–130, doi:10.1017/S0033822200030551.
- Herrero-Barbero, P., 2016, Análisis estructural del segmento Alhama – Alcantarilla de la Falla de Alhama de Murcia y sus implicaciones en el Riesgo Sísmico: Master's Thesis. Universidad Complutense de Madrid, Madrid, Spain, 50 p.
- Herrero-Barbero, P., Álvarez-Gómez, J.A., and Martínez-Díaz, J.J., 2017, Análisis estructural en el segmento Alhama de Murcia – Alcantarilla (Falla de Alhama de Murcia) y sus implicaciones en la peligrosidad sísmica: *Geogaceta*, v. 62, p. 11–14.
- Herrero-Barbero, P., Álvarez-Gómez, J.A., Martínez-Díaz, J.J., and Klimowitz, J., 2020, Neogene Basin Inversion and Recent Slip Rate Distribution of the Northern Termination of the Alhama de Murcia Fault (Eastern Betic Shear Zone, SE Spain): *Tectonics*, v. 39, p. 1–25, doi:10.1029/2019TC005750.
- Herrero-Barbero, P., Álvarez-Gómez, J.A., Williams, C., Villamor, P., Insua-Arévalo, J.M., Alonso-Henar, J., and Martínez-Díaz, J.J., 2021, Physics-based earthquake simulations in slow-moving faults: a case study from the Eastern Betic Shear Zone (SE Iberian Peninsula): *Journal of Geophysical Research: Solid Earth*, v. 126, doi:10.1029/2020jb021133.
- Herrero-Gil, A., 2014, Estudio geomorfológico y estructural de la Falla del Amarguillo: Master's Thesis. Universitat de Barcelona, Barcelona, Spain, 60 p.
- Hessami, K., Pantosti, D., Tabassi, H., Shabanian, E., Abbassi, M.R., Fegghi, K., and Solaymani, S., 2003, Paleearthquakes and slip rates of the North Tabriz Fault, NW Iran: Preliminary results: *Annals of Geophysics*, v. 46, p. 903–916, doi:10.4401/ag-3461.
- IGME, 2015a, QAFI v.3: Quaternary Active Faults Database of Iberia: Instituto Geológico y Minero de España, Madrid, Spain, <http://info.igme.es/qafi> (accessed March 2021).
- IGME, 2015b, ZESIS: Base de Datos de Zonas Sismogénicas de la Península Ibérica y territorios de influencia para el cálculo de la peligrosidad sísmica en España: Instituto Geológico y Minero de España, Madrid, Spain, <http://info.igme.es/zesis> (accessed March 2021).
- IGN-UPM, 2013, Actualización de mapas de peligrosidad sísmica de España 2012.: Centro Nacional de Información Geográfica, Instituto Geográfico Nacional, Madrid, Spain, 267 p.
- IGN, 1991, Mapa de Peligrosidad Sísmica en España: Instituto Geográfico Nacional, Madrid, Spain.
- IGN, 2011, Serie terremoto NE Lorca (Murcia): Instituto Geográfico Nacional, Madrid, Spain, <http://www.ign.es>.
- Insua-Arévalo, J.M., García-Mayordomo, J., Martín-Banda, R., Martínez-Díaz, J.J., and Masana, E., 2018, Quaternary compressive deformation in the linakge zone between the Carrascoy and Palomares faults (Eastern Betic Chain), *in* Canora, C.. ed., *Resúmenes de la 3ª Reunión Ibérica sobre Fallas Activas y Paleosismología*, Alicante, Spain, Universitat d'Alacant, p. 324.

- Insua-Arévalo, J.M., García-Mayordomo, J., Salazar, A.E., Rodríguez-Escudero, E., Martín-Banda, R., Álvarez-Gómez, J.A., Canora, C., and Martínez-Díaz, J.J., 2015, Paleoseismological evidence of holocene activity of the Los Tollos Fault (Murcia, SE Spain): A lately formed Quaternary tectonic feature of the Eastern Betic Shear Zone: *Journal of Iberian Geology*, v. 41, p. 333–350, doi:10.5209/rev_JIGE.2015.v41.n3.49948.
- Insua-Arévalo, J.M., and Martín-González, F., 2010, Contribución de la Geología al Análisis de la Pleigrosidad Sísmica. Resúmenes de la 1ª Reunión Ibérica sobre Fallas Activas y Paleosismología: Sigüenza, Spain, 214 p.
- Jiménez, M.J., and García-Fernández, M., 1999, Seismic hazard assessment in the Ibero-Maghreb region: *Annali di Geofisica*, v. 42, p. 1057–1065, doi:10.4401/ag-3774.
- Jolivet, L., Faccenna, C., and Piromallo, C., 2009, From mantle to crust: Stretching the Mediterranean: *Earth and Planetary Science Letters*, v. 285, p. 198–209, doi:10.1016/j.epsl.2009.06.017.
- Kanamori, H., 1972, Determination of effective tectonic stress associated with earthquake faulting. The Tottori earthquake of 1943: *Physics of the Earth and Planetary Interiors*, v. 5, p. 426–434, doi:10.1016/0031-9201(72)90114-8.
- Kearse, J. et al., 2018, Onshore to offshore ground-surface and seabed rupture of the Jordan–Kekerengu–Needles fault network during the 2016 Mw 7.8 Kaikoura earthquake, New Zealand: *Bulletin of the Seismological Society of America*, v. 108, p. 1573–1595, doi:10.1785/0120170304.
- Keller, E.A., and Pinter, N., 1996, *Active tectonics: Earthquakes, uplift and landscape: Upper Saddle River, New Jersey, Prentice-Hall, Inc.*, 338 p.
- Khazaradze, G., Staller, A., Martínez-Díaz, J.J., López-Escudero, R., and Masana, E., 2020, Constraints on geodetic slip partitioning between the Alhama da Murcia and Palomares faults in the SE Betics, Spain, *in All Hands on Deck: Promoting Faults in Seismic Hazard Assessment. Fault2SHA 5th Workshop - Online*, p. 30.
- King, G., and Yielding, G., 1984, The evolution of a thrust fault system: processes of rupture initiation, propagation and termination in the 1980 El Asnam (Algeria) earthquake: *Geophysical Journal of the Royal Astronomical Society*, v. 77, p. 915–933, doi:10.1111/j.1365-246X.1984.tb02229.x.
- Kondo, H., and Owen, L.A., 2013, Paleoseismology, *in Treatise on Geomorphology*, Elsevier, p. 267–299, doi:10.1016/B978-0-12-374739-6.00092-0.
- Lancaster, N., 2008, Desert dune dynamics and development: insights from luminescence dating: *Boreas*, v. 37, p. 559–573, doi:10.1111/j.1502-3885.2008.00055.x.
- Langridge, R.M. et al., 2018, Coseismic rupture and preliminary slip estimates for the Papatea fault and its role in the 2016 Mw 7.8 Kaikōura, New Zealand, earthquake: *Bulletin of the Seismological Society of America*, v. 108, p. 1596–1622, doi:10.1785/0120170336.
- De Larouzière, F.D., Bolze, J., Bordet, P., Hernandez, J., Montenat, C., and Ott d'Estevou, P., 1988, The Betic segment of the lithospheric Trans-Alboran shear zone during the Late Miocene: *Tectonophysics*, v. 152, p. 41–52, doi:10.1016/0040-1951(88)90028-5.

- Lawson, A.C., 1908, The California earthquake of April 18, 1906: Volume I, *in* Report of the State Earthquake Investigation Commission, Washington, D.C., Carnegie Institution of Washington.
- Leonard, M., 2010, Earthquake fault scaling: Self-consistent relating of rupture length, width, average displacement, and moment release: *Bulletin of the Seismological Society of America*, v. 100, p. 1971–1988, doi:10.1785/0120090189.
- Li, Q., Liu, M., and Stein, S., 2009, Spatiotemporal complexity of continental intraplate seismicity: Insights from geodynamic modeling and implications for seismic hazard estimation: *Bulletin of the Seismological Society of America*, v. 99, p. 52–60, doi:10.1785/0120080005.
- Lienkaemper, J.J., and Ramsey, C.B., 2009, OxCal: Versatile Tool for Developing Paleoequake Chronologies--A Primer: *Seismological Research Letters*, v. 80, p. 431–434, doi:10.1785/gssrl.80.3.431.
- Little, T.A., van Dissen, R., Kearse, J., Norton, K., Benson, A., and Wang, N., 2018, Kekerengu fault, New Zealand: Timing and size of late holocene surface ruptures: *Bulletin of the Seismological Society of America*, v. 108, p. 1556–1572, doi:10.1785/0120170152.
- Lonergan, L., 1993, Timing and kinematics of deformation in the Malaguide Complex, internal zone of the Betic Cordillera, southeast Spain: *Tectonics*, v. 12, p. 460–476, doi:10.1029/92TC02507.
- López-Casado, C., Sanz de Galdeano, C., Delgado, J., and Peinado, M.A., 1995, The b parameter in the Betic Cordillera, Rif and nearby sectors. Relations with the tectonics of the region: *Tectonophysics*, v. 248, p. 277–292, doi:10.1016/0040-1951(94)00278-H.
- López-Comino, J.Á., Mancilla, F.D.L., Morales, J., and Stich, D., 2012, Rupture directivity of the 2011, Mw 5.2 Lorca earthquake (Spain): *Geophysical Research Letters*, v. 39, p. 1–5, doi:10.1029/2011GL050498.
- Malservisi, R., Furlong, K.P., and Gans, C.R., 2005, Microseismicity and creeping faults: Hints from modeling the Hayward fault, California (USA): *Earth and Planetary Science Letters*, v. 235, p. 421–435, doi:10.1029/2000jb000084.
- Manighetti, I., Campillo, M., Sammis, C., Mai, P.M., and King, G., 2005, Evidence for self-similar, triangular slip distributions on earthquakes: Implications for earthquake and fault mechanics: *Journal of Geophysical Research: Solid Earth*, v. 110, p. 1–25, doi:10.1029/2004JB003174.
- Marco, S., Rockwell, T.K., Heimann, A., Frieslander, U., and Agnon, A., 2005, Late Holocene activity of the Dead Sea Transform revealed in 3D palaeoseismic trenches on the Jordan Gorge segment: *Earth and Planetary Science Letters*, v. 234, p. 189–205, doi:10.1016/j.epsl.2005.01.017.
- Marín-Lechado, C., Roldán-García, F.J., Pineda-Velasco, A., Martínez-Zubieta, P., Rodero-Pérez, J., and Díaz-Pinto, G., 2011, Mapa Geológico Digital Continuo E 1:50000, Zonas Internas de las Cordilleras Béticas (Zona-2100): GEODE. Mapa Geológico Digital Continuo de España, https://mapas.igme.es/gis/services/Cartografia_Geologica/IGME_MAGNA_50/MapServer/WMS/Server (accessed January 2001).

- Martí, A., Queralt, P., Marcuello, A., Ledo, J., Rodríguez-Escudero, E., Martínez-Díaz, J.J., Campaña, J., and Meqbel, N., 2020, Magnetotelluric characterization of the Alhama de Murcia Fault (Eastern Betics, Spain) and study of magnetotelluric interstation impedance inversion: *Earth, Planets and Space*, v. 72, doi:10.1186/s40623-020-1143-2.
- Martín-Banda, R., 2020, Segmentación y evolución reciente del sistema de fallas de la Sierra de Carrascoy: implicaciones en su potencial sismogénico: PhD Thesis. Universidad Complutense de Madrid, Madrid, Spain, 220 p.
- Martín-Banda, R., García-Mayordomo, J., Insua-Arévalo, J.M., Salazar, A.E., Rodríguez-Escudero, E., Álvarez-Gómez, J.A., Medialdea, A., and Herrero, M.J., 2015, New insights on the seismogenic potential of the Eastern Betic Shear Zone (SE Iberia): Quaternary activity and paleoseismicity of the SW segment of the Carrascoy Fault Zone: *Tectonics*, v. 35, p. 55–75, doi:10.1002/2015TC003997.
- Martín-Banda, R., Insua-Arévalo, J.M., and García-Mayordomo, J., 2021, Slip Rate Variation During the Last ~ 210 ka on a Slow Fault in a Transpressive Regime : The Carrascoy Fault (Eastern Betic Shear Zone , SE Spain): v. 8, p. 1–21, doi:10.3389/feart.2020.599608.
- Martín-Martín, A.J., 1989, Probabilistic seismic hazard analysis and damage assessment in Andalusia (Spain): *Tectonophysics*, v. 167, p. 235–244, doi:10.1016/0040-1951(89)90074-7.
- Martín-Martín, A.J., 1983, Riesgo sísmico en la Península Ibérica: PhD Thesis. Universidad Politécnica de Madrid, Madrid, Spain.
- Martínez-Díaz, J.J., 1998, Neotectónica y Tectónica Activa del Sector Centro-Occidental de la Región de Murcia y Sur de Almería (Cordillera Bética – España): PhD Thesis. Universidad Complutense de Madrid, Madrid, Spain, 466 p.
- Martínez-Díaz, J.J., Alonso-Henar, J., Insua-Arévalo, J.M., Canora, C., García-Mayordomo, J., Rodríguez-Escudero, E., Álvarez-Gómez, J.A., Ferrater, M., Ortuño, M., and Masana, E., 2018, Geological evidences of surface rupture related to a seventeenth century destructive earthquake in Betic Cordillera (SE Spain): constraining the seismic hazard of the Alhama de Murcia fault: *Journal of Iberian Geology*, doi:10.1007/s41513-018-0082-2.
- Martínez-Díaz, J.J., Bejar-Pizarro, M., Álvarez-Gómez, J.A., Mancilla, F. de L., Stich, D., Herrera, G., and Morales, J., 2012a, Tectonic and seismic implications of an intersegment rupture: *Tectonophysics*, v. 546–547, p. 28–37, doi:10.1016/j.tecto.2012.04.010.
- Martínez-Díaz, J.J., and Hernández-Enrile, J.L., 2001, Using travertine deformations to characterize paleoseismic activity along an active oblique-slip fault: The Alhama de Murcia fault (Betic Cordillera, Spain): *Acta Geologica Hispanica*, v. 36, p. 297–313.
- Martínez-Díaz, J.J., Masana, E., Hernández-Enrile, J.L., and Santanach, P., 2003, Effects of repeated paleoearthquakes on the Alhama de Murcia Fault (Betic Cordillera , Spain) on the Quaternary evolution of an alluvial fan system: *Annals of Geophysics*, v. 46, p. 775–791, doi:10.4401/ag-3455.
- Martínez-Díaz, J.J., Masana, E., and Ortuño, M., 2012b, Active tectonics of the Alhama de Murcia fault, Betic Cordillera, Spain: *Journal of Iberian Geology*, v. 38, p. 253–

- 270, doi:10.5209/rev_JIGE.2012.v38.n1.39218.
- Martínez Solares, J., 2003, Sismicidad histórica de la Península Ibérica: Física de la Tierra, v. 15, p. 13–28, doi:10.5209/rev_FITE.2003.v15.12634.
- Martínez-Díaz, J.J., 2002, Stress field variation related to fault interaction in a reverse oblique-slip fault: the Alhama de Murcia fault, Betic Cordillera, Spain: Tectonophysics, v. 356, p. 291–305, doi:10.1016/S0040-1951(02)00400-6.
- Masana, E. et al., 2018, First evidence of paleoearthquakes along the Carboneras Fault Zone (SE Iberian Peninsula): Los Trances site: Geologica Acta, v. 16, p. 461–476, doi:10.1344/GeologicaActa2018.16.4.8.
- Masana, E., Martínez-Díaz, J.J., Hernández-Enrile, J.L., and Santanach, P., 2004, The Alhama de Murcia fault (SE Spain), a seismogenic fault in a diffuse plate boundary: Seismotectonic implications for the Ibero-Magrebien region: Journal of Geophysical Research: Solid Earth, v. 109, p. 1–17, doi:10.1029/2002JB002359.
- Masana, E., Pallàs, R., Perea, H., Ortuño, M., Martínez-Díaz, J.J., García-Meléndez, E., and Santanach, P., 2005, Large Holocene morphogenic earthquakes along the Albox fault, Betic Cordillera, Spain: Journal of Geodynamics, v. 40, p. 119–133, doi:10.1016/j.jog.2005.07.002.
- Matsuda, T., Ota, Y., Ando, M., and Yonekura, N., 1978, Fault mechanism and recurrence time of major earthquakes in southern Kanto district, Japan, as deduced from coastal terrace data: GSA Bulletin, v. 89, p. 1610–1618, doi:10.1130/0016-7606(1978)89<1610:FMARTO>2.0.CO;2.
- Matthews, M. V., Ellsworth, W.L., and Reasenber, P.A., 2002, A Brownian model for recurrent earthquakes: Bulletin of the Seismological Society of America, v. 92, p. 2233–2250, doi:10.1785/0120010267.
- McCalpin, J.P., 2009, Paleoseismology: Academic Press, 588 p., doi:10.1016/S0074-6142(09)95003-3.
- McGuire, R.K., 1976, FORTRAN Computer Program for Seismic Risk Analysis: USGS Open-File Report 76-67, <https://pubs.usgs.gov/of/1976/0067/report.pdf>.
- McGuire, R.K., 1995, Probabilistic seismic hazard analysis and design earthquakes: closing the loop: Bulletin - Seismological Society of America, v. 85, p. 1275–1284, doi:10.1016/0148-9062(96)83355-9.
- Mechernich, S., Schneiderwind, S., Mason, J., Papanikolaou, I.D., Deligiannakis, G., Pallikarakis, A., Binnie, S.A., Dunai, T.J., and Reicherter, K., 2018, The Seismic History of the Pisia Fault (Eastern Corinth Rift, Greece) From Fault Plane Weathering Features and Cosmogenic ³⁶Cl Dating: Journal of Geophysical Research: Solid Earth, v. 123, p. 4266–4284, doi:10.1029/2017JB014600.
- Medialdea, A., 2012, Towards the reconstruction of flood histories : luminescence dating of palaeoflood deposits: PhD Thesis. Universidad Autónoma de Madrid, Madrid, Spain, 194 p.
- Meghraoui, M., Camelbeeck, T., Vanneste, K., Brondeel, M., and Jongmans, D., 2000, Active faulting and paleoseismology along the Bree fault, lower Rhine graben, Belgium: Journal of Geophysical Research: Solid Earth, v. 105, p. 13809–13841, doi:10.1029/1999jb900236.

- Meijninger, B.M.L., and Vissers, R.L.M., 2006, Miocene extensional basin development in the Betic Cordillera, SE Spain revealed through analysis of the Alhama de Murcia and Crevillente Faults: *Basin Research*, v. 18, p. 547–571, doi:10.1111/j.1365-2117.2006.00308.x.
- Mezcua, J., 1982, *Catálogo general de isosistas de la Península Ibérica*: Instituto Geográfico Nacional, Madrid, Spain.
- Mildon, Z.K., Roberts, G.P., Faure Walker, J.P., and Toda, S., 2019, Coulomb pre-stress and fault bends are ignored yet vital factors for earthquake triggering and hazard: *Nature Communications*, v. 10, p. 1–9, doi:10.1038/s41467-019-10520-6.
- Mildon, Z.K., Toda, S., Faure Walker, J.P., and Roberts, G.P., 2016, Evaluating models of Coulomb stress transfer: Is variable fault geometry important? *Geophysical Research Letters*, v. 43, p. 12,407–12,414, doi:10.1002/2016GL071128.
- Moernaut, J., 2020, Time-dependent recurrence of strong earthquake shaking near plate boundaries: A lake sediment perspective: *Earth-Science Reviews*, v. 210, p. 103344, doi:10.1016/j.earscirev.2020.103344.
- Montenat, C., 1973, *Les formations neogenes et quaternaires du Levant Espagnol: (provincies d’Alicante et de Murcia)*: PhD Thesis. Université de Paris Sud, Paris, France.
- Montenat, C., and Ott D’Estevou, P., 1999, The diversity of Late Neogene sedimentary basins generated by wrench faulting in the Eastern Betic Cordillera, SE Spain: *Journal of Petroleum Geology*, v. 22, p. 61–80, doi:10.1111/j.1747-5457.1999.tb00459.x.
- Montenat, C., Ott D’Estevou, P., and Masse, P., 1987, Tectonic-sedimentary characters of the Betic Neogene basins evolving in a crustal transcurrent shear zone (SE Spain): *Bulletin des centres de recherches exploration-Production Elf-Aquitaine*, v. 11, p. 1–22.
- Moreno, X., 2011, *Neotectonic and Paleoseismic Onshore-Offshore integrated study of the Carboneras Fault (Eastern Betics, SE Iberia)*: PhD Thesis. Universitat de Barcelona, Barcelona, Spain, 305 p.
- Moreno, X., Masana, E., Pallàs, R., Gràcia, E., Rodés, Á., and Bordonau, J., 2015, Quaternary tectonic activity of the Carboneras Fault in the La Serrata range (SE Iberia): *Geomorphological and chronological constraints*: *Tectonophysics*, v. 663, p. 78–94, doi:10.1016/j.tecto.2015.08.016.
- Mörner, N.-A., 2011, Paleoseismology: The application of multiple parameters in four case studies in Sweden: *Quaternary International*, v. 242, p. 65–75, doi:10.1016/j.quaint.2011.03.054.
- Mulargia, F., Stark, P.B., and Geller, R.J., 2017, Why is Probabilistic Seismic Hazard Analysis (PSHA) still used? *Physics of the Earth and Planetary Interiors*, v. 264, p. 63–75, doi:10.1016/j.pepi.2016.12.002.
- Muñoz, D., Mayer-Rosa, D., Banda, E., and Udias, A., 1984, A probabilistic calculation of seismic hazard of southern Spain: *Engineering Geology*, v. 20, p. 49–61, doi:10.1016/0013-7952(84)90042-5.
- Murray, A.S., and Wintle, A.G., 2000, Luminescence dating of quartz using an improved

- single-aliquot regenerative-dose protocol: *Radiation Measurements*, v. 32, p. 57–73, doi:10.1016/S1350-4487(99)00253-X.
- Murray, A.S., and Wintle, A.G., 2003, The single aliquot regenerative dose protocol: potential for improvements in reliability: *Radiation Measurements*, v. 37, p. 377–381, doi:10.1016/S1350-4487(03)00053-2.
- Nathan, R.P., and Mauz, B., 2008, On the dose-rate estimate of carbonate-rich sediments for trapped charge dating: *Radiation Measurements*, v. 43, p. 14–25, doi:10.1016/j.radmeas.2007.12.012.
- NCSE-02, 2002, Real Decreto 997/2002, de 27 de septiembre, por el que se aprueba la norma de construcción sismorresistente: parte general y edificación (NCSR-02): *Boletín Oficial del Estado*, v. 244, p. 35898–35967.
- Noller, J.S., 2000, Lead-210 Geochronology, *in* Noller, J.S., Sowers, J.M., and Lettis, W.R. eds., *Quaternary Geochronology*, p. 115–120, doi:10.1029/RF004p0115.
- Ortuño, M., Masana, E., García-Meléndez, E., Martínez-Díaz, J.J., Štěpančíková, P., Cunha, P.P., Sohbaty, R., Canora, C., Buylaert, J.P., and Murray, A.S., 2012, An exceptionally long paleoseismic record of a slow-moving fault: The Alhama de Murcia fault (Eastern Betic shear zone, Spain): *Bulletin of the Geological Society of America*, v. 124, p. 1474–1494, doi:10.1130/B30558.1.
- Ortuño, M., Masana, E., Gómez-Novell, O., Ferrater, M., Pallàs, R., Martínez-Díaz, J.J., Canora, C., Rockwell, T., Medialdea, A., and Rhodes, E.J., 2021, Paleoseismic chronologies from intermittent geological records: revisited sites on the Alhama de Murcia Fault: (Manuscript in preparation).
- Ortuño, M., Masana, E., Gómez-Novell, O., García-Mayordomo, J., Insua-Arévalo, J.M., and Fault2SHA-Betics Working Group, 2018, Fault rupture hypothesis at the Eastern Betics (SE Iberia); insights from the “collective thinking” within the frame of the FAULT2SHA approach: *Geophysical Research Abstracts*, v. 20.
- Pace, B., Visini, F., Scotti, O., and Peruzza, L., 2018, Preface: Linking faults to seismic hazard assessment in Europe: *Natural Hazards and Earth System Sciences*, v. 18, p. 1349–1350, doi:10.5194/nhess-18-1349-2018.
- Pagani, M., Monelli, D., Weatherill, G.A., and Garcia, J., 2014, The OpenQuake-engine Book: Hazard: Global Earthquake Model (GEM) Technical Report 2014-08, 67 p., doi:10.13117/-GEM.OPENQUAKE.TR2014.08,.
- Pantosti, D., D’Addezio, G., and Cinti, F.R., 1996, Paleoseismicity of the Ovindoli-Pezza fault, central Apennines, Italy: A history including a large, previously unrecorded earthquake in the Middle Ages (860-1300 A.D.): *Journal of Geophysical Research: Solid Earth*, v. 101, p. 5937–5959, doi:10.1029/95JB03213.
- Papanikolaou, I.D., Roberts, G.P., and Michetti, A.M., 2005, Fault scarps and deformation rates in Lazio-Abruzzo, Central Italy: Comparison between geological fault slip-rate and GPS data: *Tectonophysics*, v. 408, p. 147–176, doi:10.1016/j.tecto.2005.05.043.
- Park, J., Bazzurro, P., and Baker, J., 2007, Modeling spatial correlation of ground motion Intensity Measures for regional seismic hazard and portfolio loss estimation, *in* Kanda, Takada, and Furuta eds., *Applications of Statistics and Probability in Civil*

- Engineering, London, Taylor & Francis Group, p. 1–8.
- Parsons, T., 2008, Monte Carlo method for determining earthquake recurrence parameters from short paleoseismic catalogs: Example calculations for California: *Journal of Geophysical Research*, v. 113, p. B03302, doi:10.1029/2007JB004998.
- Peláez, J.A., Delgado, J., and López Casado, C., 2005, A preliminary probabilistic seismic hazard assessment in terms of Arias intensity in southeastern Spain: *Engineering Geology*, v. 77, p. 139–151, doi:10.1016/j.enggeo.2004.09.002.
- Peláez, J.A., and López-Casado, C., 2002, Seismic hazard estimate at the Iberian Peninsula: *Pure and Applied Geophysics*, v. 159, p. 2699–2713, doi:10.1007/s00024-002-8754-3.
- Perea, H., Alfaro, P., Iacono, C.L., Moreno, X., and Masana, E., 2012, Quaternary active tectonic structures in the offshore Bajo Segura basin (SE Iberian Peninsula – Mediterranean Sea): *Natural Hazards and Earth System Sciences*, v. 12, p. 3151–3168, doi:10.5194/nhess-12-3151-2012.
- Platt, J.P., and Vissers, R.L.M., 1989, Extensional collapse of thickened continental lithosphere: a working hypothesis for the Alboran Sea and Gibraltar arc: *Geology*, v. 17, p. 540–543, doi:10.1130/0091-7613(1989)017<0540:ECOTCL>2.3.CO;2.
- Power, M., Chiou, B., Abrahamson, N., Bozorgnia, Y., Shantz, T., and Roblee, C., 2008, An overview of the NGA project: *Earthquake Spectra*, v. 24, p. 3–21, doi:10.1193/1.2894833.
- Prescott, J.R., and Hutton, J.T., 1988, Cosmic ray and gamma ray dosimetry for TL and ESR: *International Journal of Radiation Applications and Instrumentation. Part D. Nuclear Tracks and Radiation Measurements*, v. 14, p. 223–227, doi:10.1016/1359-0189(88)90069-6.
- Quigley, M.C., Jiménez, A., Duffy, B., and King, T.R., 2019, Physical and Statistical Behavior of Multifault Earthquakes: Darfield Earthquake Case Study, New Zealand: *Journal of Geophysical Research: Solid Earth*, v. 124, p. 4788–4810, doi:10.1029/2019JB017508.
- Ramsey, C.B., and Lee, S., 2013, Recent and Planned Developments of the Program OxCal: Radiocarbon, v. 55, p. 720–730, doi:10.1017/S0033822200057878.
- Reicherter, K., and Hübscher, C., 2007, Evidence for a seafloor rupture of the Carboneras Fault Zone (southern Spain): Relation to the 1522 Almería earthquake? *Journal of Seismology*, v. 11, p. 15–26, doi:10.1007/s10950-006-9024-0.
- Reid, H.F., 1910, The California Earthquake of April 18, 1906: Volume II, *in* Report of the State Earthquake Investigation Commission, Washington, D.C., Carnegie Institution of Washington, p. 192.
- Reimer, P.J. et al., 2020, The IntCal20 Northern Hemisphere Radiocarbon Age Calibration Curve (0–55 cal kBP): *Radiocarbon*, v. 62, p. 725–757, doi:10.1017/RDC.2020.41.
- Reitman, N.G., Bennett, S.E.K., Gold, R.D., Briggs, R.W., and DuRoss, C.B., 2015, High-resolution trench photomosaics from image-based modeling: Workflow and error analysis: *Bulletin of the Seismological Society of America*, v. 105, p. 2354–2366, doi:10.1785/0120150041.

- Rick, T.C., Vellanoweth, R.L., and Erlandson, J.M., 2005, Radiocarbon dating and the “old shell” problem: direct dating of artifacts and cultural chronologies in coastal and other aquatic regions: *Journal of Archaeological Science*, v. 32, p. 1641–1648, doi:10.1016/j.jas.2005.05.005.
- Ritz, J.-F., Baize, S., Ferry, M., Larroque, C., Audin, L., Delouis, B., and Mathot, E., 2020, Surface rupture and shallow fault reactivation during the 2019 Mw 4.9 Le Teil earthquake, France: *Communications Earth & Environment*, v. 1, p. 1–11, doi:10.1038/s43247-020-0012-z.
- Rivas-Medina, A., 2014, Contribución metodológica para incorporar fallas activas en la modelización de la fuente dirigida a estimaciones de peligrosidad sísmica. Aplicación al sur de España: PhD Thesis. Universidad Politécnica de Madrid, Madrid, Spain, 245 p.
- Rivas-Medina, A., Benito, B., and Miguel Gaspar-Escribano, J., 2018, Approach for combining fault and area sources in seismic hazard assessment: Application in south-eastern Spain: *Natural Hazards and Earth System Sciences*, v. 18, p. 2809–2823, doi:10.5194/nhess-18-2809-2018.
- Roberts, G.P., 1996, Variation in fault-slip directions along active and segmented normal fault systems: *Journal of Structural Geology*, v. 18, p. 835–845, doi:10.1016/S0191-8141(96)80016-2.
- Roca, A., López Arroyo, A., and Suriñach, E., 1984, Application of the Gumbel III law to seismic data from southern Spain: *Engineering Geology*, v. 20, p. 63–71, doi:10.1016/0013-7952(84)90043-7.
- Rockwell, T.K., Ragona, D.E., Meigs, A.J., Owen, L.A., Costa, C.H., and Ahumada, E.A., 2014, Inferring a thrust-related earthquake history from secondary faulting: A long rupture record of La Laja fault, San Juan, Argentina: *Bulletin of the Seismological Society of America*, doi:10.1785/0120110080.
- Rodríguez-Cañero, R., Jabaloy-Sánchez, A., Navas-Parejo, P., and Martín-Algarra, A., 2018, Linking Palaeozoic palaeogeography of the Betic Cordillera to the Variscan Iberian Massif: new insight through the first conodonts of the Nevado-Filábride Complex: *International Journal of Earth Sciences*, v. 107, p. 1791–1806, doi:10.1007/s00531-017-1572-8.
- Rodríguez-Escudero, E., 2017, Implicaciones de la estructura interna de una zona de falla activa en la génesis de terremotos: PhD Thesis. Universidad Complutense de Madrid, Madrid, Spain, 209 p.
- Rodríguez-Escudero, E., Martínez-Díaz, J.J., Álvarez-Gómez, J.A., Insua-Arévalo, J.M., and Capote del Villar, R., 2014, Tectonic setting of the recent damaging seismic series in the Southeastern Betic Cordillera, Spain: *Bulletin of Earthquake Engineering*, v. 12, p. 1831–1854, doi:10.1007/s10518-013-9551-3.
- Rodríguez-Fernández, J., Miguel Azañón, J., and Azor, A., 2012, The Betic Intramontane Basins (SE Spain): Stratigraphy, Subsidence, and Tectonic History, *in* Busby, C. and Azor, A. eds., *Tectonics of Sedimentary Basins: Recent Advances*, Hoboken: Blackwell Publishing Ltd., p. 461–479, doi:10.1002/9781444347166.ch23.
- Roquero, E., Silva, P.G., Rodríguez-Pascua, M.A., Bardají, T., Elez, J., Carrasco-García, P., and Giner-Robles, J.L., 2019, Analysis of faulted fan surfaces and paleosols in

- the Palomares Fault Zone (Betic Cordillera, SE Spain): Paleoclimatic and paleoseismic implications: *Geomorphology*, v. 342, p. 88–102, doi:10.1016/j.geomorph.2019.06.003.
- Rosenbaum, G., Lister, G.S., and Duboz, C., 2002, Reconstruction of the tectonic evolution of the western Mediterranean since the Oligocene: *Journal of the Virtual Explorer*, v. 08, doi:10.3809/jvirtex.2002.00053.
- Ross, Z.E. et al., 2019, 2019 Ridgecrest earthquake sequence: *Science*, v. 3665, p. 346–351.
- Salditch, L., Stein, S., Neely, J., Spencer, B.D., Brooks, E.M., Agnon, A., and Liu, M., 2020, Earthquake supercycles and Long-Term Fault Memory: *Tectonophysics*, v. 774, p. 228289, doi:10.1016/j.tecto.2019.228289.
- Santamaría-López, Á., and Sanz de Galdeano, C., 2018, SHRIMP U–Pb detrital zircon dating to check subdivisions in metamorphic complexes: a case of study in the Nevado–Filábride complex (Betic Cordillera, Spain): *International Journal of Earth Sciences*, v. 107, p. 2539–2552, doi:10.1007/s00531-018-1613-y.
- Santanach, P., and Masana, E., 2001, Prospects for Paleoseismology in Spain: *Acta Geologica Hispanica*, v. 36, p. 193-196–196.
- Sanz de Galdeano, C. et al., 2019, Active Faults in Iberia, *in* *The Geology of Iberia: A Geodynamic Approach. Volume 5: Active Processes: Seismicity, Active Faulting and Relief*, Springer, v. 5, p. 126, https://doi.org/10.1007/978-3-030-11190-8_6<http://link.springer.com/10.1007/978-3-030-11190-8>.
- Schmidt, E.D., Machalett, B., Marković, S.B., Tsukamoto, S., and Frechen, M., 2010, Luminescence chronology of the upper part of the Stari Slankamen loess sequence (Vojvodina, Serbia): *Quaternary Geochronology*, v. 5, p. 137–142, doi:10.1016/j.quageo.2009.09.006.
- Scholz, C.H., 1990, *The mechanics of earthquakes and faulting*: Cambridge, United Kingdom, Cambridge University Press, doi:10.1017/9781316681473.
- Schwartz, D.P., 2018, Review: Past and future fault rupture lengths in seismic source characterization-the long and short of it: *Bulletin of the Seismological Society of America*, v. 108, p. 2493–2520, doi:10.1785/0120160110.
- Schwartz, D.P., and Coppersmith, K.J., 1984, Fault behavior and characteristic earthquakes: Examples from the Wasatch and San Andreas Fault Zones: *Journal of Geophysical Research*, v. 89, p. 5681–5698, doi:<http://dx.doi.org/10.1029/JB089iB07p05681>; doi:10.
- Scotti, O., and Peruzza, L., 2016, Fault2SHA - A European Working group to link faults and Probabilistic Seismic Hazard Assessment communities in Europe: *Geophysical Research Abstracts*, v. 18, p. 11474.
- Scotti, O., and Peruzza, L., 2017, Role of scaling laws and fault interaction. *Proceedings of the Fault2SHA - 3rd Workshop: Barcelonette, France*, 32 p.
- Sébrier, M., Ghafiri, A., and Bles, J.L., 1997, Paleoseismicity in France: Fault trench studies in a region of moderate seismicity: *Journal of Geodynamics*, v. 24, p. 207–217, doi:10.1016/s0264-3707(97)00005-7.

- Serpelloni, E., Vannucci, G., Pondrelli, S., Argnani, A., Casula, G., Anzidei, M., Baldi, P., and Gasperini, P., 2007, Kinematics of the Western Africa-Eurasia plate boundary from focal mechanisms and GPS data: *Geophysical Journal International*, v. 169, p. 1180–1200, doi:10.1111/j.1365-246X.2007.03367.x.
- Shen, Z.K., Jackson, D.D., Feng, Y.J., Cline, M., Kim, M., Fang, P., and Bock, Y., 1994, Postseismic Deformation Following the Landers Earthquake, California, 28 June 1992: *Bulletin of the Seismological Society of America*, v. 84, p. 780–791, doi:10.1029/97JB00210.
- Sieh, K., 1978a, Prehistoric large earthquakes produced by slip on the San Andreas Fault at Palmett Creek, California: *Journal of Geophysical Research*, v. 83, p. 3907, doi:10.1029/JB083iB08p03907.
- Sieh, K., 1978b, Slip along the San Andreas fault associated with the great 1857 earthquake: *Bulletin of the Seismological Society of America*, v. 68, p. 1421–1448.
- Sieh, K., and Jahns, R.H., 1984, Holocene Activity of the San Andreas Fault At Wallace Creek, California.: *Bulletin of the Geological Society of America*, v. 95, p. 883–896, doi:10.1130/0016-7606(1984)95<883:HAOTSA>2.0.CO;2.
- Sieh, K., Natawidjaja, D.H., Meltzner, A.J., Shen, C.C., Cheng, H., Li, K.S., Suwargadi, B.W., Galetzka, J., Philibosian, B., and Edwards, R.L., 2008, Earthquake supercycles inferred from sea-level changes recorded in the corals of west Sumatra: *Science*, v. 322, p. 1674–1678, doi:10.1126/science.1163589.
- Sieh, K., Stuiver, M., and Brillinger, D., 1989, A more precise chronology of earthquakes produced by the San Andreas fault in southern California: *Journal of Geophysical Research*, v. 94, p. 603–623, doi:10.1029/JB094iB01p00603.
- Silva, P.G., 1994, Evolución geodinámica de la Depresión del Guadalentín desde el Mioceno superior hasta la actualidad: neotectónica y geomorfología: PhD Thesis. Universidad Complutense de Madrid, Madrid, Spain, 642 p.
- Silva, P., 2014, Landscapes and Landforms of Spain (F. Gutiérrez & M. Gutiérrez, Eds.): Dordrecht, Springer Netherlands, *World Geomorphological Landscapes*, v. 2, 273–288 p., doi:10.1007/978-94-017-8628-7.
- Silva, P.G., Barjadí-Azcárate, T., Goy, J.L., and Zazo, C., 2004, Mapa Geomorfológico de España 1:50000. Hoja 953 (25-38): Instituto Geológico y Minero de España, Madrid, Spain.
- Silva, P.G., Goy, J.L., Somoza, L., Zazo, C., and Bardají, T., 1993, Landscape response to strike-slip faulting linked to collisional settings: Quaternary tectonics and basin formation in the Eastern Betics, southeastern Spain: *Tectonophysics*, v. 224, p. 289–303, doi:10.1016/0040-1951(93)90034-H.
- Silva, P.G., Goy, J.L., and Zazo, C., 1992a, Características estructurales y geométricas de la falla de desgarre de Lorca-Alhama: *Geogaceta*, v. 12, p. 7–10.
- Silva, P.G., Goy, J.L., Zazo, C., and Bardají, T., 2003, Fault-generated mountain fronts in southeast Spain: Geomorphologic assessment of tectonic and seismic activity: *Geomorphology*, v. 50, p. 203–225, doi:10.1016/S0169-555X(02)00215-5.
- Silva, P.G., Goy, J., Zazo, C., Lario, J., and Bardají, T., 1997, Paleoseismic indications along ‘aseismic’ fault segments in the Guadalentín depression (SE Spain): *Journal of*

- Geodynamics, v. 24, p. 105–115, doi:10.1016/S0264-3707(97)00011-2.
- Silva, P.G., Harvey, A.M., Zazo, C., and Goy, J.L., 1992b, Geomorphology, depositional style and morphometric relationships of Quaternary alluvial fans in the Guadalentin Depression (Murcia, southeast Spain): *Zeitschrift für Geomorphologie*, v. 36, p. 325–341, doi:10.1127/zfg/36/1992/325.
- Silva, P., Rodríguez-Pascua, M.A., Giner-Robles, J.L., Perez-Lopez, R., Gomez Lario, J., Perucha Atienza, M., Bardaji Azcarate, T., Huerta Hurtado, P., Roquero, E., and Bautista, M., 2014, Catálogo de los efectos geológicos de los terremotos en España: Instituto Geológico y Minero de España, Madrid, Spain, <http://igmpublicaciones.blogspot.com.es/>.
- Smedley, R.K., and Skirrow, G.K.A., 2020, Luminescence Dating in Fluvial Settings: Overcoming the Challenge of Partial Bleaching, *in* Herget, J. and Fontana, A. eds., *Palaeohydrology: Traces, Tracks and Trails of Extreme Events*, Cham, Springer International Publishing, p. 155–168, doi:10.1007/978-3-030-23315-0_8.
- Sohbati, R., Murray, A.S., Buylaert, J.-P., Ortuño, M., Cunha, P.P., and Masana, E., 2012, Luminescence dating of Pleistocene alluvial sediments affected by the Alhama de Murcia fault (eastern Betics, Spain) - a comparison between OSL, IRSL and post-IRIRSL ages: *Boreas*, v. 41, p. 250–262, doi:10.1111/j.1502-3885.2011.00230.x.
- Sornette, D., and Knopoff, L., 1997, The paradox of the expected time until the next earthquake: *Bulletin of the Seismological Society of America*, v. 87, p. 789–798.
- Spakman, W., and Wortel, R., 2004, A Tomographic View on Western Mediterranean Geodynamics, *in* The TRANSMED Atlas. The Mediterranean Region from Crust to Mantle, Berlin, Heidelberg, Springer Berlin Heidelberg, p. 31–52, doi:10.1007/978-3-642-18919-7_2.
- Stein, R.S., King, G.C.P., and Lin, J., 1994, Stress triggering of the 1994 M = 6.7 Northridge, California, Earthquake by its predecessors: *Science*, v. 265, p. 1432–1435, doi:10.1126/science.265.5177.1432.
- Stein, R.S., and Lisowski, M., 1983, The 1979 Homestead Valley Earthquake Sequence, California: Control of aftershocks and postseismic deformation: *Journal of Geophysical Research: Solid Earth*, v. 88, p. 6477–6490.
- Stich, D., Martín, J.B., and Morales, J., 2007, Deformación sísmica y asísmica en la zona Béticas-Rif-Alborán: *Revista de la Sociedad Geológica de España*, v. 20, p. 311–320.
- Stich, D., Martín, R., and Morales, J., 2010, Moment tensor inversion for Iberia-Maghreb earthquakes 2005-2008: *Tectonophysics*, v. 483, p. 390–398, doi:10.1016/j.tecto.2009.11.006.
- Stirling, M. et al., 2012, National seismic hazard model for New Zealand: 2010 update: *Bulletin of the Seismological Society of America*, v. 102, p. 1514–1542, doi:10.1785/0120110170.
- Stirling, M., and Gerstenberger, M., 2018, Applicability of the Gutenberg-Richter relation for major active faults in New Zealand: *Bulletin of the Seismological Society of America*, v. 108, p. 718–728, doi:10.1785/0120160257.
- Stirling, M., Goded, T., Berryman, K., and Litchfield, N., 2013, Selection of earthquake

- scaling relationships for seismic-hazard analysis: *Bulletin of the Seismological Society of America*, v. 103, p. 2993–3011, doi:10.1785/0120130052.
- Stuiver, M., and Polach, H.A., 1977, Discussion Reporting of 14 C Data: *Radiocarbon*, v. 19, p. 355–363, doi:10.1017/S0033822200003672.
- Sylvester, A.G., 1988, Strike-slip faults: *Geological Society of America*, v. 100, p. 1666–1703.
- Taylor, R.E., 1997, Radiocarbon Dating, *in* *Chronometric Dating in Archaeology*, Boston, MA, Springer US, p. 65–96, doi:10.1007/978-1-4757-9694-0_3.
- Toda, S., and Stein, R.S., 2020, Long- and Short-Term Stress Interaction of the 2019 Ridgecrest Sequence and Coulomb-Based Earthquake Forecasts: *Bulletin of the Seismological Society of America*, v. 110, p. 1765–1780, doi:10.1785/0120200169.
- Twiss, R., and Moores, W.H., 1992, *Structural Geology*: San Francisco, United States, Freeman & Co., 532 p., doi:10.1002/gj.3350290408.
- UNDRO, 1979, *Natural Disasters and Vulnerability Analysis. Report of Expert Group Meeting*: United Nations.
- Valentini, A., 2021, Allowing multi-fault earthquakes and relaxing fault segmentation in central Apennines (Italy): hints for fault-based PSHA: *Bollettino di Geofisica Teorica ed Applicata*, v. 62, p. 1–22, doi:10.4430/bgta0339.
- Verdecchia, A., Pace, B., Visini, F., Scotti, O., Peruzza, L., and Benedetti, L., 2018, The Role of Viscoelastic Stress Transfer in Long-Term Earthquake Cascades: Insights After the Central Italy 2016–2017 Seismic Sequence: *Tectonics*, v. 37, p. 3411–3428, doi:doi:10.1029/2018TC005110.
- Vergés, J., and Fernández, M., 2012, Tethys–Atlantic interaction along the Iberia–Africa plate boundary: The Betic–Rif orogenic system: *Tectonophysics*, v. 579, p. 144–172, doi:10.1016/j.tecto.2012.08.032.
- Vergés, J., Marzo, M., and Muñoz, J.A., 2002, Growth strata in foreland settings: *Sedimentary Geology*, v. 146, p. 1–9, doi:10.1016/S0037-0738(01)00162-2.
- Vilanova, S.P., and Fonseca, J.F.B.D., 2007, Probabilistic seismic-hazard assessment for Portugal: *Bulletin of the Seismological Society of America*, v. 97, p. 1702–1717, doi:10.1785/0120050198.
- Villani, F., Pucci, S., Civico, R., De Martini, P.M., Cinti, F.R., and Pantosti, D., 2018, Surface Faulting of the 30 October 2016 Mw 6.5 Central Italy Earthquake: Detailed Analysis of a Complex Coseismic Rupture: *Tectonics*, v. 37, p. 3378–3410, doi:10.1029/2018TC005175.
- Wallace, R., 1990, *The San Andreas Fault System, California*. USGS professional paper, 1515: USGS Professional paper, 1515.
- Wechsler, N., Rockwell, T.K., and Klinger, Y., 2018, Variable slip-rate and slip-per-event on a plate boundary fault: The Dead Sea fault in northern Israel: *Tectonophysics*, v. 722, p. 210–226, doi:10.1016/j.tecto.2017.10.017.
- Wei, S. et al., 2011, Superficial simplicity of the 2010 El Mayor-Cucapah earthquake of Baja California in Mexico: *Nature Geoscience*, v. 4, p. 615–618, doi:10.1038/ngeo1213.

- Weldon, R.J., and Sieh, K., 1985, Holocene rate of slip and tentative recurrence interval for large earthquakes on the San Andreas fault, Cajon Pass, southern California: *Geological Society of America Bulletin*, v. 96, p. 793–812, doi:10.1130/0016-7606(1985)96<793>
- Wells, D.L., and Coppersmith, K.J., 1994, New empirical relationships among magnitude, rupture length, rupture width, rupture area, and surface displacement: *Bulletin of the Seismological Society of America*, v. 84, p. 974–1002, <https://dx.doi.org/>.
- Wesnousky, S.G., 2008, Displacement and geometrical characteristics of earthquake surface ruptures: Issues and implications for seismic-hazard analysis and the process of earthquake rupture: *Bulletin of the Seismological Society of America*, v. 98, p. 1609–1632, doi:10.1785/0120070111.
- Wesnousky, S.G., 1986, Earthquakes, Quaternary Faults, and Seismic Hazard in California: *Journal of Geophysical Research*, v. 91, p. 12,587–12,631, doi:10.1029/JB091iB12p12587.
- Wesnousky, S.G., 1994, The Gutenberg-Richter or characteristic earthquake distribution, which is it? *Bulletin - Seismological Society of America*, v. 84, p. 1940–1959, doi:10.1016/0148-9062(95)99040-5.
- Wesson, R.L., Helly, E.J., Lajoie, K.R., and Wentworth, C.M., 1975, Faults and future earthquakes, in Borchardt, R.D. ed., *Studies for Seismic Hazard Zonation of the San Francisco Bay Region*, USGS professional paper 941A, p. 5–30.
- WHO, 2021, Earthquakes: World Health Organization, https://www.who.int/health-topics/earthquakes#tab=tab_1 (accessed April 2021).
- Woessner, J. et al., 2015, The 2013 European Seismic Hazard Model: key components and results: *Bulletin of Earthquake Engineering*, v. 13, p. 3553–3596, doi:10.1007/s10518-015-9795-1.
- Working Group On California Earthquake Probabilities, 2003, *Earthquake Probabilities in the San Francisco Bay Region : 2002-2031*: USGS Open-File Report 03-214, 235 p.
- Yeats, R.S., Sieh, K., and Clarence, R.A., 1997, *The geology of earthquakes*: New York.
- Youngs, R.R., and Coppersmith, K.J., 1985, Implications of fault slip rates and earthquake recurrence models to probabilistic seismic hazard estimates: *Bulletin of the Seismological Society of America*, v. 75, p. 939–964, doi:10.1016/0148-9062(86)90651-0.
- Yu, Y., and Gao, M., 2001, Effects of the hanging wall and footwall on peak acceleration during the Jiji (Chi-Chi), Taiwan Province, earthquake: *Acta Seismologica Sinica*, v. 14, p. 654–659, doi:10.1007/BF02718076.
- Zechar, J.D., and Frankel, K.L., 2009, Incorporating and reporting uncertainties in fault slip rates: *Journal of Geophysical Research: Solid Earth*, v. 114, p. 1–9, doi:10.1029/2009JB006325.
- Zhang, H., Chen, J., and Ge, Z., 2012, Multi-fault rupture and successive triggering during the 2012 Mw 8.6 Sumatra offshore earthquake: *Geophysical Research Letters*, v. 39, p. 6–11, doi:10.1029/2012GL053805.

Zimmerman, D.W., 1971, THERMOLUMINESCENT DATING USING FINE GRAINS FROM POTTERY: *Archaeometry*, v. 13, p. 29–52, doi:10.1111/j.1475-4754.1971.tb00028.x.

ANNEXES

ANNEX I

Publications in SCI Journals

Gómez-Novell, O., Chartier, T., García-Mayordomo, J., Ortuño, M., Masana, E., Insua-Arévalo, J.M., and Scotti, O., 2020a, Modelling earthquake rupture rates in fault systems for seismic hazard assessment: the Eastern Betics Shear Zone: *Engineering Geology*, v. 265, doi:10.1016/j.enggeo.2019.105452. ***Upon request to author.**

Gómez-Novell, O., García-Mayordomo, J., Ortuño, M., Masana, E., and Chartier, T., 2020b, Fault System-Based Probabilistic Seismic Hazard Assessment of a Moderate Seismicity Region: The Eastern Betics Shear Zone (SE Spain): *Frontiers in Earth Science*, v. 8, doi:10.3389/feart.2020.579398.



Fault System-Based Probabilistic Seismic Hazard Assessment of a Moderate Seismicity Region: The Eastern Betics Shear Zone (SE Spain)

Octavi Gómez-Novell^{1*}, Julián García-Mayordomo², María Ortuño¹, Eulàlia Masana¹ and Thomas Chartier³

¹RISKINAT Group, Geomodels Research Institute, Departament de Dinàmica de La Terra I de L'Oceà, Facultat de Ciències de La Terra, Universitat de Barcelona, Barcelona, Spain, ²Departamento de Riesgos Geológicos, Instituto Geológico y Minero de España, Tres Cantos, Spain, ³Hazard Team, Global Earthquake Model Foundation, Pavia, Italy

OPEN ACCESS

Edited by:

Jorge Miguel Gaspar-Escribano,
Polytechnic University of Madrid,
Spain

Reviewed by:

Chong Xu,
National Institute of Natural Hazards,
China

Sergio Molina-Palacios,
University of Alicante, Spain

*Correspondence:

Octavi Gómez-Novell
octgomez@ub.edu

Specialty section:

This article was submitted to
Geohazards and Georisks,
a section of the journal
Frontiers in Earth Science

Received: 02 July 2020

Accepted: 27 October 2020

Published: 09 December 2020

Citation:

Gómez-Novell O,
García-Mayordomo J, Ortuño M,
Masana E and Chartier T (2020) Fault
System-Based Probabilistic Seismic
Hazard Assessment of a Moderate
Seismicity Region: The Eastern Betics
Shear Zone (SE Spain).
Front. Earth Sci. 8:579398.
doi: 10.3389/feart.2020.579398

Including faults as seismogenic sources in probabilistic seismic hazard assessments (PSHA) has turned into a common practice as knowledge of active faults is improving. Moreover, the occurrence of earthquakes in multi-fault ruptures has evidenced the need to understand faults as interacting systems rather than independent sources. We present a PSHA for the Southeastern Spain obtained by including the faults of a moderate seismicity region, the Eastern Betics Shear Zone (EBSZ) in SE Spain, as the main seismogenic sources in two separate source models, one considering background seismicity. In contrast with previous studies in Spain, earthquake occurrence of the EBSZ system is modeled considering different hypotheses of multi-fault ruptures at the whole fault system scale and weighted in a logic tree. We compare the hazard levels with those from an area source PSHA and a previous fault-based approach. The results show a clear control of the EBSZ faults in the seismic hazard for all return periods, increasing drastically the hazard levels in the regions close to the fault traces and influencing up to 20 km farther with respect to the area source PSHA. The seismic hazard is dependent on the fault slip rates as peak ground accelerations and territorial extension of the fault influence appear higher around the Alhama de Murcia and Carboneras faults, while lower slip rate faults (Palomares Fault) show minor contribution to the hazard. For the return period of 475 years and near-fault locations, our models are more consistent with the ground motion values reached in the 2011 Mw 5.2 Lorca event than the building code or national seismic hazard map, which suggest that our fault system-based model performs more accurate estimations for this return period. Fault data, mainly slip rates, and its uncertainties have a clear impact on the seismic hazard and, for some faults, the lack of detailed paleoseismic studies can compromise the reliability of the hazard estimations. This, together with epistemic uncertainties concerning the background seismicity, are key discussion points in the present study, having an impact on further research and aiming to serve as a case example for other low-to-moderate seismicity regions worldwide.

Keywords: seismic hazard assessment, source modelling, fault system, peak ground acceleration, near-fault, moderate magnitude earthquakes, paleoseismology, Eastern Betics Shear Zone

INTRODUCTION

The use of geological data in probabilistic seismic hazard assessment (PSHA) has become increasingly important, since seismic catalogs do not usually extend for more than a few centuries. This is a very short time window for characterizing the occurrence of major events in regions of moderate seismic activity, even in areas where the catalogs extend for more than 1,000 years such as SE Spain or Portugal (García-Mayordomo, 2005; Vilanova and Fonseca, 2007, respectively). Traditionally, geological data and fault data have been used to characterize the occurrence of major, maximum or characteristic events (Wesnousky, 1986; Schwartz and Coppersmith, 1984). Maximum events usually have a very low impact in seismic hazard for the return periods considered in conventional building (e.g., 475 years) and so this type of fault-based PSHA has been regarded in studies interested in long return periods (e.g., critical infrastructures). However, there is increasing awareness of the fact that low-to-moderate magnitude events (Mw 4.0–6.0) are also able to produce significant damage, especially at sites located on top or very close to fault sources (e.g., 2011 Mw 5.2 Lorca earthquake in SE Spain; Alguacil et al., 2014). In this context, the identification and characterization of active faults as seismogenic sources able to produce all the range of earthquake magnitudes become critical tasks in the PSHA of moderate active regions.

For this reason, in accordance with the increasing availability and refinement of paleoseismic and geological studies, the incorporation of fault data in PSHA has become an important part of the source modeling aiming to estimate earthquake activity beyond the coverage of seismic catalogs. The use of faults in PSHA is a well-established practice worldwide (Frankel, 1995; WGCEP, 2003; Stirling et al., 2012; Woessner et al., 2015). In most of these cases, faults are modeled as independent sources following a characteristic earthquake model (Youngs and Coppersmith, 1985; Wesnousky, 1986) or a Gutenberg-Richter distribution (Gutenberg and Richter, 1945; Bungum, 2007).

During earthquakes, faults can rupture in very complex configurations involving several structures simultaneously and even with contrasting kinematics or geometries. Earthquakes such as the 2010 Mw 7.2 Cucapah (Fletcher et al., 2014), the 2012 Mw 8.6 Sumatra (Zhang et al., 2012) or the 2016 Mw 7.8 Kaikoura (Little et al., 2018) are good examples. Accordingly, in the recent years seismic hazard modelers and practitioners have developed new approaches for modeling faults as complex and interacting sources in seismic hazard. Including this complexity has demonstrated to be a turning point to model fault processes in PSHA. Approaches like UCERF-3 (Field et al., 2014) or the recent SHERIFS (Chartier et al., 2019) are emerging methodologies whose principle is modeling earthquake occurrence considering scenarios of multi-fault ruptures for source characterization in PSHA. In both cases fault rupturing is treated as an aleatory variable, whose occurrence is assumed to be linked to the randomness of the seismic process.

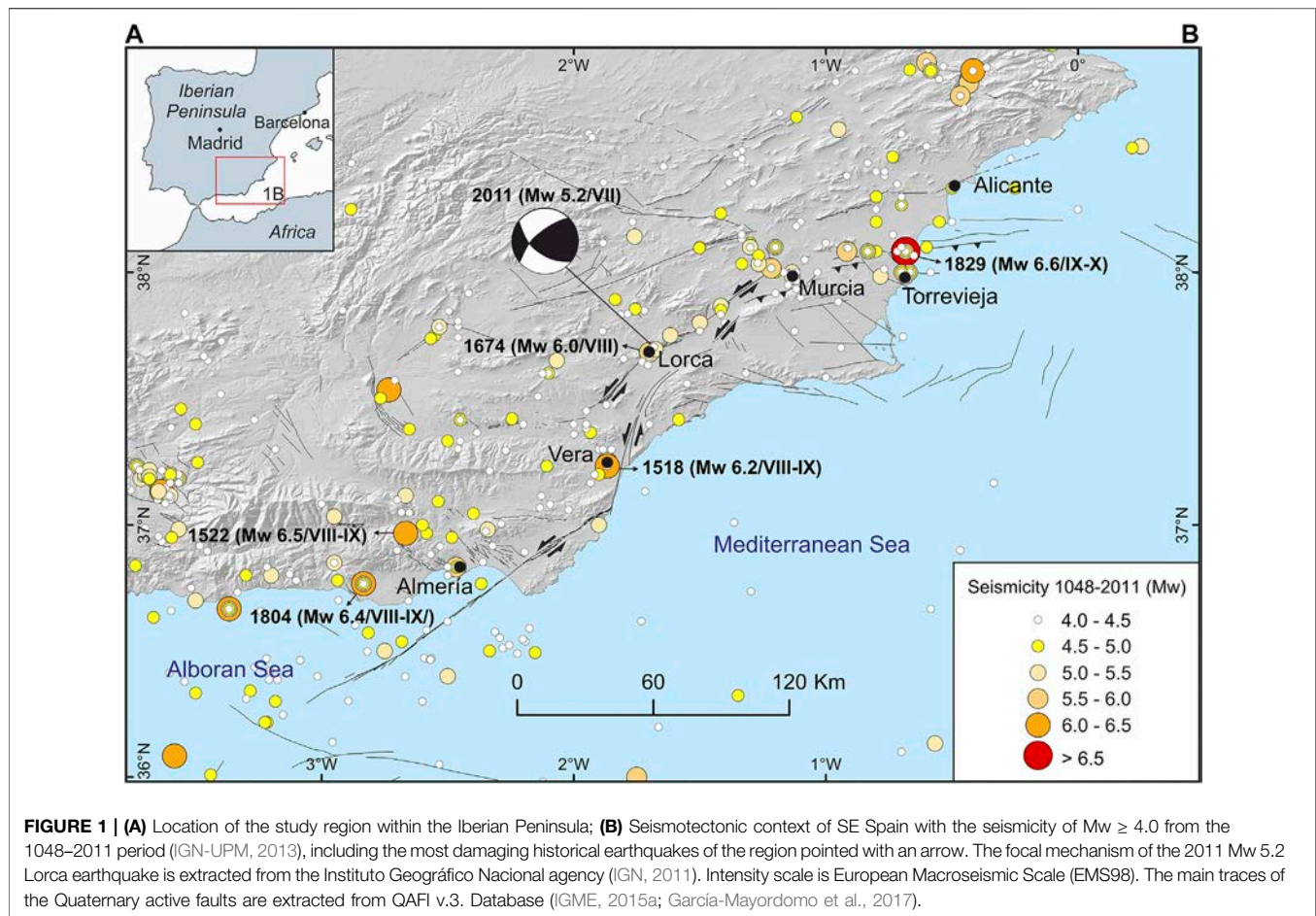
Most fault-based PSHA approaches are usually carried out in high seismicity regions with advanced paleoseismic fault knowledge to perform such studies (e.g., Stirling et al., 2012;

Field et al., 2014 for New Zealand and California, respectively). Conversely, the scarcity of paleoseismic and geological slip rate data on faults has been one of the major challenges faced by PSHA analysts in low-to-moderate seismicity regions, such as Western Europe (e.g., Spain). In Spain, PSHA has been classically modeled using area sources following Cornell (1968) and McGuire (1976) methodology, as it is the case of the latest national seismic hazard map (IGN-UPM, 2013). In that work, fault information has been included as a complementary criterion for defining area sources and, particularly, the fault length, which is used to set the upper bound of the magnitude-frequency distribution in each one. In this map, faults have not been included as seismogenic sources in the calculations due to the incompleteness of the fault data across the country. However, that is not the case of SE Spain, the most seismically active area in the country (García-Mayordomo et al., 2007) and where one of the longest active fault systems is located: the Eastern Betics Shear Zone (EBSZ).

The EBSZ is a ~400 km long transpressive tectonic corridor of mainly reverse and left-lateral strike-slip kinematics with a characteristic NE-SW sigmoidal trend (Bousquet, 1979; De Larouzière et al., 1988; Silva et al., 1993) (Figure 1B). It absorbs most part of the NW-SE convergence from the Eurasian and Nubian plates in Iberia (4–6 mm/yr; DeMets et al., 2015). Although it is a moderate seismicity region with rates lower than other European regions (e.g., Italy or Greece), many destructive earthquakes with intensities up to IX-X (I_{EMS98}) have affected this region since historical times (e.g., 1518 VIII-IX Vera, 1522 VIII-IX Almería, 1674 VIII Lorca, 1804 VIII-IX Dalías-Berja, 1829 IX-X Torrevieja; Silva et al., 2014) (Figure 1B). More recently, moderate magnitude earthquakes have taken place (e.g., 1993–1994 Adra seismic series; the 1999 Mw 4.8 Mula, 2002 Mw 5.0 Bullas; the 2005 Mw 4.8 La Paca seismic series; Rodríguez-Escudero et al., 2014), including the damaging 2011 Mw 5.2 Lorca earthquake (e.g., Martínez-Díaz et al., 2012a).

Over the last two decades, the EBSZ tectonic context has motivated many geological, geodetic and paleoseismic studies, especially since the 2011 Lorca earthquake (e.g., Moreno, 2011; Ortuño et al., 2012; Echeverría et al., 2013; Insua-Arévalo et al., 2015; Martín-Banda et al., 2015; Ferrater, 2016; Martínez-Díaz et al., 2018; Masana et al., 2018). Accordingly, PSHA studies focused here have successfully incorporated faults as independent sources either considering a characteristic earthquake or Gutenberg-Richter model (García-Mayordomo, 2005; García-Mayordomo et al., 2007; Rivas-Medina et al., 2018). However, no PSHA study has yet modeled fault sources from the perspective of multi-fault ruptures, so the present constitutes the first one in this matter. The incorporation of this variable representing fault behaviors widely observed in nature is seen as a step toward more realistic approximations of fault modeling and seismic hazard in the EBSZ.

The aim of our paper is to explore a fault-based PSHA in a moderate seismicity region as it is the EBSZ in SE Spain, using a state-of-the-art fault source modeling approach that implements fault data as inputs, considers multi-fault rupture possibilities at the whole fault system scale and treats them as aleatory



uncertainty. We use the source models computed and published in a previous article (Gómez-Novell et al., 2020). There, an emergent methodology (SHERIFS; Chartier et al., 2019) is applied to perform a source modeling of the EBSZ by computing magnitude-frequency distributions (MFDs) at the scale of the whole EBSZ fault system considering different scenarios of fault ruptures. The adequacy of the models is evaluated and ranked in terms of their agreement with the regional seismic catalog and paleoseismic data. For the present study, we adapt and re-compute these models, weight them in a logic tree and use them as inputs for the hazard calculations. We compute seismic hazard using the OpenQuake engine (Pagani et al., 2014), evaluate the influence of the selected fault source models on the seismic hazard and compare them with previous PSHA approaches in SE Spain. We also place the interest of our study for other low-to-moderate seismicity regions worldwide.

GEOLOGICAL SETTING

The EBSZ is a main active fault system in SE Spain. The faults affect Quaternary sedimentary deposits and generate geomorphological and morphotectonic features (e.g., fluvial channel offsets, fault scarps) along a left-lateral transpressive

corridor, evidencing tectonic activity during the recent Quaternary (De Larouzière et al., 1988; Silva et al., 1993). The onset of the neotectonic activity under the nowadays compressional transpressive regime in the Eastern Betics occurred during the Late Miocene (e.g., Rodríguez-Fernández et al., 2012). From SW to NE these faults are (Figure 2A): Carboneras Fault (CF), Palomares Fault (PF), Alhama de Murcia Fault (AMF), Los Tollos Fault (LTF), Carrascoy Fault (CAF) and Bajo Segura Fault (BSF) (Bousquet, 1979; Silva et al., 1993). Characterizing the role and activity degree of these faults during the Quaternary has been the aim of many geomorphological, paleoseismic and geodetic studies in the last two decades, making the EBSZ one of the most studied fault systems in the Iberian Peninsula so far.

The EBSZ is one of the most seismically active regions of the Western Mediterranean and it has hosted many damaging earthquakes since the historical period. Most damaging earthquakes in the area have been attributed to the main faults forming the EBSZ. Important examples are the 1518 Vera earthquake, attributed to PF (e.g., García-Mayordomo, 2005), the 1522 Almería earthquake to CF (e.g., Reicherter and Hübscher, 2007), the 1674 Lorca earthquake to AMF (Martínez-Díaz et al., 2018), the 1829 Torrevieja earthquake to BSF (e.g., Alfaro et al., 2012) or, in recent times, the 2011 Lorca

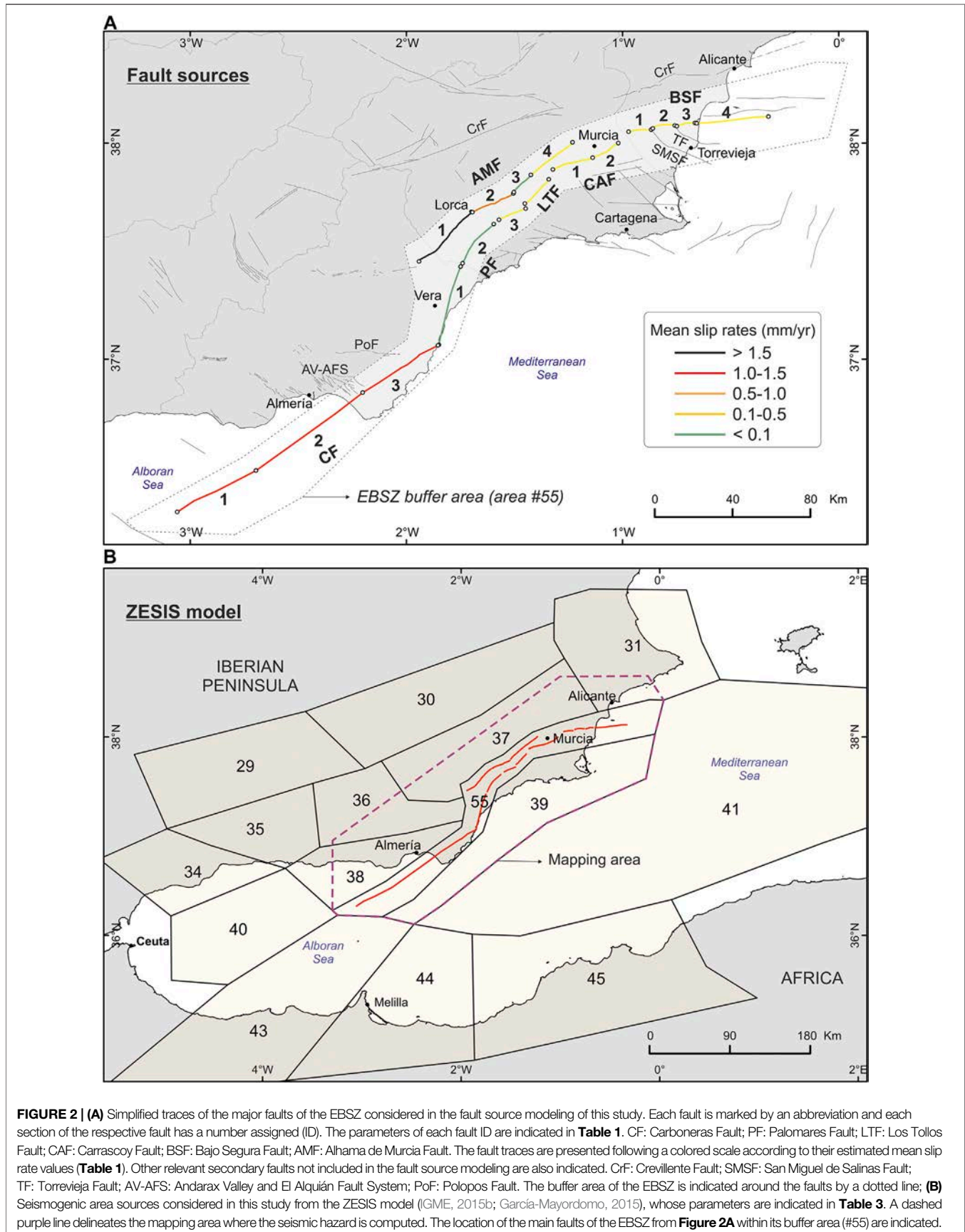


FIGURE 2 | (A) Simplified traces of the major faults of the EBSZ considered in the fault source modeling of this study. Each fault is marked by an abbreviation and each section of the respective fault has a number assigned (ID). The parameters of each fault ID are indicated in **Table 1**. CF: Carboneras Fault; PF: Palomares Fault; LTF: Los Tollos Fault; CAF: Carrascoy Fault; BSF: Bajo Segura Fault; AMF: Alhama de Murcia Fault. The fault traces are presented following a colored scale according to their estimated mean slip rate values (**Table 1**). Other relevant secondary faults not included in the fault source modeling are also indicated. CrF: Crevillente Fault; SMSF: San Miguel de Salinas Fault; TF: Torrevieja Fault; AV-AFS: Andarax Valley and El Alquían Fault System; PoF: Polopos Fault. The buffer area of the EBSZ is indicated around the faults by a dotted line; **(B)** Seismogenic area sources considered in this study from the ZESIS model (IGME, 2015b; García-Mayordomo, 2015), whose parameters are indicated in **Table 3**. A dashed purple line delineates the mapping area where the seismic hazard is computed. The location of the main faults of the EBSZ from **Figure 2A** within its buffer area (#55) are indicated.

earthquake to AMF (Martínez-Díaz et al., 2012a) (Figure 1B). Some of these historical earthquakes are known to have ruptured the surface, as recently unveiled for the 1674 Lorca earthquake (Martínez-Díaz et al., 2018). Importantly, most of the instrumental seismicity in the EBSZ occurs relatively at shallow depths and focal mechanisms are consistent with the strike-slip and reverse character of the main faults (Stich et al., 2007, Stich et al., 2010).

Paleoseismic trenching and detailed geomorphological studies have demonstrated the capability of the system to generate large magnitude earthquakes ($M_w > 6.0$) and allowed to constrain critical seismic parameters (slip rate) in several of the main faults: AMF, CF, CAF or LTF (Table 1). The slip rate ranges between 1.0 and 1.7 mm/yr for AMF, according to estimates from Ferrater et al. 2017; 1.0 and 1.3 mm/yr for CF (Moreno, 2011); 0.37 ± 0.08 mm/yr for CAF (Martín-Banda et al., 2015) and 0.12–0.17 mm/yr for LTF (Insua-Arévalo et al., 2015). Conversely, PF, BSF and the northern termination of AMF have not been studied using detailed paleoseismic trenching analysis and their slip rate estimations are based mainly on long-term displacements of geological markers (e.g., Herrero-Barbero et al., 2020), which may be affected by larger uncertainties.

Continued tectonic activity in the EBSZ is also inferred from the current geodetic data. The obtained velocities of AMF-PF combined (1.5 ± 0.3 ; Echeverría et al., 2013) are consistent with the paleoseismic and geomorphologic slip rates of AMF, suggesting a main role of this fault into the deformation. Similarly, geodetic velocities of CF are in agreement with its geological slip rates (1.3 ± 0.2 mm/yr; Echeverría et al., 2015). In the NE end of the EBSZ GPS data indicates a partitioning of the deformation into lateral and reverse components, and compatibility with the kinematics of CAF and BSF, respectively (Borque et al., 2019).

DATA AND METHODS FOR THE HAZARD ASSESSMENT

Source Modeling

In this work, we consider two types of seismogenic sources that are combined: faults and area sources (Figure 2). Fault sources are modeled within the EBSZ and area sources are modeled outside of it. The resulting composite source models are not a classical hybrid approach where faults accommodate earthquakes from a cutoff magnitude and area sources accommodate background seismicity (e.g., García-Mayordomo et al., 2007); instead, in our models both fault and area sources are modeled following a Gutenberg-Richter (GR) MFD for all the magnitude range ($M_w \geq 4.0$), as we explain in the following sections.

Fault Sources

Fault sources are modeled exclusively for the EBSZ. The source modeling performed is based on the SHERIFS methodology as published in Gómez-Novell et al., 2020, where the first step of a source modeling for PSHA is performed at the EBSZ: the feasibility of multi-fault rupture scenarios is analyzed and

earthquake occurrence on faults is modeled at the whole fault system scale following a GR distribution.

SHERIFS (Chartier et al., 2019) is a method of fault source modeling that uses geological fault data as inputs to calculate fault earthquake rates. Among its advantages, 1) it allows to model earthquake occurrence in fault systems as a whole and considering sets of multi-fault ruptures; 2) is well adapted for regions, such as the EBSZ, where geological data is the prime source of information for characterizing faults. In this sense, SHERIFS requires: i) a 3D geometry of the fault system, ii) slip rate of each fault source, iii) a target shape MFD of the fault system (e.g., GR) which is based on published studies or seismic databases and iv) a scaling relationship to estimate the upper bound of the MFD distribution (M_{max}). The slip rate of each fault is treated as a budget and it is consumed following an iterative process to fit the target MFD, in which the different rupture scenarios are computed separately until the budget of the limiting faults is exhausted. The resulting MFDs are representative of the whole fault system and are weighted in a logic tree according to their consistency with data from the regional seismic catalog and paleoseismic studies (see Gómez-Novell et al., 2020 for details on how SHERIFS is applied to compute and weight the fault system MFDs).

Only the faults of the EBSZ have been considered for the SHERIFS modeling, because they are the ones absorbing most of the plate convergence motion in SE Spain (Bousquet, 1979; Silva et al., 1993) and because they show the best geological and paleoseismic data available in the region for seismogenic source modeling. The main fault sources are shown in Figure 2A. Faults outside of the EBSZ or secondary faults have not been considered mainly due to lack of enough quality data (e.g., Crevillente Fault, Torrevieja Fault, San Miguel de Salinas Fault, El Andarax Valley Fault, El Alquíán Fault System, among others; Figure 2A).

For the fault source modeling we adopted the fault data and characteristics used in Gómez-Novell et al., 2020, obtained from available and mainly published data. Faults are sectioned (Figure 2A) according to segmentation in literature based on their geometry, geomorphic expression, seismicity, kinematics and activity evidence. Offshore segmentation of CF is adopted from Moreno (2011), onshore CF and PF from García-Mayordomo, 2005. Segmentation of CAF is based on Martín-Banda et al., 2015, BSF on Alfaro et al., 2012 and AMF on Martínez-Díaz et al., 2012b. These sections are then linked to create multi-fault rupture scenarios of the different fault rupture hypothesis explored in this study (see Table 2). Fault traces are simplified with respect to the ones depicted in the Quaternary Active Faults database of Iberia (QAFI v.3) (IGME, 2015a; García-Mayordomo et al., 2017) for the purposes of this study and multi-branch sections are simplified to a single one. This is consistent with studies that suggest that fault traces likely link at depth (e.g., CF: Moreno, 2011; AMF: Martínez-Díaz et al., 2012b). Dip, kinematics and seismogenic depths (Table 1) are extracted from the QAFI database, which compiles data from published studies on these faults. Fault slip rates are directly extracted from published works and, in selected cases, from unpublished data or expert opinion, as specified in Table 1 (see also the Appendix in

TABLE 1 | Fault input data used to calculate the earthquake rates of the EBSZ fault system with the SHERIFS approach in the fault source modeling. The sources of information and references from where fault slip rate data are extracted are specified (see details in Gómez-Novell et al., 2020). Other fault parameters are extracted from the QAFI v.3. Database (IGME, 2015a; García-Mayordomo et al., 2017). See the map in **Figure 2A** for the location of each fault section mentioned in the table. Adapted from Gómez-Novell et al., 2020.

Fault name	Fault section ID	Dip (°)	Main kinematics	Seismogenic depth range (km)	Fault length (km)	Net slip rate (mm/yr)			Type of information used to infer slip rate (references) and time frame covered
						Min	Mean	Max	
Carboneras (CF)	CF-1	90	Strike-slip	0–11	39.1	1.1	1.2	1.3	Displaced fluvial channels, trench offsets and GPS data (Moreno, 2011; Echeverria et al., 2015); since Pliocene–Holocene
	CF-2	90	Strike-slip	0–11	59.6	1.1	1.2	1.3	
	CF-3	90	Strike-slip	0–11	39.5	1.1	1.2	1.3	
Palomares (PF)	PF-1	90	Strike-slip	0–8	41.1	0.01	0.04	0.08	Tectonic uplift of terraces and alluvial fans (García-Mayordomo, 2005 and references); since Lower-Middle Pleistocene
	PF-2	90	Strike-slip	0–8	24.0	0.01	0.04	0.08	
	PF-3	90	Strike-slip	0–8	12.0	0.04	0.1	0.16	
Los Tollos (LTF)	LTF	85	Strike-slip	0–8	16.0	0.06	0.16	0.25	Recurrence intervals in paleoseismic trenches (Insua-Arévalo et al., 2015); since 12 kyr
Carrascoy (CAF)	CAF-1	70	Reverse	0–12	18.2	0.29	0.37	0.45	Restoration of deformed units, consistent with offsets in trenches (Martín-Banda et al., 2015); since 209.1 kyr
	CAF-2	85	Strike-slip	0–12	13.1	0.48	0.53	0.58	
Bajo Segura (BSF)	BSF-1	60	Reverse	1.0–12	11.6	0.25	0.33	0.41	Tectonic uplift (Alfaro et al., 2012); since 2–3 kyr
	BSF-2	60	Reverse	1.0–12	9.2	0.25	0.33	0.41	
	BSF-3	60	Reverse	1.0–12	7.7	0.12	0.2	0.3	
	BSF-4	60	Reverse	1.0–12	29.3	0.12	0.2	0.3	
Alhama de Murcia (AMF)	AMF-1	70	Strike-slip	0–12	34.1	1.6	1.65	1.7	Displaced fluvial channels (Ferrater, 2016; Ferrater et al., 2017); since 200 kyr for AMF-1, 30 kyr for AMF-2
	AMF-2	70	Strike-slip	0–12	19.7	0.8	1.0	1.2	
	AMF-3	70	Strike-slip	0–12	11.3	0.01	0.07	0.1	Based on expert opinion from QAFI database (IGME, 2015a)
	AMF-4	45	Strike-slip	0–12	23.9	0.07	0.2	0.37	Tectonic uplift (Herrero-Barbero, 2016); since late Miocene-Pliocene

TABLE 2 | Fault sections involved in the maximum fault and multi-fault ruptures envisaged in each hypothesis of the fault source modeling. See **Figure 2A** for the location of the mentioned fault sections. The maximum magnitude ranges of each hypothesis of the FM and FM_bg models are indicated. These ranges result from the random sampling of different fault ruptures allowed within a same hypothesis by the SHERIFS methodology.

Hypothesis/fault rupture scenario	Maximum expected multi-fault ruptures	Maximum magnitude range (Mw)
1	Only single fault section ruptures are allowed	6.6–7.3
2	–CF–1 + CF–2 + CF–3 –PF–1 + PF–2 + PF–3 –LTF –CAF–1 + CAF–2 –BSF–1 + BSF–2 + BSF–3 + BSF–4 –AMF–1 + AMF–2 + AMF–3 + AMF–4	6.7–7.5
3	–CF–1 + CF–2 + CF–3 + PF–1 + PF–2 + PF–3 –LTF + CAF–1 + CAF–2 + BSF–1 + BSF–2 + BSF–3 + BSF–4 –AMF–1 + AMF–2 + AMF–3 + AMF–4	6.9–7.7
4	–CF–1 + CF–2 + CF–3 + PF–1 + PF–2 + PF–3 + LTF + CAF–1 + CAF–2 + BSF–1 + BSF–2 + BSF–3 + BSF–4 –AMF–1 + AMF–2 + AMF–3 + AMF–4	7.1–7.8

Gómez-Novell et al., 2020 for specific details on the criteria followed for slip rate selection, especially for unpublished work).

The fault-system source model considered is spatially constrained to the limits of area source #55 of the ZESIS national scale area source model (García-Mayordomo, 2015), available at the ZESIS database (IGME, 2015b), which was delineated as the envelope of the surface projection of the EBSZ fault planes and characterized by the seismic record within (IGN-UPM, 2013). In this present approach, earthquake occurrence in this area (hereinafter called EBSZ buffer area) is completely modeled on faults from the geological fault data shown in Table 1. However, we also consider the alternative possibility that a small portion of the seismic moment release in the EBSZ is due to unknown faults (e.g., blind, unmapped) different from the considered ones, by modeling background seismicity in one of our models. Although the EBSZ buffer area is a narrow area constrained to the surface projection of well-known faults, it cannot be precluded that some activity may occur on unknown active faults not considered in this study (section 3.1.1.2).

Therefore, two alternative fault source models are envisaged within the EBSZ buffer area, one exclusively considering the faults' activity (FM model) and another one considering a fraction of background seismic activity overlapped with the faults (FM_bg model).

Fault Sources: FM Model

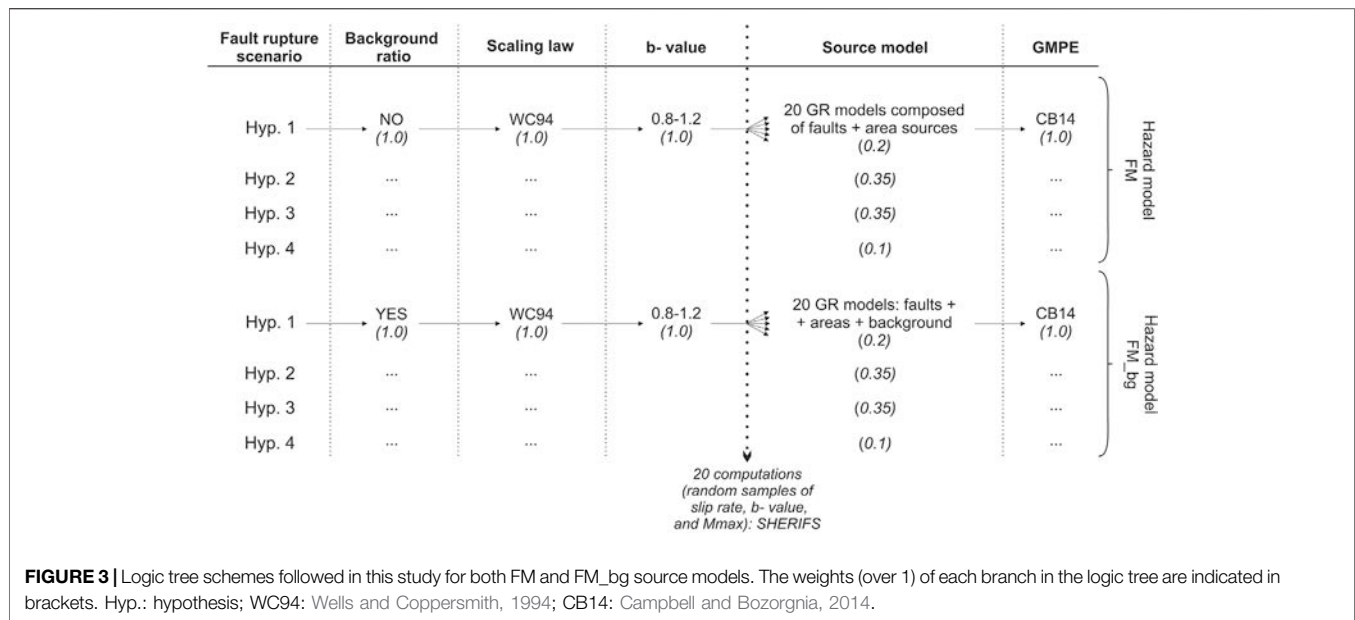
For this model, earthquake rates in the EBSZ buffer area are modeled only on the EBSZ fault system, assuming that all seismicity over Mw 4.0 occurring within its limits is related to these faults. This fault-system source model is based on the results of the modeling performed in Gómez-Novell et al., 2020 without any additional modifications. Four scenarios or hypotheses of fault and multi-fault ruptures involving from single fault sections to nearly the whole system (hypothesis 1 to 4; Table 2) are modeled using SHERIFS and the fault data in Table 1 to obtain different GR distributions for the whole EBSZ system. In order to incorporate the epistemic uncertainty in the input data, the GR of each scenario is composed by 20 GR curves

resulting from 20 computations exploring random values of input parameters, i.e., fault slip rates, b-values and Mmax of GR distribution. Slip rates are explored within the ranges provided in Table 1 and the b-values within the 0.8–1.2 range (Figure 3), whose mean (1.0) is in agreement with the one of the EBSZ in the ZESIS model (García-Mayordomo, 2015). The Mmax is set following Wells and Coppersmith, 1994 for rupture area and all kinematics. The resulting earthquake occurrences of each scenario (80 GR curves for all four scenarios) are expressed as the seismicity rates of each fault-rupture involved in that scenario (see Gómez-Novell et al., 2020 for details on the criteria applied to define the fault rupture scenarios, the input parameters used for the modeling with SHERIFS and the calculations). Furthermore, in the previous paper, the agreement of the resulting MFDs with the earthquake distribution from the catalog and paleoseismic record is analyzed and a qualitative ponderation of each hypothesis for PSHA is proposed, which we use here to set our logic tree weighting scheme (section 3.3 and Figure 3). All these outputs are used to build the source models in hazard calculations.

Fault Sources Including Background Seismicity: FM_bg Model

We introduced, by means of a background ratio, a modification respect to the previous FM model in order to consider that part of the seismic moment release in the EBSZ could be due to unknown active faults apart from the main ones. The rest of the input parameters are the same as mentioned for the FM model.

The background ratio is a parameter from SHERIFS that allows sharing a fraction (percentage) of the seismicity rate of a given magnitude between the faults and the background or the area directly surrounding the faults. For instance, a background ratio of 70% for Mw 4.0 means that 70% of the total seismicity rate of Mw 4.0 is modeled on faults and 30% as background seismicity. Therefore, the occurrence rates of the selected magnitude range on the faults are lowered with respect to the FM model consistently with the ratio adopted, avoiding double-counting of seismicity and respecting the GR distribution (see Chartier et al., 2019 for details on the



background ratio). In our case, the background area corresponds to the EBSZ buffer area, whose seismic potential is then not only defined by the faults contained but also by the background seismicity as an area source.

Chartier et al., 2019 recognize that the user may rely on expert opinion to set this ratio due to its difficulty but propose to use the distance between earthquake epicenters and faults as possible criteria to set it. We cannot follow this approach due to large location errors at the EBSZ: 67% of the $M_w \geq 4.0$ earthquakes are previous to year 1962 (IGN-UPM, 2013) and hence show epicentral errors larger than 10 km or even 20 km (García-Mayordomo, 2005). We then set the background ratios following expert opinion but based on criteria from seismicity data of the region as we explain below. These ratios are 70%, 80%, 90%, 95% for M_w 4.0, 4.5, 5.0, and 5.5, respectively, which represent the percentage of the total EBSZ seismic moment that is actually modeled on faults for each 0.5 magnitude bin. The remaining is modeled as background in the area of about 10 km around the faults.

The selected percentages are consistent with the fact that most of the instrumental earthquakes of $M_w \geq 4.0$ in the EBSZ have occurred in the modeled faults. This is supported by the location of recent moderate earthquakes (e.g., 2011 Lorca seismic series related to AMF; Martínez-Díaz et al., 2012b) and by the fact that focal mechanisms of seismicity are in agreement with the main faults of the region (Stich et al., 2007, Stich et al., 2010). On the other hand, the GR distributions modeled with SHERIFS for the EBSZ in Gómez-Novell et al., 2020 predict good fits with the regional seismic catalog for most of the rupture scenarios in the $M_w < 6.0$ magnitude range. This supports that known faults might be responsible of most of the seismicity within the EBSZ. Consequently, we select ratios that do not modify significantly the GR distributions, hence that do not

invalidate the proposed logic tree weighting in that study and comparison can be directly done with the FM model.

Only events in the range of M_w 4.0–5.5 are affected by the background ratio in our study, because earthquakes this size rarely cause surface rupture (Biasi and Weldon, 2006) and thus, they may occur in unrecognized faults and unadvertised by the paleoseismic studies. $M_w > 6.0$ earthquakes though, are considered to be produced in larger faults with geomorphic expression so they are modeled exclusively on the known EBSZ faults.

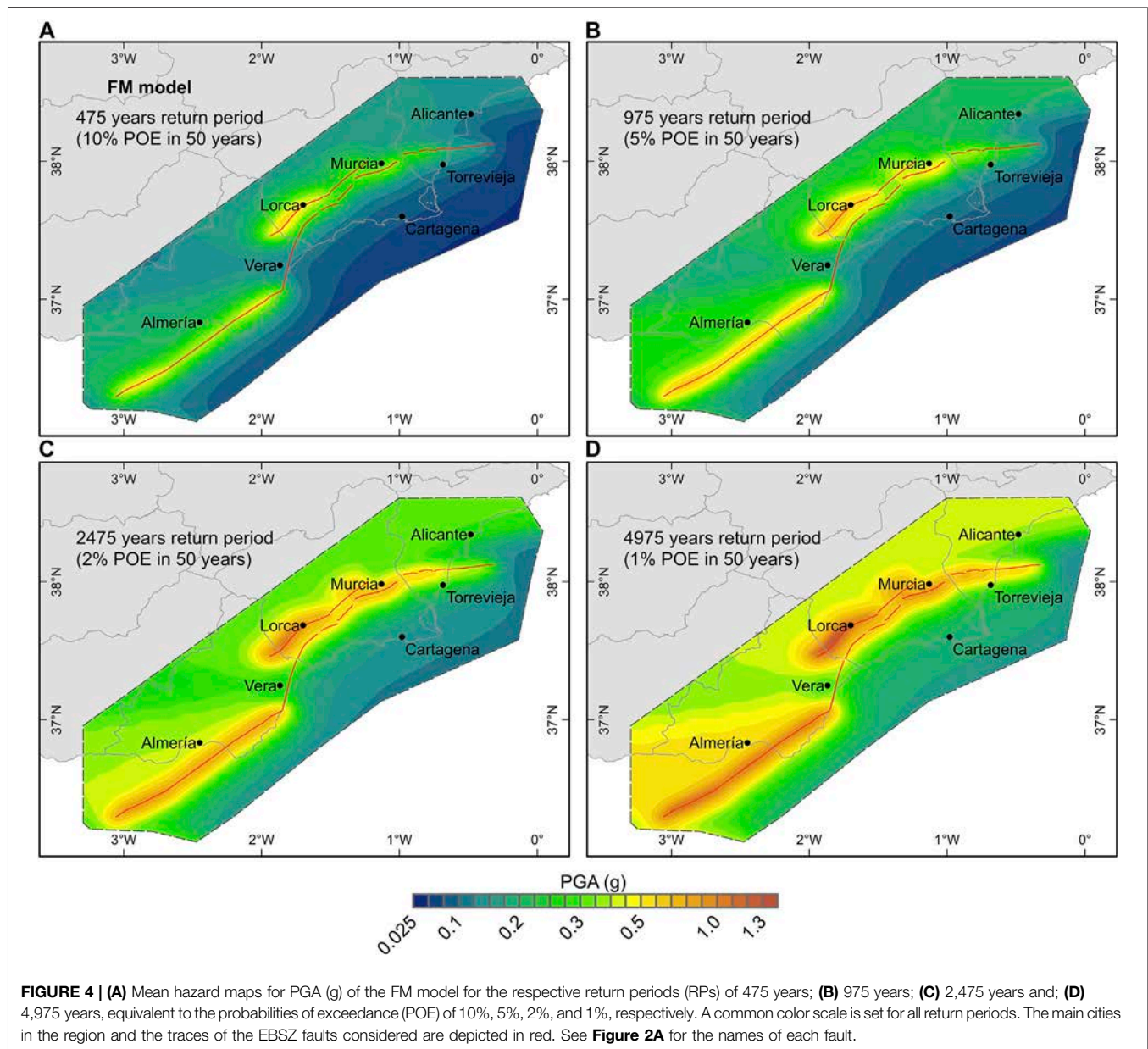
Area Sources

Outside the bounds of the EBSZ buffer area we consider the area sources of ZESIS model (García-Mayordomo, 2015). The area sources considered here are (Figure 2B): #29, #30, #31, #34, #35, #36, #37, #38, #39, #40, #41, #43, #44, #45 and, for the FM_{bg} model only, #55. These areas are all located within a radius of 50 km from the external boundary of the mapping area in order to account for the influence of seismogenic sources adjacent to the EBSZ buffer area (#55). The potential influence of farther sources is considered negligible for the purposes of this study. The earthquake occurrence in these areas is modeled according to GR distributions obtained in the frame of the project to update the national seismic hazard map of Spain (IGN-UPM, 2013), and their parameters (a and b-value, M_{min} , M_{max} ; Table 3) are adopted here from the ZESIS database (IGME, 2015b). In the case of area #55, earthquake occurrence is controlled by the seismic moment assigned by the background ratios in each source model and following the target MFD of the faults (section 3.1.1.2). The area sources are added to the fault sources modeled with SHERIFS to build the different source models for the hazard calculations.

The characterization of the area sources is further completed defining a distribution of nodal planes and hypocentral depths in each area (OpenQuake manual v.3.7.1; GEM, 2019). The former controls the strike, dip and rake of earthquake ruptures inside the

TABLE 3 | Parameters of the area sources used for the area source model in this study. Mmin, Mmax (Mw range), a and b-values of the GR distribution are extracted from the ZESIS area source model (IGME, 2015b; García-Mayordomo, 2015). OpenQuake required parameters such as nodal planes are inferred from main fault orientations of the QAFI v.3. Database (IGME, 2015a; García-Mayordomo et al., 2017) or focal mechanisms of the studies indicated in the table. Seismogenic depths are based on fault data compiled in the QAFI database.

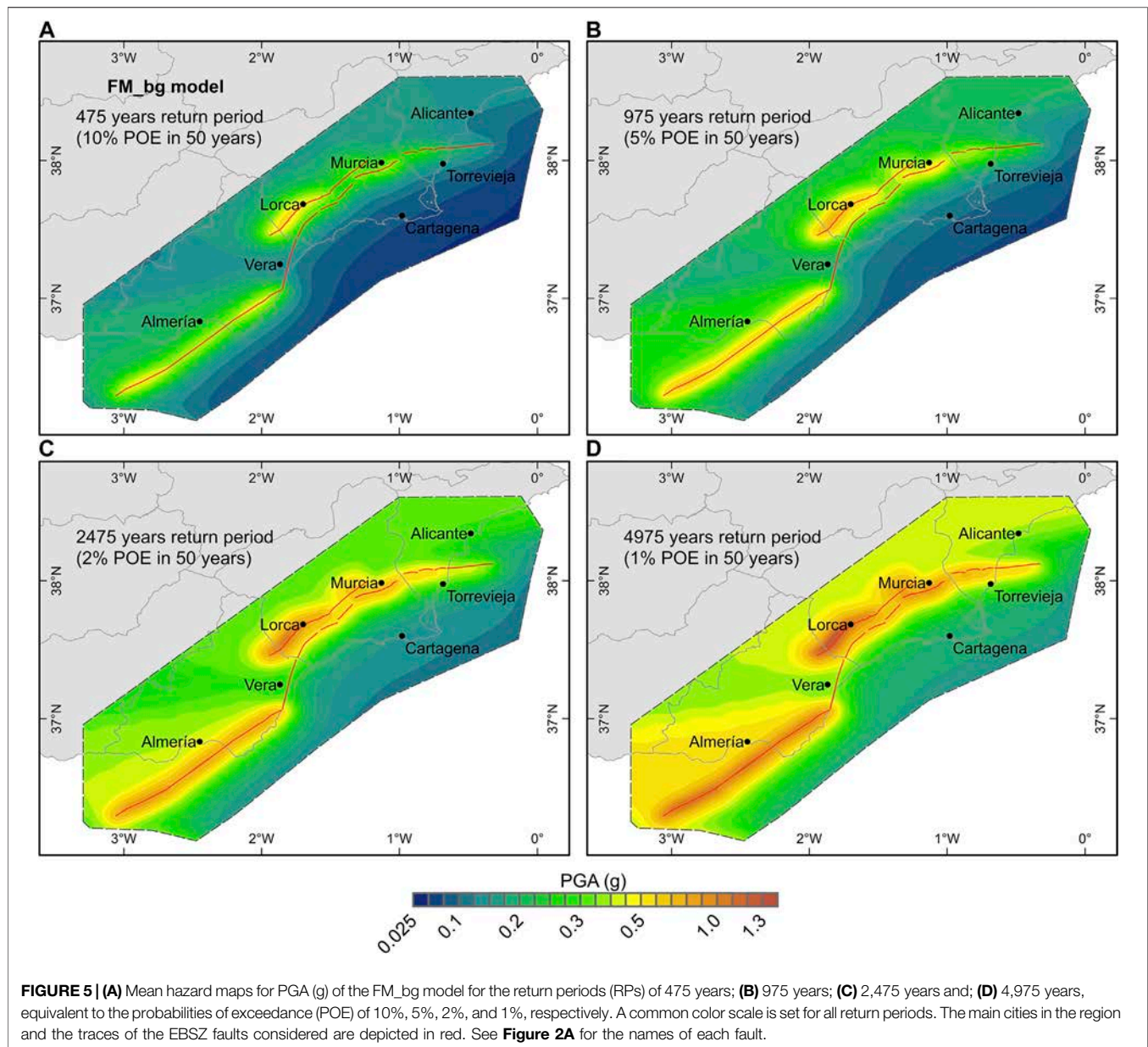
ZESIS parameters				OpenQuake parameters					
Area source	Mw range (Mw)	GR parameters		Seismogenic depth (km)	Hypocentral depths (km)		Nodal planes		References
		a	b		Depth (km)	Probability	Dip/rake/strike (°)	Probability	
29	4.0–6.6	3.36	1.02	20	a) 5 b) 10	a) 0.5 b) 0.5	a) 90/180/060	a) 1.0	Mean fault orientations inferred from the QAFI database (IGME, 2015a)
30	4.0–5.0	3.84	1.26	11	a) 5 b) 10	a) 0.5 b) 0.5	a) 85/–140/125 b) 90/–140/040	a) 0.5 b) 0.5	
31	4.0–6.6	2.99	0.89	15	a) 5 b) 10	a) 0.5 b) 0.5	a) 90/30/065 b) 60/–90/330	a) 0.5 b) 0.5	
34	4.0–6.6	3.30	1.0	8	a) 5 b) 8	a) 0.5 b) 0.5	a) 70/5/151 b) 85/160/060 c) 88/–170/243 d) 80/–2/152	a) 0.25 b) 0.25 c) 0.25 d) 0.25	Focal mechanisms by Stich et al. (2010)
35	4.0–6.8	4.24	1.12	9	a) 5 b) 9	a) 0.5 b) 0.5	a) 60/–90/150 b) 60/–90/330	a) 0.5 b) 0.5	Mean fault orientations (QAFI)
36	4.0–6.5	3.08	0.98	9	a) 5 b) 9	a) 0.5 b) 0.5	a) 60/–90/150 b) 60/–90/330	a) 0.5 b) 0.5	
37	4.0–6.8	4.23	1.16	11	a) 5 b) 10	a) 0.5 b) 0.5	a) 90/30/240 b) 90/–135/325	a) 0.5 b) 0.5	
38	4.0–6.7	3.34	0.96	8	a) 5 b) 8	a) 0.5 b) 0.5	a) 60/–135/150	a) 1.0	
39	4.0–6.7	4.29	1.34	8	a) 5 b) 8	a) 0.5 b) 0.5	a) 90/180/100 b) 60/–90/140	a) 0.5 b) 0.5	
40	4.0–6.5	2.88	0.94	10	a) 5 b) 10	a) 0.5 b) 0.5	a) 23/135/120 b) 85/5/214	a) 0.5 b) 0.5	Fault orientations from QAFI database and focal mechanisms by Gràcia et al. (2019)
41	4.0–6.5	4.5	1.35	8	a) 5 b) 8	a) 0.5 b) 0.5	a) 90/180/120 b) 90/0/014	a) 0.5 b) 0.5	Mean fault orientations (QAFI)
43	4.0–7.0	4.23	1.07	11	a) 5 b) 10	a) 0.5 b) 0.5	a) 85/5/214 b) 84/175/124 c) 90/0/210 d) 45/85/070	a) 0.25 b) 0.25 c) 0.25 d) 0.25	Focal mechanisms by Stich et al. (2010) and Gràcia et al. (2019)
44	4.0–6.4	3.08	0.9	11	a) 5 b) 10	a) 0.5 b) 0.5	a) 90/170/104 b) 90/170/001	a) 0.5 b) 0.5	Mean fault orientations (QAFI)
45	4.0–7.3	2.96	0.8	11	a) 5 b) 10	a) 0.5 b) 0.5	a) 18/102/59 b) 73/86/226	a) 0.5 b) 0.5	Focal mechanisms by Stich et al. (2010)
55	Earthquake occurrence is modeled with SHERIFS for Mw 4.0–5.5 considering the seismic rates assigned by the background ratios and following the target MFD shape (b-value) of the EBSZ faults			12	a) 5 b) 8	a) 0.5 b) 0.5	a) 90/20/050 b) 60/90/080	a) 0.5 b) 0.5	Mean fault orientations (QAFI)



zone, while the latter controls the depth of the center of the ruptures. Nodal planes in each area are defined based on the predominant fault orientations from the QAFI v.3 database (IGME, 2015a), as well as by the distribution of focal mechanisms available in SE Spain and North-Africa (Stich et al., 2010), and the Alboran Sea (Gràcia et al., 2019) (Table 3). Eventually, a set of different nodal planes is defined for each area source representing each one the same probability of occurrence. Similarly, two equally probable hypocentral depths are defined for each source area (Table 3): the upper is set at 5 km and the lower between 8 and 10 km depending on the minimum common seismogenic depth of all faults contained in the area. The maximum seismogenic depth of the faults in the QAFI database defines the seismogenic depth for each area source.

Final Composite Seismogenic Source Models for Hazard Calculations

Two resulting composite source models are used for the calculations: FM + area sources and FM_bg + area sources. The “composite” term is used here to remark that each source model is composed by a fault source model and an area source model (Figure 3). The former sets the occurrence rates of all the fault ruptures envisaged in each fault rupture hypothesis modeled with SHERIFS within the EBSZ buffer area. The latter sets the occurrence rates of the different area sources considered outside the EBSZ buffer area and the background seismicity in the case of FM_bg model. The final models are referred by the distinctive fault source model name henceforth (i.e., FM and FM_bg). Because each of the four multi-fault rupture scenarios is composed of 20 different GR curves, a total of 80 input source



models for OpenQuake compose both FM and FM_bg source models (Figure 3). The fault source part (e.g., earthquake rates, M_{max}) is different for each 80 models because it depends on a) on the rupture scenario considered and b) the values of the input parameters explored randomly during the SHERIFS calculation. Each FM and FM_bg are computed separately in a different hazard calculation in order to better test and highlight the influence of including a background ratio, and to compare results more directly.

Ground Motion Prediction Equation

We selected the ground motion prediction equation (GMPE) derived by Campbell and Bozorgnia, 2014 from the PEER NGA project (Power et al., 2008). This equation is well adapted for fault-based PSHAs since it accounts for near-fault features such

as fault geometry, style of faulting, depth of rupture and hanging wall effects. For the fault-based approach that we propose, this equation is then suitable to show the sensibility of the seismic hazard results to the fault source models. Additionally this equation is the one that Rivas-Medina et al., 2018 selected for a fault-based PSHA in SE Spain after an analysis of several GMPEs. According to the authors, this equation allowed better estimations of the expected accelerations in the study region considering the characteristics of the sources and the available data.

We acknowledge that considering a set of GMPEs is a normal practice in the attempt to capture the epistemic uncertainty related to ground motion. However, we consider just one GMPE to facilitate the detection of the impact of fault incorporation into PSHA and to be able to perform direct comparisons with

previous studies. In order to quantify the influence of the GMPE on the results related to the fault source model and compared to other GMPEs not sensible to near-fault effects, we perform a sensibility analysis to the FM model by using the Akkar et al., 2014 equation. This is the latest GMPE derived from pan-European databases and does not include fault parameters in its functional form apart from style of faulting as a dummy variable. The implications of this analysis are discussed in section 5.3.

Logic Trees Explored

Each source model is computed separately. Thus, two logic trees are explored in this study as depicted in Figure 3. For each logic tree, the four different hypotheses of multi-fault ruptures are considered in order to incorporate the epistemic uncertainty of earthquake occurrence on faults. Each rupture hypothesis constitutes a branch of the logic tree, weighted based on the analysis of the agreement with the seismic catalog and paleoseismic data performed in Gómez-Novell et al., 2020. That study concluded that hypotheses 2 and 3 were the ones with better agreement with the regional seismic catalog and paleoseismic data, followed by hypothesis 1 and lastly, hypothesis 4. A better agreement implies a more suitable hypothesis for the study region. Accordingly, we assigned a weight of 35% to both hyp. 2 and 3, 20% to hyp. 1 and 10% to hyp. 4. Each hypothesis is composed by 20 GR curves, hence 20 input source models for OpenQuake that include a fault source model and an area sources model. The weight of each of the 20 branches or models that form a hypothesis equals 1/20 of the weight of the whole branch (Figure 3).

Hazard Calculations

Hazard calculations are performed using the OpenQuake engine (Pagani et al., 2014). We compute a set of mean hazard maps in terms of PGA as function of probabilities of exceedance of 10, 5, 2 and 1% in a time window of 50 years, which correspond to return periods (RPs) of 475-, 975-, 2,475- and 4,975-years, respectively (Figures 4, 5). The region considered is depicted in Figure 2B and follows a 2×2 km grid, accounting for a total of 10,556 calculation points for each return period. This region is defined to comprise completely the EBSZ buffer area and include important cities of the region (Murcia, Lorca, Almería, Vera, Torrevieja, Alicante and Cartagena). To analyze fault influence, in the cities adjacent to the EBSZ faults (Murcia, Lorca, Almería, Vera, Torrevieja) we produce mean hazard curves in terms of PGA (Figure 6) and hazard disaggregation for distance-magnitude (Figure 7 and Supplementary material). Soil conditions are always considered to be rock or hard soil ($V_{s30} = 760$ m/s). The maximum distance considered for the hazard calculations is 100 km in order to better reproduce the near-fault related hazard of the EBSZ and because farther sources have negligible impact in the study area (see disaggregation results in section 4.1). Source input files of the hazard calculations including source models, GMPE, logic tree and calculation specifications are included in the Supplementary material of the article.

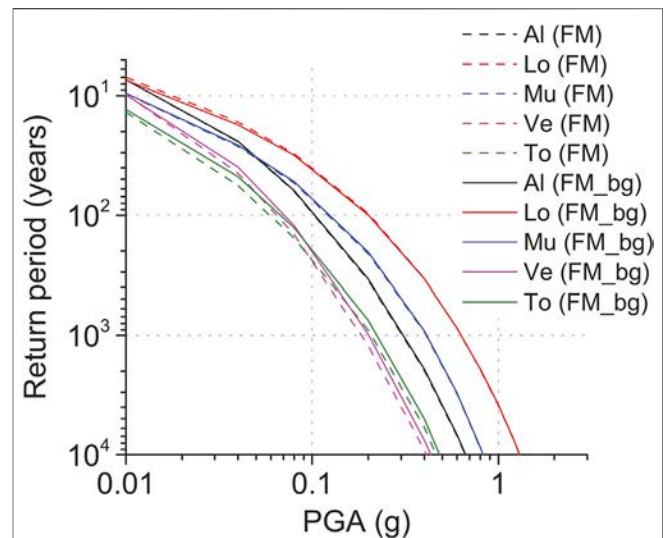


FIGURE 6 | Mean hazard curves for PGA (g) of the FM and FM_bg models in the cities of Almería (Al), Lorca (Lo), Murcia (Mu), Vera (Ve) and Torrevieja (To). Their location is indicated in the maps from Figures 4, 5.

RESULTS

The results of the calculations are presented in mean hazard maps (Figures 4, 5) and mean hazard curves for five cities of the region (Figures 6). Maps were obtained after interpolation using the natural neighbor approach from the OpenQuake outputs. A common colored scale has been set for all maps to facilitate comparison. Mean hazard curves for the cities of Murcia, Lorca, Almería, Vera, Torrevieja are also depicted in terms of PGA on rock (Figure 6). To test the influence of the different fault sources and the seismic background on the hazard, we computed hazard disaggregation of the FM_bg model for the magnitude-distance relationship. In Figure 7, we depict representative disaggregation results in three cities and for two RPs (475 and 2,475 years). For complete disaggregation, figures of all the cities considered in Figure 6 and all four RPs are available the Supplementary material.

The results show a clear control of the EBSZ fault over the seismic hazard of SE Spain for all RPs, especially in the vicinity of faults (10–20 km). Slip rate values directly affect fault influence into the hazard because highest accelerations are located around faults with higher slip rates of the system, while lower slip rate faults have much less influence. The impact of the background into the models is very limited given the similarity of results from both FM and FM_bg.

Mean Hazard Maps and Disaggregation Fault Influence

The mean hazard maps from both FM and FM_bg models (Figures 4, 5) produce very similar results in terms of absolute hazard levels and distribution and increments between them are very low (Figure 8). The modeled EBSZ fault system exerts a clear control into the seismic hazard of SE Spain for all RPs, especially

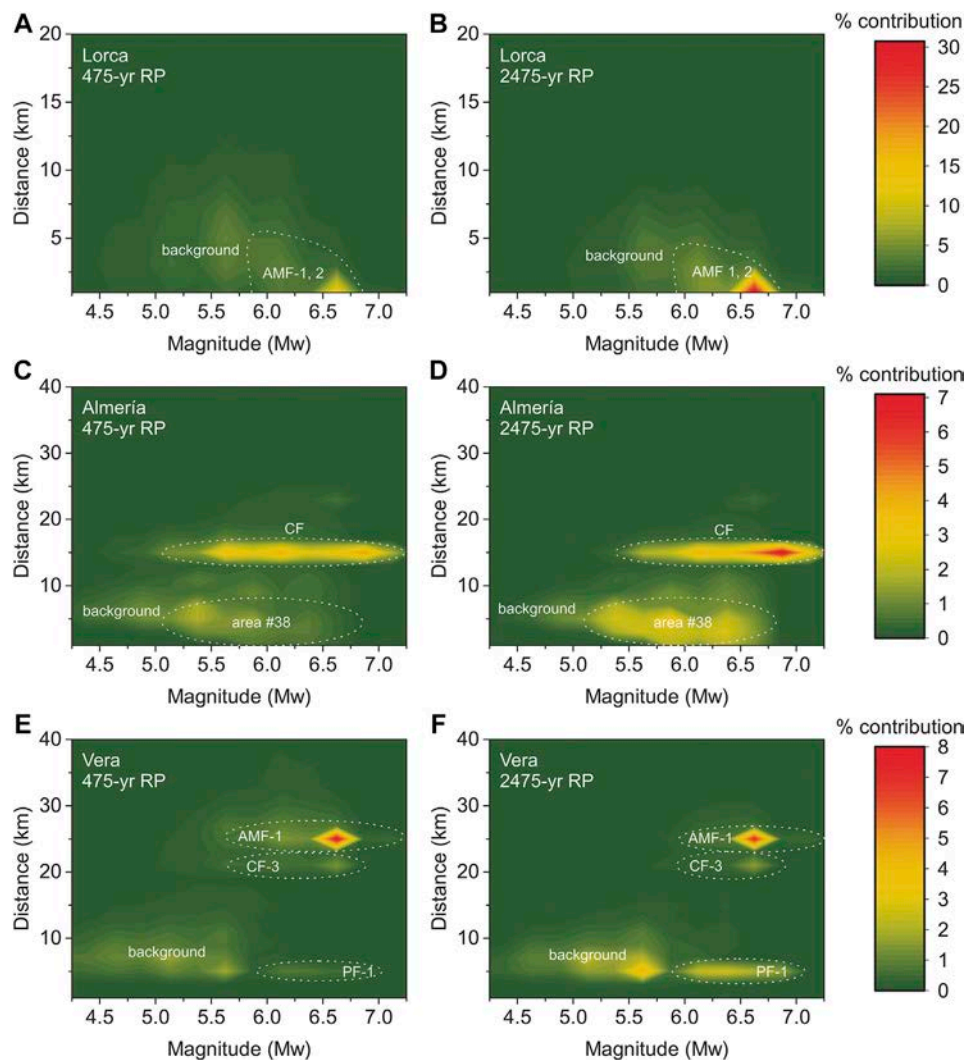


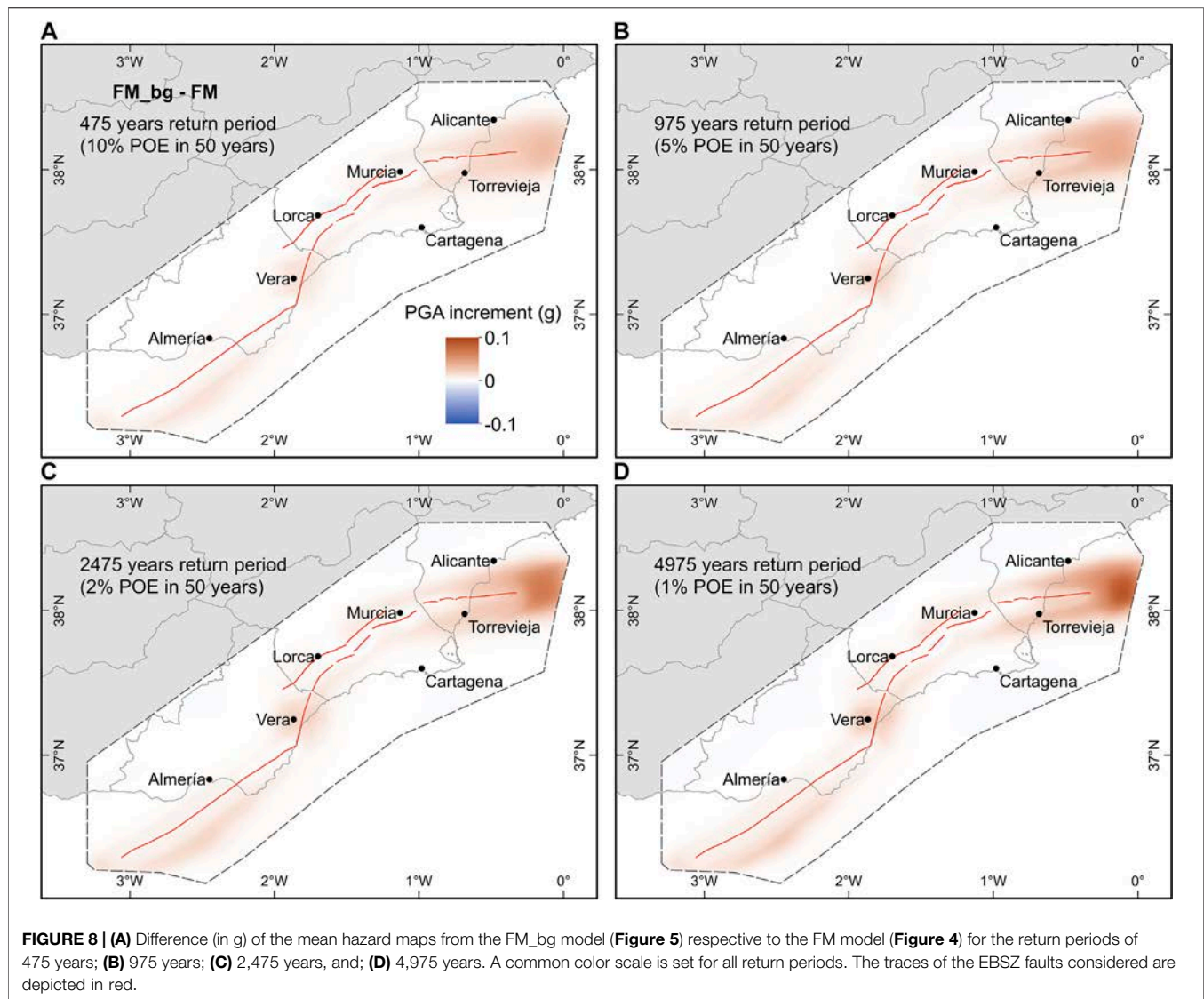
FIGURE 7 | (A) Hazard disaggregation for the magnitude-distance relationship of the FM_bg model in the cities of Lorca for the return periods of 475 years and; **(B)** 2,475 years; **(C)** Almería for 475 years and; **(D)** 2,475 years; **(E)** Vera for 475 years and; **(F)** 2,475 years. A common color scale is set for the two return periods representing each city. The main sources contributing to the hazard of each city and return period are highlighted. For disaggregation figures of all the cities in **Figure 6** and for the four return periods of 475, 975, 2,475, and 4,975 years, see the Supplementary Material of this paper.

noticeable in the near-fault regions, where maximum PGA values are located.

In both models, the maximum acceleration values range from 0.5–0.6 g for the 475 years RP to 1.2–1.3 g for the 4,975 years RP (Figures 4, 5) and are located along the faults with higher slip rates. That is the case of the Southwestern termination of AMF, near Lorca (AMF-1 and 2) or CF near Almería, which have the highest slip rates of the system (>1.0 mm/yr; Table 1 and Figure 2A). On the other hand, lower slip rate faults have minor influence in the hazard levels for all RPs, also depending on their slip rates. Mean hazard maps from both FM and FM_bg models (Figures 4, 5, respectively) show that PF is the fault with less footprint on the hazard for all RPs, which is consistent with its slip rate being the lowest of all the system according to the available estimations (<0.1 mm/yr; Table 1).

Other faults such as the Eastern termination of BSF (BSF-3 and 4), AMF-4 or LTF, have higher slip rates (~0.1–0.4 mm/yr; Table 1) but their influence to the hazard is limited compared to AMF-1, 2 or CF (Figures 4, 5).

The hazard disaggregation of the FM_bg model (Figure 7) shows that all the contributions to the seismic hazard in a specific site are from sources located within a 20–30 km radius, suggesting that farther sources do not influence the hazard. Higher slip rate faults contribute the most to the seismic hazard values of the closer zones, while lower slip rate faults have very small contributions, even in the sites in their closest vicinity. In the cities of Lorca and Almería (Figures 7A–D), the magnitude-distance relationships that influence most the hazard coincide with the location of AMF-1 and 2, and CF-3, respectively, which are the fault sections with higher slip rates in the system (Table 1).

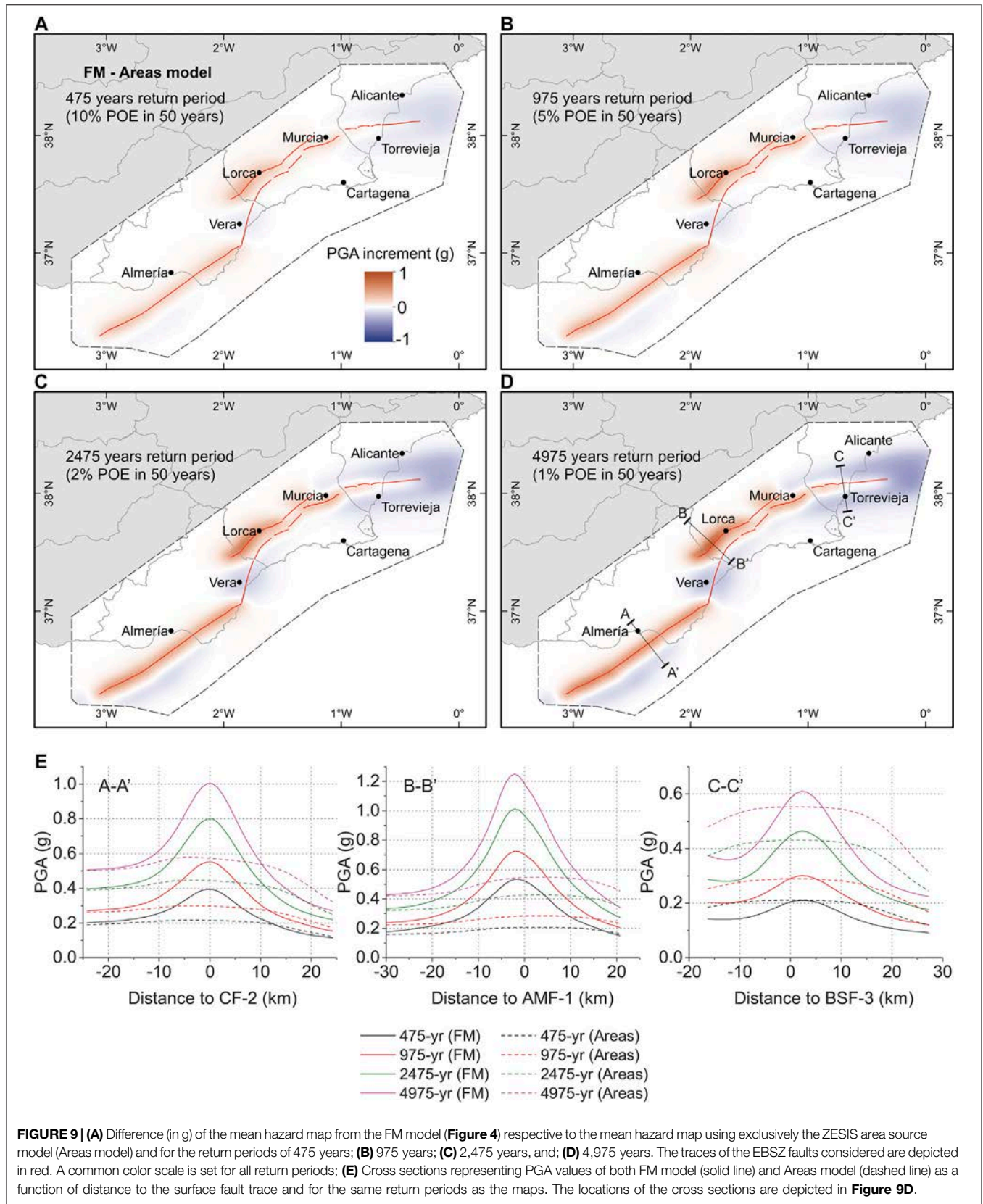


Lorca is located <1 km from AMF in the limit between AMF-1 and 2, which explains the maximum influence from sources located between 1–5 km. These maximum AMF-1 and 2 contributions are in a tight Mw 6.5–6.75 range for both RPs (Figures 7A, B), which might suggest the controlling earthquakes in this city. Almería is located at ~15 km from CF-3, consistent with the distance of the source's maximum contribution. The higher distance of the fault from the city causes its contribution to be considerably lower than AMF-1 and hence other non-fault sources influence the hazard as well (Figures 7C, D). The contributions of CF-3 comprise a wider magnitude range (Mw 5.0–7.0) in the 475 years RP (Figure 7C), while they concentrate around Mw 6.5–7.0 in the 2,475 years RP (Figure 7D). Conversely, in zones such as Vera, located next to very low slip rate faults (i.e. PF), the main contributions to the seismic hazard are not from the closer faults, but from other farther faults (Figures 7E, F). In this city AMF-1 is the main contribution despite this fault being ~25 km farther, while PF is the least even for long RPs (Figure 7F).

A hanging wall effect can be observed in non-vertical dipping faults such as AMF, CAF or BSF (Figures 4, 5). Such near-fault effect is more visible at longer RPs (i.e., 2,475 and 4,975 years), where PGAs for two selected sites at the same distance of a fault trace but on opposite sides, are higher on the hanging wall. A clear example is the transect perpendicular to AMF near the city of Lorca (Figure 9E). This is a significant observation for seismic hazard assessment in near-fault zones as we discuss in section 5.1.1.

Background Influence

The similarities between the mean hazard maps from the FM and FM_{bg} models suggest that adding a seismic activity background ratio in the FM_{bg} model produces minor changes to the final hazard results within the EBSZ buffer for any RP (Figure 8). In general, the background contributes to raise the hazard values with respect to the FM model, while the decreases are depreciable. PGA increments, especially for



the shorter RPs, are mild (Figures 8A–C), but for the 4,975 years RP the hazard values are incremented up to a maximum of ~ 0.1 g in some zones (e.g., E of BSF; Figure 8D). For the faults, PGA values remain practically identical for all RPs, which means that earthquake occurrence on most faults is higher than the one generated by the background. However, the background contributes to slightly increment the hazard within the EBSZ buffer area in the zones farther from the traces and influence of the faults (e.g., E of BSF-4) or next to faults with slip rates much lower than the average of the system (~ 0.5 mm/yr; based on the mean values in Table 1); mainly PF. In these zones, the poor influence of faults allows the background of the FM_bg model to overcome the occurrence rates (i.e., probabilities of exceedance) of the hazard from the FM model, thus higher values are found in the FM_bg model within a same RP.

The maximum hazard increments caused by the background take place E of BSF-4 (Figure 8), where the Bajo Segura fault-system terminates. This is because fault-related seismic hazard influence is larger and wider in the transversal sections across faults rather than in their longitudinal ends, as it can be seen in CF or the Southwestern termination of AMF (Figures 4, 5). In addition, BSF-4 has a lower slip rate (~ 0.2 mm/yr; Table 1) than the average of the faults in the system and the closest area sources in this zone, i.e., #31, #39 and especially #41 (Figure 2B), have very low activity rates (IGME, 2015b). This particular situation causes low occurrence rates of the hazard from the FM model in this zone and allows the background (FM_bg) to overcome such rates more remarkably than any other zone.

These observations are consistent with the disaggregation results of the FM_bg model as in general the background shows low contributions on the hazard, especially where faults dominate the hazard (Figure 7 and Supplementary material). Only in the case of Vera, the seismic background has a significant contribution due to the lower slip rates, hence activity rates, of the PF (Figures 7E,F). This causes the background to overcome the contribution of PF in the Mw 4.0–5.5 range and to contribute significantly to the seismic hazard levels of the city, especially in longer RPs (Figure 7F).

Area Sources Influence

From the mean hazard maps of both FM and FM_bg models it can be observed that the area sources have a much minor footprint in the seismic hazard distribution of the EBSZ than the faults. This is mainly because the activity rates of the area sources modeled are either very low (#31, #36, #39 or #41; IGME, 2015b) or are located too far (>100 km) to have a significant impact in the hazard of the mapped region, such as the North-African source areas (#43, #44 and #45) (Figure 2B). Nevertheless, area sources such as #37 and #38 have a recognizable influence on the hazard results as their shapes can be recognized in the hazard maps especially for the 2,475 and 4,975 years RPs (Figures 4, 5). These area sources have high activity rates comparable to the EBSZ buffer area (IGME, 2015b) and contain faults known to be capable of producing Mw > 5.0 earthquakes, such as the Crevillente Fault or the Andarax Valley

and El Alquíán fault systems (#37 and #38, respectively; Figure 2).

The hazard disaggregation shows the contribution of area source #38 on the hazard of Almería for RPs of 2,475-years RP (Figure 7D) as the city is located inside this area source. Contrarily, neither Lorca or Vera have contribution of area sources into their hazard (Figures 7A–F, respectively) as they are located ~ 8 – 9 km from the closest area source limit. Although these areas are at relatively close distances, the higher proximity of AMF-1 in Lorca and the low activity rates of the closer area #36 in Vera prevent them to contribute to the hazard in these cities.

Mean Hazard Curves

Figure 6 shows the mean hazard curves obtained for five cities located close to the EBSZ faults (Almería, Lorca, Murcia, Vera and Torreveja) for both the FM and FM_bg models. It is clear that setting a background ratio for the EBSZ buffer area does not imply dramatic changes in the hazard curves of these cities, which are all very close to active faults. In the case of the Almería, Lorca and Murcia, the respective hazard curves of both models predict practically identical PGA values for any RP. Conversely, in Torreveja and, especially, in Vera, the FM_bg model predicts higher PGAs than the FM model, although these differences are very small: less than <0.1 g for the $\sim 10,000$ years RP. The reason for these differences between models is the lower slip rates of the BSF and PF, respectively for Torreveja and Vera, compared to the other faults close to the other studied cities.

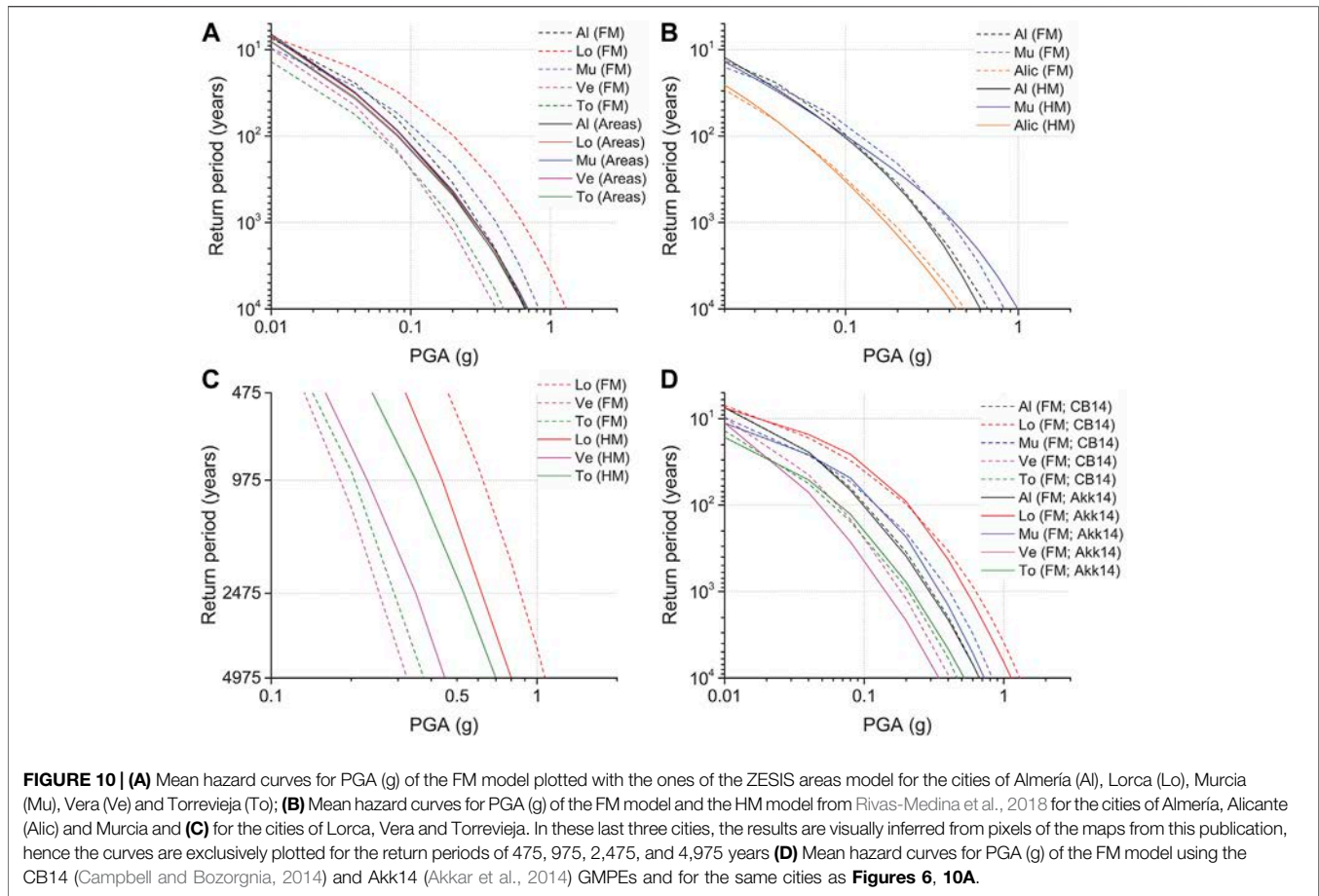
DISCUSSION

Comparison With Previous Probabilistic Seismic Hazard Assessment in SE Spain: Implications of the Modeling

The results presented in this study highlight a clear influence of the faults of the EBSZ in the seismic hazard values of SE Spain, as shown in Figures 4–7. Both of the FM and FM_bg source models applied for the hazard calculations show very similar results, meaning that the application of a background ratio has minor influence on the hazard, especially in those zones closer to faults (Figure 8). Hence, for the comparison analysis that follows we will focus on results of the FM model, though practically all the observations are also applicable to the FM_bg model results. In the same way and due to the low impact of the background on the hazard, the fault influence observations from the disaggregation of the FM_bg model (Figure 7) are valid for the FM model. We compare our results with a PSHA produced only considering the ZESIS area sources model, as well as with a recent fault-based PSHA done in SE Spain (Rivas-Medina et al., 2018).

Comparison With a Probabilistic Seismic Hazard Assessment Using the ZESIS Area Source Model

The PSHA results of our FM model are compared with a PSHA reached here by using exclusively the area sources of the ZESIS model (Figure 2B) and the same GMPE as our calculations (Campbell and Bozorgnia, 2014). Significant changes in PGA



are found between both models within the limits of the EBSZ, where the faults are modeled (Figures 9A–D); outside these limits, the hazard values do not experience any change since all use the same area sources model. The FM model increases the PGA with respect to the areas approach in the zones strictly around the faults. Hence, faults concentrate the hazard highlighting the controlling effect of the faults on the hazard levels. The curves in Figure 10A depict this effect as Lorca, which is located nearly on top of AMF (Figure 2A), shows the highest increment in the FM model. Next, Murcia and Almería show progressively lower PGA increments with respect to the areas model as the distance to the fault increases. These hazard increments in the near-fault zones are achieved by reducing the hazard in the zones farther from the faults with respect to the areas approach and are more visible in longer RPs (975 years RP or larger; Figures 9B–D), where the faults have more influence.

The influence of faults on the hazard (net PGA and areal extension) respect to the areas approach, strongly depend on the fault slip rates. The cross sections A-A' and B-B' (Figure 9E), show that higher slip rate faults in the system such as CF or AMF-1, respectively (1–2 mm/yr; Table 1) influence the hazard up to 10–20 km far from the fault trace for all return periods. This causes significant increments in the PGA values within 20–40 km-wide influence zones of ~70–80% for all RPs in CF-

3 and ~130–150% for all RPs in AMF-1 (Figure 9E). Such increments are slip rate dependent, thus higher for AMF-1 because it has the highest slip rate. Despite this, the disaggregation results of the FM_bg model show that faults can control the hazard in regions farther than the influence zone of the faults up to 20–30 km from its traces, as it is the case of AMF-1 in Vera (Figures 7E,F). Farther than this distance limit however, no source has significant influence in any part of the studied area. Fault influence zones are also dependent on the dip direction in non-vertical dipping faults (AMF, BSF), wider in the hanging wall (Figure 9E), implying a hanging wall effect.

Contrarily, lower slip rate faults have much less impact on the hazard with respect to the areas approach. Although no exhaustive slip rate analysis has been performed, it can be observed that the faults that have slip rates <0.1 mm/yr do not increase the seismic hazard and it is overcome by the areas approach, as it is the clear case of PF (Figures 9, 10A in Vera). Even so, faults with slightly higher slip rates (~0.1–0.4 mm/yr; AMF-4, LTF or BSF) do influence the hazard, but their impact is more limited than AMF-1, 2 or CF, even for long RPs (Figure 9D). The cross section in BSF-3 (C-C'; Figure 9E) depicts one of these latter examples. This fault section has a slip rate range 4–14 times smaller than AMF-1 and CF (0.12–0.3 mm/yr; Table 1), which causes its influence zone to be over 2–3 times smaller (<10 km wide). In this case the near-

fault PGA increments are negligible for short RPs of 475- and 975-years and very small (<0.1 g) for longer RPs (Figure 9E). The small influence of the fault causes the FM's PGA values to be overcome by the ones of the areas approach in less than 5 km from the peak of maximum fault influence. This is also depicted by the Torrevieja curves (Figure 10A) and the maps of Figure 9. The implications of lower slip rate faults on the hazard are discussed in section 5.2.

The consideration of near-fault hazard in zones in the vicinity of the EBSZ faults as both FM and FM_bg models do, including effects such as the hanging wall, provides more realistic estimations of the seismic hazard. This is relevant because during earthquakes, zones close to active faults are exposed to higher accelerations than farther zones due to these near-source effects (e.g., 2011 Lorca earthquake; Alguacil et al., 2014). Their location respect to the dip direction of the fault is also relevant for the ground motion, usually higher in the hanging wall (e.g., Yu and Gao, 2001). Conversely, area source approaches do not reproduce these effects, but uniform PGA distributions within an area, as depicted by the nearly identical mean hazard curves of the cities within the EBSZ buffer area (Figure 10A). A detailed and representative analysis of the relationship between PGA, distance to the fault and influence of fault slip rate is a necessary step to be taken in further hazard studies in the region, as it could be useful to define amplification coefficients in earthquake resistant provisions to account for near-fault effects at sites located next to active faults.

Comparison With Rivas-Medina et al., 2018 Fault-Based Approach

We compare the results from the FM model with the fault-based study of Rivas-Medina, 2014, recently published in Rivas-Medina et al., 2018. In that study a PSHA of Southern Spain is performed considering faults as independent, non-interacting sources, following a hybrid methodology (HM model) that avoids setting an arbitrary cutoff magnitude for modeling seismicity in the background (see details in Rivas-Medina et al., 2018). The PSHA was performed for a larger territory of SE Spain than the present study and for all the active faults of the region as compiled in the old QAFI v.2 database back in 2012. The areal model for this study (GM10) is different from the ZESIS model (aka GM12; IGN-UPM, 2013) as it does not identify the EBSZ buffer area (area #55; Figure 2B). The GMPE used is the same as in our study. We compare the mean hazard curves of the FM model with the HM model, including Alicante (Figures 10B, 10C). The hazard curves for the cities of Lorca, Vera and Torrevieja were not computed specifically by the authors, hence we inferred visually the PGA values at these cities from pixel screening of the hazard maps for each of the four RPs calculated (475, 975, 2,475 and 4,975 years; Figure 10C).

The main contribution of our work with respect to Rivas-Medina et al., 2018 is the consideration of multi-fault ruptures in the source modeling, which causes differences in the hazard estimations mainly for long RPs. Regarding the EBSZ as a whole in PSHA is a novelty in Spain and might constitute a more realistic approach to model the seismic hazard. The main point is that multi-fault ruptures are regarded as a frequent

phenomenon, demonstrated by numerous morphogenetic earthquakes in the last decades (e.g., Choi et al., 2012; Hamling et al., 2017; Villani et al., 2018).

In general, the study by Rivas-Medina et al., 2018 provides hazard levels in the range of the ones obtained by the FM model, however there are noteworthy differences. These are mainly due to 1) the consideration of multi-fault ruptures in the FM model, 2) differences in the fault data used in each source modeling, 3) the background seismicity of the HM model and 4) the number of faults considered. The FM model treats the fault system as a whole by allowing the possibility for faults to rupture simultaneously in multi-fault ruptures including large rupturing scenarios. This consideration allows a larger number of fault rupture possibilities to host a certain magnitude and therefore hazard values are generally higher for this model, as shown by the curves of Lorca, Almería and Alicante (Figures 10B,C). These differences are more notable in RPs over $\sim 1,000$ years because multi-fault ruptures produce higher magnitudes that control the longer RPs. Moreover, the discrepancies in the slip rate values and segmentation between both FM and HM models are also responsible for the hazard differences. For instance, the higher values of the FM in Lorca are because updated slip rate data for AMF-1 and AMF-2 are used (1.65 and 1.0 mm/yr, respectively; Table 1), contrary to the HM model (0.3 and 0.5 mm/yr). The higher values in Almería, on the other hand, are because CF is divided in three segments with a mean slip rate of 1.1 mm/yr (Table 1) in the FM model, while in the HM it is divided in two segments, one of which uses an outdated slip rate (0.04 mm/yr).

In the cities of Murcia, Vera and Torrevieja, the curves of the HM model predict higher values than the FM model (Figures 10B,C). In Murcia this is only for RPs over ~ 500 years, as for lower RPs the tendency is the same as the mentioned for Almería and Lorca. We attribute this to the fact that CAF, which controls the hazard of this city (see disaggregation in the Supplementary material), is considered as a single-segment fault in the HM model (CAF; 0.54 mm/yr), while in the FM as two segments with different and lower mean slip rates (0.37 and 0.53 mm/yr for CAF-1 and 2, respectively; Table 1). In RPs over 500 years this implies that probably a big part of the magnitudes that in the HM model are achieved independently by CAF, in the FM model are achieved by multi-fault ruptures involving CAF-1 and 2. As the slip rates of CAF-1 are lower than CAF-2, the occurrence rates of these multi-fault ruptures are limited by the former (see slip rate treatment in SHERIFS on section 3.1.1) and hence are lower than the HM model in this area. On the other hand, the fact that the fault is divided in two segments increases the earthquake rates of lower magnitudes and consequently the PGA values for low RPs (<500 years) in this city with respect to the HM model (Figure 10B). As such, linked ruptures between segments, i.e., higher magnitudes, are less frequent in low RPs.

In Vera and especially Torrevieja the higher values of the HM model are visible in all four RPs represented (Figure 10C). In the former, the hazard is not controlled by the nearest faults due to the low activity rates of PF, so the background seismicity of the HM model overcomes the ones from the FM. Remarkably, performing this comparison with the curves from the FM_bg model would produce practically the same results, as the

background seismicity of the HM model is modeled for a larger magnitude range (M_w 4.0–6.9) and implies higher seismicity rates. In the latter, the higher HM values are because in this area, additional fault sources apart from the BSF are considered in the modeling (Torrevieja and San Miguel de Salinas faults; Figure 2A). While the incorporation of more fault sources on the hazard might suggest that the results from the HM model in the Torrevieja zone are more accurate than the FM, it should be noted that including more faults on the hazard does not necessarily imply more accurate results. These additional faults are not included in our models because are secondary faults to the BSF system (Alfaro et al., 2012) and hence are not part of the main structures in the EBSZ. Moreover, neither their relationship with the EBSZ system and their geological parameters have been studied in detail. The inclusion of such faults on the hazard should account for these uncertainties as they could imply misguided hazard estimations.

Implications for Moderate Magnitude Earthquakes

The hazard results from the disaggregation show that moderate magnitudes in the M_w 4.5–6.0 range, although not being the most remarkable, have a non-depreciable contribution to the final hazard in the selected studied sites even in long RPs (e.g., Almería and Vera; Figures 7D,F, respectively). Moreover, according to Gaspar-Escribano et al., 2008, in SE Spain, low-to-moderate magnitude earthquakes between M_w 4.0 and 5.5 control seismic hazard for the 475 years RP. Such kind of earthquakes are relatively frequent in SE Spain and have demonstrated to be quite destructive. The 1999 M_w 4.8 Mula, 2002 M_w 5.0 Bullas and 2005 M_w 4.8 La Paca earthquake series are some recent examples (Benito et al., 2007), being the 2011 M_w 5.2 Lorca earthquake the latest one (Martínez-Díaz et al., 2012a).

The near-source effects of the 2011 M_w 5.2 Lorca earthquake produced exceptionally high accelerations around 0.37 g in the city of Lorca (Cabañas et al., 2011) due to: 1) the proximity of the epicenter to the city, 2) the shallow depth of the earthquake and 3) the directivity of the rupture propagation toward Lorca (Alguacil et al., 2014). The hazard map of the current Spanish Building Code (NCSE-02, 2002) for the 500 years RP and the updated national seismic hazard map for the 475 years RP (IGN-UPM, 2013) predict PGA values in Lorca (0.12 and 0.19 g, respectively) that underestimate the PGA reached in the Lorca earthquake. Conversely, the results of the FM model, but also FM_bg, predict values that differ less than 0.1 g from the ones reached in the 2011 Lorca earthquake: ~0.45 g for the 475 years RP. Rivas-Medina et al., 2018 predict slightly lower values of 0.3 g in Lorca for the same RP, but that are also close to the measured ones.

The fact that fault-based PSHAs in SE Spain predict PGA values for the 475 years RP coherent to the ones of the Lorca earthquake, whose moderate magnitude produced severe damage, may suggest that fault-based approaches perform more realistic hazard predictions than classical area source approaches, particularly for sites located on top of faults or in their vicinity. The PSHA such as the one presented in this study or the one from Rivas-Medina et al., 2018 approximate better the hazard for short RPs due to the effect of faults. However, other site

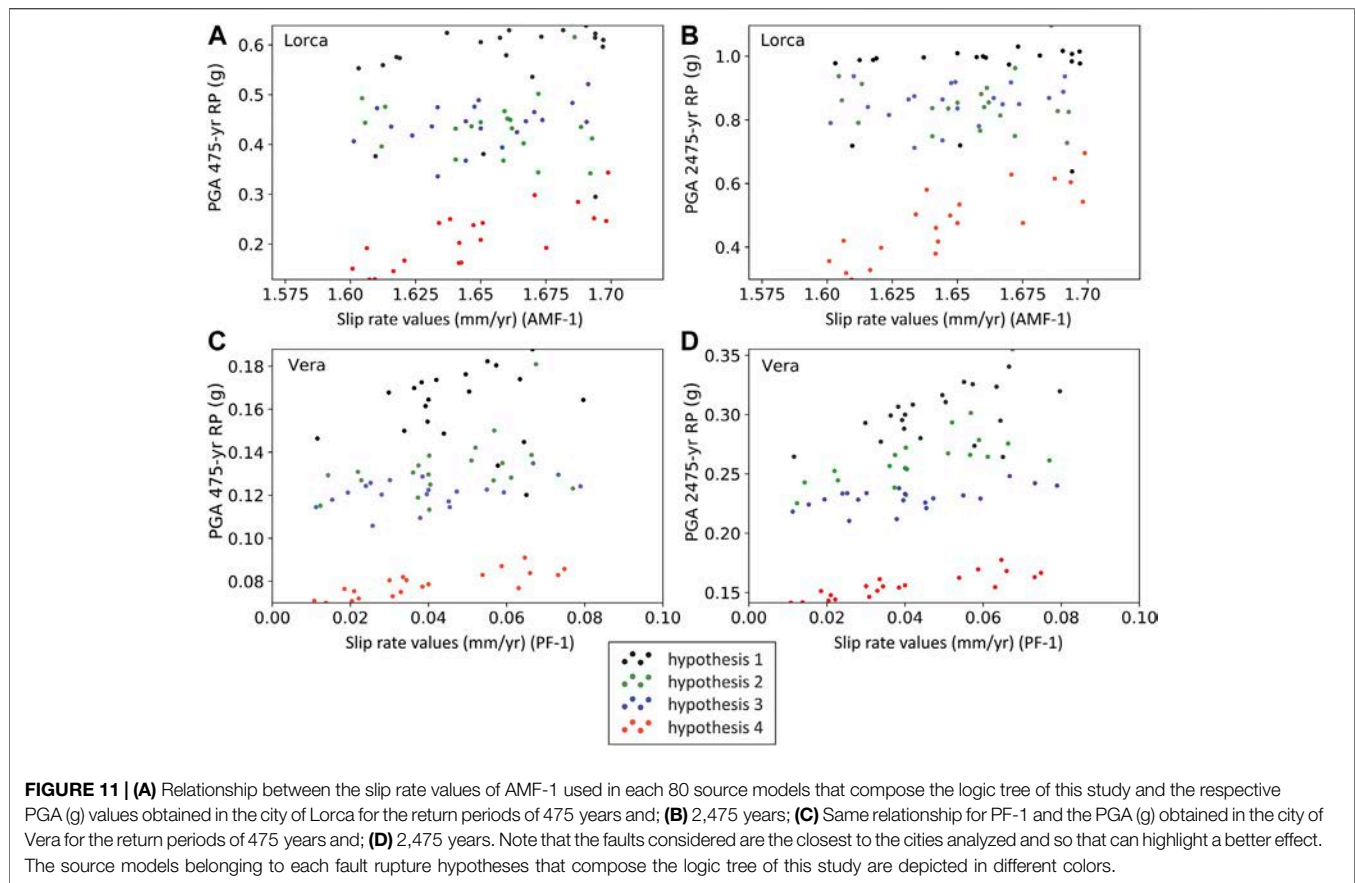
effects such as topography, directivity and changes in soil properties should be incorporated for a more accurate hazard estimation, especially in seismic microzonation.

Implications of the Fault Slip Rates

Slip rate data of faults is a controlling factor in the hazard values obtained in this study as it has a direct impact on the probabilities of exceedance in a given observational period. Higher slip rate faults (e.g., AMF-1 and 2 or CF) imply higher PGA values and influence than lower slip rate faults, some of which have slip rate values so low (<0.1 mm/yr; PF) that are not able to influence significantly the hazard at any RP. This is also observable in the slip rate values used by the source models that compose each branch of the logic tree in relationship with the resulting PGA for each model (Figure 11). Each source model is built by picking a random slip rate value from the fault uncertainty ranges provided as inputs (Table 1). Thus, aside from the fault rupture hypotheses considered, the models that use higher slip rate values within the uncertainty range show an overall tendency to produce higher PGA estimations at closer sites within the same hypothesis (e.g., AMF-1 in Lorca; Figures 11A,B). Nevertheless, the data in the plots from Figure 11 show high dispersion, which suggests that the slip rate uncertainty is not the only parameter affecting seismic hazard variability. In fact, the proximity of the analyzed site to the fault, the rupture hypothesis in question or the RP might control the slope of the mentioned tendency for each hypothesis. Closer sites, i.e., Lorca, result in steeper slopes, similarly to higher RPs (Figures 11A,B).

PGA variations as a function of slip rate uncertainty are more remarkable in higher slip rate faults (Figures 11A,B), despite their uncertainties being smaller than for lower slip rate faults (Figures 11C,D). AMF-1 has an uncertainty that represents only the ~3% of the mean, while it is ~100% for PF-1 (Table 1), however the hazard variations linked to the slip rate variations are considerably higher for the former in Lorca than the latter in Vera. This is because lower slip rates have less impact on the return periods studied than higher slip rate faults, which is consistent with the low influence of PF in our hazard calculations (Figures 7E,F).

The identification of the method and source of information upon which slip rate data is based on for each individual fault (Table 1) is a crucial step, as it affects the reliability of such data and ultimately the hazard results. At the EBSZ, this is one of the main challenges today as most paleoseismic studies focus only on specific fault sections or single strands of faults with multiple branches, while others remain poorly studied. The faults that concentrate most part of these studies and thus have a better characterization are AMF-1 and 2, CAF and CF. Although most of these focus only on the major fault branches, their slip rate estimations are robust and consistent with overall geodetic data (see section 2 and references of Table 1). Conversely, PF, AMF-3 and 4 or BSF have not been object of detailed paleoseismic research to date and fault data is inferred based on qualitative geomorphological indicators and from geodetic data. These less studied faults at the EBSZ are the ones that have lower slip rate estimations (Table 1) and contribute poorly to the hazard, which could imply a bias of such hazard towards well-studied faults.



Considering the clear sensitivity of the seismic hazard to the fault slip rates, the acquisition of new data in the less studied faults is critical to increase the quality and reliability of the current available data compared to other faults in the EBSZ. Updated parameters can have important implications in the hazard results around them, especially PF. On the other hand, in the zones farther from the mentioned faults and controlled by faults with more paleoseismic research, seismic hazard estimations are more reliable and critical seismic parameters are well constrained (see references in Table 1).

Implications of the Ground Motion Prediction Equation Selection

The selection of GMPEs for PSHA is also a difficult task as it has a great influence on the hazard results obtained for a particular study region and sometimes can mask or exaggerate the influence of a seismic source. In this study, we selected a NGA GMPE that is well adapted for fault-based PSHA (Campbell and Bozorgnia, 2014; section 3.2) as it is sensitive to near-fault effects. Therefore, the strong contribution of the faults into our hazard models could be seen as a result of applying such equation. In order to test the sensitivity of the hazard models to the GMPEs we performed the hazard calculation of the FM model using the equation by Akkar et al., 2014 (henceforth Akk14). We used this equation because is not as specifically designed for near-fault effects as the one by

Campbell and Bozorgnia, 2014 (henceforth CB14) and the source characteristics of earthquakes are exclusively represented by magnitude and style of faulting. The mean hazard maps of the FM model using Akk14 are shown in Figures 12A,B for the 475- and 4,975-years RPs. The differences with the CB14 equation are depicted in the maps of Figures 12C and 12D and the cross sections of Figure 12E for the same RPs. Only these two extreme RPs are shown in order to point out the maximum variations with the CB14 equation.

The sensitivity test performed with the Akk14 equation evidences that the influence of the EBSZ faults on the hazard results performed in this paper is independent of the GMPE used. Therefore, the marked influence of the faults into the PSHA is not a consequence of the GMPE. The resulting mean hazard maps of Akk14 (Figures 12A,B) are very similar to the ones obtained with the CB14 equation (Figure 4) showing a similar hazard distribution. Faults have a clear influence on the hazard for both RPs explored in the near-fault zones and the highest PGA values are found along the traces of the faults, especially the most active according to their slip rates (e.g., AMF-1 and CF). Hanging wall effects are also recognized in the map using Akk14 for non-vertical dipping faults (AMF, CAF and BSF; Figures 12A and 12B).

Despite this, due to its less sensitivity to near-fault hazard estimations, Akk14 computes a more diffuse hazard estimation around the faults, with lower PGA values in general and lower

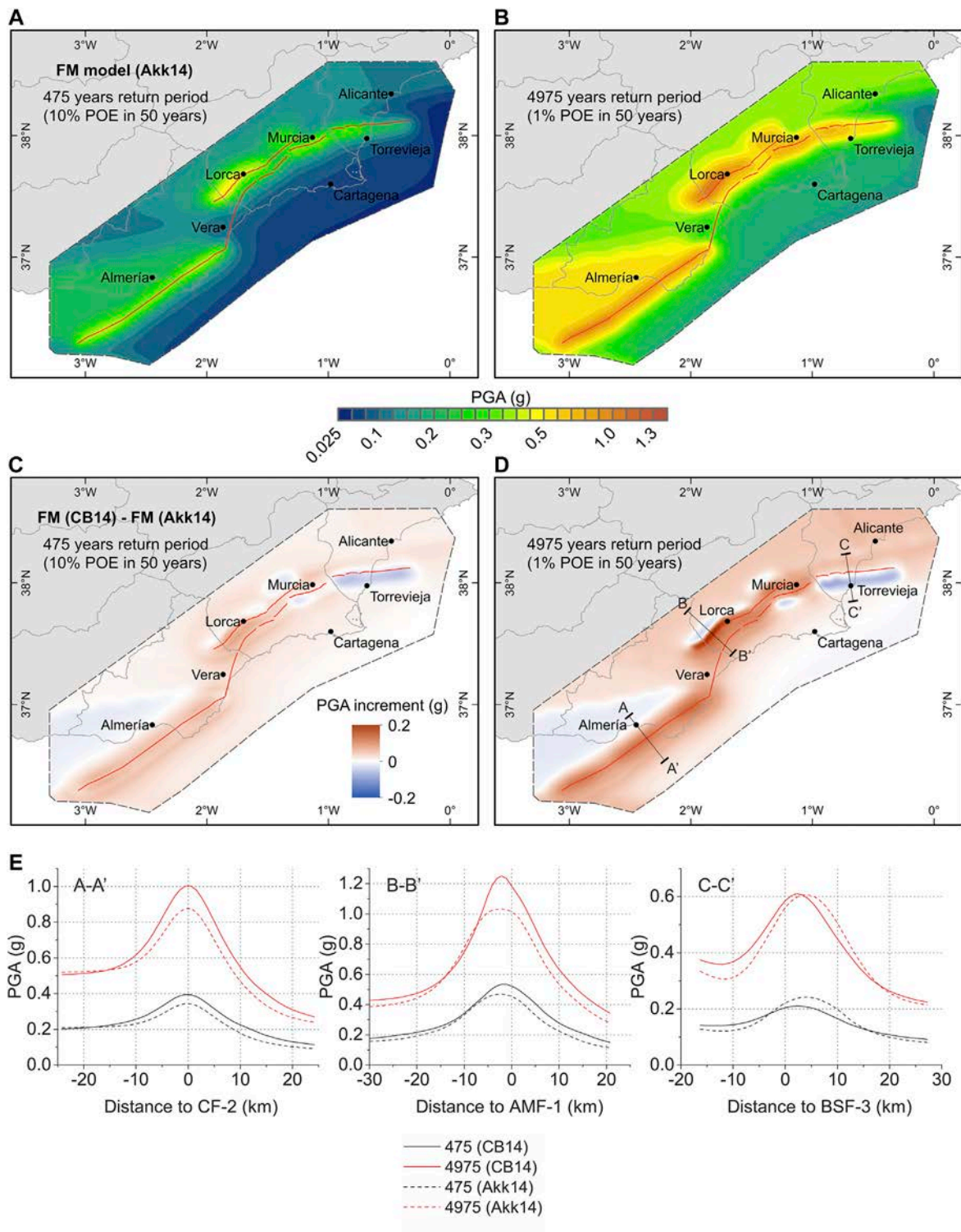


FIGURE 12 | (A) Mean hazard maps for PGA (g) of the FM model using the Akk14 GMPE (Akkar et al., 2014) for the return periods of 475 years and; **(B)** 4,975 years. The color scale is common for both return periods; **(C)** Difference (in g) of the mean hazard maps from the FM model using the CB14 equation with respect to using Akk14 for the return periods of 475 years and; **(D)** 4,975 years. The color scale is common for both return periods. The traces of the EBSZ faults considered are depicted in red in all panels; **(E)** Cross sections representing PGA (g) values of the FM model using the CB14 (solid line) and Akk14 (dashed line) GMPEs as a function of distance to the surface fault trace and for the same return periods as the maps. The locations of the cross sections are indicated in **Figure 12D**.

PGA increments as a function of distance to the fault trace (Figure 12E). Therefore, CB14 produces higher PGA values than Akk14 for most of the mapped area and especially around faults, accentuating near-fault effects on the hazard levels. Maximum variations are located close to the traces of faults with higher slip rates, importantly around CF or AMF-1, where these are up to 0.1 and 0.2 g, respectively for the 4,975 years RP and <0.1 g for the 475 years RP (A-A' and B-B', respectively; Figure 12E). The mean hazard curves from Lorca, Almería, Murcia and Vera also depict PGA increments for the CB14 equation in RPs over ~100 years (Figure 10D). In other lower slip rate faults such as BSF, the use of different GMPEs implies practically negligible PGA variations for all RPs (C-C' cross section along BSF-3; Figure 12E). In this case, for the 475 years RP, the use of Akk14 provides slightly higher PGA values (~0.05 g) due to the less sensitivity of the equation to the fault slip rates, up to one order of magnitude lower than AMF-1 or CF (Table 1).

In non-vertical dipping faults, hanging wall effects are more accentuated with the CB14 equation (Figures 12C–E). In the zones further away from the fault trace on the hanging wall, hazard decreases more abruptly with CB14 with respect to Akk14, especially in long RPs. The higher PGA gradient around the fault trace causes a rapid drop on the hazard values with respect to the lower gradient of Akk14 as distance to the fault increases. AMF, CAF and BSF are clear examples of this effect and, in particular, BSF is the one affected by highest reductions on the hanging wall for all RPs, because the surface projection of its fault plane is larger (Figures 12C,D). The curve of Torrevieja represents this effect related to the BSF (Figure 10D).

Overview: Limitations and Perspectives

The high hazard values in the near-fault zones, the high contribution of faults on the sites hazard and the agreement of the 475 years RP PGA values with the 2011 Lorca earthquake represent more coherent results with the observed values than classical area source methods. Examples of these classical methods are the current Spanish Building Code (NCSE, 2002) and the updated national seismic hazard map (IGN-UPM, 2013). The inclusion of multi-fault ruptures into fault-based PSHA is a novelty for Spain and yet unusual in other low-to-moderate seismicity regions worldwide. Generally, the lack of fault data prevents such kind of analysis in these regions, but as seen, it can imply very important hazard (PGA) changes respect to classical approaches. Moreover, considering multi-fault ruptures is a step forward towards a more realistic seismic hazard assessment, as the occurrence of multi-fault ruptures in nature is becoming an increasingly identified phenomena (e.g., Langridge et al., 2018; Quigley et al., 2019). We therefore aim that our study could serve as a case example for other studies focused in low-to-moderate seismicity regions, such as the EBSZ.

Nevertheless, it is necessary to assess the uncertainties of our study that affect the results presented and need to be considered when interpreting them. One remarkable topic is the background ratio selection of our study. The ratios modeled are an assumption that is established following expert opinion, based on available geological and seismological data from earthquakes

in the region. This means that the ratios are not necessarily defining of the study area, but an approximation. The option selected here considers that a big part of the earthquakes in the Mw 4.0–5.5 range are related to the faults modeled because it is consistent with observations (section 3.1.1.2). However, we acknowledge the existent implicit epistemic uncertainties within this assumption, as exemplified by the main shocks of the 2019 Ridgecrest sequence (Mw 6.4 and 7.1), which developed in non-previously mapped faults (Ross et al., 2019). In this sense, other background ratios could and should be explored in a logic tree in further research to account for the epistemic uncertainty of earthquakes happening outside of the known faults. In the line of Chartier et al., 2019, we also recognize the difficulty of setting this parameter and encourage the discussion among researchers on what parameters could help its determination. This is a key issue in SE Spain considering the aforementioned large uncertainties affecting the seismicity epicenter locations of most Mw ≥ 4.0 earthquakes.

Another limitation of our results is the fact that the present hazard calculations may be underestimating the contribution of other fault sources in SE Spain outside of the EBSZ fault system. There are many Quaternary-active faults within the mapping area selected in our study that have not been considered in the source modeling mainly because of a lack of quality data, contrary to the faults within the EBSZ. Fault systems such as El Alquián and Andarax Valley, Polopos or San Miguel de Salinas (Figure 2A) are some examples of active faults in the area with evidence of related seismicity (QAFI database; IGME, 2015a). These faults could also contribute to the seismic hazard, especially outside the EBSZ buffer area, although none of them have the dimensions (length) of the ones in the EBSZ considered in our study and thus their contribution should not be expected to be that relevant.

Further research is then encouraged to focus on incorporating such uncertainties in the light of a more complete and accurate PSHA analysis. As such, in the zones where there is a lack of paleoseismological studies, obtaining well-constrained and updated fault parameters, especially slip rate values, is critical because they can compromise the reliability or bias of the hazard results. This is not only important for the EBSZ faults but also for the ones outside of it and not included in this study. Updated paleoseismic and geodetic data on faults and the inclusion of more faults as sources would necessarily lead to a reassessment of the source modeling and the hazard in the region. In the meanwhile and given the need of updated and more realistic hazard assessments, it would be useful to consider the near-fault hazard estimations in our models as they could help to set near-fault amplification coefficients to be applied at sites located on top of active faults or in close vicinity. Further research should also focus on exploring the use of other parameters rather than PGA to quantify the seismic hazard such as the spectral acceleration or peak ground velocity and displacement. These parameters are more indicative of the damage generated by an earthquake than PGA as they highlight possible amplification effects in buildings and structures at a given site that ultimately are of interest for seismic engineering purposes. In this sense, and additionally to the use of GMPEs, exploring approaches of spatially correlated ground motion intensity measures (e.g., Park et al., 2007) could be

interesting for further research in order to better characterize expected ground motion, damage and loss estimates for seismic hazard and risk assessment.

CONCLUSIONS

This paper presents a fault system-based PSHA of SE Spain in which earthquake occurrence in the EBSZ is modeled at the scale of the whole fault system and using geological fault data. We devised two alternative models for characterizing the seismicity in the EBSZ, one assuming that all seismic activity is due to known faults of the EBSZ (FM) and another in which part of the seismicity (Mw 4.0–5.5) also occurs as background, related to unknown active faults (FM_bg).

The main conclusion is that, for both models analyzed, faults dominate the seismic hazard in the areas located around faults up to 20–30 km from them, even for short return periods of 475 years. This is remarkable for SE Spain as most of the important cities or towns in this area are commonly found on top or very close to Quaternary active faults (e.g., Lorca, Murcia, Totana, Alhama de Murcia, etc.). Fault effects increase PGA values compared to previous PSHAs based on classical area source methods, but their influence zone is strongly dependent on their slip rates. Around the faults with the higher slip rates of the system, such as the Carboneras Fault or the southwestern end of the Alhama de Murcia Fault (>1 mm/yr), the PGA values are increased up to 150% respect to area source methods for all return periods and the fault influence extends up to 10–20 km from the fault traces. On the other hand, lower slip rate faults such as Bajo Segura Fault (~0.2 mm/yr) produce minor PGA increments, only significant for long return periods, and their influence zones extend up to 5 km from the trace. Around non-vertical dipping faults (e.g., Alhama de Murcia and Bajo Segura faults), the higher hazard values are found in the hanging wall, implying hanging wall effects. Lastly, the faults with the lowest estimated slip rates of the system such as Palomares Fault (<0.1 mm/yr) have no significant impact in the hazard whatsoever. The very similar results from both models evidence that modeling a small portion of the Mw 4.0–5.5 seismicity rate as background (FM_bg) has a minor impact on the seismic hazard of the EBSZ, because fault activity generally overcomes the rates of the background.

The fault-based approach presented seems to provide more accurate hazard estimations than classical area source approaches in sites located close to the faults, at least for the return period of 475 years typically dominated by moderate-magnitude earthquakes. Our hazard results in Lorca for this return period appear to be more consistent with the instrumental PGA values recorded during the 2011 Mw 5.2 earthquake than the ones predicted in the Spanish Building Code or in the updated national seismic hazard map. Also, the consideration of multi-fault ruptures in the source modeling causes significant differences with previous fault-based PSHA in SE Spain and it is a step forward to account for the complexity observed in nature. This kind of approach is a novelty in Spain and might serve as a case example for other low-to-moderate seismicity regions worldwide.

Fault slip rate and its uncertainties have an important influence on the seismic hazard, especially in higher slip rate faults that have more impact in the studied return periods. However, the lack of detailed paleoseismic studies in some lower slip rate faults of the EBSZ (Palomares Fault, Bajo Segura Fault and northeastern termination of Alhama de Murcia Fault) compromises the reliability of the hazard in their surroundings. We identify thus that further research should focus primarily on the obtention of new data to characterize these faults. In the meanwhile, we suggest the use of a near-fault amplification coefficients to be applied to the basic design acceleration provided in the current seismic code for the buildings near Quaternary active faults in this region.

DATA AVAILABILITY STATEMENT

The original contributions presented in the study are included in the article/Supplementary Material, further inquiries can be directed to the corresponding author.

AUTHOR CONTRIBUTIONS

OGN and JGM conceived the original idea of the paper, prepared the input data and performed the hazard calculations. OGN, JGM and TC contributed to the interpretation of the results. All authors contributed to the discussions and preparation of the manuscript.

FUNDING

This work was funded by the PREVENT project (CGL2015-66263-R) and FPI predoctoral grant of Octavi Gómez-Novell (BES-2016-077048) from the Spanish Ministry of Science, Innovation and Universities. Open access fees were partially funded by the Vice-rectorate for Ph.D. and Research Promotion of the University of Barcelona.

ACKNOWLEDGMENTS

The authors want to thank Alicia Rivas-Medina for providing files for the comparison performed in the present paper and the ESC Fault2SHA working group for the discussions on the main topics of fault data as inputs for PSHA. We also want to thank Chong Xu, Sergio Molina-Palacios and an anonymous reviewer for their comments and suggestions that contributed to improve this paper.

SUPPLEMENTARY MATERIAL

The Supplementary Material for this article can be found online at: <https://www.frontiersin.org/articles/10.3389/feart.2020.579398/full#supplementary-material>.

REFERENCES

- Akkar, S., Sandikkaya, M. A., and Bommer, J. J. (2014). Empirical ground-motion models for point- and extended-source crustal earthquake scenarios in Europe and the Middle East. *Bull. Earthq. Eng.* 12, 359–387. doi:10.1007/s10518-013-9461-4
- Alfaro, P., Bartolomé, R., Borque, M. J., Estévez, A., García-Mayordomo, J., García-Tortosa, F. J., et al. (2012). The Bajo Segura fault zone: active blind thrusting in the eastern betic cordillera (SE Spain). *J. Iber. Geol.* 38, 287–300. doi:10.5209/rev_JIGE.2012.v38.n1.39217
- Benito, B., Capote, R., Murphy, P., Gaspar-Escribano, J. M., Martínez-Díaz, J. J., Tsige, M., et al. (2007). An overview of the damaging and low magnitude Mw 4.8 La Paca earthquake on 29 January 2005: context, seismotectonics, and seismic risk implications for southeast Spain. *Bull. Seismol. Soc. Am.* 97, 671–690. doi:10.1785/0120050150
- Borque, M. J., Sánchez-Alzola, A., Martín-Rojas, I., Alfaro, P., Molina, S., Rosa-Cintas, S., et al. (2019). How much nubia- Eurasia convergence is accommodated by the NE end of the eastern betic shear zone (SE Spain)? constraints from GPS velocities. *Tectonics* 38, 1824–1839. doi:10.1029/2018TC004970
- Bousquet, J.-C. (1979). Quaternary strike-slip faults in southeastern Spain. *Dev. Geotectonics*. 13, 277–286. doi:10.1016/B978-0-444-41783-1.50044-1
- Bungum, H. (2007). Numerical modelling of fault activities. *Comput. Geosci.* 33, 808–820. doi:10.1016/j.cageo.2006.10.011
- Cabañas, L., Carreño-Herrero, E., Izquierdo-Álvarez, A., Martínez-Solares, J. M., Capote, R., Martínez-Díaz, J. J., et al. (2011). *Informe del sismo de Lorca del 11 de Mayo de 2011*, Madrid, Spain, Available at: <http://hdl.handle.net/10261/62381> (Accessed February 20, 2011).
- Campbell, K. W., and Bozorgnia, Y. (2014). NGA-West2 ground motion model for the average horizontal components of PGA, PGV, and 5% damped linear acceleration response spectra. *Earthq. Spectra*. 30, 1087–1114. doi:10.1193/062913EQS175M
- Chartier, T., Scotti, O., and Lyon-Caen, H. (2019). SHERIFS: open-source code for computing earthquake rates in fault systems and constructing hazard models. *Seismol. Res. Lett.* 90, 1678–1688. doi:10.1785/0220180332
- Choi, J.-H., Jin, K., Enkhbayar, D., Davvasambuu, B., Bayasgalan, A., and Kim, Y.-S. (2012). Rupture propagation inferred from damage patterns, slip distribution, and segmentation of the 1957 MW8.1 Gobi-Altay earthquake rupture along the Bogd fault, Mongolia. *J. Geophys. Res.* 117, a–n. doi:10.1029/2011JB008676
- Cornell, C. A. (1968). Engineering seismic risk analysis. *Bull. Seismol. Soc. Am.* 58, 1583–1606.
- De Larouzière, F. D., Bolze, J., Bordet, P., Hernandez, J., Montecat, C., and Ott d'Estevou, P. (1988). The Betic segment of the lithospheric Trans-Alboran shear zone during the Late Miocene. *Tectonophysics* 152, 41–52. doi:10.1016/0040-1951(88)90028-5
- DeMets, C., Iaffaldano, G., and Merkuriev, S. (2015). High-resolution neogene and quaternary estimates of nubia- Eurasia-north America plate motion. *Geophys. J. Int.* 203, 416–427. doi:10.1093/gji/ggv277
- Echeverría, A., Khazaradze, G., Asensio, E., Gárate, J., Dávila, J. M., and Suriñach, E. (2013). Crustal deformation in eastern Betics from CuaTeNeo GPS network. *Tectonophysics* 608, 600–612. doi:10.1016/j.tecto.2013.08.020
- Echeverría, A., Khazaradze, G., Asensio, E., and Masana, E. (2015). Geodetic evidence for continuing tectonic activity of the carboneras fault (SE Spain). *Tectonophysics* 663, 302–309. doi:10.1016/j.tecto.2015.08.009
- Ferrater, M., Ortuño, M., Masana, E., Martínez-Díaz, J. J., Pallàs, R., Perea, H., et al. (2017). Lateral slip rate of Alhama de Murcia fault (SE Iberian Peninsula) based on a morphotectonic analysis: comparison with paleoseismological data. *Quat. Int.* 451, 87–100. doi:10.1016/j.quaint.2017.02.018
- Field, E. H., Biasi, G. P., Bird, P., Dawson, T. E., Felzer, K. R., Jackson, D. D., et al. (2014). Uniform California earthquake rupture forecast, version 3 (UCERF3): the time-independent model. *Bull. Seismol. Soc. Am.* 3, 1122–1180. doi:10.13133/0fr20131165
- Fletcher, J. M., Teran, O. J., Rockwell, T. K., Oskin, M. E., Hudnut, K. W., Mueller, K. J., et al. (2014). Assembly of a large earthquake from a complex fault system: surface rupture kinematics of the 4 April 2010 El Mayor-Cucapah (Mexico) Mw 7.2 earthquake. *Geosphere* 10, 797–827. doi:10.1130/GES00933.1
- Frankel, A. (1995). Mapping seismic hazard in the central and eastern United States. *Seismol. Res. Lett.* 66, 8–21. doi:10.1785/gssrl.66.4.8
- Ferrater, M. (2016). *Velocitat de desplaçament de la falla d'Alhama de Murcia (Bètiques Orientals); implicacions en el seu potencial sísmic*. Dissertation thesis. Barcelona (Spain): Universitat de Barcelona.
- García-Mayordomo, J. (2005). *Caracterización y análisis de la peligrosidad sísmica en el sureste de España*. Dissertation thesis. Madrid (Spain): Universidad Complutense de Madrid.
- García-Mayordomo, J. (2015). *Creación de un modelo de zonas sísmogénicas para el cálculo del mapa de peligrosidad sísmica de España*. Dissertation thesis. Madrid (Spain): Instituto Geológico y Minero de España.
- García-Mayordomo, J., Gaspar-Escribano, J. M., and Benito, B. (2007). Seismic hazard assessment of the Province of Murcia (SE Spain): analysis of source contribution to hazard. *J. Seismol.* 11, 453–471. doi:10.1007/s10950-007-9064-0
- García-Mayordomo, J., Martín-Banda, R., Insua-Arévalo, J. M., Álvarez-Gómez, J. A., Martínez-Díaz, J. J., and Cabral, J. (2017). Active fault databases: building a bridge between earthquake geologists and seismic hazard practitioners, the case of the QAFI v.3 database. *Nat. Hazards Earth Syst. Sci.* 17, 1447–1459. doi:10.5194/nhess-17-1447-2017
- Gaspar-Escribano, J. M., Benito, B., and García-Mayordomo, J. (2008). Hazard-consistent response spectra in the Region of Murcia (Southeast Spain): comparison to earthquake-resistant provisions. *Bull. Earthq. Eng.* 6, 179–196. doi:10.1007/s10518-007-9051-4
- Gil, G., Vidal, F., Navarro, M., García-Jerez, A., and Pérez-Muelas, J. (2014). Characterization of earthquake shaking severity in the town of Lorca during the May 11, 2011 event. *Bull. Earthq. Eng.* 12, 1889–1908. doi:10.1007/s10518-013-9475-y
- Global Earthquake Model (GEM) (2019). The OpenQuake-engine user manual. Global earthquake model (GEM) open-quake manual for engine version 3.7.1. doi:10.13117/GEM/OPENQUAKE.MANENGINE.3.7.1
- Gómez-Novell, O., Chartier, T., García-Mayordomo, J., Ortuño, M., Masana, E., Insua-Arévalo, J. M., et al. (2020). Modelling earthquake rupture rates in fault systems for seismic hazard assessment: the eastern betics shear zone. *Eng. Geol.* 265 105452. doi:10.1016/j.enggeo.2019.105452
- Gràcia, E., Grevemeyer, I., Bartolomé, R., Perea, H., Martínez-Loriente, S., Gómez de la Peña, L., et al. (2019). Earthquake crisis unveils the growth of an incipient continental fault system. *Nat. Commun.* 10, 1–12. doi:10.1038/s41467-019-11064-5
- Hamling, I. J., Hreinsdóttir, S., Clark, K., Elliott, J., Liang, C., Fielding, E., et al. (2017). Complex multifault rupture during the 2016 Mw7.8 Kaikōura earthquake, New Zealand. *Science* 356, eaam7194. doi:10.1126/science.aam7194
- Herrero-Barbero, P. (2016). *Análisis estructural del segmento Alhama–alcantarilla de la Falla de Alhama de Murcia y sus implicaciones en el Riesgo Sísmico*. Master's thesis Madrid (Spain): Universidad Complutense de Madrid.
- Herrero-Barbero, P., Álvarez-Gómez, J. A., Martínez-Díaz, J. J., and Klimowitz, J. (2020). Neogene basin inversion and recent slip rate distribution of the northern termination of the Alhama de Murcia fault (eastern betic shear zone, SE Spain). *Tectonics* 39, 1–25. doi:10.1029/2019TC005750
- Instituto Geográfico Nacional–Universidad Politécnica de Madrid Working Group (IGN-UPM) (2013). *Actualización de mapas de peligrosidad sísmica de España 2012*. Madrid, Spain: Centro Nacional de Información Geográfica, Instituto Geográfico Nacional.
- Instituto Geológico y Minero de España (IGME) (2015a). QAFI v.3: quaternary active faults database of Iberia. Available at: <http://info.igme.es/qafi> (Accessed March 9, 2020).
- Instituto Geológico y Minero de España (IGME) (2015b). ZESIS: base de Datos de Zonas Sísmogénicas de la Península Ibérica y territorios de influencia para el cálculo de la peligrosidad sísmica en España. Available at: <http://info.igme.es/zesis> (Accessed March 9, 2020).
- Instituto Geográfico Nacional (2011). Serie terremoto NE Lorca (Murcia). Available at: <http://www.ign.es> (Accessed May 11, 2020).
- Insua-Arévalo, J. M., García-Mayordomo, J., Salazar, A. E., Rodríguez-Escudero, E., Martín-Banda, R., Álvarez-Gómez, J. A., et al. (2015). Paleoseismological evidence of holocene activity on Los Tollos Fault (Murcia, SE Spain): a lately formed quaternary tectonic feature of the eastern betic shear zone. *J. Iber. Geol.* 41, 333–350. doi:10.5209/rev_JIGE.2015.v41.n3.49948
- Langridge, R. M., Rowland, J., Villamor, P., Mountjoy, J., Townsend, D. B., Nissen, E., et al. (2018). Coseismic rupture and preliminary slip estimates for the papatea fault and its role in the 2016 Mw 7.8 kaikōura, New Zealand, earthquake. *Bull. Seismol. Soc. Am.* 108, 1596–1622. doi:10.1785/0120170336

- Little, T. A., van Dissen, R., Kearse, J., Norton, K., Benson, A., and Wang, N. (2018). Kekerengu fault, New Zealand: timing and size of late holocene surface ruptures. *Bull. Seismol. Soc. Am.* 108, 1556–1572. doi:10.1785/0120170152
- Martín-Banda, R., García-Mayordomo, J., Insua-Arévalo, J. M., Salazar, Á. E., Rodríguez-Escudero, E., Álvarez-Gómez, J. A., et al. (2016). New insights on the seismogenic potential of the eastern betic shear zone (SE Iberia): quaternary activity and paleoseismicity of the SW segment of the Carrascoy Fault zone. *Tectonics* 35, 55–75. doi:10.1002/2015TC003997
- Martínez-Díaz, J. J., Bejar-Pizarro, M., Álvarez-Gómez, J. A., Mancilla, F. d. L., Stich, D., Herrera, G., et al. (2012a). Tectonic and seismic implications of an intersegment rupture. *Tectonophysics* 546–547, 28–Q17 37. doi:10.1016/j.tecto.2012.04.010
- Martínez-Díaz, J. J., Masana, E., and Ortuño, M. (2012b). Active tectonics of the Alhama de Murcia fault, betic cordillera, Spain. *J. Iber. Geol.* 38, 253–270. doi:10.5209/rev_JIGE.2012.v38.n1.39218
- Masana, E., Moreno, X., Gràcia, E., Pallàs, R., Ortuño, M., López, R., et al. (2018). First evidence of paleoearthquakes along the Carboneras fault zone (SE Iberian Peninsula): Los trances site. *Geol. Acta.* 16, 461–476. doi:10.1344/GeologicaActa2018.16.4.8
- McGuire, R. K. (1976). USGS Open-File Report 76-67. *FORTRAN computer program for seismic risk analysis*. Available at: <https://pubs.usgs.gov/of/1976/0067/report.pdf>. (Accessed January 26, 1976).
- Medialdea, J. J., Alonso-Henar, J., Insua-Arévalo, J. M., Canora, C., García-Mayordomo, J., Rodríguez-Escudero, E., et al. (2018). Geological evidences of surface rupture related to a seventeenth century destructive earthquake in Betic Cordillera (SE Spain): constraining the seismic hazard of the Alhama de Murcia fault. *J. Iber. Geol.* 45, 73. doi:10.1007/s41513-018-0082-2
- Moreno, X. (2011). *Neotectonic and paleoseismic onshore-offshore integrated study of the Carboneras fault (eastern Betics, SE Iberia)*. Dissertation thesis. Barcelona (Spain): Universitat de Barcelona.
- Norma de la Construcción Sismorresistente Española (NCSE-02) (2002). Real Decreto 997/2002, de 27 de septiembre, por el que se aprueba la norma de construcción sismorresistente: parte general y edificación (NCSR-02). *Boletín Oficial del Estado*. 244, 35898–35967.
- Ortuño, M., Masana, E., García-Meléndez, E., Martínez-Díaz, J., Stepánikova, P., Cunha, P. P., et al. (2012). An exceptionally long paleoseismic record of a slow-moving fault: the Alhama de Murcia fault (Eastern Betic shear zone, Spain). *Geol. Soc. Am. Bull.* 124, 1474–1494. doi:10.1130/B30558.1
- Pagani, M., Monelli, D., Weatherill, G. A., and Garcia, J. (2014). Global earthquake model (GEM) technical report 2014-08. *The OpenQuake-engine book: hazard*. 67. doi:10.13117/-GEM.OPENQUAKE.TR2014.08
- Park, J., Bazzurro, P., and Baker, J. (2007). “Modeling spatial correlation of ground motion Intensity Measures for regional seismic hazard and portfolio loss estimation,” in *Applications of Statistics and Probability in civil engineering*. editors T. Kanda and Furuta (London, UK: Taylor and Francis Group), 579.
- Power, M., Chiou, B., Abrahamson, N., Bozorgnia, Y., Shantz, T., and Roblee, C. (2008). An overview of the NGA project. *Earthq. Spectra*. 24, 3–21. doi:10.1193/1.2894833
- Quigley, M. C., Jiménez, A., Duffy, B., and King, T. R. (2019). Physical and statistical behavior of multifault earthquakes: darfield earthquake case study, New Zealand. *J. Geophys. Res. Solid Earth*. 124, 4788–4810. doi:10.1029/2019JB017508
- Reicherter, K., and Hübscher, C. (2007). Evidence for a seafloor rupture of the Carboneras fault zone (southern Spain): relation to the 1522 Almería earthquake? *J. Seismol.* 11, 15–26. doi:10.1007/s10950-006-9024-0
- Rivas-Medina, A., Benito, B., and Gaspar-Escribano, J. M. (2018). Approach for combining fault and area sources in seismic hazard assessment: application in south-eastern Spain. *Nat. Hazards Earth Syst. Sci.* 18, 2809–2823. doi:10.5194/nhess-18-2809-2018
- Rivas-Medina, A. (2014). *Contribución metodológica para incorporar fallas activas en la modelización de la fuente dirigida a estimaciones de peligrosidad sísmica Aplicación al sur de España*. PhD thesis. Madrid (Spain): Universidad Politécnica de Madrid.
- Rodríguez-Escudero, E., Martínez-Díaz, J. J., Álvarez-Gómez, J. A., Insua-Arévalo, J. M., and Capote del Villar, R. (2014). Tectonic setting of the recent damaging seismic series in the Southeastern Betic Cordillera, Spain. *Bull. Earthq. Eng.* 12, 1831–1854. doi:10.1007/s10518-013-9551-3
- Rodríguez-Fernández, J., Miguel Azañón, J., and Azor, A. (2012). “The betic intramontane basins (SE Spain): stratigraphy, subsidence, and tectonic history,” in *Tectonics of sedimentary basins: recent advances*. editors C. Busby and A. Azor (Hoboken: Blackwell Publishing Ltd.), 461–479.
- Ross, Z. E., Idini, B., Jia, Z., Stephenson, O. L., Zhong, M., Wang, X., et al. (2019). Hierarchical interlocked orthogonal faulting in the 2019 Ridgecrest earthquake sequence. *Science* 366, 346–351. doi:10.1126/science.aaz0109
- Schwartz, D. P. and Coppersmith, K. J. (1984). Fault behavior and characteristic earthquakes: examples from the Wasatch and San Andreas fault zones. *J. Geophys. Res.* 89, 5681–5698. doi:10.1029/JB089iB07p05681
- Silva, P. G., Goy, J. L., Somoza, L., Zazo, C., and Bardají, T. (1993). Landscape response to strike-slip faulting linked to collisional settings: Quaternary tectonics and basin formation in the Eastern Betics, southeastern Spain. *Tectonophysics* 224, 289–303. doi:10.1016/0040-1951(93)90034-H
- Silva, P. G., Rodríguez-Pascua, M. A., Giner-Robles, J. L., Perez-Lopez, R., Gomez Lario, J., Perucha Atienza, M., et al. (2014). *Catálogo de los efectos geológicos de los terremotos en España*. Available at: <http://igmpublicaciones.blogspot.com.es/> (Accessed April 6, 2015).
- Stich, D., Martín, J. B., and Morales, J. (2007). Deformación sísmica y asísmica en la zona Béticas-Rif-Alborán. *Rev. Soc. Geol. Espana.* 20, 311–320.
- Stich, D., Martín, R., and Morales, J. (2010). Moment tensor inversion for Iberia-Maghreb earthquakes 2005–2008. *Tectonophysics* 483, 390–398. doi:10.1016/j.tecto.2009.11.006
- Stich, G. P., and Weldon, R. J. (2006). Estimating surface rupture length and magnitude of paleoearthquakes from point measurements of rupture displacement. *Bull. Seismol. Soc. Am.* 96, 1612–1623. doi:10.1785/0120040172
- Stirling, M., McVerry, G., Gerstenberger, M., Litchfield, N., Van Dissen, R., Berryman, K., et al. (2012). National seismic hazard model for New Zealand: 2010 update. *Bull. Seismol. Soc. Am.* 102, 1514–1542. doi:10.1785/0120110170
- Vilanova, S. P., and Fonseca, J. F. B. D. (2007). Probabilistic seismic-hazard assessment for Portugal. *Bull. Seismol. Soc. Am.* 97, 1702–1717. doi:10.1785/0120050198
- Villani, F., Pucci, S., Civico, R., De Martini, P. M., Cinti, F. R., and Pantosti, D. (2018). Surface faulting of the 30 October 2016 Mw 6.5 Central Italy earthquake: detailed analysis of a complex coseismic rupture. *Tectonics* 37, 3378–3410. doi:10.1029/2018TC005175
- Villaseñor, B., and Richter, C. F. (1945). Frequency of earthquakes in California. *Nature* 156, 371. doi:10.1038/156371a0
- Wells, D. L., and Coppersmith, K. J. (1994). New empirical relationships among magnitude, rupture length, rupture width, rupture area, and surface displacement. *Bull. Seismol. Soc. Am.* 84, 974–1002.
- Wesnousky, S. G. (1986). Earthquakes, quaternary faults, and seismic hazard in California. *J. Geophys. Res.* 91 (12), 12587–12631. doi:10.1029/JB091i12p12587
- Woessner, J., Laurentiu, D., Laurentiu, D., Giardini, D., Crowley, H., Cotton, F., et al. (2015). The 2013 European Seismic Hazard Model: key components and results. *Bull. Earthq. Eng.* 13, 3553–3596. doi:10.1007/s10518-015-9795-1
- Working Group on California Earthquake Probability (WGCEP) (2003). USGS Open-File Report 03-214. *Earthquake probabilities in the san francisco bay Region: 2002-2031*.
- Youngs, R. R., and Coppersmith, K. J. (1985). Implications of fault slip rates and earthquake recurrence models to probabilistic seismic hazard estimates. *Int. J. Rock Mech. Min. Sci. Geomech. Abstr.* 23, 125. doi:10.1016/0148-9062(86)90651-0
- Yu, Y.-X., and Gao, M.-T. (2001). Effects of the hanging wall and footwall on peak acceleration during the Jiji (Chi-Chi), Taiwan Province, earthquake. *Acta Seimol. Sin.* 14, 654–659. doi:10.1007/BF02718076
- Zhang, H., Chen, J., and Ge, Z. (2012). Multi-fault rupture and successive triggering during the 2012 Mw 8.6 Sumatra offshore earthquake. *Geophys. Res. Lett.* 39, a–n. doi:10.1029/2012GL053805

Conflict of Interest: The authors declare that the research was conducted in the absence of any commercial or financial relationships that could be construed as a potential conflict of interest.

Copyright © 2020 Gómez-Novell, García-Mayordomo, Ortuño, Masana and Chartier. This is an open-access article distributed under the terms of the Creative Commons Attribution License (CC BY). The use, distribution or reproduction in other forums is permitted, provided the original author(s) and the copyright owner(s) are credited and that the original publication in this journal is cited, in accordance with accepted academic practice. No use, distribution or reproduction is permitted which does not comply with these terms.

ANNEX II

Supporting data of the thesis contents

- A) Uninterpreted digital elevation models (DEM)
- B) OSL dating laboratory reports
- C) Uninterpreted field images
- D) High quality trench photologs and interpreted logs
- E) OxCal scripts
- F) Slip rate PDFs

The data and details from this annex are available at the *Figshare* digital repository in the following link:

<https://figshare.com/s/5afe98d9a785904c8903>